A Porous Media Model for Sprinkler Wetting

By

Joel Edwards Sipe

A Dissertation

Submitted to the Faculty

of

Worcester Polytechnic Institute

In partial fulfillment of the requirements for the

Degree of Doctor of Philosophy

in

Fire Protection Engineering

May 2010

APPROVED

_____

Professor Nicholas A. Dembsey, Major Advisor

_____

Dr. Hong-Zeng Yu, FM Global

_____

Professor Ali Rangwala, Co-Advisor

_____

Professor John Sullivan, Co-Advisor

_____

Professor Kathy A. Notarianni, Head of Department

Abstract

A one-dimensional porous media model has been developed to investigate water based fire suppression. The model is for heat and mass transfer in porous materials subjected to external water sprays and radiant heating. In the model, heat transfer inside the material occurs by conduction, convection, and phase change. Mass transfer occurs by gas phase diffusion and convection in the liquid and gas phases. Convective mass fluxes in the gas phase are driven by gas phase pressure gradients according to Darcy's law. Similarly, liquid phase convective mass fluxes are driven by liquid pressure gradients. Surface tension forces are included in the liquid pressure by means of an empirical correlation called the J-Function. The model was validated using experimental data for wetting and heating. Data from the literature for convective heating of particulate media, brick, and wood, compared well with model predictions. Wetting and heating experiments were conducted in the WPI Fire Science Lab with ceramic fiberboard samples. The samples were wetted in two ways: placing the sample in contact with a reservoir of water, and spray wetting using a water mist nozzle. The heating tests were conducted in the cone calorimeter with pre-wetted samples. The data from these tests also compares well with model predictions.

Acknowledgements

I believe that great accomplishments by individuals are most accurately viewed as the result of tremendous help from others, sometimes in unseen ways, rather than a personal triumph alone. With that in mind, there are so many individuals that helped to make this project possible and deserve my sincere thanks. Without an overwhelming amount of help along the way, my own personal efforts would have been fruitless.

First and foremost I would like to thank my advisor Prof. Nicholas Dembsey. He is an outstanding instructor of the highest caliber that is only encountered once in a lifetime. No matter what problems arose over the course of this project, he always had the right advice. I entered every meeting stressed out and holding a list of problems with my research, and left several hours later, relaxed, and with a clear plan to solve each problem. Prof. Dembsey's endless guidance, patience, and wisdom kept me going in the right direction. Without his help, this dissertation would not have been possible.

I must also thank the other members of my committee for their help and input. Prof. Ali Rangwala helped teach me so much fundamental material in his classes, and through working as his TA. Prof. John Sullivan provided expert advice and guidance on the numerical solution algorithm used for the model, and many other issues. Dr. Bert Yu provided much helpful advice in meetings at FM Global, and his support helped secure continued funding for the project. Without the financial support of FM Global, this project never would have gotten off the ground. Prof. Kathy Notarianni provided helpful oversight of the project and encouragement.

Hearty thanks are also due to Dr. John Woycheese, who served as my advisor before he left his career in academia to work in the fabled "real world" of fire protection engineering consulting. Dr. Woycheese was instrumental in helping me get into the Ph.D. program at WPI, and helped get my project started before his departure. He sparked my interest in so many areas of math and science, and we had many enjoyable discussions on so many issues. His ever-cheerful demeanor is still missed at WPI by everyone that knew him.

I would also like to thank Randy Harris, the lab manager of the WPI Fire Science Laboratory. His help was invaluable to the successful completion of my experiments, and he made working in the lab a real pleasure.

While working out problems related to my research, I had countless discussion sessions and helpful comments from my fellow graduate students in HL 034. My sincere thanks go out to Esther Kim, Scott Rockwell, Hae Jun Park, Kulbushian Joshi,

and Alberto Alvarez. All of them made working in the grad student office a much more pleasurable experience.

A very special thanks is due to Jim and Katie Pietrovito, and Dr. Jeanine Skorinko for assisting with my living arrangement when my apartment lease expired close to the completion of this project. I can't thank you all enough. Jeanine, you helped keep me sane, well fed, and motivated, and for this I am eternally grateful. I can't thank you enough.

My friends provided a healthy balance of denigration over my seemingly permanent status as a grad student, and generous financial assistance in acquiring libations. They helped me find fun things to do while not studying, which helped me to retain some amount of sanity.

Last, but not at all least, I must thank my mom and dad for always being very supportive of my decision to pursue a doctorate degree. My parents are the type of people that would have given me their last dollar if I needed it, without thinking twice. They have always been quick to lend moral support and encouragement when I needed it. I couldn't ask for better parents, and I am so grateful for that.

I would also like to thank generous financial support from FM Global, the SFPE Educational and Scientific Foundation, and the Department of Fire Protection Engineering at WPI.

Table of Contents

List of Tables

List of Figures

Nomenclature

Roman Letters

a_λ = monochromatic absorption coefficient $\left[m^{-1}\right]$

A = area $\left[m^2\right]$

B_i = body force in the i-direction $\left[\frac{N}{m^3}\right]$

c_A = fluid A mass content $\left[\frac{kg}{m^3}\right]$

C = molar concentration $\left[\frac{kmol}{m^3}\right]$

C_E = Ergun coefficient $[-]$

C_p = specific heat $\left[\frac{kJ}{kgK}\right]$

D_A^T = thermal diffusion coefficient $\left[\frac{kg}{ms}\right]$

D_{eff} = effective diffusivity $\left[\frac{m^2}{s}\right]$

D_{ij} = binary diffusion coefficient $\left[\frac{m^2}{s}\right]$

D_o = reference diffusivity $\left[\frac{m^2}{s}\right]$

D_{va} = diffusivity of vapor in air $\left[\frac{m^2}{s}\right]$

D_w = moisture diffusion coefficient $\left[\frac{m^2}{s}\right]$

e = specific internal energy $\left[\frac{J}{m^3}\right]$

e_t = total internal energy $\left[\frac{J}{m^3}\right]$

f = function representing model output

$f(\delta)$ = pore size distribution function $[-]$

f_k = force acting on the k molecules $[N]$

F = force $[N]$

g = gravity $\left[\frac{m}{s^2}\right]$

Gr_h = heat transfer Grashof number $[-]$

Gr_m = mass transfer Grashof number $[-]$

h = enthalpy $\left[\frac{J}{m^3}\right]$

h = heat transfer coefficient $\left[\frac{W}{m^2K}\right]$

h_m = mass transfer coefficient $\left[\frac{m}{s}\right]$

i = total infiltration $[m]$

$\dot{j}''$ = diffusive mass flux $\left[\frac{kg}{m^2s}\right]$

J = J-function $[-]$

k = thermal conductivity $\left[\frac{W}{mK}\right]$

k_o = shape parameter $[-]$

k_λ = monochromatic extinction coefficient $\left[m^{-1}\right]$

k_T = thermal diffusion ratio $[-]$

K = permeability $\left[m^2\right]$

K_r = relative permeability

Kn = Knudsen number $[-]$

$K_1 - K_{20}$ = coefficients

l = length $[m]$

L = length $[m]$

L_e = effective length $[m]$

L_t = excess length $[-]$

L^* = dummy placeholder $[-]$

m = mass $[kg]$

$\dot{m}''$ = mass flux $\left[\frac{kg}{m^2 s}\right]$

$\dot{m}'''_{evap}$ = evaporation rate $\left[\frac{kg}{m^3 s}\right]$

M = molecular weight $\left[\frac{kg}{kmol}\right]$,
moisture content $[-]$

n = normal vector

n_λ = index of refraction $[-]$

N = number of moles

Nu = Nusselt number $[-]$

Oh = Ohnesorge number $[-]$

p = partial pressure $[Pa]$

p_c = capillary pressure $[Pa]$

p_{vs} = vapor pressure above flat surface $[Pa]$

P = total pressure $[Pa]$

Pr = Prandtl number $[-]$

$\dot{q}''$ = heat flux $\left[\frac{W}{m^2}\right]$

$\dot{Q}$ = fluid flow rate $\left[\frac{m^3}{s}\right]$

$\dot{Q}'''$ = heat source $\left[\frac{W}{m^3}\right]$

r = radius $[m]$

R = universal gas constant $\left[\frac{J}{molK}\right]$

R = radius of tube $[m]$

R_i = gas constant for gas i $\left[\frac{J}{kgK}\right]$

R_λ = monochromatic reflectivity $[-]$

Ra_h = heat transfer Rayleigh number $[-]$

Ra_m = mass transfer Rayleigh number $[-]$

Re_d = Reynolds number based on diameter $[-]$

$\mathrm{Re}_{\sqrt{K}}$ = Reynolds number based on permeability $[-]$

S = saturation $[-]$

S_i = sensitivity coefficient $[-]$

Sc = Schmidt Number $[-]$

Sh = Sherwood Number $[-]$

t = time $[s]$

T = temperature $[K]$

$\tilde{T}$ = spatial temperature deviation $[K]$

u = uncertainty, internal energy $\left[\frac{J}{kg}\right]$

u_c = combined standard uncertainty

u_{int} = interfacial velocity $\left[\frac{m}{s}\right]$

u = x-direction velocity $\left[\frac{m}{s}\right]$

u_D = Darcean velocity $\left[\frac{m}{s}\right]$

u_i=i-direction velocity $\left[\frac{m}{s}\right]$

U_A = fluid A volume content $\left[\frac{m^3}{m^3}\right]$

v = y-direction velocity $\left[\frac{m}{s}\right]$

v_o = infiltration velocity $\left[\frac{m}{s}\right]$

V = volume $\left[m^3\right]$

V_i = diffusional velocity $\left[\frac{m}{s}\right]$

w = z-direction velocity $\left[\frac{m}{s}\right]$

We = Weber number $[-]$

x_i = i$^{\text{th}}$ direction, input parameter i

x=x-direction

X_i = mol fraction $[-]$

y=y-direction, model output

Y_i = i$^{\text{th}}$ species mass fraction $[-]$

z=z-direction, distance $[m]$

Greek Letters

α = thermal diffusivity $\left[m^2/s\right]$

β_h = coefficient of thermal expansion $\left[K^{-1}\right]$

β_m = composition expansion coefficient $\left[m^3/kg\right]$

δ = pore diameter $\left[m\right]$

δ_{ij} = kronecker delta function $\left[-\right]$

$\delta_{0.99}$ = boundary layer thickness $\left[m\right]$

ε = emissivity $\left[-\right]$

Δh_f^o = enthalpy of formation $\left[\frac{kJ}{kg}\right]$

Δh_{vap} = enthalpy of vaporization $\left[\frac{kJ}{kg}\right]$

Δh_w = heat of wetting $\left[\frac{kJ}{kg}\right]$

Δt = timestep $\left[s\right]$

$\Delta x, \Delta y, \Delta z$ = control volume dimensions $\left[m\right]$

θ = contact angle $\left[\text{deg, } rad\right]$

λ = wavelength $\left[m\right]$

μ = viscosity $\left[\frac{kg}{ms}\right]$

ν = kinematic viscosity $\left[\frac{m^2}{s}\right]$

ρ = density $\left[\frac{kg}{m^3}\right]$

σ = surface tension $\left[\frac{N}{m}\right]$,

Stephan Boltzmann constant $\left[\frac{W}{m^2T^4}\right]$

σ_{ij} = stress tensor $\left[\frac{N}{m^2}\right]$

τ = transmissivity $\left[-\right]$

φ = porosity $\left[-\right]$

Φ = heat sink or source term $\left[\frac{W}{m^3}\right]$

ψ = volume fraction $\left[\frac{m^3}{m^3}\right]$

$\dot{\omega}_A'''$ = species reaction rate $\left[\frac{kg}{m^3 s}\right]$

Ω = random function

Symbols

$\Delta\hat{T}$ = largest change in $\Delta\hat{T}$ $\left[K\right]$

$\nabla(\ ) = \frac{\partial(\ )}{\partial x} + \frac{\partial(\ )}{\partial y} + \frac{\partial(\ )}{\partial z}$

$\vec{u}$ = vector quantity

$\langle\Omega\rangle$ = spatial average of Ω

$\langle\Omega_i\rangle$ = i phase average of Ω

$\langle\Omega_i\rangle^i$ = intrinsic i phase average of Ω

$\tilde{\Omega}$ = deviation of Ω

∞ = ambient

Subscripts

a = air

A = fluid A

Air = air

Avg = average value

B = fluid B

eff = effective

g = gas phase

h = hydraulic

$H_2 0$ = water

i = counter for index notation

int = interface

ir = irreducible

j = counter for index notation

l = liquid phase

o = reference, initial

s = solid phase

$surf$ = surface

v=vapor

w = water

x = x-direction

y = y-direction

z = z-direction

1. Introduction

The ability to accurately model water based fire suppression is an important long term goal of fire research. The current state of the art of suppression research and product development relies heavily on large scale fire testing. It is desirable for many reasons to reduce the number of large scale tests necessary. They can be expensive, time consuming, and pose environmental concerns over the products of combustion released. Computer fire modeling has the potential to reduce our reliance on full scale testing. As computing power has increased, so too has the sophistication of computer fire models which predict fire behavior and consequences. The suppression algorithms in most available computer fire models are considerably less sophisticated, and in many cases much reliance is placed on empirical data for the prediction of suppression. There is a clear need for improved models for water based fire suppression that can augment larger models which predict fire behavior and consequences. As a step towards achieving that goal, a model has been developed for the heat and mass transfer in porous materials exposed to water sprays in a compartment fire environment.

Much previous work has focused on water spray cooling of non-porous solids, with little attention paid to water absorption. Many investigations focused on single drops impacting a non-porous solid heated from below [1-10] and by a radiant heat source [11-14]. Evaporative cooling of hot plates by a stream of droplets randomly deposited one at a time was investigated by Klassen et al. [15]. The same conditions were also investigated using radiant heating [16-18]. The effectiveness of spray cooling of non-porous materials was investigated by Toda [19] and Bonacina et al. [20] and a review is presented by Bolle and Moreau [21]. Of these investigations, only two [10, 14] looked at the cooling effect of drops impacting porous materials, and only experimentally. No water absorption measurements were made. Yu and Jayaweera [22] investigated rates of water absorption by corrugated board subjected to water sprays and show that the mass of water absorbed is proportional to the time to the half power, as predicted by a simple capillary tube model. Outside of the realm of fire research, much work has been performed in other areas of porous media study that can give insight into fire related problems. Many porous media textbooks are available [23-26] and many models have been developed for wetting and drying applications that closely resemble fire suppression related problems. In the field of hydrogeology, models have been developed to predict the flow of fluids in soils, clays, and porous rock. The modeling approach for isothermal conditions is described by Philip [27-33], and models for soils with thermal gradients are given by Philip and DeVries [34] and

DeVries [35]. The infiltration of water into soils by means of surface tension forces closely resembles the case of isothermal wetting of porous materials by fire sprinklers. One important difference is that the length and time scales of interest often differ by several orders of magnitude. The characteristic length and time scales of solid items being wetted by sprinklers are often on the order of millimeters and minutes. For water penetration into soils, the characteristic length and time scales can be measured in meters and hours. As a result, the thermal and saturation gradients are much greater for sprinkler wetting problems than for groundwater infiltration problems. Many models have been developed for industrial drying applications for various materials. Drying of materials is a highly energy intensive process [36] and drying models have been developed to maximize the efficiencies of drying processes. Two of the earliest comprehensive drying models for the general heat and mass transfer in porous materials are the phenomenological model developed by Luikov [37] and the mechanistic model of Whitaker [36]. Many recent models have been based on the modeling frameworks proposed by these researchers. Models were later developed for the convective drying of materials, such as the models of Nasrallah and Perre [38], Chen and Pei [39], and Ilic and Turner [40]. A microwave drying model was developed by Ni [41]. The problem of drying of materials exhibits some similarities to the problem encountered in fire science of heating a wet object to the point of ignition. Objects being dried for industrial applications often have similar length scales as fuel packages in a fire environment, but much longer timescales, and lower temperature scales. As a result, thermal gradients are much greater in an ignition problem, as compared to an industrial drying problem. Despite the differences, there are sufficient similarities between these related problems to suggest that a similar type of porous media model could predict certain aspects of fire suppression behavior.

The current research project uses porous media modeling techniques for hydrogeology and industrial drying applications to investigate water based fire suppression. The scenario being investigated is of a porous material exposed to spray wetting and radiant heating, as shown in Figure 1.

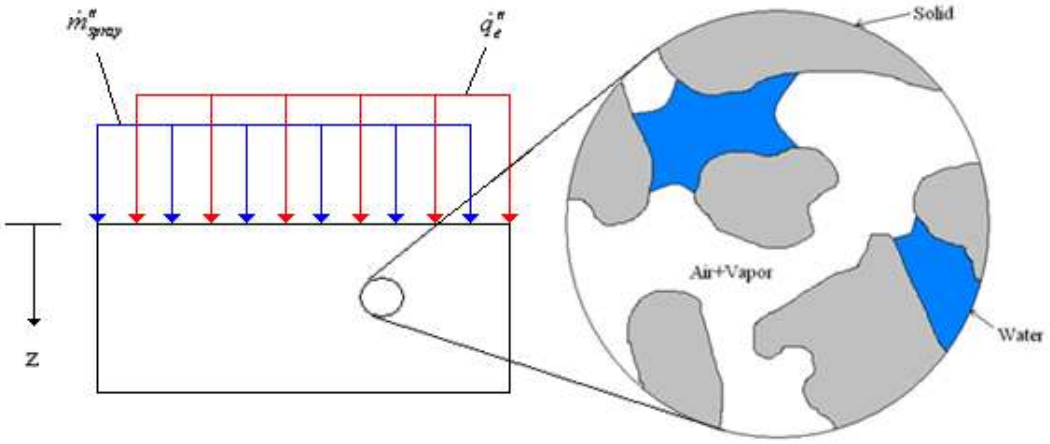

Figure 1 – Representative Porous Material Subjected to Spray Wetting and Radiant Heating

This scenario represents an object in a compartment fire environment where a sprinkler has actuated. In the case of real world combustible materials, sufficient heating rates will lead to pyrolysis and possibly an ignition event. The model presented here assumes an inert solid material, and is only applicable to the time period leading up to pyrolysis. Thermal heating effects will be countered by the cooling and wetting effects of the water spray. Water that is absorbed into combustible materials can increase the time to ignition, and lower flame spread rates for a given thermal insult. This is due to the observation that some of the absorbed water must be evaporated before ignition can occur. While this can be observed and measured, there are currently few tools available to fire researchers and engineers that can quantitatively predict wetting rates or the effects of absorbed water. As part of the current research project, a porous media model was developed and used to investigate two simplified scenarios that relate to the more general water suppression problem. The scenarios are the case of the wetting of an initially dry material, and the heating of an initially wet material. These are shown in Figure 2**.**

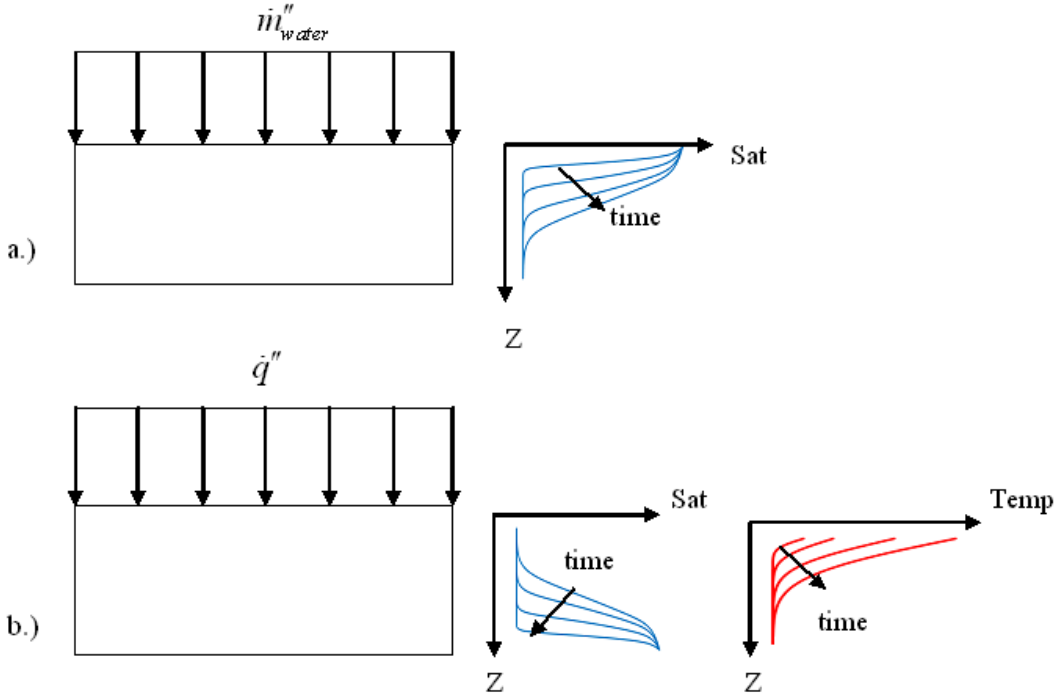

Figure 2 – Wetting Scenario (a) and Heating Scenario (b)

The wetting scenario represents an event occurring early in the fire development or at a distance from the fire where thermal effects are not significant. The process is nominally near isothermal if sufficiently far from the fire. Water from the sprinkler that is delivered to the surface is drawn into the material primarily by surface tension forces and gravity, provided that the surface is outside of the direct spray impingement area. If the water application rate is sufficiently high, a film of water will form on the surface of the material blocking gas phase mass transfer between the material and the ambient environment. The heating scenario represents an event where an object that has absorbed significant amounts of water is now exposed to a radiant heat exposure. The material surface will remain below 100^{o}C until a sufficient amount of water has evaporated, allowing the surface to become dry. At this time the surface temperature will rise dramatically. In the case of a combustible material, this temperature rise could lead to ignition. The model that has been developed here provides a tool for quantifying the above described processes for porous materials. This dissertation presents the model framework, solution method, and attempts to give the reader an understanding of how well the model works by means of an uncertainty analysis, and describes the model validation with six sets of experimental data for wetting and heating

2. Development of Porous Media Model

The framework used for the current porous media model is as follows. The porous material itself is assumed to be a solid matrix with liquid water, vapor and air in the pore spaces as illustrated in Figure 1. The material is treated as a continuum, with volume averaged representative properties that characterize its porous nature. The exact structure of the solid material and the flow patterns are not resolved. The material is treated as an isotropic, non-hygroscopic, inert material. Pyrolysis, combustion reactions, and internal radiation are not considered. One dimensional transfer is assumed. The porosity ϕ is defined as the volume ratio of void space to solid material. The amount of liquid water in the pore space of the material is characterized by the volume fraction of void space filled with water, called the liquid saturation, S_w. The amount of gas (vapor + air) in the material is characterized by the fraction of void space filled with gas, called the gas saturation, S_g. Since all of the pore space is filled with gas or liquid, the liquid and gas saturations must sum to 1. It is sometimes useful to characterize the amount of water in the material on a mass basis. The moisture content, M, is the mass ratio of water to solid material. This can be used to describe the amount of water at a point in space, or in an entire object. Many real-world materials are hygroscopic, meaning that water is absorbed into the solid matrix. This can cause swelling and shrinking of the solid matrix under wetting and drying conditions, and causes the porosity to change. In the current model materials are assumed to be non-hygroscopic with a constant porosity. Transport in the material is also simplified by making the assumption of local thermal equilibrium. This means that at a particular point in space, the solid, liquid, and gas phases are at the same temperature. This allows the thermal transport to be characterized by a single equation for conservation of energy. It also allows vapor pressure to be calculated as a function of temperature and saturation only. The conditions for local thermal equilibrium to be valid are discussed in appendix B.

In the current model, liquid water fluxes are driven by pressure gradients and gravity forces according to Darcy's law [23-25],

$$\dot{m}''_w = -\rho_w \frac{KK_{r,l}}{\mu_w}\left(\frac{\partial p_w}{\partial z} - \rho_w g\right), \tag{1}$$

where ρ_w and μ_w are the density and viscosity of the water, K is the permeability of the solid porous material, K_{rl} is the liquid relative permeability, p_w is the pressure in the water, and g is gravity. The liquid density is approximated as having constant values. The water viscosity is assumed to vary with temperature. The permeability is a measure of the ability of a single fluid phase to flow through a porous material under saturated conditions. The permeability is material specific and must be determined empirically. Tables of values of permeability for various materials are available in the literature [25, 42, 43]. The liquid relative permeability is a measure of the restriction of the flow rate when two or more fluids are present in the porous material (multiphase flow) as compared to the case of single phase flow. For the scenarios of interest here, the two fluids are water and a gas mixture consisting of air and water vapor. The relative permeability varies between zero and one and is a complex function of saturation, porosity, pore size distribution of the solid material, and the properties of the fluids. The relative permeability can be approximated as a function of saturation [23], as shown in Figure 3 for particulate media. The characteristic shapes of these functions is discussed in Appendix B. Empirical functional relationships for relative permeability for various solid – fluid combinations are given by Kaviany [23]. The pressure in the water, p_w, at any point in the material differs from the total gas phase pressure, P, due to interfacial surface tension forces. The difference between the gas phase pressure and water pressure is called the capillary pressure. The capillary pressure is modeled using a correlation with the form:

$$p_c = P - p_w = \left(\frac{\varphi}{K}\right)^{\frac{1}{2}} \sigma J. \tag{2}$$

Where ϕ is the porosity, σ is the surface tension, and J is a material specific empirical correlation called the J-Function. The J function is a function of liquid saturation and accounts for the pore size distribution in the porous material [44]. J-Functions for various materials are available in the literature [23, 25, 45]. For example, the J-Function for a particulate media is [23]

$$J = \left[0.364\left(1-\exp\left(-40\left(1-S_w\right)\right)\right) + 0.221\left(1-S_w\right) + \frac{0.005}{S_w - 0.08} \right], \tag{3}$$

and is shown in Figure 4.

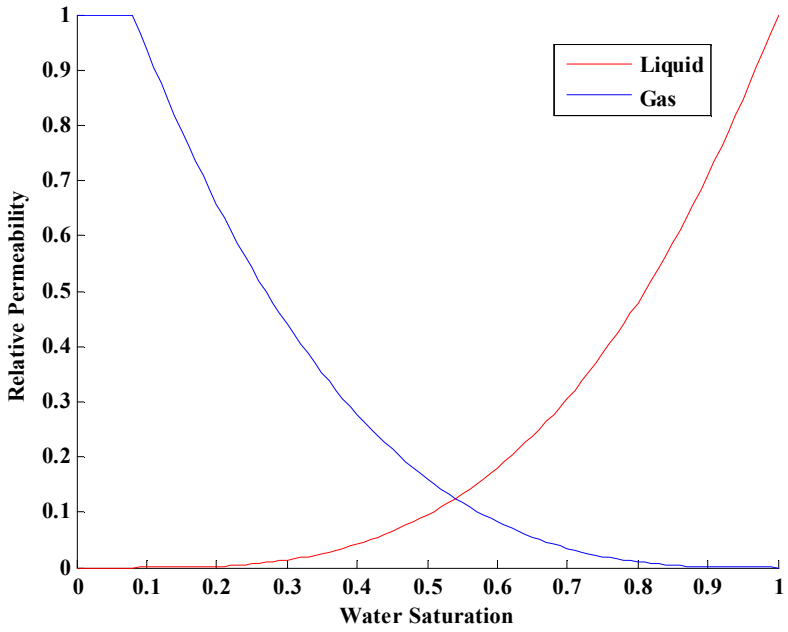

Figure 3 – Relative Permeability vs. Saturation for Liquid and Gas in Particulate Media

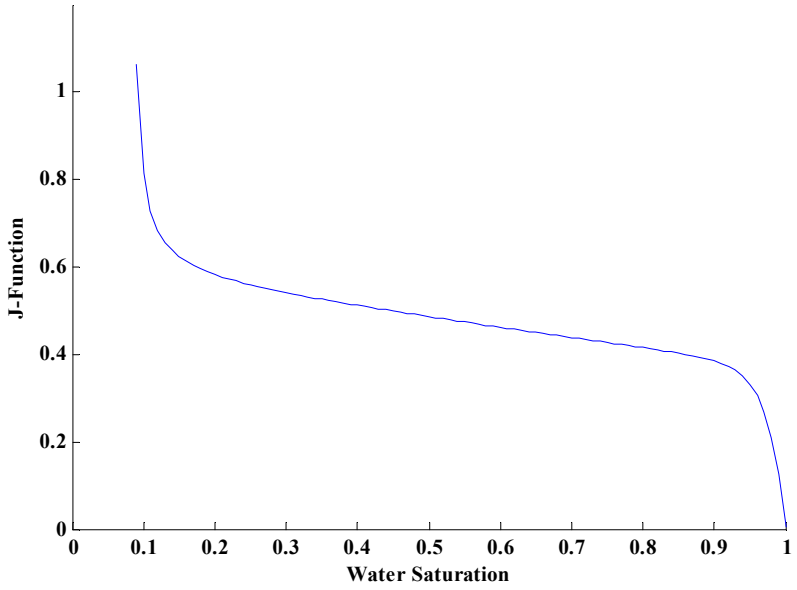

Figure 4 – J-Function vs. Saturation for Particulate Media

Slightly different J-Function curves have been observed for wetting and drying. This is called hysteresis, and is discussed in Appendix B. This model assumes that a single J-Function can reasonably describe the effects of surface tension forces on water in a porous material. The gas phase total mass fluxes contain convective and diffusive components [41]:

$$\dot{m}_v'' = -\rho_v \frac{KK_{r,g}}{\mu_g}\frac{\partial P}{\partial z} - \frac{C^2}{\rho} M_a M_v D_{eff} \frac{\partial X_v}{\partial z}, \tag{4}$$

$$\dot{m}_a'' = -\rho_a \frac{KK_{r,g}}{\mu_g}\frac{\partial P}{\partial z} - \frac{C^2}{\rho} M_v M_a D_{eff} \frac{\partial X_a}{\partial z}. \tag{5}$$

The convective terms of Eqs. (4) and (5), are given by Darcy's law, where ρ_v and ρ_a are the densities of the vapor and air, μ_g is the viscosity of the gas mixture, $K_{r,g}$ is the gas relative permeability, and P is the total gas phase pressure. The gas viscosity is approximated as having a value. The gas relative permeability accounts for the reduced

convective mass flow rate of gas due to the presence of water in the pores. It is an empirical correlation that is modeled as a function of liquid saturation as shown in Figure 3 for a particulate material. The diffusive terms of Eqs. (4) and (5) are given by Fick's law, where C is the molar concentration of the gas mixture, ρ is the total gas phase density, M_a and M_v are the molar masses of air and vapor, D_{eff} is the effective diffusivity for gas phase diffusion, and X is the molar fraction. The effective diffusivity is a material specific empirical correlation which multiplies the diffusivity of vapor in air by a scaling function that varies between zero and 1. This scaling function accounts for the decreased diffusive mass flux due to the constricted and tortuous path through which diffusion occurs. For example the effective diffusivity for soils was measured by Baver and Gardner [46] to be:

$$D_{eff,g} = D_{va}\left(S_g\phi\right)^{\frac{4}{3}}. \tag{6}$$

Eq (6) is assumed to apply to all of the porous materials used in this study, except for wood. The diffusivity of vapor in air is calculated as a function of temperature and pressure (Bejan, 1992):

$$D_{va} = 2.6\times10^{-5}\left(\frac{T}{298}\right)^{1.75}\frac{101300}{P}. \tag{7}$$

When the material is very wet the partial pressure of water vapor in the pore spaces is assumed to obey the Clausius-Clapeyron thermodynamic relation [47]:

$$p_{vs} = 101300\exp\left[-\frac{\Delta h_{vap}}{R_v}\left(\frac{1}{T}-\frac{1}{373}\right)\right], \tag{8}$$

where Δh_{vap} is the enthalpy of vaporization, and R_v is the water vapor gas constant.

When the material is very dry, water is held in very small pores, and surface tension forces can significantly decrease the vapor pressure below the value predicted by Eq. (8). In some dry materials the water will be chemically bound to the solid matrix. To account for these effects, an empirical sorption relation is used to calculate the vapor

pressure as a function of water saturation and temperature. When the material is very dry, the vapor pressure approaches zero. For example, the sorption relation for brick is given by Haertling [48] and assumed to represent the behavior of a range of solid materials:

$$S = \frac{(1-\phi)\rho_s}{\phi\rho_w}\left(0.0105\left(\frac{p_v}{p_{vs}}\right)^{0.2} + 0.0125\exp\left(20\frac{p_v}{p_{vs}} - 20\right)\right), \tag{9}$$

where p_v is the vapor pressure in the pores, p_{vs} is the equilibrium vapor pressure over a non-curved liquid water surface, and the ratio $\frac{p_v}{p_{vs}}$ is the relative humidity. The ideal gas law is used to calculate the densities of air and vapor:

$$\rho_a = \frac{p_a}{R_a T}, \tag{10}$$

$$\rho_v = \frac{p_v}{R_v T}. \tag{11}$$

2.1. Governing Equations

The model is formed from three equations for conservation of species, and one equation for conservation of energy. Momentum is implicitly conserved by using Darcy's law for convective mass fluxes. The governing equations can be derived from a control volume analysis. The complete derivation is given in Appendix C. The equations in one dimensional form are:
conservation of mass for liquid water,

$$\phi\frac{\partial(\rho_w S_w)}{\partial t} + \frac{\partial}{\partial z}(\dot{m}''_w) = -\dot{m}'''_{evap}, \tag{12}$$

conservation of mass for vapor water,

$$\phi \frac{\partial \left(\rho_v S_g \right)}{\partial t} + \frac{\partial}{\partial z} \left(\dot{m}_v'' \right) = \dot{m}_{evap}''' \quad , \tag{13}$$

conservation of mass for air,

$$\phi \frac{\partial \left(\rho_a S_g \right)}{\partial t} + \frac{\partial}{\partial z} \left(\dot{m}_a'' \right) = 0 \quad , \tag{14}$$

and conservation of energy,

$$\left(\rho c_p \right)_{eff} \frac{\partial T}{\partial t} + \left[\dot{m}_w'' C_{p,w} + \dot{m}_v'' C_{p,v} + \dot{m}_a'' C_{p,a} \right] \frac{\partial T}{\partial z} + \Delta h_{vap} \dot{m}_{evap}''' = \frac{\partial}{\partial z} \left(k_{eff} \frac{\partial T}{\partial z} \right) . \tag{15}$$

The evaporation rate, $\dot{m}_{evap}'''$, appears as a sink in Eq. (12), and as a source in Eq. (13), $C_{p,w}$,. $C_{p,v}$, and $C_{p,a}$ are the specific heats of the water, vapor, and air components, and T is the temperature of all phases at a point in space. The effective thermal properties of the material are calculated by assuming volumetric contributions from all phases present [41]:

$$\left(\rho C_p \right)_{eff} = \phi S_w \rho_w C_{p,w} + \phi S_g \rho_v C_{p,v} + \phi S_g \rho_a C_{p,a} + \left(1 - \phi \right) \rho_s C_{p,s} \tag{16}$$

$$k_{eff} = \phi S_a k_a + \phi S_v k_v + \phi S_w k_w + \left(1 - \phi \right) k_s \tag{17}$$

Following the method and notation of Ni [41] the conservation equations can be rearranged and rewritten as a system of three partial differential equations. The details are given in Appendix C. First add Eqs. (12) and (13) together, substitute using Eq. (4), Eq. (5), and Eq. (11), and expand terms so that a single conservation equation for water and water vapor is achieved, with the evaporation terms removed:

$$K_4 \frac{\partial S_w}{\partial t} + K_5 \frac{\partial T}{\partial t} + K_6 \frac{\partial P}{\partial t} = \frac{\partial}{\partial z} \left(K_1 \frac{\partial S_w}{\partial z} \right) + \frac{\partial}{\partial z} \left(K_2 \frac{\partial T}{\partial z} \right) + \frac{\partial}{\partial z} \left(K_3 \frac{\partial P}{\partial z} \right) - \frac{\partial}{\partial z} \left(K_{19} \right) . \tag{18}$$

The coefficients are functions of the dependant variables and defined in Appendix A. Next take Eq. (14), and substitute using Eq. (5) and Eq. (10) to form a new equation for the conservation of air:

$$K_{10}\frac{\partial S_w}{\partial t}+K_{11}\frac{\partial T}{\partial t}+K_{12}\frac{\partial P}{\partial t}=\frac{\partial}{\partial z}\left(K_7\frac{\partial S_w}{\partial z}\right)+\frac{\partial}{\partial z}\left(K_8\frac{\partial T}{\partial z}\right)+\frac{\partial}{\partial z}\left(K_9\frac{\partial P}{\partial z}\right). \tag{19}$$

Finally, take Eq. (15) and substitute using Eq. (1), Eq. (16), and Eq. (17) to form a new equation for the conservation of energy:

$$\begin{aligned}K_{16}\frac{\partial S_w}{\partial t}+K_{17}\frac{\partial T}{\partial t}+K_{18}\frac{\partial P}{\partial t}=&-\left(C_{pv}\dot{m}_v''+C_{pa}\dot{m}_a''+C_{pv}\dot{m}_w''\right)\frac{\partial T}{\partial z}\\&+\frac{\partial}{\partial z}\left(K_{13}\frac{\partial S_w}{\partial z}\right)+\frac{\partial}{\partial z}\left(K_{14}\frac{\partial T}{\partial z}\right)+\frac{\partial}{\partial z}\left(K_{15}\frac{\partial P}{\partial z}\right)+\frac{\partial}{\partial z}\left(K_{20}\right).\end{aligned} \tag{20}$$

This is a system of three non-linear parabolic partial-differential equations. It requires six boundary conditions in space and three boundary conditions in time to be a well posed problem. The dependant variables are water saturation, temperature, and the total gas phase pressure. All other quantities can be calculated from these three dependant variables, using the constitutive relations discussed previously.

2.2. Boundary Conditions

Initially the material is at a uniform specified saturation, and the temperature and pressure are at the ambient values. At t = 0:

$$S = S_o, \tag{21}$$

$$T = T_\infty, \tag{22}$$

$$P = P_\infty. \tag{23}$$

The simplest possible spatial boundary conditions are type 1 boundary conditions, where the values of saturation, temperature, and pressure are specified at z = 0:

$$S = S_{surf}, \tag{24}$$

$$T = T_\infty, \tag{25}$$

$$P = P_{\infty}, \tag{26}$$

and at z = L:

$$S = S_o, \tag{27}$$
$$T = T_{\infty}, \tag{28}$$
$$P = P_{\infty}. \tag{29}$$

Eqs. (21)-(29) are used for model verification tests and one of the wetting validation tests. Eq. (26) is used for all validation tests. For many wetting and heating scenarios however, more complicated flux boundary conditions are required for water saturation and temperature.

Surface Flux Boundary Conditions

The flux boundary conditions at the top surface for saturation and temperature are shown symbolically in Figure 5.

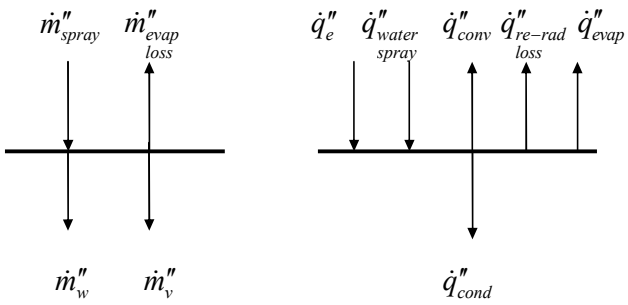

Figure 5 – Surface Boundary Conditions for Saturation and Temperature

At the top surface, water is transported externally by liquid water spray that is applied to the surface $\dot{m}''_{spray}$ and evaporative vapor losses $\dot{m}''_{\substack{evap \\ loss}}$, and internally it is transported by liquid convective fluxes $\dot{m}''_{w}$ and convective and diffusive fluxes of vapor $\dot{m}''_{v}$ as shown in Figure 5. The saturation boundary condition can be written as

$$\dot{m}''_{w} + \dot{m}''_{v} = \dot{m}''_{spray} - \dot{m}''_{\substack{evap \\ loss}}. \tag{30}$$

By substituting Eqs. (1) and (4), Eq. (30) can be rewritten,

$$-K_1 \frac{\partial S_w}{\partial z} - K_2 \frac{\partial T}{\partial z} - K_3 \frac{\partial P}{\partial z} + K_{19} = \dot{m}''_{spray} - h_m \left(\rho_{v,surf} - \rho_{v,\infty} \right) \quad (31)$$

.

The LHS of Eq. (31) represents the total internal flux of water and vapor, under the driving forces of saturation, temperature, pressure, and gravity. Water is added by means of the water spray flux. The only way that water leaves the material in the model, is by evaporation. In some convective drying cases, water is added by means of condensation on the surface in the early stages of the drying process. This only occurs if the ambient air is relatively humid and the surface of the material is still relatively cold. This boundary condition ignores the inertial force of the water droplets impacting the surface of the material. In many cases this impact pressure is much less than the capillary pressure from surface tension forces in the material. For an incident mass flux, $\dot{m}''_{spray}$, with a spray velocity, u, the spray impact pressure at the surface is assumed to be approximately the stagnation point pressure, $p_{spray} = \dot{m}''_{spray} u$. The maximum capillary pressure in the material is approximately of the order $\sigma\sqrt{\phi / K}$. The porosity of the materials used in this study ranged from 0.435 to 0.8 and the permeability ranged from 10^{-11} to 10^{-16} m. Typical mass fluxes associated with fire sprinklers range from 0.0475 to 0.272 kg/m^{2}s (0.07 – 0.4 gpm/ft^2) and velocities of sprinkler droplets can reach up to 20 m/s. For these scenarios, the impact pressure is several orders of magnitude lower than the capillary pressure. The issue of impact forces from water droplets is discussed in more detail in Appendix B.

The thermal boundary condition at the surface involves many transport processes. Heat transfer occurs externally by radiant heating from an external source, convective transfer by the water spray, convective loss to the ambient air, re-radiative losses from the surface to the ambient, and evaporative cooling losses. Internally heat transport occurs by conduction. These are shown in Figure 5. In-depth absorption of radiation is not considered. The surface thermal boundary condition can be written as

$$\dot{q}''_{cond} = \dot{q}''_e + \underset{spray}{\dot{q}''_{water}} - \dot{q}''_{conv} - \underset{loss}{\dot{q}''_{re-rad}} - \dot{q}''_{evap} \quad (32)$$

.

By defining the heat flux terms, Eq. (32) can be written as

$$-K_{14}\frac{\partial T}{\partial z} = \dot{q}_e'' + \dot{m}_{spray}'' C_{p,w}\left(T_{spray} - T_{surface}\right) - h\left(T_s - T_\infty\right) - \varepsilon_s \sigma\left(T_s^4 - T_\infty^4\right) - \Delta h_v h_m\left(\rho_{v,surf} - \rho_{v,\infty}\right). \quad (33)$$

The surface pores are assumed to be open to the ambient, and therefore the pressure at the top surface given by Eq. (26).

Back Face Flux Boundary Conditions

The back face of the material is sealed to liquid and gas flow and insulated. This is shown symbolically in Figure 6.

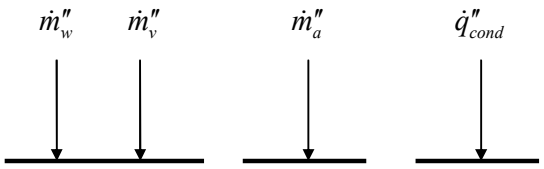

Figure 6 – Back Face Boundary Conditions for Saturation, Pressure, and Temperature

The liquid and vapor water fluxes reaching the back face are zero, as shown in Figure 6. This boundary condition is

$$\dot{m}_v'' + \dot{m}_w'' = 0 \quad (34)$$

Using Eqs. (1) and (4), Eq. (34) can be written as

$$-K_1\frac{\partial S_w}{\partial z} - K_2\frac{\partial T}{\partial z} - K_3\frac{\partial P}{\partial z} + K_{19} = 0 \quad (35)$$

The air flux reaching the back face is equal to zero, as shown in Figure 6. This boundary condition is

$$\dot{m}_a'' = 0 \quad . \tag{36}$$

Using Eq. (5), Eq. (36) can be written as

$$-K_7 \frac{\partial S_w}{\partial z} - K_8 \frac{\partial T}{\partial z} - K_9 \frac{\partial P}{\partial z} = 0 \quad . \tag{37}$$

Heat transfer by conduction reaching the back face is equal to zero, as shown in Figure 6. This boundary condition is

$$\dot{q}_{cond}'' = 0 \quad . \tag{38}$$

Using Fourier's law, this can be rewritten as

$$-K_{14} \frac{\partial T}{\partial z} = 0 \quad . \tag{39}$$

The model is now comprised of Eqs. (18), (19), and (20), with boundary conditions for most cases given for the front surface by Eqs. (26), (31), and (33), and the back face by Eqs. (35), (37), and (39).

3. Solution Method

The model is solved using the finite difference method with a code written in MATLAB. The discretization of the spatial domain is shown in Figure 7.

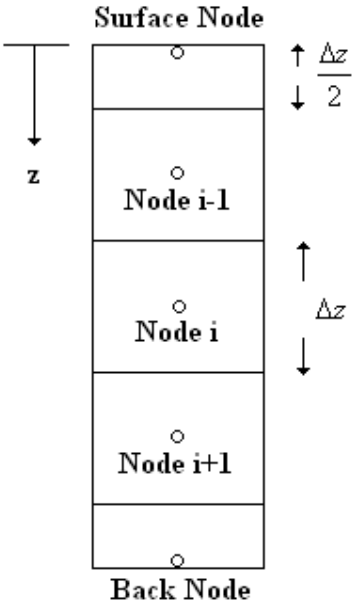

Figure 7 – Discretization of Spatial Domain

The domain is divided into nodes with a finite length. The interior nodes have a length of Δz, and the surface and back face nodes have a length of $\Delta z/2$. The length Δz is equal to $l/(N-1)$ where l is the length of the domain, l, and N is the number of nodes. Second order spatial derivatives are approximated numerically by calculating fluxes into and out of the node i

$$\frac{\partial}{\partial z}\left(K_1\frac{\partial S}{\partial z}\right)\approx\frac{\left(K_1\frac{\partial S}{\partial z}\right)_{i+1/2}-\left(K_1\frac{\partial S}{\partial z}\right)_{i-1/2}}{\Delta z} \tag{40}$$

where the fluxes $\left(K_1\frac{\partial S}{\partial z}\right)_{i\pm1/2}$ are calculated at the respective adjacent node boundaries (i ± 1/2 node spacing) using forward and backward difference schemes. For example:

$$\left(K_1\frac{\partial S}{\partial z}\right)_{i+1/2}\approx K1_{i+1/2}^{n}\frac{S_{i+1}^{n}-S_{i}^{n}}{\Delta z}. \tag{41}$$

where the superscript n denotes the n^{th} time step. So Eq. (40) can be written

$$\frac{\partial}{\partial z}\left(K_1 \frac{\partial S}{\partial z}\right) \approx \left(\frac{K1^n_{i+\frac{1}{2}} \frac{S^n_{i+1} - S^n_i}{\Delta z} - K1^n_{i-\frac{1}{2}} \frac{S^n_i - S^n_{i-1}}{\Delta z}}{\Delta z} \right). \tag{42}$$

The labeling convention for the coefficients has been changed here to avoid confusion with the numerical subscripts. For example $K_1 = K1$. The first order derivatives are calculated using a central difference scheme. For example the convective heat fluxes are approximated as:

$$C_{pv} \dot{m}''_w \frac{\partial T}{\partial z} \approx C_{pv} \dot{m}''_w \frac{T^n_{i+1} - T^n_{i-1}}{2\Delta z} \tag{43}$$

And

$$\frac{\partial}{\partial z}\left(K_{20}\right) \approx \frac{K20^n_{i+1} - K20^n_{i-1}}{2\Delta z}. \tag{44}$$

Temporal derivatives are calculated using a forward difference scheme with coefficients calculated at the temporal half step:

$$K_4 \frac{\partial S_w}{\partial t} \approx K4^{n+\frac{1}{2}}_i \frac{S^{n+1}_i - S^n_i}{\Delta t}. \tag{45}$$

A Crank-Nicholson discretization scheme is used to provide improved accuracy in time and greater stability than would be realized with a fully explicit or implicit scheme. By discretizing each of the three governing equations in this manner, they can be arranged in matrices as discussed by Ames [49], and solved using Matrix manipulation techniques. The equations, in matrix form, are written as $[Coefficients][Unknowns] = [RHS]$, where [Coefficients] is a 3N by 3N matrix

containing the coefficients of the equations, [Unknowns] is a 3N by 1N matrix containing the dependant variables, and [RHS] is a 3N by 1N matrix containing the RHS terms. This allows the equations to be solved using matrix manipulation techniques. A code has been written using the software program MATLAB to solve this system of equations with the boundary conditions given. Since the coefficients K_1 – K_{20} are functions of the dependant variables, the solution algorithm will step forward in time and then iterate until convergence is achieved, before stepping forward in time again. The conditions for convergence used are: $\Delta S < 1\times10^{-6}$, $\Delta T < 1\times10^{-6} K$, $\Delta P < 0.1 Pa$. As with other parameters, these are adjustable through an input file. The user must specify the values of the initial conditions, the type of boundary conditions, and values for the ambient conditions, radiant heat flux, water spray mass flux, material properties, and numerical inputs. The time step is allowed to adjust if needed. For some scenarios a large time step is possible for some initial period but will crash a later time when a smaller time step is needed. For these cases the time step will be decreased partway through a simulation, usually by a factor of 10 or more. This can be set to occur at a predetermined time, or when a particular value of a parameter is reached. For example the time step can be decreased when the surface saturation drops below the irreducible saturation. The complete details of the solution algorithm are given in Appendix D.

4. Verification

In order to verify that the model code has been correctly implemented, a series of tests were performed. Model outputs were compared to analytical solutions for simplified scenarios to show that the governing equations are being solved correctly. For each dependant variable, two analytical solutions were compared with the model output. Analytical solutions for saturation profiles can be obtained from the equation for conservation of mass for liquid water if isothermal behavior is assumed. This allows analytical solutions for conditions with and without the effects of gravity. Analytical solutions for temperature profiles in the material can be obtained by assuming that the material is completely impermeable and dry. Solutions are available for constant temperature and constant surface heat flux boundary conditions. Analytical solutions for pressure profiles in the material can be derived if the gas relative permeability is set to zero. Solutions were determined for cases where the pressure was increased by heating and the compressive effects of wetting. In all six cases the model was shown to be working correctly. The complete details of the

verification tests are given in Appendix E.

5. Sensitivity Analysis

A sensitivity analysis was conducted on the model for each of the 6 validation cases that will be described in section 6. These cases are: wetting of pieces of ceramic fiberboard (CFB) using two means of applying the water, convective drying of a particulate media, brick, and wood, and radiant heating of wet ceramic fiberboard. The details of the sensitivity analysis are given in Appendix G. A one factor at a time local sensitivity analysis was chosen for low computational effort and applied to each of the validation cases. This method consists of measuring the effect on the model output when one single input parameter is adjusted and all others are held constant. The measure of the sensitivity of the model output, y, to a single parameter x_i is given by a sensitivity coefficient S_i [50]:

$$S_i = \frac{x_i}{y}\frac{\partial y}{\partial x_i} \quad . \tag{46}$$

Since this model is solved numerically, Eq. (46) is approximated numerically as

$$S_i = \frac{x_i}{y}\frac{\Delta y}{\Delta x_i} \quad . \tag{47}$$

Eq. (47) was used to calculate a sensitivity coefficient for each parameter by adjusting the parameter while holding all others constant, and observing the change in model output. The sensitivity coefficient for the input parameters was used to create sensitivity rankings of the input parameters. The model output that was compared and used to calculate the sensitivity coefficients was different for each validation case. For the two wetting cases, the water penetration depth was integrated over time, and the sum was used as a quantitative measure of wetting. For the wood and brick heating cases, the surface temperature was integrated over time, and this sum was used as the quantitative measure of heating. For the particulate media and CFB heating cases, the time that the surface temperature jumped dramatically was used. For each case, a cutoff value was chosen to separate the most sensitive input parameters. For the wetting tests, the inputs with a sensitivity coefficient greater than 0.5 are shown in

Table 1. The Capillary Pressure Coefficients in Table 1 are defined in Appendix G. For Type 1 BC wetting, the model is extremely sensitive to the surface saturation value. This value determines how rapidly water can enter the material. The relative permeability and capillary pressure are very sensitive to the saturation at values close to one, as can be seen in Figure 3 and Figure 4.

Table 1 – Sensitivity Coefficients for Wetting of CFB

Type 1 BC		**Spray Wetting**	
Parameter	**S_i**	**Parameter**	**S_i**
Surface Saturation	17.05	Porosity	0.9357
Cap Press Coeff 1	0.82761	Water flux	0.85056
Permeability	0.66859	Liq Rel Permeability	0.79437
Porosity	0.63037		
Liq Rel Permeability	0.55899		
Cap Press Coeff 2	0.5139		

The inputs with a sensitivity coefficient greater than 0.1 for the convective heating validation tests using brick and wood are shown in Table 2. For both cases, the model is very sensitive to the ambient temperature. This is due to the dependence of the convective heating rate on the ambient temperature. The sensitivity coefficient is scaled using the absolute value of the input, so a change from 353K to 355K is only a 0.567% change, but for a convective heating scenario it can have significant effects on the model output. The ambient temperature is usually known very precisely, so this is not a serious concern for the uncertainty of the model.

Table 2 – Sensitivity Coefficients for Heating of Brick and Wood

Brick		**Wood**	
Parameter	**S_i**	**Parameter**	**S_i**
Ambient Temp	6.0505	Ambient Temp	14.8
Initial Temp	0.2887	Initial Temp	0.269
Heat Trans. Coeff.	0.26033	Heat Trans Coeff	0.195
Initial Saturation	0.2574	Initial Saturation	0.146
Length	0.12885	Porosity	0.119
Liq Rel Permeability	0.10521	Length	0.102

For the cases of heating of particulate media and CFB, the model inputs with a sensitivity coefficient above 0.5 are shown in Table 3. The particulate media case is most sensitive to the ambient temperature, just as with the other convective heating cases. The case of radiant heating of CFB is most sensitive to the initial saturation.

Table 3 – Sensitivity Coefficients for Heating of Particulate Media and CFB

Particulate Media (Convective Heating)		**CFB (Radiant Heating)**	
Ambient Temp	16.451	Initial Saturation	2.1843
Initial Saturation	1.172	Radiant Heat Flux	1.0731
Heat Trans Coeff	0.90585	Surface Emissivity	1.0457
Relative Humidity	0.77966	Length	0.87902
Initial Temp	0.66094	S_{ir}	0.78212
		Porosity	0.64016
		Liq. Rel. Perm.	0.50723

The uncertainty of the model output was calculated for each validation case by first calculating the maximum uncertainty of the each of the input parameters shown in Table 1 through Table 3. The method of calculating the maximum uncertainty of each input parameter is discussed in Appendix H. Each input has a range of possible values and a probability of each one being correct. This range is assumed to follow a normal distribution, where the base value that has been used for model calculations represents the mean value. The maximum uncertainty that is calculated for each parameter is assumed to represent 3 standard deviations of the input distribution as shown in Figure 8.

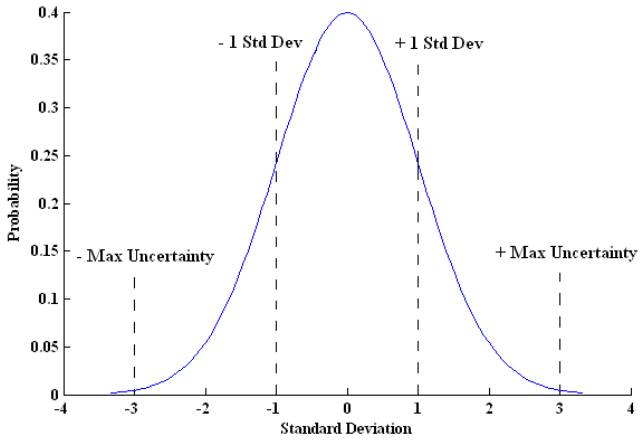

Figure 8- Distribution of Uncertainty of Input Parameters

This means that 99.7% of all possible values of a given input parameter are contained between the calculated maximum and minimum values of that parameter. The values that lie outside of the single standard deviation range are assumed to represent extreme cases, with a low probability of occurrence. The input uncertainty of each parameter was assumed to be ± one standard deviation. This range includes 68.3% of all possible values of each input parameter, and is assumed to represent a reasonable range. The uncertainties of the input parameters for wetting are shown in Table 4 and Table 5.

Table 4 – Uncertainty of Input Parameters for CFB Wetting – Type 1 BC

Parameter	**Base Value**	**Max Uncertainty**	**1 Std Dev**
Surface Saturation	0.99	± 0.01	± 0.0033
Cap Press Coeff 1	0.4	± 0.04	± 0.0133
Permeability	$5\times10^{-11} m^2$	$\pm\ 2\times10^{-11} m^2$	$\pm\ 0.66\times10^{-11} m^2$
Porosity	0.8	± 0.05	± 0.0166
Liq Rel Perm	$K_{rl} = S_{eff}^3$	± 1	± 0.333
Cap Press Coeff 2	0.364	± 0.073	± 0.0243

Table 5 – Uncertainty of Input Parameters for CFB Spray Wetting

Parameter	Base Value	Max Uncertainty	1 Std Dev
Porosity	0.8	± 0.05	± 0.0167
Water flux	Test 1 - 0.104 kg/m^{2}s Test 2 - 0.128 kg/m^{2}s Test 3 - 0.188 kg/m^{2}s	± 10%	± 3.33%
Liq Rel Perm	$K_{rl} = S_{eff}^3$	± 1	± 0.333

The maximum uncertainties of the inputs for the four heating validation cases are shown in Table 6 through Table 9.

Table 6 – Uncertainties of Parameters for Particulate Media Drying

Parameter	Base Value	Uncertainty	1 Std Dev
Ambient Temp	321K	± 1K	± 0.33K
Initial Saturation	0.915	± 0.015	± 0.005
Heat Trans Coeff	57.7 W/m^2K	± 5.77 W/m^2K	± 1.92 W/m^2K
Relative Humidity	33%	± 2%	± 0.66%
Initial Temp	289.9K	± 1K	± 0.33K

Table 7 – Uncertainty of Input Parameters for Brick Drying

Parameter	Base Value	Uncertainty	1 Std Dev
Ambient Temp	80^{o}C	± 2 ^{o}C	± 0.66
Initial Temp	25^{o}C	± 2^{o}C	± 0.66
Heat Trans Coeff	f(S)	± 10%	± 3.33
Initial Saturation	0.56	± 0.056	± 0.0187
Length	0.05m	± 0.001	± 0.000333
Liq. Rel. Perm. Coeff	4	± 1	± 0.333

Table 8 – Uncertainty of Input Parameters for Wood Drying

Parameter	Base Value	Max Uncertainty	1 Std Dev
Ambient Temp	40°C	$\pm 2^o C$	$\pm 0.66^o C$
Initial Temp	10°C	$\pm 2^o C$	$\pm 0.66^o C$
Heat Trans Coeff	$92.5 W/m^2 K$	$\pm 15 W/m^2 K$	$\pm 5 W/m^2 K$
Initial Saturation	0.99	± 0.02	± 0.0066
Porosity	0.61	± 0.0305	± 0.0101
Length	0.019m	± 0.01	± 0.0033

Table 9 - Uncertainty of Input Parameters for CFB Heating Tests

Parameter	Base Value	Max Uncertainty	1 Std Dev
Initial Saturation	Test 1 - 0.3 Test 2 - 0.5 Test 3 - 0.7	± 0.043 ± 0.070 ± 0.099	± 0.0143 ± 0.0233 ± 0.033
Radiant Heat Flux	20kW/m^2	± 1kW/m^2	± 0.333 kW/m^2
Surface Emissivity	0.96	± 0.02	± 0.0667
Length	0.0254m	± 0.00151m	± 0.000503
S_{ir}	0.15	± 0.015	± 0.005
Porosity	0.8	± 0.85	± 0.0167
Liq. Rel. Perm. Coeff	3	± 1	± 0.333

To calculate the effect of uncertainty of the input parameters on the model output, an uncertainty analysis was performed. The model output for each validation case with the base values of all parameters was taken as the base case output. Then individual simulations were performed while adjusting the input parameters one at a time by plus or minus one standard deviation. The combined standard uncertainty for each model output can be expressed as [51]

$$u_c^2(y) = \sum_{i=1}^{N} \left(\frac{\partial f}{\partial x_i} \right)^2 u^2(x_i) \quad (48)$$

,

where the model output, y, is represented as $y = f(x_1, x_2, .., x_i, ...x_n)$, $u_c(y)$ is the combined standard uncertainty of y, and $u(x_i)$ is the uncertainty of input parameter xi. Since the model obtains numerical solutions to the governing equations, the Eq. (48)

is approximated as

$$u_c^2(y) = \sum_{i=1}^{N} \left(\frac{\Delta y}{\Delta x_i} \right)^2 (\Delta x_i)^2 = \sum_{i=1}^{N} (\Delta y)^2 \quad (49)$$

This was used to calculate a reasonable error band for each of the validation cases. This error band represents the sum of the uncertainties associated with adjusting each of the most important input parameters by one standard deviation. The combined standard uncertainty was calculated at discrete points in time and space to provide the error bars for the validation figures. The complete details of the uncertainty analysis are given in Appendix H.

6. Model Validation

A series of model validation tests were conducted using experimental data for wetting and heating. Convective heating data was gathered from the literature, but little data is currently available for spray wetting of materials and radiant heating of wet materials. For these cases experiments were performed in the WPI Fire Science Lab. The complete details of all validation work are given in Appendix F.

6.1. Ceramic Fiberboard Parameter Estimation

Ceramic fiberboard (CFB) was chosen as a test material for the wetting tests. CFB was chosen because it is hydrophilic, inert, and on the macro level it is isotropic and homogeneous. The CFB was a Kaowool M-Board manufactured by Thermal Ceramics. The material was purchased in 2' by 3' sheets of 1" and 2" thicknesses, which were then cut into smaller samples for the tests. The CFB was determined to be 80% porous by weighing a 6" by 6" by 2" sample in its dry and completely wet state. Correlations for the capillary pressure, relative permeabilities, and vapor pressure are required as model inputs. Experimentally determined correlations for capillary pressure are provided in the literature for a number of materials [23], but none are available for any fiberboard product. A series of experiments were conducted in the WPI Fire Science Laboratory to determine an expression for the capillary pressure in CFB. The method is described by Youngs [52] for tests using sectioned tubes of particulate media. Here the same process is used with a solid material. Details are given in Appendix F.

The experiments were conducted using a sample of CFB that initially measured 2" by 3" by 24". This larger sample was cut into 24 smaller samples that measured 2" by 3" by 1". Three tests were conducted on these samples in two different configurations. Two tests were conducted with stacks of 12 of the CFB samples, and one test was conducted using all 24 samples. The columns were placed in a shallow pan of water that was maintained at a depth of approximately 1cm. The samples were allowed to sit for 24 hours while capillary action drew water into the columns. The interface between individual samples where the CFB was cut was observed to significantly slow the transfer of liquid water. For this test the samples were left for a long period until equilibrium was reached, so this resistance is believed to be negligible. After 24 hours the saturation profile in the columns was determined by weighing the individual samples. The capillary pressure in each sample was determine by observing that it must be equal to the hydrostatic pressure, $\rho_w gh$, associated with the height of the sample, h, above the water source. This data was used to determine the capillary pressure as a function of saturation and is shown in Figure 9.

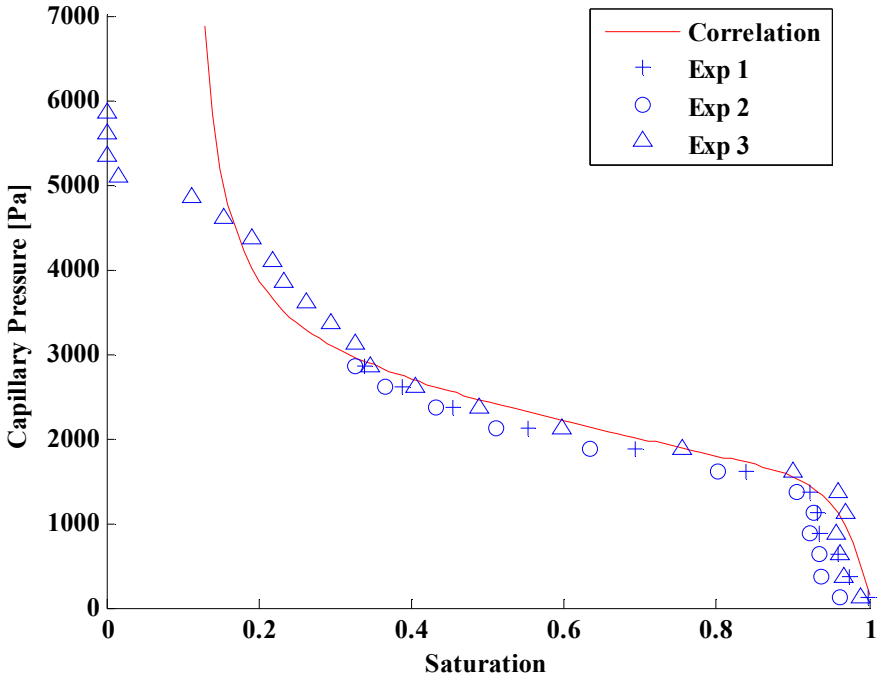

Figure 9 – Capillary Pressure in Ceramic Fiberboard as a Function of Saturation

Using this experimental data and Eq. (2) the J-Function for CFB was determined to be:

$$J(S) = 0.4\left[0.364\left(1-\exp\left(-30\left(1-S\right)\right)\right)+0.471\left(1-S\right)+\frac{0.035}{S-0.1}\right] . \quad (50)$$

Eq. (50) was determined by adjusting the coefficients of Eq. (3) until good agreement was observed with the experimental data. The relative permeabilities of CFB are assumed to obey cubic functions of saturation [23]:

$$K_{rl} = S_{eff}^3 , \quad (51)$$

$$K_{rg} = \left(1-S_{eff}\right)^3 . \quad (52)$$

Where S_{eff} is the effective saturation and varies between 0 and 1:

$$S_{eff} = \frac{S_w - S_{ir}}{1-S_{ir}} \quad for\ S > S_{ir} , \quad (53)$$

$$S_{eff} = 0 \quad for\ S < S_{ir} .$$

When the saturation is below the irreducible saturation, S_{ir}, water in the material is in non-interconnected pockets, and cannot flow. For CFB, S_{ir} is determined to be 0.15 based on the experiments shown in Figure 9. The Capillary pressure correlation takes on unreasonable values below this value, and contains a singularity at S=0.1. The relative permeability has a value of 0 for saturation values below the irreducible saturation, so the unreasonable behavior of the capillary pressure correlation has no effect.

The vapor pressure in the CFB is assumed to obey Eq. (9). To test this, a series of experiments were conducted to measure the saturation of samples of CFB at equilibrium in atmospheres of varying relative humidity. Samples of CFB measuring 2" by 3" by 1" were sealed in a Tupperware container with the relative humidity inside increased or decreased from the ambient value of ~60% in the lab. The relative humidity was controlled by placing either a damp paper towel or a pan containing a small amount (~1g) of Dri-Rite dessicant in the container with the CFB sample. For each test, the relative humidity in the container was measured using an Omega RH411 Thermo-Hygrometer. The dry mass of the samples was determined by placing them in

a Tupperware container for 24 hours with 100 g of Dri-Rite. The samples were weighed after 24 hours. The saturation was calculated from the mass at equilibrium and the completely dry mass. The relative humidity predicted by the sorption relation for brick by Eq. (9) and the experimental data for CFB are shown in Figure 10. Sorption relations are commonly expressed as relative humidity or vapor pressure as a function of saturation or moisture content. Eq. (9) cannot be expressed in this manner due to the exponential function, but is plotted as such in Figure 10.

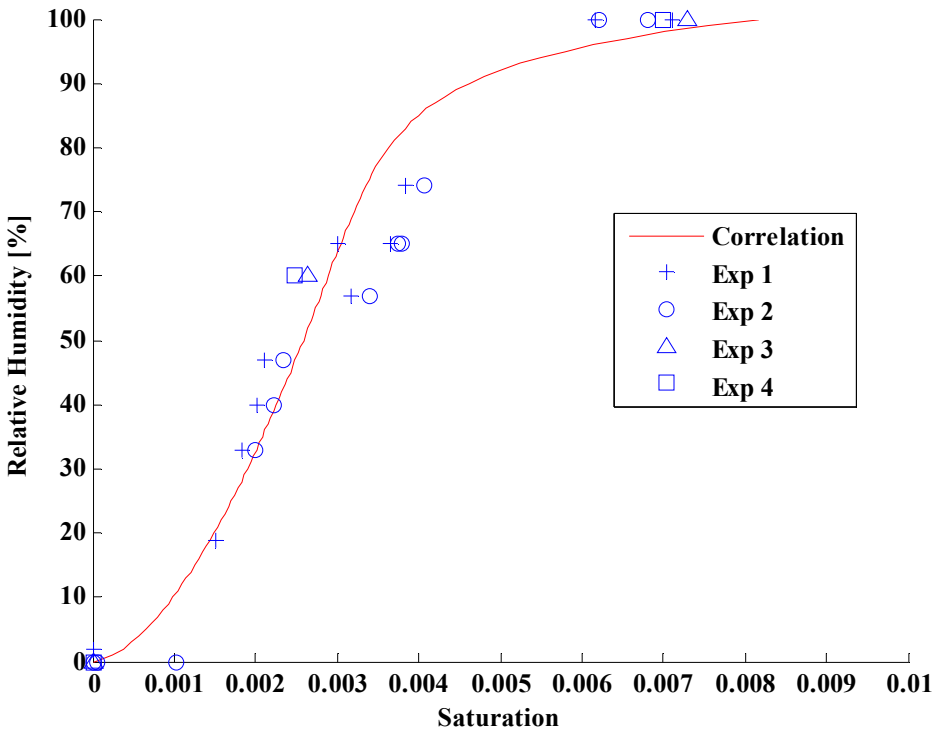

Figure 10 – Relative Humidity vs Saturation at Equilibrium in Ceramic Fiberboard at 22^0C

6.2. Wetting Validation

Wetting tests were conducted using samples of CFB that measured 2” by 3” by 6” and rates of water absorption were measured. For all wetting tests, the 6” sides of the CFB blocks were sealed with silicone caulking and oriented so that the smaller unsealed edges faced up and down. When the blocks had to be reused, they were allowed to dry until they returned to their initial dry mass. The water that enters the CFB is assumed to form a saturation profile with a sharp transition, or wetting front, where the material transitions from wet to completely dry material over a short

distance. This assumption is supported by model predictions, and visual observations of the wetted material. A method for determining the location of this wetting front was developed using resistance probes. The probes consist of two 1" long 13 gauge nails as terminals that are inserted into the material at 5 locations. The resistance between the two terminals of each probe is measured using a National Instruments data acquisition system that consists of a SCXI 1001 multiplexor, SCXI 1181 module, and SCXI 1301 terminal block. A sudden drop in resistance between the terminals is observed when the wetting front reaches the probe location. This method was used for all wetting tests to determine the wetting front location as a function of time. Water was applied in two ways: by placing one unsealed face of the sample in contact with a reservoir of water (type 1 boundary condition), or by applying a water spray to one end of the sample (type 2 boundary condition).

For the type 1 boundary condition tests, water was applied to the top and bottom of the CFB samples so that the surface being wetted was completely saturated. For the bottom wetting tests, this was accomplished by placing the sample in a wide shallow pan of water that was maintained at a depth of 1 cm. For the top wetting tests, a pan with a 1.75" by 2.75" hole was attached to the top of the sample, so that the hole covered the unsealed top end of the sample. Silicone caulking was used to seal the edges, so that no water was allowed to leak between the pan and the sample. Water was poured into the pan and maintained at a depth of no greater than 1cm, to minimize the effects of hydrostatic pressure from the water. Seven wetting tests were conducted in this manner; 4 bottom wetting tests, and 3 top wetting tests. The model was used to predict the behavior under similar wetting conditions. The boundary and initial condtions used for the model simulations are given by Eqs. (21)-(29). The ambient temperature was 295K, the initial saturation was 0.004, and a surface saturation of 0.99 was specified. The surface saturation condition of 0.99 was chosen for three reasons: the model cannot accept a saturation value of 1 due to numerical instabilities, the material is assumed to have some very small pores that are inaccessible to water penetration, and 0.99 gives good agreement with experimental results. The wetting front was determined from the model output as the location where the saturation had increased from the initial value by 0.05. The experimental data for this wetting scenario was used to determine the permeability of the material. Since the permeability is also an unknown in the capillary pressure calculation, several modeling iterations were required. The ceramic fiberboard was determined to have a permeability of $5\times10^{-11}m^2$ by adjusting the permeability in the model until good agreement was

observed between the model predictions and experimental results for capillary rise tests and Type 1BC wetting tests. This value for permeability was then used for the modeling of the spray wetting tests and radiant heating tests. The results of experimental wetting tests and model predictions are shown in Figure 11.

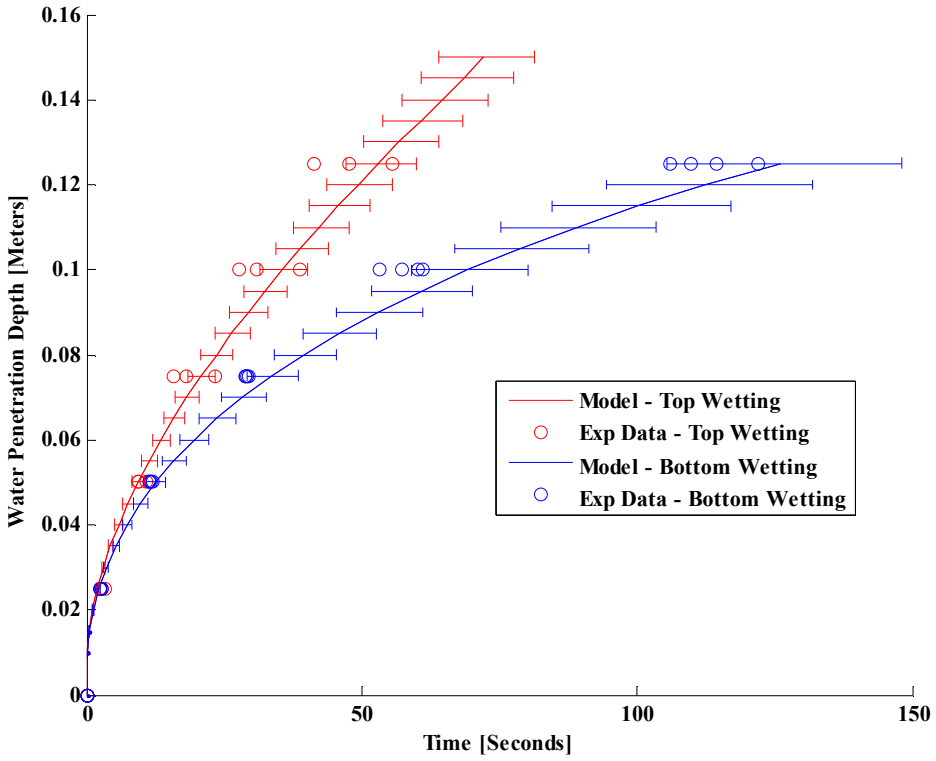

Figure 11 – Water Penetration Depth as a Function of Time for Wetting of Ceramic Fiberboard Using Type 1 Boundary Condition

The difference between the top wetting and bottom wetting scenarios, as observed in the model and experimental results, is due to the effects of gravity. The water penetration depth for both scenarios follows an approximate time to the half power trend. The model is able to match this behavior qualitatively and quantitatively. The model results do exhibit a fair amount of uncertainty, mostly due to the surface saturation value chosen. At saturations close to one, the capillary pressure and relatively permeability are extremely sensitive to the saturation. This behavior is similar to that of particulate media, as shown in Figure 3 and Figure 4. Spray wetting tests were conducted at three water flow rates. The water was delivered by means of a water mist nozzle mounted 41.5” above the surface of the sample. The water flow rate

was controlled by using a needle valve to adjust the pressure at the nozzle, which was monitored using a pressure gauge. Tests were conducted with a nozzle pressure of 5, 10, and 20 psig. Independent tests were conducted to measure the water mass flux delivered to the horizontal plane at the level of the surface of the sample prior to the wetting tests. This was accomplished by using a grid of square water collection tubes. The average water mass fluxes were determined to be 0.104, 0.128, and 0.188 kg/m^{2}s at pressure values of 5, 10, and 20 psi at the nozzle. The moisture sensor probes inserted in 5 locations to monitor the location of the wetting front. Boundary conditions for the model simulations are given for the surface by Eqs. (26), (31), (33), and for the back face by Eqs. (35), (37), and (39). No overflow was observed on the top surface during the experiments. The initial saturation was 0.004, the ambient temperature was 295K, and the three measured water spray mass fluxes were used for separate tests. The experimental results and model predictions are shown in Figure 12.

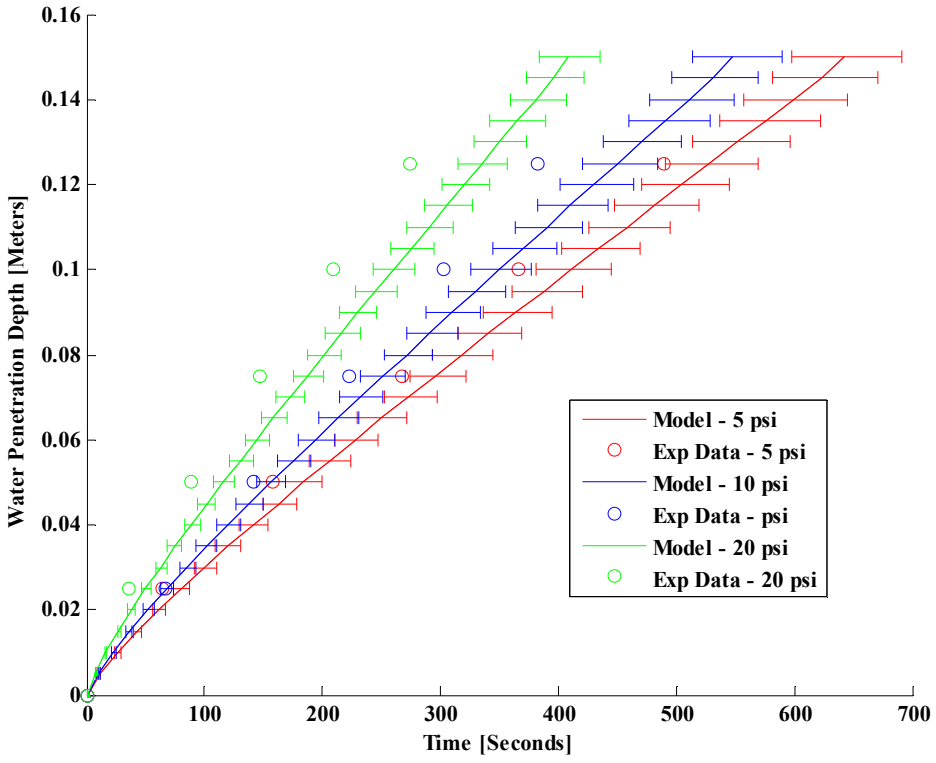

Figure 12 – Water Penetration Depth as a Function of Time for Spray Wetting of Ceramic Fiberboard

The experimental data approximately follows a linear trend for water

penetration depth vs. time which is matched qualitatively by the model. The model under-predicts the water penetration depth for each applied water flux. It is possible that the correlations used for CFB are not accurately characterizing the materials behavior at lower saturations. For this scenario the predicted saturation values are lower than those from the Type 1 boundary condition wetting case. For all three water mass fluxes the model predicts that the surface saturation remains below 0.8. The discrepancy between the model predictions and experimental results in Figure 12 could be explained by issues with the relative permeability correlation and capillary pressure not fully capturing the behavior of CFB at low saturation values.

6.3. Heating Validation

The thermal transport processes of the model were validated using data for convective heating of particulate media [53], brick [54], and wood [55] [56] [45], and radiant heating tests using CFB. The radiant heating tests will be discussed in detail, due to their applicability to fire ignition phenomena. The material properties and experimental conditions for all of the heating validation tests are given in Table 10.

Table 10 – Model Inputs for Heating Validation Tests

	Quartz Particles	Brick	Wood	CFB
Solid Density, ρ_s [kg/m^3]	2610 [53]	2566 [39]	1500 [57]	1355 [58]
Therm Cond, k [W/mK]	1.4 [43]	0.885 [39]	0.377 [57]	0.117 [58]
Specific Heat, C_p [J/kgK]	780 [43]	750 [39]	2800 [57]	1046 [58]
Porosity, ϕ	0.46 [53]	0.435 [39]	0.61 [56]	0.8 [58]
Permeability, K [m^2]	3.75×10^{-11} [58]	5×10^{-14} [25]	2×10^{-16} [59]	5×10^{-11} [58]
Initial Saturation, S_o	0.915 [53]	0.56 [39]	0.99 [56]	0.3,0.5,0.7 [58]
Irr. Saturation, S_{ir}	0.1 [58]	0.09 [40]	N/A	0.15 [58]
Initial Temp, T_o [K]	298 [53]	298 [39]	289 [56]	295 [58]
Amb. Temp, T_∞ [K]	321 [53]	353 [39]	313 [56]	295 [58]
Rel. Hum, RH_∞ [%]	33 [53]	9.3 [39]	5 [56]	20 [58]

Particulate Media Heating

Convective drying tests were conducted by Lu et al. [53] with a bed of quartz particles. Particles with a diameter of 1-1.5mm were placed in a cylindrical bed 45mm

in diameter, and 15mm deep that was flush mounted in the floor of a heated wind tunnel. The surface heat and mass transfer coefficients were determined to be 43W/m^{2}K and 0.0723 m/s. The sample had an initial moisture content of 0.3 kg/kg. The total mass loss rate was measured using a digital balance. Thermocouples were placed 0, 6, 8, 10, and 12 mm from the bottom surface. The capillary pressure is given by Eq. (3), and relative permeabilities are given by Eqs. (51)-(53). The effective diffusivity of the media is given by Eq. (6). The sorption relation for brick, given by Eq. (9), is used to calculate the vapor pressure. The model simulations were performed using 16 nodes and an adjustable time step that drops from 1 second to 0.1 seconds when the surface saturation drops below the irreducible saturation. The experimental data from Lu et al. [53] and model predictions are shown in Figure 13 and Figure 14. The model is shown to have reasonably good agreement with the experimental data.

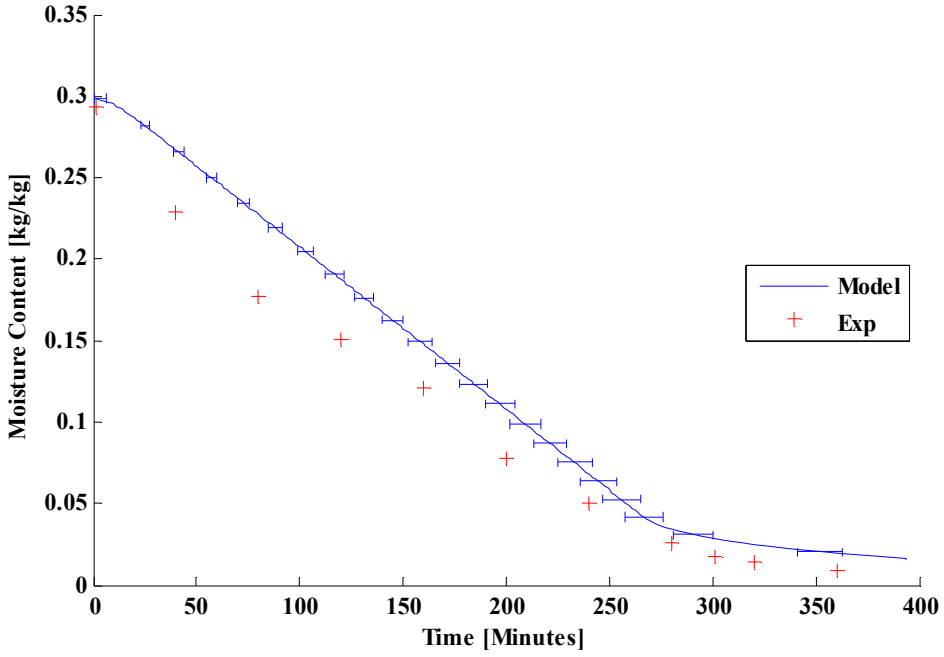

Figure 13 – Total Sample Moisture Content as a Function of Time for Convective Heating of Particulate Media

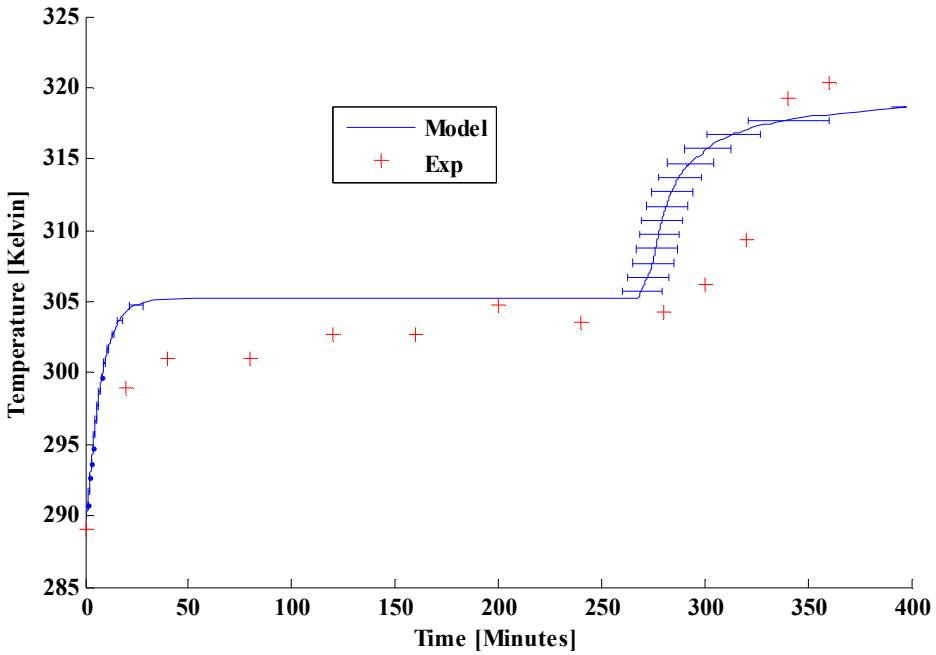

Figure 14 – Temperature at 2mm Depth as a Function of Time for Convective Heating of Particulate Media

The model predicts that the particulate media is at approximately 305K from 50 to 270 minutes. This is the wet bulb temperature for the drying conditions of the test. During this time, evaporation occurs at the surface, lowering the saturation at the surface, and drawing water to the surface by means of surface tension forces. After 270 minutes the surface saturation drops below the irreducible saturation, and water is no longer transported to the surface by capillary action. This causes the surface saturation to rapidly approach zero, and as this happens the vapor pressure at the surface is limited by the vapor pressure correlation. The resulting decrease in vapor pressure results in a decrease in evaporative cooling at the surface, and a jump in temperature, as observed in Figure 14. When the surface is below the irreducible saturation, moisture is only transported to the surface by means of vapor phase diffusion. This results in an abrupt change in the slope of the mass vs. time curve (decrease in mass loss rate), as shown in Figure 13. The model seems to under-predict the rate of mass loss, and over-predict the temperature of the particulate media until close to the end of the experiments. This could be due to errors associated with the calculation of the heat transfer coefficient or simply a case of physical phenomena not being completely captured by the model. In this case, the assumption that no vapor escapes from inside the material is possibly

being violated. Lu et al. [53] give an experimental uncertainty of 0.1% for their temperature measurements. This does not address the repeatability of the tests. Tests conducted with ceramic fiberboard exhibit a large degree of variation between virtually identical tests. For this reason, it is suspected that the experimental data from Lu et al [53] could have a similar experimental uncertainty to the CFB heating tests that will be discussed later.

Brick Heating

Convective drying tests with brick slabs were conducted by Przesmycki and Strumillo [54]. Data for the experimental conditions is provided by Chen and Pei [39] and properties for brick are given in Table 10. The experiment was conducted by placing a brick sample in a convective drying environment where mass loss and temperature at 6 locations was measured. The brick sample had a surface area of 20 cm^2 and a thickness of 5 cm. The surface heat and mass transfer coefficients are assumed by Chen and Pei [39] to obey empirical correlations developed for convective drying:

$$h = 75\left(0.8 + 0.2\frac{M_{surf} - 0.015}{0.09 - 0.015}\right), \tag{54}$$

$$h_m = 0.083\left(0.1 + 0.9\frac{M_{surf} - 0.015}{0.09 - 0.015}\right), \tag{55}$$

where M_{surf} is the surface moisture content. The capillary pressure and relative permeabilities of sandstone given by Kaviany [23] are assumed to characterize the brick:

$$p_c = \frac{\sigma}{\sqrt{K/\phi}}\left[0.3 - 0.0663\ln\left(S_w - S_{ir}\right)\right], \tag{56}$$

$$K_{rl} = S_{eff}^4, \tag{57}$$

$$K_{rg} = \frac{\left(1 - S_{eff}\right)^2}{\left(1 - S_{eff}^2\right)} \tag{58}$$

.

The effective diffusivity is given by Eq. (6). Model simulations were conducted with 26 nodes and a time step of 1 second. The model predictions in Figure 15 show good agreement with the experimental mass loss rate. The internal temperature at 0.1, 1, 3.5, and 9.5 hours is shown in Figure 16 and the surface temperature over the entire simulation is shown in Figure 17. The overall agreement between the model and experimental results is good. The model predicts that the surface saturation falls below the irreducible saturation around 0.75 hours. After this occurs, the only means of moisture transport to the surface is by gas phase diffusion. The temperature profile develops an abrupt change in slope at the location where the saturation is equal to the irreducible saturation. This can be seen in Figure 16 at 3.5 and 9.5 hours.

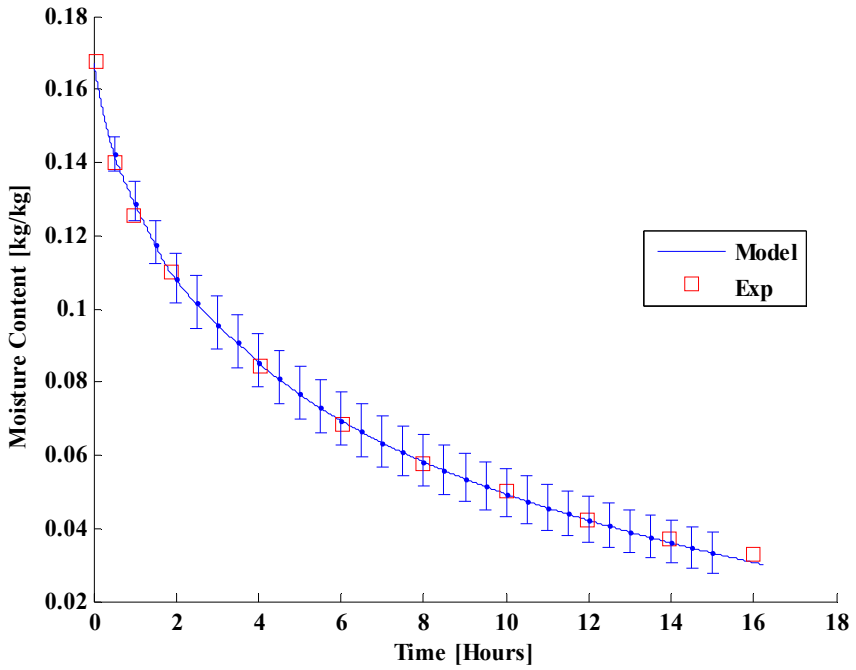

Figure 15 – Total Sample Moisture Content as a Function of Time for Convective Heating of Brick

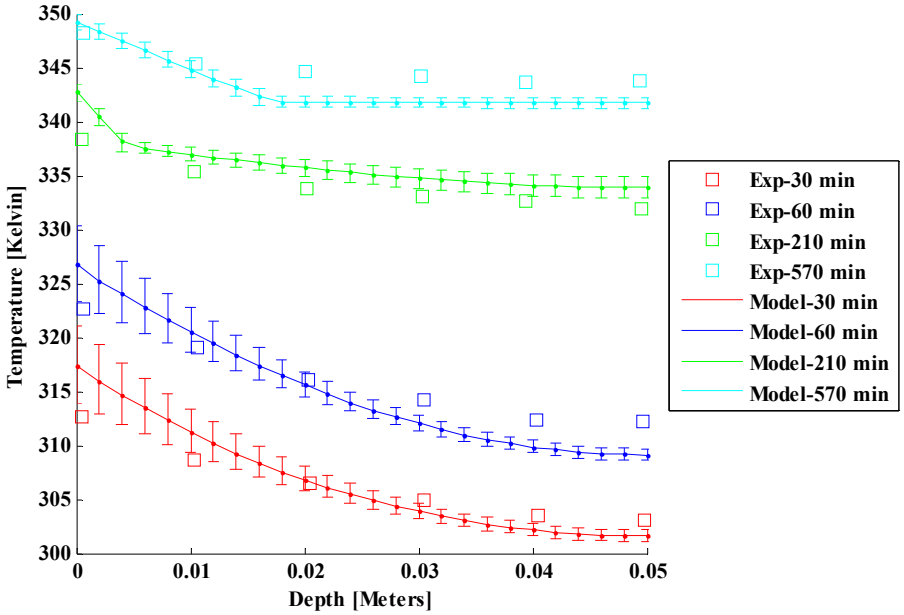

Figure 16 – Internal Temperature as a Function of Depth for Convective Heating of Brick

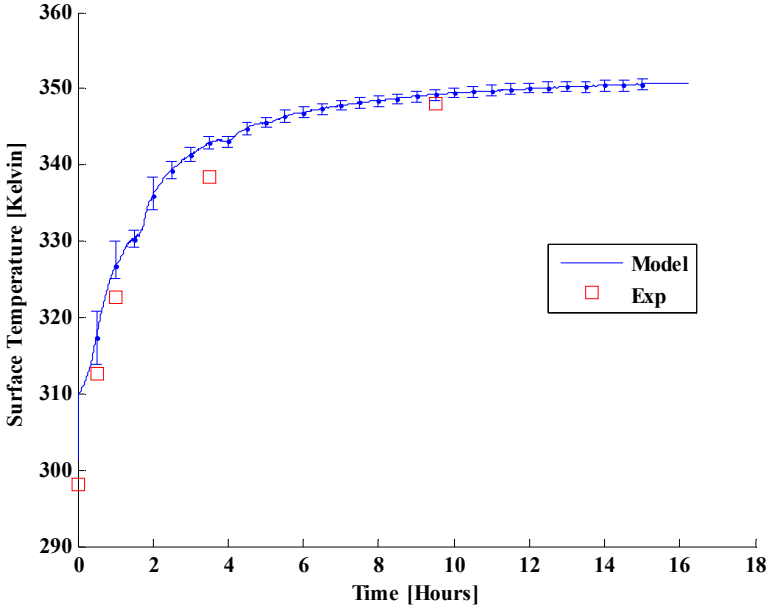

Figure 17 – Surface Temperature as a Function of Time for Convective Heating of Brick

In this case there is no sudden jump when the surface dries out as was observed in the case of particulate media. The brick surface dries out much more gradually, and sample mass goes down at a gradually decreasing rate as shown by both the experimental and model results in Figure 15. This is caused by the surface heat and mass transfer coefficients' dependence on surface moisture content. As the surface becomes dry, the rate of heat and mass transfer is reduced, according to Eqs. (54) and (55), and the surface vapor is reduced according to Eq. (9). As the surface vapor pressure is reduced, gas-phase diffusion draws vapor to the surface, increasing the evaporation rate below the surface. The model predicts a saturation profile that transitions rapidly from dry to wet and is marked by an abrupt changes in the slope of the internal temperature. This is observed in the predicted temperature profiles at 210 and 570 minutes shown in Figure 16. The experimental data shown in Figure 16 does not exhibit the same sharp changes of slope of temperature that the model predicts. It appears that the brick exhibits a more smooth transition from wet to dry, and as a result flatter temperature profiles, as evidenced by the data in Figure 16.

Wood Heating

Plumb et al. [55, 56] ran drying experiments using samples of southern pine. In these experiments, temperature and moisture content were measured at various locations in the material during the drying process. The wood samples measured 3.8 cm thick by 8.9 cm wide and 45 cm long. The samples were stored submerged in water until just before the test was initiated to ensure a saturation as close to one as possible. The test was conducted in a heated wind tunnel where the ambient air was 40^{o}C and at a relative humidity of 5%. The sample was mounted so that the two 8.9 cm by 45 cm sides of the sample were exposed to the heated stream of air. The other edges were sealed and insulated. The surface heat and mass transfer coefficients are determined to be 92.5 W/m^{2}K and 0.099 m/s. The properties of wood are given in Table 10. Half of the sample was modeled by assuming a line of symmetry across the center, with no-flux boundary conditions at the central plane of the model domain. Convective heating and drying conditions are used for the front face. The evaporation rate is determined from experimental results to be [56]

$$\dot{m}''_{evap} = \beta^3 h_m \left(\rho_{v,surf} - \rho_{v,\infty} \right) . \tag{59}$$

Where the surface drying coefficient, β, is defined as

$$\beta = \frac{M_{surf} - EMC}{M_{\max} - EMC}, \tag{60}$$

where M_{surf} is the moisture content (kg/kg) at the surface, M_{max} is the maximum possible moisture content, and EMC is the equilibrium moisture content. For this test M_{max} is 1.34 and the EMC is assumed to be zero. The capillary pressure in wood is given by Spolek and Plumb [45] to be

$$p_c = 1.24 \times 10^4 S^{-0.61}. \tag{61}$$

Relative permeabilities for wood are given by [56] to be

$$K_{rl} = S_{eff}, \tag{62}$$

$$K_{rg} = 0.05\left(1 - S_{eff}\right). \tag{63}$$

The relative humidity in wood is given by Nasrallah and Perre [38] to be

$$p_v = p_{vs} \exp\left(\left(17.884 - 0.1423T + 0.0002363T^2\right)\left(1.0327 - 0.000674T\right)^{92M}\right). \tag{64}$$

The effective gas diffusivity of wood can be modeled as [60]

$$D_{eff} = D_{va} \frac{K_{rg}}{45}. \tag{65}$$

This validation case is problematic because wood is a hygroscopic material and the model cannot handle hygroscopic behavior. For this reason the model is only appropriate for wood early in the drying process when liquid water is present in the pore spaces. Wood fibers absorb water which becomes chemically bound to the hydroxyl groups of the cellulose [61]. The maximum amount of water that can be

absorbed into the wood fibers in this manner is called the fiber saturation point. Siau [60] gives the fiber saturation point as 0.3 kg/kg. Below the fiber saturation point, all of the moisture is contained in the solid fibers and the current model is not appropriate. The model simulation was terminated when the surface moisture content dropped below this value. Model simulations were conducted with 31 nodes and a time step of 10 seconds. The predicted spatial moisture content profile and experimental results for 0 min, 180 min, and 780 min for wood are shown in Figure 18. The variations in the experimental data points are due to variations in the density of the wood due to seasonal growth rings. The predicted mass loss rate and experimental data points are shown in Figure 19. The model predicted surface temperature and experimental data points are shown in Figure 20.

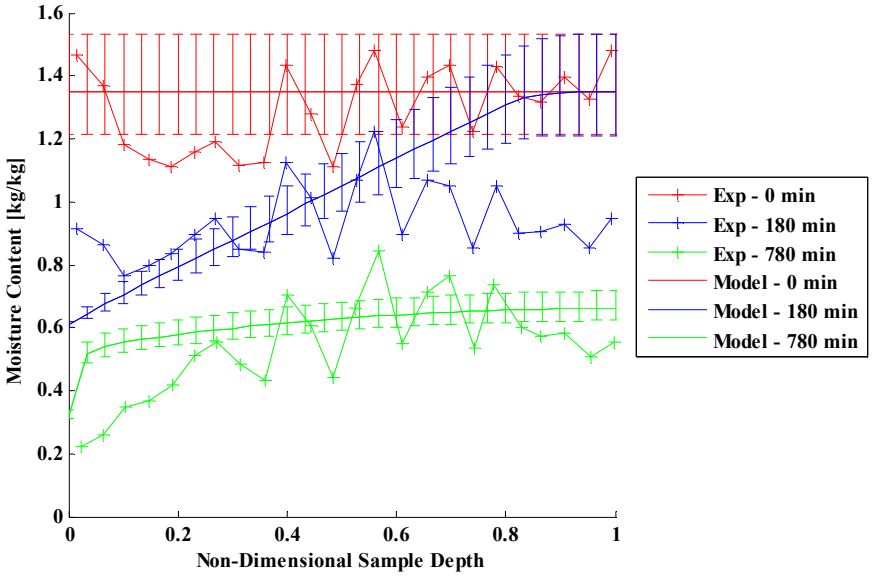

Figure 18 – Moisture Content as a Function of Non-Dimensional Sample Depth at Three Times for Convective Heating of Wood

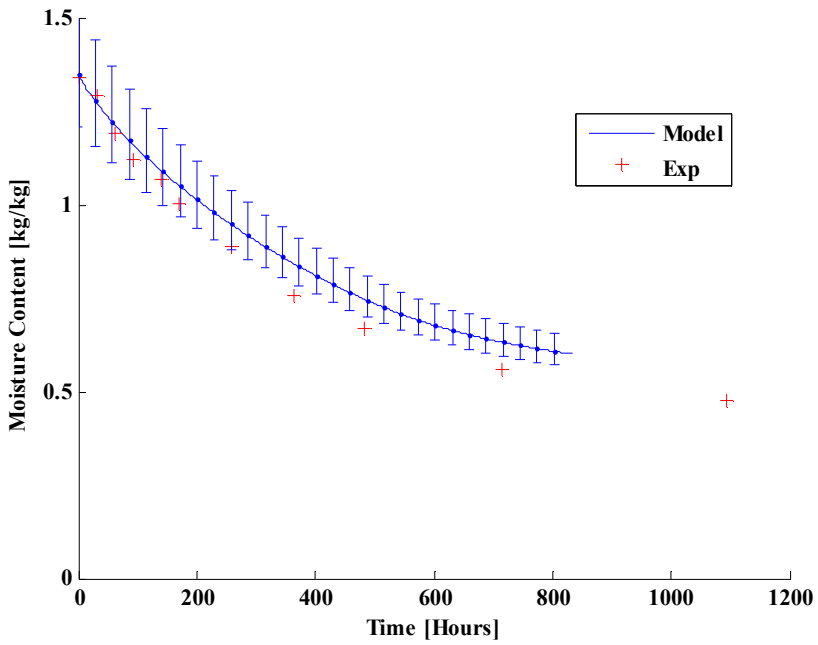

Figure 19 – Total Sample Moisture Content as a Function of Time for Convective Heating of Wood

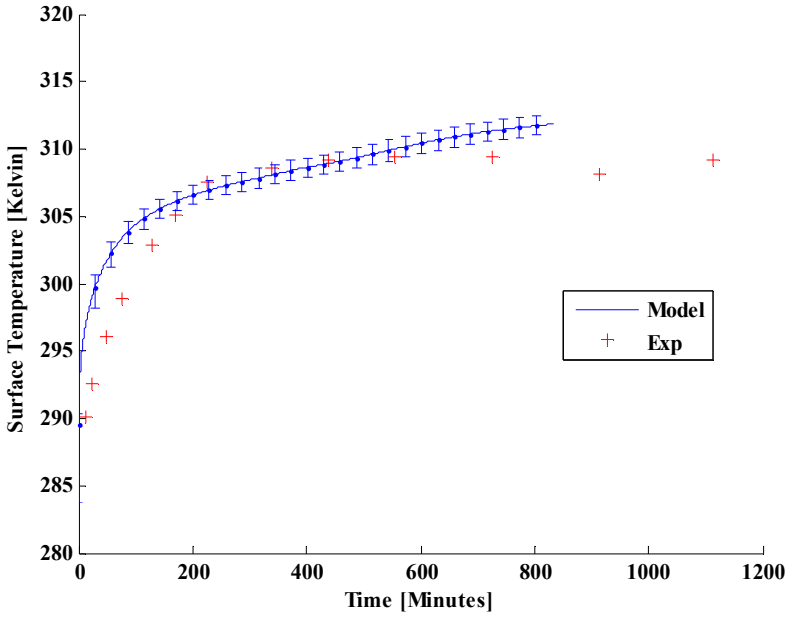

Figure 20 – Surface Temperature as a Function of Time for Convective Heating of Wood

The moisture content profiles in Figure 18 show that the model is under-predicting the internal rate of moisture movement early in the drying process. Model simulations were conducted which show that the internal moisture profiles for wood are a strong function of the effective diffusivity correlation used. These are discussed in Appendix F. There exists little data on alternative empirical correlations, and this parameter was not optimized for this investigation. Wood samples also exhibit a large degree of variation in the measured permeability [60] and the measured capillary pressure [45], which might explain some of the discrepancies between the model and experimental results. The model does not account for the hygroscopic, non-homogeneous, and non-isotropic nature of the wood. Movement of bound water, which is not included in the model, could account for the divergence of the predicted and observed mass and temperature towards the end of the simulation, as shown in Figure 19 and Figure 20. Despite these factors, the predicted sample mass and temperature shown in Figure 19 and Figure 20 give very good qualitative agreement with the experimental results, and the quantitative agreement is reasonable. This case should be considered to be an extreme case, perhaps the limit of what the model, in its current capacity, can handle.

CFB Heating

Radiant heating tests using wet ceramic fiberboard samples were conducted in the cone calorimeter in the WPI Fire Science Lab. Details are given in Appendix F. The samples were 4" by 4" by 1" thick (0.102m by 0.102 m by 0.0254m). Temperatures were measured at the surface and at the center of the sample (1/2" depth). The surface temperature was measured using a bare bead thermocouple that was gently inserted about 0.5-1.0 mm into the surface of the CFB, just deep enough to remain in place for the duration of the test. During one test the surface thermocouple became detached from the surface. The centerline temperature was measured by inserting a 40 gauge sheathed thermocouple probe into the sample horizontally. The sample was insulated on the edges and back face with 1" thick Kaowool blanket insulation manufactured by Thermal Ceramics. The sample with insulation was placed on the cone calorimeter load cell to measure mass loss from evaporation. The experimental set up is shown in Figure 21. Three sets of heating tests were conducted with an imposed radiant heat flux of 20 kW/m^2. Tests were conducted at three initial saturation values. Seven tests were conducted with an initial saturation of 0.3, seven tests were conducted with an initial saturation of 0.5, and four tests were conducted at an initial saturation of 0.7. The initial saturation was achieved by adding a known mass of water to the samples. Eight different samples of CFB were used, some of which were re-used for multiple heating

tests. The samples were allowed to cool down for several hours between tests before being re-used. Any residual water in the samples was accounted for by weighing the samples before and after every test.

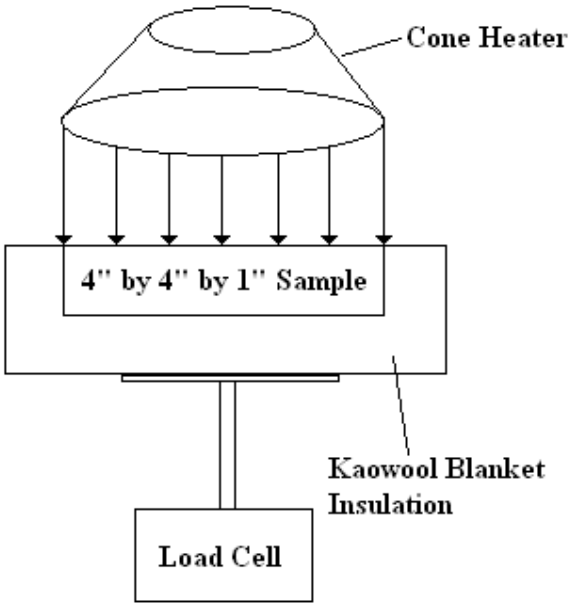

Figure 21 – Experimental Set up for CFB Heating

The bulk properties provided by Thermal Ceramics were used to determine properties of the solid phase of the CFB. The solid density is 1355 kg/m^3, the specific heat of the solid is 1046 J/kgK, and the thermal conductivity of the solid is 0.117 W/mK. The emissivity of CFB is assumed to be 0.96, which is the measured value for asbestos board [62]. The capillary pressure is given by Eq. (50), relative permeabilities are given by Eqs. (51)-(53), and the vapor pressure is given by (9). The surface heat and mass transfer coefficients are calculated from correlations for free convection on a flat plate. The heat transfer coefficient, h, is typically calculated from the Nusselt number [57],

$$\overline{Nu} = \frac{hL}{k} = 0.54 Ra_h^{1/4} \quad for\ 10^5 < Ra_h < 10^7 \tag{66}$$

,

Where the heat transfer Rayleigh number, Ra_h, is the product of the heat transfer Grashof number, Gr_h, and the Prandtl number, Pr,

$$Ra_h = Gr_h \,\mathrm{Pr} = \frac{g\beta_h \left(T_s - T_\infty\right) L^3}{\nu^2} \frac{\nu}{\alpha} \,. \tag{67}$$

The mass transfer coefficient, h_m, is typically calculated from the Sherwood number,

$$\overline{Sh} = \frac{h_m L}{D} = 0.54 Ra_m^{1/4} \quad for\ 10^5 < Ra_m < 10^7 \quad , \tag{68}$$

where the mass transfer Rayleigh number is the product of the mass transfer Grashof number and the Schmidt number,

$$Ra_m = Gr_m Sc = \frac{g\beta_m \left(\rho_s - \rho_\infty\right) L^3}{\nu^2} \frac{\nu}{D} \,. \tag{69}$$

The convective flows above a wet heated surface must account for the driving forces arising from both thermal and species diffusion. If the Schmidt number is equal to the Prandtl number, the problem reduces to a single buoyancy effect [63]. In this case the total Rayleigh number is calculated by summing the heat and mass transfer Grashof numbers:

$$Ra = \left(Gr_h + Gr_m\right) \mathrm{Pr} \,. \tag{70}$$

The heat and mass transfer coefficients are calculated in the model by substituting Eq. (70) for the heat and mass transfer Rayleigh numbers in Eqs. (66) and (68). The properties of air are calculated at the film temperature, $T_{film} = 0.5\left(T_{surf} + T_\infty\right)$. This method produces a surface heat transfer coefficient between 10 and 15 W/m^{2}K and a mass transfer coefficient between 0.01 and 0.02 m/s. The model simulations used 26 nodes and a variable time step that dropped from 1 second to 0.001 seconds when the surface saturation dropped below the irreducible saturation.

For tests at each of the three initial saturations the model predicts the surface temperature rising initially to the wet bulb temperature, where it remains approximately constant as long as the surface of the material is wet. As the predicted surface saturation approaches the irreducible saturation, the relative permeability approaches zero according to Eq. (51), water flow to the surface by means of surface tension forces is choked off, and the surface saturation drops rapidly. As the surface

saturation approaches zero the surface vapor pressure is reduced according to Eq. (9), and as a result evaporative cooling is reduced, and the surface temperature jumps dramatically. As the surface vapor pressure is reduced, evaporation is increased inside the material due to an increase in the rate of vapor transport to the surface. This increase in internal evaporation causes a sudden drop in internal temperature. The drop in surface evaporation rate also causes a drop in the rate of sample mass loss.

The model results for an initial saturation of 0.3 are in very good qualitative agreement with experimental data. The surface temperature is shown in Figure 22. This case has the lowest initial saturation, and the wet bulb period is relatively short. After the surface dries out, the predicted surface temperature jumps dramatically at five and a half minutes. When compared to the experiments, the model slightly under predicts the observed jump times, but there is significant overlap with the uncertainty band. The maximum surface temperature reached is slightly over predicted by the model. The predicted internal temperature is shown in Figure 23, and gives good agreement with the experimental data for the first ten minutes. The predicted temperature drops significantly below the experimental temperatures at the end of the test. The mass of water in the sample is shown in Figure 24. The uncertainty band overlaps some of the experimental data, but the model appears to be slightly under predicting the mass loss rate.

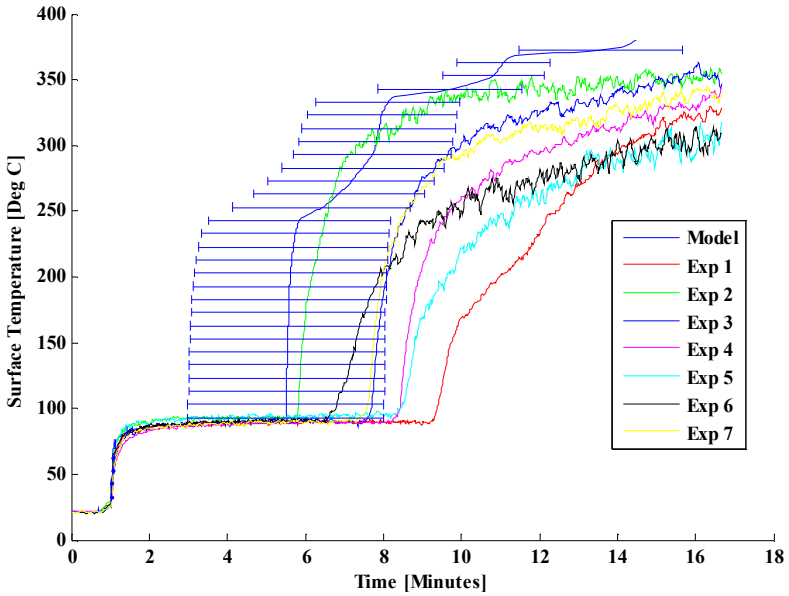

Figure 22 – Surface Temperature as a Function of Time for Radiant Heating of Ceramic Fiberboard with an Initial Saturation of 0.3

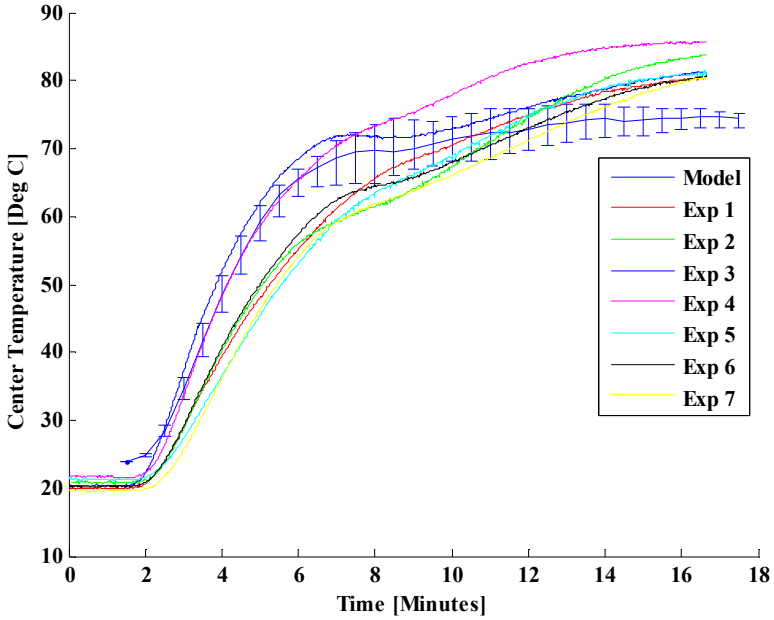

Figure 23 – Centerline Temperature as a Function of Time for Radiant Heating of Ceramic Fiberboard with an Initial Saturation of 0.3

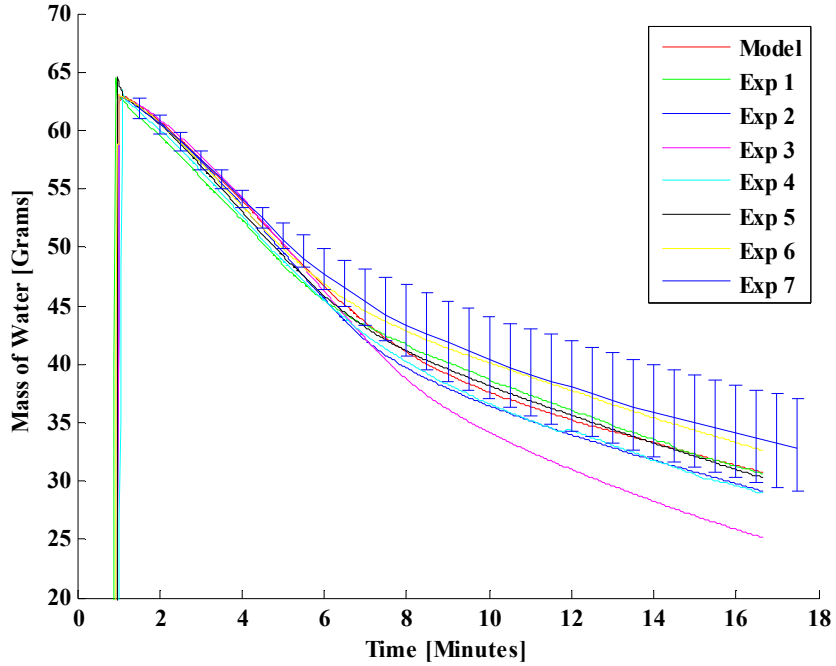

Figure 24 – Mass of Water in Sample as a Function of Time for Radiant Heating of Ceramic Fiberboard with an Initial Saturation of 0.3

For the case where the initial saturation is increased to 0.5, the surface temperature remains at the wet bulb temperature for a longer period of time, as shown in Figure 25. This is due to the fact that more water must be removed by evaporation before the flow to the surface is choked off, causing the surface to dry out, and the surface temperature to jump. In this case, the predicted surface temperature jump gives very good agreement with the experimental results. The maximum surface temperature reached towards the end of the test is slightly over predicted. The predicted centerline temperature gives very good agreement with the experimental data up until the surface temperature jumps at approximately 17 minutes as shown in Figure 26. At this point the model predicts a more dramatic reduction in centerline temperature than is observed by experiment. The rate of mass loss is slightly under predicted, as shown in Figure 27, but there is significant overlap with the uncertainty band.

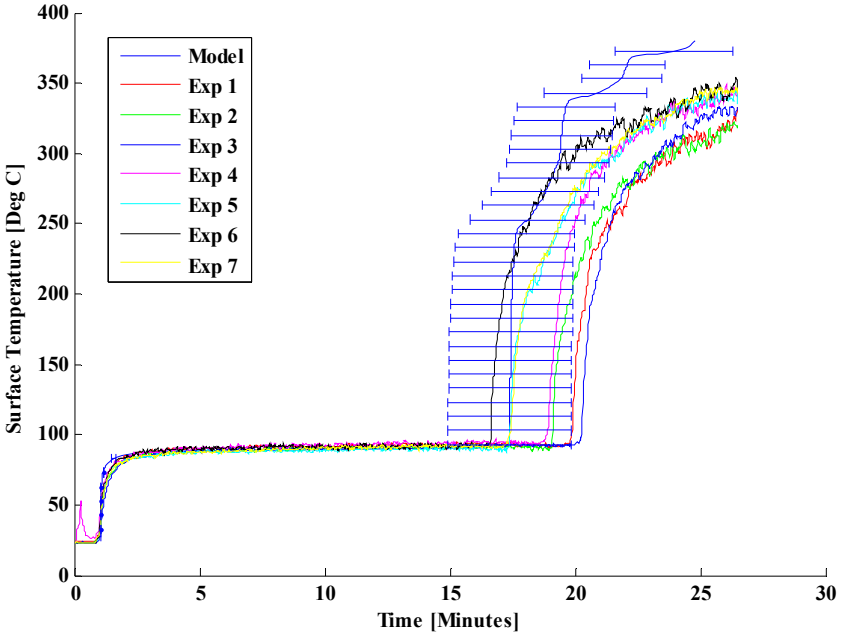

Figure 25 – Surface Temperature as a Function of Time for Radiant Heating of Ceramic Fiberboard with an Initial Saturation of 0.5

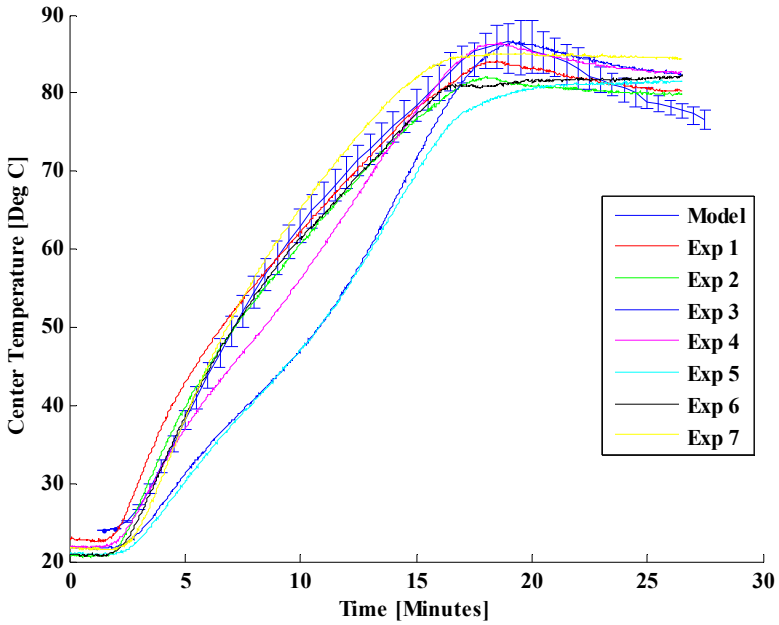

Figure 26 – Centerline Temperature as a Function of Time for Radiant Heating of Ceramic Fiberboard with an Initial Saturation of 0.5

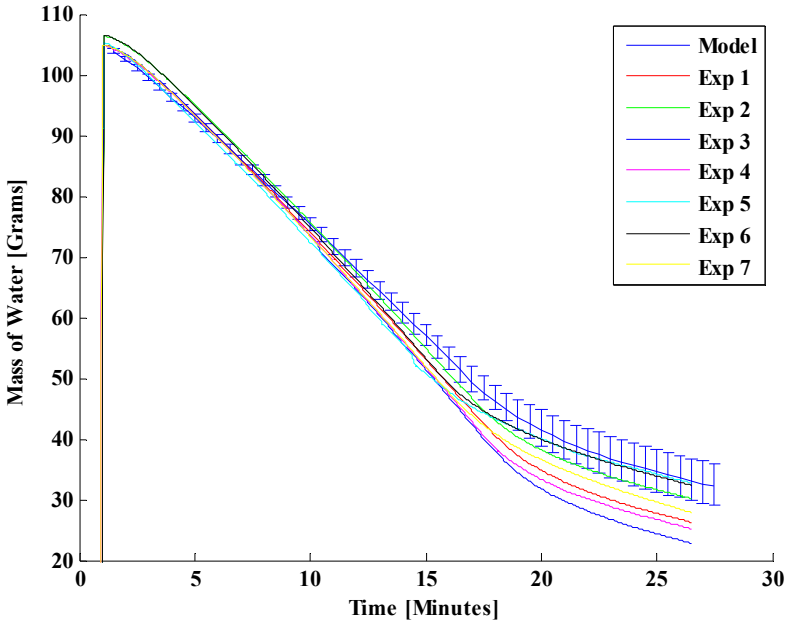

Figure 27 – Mass of Water in Sample as a Function of Time for Radiant Heating of Ceramic Fiberboard with an Initial Saturation of 0.5

The case of heating CFB with an initial saturation of 0.7 follows the same general trends as the previous two cases, and the qualitative agreement between the model and experiment is very good for this case. The surface temperature remains at the wet bulb temperature for longer because there is more water to remove before the surface temperature jumps, as shown in Figure 28. The jump time is slightly over predicted in this case. The predicted centerline temperature is shown in Figure 29. The model gives good agreement with the experimental data up until approximately 25 minutes, when the experimental surface temperature jumps. After this time, the model over predicts the drop in centerline temperature caused by the increase of internal evaporation. The rate of mass loss is slightly under predicted for this case, as shown in Figure 30.

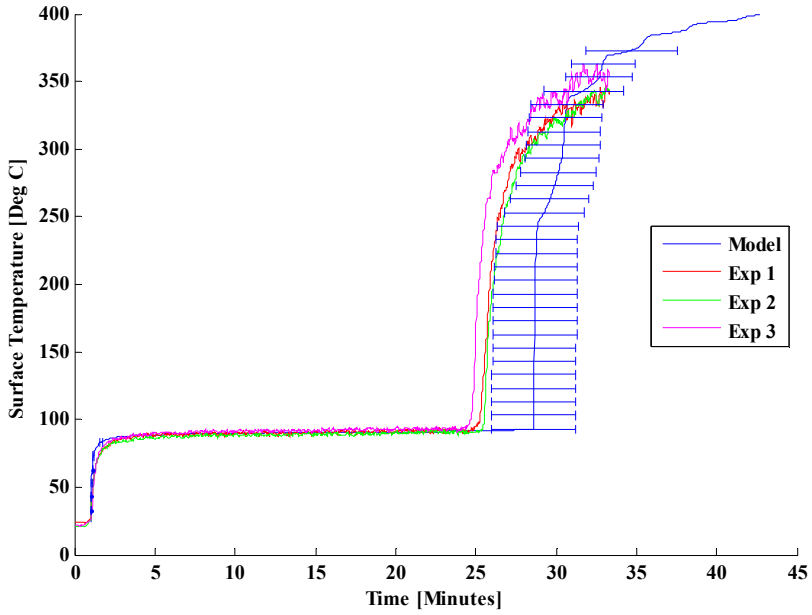

Figure 28 – Surface Temperature as a Function of Time for Radiant Heating of Ceramic Fiberboard with an Initial Saturation of 0.7

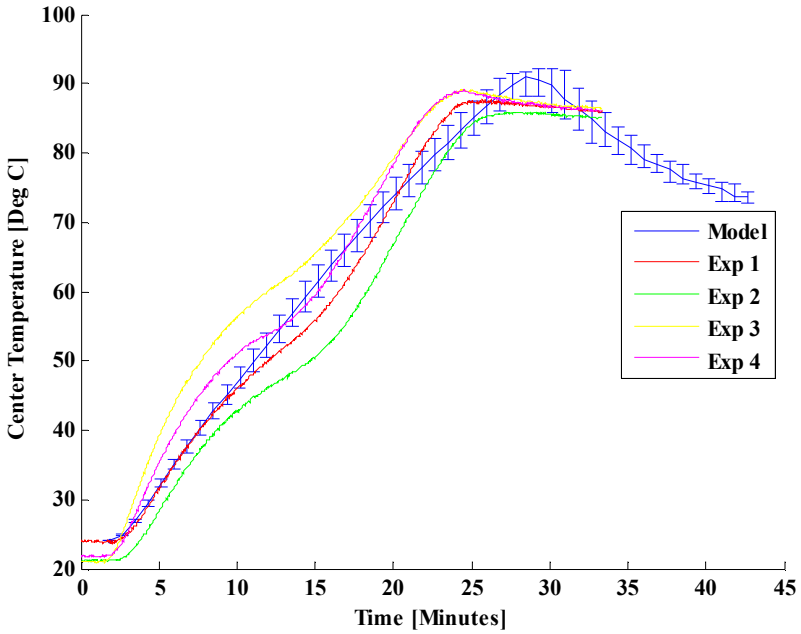

Figure 29 – Centerline Temperature as a Function of Time for Radiant Heating of Ceramic Fiberboard with an Initial Saturation of 0.7

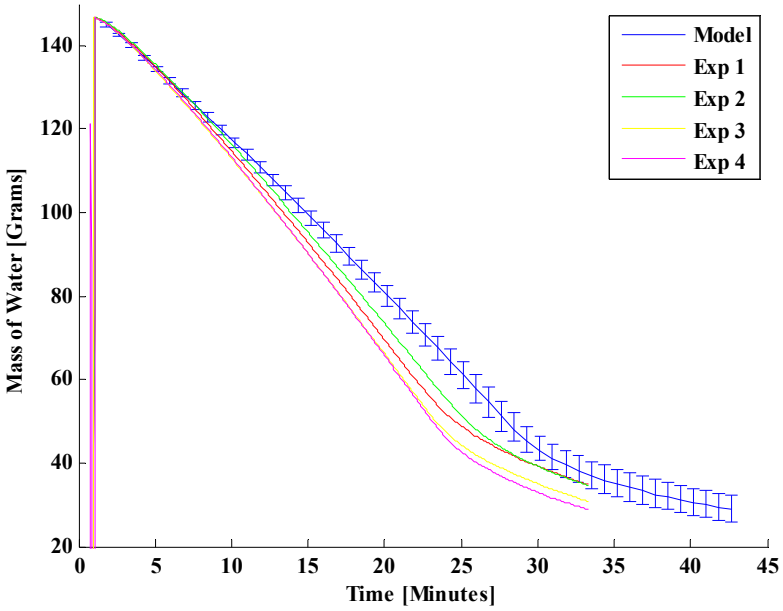

Figure 30 – Mass of Water in Sample as a Function of Time for Radiant Heating of Ceramic Fiberboard with an Initial Saturation of 0.7

Overall, the model gives good agreement with the experimental data for all three radiant heating cases. All of the general trends observed in the experiments are matched by the model output. The surface temperature wet bulb period and jump, initial increase and subsequent decrease of the internal temperature, and the change in mass loss rate as the surface dries out are all predicted very well qualitatively by the model. There are several cases where significant quantitative differences are observed between the model and experiments. As the initial saturation is increased from 0.3 to 0.7, the model switches from under-predicting to over-predicting the jump time. Possible reasons for this behavior include physical phenonema not included in the model, such as temperature dependant surface tension, migration of bound water, and hysteresis of the capillary pressure. Also the sorption relation was validated at room temperature, and it is unclear how appropriate it is for high temperature applications. The maximum surface temperature reached is also over-predicted by the model. This could be caused by issues with the sorption relation, or movement of bound water, both of which could affect the evaporation rate at the surface. It is also possible that there is experimental uncertainty associated with the thermocouple bead location, and radiation reaching the thermocouple bead. The internal temperature drop after the surface dries out is over-predicted by the model in each case. This could also be caused by errors associated with the sorption relation, movement of bound water, or the effective diffusivity relation. The mass loss rate is under-predicted in each case. This is possibly caused by uneven initial distribution of water, vapor loss through the surface from inside the sample, or movement of bound water to the surface, none of which are included in the model. Modeling results from Lu et al [53] show that including movement of bound water increases the predicted mass loss rate. In addition to not accounting for all physical phenomena, the model is a simplified framework does not completely characterize all materials. The J-Function and relative permeability relations are approximations of observed behavior that do not always match the behavior of real materials. Overall, the model is shown here to do a good job at predicting the behavior of a heating scenario that is of key interest to fire researchers.

7. Conclusions

A model for heat and mass transfer in porous media has been presented in detail. The model has been shown to be capable of simulating wetting and heating scenarios that are relevant to water based fire suppression. Reasonable agreement is

observed with six validation cases using four materials, and representing two wetting scenarios, and two heating scenarios. The model gives very good qualitative agreement with the experimental data and reasonable quantitative agreement. These processes are of significant interest to fire researchers and engineers because they represent the wetting and subsequent drying processes that precede ignition of an object during water based suppression of a fire. The research that is presented in this paper constitutes a significant step towards the prediction of water based fire suppression.

8. Future Work

In order to extend the current model to materials that are of interest to fire researchers and engineers, more material data is required. Hydraulic properties are available for many soils, rocks, and particulate media, but few materials that represent fuel packages in a fire scenario. The authors believe that the model has many potential applications. Chemical kinetics could be added, to extend its use to pyrolysis applications. Current pyrolysis models do not have the capability to handle the presence of liquid water. The model could be extended to handle the pyrolysis of wood, but must be modified first, since hygroscopic behavior is not included. In theory, the model also has the potential to predict burning rates of flammable liquids spilled on porous materials. This application has not yet been investigated. Future validation work should also be performed with simultaneous water and heat application. At this time, due to significant uncertainty in some of the model inputs, a multi-dimensional model is not recommended.

Bibliography

1. di Marzo, M., and Evans, D., *Dropwise evaporative cooling of high thermal conductivity materials.* Heat and Technology, 1987. **5**(1-2): p. 29-40.
2. di Marzo, M., and Evans, D.,, *Evaporation of a water droplet deposited on a high thermal conductivity surface.* Trans. ASME, J. of Heat Transfer, 1989. **111**: p. 210-213.
3. di Marzo, M., Liao, P., Tartarini, Y., Evans. D., and Baum, H., *Dropwise evaporative cooling of a low thermal conductivity solid*, in *Fire Safety Science – Proceedings of the Third International Symposium*. 1991, International Association of Fire Safety Science. p. 987-996.
4. di Marzo, M., Tartarini, P., Liao, Y., Evans. D., and Baum, H., *Evaporative cooling due to a gently deposited droplet.* International Journal of Heat and Mass Transfer, 1993. **36**(17): p. 4133-4139.
5. Tartarini, P., and di Marzo, M., *The solid-liquid interfacial conditions for dropwise evaporative cooling.* Heat and Technology, 1992. **10**(3-4): p. 57-71.
6. White, G., Tinker, S., di Marzo, M.,. *Modelling of dropwise evaporative cooling on a semi-infinite solid subjected to radiant heat input*. in *Fire Safety Science – Proceedings of the Fourth International Symposium*. 1994.
7. Chandra, S., di Marzo, M., Qiau, Y. M., and Tartarini, P., *Effect of liquid-solid angle on droplet evaporation.* Fire Safety Journal, 1996. **27**(2): p. 141-158.
8. di Marzo, M., *Dropwise evaporative cooling*, in *National Heat Transfer Conference*. 1995: Bologna Italy.
9. Pasandideh-Fard, M., Chandra, S, and Mostaghimi, J., *A three-dimensional model of droplet impact and solidification* International Journal of Heat and Mass Transfer, 2002. **45**(11): p. 2229-2242.
10. Abu-Zaid, M., and Atreya, A., *Transient cooling of hot porous and non-porous ceramic solids.* Transactions of the ASME, 1994. **116**.
11. di Marzo, M., Kidder, C. H., and Tartarini, P., *Infrared thermography of dropwise evaporative cooling of a semiinfinite solid subjected to radiant heat input.* Experimental Heat Transfer, 1992. **5**: p. 101-114.
12. Tartarini, P., Liao, Y., and di Marzo, M., *Transient cooling of a hot surface by droplets evaporation*, in *NIST Interagency Report*. 1993.
13. Tartarini, P., and di Marzo, M. *Evaporative cooling in radiative field*. in *Proceedings of the 10th International Heat Transfer Conference*. 1994.
14. Abu-Zaid, M., *Droplet evaporation on porous and non-porous ceramic solids*

heated from top. Heat and Mass Transfer, 2002. **38**: p. 203-211.

15. Klassen, M., diMarzo M., and Sirkis, J., *Infrared thermography of dropwise evaporative cooling.* Experimental Thermal and Fluid Science, 1992. **5**: p. 136-141.
16. Dawson, H., and di Marzo, M., *An Experimental Study of Multiple Droplet Evaporative Cooling*, in *NIST Interagency Report*. 1993.
17. di Marzo, M., and Tinker, S., *Evaporative cooling due to a sparse spray.* Fire Safety Journal, 1996. **27**(4): p. 289-303.
18. Milke, J.A., Tinker, S. C., and di Marzo, M., *Effect of Dissolved Gases on Spray Evaporative Cooling With Water.* Fire Technology, 1997. **33**(2).
19. Toda, S., *A study of mist cooling – Thermal behaviors of liquid films formed from mist drops on a heated surface at high temperatures and high heat fluxes*, in *Technology Reports*. 1971, Tohoku University.
20. Bonacina, C., Del Giudice, S., and Comini, G., *Dropwise Evaporation.* Journal of Heat Transfer, 1979. **101**: p. 441-446.
21. Bolle, L., and Moreau, J. C. , *Spray cooling of hot surfaces.* Multiphase Science and Technology, 1982.
22. Yu, H.Z., and Jayaweera, Tina, *Water Absorption in Horizontal Corrugated Board Under Water Sprays*, in *FM Global Technical Report*. 2004: Norwood MA.
23. Kaviany, M., *Principles of Heat Transfer in Porous Media*. 2nd ed. 1995, New York: Springer-Verlag.
24. Dullien, F.A.L., *Porous Media - Fluid Transport and Pore Structure*. 1992, San Diego CA: Academic Press.
25. Scheidegger, A., *The Physics of Flow Through Porous Media*. 3rd ed. 1974: University of Toronto Press.
26. Bear, J., *Dynamics of Fluids in Porous Media*. Dover Publications Inc. 1972, New York.
27. Philip, J.R., *The theory of infiltration: 1. The infiltration equation and it's solution.* Soil Science, 1957. **83**: p. 345-357.
28. Philip, J.R., *The theory of infiltration: 2. The profile at infinity.* Soil Science, 1957. **83**: p. 435-448.
29. Philip, J.R., *The theory of infiltration: 3. Moisture profiles and relation to experiment.* Soil Science, 1957. **84**: p. 163-178.
30. Philip, J.R., *The theory of infiltration: 4. Sorptivity and algebraic infiltration equations.* Soil Science, 1957. **84**: p. 257-264.

31. Philip, J.R., *The theory of infiltration: 5. The influence of initial moisture content.* Soil Science, 1957. **84**: p. 329-339.
32. Philip, J.R., *The theory of infiltration: 6. The effect of water depth over soil.* Soil Science, 1958. **85**: p. 345-357.
33. Philip, J.R., *Theory of infiltration.* Advances in Hydroscience, 1969. **5**: p. 215-296.
34. Philip, J.R., and De Vries, D. A., *Moisture movement in porous materials under temperature gradients.* Transactions of the American Geophysical Union, 1958. **38**(2).
35. De Vries, D.A., *Simultaneous transfer of heat and moisture in porous media.* Transactions of the American Geophysical Union, 1958. **39**(5).
36. Whitaker, S., *Heat, mass, and momentum transfer in porous media: A theory of drying*. Advances in Heat Transfer. Vol. 13. 1977: Academic Press.
37. Luikov, A.V., *Systems of differential equations of heat and mass transfer in capillary porous bodies,.* International Journal of Heat and Mass Transfer, 1975. **18**: p. 1-13.
38. Nasrallah, B.S., and Perre, P., *Detailed study of a model of heat and mass transfer during convective drying of porous media.* International Journal of Heat and Mass Transfer, 1988. **31**(5): p. 957-967.
39. Chen, P., and Pei, David C. T., *A Mathematical Model of Drying Processes.* International Journal of Heat and Mass Transfer, 1989. **32**(2): p. 297-310.
40. Ilic, M., and Turner, I. W., *Convective Drying of a Consolidated Slab of Wet Porous Material.* International Journal of Heat and Mass Transfer, 1989. **32**(12): p. 2351-2362.
41. Ni, H., *Multiphase Moisture Transport in Porous Media Under Intensive Microwave Heating*, in *Department of Agricultual and Biological Engineering*. 1997, Cornell University: Cornell NY.
42. Luikov, A.V., *Heat and Mass Transfer in Capillary-Porous Bodies*. 1966, Oxford: Pergammon Press.
43. Bejan, A., *Heat Transfer*. 1993, New York: John Wiley and Sons, Inc.
44. Leverett, M.C., *Capillary behavior in porous solids.* Transactions of the AIME, 1941. **142**: p. 159-172.
45. Spolek, G.A., and Plumb, O. A., *Capillary Pressure in Softwoods.* Wood Science Technology, 1981. **15**: p. 189-199.
46. Baver, L.D., Gardner W. R., and Gardner, W. H. , *Soil Physics*. 4th ed. 1972, New York: John Wiley and Sons, Inc.

47. Moran, M.J., and Shapiro, Howard N., *Fundamentals of Engineering Thermodynamics*. 2000, New York: John Wiley and Sons, Inc. .
48. Haertling, M., *Prediction of Drying Rates*, in *Drying '80*, A.S. Mujumdar, Editor. 1980, Hemisphere. p. 88-98.
49. Ames, W.F., *Numerical Methods for Partial Differential Equations*. 2nd ed. 1977, New York: Academic Press.
50. Saltelli, A., Chan., K., Scott., E. M., *Sensitivity Analysis*. 2000, New York: John Wiley and Sons, Inc. .
51. Institute, A.N.S., *U.S. Guide to the Uncertainty in Measurement*. 1997, Boulder CO: NCSL International.
52. Youngs, E.G., *Moisture profiles during vertical infiltration.* Soil Science, 1957. **84**: p. 283-290.
53. Lu, T., Jiang, P., Shen, S., *Numerical and experimental investigation of convective drying in unsaturated porous media with bound water.* Heat and Mass Transfer, 2005. **41**: p. 1103-1111.
54. Przesmyki, Z., and Strumillo, C., *The mathematical modeling of drying process based on moisture transfer mechanism*, in *Drying '85*, R. Toei, and Mujumdar, A. S., Editor. 1985, Hemisphere: Washington DC. p. 126-134.
55. Plumb, O.A., Brown, C. A., and Olmstead B. A., *Experimental measurements of heat and mass transfer during convective drying of southern pine.* Wood Science Technology, 1984. **18**: p. 187-204.
56. Plumb, O.A., Spolek, G. A., and Olmstead, B. A., *Heat and mass transfer in wood during drying.* International Journal of Heat and Mass Transfer, 1985. **28**(9): p. 1669-1678.
57. DiNenno, P.J., *SFPE Handbook of Fire Protection Engineering*. 3rd ed. 2002, Quincy MA: National Fire Protection Association.
58. Sipe, J., *A Porous Media Model for Sprinkler Wetting*, in *Department of Fire Protection Engineering*. 2010, Worcester Polytechnic Institute: Worcester, MA.
59. Comstock, G.L., *Directional permeability of softwoods.* Wood Fiber, 1970. **1**: p. 283-289.
60. Siau, J.F., *Flow in Wood*. 1971, New York: Syracuse University Press.
61. Spolek, G.A., *A Model of Simultaneous Convective, Diffusive, and Capillary Heat and Mass Transport in Drying Wood*. 1981, Washington State University.
62. Luikov, A.V., *Heat and Mass Transfer in Capillary Porous Bodies*. 1961, London: Pergamon Press.
63. Gebhart, B., Jaluria, Yogesh, Mahajan, Roop. L. and Sammakia, Baghat,

Buoyancy Induced Flows and Transport. 1988: Hemisphere Publishing Corporation.

Appendix A. Definitions of Coefficients

$$K_1 = \frac{M_a M_v D_{eff,g}}{RT\left[(P-p_v)M_a + p_v M_v\right]} P \frac{\partial p_v}{\partial S_w} - \rho_w \frac{KK_{r,w}}{\mu_w} \frac{\partial p_c}{\partial S_w}$$

$$K_2 = \frac{M_a M_v D_{eff,g}}{RT\left[(P-p_v)M_a + p_v M_v\right]} P \frac{\partial p_v}{\partial T}$$

$$K_3 = \frac{p_v}{R_v T} \frac{KK_{r,g}}{\mu_g} - \frac{M_a M_v D_{eff,g}}{RT\left[(P-p_v)M_a + p_v M_v\right]} p_v + \rho_w \frac{KK_{r,w}}{\mu_w}$$

$$K_4 = -\phi \frac{p_v}{R_v T} + \frac{\phi(1-S_w)}{R_v T}\left(\frac{\partial p_v}{\partial S_w}\right) + \phi \rho_w$$

$$K_5 = \frac{\phi(1-S_w)}{R_v} \frac{\partial}{\partial T}\left(\frac{p_v}{T}\right)$$

$$K_6 = 0$$

$$K_7 = -\frac{M_a M_v D_{eff,g}}{RT\left[(P-p_v)M_a + p_v M_v\right]} P \frac{\partial p_v}{\partial S_w}$$

$$K_8 = -\frac{M_a M_v D_{eff,g}}{RT\left[(P-p_v)M_a + p_v M_v\right]} P \frac{\partial p_v}{\partial T}$$

$$K_9 = \frac{P-p_v}{R_a T} \frac{KK_{r,g}}{\mu_g} + \frac{M_a M_v D_{eff,g}}{RT\left[(P-p_v)M_a + p_v M_v\right]} p_v$$

$$K_{10} = -\frac{\phi}{R_a}\left(\frac{P-p_v}{T} + \frac{1-S_w}{T}\frac{\partial p_v}{\partial S_w}\right)$$

$$K_{11} = -\frac{\phi}{R_a}\left(\frac{p}{T^2} - \frac{PS_w}{T^2} + (1-S_w)\frac{\partial}{\partial T}\left(\frac{p_v}{T}\right)\right)$$

$$K_{12} = \frac{\phi(1-S_w)}{R_a T}$$

$$K_{13} = \rho_w \frac{KK_{r,l}}{\mu_w} \frac{\partial p_c}{\partial S_w} \Delta h_v$$

$$K_{14} = \left(\phi S_a k_a + \phi S_v k_v + \phi S_l k_l + (1-\phi) k_s\right)$$

$$K_{15} = -\rho_w \frac{KK_{r,w}}{\mu_w} \Delta h_v$$

$$K_{16} = -\Delta h_v \phi \rho_w$$

$$K_{17} = \phi S_l \rho_l C_{p,l} + \phi S_v \rho_v C_{p,v} + \phi S_a \rho_a C_{p,a} + (1-\phi) \rho_s C_{p,s}$$

$$K_{18} = 0$$

$$K_{19} = \rho_w \frac{KK_{r,l}}{\mu} \rho_w g$$

$$K_{20} = \Delta h_v \rho_w \frac{KK_{r,l}}{\mu_w} \rho_w g$$

Appendix B. Background Material

In this appendix the fundamentals of transport phenomena in porous media will be discussed. It is beneficial to first discuss the reasons why porous media is of interest to fire protection engineers. Many areas of fire protection engineering involve transport phenomena in porous media. Some examples include spray wetting of porous materials by fire sprinklers, combustion applications such as pyrolysis of porous materials and fuel wicking, heat losses from fire compartments, concrete exposure to fire, and thermal exposure of firefighter's protective clothing. These areas are quite diverse, yet each involves heat and mass transfer through porous media. An understanding of the basic physics of transport phenomena in porous media will aid in their understanding.

Water is the most widely used fire extinguishing agent for many reasons [64]. Most importantly it is readily available, inexpensive, non-toxic, stable, and has a high latent heat of vaporization. Sprinklers are a common form of water based automatic fire suppression. In many cases they are a building's first line of defense against fire. Upon actuation, sprinklers will discharge water on and in the vicinity of the fire, wetting and cooling both the burning materials, and adjacent items. This can reduce the heat release rate, slow the rate of flame spread, and prevent other nearby items from igniting. The sprinkler's ability to perform these tasks is affected by many factors including the interaction of the water with various porous media. If water is absorbed into a material the time until ignition is increased for a particular heat flux [65]. This can slow flame spread rates, and prevent other items from igniting and contributing to a fire. The splash dynamics of water droplets impacting a burning surface are believed to be an important process affecting fire suppression [66]. Despite the importance of water absorption, the physics of spray wetting are not very well understood.

Porous media is often encountered in combustion applications. Pyrolysis of porous materials will involve the flow of pyrolyzates through the pore spaces. Common porous combustibles include wood, paper products such as corrugated board, synthetic foams, and woven materials and fabrics. When a material is sufficiently heated to undergo pyrolysis, it will not occur only at the surface, but also at depth. Pyrolyzates will flow through the pores of the material and exit at the surface. For materials such as wood, the pore structure will greatly affect its behavior during pyrolysis. In cases of fuel spills on porous surfaces and ignition of the spill, the burning behavior will differ from a simple pool fire [67]. Fuel can initially enter the material due to gravity, inertial, or surface tension forces. When the fuel is ignited, a complicated system of transport processes will be set up. Surface fuel will evaporate

and burn, while subsurface fuel will evaporate and flow through the pore spaces to reach the surface. Subsurface fuel will be transported to the surface by capillary action as the surface material dries. If the porous solid is combustible, then pyrolysis of the solid will occur as well, further complicating the scenario. The burning behavior of such a fire will differ from a fire resulting from a fuel spill on a non-porous surface.

Many fire scenarios will expose porous materials to a thermal insult. Compartment walls are often constructed from porous materials such as wood and fiberglass insulation. Heat transfer through such walls often has accompanying mass transfer. Water will always be present in building materials, and evaporation and condensation can transport large amounts of heat. Models for heat transfer through walls will often account for the coupling between heat and mass transfer. This coupling cannot be ignored when modeling the exposure of concrete to fire. As concrete is heated physically bound water will evaporate, cement paste will break down and release chemically bound water, and other materials will evaporate producing convective and diffusive mass fluxes in the material and possibly very high internal pressures [68]. If sufficiently high internal pressures are reached, then explosive spalling can occur [69]. Coupled heat and mass transfer also occurs during fire exposure of fabrics. Fire exposure of firefighter's protective clothing is one example. Attempts have been made to model heat transfer through firefighters clothing for the purposes of predicting skin burns [70, 71]. When water is present in the various layers of material, simultaneous mass transfer will occur.

B.1. Transport Phenomena in Porous Media

B.1.1. Pore structure and properties

Porous materials consist of interconnected and non-interconnected pore spaces in a solid material, fibrous material, or bed of granular material. All macroscopic properties of porous materials are affected by their pore structure [24]. The size and geometry of the pores can vary greatly, and lead to further classification of porous media. Pores that are on the meter scale will be called caves or caverns. Pore diameters on the molecular scale are called micropores, ultramicropores [23] or the material is simply referred to as "capillary-porous" [72]. Granular materials can range from fine silts and powders to soils and sands to pebbles, rocks, and boulders. A representative porous material is shown in Figure 31.

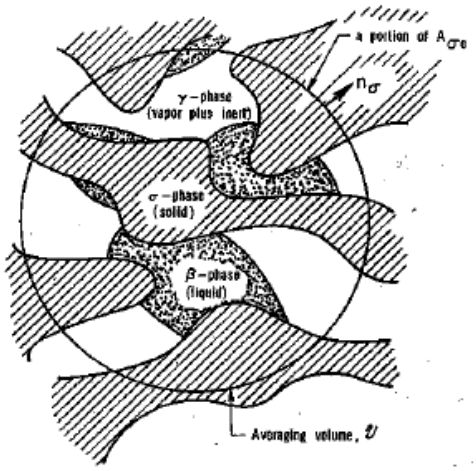

Figure 31 – Representative Porous Material (from [36])

There are many parameters that can describe a porous material, but the most common is the porosity ϕ. Porosity is defined as the ratio of void space to total volume in a porous material. The connectivity of pores is important for fluid flow. Some pores will be connected to other pores through a pore network. It is through these interconnected pores that fluids can move throughout the material. Other pores are non-interconnected and will not permit fluid flow. These could be bubbles in a solid material or isolated air pockets in foam. The porosity calculated with the interconnected pores and ignoring small pores that are hard to fill is sometimes called the effective porosity [23]. Porosity measurements can be made several ways [24].

- Direct – Bulk Volume is compared to crushed volume.
- Photography – Sum of areas of solids is compared to area of voids.

- Imbibition – Mass of completely wetted material is compared to mass of dry material. This method measures the effective porosity.
- Mercury Injection – Volume of mercury injected into material is measured. This method measures the effective porosity.
- Gas Injection – Pressure in container housing the material is measured before and after expansion via a second container.
- Density Methods – The density of the bulk material can be determined and compared to the density of the pure solid.
- Gamma Ray and X-Ray Attenuation – Intensity of a beam passing through the material is compared to that passing through a solid slab of the same material.

Porosity values of common porous materials given by [25] are shown in Table 11.

Table 11 - Values of Porosity for Several Materials

Substance	Porosity
Foam metal	0.98
Fiberglass	0.88
Berl Saddles	0.68-0.83
Wire crimps	0.68-0.76
Silica grains	0.65
Black slate powder	0.57-0.66
Raschig rings	0.56-0.65
Leather	0.56-0.59
Catalyst granules	0.45
Granular crushed rock	0.44-0.45
Soil	0.43-0.54
Sand	0.37-0.50
Silica powder	0.37-0.49
Spherical packings, well shaken	0.36-0.43
Cigarette filters	0.17-0.49
Brick	0.12-0.34
Hot compacted copper powder	0.09-0.34
Sandstone (oil sand)	0.08-0.38
Limestone, dolomite	0.04-0.10
Coal	0.02-0.12
Concrete (ordinary mixes)	0.02-0.07

Another important parameter of a porous material is the pore diameter. For many engineering materials, however, the pore diameter is a nebulous quantity. Most materials will have pores of varying diameters, and bonded fibrous materials such as paper may not have any spaces resembling cylindrical pores. It is more appropriate to define a pore size distribution $f(\delta)$ equal to the fraction of pore space of diameter, δ, such that,

$$\int_{\delta=0}^{\infty} f(\delta) d\delta = 1$$

Pore size distributions can be measured using mercury injection measurements, optical methods, x-ray and gamma ray absorption, and acoustical methods [24]. Dullien [24] gives the pore size distribution of various porous materials. Figure 32 shows his data points for 250 μm glass beads.

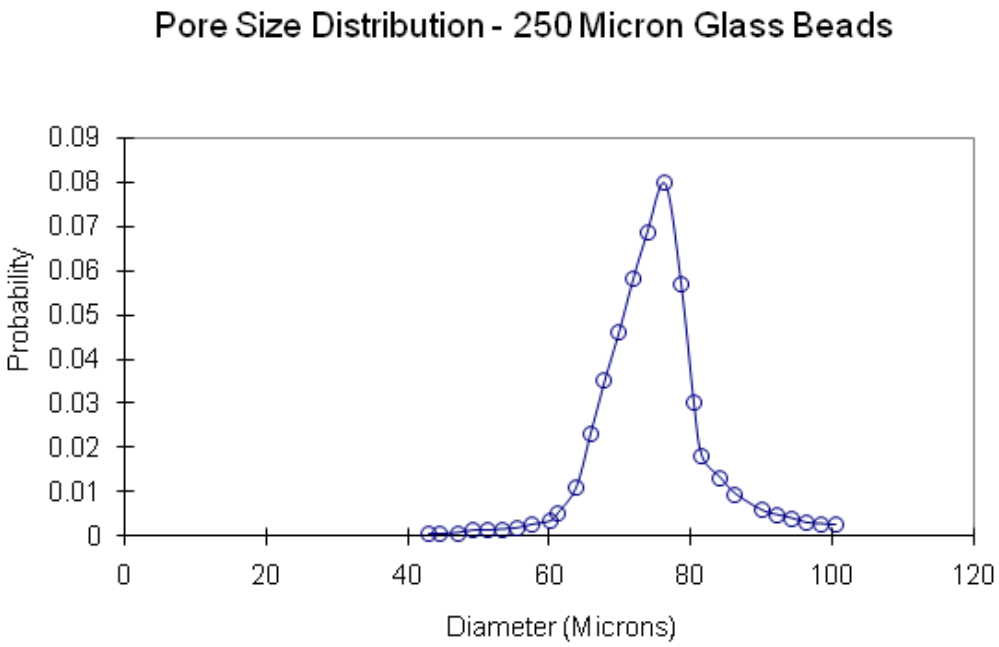

Figure 32 – Pore Size Distribution

When discussing fluids in porous media it is necessary to be able to quantify the amount of a particular fluid phase present. Three common parameters for this are the mass content, volumetric content, and saturation. The mass content c_A [kg/m^3] of a fluid A, is the mass of fluid per unit volume of the material. The volumetric content U_A [m^3/m^3] of fluid A is the volume of fluid per unit volume. The saturation S_A of fluid A is fraction of the pore space filled with fluid A. The saturation is proportional to the volumetric and mass contents by the following relationship

$$S_A = \frac{U_A}{\phi} = \frac{c_A}{\rho_A \phi}$$

A more useful quantity is the effective liquid saturation S_{eff} [23].

$$S_{eff} = \frac{S - S_{ir,l}}{1 - S_{ir,l} - S_{ir,g}}$$

When a fluid displaces another fluid in the void space of a porous material, it will not be able to penetrate some of the smaller pores or disconnected spaces. In many cases it is impossible to reach 100% saturation. The effective saturation represents the fraction of maximum achievable saturation. $S_{ir,l}$ is the irreducible liquid saturation, and $S_{ir,g}$ is the irreducible gas saturation. The irreducible saturation is the amount of fluid that cannot be easily removed from the material during imbibition or drainage. When draining the liquid from a saturated material, a small amount of liquid will remain in the material unless the material is specially conditioned by heating or extended exposure to very dry air. This small amount of liquid is the irreducible liquid saturation. For gases, a similar definition applies. During imbibition, a liquid will displace the air occupying the void spaces of an initially dry material. The liquid will not be able to penetrate all of the small pores to displace 100% of the air. This small amount of air that remains is the irreducible gas saturation. When referring to "saturation" the term usually refers to liquid saturation, unless otherwise specified. An ambiguity arises however from this choice of nomenclature when two immiscible liquids are present in a porous material. Such is the case when water is pumped into underground oilfields for purposes of petroleum extraction. In other cases water and oil can be present in porous materials. In such cases the wetting phase is considered to be the liquid, and the non-wetting phase is considered to be the gas. With this in mind, all of the analyses made with respect to liquids – gas systems can be applied to liquid –liquid systems. Porous materials can also be classified based on how they interact with the most common wetting fluid: water. Most materials will contain a small amount of water in their pore space under normal conditions unless they have been oven dried or otherwise conditioned to remove the moisture. All other materials will retain a small amount of moisture in the form of free water or bound water. Free water is present in the pores of the material and is free to move throughout the material. Bound water can

be physically or chemically bound. Physically bound water is held in very small pores of the solid matrix by surface tension forces. For a particular material, the physically bound moisture content is a function of temperature and humidity. Water that bonds with the solid material to form a hydrate is chemically bound water. Chemically bound water is also called “water of crystallization” or “water of hydration”. Some examples are cement paste and gypsum. These materials will break down at high temperatures and release the chemically bound water in a process called dehydration. Some materials will undergo volume changes with the addition or removal of water. Hygroscopic materials are materials which absorb significant amounts of bound water in the solid matrix during wetting. These materials will often shrink during drying and swell during imbibition. The vapor pressure in hygroscopic materials is a function of temperature and the saturation of the material. Non-hygroscopic materials will not absorb water into the solid matrix, and swelling and shrinkage are not generally considered. In non-hygroscopic materials, the vapor pressure can be calculated as a function of temperature only [72].

B.1.2. Continuum Assumption

For purposes of modeling, the continuum assumption will be invoked in this study. This means that materials are treated as being continuous and having properties defined everywhere in space, even if the properties are not continuous (such as at a solid-fluid interface) [73]. As the length scale of interest is reduced, molecular interactions become more important, and the continuum assumption breaks down. An example of this is the motion of small particles due to random interactions with surrounding molecules. This is known as Brownian motion. For many purposes, it is not necessary to know details of the molecular motion, but instead the bulk fluid motion is of interest. The point at which a continuum treatment is appropriate for a flow is determined by the Knudsen number Kn [23].

$$Kn = \frac{mean\ \ free\ \ path\ \ of\ \ molecules}{average\ \ pore\ \ size\ \ or\ \ interparticle\ \ clearance}$$

When a flow has Kn>>1, it is called Knudsen flow, and the continuum assumption is not valid. When Kn<<1, the flow is called viscous flow, and the continuum assumption is appropriate. The region in between is called the transition region [23]. If the properties of a material are considered to be continuous, some care is required when

defining properties such as density and porosity. These properties require a measurement volume whose size will affect their values. Density is defined as the ratio of the mass of an amount of matter to the volume that it occupies [26]. As the measuring volume is made smaller and smaller it will converge on the value of density at a point. If it is made smaller than a limiting size, however it will not contain enough molecules to give an appropriate value. If it is too small it may not contain any molecules. This is illustrated in Figure 33.

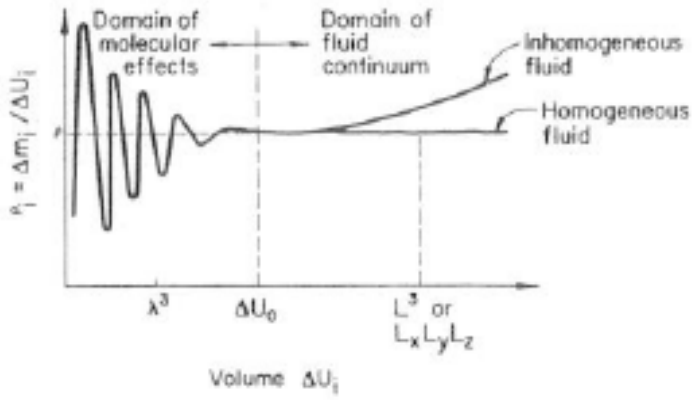

Figure 33 – Effect of Measuring Volume on Density [26]

In a similar manner porous materials can be treated as a continuum with properties of porosity, permeability, etc defined everywhere in space. This does not capture all of the fine details such as actual flow velocities in the pores, but gives statistical averages over a measuring volume. Porosity can be analyzed in the same manner used for density. Porosity is defined as the ratio of the volume of void space to the measuring volume. If the measuring volume is too large it will not be representative of the local porosity at a point. If it is too small it will not contain enough pores to give an appropriate value for the point. This is illustrated in Figure 34.

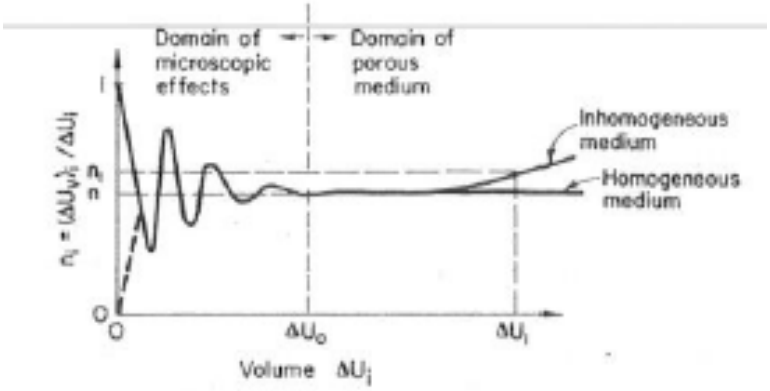

Figure 34 – Effect of Measuring Volume on Porosity [26]

B.1.3. Constitutive Relationships

Relationships are required to calculate heat and mass fluxes, vapor pressure, capillary pressure, relative permeability, and other parameters from dependant variables.

B.1.4. Mass Fluxes

The total mass flux in a multi-component system is comprised of convective and diffusive components. The convective mass flux ρu_i in a porous material is determined using Darcy's Law, which will be covered later. The diffusive mass flux in a fluid arises due to 4 primary driving forces: the concentration gradient, pressure gradient, external forces, and temperature gradients [74]. Fick's law governs mass fluxes due to concentrations gradients which are often the most significant driving force. Pressure gradients can result in mass fluxes, for example in rotating fluids or centrifuges where the heavier molecules are forced away from the axis of rotation. Fluxes from external forces can arise when an electric or magnetic field is applied to an ionized fluid containing charged particles. Mass fluxes driven by temperature gradients are called Soret mass fluxes, and the process is called thermal diffusion. Thermal diffusion tends to draw lighter molecules into hotter regions and heavier molecules into cold regions of a fluid. Combustion of hydrogen is likely to be influenced by thermal diffusion [75]. The discovery of thermal diffusion in gases is interesting in that it was predicted by Chapman-Enskog theory before it was observed experimentally. Soret investigated the phenomenon in liquids, and his name is often

associated with the process [76]. The total diffusive flux of component A of a N gas is given by Hirschfelder et al. [74]

$$\dot{j}''_{A,i} = \frac{C^2}{\rho}\sum_{j=1}^{N} M_A M_B D^m_{Aj} d_{A,j} - D^T_A \frac{\partial \ln T}{\partial x_i}$$

Where C is the molar concentration, M is the molar weight of the components, D^m_{Aj} is the Fick's multi-component diffusivity, D^T_A is the thermal diffusion coefficient, and the diffusive driving forces $d_{A,i}$ are defined as

$$d_{A,i} = \frac{\partial X_A}{\partial x_i} + \left(X_A - \frac{C_A M_A}{\rho} \right) \frac{\partial \ln P}{\partial x_i} - \left(\frac{C_A M_A}{P\rho} \right) \left[\frac{\rho}{M_A} f_{A,i} - \sum_{k=1}^{N} C_k f_{k,i} \right]$$

Where P is the pressure, and $f_{i,j,}$ is the body force acting on component i in the j direction. The pressure diffusion and body force diffusion terms (second and third terms) are only significant in certain situations and are most often negligible [77]. In the absence of electrical or magnetic fields the body force term can be ignored. For many porous media applications the pressure, body force, and thermal diffusion terms can be ignored. To compare the relative effects of each, consider the microwave drying of a slab of a porous material 10 cm in thickness. Assume that the material is heated in a manner that the center of the material is at 100^{o}C and the surface is cooled to 20^{o}C. The vapor pressure of water at the center will be 1atm gage or 2 atm absolute. The material can be treated as one-dimensional and symmetric about the center plane. Figure 35 shows the representative scenario. Temperature, pressure, and mass fraction will not necessarily behave in a linear fashion as they are depicted here.

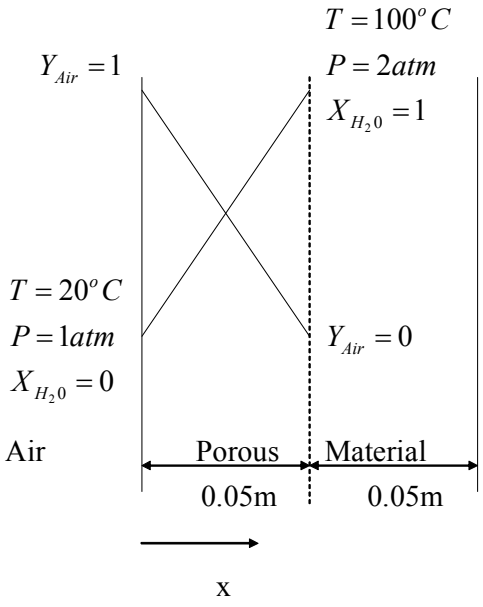

Figure 35 – Porous Material Subjected to Microwave Heating

To calculate the exact values of the diffusive flux terms is complicated but approximations and limiting values can be estimated. In the absence of electric or magnetic fields the body force diffusion term is zero

$$\frac{P}{M_j} f_{A,i} - \sum_{k=1}^{N} C_k f_{k,i} = 0$$

The molar fraction gradient driving force term is approximately

$$\frac{\partial X_{H_20}}{\partial x_i} \approx \frac{1}{0.05} = 20$$

Now calculate the pressure gradient driving force. Where mol fraction, pressure, and temperature are needed, use the average value.

$$X_{H_20} = X_{Air} = \frac{1+0}{2} = 0.5$$
$$T_{avg} = \frac{373+293}{2} = 333K$$
$$P_{avg} = \frac{1+2}{2} = 1.5atm$$

Calculate mass fraction based on molar fraction

$$Y_A = \frac{X_A M_A}{X_A M_A + X_B M_B}$$

So

$$Y_{H_20,avg} = \frac{(0.5)(18)}{(0.5)(18)+(0.5)(29)} = 0.383$$
$$Y_{Air,avg} = \frac{(0.5)(29)}{(0.5)(18)+(0.5)(29)} = 0.617$$

$$X_{H_20} - \frac{C_{H_20} M_{H_20}}{\rho} = X_{H_20} - Y_{H_20} \le 0.5 - 0.383 = 0.117$$
$$X_{Air} - \frac{C_{Air} M_{Air}}{\rho} = X_{Air} - Y_{Air} \le 0.5 - 0.617 = -0.117$$

and

$$\frac{\partial \ln P}{\partial x} = \frac{1}{P}\frac{\partial P}{\partial x} = \frac{1}{1.5}\frac{1}{0.05} = 13.3$$

So the maximum value of the pressure gradient driving force is

$$\left(X_A - \frac{C_A M_A}{\rho}\right)\frac{1}{P}\frac{\partial P}{\partial x} = (0.5 - 0.383)\frac{1}{1.5}\frac{1}{0.05} = 1.56$$

This is more than an order of magnitude less than the molar fraction driving force. So in the absence of larger pressure gradients and electric or magnetic fields, the diffusive

mass flux reduces to

$$\dot{j}''_{A,i} = \frac{C^2}{\rho}\sum_{j=1}^{N} M_A M_B D^m_{Aj} \frac{\partial X_A}{\partial x_i} - D^T_A \frac{\partial \ln T}{\partial x_i}$$

Which can be written in terms of diffusional velocities for a 2 component mixture consisting fluids of A and B as

$$V_A - V_B = -\frac{C^2}{C_A C_B} D_{AB}\left(\frac{\partial X_A}{\partial x_i} - k_T \frac{\partial \ln T}{\partial x_i}\right)$$

Where V_A and V_B are the average diffusion velocities of fluids A and B, D_{AB} is the binary diffusion coefficient, and k_T is the thermal diffusion ratio which is defined as

$$k_T = \frac{\rho}{C^2 M_A M_B}\frac{D^T_A}{D_{AB}}$$

The thermal diffusion ratio is a measure of the relative importance of thermal and ordinary diffusion. For most fluid combinations it is less than 0.1 [74]. Table 12 contains values of k_T for common gas combinations.

Table 12 – Values of Thermal diffusion ratio (Hirschfelder et al. 1954)

Gas Pair	% of Lighter Gas	$k_T \times 10^2$		$\overline{T}$ [K]
		Experimental	Calculated	
H_2-CO_2	53	6.89	8.39	300
	53	8.99	9.60	370
H_2-CO	24	3.76	3.21	142
	53	5.83	5.08	142
	24	4.45	4.81	246
	53	7.38	7.66	246
H_2-N_2	29.4	3.95	3.97	143
	42.0	5.21	5.01	143
	77.5	4.84	4.44	143
	29.4	5.48	5.90	264
	42.0	7.49	7.37	264
	77.5	6.63	6.36	264

If we continue to use the example of microwave drying of a porous material, the relative importance of thermal diffusion can be estimated. Examine the diffusion velocities for a 2-component fluid mixture. Once again the driving force terms can be approximated for purposes of comparison. A value for the thermal diffusion ratio for water vapor and air could not be found in the literature. Since for most binary gas combinations the thermal diffusion ratio is less than 0.1, use that value. Now calculate the two driving force terms from the diffusion velocity equation.

$$\frac{\partial X_A}{\partial x_i} \approx \frac{\Delta X_A}{\Delta x_i} = \frac{1}{0.05} = 20$$

$$k_T \frac{\partial \ln T}{\partial x_i} = k_T \frac{\partial \ln T}{\partial T}\frac{\partial T}{\partial x_i} = k_T \frac{1}{T}\frac{\partial T}{\partial x_i} \approx k_T \frac{1}{T}\frac{\Delta T}{\Delta x_i} = 0.1\frac{1}{333}\frac{80}{0.05} = 0.48$$

This indicates that the effects of thermal diffusion are more than an order of magnitude less than that of molar fraction driven diffusion. For porous media applications the diffusive mass flux is often approximated using Fick's law. Fick's law can be written many ways. It can be written as a diffusive velocity, molar flux, or mass flux, with the driving force as mass fraction, or molar fraction gradient. Two convenient forms of Fick's law of mass diffusion are [78]

$$\dot{j}''_{A,i} = \rho V_{A,i} = \rho\left(u_{A,i} - u_i\right) = -\rho D_{AB}\frac{\partial Y_A}{\partial x_i}$$

and

$$\dot{j}''_{A,i} = -\frac{C^2}{\rho} M_A M_B D_{AB}\frac{\partial X_A}{\partial x_i}$$

Here $j''_{A,i}$ is the diffusive mass flux in the i^{th} direction, $V_{A,I}$ is the diffusion velocity, $u_{A,i}$ is the average velocity of species A in the i-direction, and u_i is the bulk average velocity in the i-direction. The various forms of Fick's Law are described by Bird et al. [78].

B.1.5. Heat Fluxes

There are three components of the total heat flux in a multi-component system. They are conductive heat flux, inter-diffusion heat flux, and Dufour heat flux [79]. The conductive heat flux is driven by temperature gradients according to Fourier's Law of heat conduction and is the main cause of heat flux. Fourier's Law is an observed relationship between heat flux and temperature gradient which states

$$\dot{q}''_{conduction} = -k\nabla T = -k\frac{\partial T}{\partial x_i}$$

where k is the thermal conductivity of an isotropic material. If a material is anisotropic, then k is a symmetric second order tensor [78]. In this case, the heat flux does not necessarily point in the direction of the temperature gradient. Inter-diffusion heat flux arises when gas component i has an average velocity that differs from the mass average velocity of the mixture. In this case, the extra enthalpy flux carried by the j^{th} gas molecules is [79]

$$\dot{q}''_{i,\mathrm{int}erdiffusion} = \rho h_j Y_j V_{j,i}$$

The overall inter-diffusion enthalpy flux of all species in the mixture is [79]

$$\dot{q}''_{i,interdiffusion} = \rho \sum_{j=1}^{N} h_j Y_j V_{j,i}$$

Dufour heat fluxes are due to mass fraction gradients and are the reciprocal effect of Soret mass fluxes. The process is also called the diffusion thermal effect. Dufour heat fluxes are expressed as [79]

$$\dot{q}''_{Dufour} = RT \sum_{j=1}^{N} \sum_{k=1}^{N} \frac{X_k D_j^T}{M_j D_{jk}} \left(V_{j,i} - V_{k,i} \right)$$

So the total heat flux vector is

$$\dot{q}''_i = k \frac{\partial T}{\partial x_i} + \rho \sum_{j=1}^{N} h_j Y_j V_{j,i} + RT \sum_{j=1}^{N} \sum_{k=1}^{N} \frac{X_k D_{j\,j}^T}{M_j D_{jk}} \left(V_{j,i} - V_{k,i} \right)$$

where $V_{j,i}$ is the mass diffusion velocity of the j^{th} component in the i direction, and h_j is the enthalpy of the j^{th} component. In general, the inter-diffusive and Dufour heat fluxes are ignored since they are small compared to the conduction heat flux. To show this consider again the wet porous material subjected to microwave heating. Assume that the material has thermal properties similar to that of yellow pine (k=0.147W/m^{2}K, [57] First the estimate the conductive heat flux

$$\dot{q}''_{cond,x} = -k \frac{\partial T}{\partial x} \approx -k \frac{\Delta T}{\Delta x} = -0.147 \frac{80}{0.05} = -235 \frac{W}{m^2}$$

Now estimate the inter-diffusive heat flux

$$\dot{q}''_{interdiffusion,x} = \rho \sum_{j=1}^{N} h_j Y_j V_{j,i} = \rho \left(h_{H_20} Y_{H_20} V_{H_20} + h_{Air} Y_{Air} V_{Air} \right)$$

First calculate the diffusional velocities.

$$V_A = -D_{AB}\frac{\partial Y_A}{\partial x}$$

$$V_{H_20} \approx -D_{Air-H_20}\frac{\Delta Y_{H_20}}{\Delta x} = -D_{Air-H_20}\frac{1}{0.05}$$

$$V_{Air} \approx -D_{Air-H_20}\frac{\Delta Y_{Air}}{\Delta x} = -D_{Air-H_20}\frac{-1}{0.05}$$

The binary diffusion coefficient for air – water vapor is given in Turns [80] as

$$D_{Air-H_20} = 2.2\times10^{-5}\frac{m^2}{s} \quad @\ 273\ \text{K}$$

An approximate correlation that includes temperature and pressure effects is given by Ni [41] as

$$D_{Air-H_20} = 2.3\times10^{-5}\frac{P_o}{P}\left(\frac{T}{T_o}\right)^{1.81}$$

Where T_o=256K and P_o=1atm. Since the exact shape of the temperature, pressure, and mass fraction gradients is not known, calculate diffusivity and enthalpies at the average temperature, pressure, and mass fraction

$$T_{avg} = \frac{100+20}{2} = 60^oC$$

$$Y_{H_20,avg} = Y_{Air,avg} = \frac{1+0}{2} = 0.5$$

$$P_{Avg} = \frac{1+2}{2} = 1.5$$

$$D_{Air-H_20} = 2.3\times10^{-5}\frac{1}{1.5}\left(\frac{333}{256}\right)^{1.81} = 2.47\times10^{-5}\frac{m^2}{s}$$

So the diffusion velocities are

$$V_{H_20} \approx -2.47\times10^{-5}\frac{1}{0.05} = -4.94\times10^{-4}\frac{m}{s}$$
$$V_{Air} \approx 2.47\times10^{-5}\frac{1}{0.05} = 4.92\times10^{-4}\frac{m}{s}$$

And the enthalpy and density of the gas mixture are

$$h_{H_20} = 2610\frac{kJ}{kg}\ \ (Moran\,and\,Shapiro, 2000)$$
$$h_{Air} = 333\frac{kJ}{kg}\ \ (Moran\,and\,Shapiro, 2000)$$
$$\rho = Y_{H_20}\rho_{H_20} + Y_{Air}\rho_{Air} = Y_{H_20}\frac{P}{R_{H_20}T} + Y_{Air}\frac{P}{R_{Air}T}$$
$$\rho = 0.5\frac{152000}{(461)(333)} + 0.5\frac{152000}{(287)(333)} = 0.495 + 1.59 = 2.09\frac{kg}{m^3}$$

So the inter-diffusion heat flux is

$$\dot{q}''_{\text{int}erdiffusion,x} = 2.09\left((2610)(0.5)\left(-4.94\times10^{-4}\right) + (333)(0.5)\left(4.94\times10^{-4}\right)\right)$$
$$\dot{q}''_{\text{int}erdiffusion,x} = -1.18\frac{W}{m^2}$$

This is much smaller than the conduction heat flux so it seems reasonable to ignore it. Next examine the Dufour heat flux.

$$\dot{q}''_{Dufour} = RT\sum_{j=1}^{N}\sum_{k=1}^{N}\frac{X_k D_j^T}{M_j D_{jk}}\left(V_{j,i} - V_{k,i}\right)$$

Hirschfelder et al. give values for the thermal diffusion ratio k_T which can be used to calculate the ratio D_j^T / D_{jk}

$$k_T = \frac{\rho}{C^2 M_{Air} M_{H_20}} \frac{D^T_{Air}}{D_{Air-H_20}}$$

$$\frac{D^T_{Air}}{D_{Air-H_20}} = k_T \frac{C^2 M_{Air} M_{H_20}}{\rho}$$

And the diffusion velocities can be calculated by [74]

$$V_{Air} - V_{H_20} = -\frac{C^2}{C_{Air} C_{H_20}} D_{Air-H_20} \frac{\partial X_{Air}}{\partial x}$$

Where

$$C = \frac{P}{RT} = \frac{152000}{(8314)(333)} = 0.055 \frac{mol}{m^3}$$

$$C_{Air} = CY_{Air} = 0.055(0.5) = 0.0275 \frac{mol}{m^3}$$

$$C_{H_20} = CY_{H_20} = 0.055(0.5) = 0.0275 \frac{mol}{m^3}$$

So the diffusion velocities can be calculated as

$$V_{Air} - V_{H_20} \approx -\frac{(0.055)^2}{(0.0275)(0.0275)} \left(2.47 \times 10^{-5}\right) \frac{-1}{0.05} = 0.002 \frac{m}{s}$$

and

$$V_{H_20} - V_{Air} = -\frac{C^2}{C_{H_20} C_{Air}} D_{Air-H_20} \frac{\partial X_{H_20}}{\partial x}$$

$$V_{H_20} - V_{Air} \approx -\frac{(0.055)^2}{(0.0275)(0.0275)} \left(2.47 \times 10^{-5}\right) \frac{1}{0.05} = -0.002 \frac{m}{s}$$

So the Dufour heat fluxes can be calculated as

$$\dot{q}''_{Dufour} = RT\sum_{i=1}^{2}\sum_{j=1}^{2}\frac{X_j}{M_i}k_T\frac{C^2 M_i M_j}{\rho}\left(V_i - V_j\right)$$

$$\dot{q}''_{Dufour} = RT\frac{X_{H_20}}{M_{Air}}k_T\frac{C^2 M_{Air}M_{H_20}}{\rho}\left(V_{Air} - V_{H_20}\right) + RT\frac{X_{Air}}{M_{H_20}}k_T\frac{C^2 M_{Air}M_{H_20}}{\rho}\left(V_{H_20} - V_{Air}\right)$$

$$\dot{q}''_{Dufour} = (8314)(333)\frac{0.5}{29}0.1\frac{(0.055)^2(29)(18)}{(2.09)}(0.002) + (8314)(333)\frac{0.05}{18}0.1\frac{(0.055)^2(29)(18)}{(2.09)}(-0.002)$$

$$\dot{q}''_{Dufour} = 7.21 - 11.6 = -4.39\frac{kW}{m^2}$$

B.1.6. Vapor Pressure

The vapor pressure above a flat liquid surface can be calculated using the Clausius-Clapeyron thermodynamic relation which states [36]

$$P_v = P_o \exp\left[-\frac{\Delta h_{vap}}{R_v}\left(\frac{1}{T} - \frac{1}{T_o}\right)\right]$$

Where P_o is the reference pressure (101300 Pa) at the reference temperature T_o (373K), R_v is the vapor gas constant, and Δh_{vap} is the enthalpy of vaporization of the liquid.

For very wet materials, the Clausius-Clapeyron equation can be used to calculate the vapor pressure in the pore spaces. For very dry materials, or materials with vary small pore diameters, surface tension effects will change the vapor pressure-temperature relation and the Kelvin relation might be more appropriate. The Kelvin equation states [36]

$$P_v = P_o \exp\left[-\frac{2\sigma}{r\rho_l R_v T}\right]$$

Where P_o is the reference pressure (101300 Pa), σ is the surface tension, r is the radius of curvature for a single interface, ρ_l is the density of the liquid, R_v is the vapor gas constant, and T is the temperature. When the Kelvin equation is used to

calculate the vapor pressure in a porous material, r is not explicitly known due to the range of pore diameters. Whitaker [36] states that r will become an experimentally determined characteristic length of the material. For many materials the radius of curvature can be modeled as a function of saturation and temperature.

Another important means of modeling the vapor pressure in a porous material is called a moisture sorption isotherm. This is a relationship between the vapor pressure in the pores of a material and the moisture content at a certain temperature. For brick, the relation between relative humidity and moisture content is given as

$$M = 0.0105\left(RH\right)^{0.2} + 0.0125\exp\left(20 \cdot RH - 20\right)$$

This is shown graphically in Figure 36.

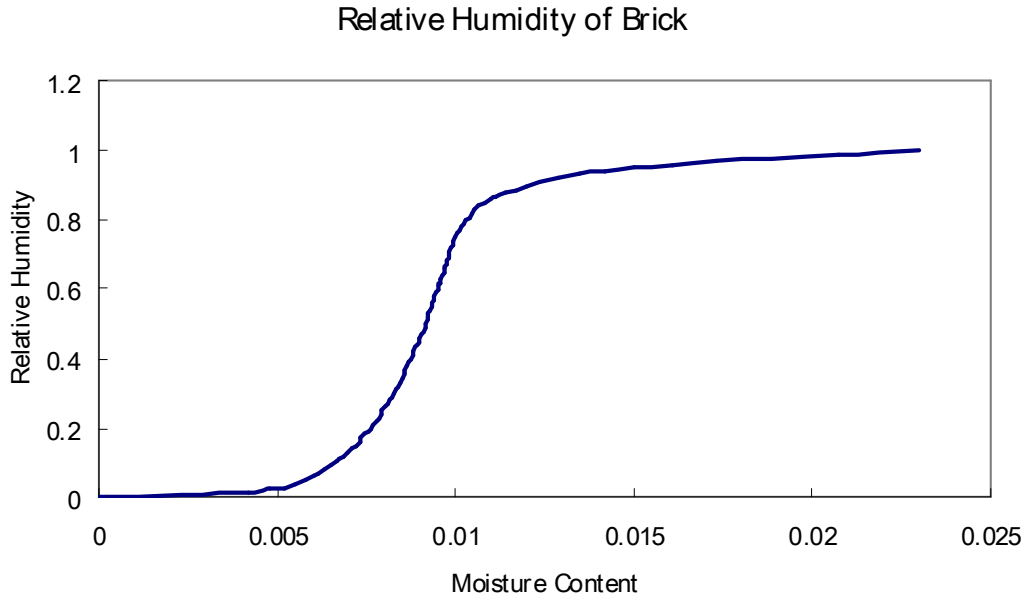

Figure 36 – Relative Humidity of Brick (From [48])

Since brick reaches 100% relative humidity at a very low moisture content, it is considered to be a non-hygroscopic material. That is, it absorbs very little moisture into the solid material. Other materials will absorb significant amounts of water into the solid matrix and exhibit reduced vapor pressure at higher moisture contents due to

higher levels of bound water. The sorption relation for wood is given by Nasrallah and Perre [38] as

$$p_v = p_{vs} \exp\left(\left(17.884 - 0.1423T + 0.0002363T^2\right)\left(1.0327 - 0.000674T\right)^{92M}\right)$$

The sorption isotherms for wood at three different temperatures are shown in Figure 37.

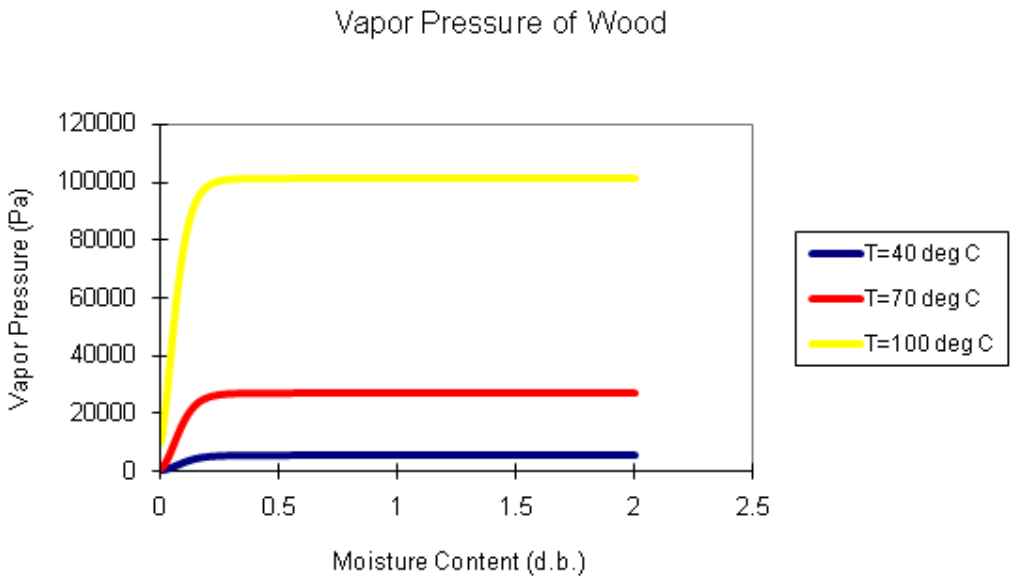

Figure 37 – Sorption Isotherms for Wood (from [38])

B.1.7. Darcy's Law

Fluid will flow through a porous material under a pressure gradient according to Darcy's Law

$$\vec{u}_D = -\frac{K}{\mu}\left(\nabla P - \rho g\right) \quad or \qquad u_{D,i} = -\frac{K}{\mu}\left(\frac{\partial P}{\partial x_i} - \rho g_i\right)$$

Where the factor K is the permeability of the material in m^2, μ and ρ are the viscosity and density of the fluid in kg/ms and kg/m^3, and the Darcean velocity u_D is related to the average pore velocity u_p by the porosity of the material

$$\vec{u}_D = \phi \vec{u}_p$$

Values of K for some common porous materials given by [25] are shown in Table .

Table 13 - Permeability of Several Materials

Substance	Permeability $\left(m^2\right)$
Sandstone (oil sand)	5.0×10^{-16} to 3.0×10^{-12}
Brick	4.8×10^{-15} to 2.2×10^{-13}
Limestone, dolomite	2.0×10^{-15} to 4.5×10^{-14}
Leather	9.5×10^{-14} to 1.2×10^{-13}
Black slate powder	4.9×10^{-14} to 1.2×10^{-13}
Agar	2.0×10^{-14} to 4.4×10^{-13}
Silica powder	1.3×10^{-14} to 5.1×10^{-14}
Soils	2.9×10^{-13} to 1.4×10^{-11}
Bituminous concrete	1.0×10^{-13} to 2.3×10^{-11}
Fiberglass	2.4×10^{-11} to 5.1×10^{-11}
Sand	2.0×10^{-11} to 1.8×10^{-10}
Hair felt	8.3×10^{-10} to 1.2×10^{-9}
Cork board	3.3×10^{-10} to 1.5×10^{-9}
Wire crimps	3.8×10^{-9} to 1.0×10^{-8}
Cigarettes	1.1×10^{-9}
Berl saddles	1.3×10^{-7} to 3.9×10^{-7}

Darcy's Law can be rearranged and written as

$$-\frac{\partial P}{\partial x_i} = u_{D,i}\frac{\mu}{K} - \rho g$$

Kaviany (1995) describes the various flow regimes in porous media flows. As velocity is increased the flow will transition from the Darcy regime (Re_d<1,viscous forces dominate), to the inertial regime (1<Re_d<150, inertial forces affect the pressure drop significantly), to the unsteady laminar regime (150<Re_d<300, some oscillations are observed but flow is still laminar), to finally the fully turbulent regime (Re_d>300, flow is highly unsteady and chaotic). To account for these effects as well as transient acceleration a longer form of Darcy's law is sometimes used (Kaviany, 1995)

$$\frac{\rho_o}{\phi}\left(\frac{\partial u_{D,i}}{\partial t} + u_{D,i}\cdot\nabla u_{D,i}\right) = -\frac{\partial P}{\partial x_i} + \rho g + \frac{\mu}{\phi}\nabla^2 u_{D,i} - \frac{\mu}{K}u_{D,i} - \frac{C_E}{\sqrt{K}}\rho\left|u_{D,i}\right|u_{D,i}$$

The terms is this equation represent fluid acceleration (material or co-moving derivative), the pore pressure gradient, body forces, macroscopic or bulk viscous diffusion (this is also called the Brinkman viscous term), microscopic visous shear stresses (Darcy term), and the last term is called the microscopic inertial force or the Ergun inertial term. The coefficient C_E is the Ergun coefficient and usually takes on a value of 0.550 [23]. As the porosity of a material goes to 1 $(\phi \to 1)$, the permeability K will get large and the last two terms will approach zero and the transient version of Darcy's Law will reduce to the Navier Stokes equations. The steady state version of Darcy's law is by far the most commonly used.

B.2. Conservation Laws

The basic laws of conservation of mass, momentum, and energy apply to single phase systems as well as multiple phase systems such as porous materials. When dealing with a porous material there must be a means of coupling between the solid and fluid phases at the interfaces. This is quite complicated given the three dimensional structure of many porous materials. It is common to invoke the continuum assumption and use modified conservation laws when dealing with a fluid in a porous material. The conservation laws will be discussed, and then the common simplifications that are used to model porous media will be covered.

B.2.1. Mass Conservation

The conservation of mass for a multi-component fluid can be derived as follows. Consider the 2 dimensional differential control volume of dimensions $\Delta x \Delta y$ shown in Figure 38

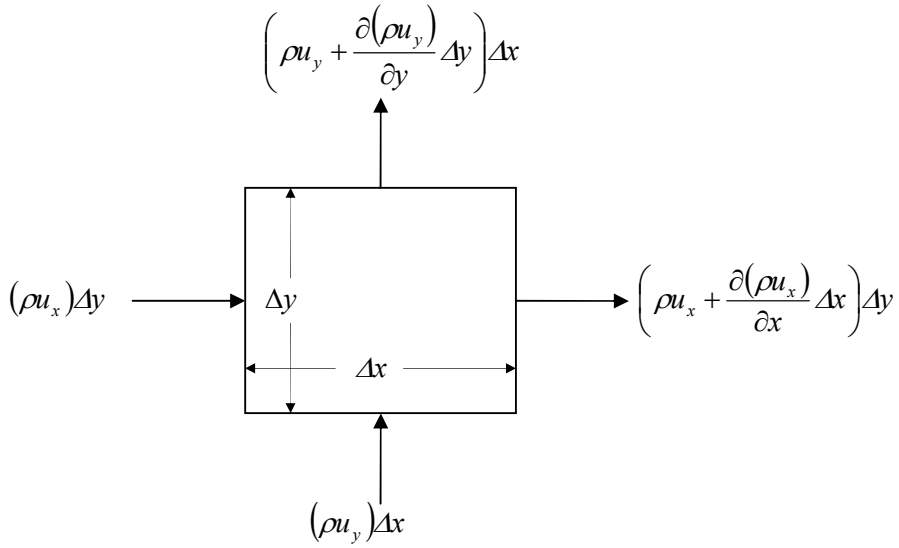

Figure 38 – A fixed infinitesimal control volume in a 2 dimensional flow field

Summing all of the mass fluxes in Figure 38 gives

$$\frac{\partial(\rho u_x)}{\partial x}\Delta x\Delta y + \frac{\partial(\rho u_y)}{\partial y}\Delta x\Delta y$$

This is equal to the rate of change of mass in the control volume

$$\frac{\partial \rho}{\partial t}\Delta x\Delta y = \frac{\partial(\rho u_x)}{\partial x}\Delta x\Delta y + \frac{\partial(\rho u_y)}{\partial y}\Delta x\Delta y$$
$$\frac{\partial \rho}{\partial t} = \frac{\partial(\rho u_x)}{\partial x} + \frac{\partial(\rho u_y)}{\partial y}$$

or more generally

$$\frac{\partial \rho}{\partial t} + \frac{\partial}{\partial x_i}(\rho u_i) = 0$$

When individual species are considered, such as when a chemical reaction is occurring, the conservation equation for species A is [79]

$$\rho \frac{DY_A}{Dt} = \frac{\partial}{\partial x_i}\left(\rho D_A \frac{\partial Y_A}{\partial x_i}\right) + \dot{\omega}_A'''$$

Where Y_A, D_A, and $\dot{\omega}_A'''$ are the mass fraction, mass diffusion coefficient, and chemical generation rate for species A.

B.2.2. Momentum Conservation

To derive the differential form of the conservation of momentum consider a 2 dimensional fluid particle of dimensions $\Delta x \Delta y$ shown in Figure 39. σ_{ij} is a surface stress on the i=constant plane and acting in the j direction.

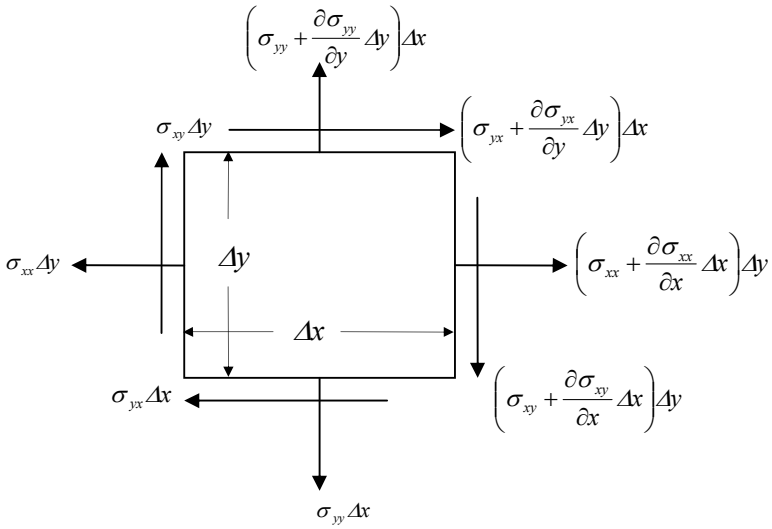

Figure 39 – Forces acting on a 2 dimensional fluid particle

The sum of all the surface forces acting on the fluid particle in the x direction is

$$\sum F_x = -(\sigma_{xx})\Delta y + \left(\sigma_{xx} + \frac{\partial \sigma_{xx}}{\partial x}\Delta x\right)\Delta y - (\sigma_{yx})\Delta x + \left(\sigma_{yx} + \frac{\partial \sigma_{yx}}{\partial y}\Delta y\right)\Delta x$$

$$= \frac{\partial \sigma_{xx}}{\partial x}\Delta x \Delta y + \frac{\partial \sigma_{yx}}{\partial y}\Delta x \Delta y$$

And in the y direction

$$\sum F_y = -\left(\sigma_{yy}\right)\Delta x + \left(\sigma_{yy} + \frac{\partial \sigma_{yy}}{\partial x}\Delta y\right)\Delta x - \left(\sigma_{xy}\right)\Delta y + \left(\sigma_{xy} + \frac{\partial \sigma_{xy}}{\partial x}\Delta x\right)\Delta y$$

$$\sum F_y = \frac{\partial \sigma_{yy}}{\partial y}\Delta x \Delta y + \frac{\partial \sigma_{xy}}{\partial x}\Delta x \Delta y$$

Newton's second law of motion states that the sum of all forces on an object equals the temporal derivative of its momentum.

$$\sum F = ma = m\frac{Du_i}{Dt} = \rho\left(\frac{\partial u_i}{\partial t} + u_j \frac{\partial u_i}{\partial x_j}\right)\Delta x \Delta y$$

Where the material derivative is defined as

$$\frac{D(\ )}{Dt} = \frac{\partial(\ )}{\partial t} + u_i \frac{\partial(\ )}{\partial x_i}$$

Equating this to the sum of all forces in the i direction produces the momentum equation shown here in indicial notation [79].

$$\rho \frac{Du_i}{Dt} = \frac{\partial \sigma_{ij}}{\partial x_j} + B_i \qquad where\ i = x, y, z$$

B is the body force acting on the fluid

$$B_i = \rho \sum_{k=1}^{n} Y_k f_{k,i}$$

and the stress tensor σ_{ij} is defined as

$$\sigma_{ij} = -P\delta_{ij} + \left(\mu' - \frac{2}{3}\mu\right)\frac{\partial u_k}{\partial x_k}\delta_{ij} + \mu\left(\frac{\partial u_i}{\partial x_j} + \frac{\partial u_j}{\partial x_i}\right)$$

Where μ' is the bulk viscosity and is often assumed to be zero [79], and δ_{ij} is the Kronecker delta function defined as

$$\delta_{ij} = \begin{cases} 1 & for\ i = j \\ 0 & for\ i \neq j \end{cases}$$

When the material properties ρ and μ are constant, the momentum equation can be simplified to a form shown here in Gibbs (symbolic) notation

x-component

$$\rho\left(\frac{\partial u}{\partial t} + u\frac{\partial u}{\partial x} + v\frac{\partial u}{\partial y} + w\frac{\partial u}{\partial z}\right) = -\frac{\partial P}{\partial x} + \mu\left(\frac{\partial^2 u}{\partial x^2} + \frac{\partial^2 u}{\partial y^2} + \frac{\partial^2 u}{\partial z^2}\right) + B_x$$

y-component

$$\rho\left(\frac{\partial v}{\partial t} + u\frac{\partial v}{\partial x} + v\frac{\partial v}{\partial y} + w\frac{\partial v}{\partial z}\right) = -\frac{\partial P}{\partial y} + \mu\left(\frac{\partial^2 v}{\partial x^2} + \frac{\partial^2 v}{\partial y^2} + \frac{\partial^2 v}{\partial z^2}\right) + B_y$$

z-component

$$\rho\left(\frac{\partial w}{\partial t} + u\frac{\partial w}{\partial x} + v\frac{\partial w}{\partial y} + w\frac{\partial w}{\partial z}\right) = -\frac{\partial P}{\partial z} + \mu\left(\frac{\partial^2 w}{\partial x^2} + \frac{\partial^2 w}{\partial y^2} + \frac{\partial^2 w}{\partial z^2}\right) + B_z$$

These three components of the simplified momentum equation and the continuity equation form a system of four equations with four unknowns (u, v, w, P). For non-isothermal conditions the energy equation must be also included, since temperature adds a fifth unknown. The momentum equation is a system of non-linear PDE's which has not been solved analytically, except for certain simplified geometries. The system can be solved numerically using computational fluid dynamics software, but this is not practical for flow through complex pore geometries. Techniques for modeling flow will be discussed later.

B.2.3. Conservation of Energy

To derive the energy equation, consider the control volume of dimensions $\Delta x \Delta y$ shown in Figure 40.

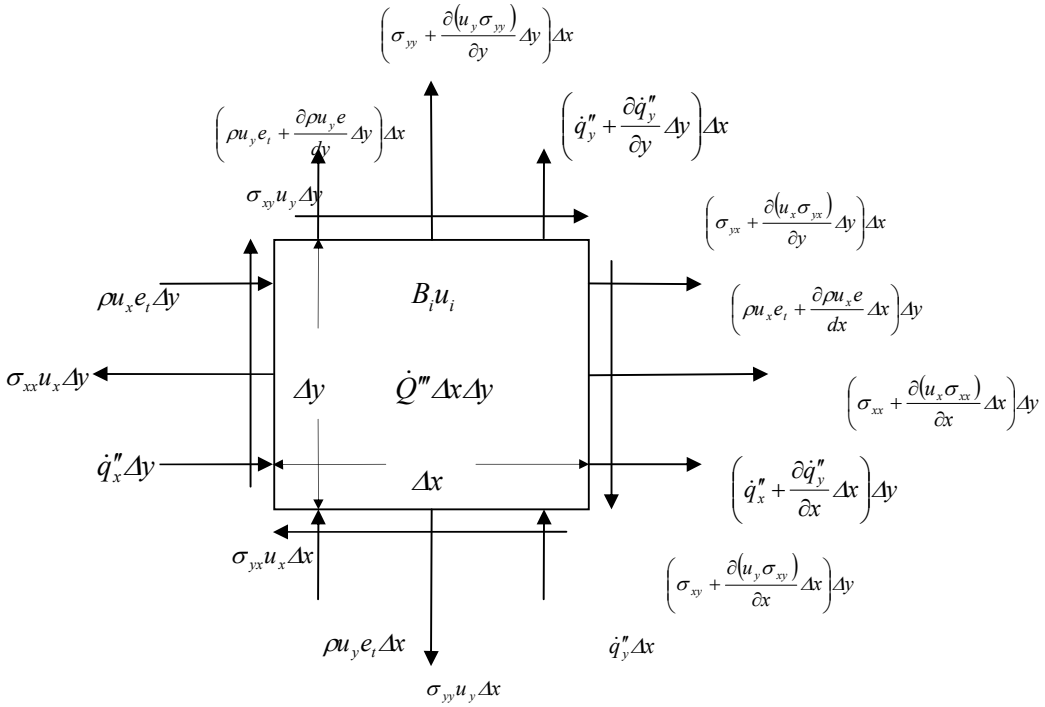

Figure 40 – Enthalpy fluxes in a 2 dimensional reacting flow field

Here e_t represents the total internal energy and B_iu_i represents body force work and they are defined as

$$e_t = e + \frac{u_i u_i}{2} \quad \text{and} \quad B_i u_i = \rho \sum_{k=1}^{n} Y_k f_{k,i}\left(u_i + V_{k,i}\right)$$

Where e is the specific internal energy and $V_{k,i}$ is the diffusional velocity of species k in the i direction.
The total change in internal and kinetic energy is

$$\frac{\partial}{\partial t}(\rho e_t) = -\frac{\partial}{\partial x_i}(\rho u_i e_t) - \frac{\partial \dot{q}''_i}{\partial x_i} + \dot{Q}''' + \frac{\partial(u_i \sigma_{ji})}{\partial x_j} + \rho \sum_{k=1}^{n} Y_k f_{k,i}\left(u_i + V_{k,i}\right)$$

or

$$\frac{\partial}{\partial t}(\rho e_t) + \frac{\partial}{\partial x_i}(\rho u_i e_t) = -\frac{\partial \dot{q}''_i}{\partial x_i} + \dot{Q}''' + \frac{\partial(u_i \sigma_{ji})}{\partial x_j} + \rho \sum_{k=1}^{n} Y_k f_{k,i}\left(u_i + V_{k,i}\right)$$

This can be simplified. First expand the derivatives on the LHS

$$\rho\frac{\partial e_t}{\partial t}+e_t\frac{\partial \rho}{\partial t}+\rho u_i\frac{\partial e_t}{\partial x_i}+e_t\frac{\partial(\rho u_i)}{\partial x_i}=-\frac{\partial \dot{q}_i''}{\partial x_i}+\dot{Q}'''+\frac{\partial(u_i\sigma_{ji})}{\partial x_j}+\rho\sum_{k=1}^{n}Y_k f_{k,i}(u_i+V_{k,i})$$

From the continuity equation we know that

$$\frac{\partial \rho}{\partial t}+\frac{\partial(\rho u_i)}{\partial x_i}=0$$

So the energy equation becomes

$$\rho\frac{\partial e_t}{\partial t}+\rho u_i\frac{\partial e_t}{\partial x_i}=-\frac{\partial \dot{q}_i''}{\partial x_i}+\dot{Q}'''+\frac{\partial(u_i\sigma_{ji})}{\partial x_j}+\rho\sum_{k=1}^{n}Y_k f_{k,i}(u_i+V_{k,i})$$

Using the definition of total internal energy and expanding terms

$$\rho\frac{\partial e_t}{\partial t}+\rho\frac{\partial\left(\frac{1}{2}u_iu_i\right)}{\partial t}+\rho u_i\frac{\partial e_t}{\partial x_i}+\rho u_j\frac{\partial\left(\frac{1}{2}u_iu_i\right)}{\partial x_j}=-\frac{\partial \dot{q}_i''}{\partial x_i}+\dot{Q}'''+u_i\frac{\partial \sigma_{ji}}{\partial x_j}+\sigma_{ji}\frac{\partial u_i}{\partial x_j}$$
$$+\rho\sum_{k=1}^{n}Y_k f_{k,i}u_i+\rho\sum_{k=1}^{n}Y_k f_{k,i}V_{k,i}$$

Now if we multiply the momentum equation by u_i it becomes

$$\rho u_i\left(\frac{\partial u_i}{\partial t}+u_j\frac{\partial u_i}{\partial x_j}\right)=u_i\frac{\partial \sigma_{ij}}{\partial x_j}+\rho\sum_{k=1}^{n}Y_k f_{k,i}u_i$$

Which can be rearranged as

$$\rho\left(\frac{\partial\left(\frac{1}{2}u_iu_i\right)}{\partial t}+u_j\frac{\partial\left(\frac{1}{2}u_iu_i\right)}{\partial x_j}\right)=u_i\frac{\partial \sigma_{ij}}{\partial x_j}+\rho\sum_{k=1}^{n}Y_k f_{k,i}u_i$$

Subtract this from the total energy equation and we have

$$\rho\frac{\partial e}{\partial t}+\rho u_i\frac{\partial e}{\partial x_i}+=-\frac{\partial \dot{q}_i''}{\partial x_i}+\dot{Q}'''+\sigma_{ji}\frac{\partial u_i}{\partial x_j}+\rho\sum_{k=1}^{n}Y_k f_{k,i}V_{k,i}$$

Using the definition of internal energy

$$e=h-\frac{P}{\rho}$$

and assuming that heat input, $\dot{Q}'''$, is zero, the law of conservation of energy can be written in terms of enthalpy [79]

$$\rho\frac{Dh}{Dt}-\frac{DP}{Dt}=\frac{\partial \dot{q}_i''}{\partial x_i}+\tau_{ij}\frac{\partial u_i}{\partial x_j}+\rho\sum_{k=1}^{N}Y_k f_{k,i}V_{k,i}$$

Where τ is the shear stress and is given by

$$\tau_{ij}=\left(\mu'-\frac{2}{3}\mu\right)\frac{\partial u_k}{\partial x_k}+\mu\left(\frac{\partial u_i}{\partial x_j}+\frac{\partial u_j}{\partial x_i}\right)$$

Using the definition of enthalpy

$$h=\Delta h_f^o+\int_{T^o}^{T}C_p dT$$

and Fourier's law of heat conduction

$$\dot{q}_i''=k\frac{\partial T}{\partial x_i}$$

the conservation of energy can be written in terms of temperature

$$\rho C_p\frac{DT}{Dt}-\frac{DP}{Dt}=\frac{\partial}{\partial x_i}\left(k\frac{\partial T}{\partial x_i}\right)+\tau_{ij}\frac{\partial u_i}{\partial x_j}-\sum_{i=1}^{N}\dot{\omega}_i'''\Delta h_{f,i}^o+\rho\sum_{k=1}^{N}Y_k f_{k,i}V_{k,i}$$

Where $\sum_{i=1}^{N}\dot{\omega}_i'''\Delta h_{f,i}^o$ and $\rho\sum_{k=1}^{N}Y_k f_{k,i}V_{k,i}$ represent the heat generated by chemical reaction or phase change and body force work. This formulation assumes that inter-diffusion heat fluxes and Dufour effects are negligible.

B.3. Modeling Techniques for Porous Media

B.3.1. Quasi-analytical derivation of Darcy's Law

Flow through a single capillary is a case where an analytical solution of the Navier Stokes equations is possible. An idealized porous material can be considered to be a solid with uniform parallel capillary tubes as shown in Figure 41.

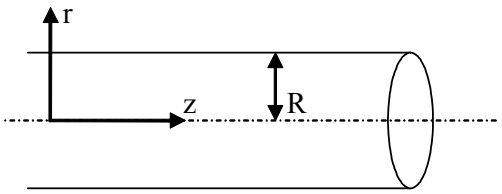

Figure 41 – Capillary Tube

In this case there is a clearly defined pore diameter. The average velocity for fully developed fluid flow in a tube can be obtained by integrating the momentum equation in cylindrical coordinates.

z-direction momentum [73]

$$\rho\left(\frac{\partial u_z}{\partial t}+u_r\frac{\partial u_z}{\partial r}+\frac{u_r}{r}\frac{\partial u_z}{\partial \theta}+u_r\frac{\partial u_z}{\partial z}\right)=-\frac{\partial P}{\partial z}+\mu\left(\frac{1}{r}\frac{\partial}{\partial r}\left(r\frac{\partial u_z}{\partial r}\right)+\frac{1}{r^2}\frac{\partial^2 u_z}{\partial \theta^2}+\frac{\partial^2 u_z}{\partial z^2}\right)+\rho g_z$$

Since the flow is in the z direction and is only a function of r, if we ignore the effects of gravity, the momentum equation simplifies to

$$\frac{1}{r}\frac{\partial}{\partial r}\left(r\frac{\partial u_z}{\partial r}\right)=-\frac{1}{\mu}\frac{\partial P}{\partial z}$$

Subject to the following boundary conditions

$$@\, r=0, \quad \frac{\partial u_z}{\partial r}=0$$
$$@\, r=R, \quad u_z=0$$

Integrate this twice

$$\int \frac{\partial}{\partial r}\left(r\frac{\partial u_z}{\partial r} \right) = -\int \frac{1}{\mu}\frac{\partial P}{\partial z} r$$

$$r\frac{\partial u_z}{\partial r} = -\frac{1}{\mu}\frac{\partial P}{\partial z}\frac{r^2}{2} + C_1$$

$$\int \frac{\partial u_z}{\partial r} = -\int \frac{1}{\mu}\frac{\partial P}{\partial z}\frac{r}{2} + \frac{C_1}{r}$$

$$u_z = -\frac{1}{\mu}\frac{\partial P}{\partial z}\frac{r^2}{4} + C_1 \ln\left(r\right) + C_2$$

Apply the boundary conditions for this case

BC 1

$$r\frac{\partial u_z}{\partial r} = -\frac{1}{\mu}\frac{\partial P}{\partial z}\frac{r^2}{2} + C_1$$

$$0 = 0 + C_1$$

$$C_1 = 0$$

BC 2

$$u_z = -\frac{1}{\mu}\frac{\partial P}{\partial z}\frac{r^2}{4} + C_1 \ln\left(r\right) + C_2$$

$$0 = -\frac{1}{\mu}\frac{\partial P}{\partial z}\frac{R^2}{4} + C_2$$

$$C_2 = \frac{1}{\mu}\frac{\partial P}{\partial z}\frac{R^2}{4}$$

So,

$$u_z = \frac{R^2}{4\mu}\frac{\partial P}{\partial z}\left(1 - \frac{r^2}{R^2} \right)$$

Where the maximum velocity is

$$u_{\max} = \frac{R^2}{4\mu}\frac{\partial P}{\partial z}$$

The average velocity is obtained by integrating over the capillary tube cross sectional area

$$u_{avg} = \frac{Q}{A} = \frac{1}{\pi R^2}\int_{\theta=0}^{2\pi}\int_{r=0}^{R}\frac{1}{4\mu}\frac{\partial P}{\partial z}\left(R^2 - r^2\right) r\,\partial r\partial\theta$$

$$u_{avg} = \frac{1}{\pi R^2}\frac{2\pi}{4\mu}\frac{\partial P}{\partial z}\left(\frac{R^2 r^2}{2} - \frac{r^4}{4}\right)\Bigg|_0^R$$

$$u_{avg} = \frac{R^2}{8\mu}\frac{\partial P}{\partial z} = \frac{d^2}{32\mu}\frac{\partial P}{\partial z}$$

Where d is the diameter of the capillary tube. This is the Hagen-Poiseuille equation [23]. The equation can be written in terms of Darcean velocity, u_D, using $\varphi = n\pi d^2/4$, where n is the number of capillary tubes per unit cross sectional area.

$$u_D = -\phi\frac{d^2}{32\mu}\frac{dp}{dx} = -\frac{n\pi d^4}{128\mu}\frac{dp}{dx}$$

Relating this flow to Darcy's law in one dimension allows for an analytical solution for the permeability K

$$u_D = -\frac{K}{\mu}\frac{\partial P}{\partial x} = -\frac{n\pi d^4}{128\mu}\frac{dp}{dx}$$

$$K = \frac{n\pi d^4}{128} = \frac{\phi d^2}{32}$$

Real porous materials usually have complex pore networks, and do not strictly obey this simple capillary model. It is, however, useful to relate this model to pores that have irregular diameters. A simple model for flow through solid matrices can be used to predict the permeability of other simple porous materials. Carmen-Kozeny theory [24] predicts permeability based on the pore hydraulic diameter and tortuosity

$$d_h = \frac{4 \times void\ \ volume}{surface\ \ area} = \frac{4\phi}{A_o^*(1-\phi)}$$

$$\tau = \frac{L_e}{L}$$

Where L_e is the effective length in a curved pore through which fluid must flow to travel a distance L. The modified equation for K now becomes [23]

$$K = \frac{\phi d_h^2}{16 k_o \tau^2} = \frac{\phi^3}{k_o \tau^2 (1-\phi)^2 A_o^{*2}}$$

Where k_o is a shape parameter and is equal to 2 for circular capillaries, and 2-2.5 for rectangular, elliptical, and annular shapes [81] and A_o^* is a special version of the specific surface area and has units of m^2/m^3. It is defined as the ratio of wetted surface area to solid volume $\frac{A_{sg}}{V_s}$. For packed spheres this is

$$A_o^* = \frac{A_{fs}}{V_s} = \frac{4\pi r^2}{\frac{4}{3}\pi r^3} = \frac{3}{r} = \frac{6}{d}$$

Happel and Brennar [81] suggest a value of $\sqrt{2}$ for the tortuosity τ and 2.5 for the shape factor k_o for packed beds of spheres. This leads to the prediction of permeability known as the Carmen Kozeny equation [23]. For a packed bed of spheres this is

$$K = \frac{\phi^3}{180(1-\phi)^2} d^2$$

.

For particles that have a narrow range of diameter distribution, Rumpf and Gupte [82] give an empirical equation that shows better agreement with experimental data [23]

$$K = \frac{\phi^{5.5}}{5.6} d^2$$

Most single phase flows through porous media are modeled using Darcy's law with either quasi-analytical or empirical values for K. Direct application of the Navier Stokes equations usually is not practical for porous media flows. Mapping the pore structure and solving flow problems using a CFD code is prohibitively time consuming except in cases of simple pore structures.

B.3.2. Gas Phase Diffusion in Porous Media

As was discussed earlier, the driving forces for diffusion of gases are often dominated by the concentration gradient driving force. For this reason gas phase diffusion is frequently written as a form of Fick's Law. It is convenient to write it in terms of a mass flux with the molar fraction as the driving force. The mass flux of component A in the i-direction is written as

$$\dot{j}''_{A,i} = -\frac{C^2}{\rho} M_A M_B D_{AB} \frac{\partial X_A}{\partial x_i}$$

This is convenient because the molar fraction of gases is proportional to the partial pressure of the gas. At equilibrium the partial pressure is the vapor pressure which can be calculated using the Clausius-Clapeyron relation from Thermodynamics. In porous materials gas phase diffusion will occur through a smaller cross sectional area due to the presence of the solid and liquid phase. There will be further reduction in the diffusion mass flux due to the tortuous path through which the gas must travel. A general formula for the diffusivity of a binary gas mixture in a porous media is given by Geankoplis [83] as

$$D_{eff,g} = D_{AB} \frac{\psi_g}{\tau}$$

Where ψ_g is the volume fraction of gas in the porous material, and τ is the tortuosity of the gas path. The tortuosity is the ratio of the average path that a fluid particle must travel between two points (also called the effective length) in the porous material to the linear distance between the two points (or the actual length)[23].

$$\tau = \frac{L_e}{L}$$

Some authors will write this as

$$\frac{L_e}{L} = 1 + L_t$$

Where L_t is the excess length. Some authors will call L_t the tortuosity [84]. In this study the first definition will be used, but the reader should be aware that there are other extant naming conventions. The tortuosity τ of porous food materials varies between 2 and 6 [83]. This value must be obtained from experiments, and is hard to get [41]. A more practicable relation is given by [46] for soils

$$D_{eff,g} = D_{AB}\left(S_g \phi\right)^{\frac{4}{3}}$$

This can be written in terms of the liquid saturation

$$D_{eff,g} = D_{AB}\left(\left(1 - S_l\right)\phi\right)^{\frac{4}{3}}$$

For wood, Nasrallah and Perre [38] use

$$D_{eff} = D_{va}\frac{K_g}{45}$$

The binary diffusion coefficient, D_{va}, can be calculated from Chapman Enskog theory of binary mixtures of gases at low to moderate pressures [80, 85]. A very detailed description of this is given by Hirschfelder et al. [74] or Bird et al.[78]. For many scenarios of interest the liquid phase present in the porous material is water, and the binary diffusion coefficient can be approximated as a function of pressure and temperature [41]

$$D_{va} = 2.3\times10^{-5}\frac{P_o}{P}\left(\frac{T}{T_o}\right)^{1.81}$$

Turns (2000) gives a value of D_{va} of $2.3\times10^{-5}\frac{m^2}{s}$ at 273K and 1atm. Ni [41] uses a constant value of $2.6\times10^{-5}\frac{m^2}{s}$ in a model for the microwave drying of foods.

The molar concentration C can be obtained from the ideal gas law.

$$PV = nRT$$

$$C = \frac{n}{V} = \frac{P}{RT} = \left[\frac{\frac{N}{m^2}}{\frac{Nm}{molK}K}\right] = \left[\frac{mol}{m^3}\right]$$

The densities of gases can also be calculated using the ideal gas law.

$$\rho_g = \frac{nM_g}{V} = \frac{p_g M_g}{RT} = \frac{p_g}{R_g T} = \left[\frac{\frac{N}{m^2}}{\frac{Nm}{kgK}K}\right] = \left[\frac{kg}{m^3}\right]$$

Where R_g is the specific gas constant, R is the universal gas constant, and M_g is the molecular weight of gas g.

$$R_g = \frac{R}{M_g}$$

For air and water vapor the gas constants are

$$R_a = \frac{R}{M_a} = \frac{8314\frac{J}{molK}}{28.8\frac{kg}{mol}} = 289\frac{J}{kgK}$$

$$R_v = \frac{R}{M_v} = \frac{8314\frac{J}{molK}}{18\frac{kg}{mol}} = 462\frac{J}{kgK}$$

B.3.3. Local Thermal Equilibrium

When modeling heat transfer in porous media, another important simplification that is often made is that of local thermal equilibrium. This means that at a point in the material, all phases present are at the same temperature. In reality there will be differences in temperature between the solid matrix and the fluids in the pore space. Many times however these temperature differences are small compared to temperature differences that are occurring over the system dimension. This is the basis for the assumption of local thermal equilibrium [23]. The conditions for local thermal equilibrium to be appropriate are given by Whitaker [86]. Whitaker [86] uses the method of volume averaging to transform the governing equations for each phase into a condensed form that is more tractable. He uses the same method to derive conditions for local thermal equilibrium. The details of his derivation are given here. First define a spatial average of a function Ω.

$$\langle \Omega \rangle = \frac{1}{V} \int_V \Omega dV$$

In this manner, $\langle \Omega \rangle$ becomes the spatially smoothed version of Ω [86]. This process can be used to define phase averaged quantities. For example, the phase average density of the gas phase is defined as

$$\langle \rho_g \rangle = \frac{1}{V} \int_V \rho_g dV$$

Here we use the convention that ρ_g is zero in the solid and liquid phases. This means that the gas phase average density reduces to

$$\langle \rho_g \rangle = \frac{1}{V} \int_{V_g(t)} \rho_g dV$$

The phase average value of a function is averaged over the entire volume including space where it has a value of zero. Therefore if the gas density has a constant value, the phase average density is not equal to this value. For this reason it is useful to define an intrinsic phase average, which is defined as

$$\langle \rho_g \rangle^g = \frac{1}{V_g(t)} \int_{V_g(t)} \rho_g dV$$

Another useful tool is the spatial averaging theorem [87] which states that for some property of a phase, for example Ω_s

$$\langle \nabla \Omega_s \rangle = \nabla \langle \Omega_s \rangle + \frac{1}{V} \int_{A_{sl}} \Omega_s n_{sl} dA + \frac{1}{V} \int_{A_{sg}} \Omega_s n_{sg} dA$$

This is a special case of the more general transport theorem [87]

$$\frac{d}{dt} \int_V \Omega_s dV = \int_V \frac{\partial \Omega_s}{\partial t} dV + \int_A \Omega_s \vec{u} \cdot \vec{n} \, dA$$

Also define volume fractions for the solid, liquid, and gas phases.

$$\psi_s = \frac{V_s}{V} \qquad \psi_l = \frac{V_l}{V} \qquad \psi_g = \frac{V_g}{V}$$

Where the sum of the volume fractions must be equal to one

$$\psi_s + \psi_g(t) + \psi_l(t) = 1$$

and the phase average and intrinsic phase average are related by the volume fraction.

$$\psi_g \langle \rho_g \rangle^g = \langle \rho_g \rangle$$

To determine whether local thermal equilibrium is valid, first consider the energy equation for a three phase system. Derive the volume averaged energy equation for each individual phase and add them together. Assume a porous solid contains a liquid and gas phase in the pore spaces. If the gas is considered incompressible, the quasi-steady creep flow form of the Navier Stokes equations are considered appropriate for the fluids. Here viscous dissipation is neglected, and material properties are considered constant. The problem can be expressed mathematically as follows [86].

Solid Phase

$$\rho_s c_{p,s} \frac{\partial T_s}{\partial t} = k_s \nabla^2 T_s + \Phi_s \qquad \text{(energy)}$$

Liquid Phase

$$\nabla \cdot v_l = 0 \qquad \text{(continuity)}$$

$$-\nabla P_l + \rho_l g + \mu_l \nabla^2 v_l = 0 \qquad \text{(momentum)}$$

$$\rho_l c_{p,l} \left(\frac{\partial T_l}{\partial t} + v_l \cdot \nabla T_l \right) = k_l \nabla^2 T_l + \Phi_l \qquad \text{(energy)}$$

Gas phase

$$\nabla \cdot v_g = 0 \qquad \text{(continuity)}$$

$$-\nabla P_g + \rho_g g + \mu_g \nabla^2 v_g = 0 \qquad \text{(momentum)}$$

$$\rho_g c_{p,g} \left(\frac{\partial T_g}{\partial t} + v_g \cdot \nabla T_g \right) = k_g \nabla^2 T_g + \Phi_g \qquad \text{(energy)}$$

Subject to the following boundary conditions on the interfaces. On the solid-liquid interface A_{sl}

$$v_l = 0 \qquad on \qquad A_{sl}$$
$$\dot{q}_s'' \cdot n_{sl} + \dot{q}_l'' \cdot n_{ls} = 0 \qquad on \qquad A_{sl}$$
$$T_s = T_l \qquad on \qquad A_{sl}$$

On the solid-gas interface A_{sg}

$$v_g = 0 \qquad on \qquad A_{sg}$$
$$\dot{q}_s'' \cdot n_{sg} + \dot{q}_g'' \cdot n_{gs} = 0 \qquad on \qquad A_{sg}$$
$$T_s = T_g \qquad on \qquad A_{sg}$$

On the liquid-gas interface

$$\rho_l\left(v_g - u_{int}\right)\cdot n_{lg} + \rho_g\left(v_l - u_{int}\right)\cdot n_{gl} = 0 \qquad on \qquad A_{lg}$$
$$\rho_l h_l\left(v_g - u_{int}\right)\cdot n_{lg} + \rho_g h_l\left(v_l - u_{int}\right)\cdot n_{gl} = -\left(\dot{q}_l''\cdot n_{lg} + \dot{q}_g''\cdot n_{gl}\right) \qquad on \qquad A_{lg}$$
$$T_l = T_g \qquad on \qquad A_{lg}$$
$$P_l = P_g + \sigma\left(\frac{1}{r_1} + \frac{1}{r_2}\right) \qquad on \qquad A_{lg}$$

Here Φ is energy addition from electromagnetic radiation absorption. The radii r_1 and r_2 are the principle radii of curvature of the curved interface A_{lg}. In the case of an interface in a capillary tube the two radii would be equal. The vector n_{sl} is the unit normal vector for the solid phase surface in contact with the liquid phase that points into the liquid phase. The vectors n_{sg}, and n_{gl} are defined in the same manner and u_{int} is the velocity of the liquid-gas interface. It should be noted that

$$n_{sl} = -n_{ls} \qquad on \qquad A_{sl} = A_{ls}$$

Next calculate the volume averaged equations. Start with the solid phase

$$\rho_s c_{p,s}\frac{\partial T}{\partial t} = -\nabla\cdot\dot{q}_s'' + \Phi_s$$

Forming the volume average and using the averaging theorem gives [86]

$$\rho_s c_{p,s}\frac{\partial\langle T_s\rangle}{\partial t} = -\nabla\cdot\langle\dot{q}_s''\rangle - \frac{1}{V}\int_{A_{sl}}\dot{q}_s''\cdot n_{sl}dA - \frac{1}{V}\int_{A_{sg}}\dot{q}_s''\cdot n_{sg}dA + \Phi_s$$

Where the heat flux can be expressed as

$$\langle\dot{q}_s''\rangle = -k_s\langle\nabla T_s\rangle = -k_s\left(\nabla T_s + \frac{1}{V}\int_{A_{sl}}T_s n_{sl}dA + \frac{1}{V}\int_{A_{sg}}T_s n_{sg}dA\right)$$

Combining these two equations with the relation between phase average and intrinsic phase average gives

$$\psi_s \rho_s c_{p,s} \frac{\partial \langle T \rangle^s}{\partial t} = \nabla \cdot \left[k_s \left(\nabla \left(\psi_s \langle T_s \rangle^s \right) + \frac{1}{V} \int_{A_{sl}} T_s n_{sl} dA + \frac{1}{V} \int_{A_{sg}} T_s n_{sg} dA \right) \right]$$
$$- \frac{1}{V} \int_{A_{sl}} \dot{q}_s'' \cdot n_{sl} dA - \frac{1}{V} \int_{A_{sg}} \dot{q}_s'' \cdot n_{sg} dA + \Phi_s$$

The derivation of the volume averaged form of the energy equation for the liquid and gas phases is similar to the process just completed for the solid phase but much lengthier. It is complicated by the convective transport terms and phase change occurring at the gas-liquid interface. The complete derivation is given by Whitaker [36, 86]. He ends up with the following form of the volume averaged liquid phase energy equation

$$\psi_l \rho_l c_{p,l} \frac{\partial \langle T_l \rangle^l}{\partial t} + \rho_l c_{p,l} \langle v_l \rangle \cdot \nabla \langle T_l \rangle^l + \rho_l c_{p,l} \nabla \cdot \langle \tilde{v}_l \tilde{T}_l \rangle + \frac{1}{V} \int_{A_{lg}} \rho_l c_{p,l} \tilde{T}_l (v_l - w) \cdot n_{lg} dA$$
$$= \nabla \cdot \left\{ k_l \left[\nabla \left(\psi_l \langle T_l \rangle^l \right) + \frac{1}{V} \int_{A_{ls}} T_l n_{ls} dA + \frac{1}{V} \int_{A_{lg}} T_l n_{lg} dA \right] \right\} - \frac{1}{V} \int_{A_{ls}} \dot{q}_l'' \cdot n_{ls} dA - \frac{1}{V} \int_{A_{lg}} \dot{q}_l'' \cdot n_{lg} dA + \langle \Phi_l \rangle$$

For the gas phase the volume averaged form of the energy equation is

$$\left[\sum_{i=1}^{N} \langle \rho_i \rangle c_{p,i} \right] \frac{\partial \langle T_g \rangle^g}{\partial t} + \left[\sum_{i=1}^{N} c_{p,i} \langle \rho_i v_i \rangle \right] \cdot \nabla \langle T_g \rangle^g + \nabla \cdot \left[\sum_{i=1}^{N} c_{p,i} \langle \tilde{\rho}_i \tilde{v}_i \tilde{T}_g \rangle \right]$$
$$+ \frac{1}{V} \int_{A_{gl}} \sum_{i=1}^{N} \rho_i c_{p,i} \tilde{T}_g (v_i - w) \cdot n_{gl} dA + \frac{\partial}{\partial t} \left[\sum_{i=1}^{N} c_{p,i} \langle \tilde{\rho}_i \tilde{T}_g \rangle \right]$$
$$= \nabla \cdot \left\{ k_g \left[\nabla \left(\psi_g \langle T_g \rangle^g \right) + \frac{1}{V} \int_{A_{gs}} T_g n_{gs} dA + \frac{1}{V} \int_{A_{gl}} T_g n_{gl} dA \right] \right\} - \frac{1}{V} \int_{A_{gs}} \dot{q}_g'' \cdot n_{gs} dA - \frac{1}{V} \int_{A_{gl}} \dot{q}_g'' \cdot n_{gl} dA + \langle \Phi_g \rangle$$

Here quantities marked with a tilda ($\tilde{\rho}$) represent the fluctuations of that quantity about it's average. The system of equations governing multiphase heat transfer in a porous material that have been given are quite complex. If the assumption of local thermal equilibrium can be invoked, the problem will be greatly simplified. First consider the simplifying effect of the assumption on the energy equations. To do so,

first define spatial temperature deviations

$$\langle T_s \rangle^s = \langle T \rangle + \hat{T}_s$$
$$\langle T_l \rangle^l = \langle T \rangle + \hat{T}_l$$
$$\langle T_g \rangle^g = \langle T \rangle + \hat{T}_g$$

Where the average temperature is defined as

$$\langle T \rangle = \frac{1}{V}\int_V T dV = \psi_s \langle T_s \rangle^s + \psi_l \langle T_l \rangle^l + \psi_g \langle T_g \rangle^g$$

Using these definitions, the solid phase thermal energy equation can be written as

$$\psi_s \rho_s c_{p,s} \frac{\partial \langle T \rangle}{\partial t} = \nabla \cdot \left[k_s \left(\nabla \left(\psi_s \langle T \rangle \right) + \frac{1}{V}\int_{A_{sl}} T_s n_{sl} dA + \frac{1}{V}\int_{A_{sg}} T_s n_{sg} dA \right) \right]$$
$$- \frac{1}{V}\int_{A_{sl}} \dot{q}_s'' \cdot n_{sl} dA - \frac{1}{V}\int_{A_{sg}} \dot{q}_s'' \cdot n_{sg} dA + \Phi_s - \left\{ \psi_s \rho_s c_{p,s} \frac{\partial \hat{T}}{\partial t} - \nabla \cdot \left[k_s \nabla \left(\psi_s \hat{T}_s \right) \right] \right\}$$

If the deviations are much smaller than the spatial average temperature, then the last term can be neglected. So if

$$\frac{\partial \hat{T}_s}{\partial t} << \frac{\partial \langle T \rangle}{\partial t} \quad and \quad \nabla \hat{T}_s << \nabla \langle T \rangle$$

then

$$\psi_s \rho_s c_{p,s} \frac{\partial \hat{T}}{\partial t} - \nabla \cdot \left[k_s \nabla \left(\psi_s \hat{T}_s \right) \right] \approx 0$$

If these terms can be neglected in the gas and liquid thermal energy equations as well, the three equations can be added to give

$$\langle\rho\rangle\bar{c}_p\frac{\partial\langle T\rangle}{\partial t}+\left[\rho_l c_{p,l}u_l+\langle\rho_g\rangle^g\langle c_{p,g}\rangle^g u_g\right]\cdot\nabla\langle T\rangle+\Delta h_{vap}\langle\dot{m}'''_{evap}\rangle=\nabla\cdot\left(k_{eff}\cdot\nabla T\right)+\Phi$$

Where

$$\langle\rho\rangle=\psi_s\rho_s+\psi_l\rho_l+\psi_g\sum_{i=1}^{N}\langle\rho_i\rangle^g$$

$$\bar{c}_p=\frac{\psi_s\rho_s c_{p,s}+\psi_l\rho_l c_{p,l}+\psi_g\sum_{i=1}^{N}\langle\rho_i\rangle^g c_{p,g}}{\langle\rho\rangle}$$

In order to develop the constraints for local thermal equilibrium to be valid, consider a two phase system consisting of a porous material with a liquid in the pore spaces. We are concerned with the temperature difference between the solid and liquid. Define spatial temperature deviations

$$\hat{T}_s=\langle T_s\rangle^s-\langle T\rangle$$
$$\hat{T}_s=\langle T_l\rangle^l-\langle T\rangle$$

This is similar to the definition of an average fluid velocity for turbulent flows. The phase average temperature can be written as

$$\langle T\rangle=\frac{1}{V}\int_V TdV=\psi_s\langle T_s\rangle^s+\psi_l\langle T_l\rangle^l+\psi_g\langle T_g\rangle^g$$

For this two phase system it reduces to

$$\langle T\rangle=\psi_s\langle T_s\rangle^s+\psi_l\langle T_l\rangle^l$$

The volume fractions can be written as

$$\psi_s=1-\psi_l$$
$$\psi_l=1-\psi_s$$

Now the spatial temperature deviations can be written as

$$\hat{T}_s = \langle T_s \rangle^s - \psi_s \langle T_s \rangle^s - \psi_l \langle T_l \rangle^l = \langle T_s \rangle^s (1 - \psi_s`) - \psi_l \langle T_l \rangle^l = \psi_l \left(\langle T_s \rangle^s - \langle T_l \rangle^l \right)$$
$$\hat{T}_l = \langle T_l \rangle^l - \psi_s \langle T_s \rangle^s - \psi_l \langle T_l \rangle^l = \langle T_l \rangle^l (1 - \psi_l) - \psi_s \langle T_s \rangle^s = \psi_s \left(\langle T_l \rangle^l - \langle T_s \rangle^s \right)$$

In order to allow the assumption of local thermal equilibrium, we must ensure that

$$\Delta \hat{T}_s << \Delta \langle T \rangle \quad and \quad \Delta \hat{T}_l << \Delta \langle T \rangle$$

Where $\Delta \hat{T}_s, \Delta \hat{T}_l,$ *and* $\Delta \langle T \rangle$ are the largest changes that occur in $\hat{T}_s, \hat{T}_l, and \langle T \rangle$ during the time frame of interest. This can be written as

$$\Delta \left[\psi_l \left(\langle T_s \rangle^s - \langle T_l \rangle^l \right) \right] << \Delta \left[\psi_s \langle T_s \rangle^s + \psi_l \langle T_l \rangle^l \right]$$
and
$$\Delta \left[\psi_s \left(\langle T_l \rangle^l - \langle T_s \rangle^s \right) \right] << \Delta \left[\psi_s \langle T_s \rangle^s + \psi_l \langle T_l \rangle^l \right]$$

Which will be satisfied if

$$\langle T_s \rangle^s - \langle T_l \rangle^l << \Delta \langle T_s \rangle^s$$
or
$$\langle T_s \rangle^s - \langle T_l \rangle^l << \Delta \langle T_l \rangle^l$$

Consider the porous solid with a single fluid phase, liquid in this case, in the pore spaces as shown in Figure 42.

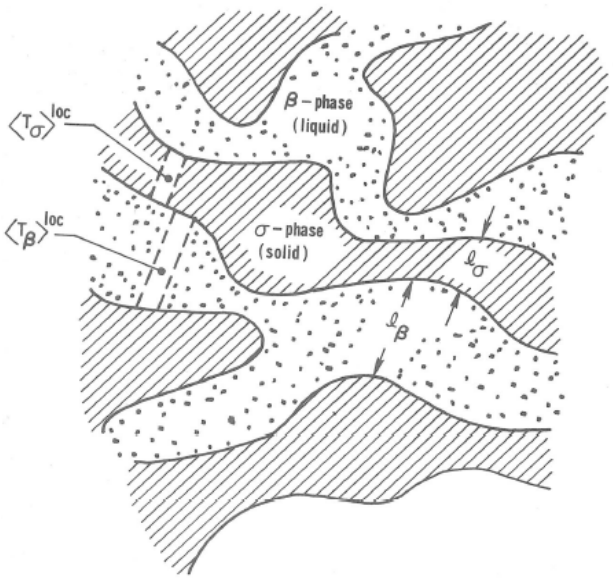

Figure 42 – Local Thermal Equilibrium in a Solid – Liquid System (from [86])

If we examine the solid phase thermal energy equation

$$\psi_s \rho_s c_{p,s} \frac{\partial \langle T \rangle^s}{\partial t} = \nabla \cdot \left[k_s \left(\nabla \left(\psi_s \langle T_s \rangle^s \right) + \frac{1}{V} \int_{A_{sl}} T_s n_{sl} dA \right) \right] - \frac{1}{V} \int_{A_{sl}} \dot{q}_s'' \cdot n_{sl} dA + \Phi_s$$

No single term in this equation can be much larger than any other term, but a term can be much smaller than every other term [86], so we can write

$$\frac{1}{V} \int_{A_{sl}} \dot{q}_s'' \cdot n_{sl} dA = O \begin{cases} \psi_s \rho_s c_{p,s} \dfrac{\partial \langle T \rangle^s}{\partial t} \\ \nabla \cdot \left[k_s \left(\nabla \left(\psi_s \langle T_s \rangle^s \right) + \dfrac{1}{V} \displaystyle\int_{A_{sl}} T_s n_{sl} dA \right) \right] \\ \Phi_s \end{cases}$$

The order of magnitude of each of these terms can be estimated. Start with the interfacial heat flux. From Figure 42 we see that the heat flux from the solid to the

liquid can be approximated as

$$\dot{q}''_s \cdot n_{sl} = O\left[\frac{k_s}{l_s}\left(\langle T_s \rangle^{loc} - T_i\right)\right]$$

The notation O means "on the order of magnitude of", T_i is the temperature of the solid liquid interface, and $\langle T_s \rangle^{loc}$ is the temperature in a small local region of the solid. In the same manner we can estimate the heat flux in the liquid at the solid liquid interface to be

$$\dot{q}''_l \cdot n_{ls} = O\left[\frac{k_l}{l_l}\left(\langle T_l \rangle^{loc} - T_i\right)\right]$$

And from the boundary conditions given for the solid liquid interface we know that

$$\dot{q}''_s \cdot n_{sl} + \dot{q}''_l \cdot n_{ls} = 0 \qquad on \qquad A_{sl}$$

So the interfacial temperature T_i can be eliminated to give

$$\dot{q}''_s \cdot n_{sl} = O\left[\frac{\langle T_s \rangle^{loc} - \langle T_l \rangle^{loc}}{\frac{l_s}{k_s} + \frac{l_l}{k_l}}\right]$$

The integral can now be performed to evaluate the last term in the solid phase energy equation

$$\frac{1}{V}\int_{A_{sl}} \dot{q}''_s \cdot n_{sl} dA = \frac{1}{V}\int_{A_{sl}} \dot{q}''_s \cdot n_{sl} dA === O\left[\left(\frac{A_{sl}}{V}\right)\frac{\langle T_s \rangle^{s} - \langle T_l \rangle^{l}}{\frac{l_s}{k_s} + \frac{l_l}{k_l}}\right]$$

Using a procedure discussed by Whitaker [88] the order of magnitude of the first and

second terms in the solid phase thermal energy equation can be estimated

$$\psi_s \rho_s c_{p,s} \frac{\partial \langle T \rangle^s}{\partial t} = O\left[\psi_s \rho_s c_{p,s} \frac{\Delta \langle T \rangle^s}{\tau} \right]$$

$$\nabla \cdot \left[k_s \left(\nabla \left(\psi_s \langle T_s \rangle^s \right) + \frac{1}{V} \int_{A_{sl}} T_s n_{sl} dA \right) \right] = O\left[\frac{k_s \psi_s \Delta \langle T_s \rangle^s}{L^2} \right]$$

Where $\Delta \langle T_s \rangle^s$ represents the change in $\langle T_s \rangle^s$ that occurs during a characteristic time τ and over a characteristic length L. The estimate for the second term makes use of an analysis by Whitaker [36] that shows

$$\frac{1}{V} \int_{A_{sl}} T_s n_{sl} dA = O\left[\nabla \left(\psi_s \langle T_s \rangle^s \right) \right]$$

Comparing the order of magnitude of the terms again

$$\left(\frac{A_{sl}}{V} \right) \frac{\langle T_s \rangle^s - \langle T_l \rangle^l}{\frac{l_s}{k_s} + \frac{l_l}{k_l}} = O\left\{ \begin{array}{l} \psi_s \rho_s c_{p,s} \dfrac{\Delta \langle T \rangle^s}{\tau} \\ \dfrac{k_s \psi_s \Delta \langle T_s \rangle^s}{L^2} \\ \langle \Phi_s \rangle \end{array} \right.$$

Which can be rearranged to give the order of magnitude of the difference in local temperature between the solid and liquid phase

$$\left\langle T_s \right\rangle^s - \left\langle T_l \right\rangle^l = O\begin{cases} \dfrac{\psi_s \rho_s c_{p,s} \Delta \left\langle T \right\rangle^s}{\dfrac{A_{sl}}{V}\tau}\left(\dfrac{l_s}{k_s}+\dfrac{l_l}{k_l}\right) \\ \dfrac{k_s \psi_s \Delta \left\langle T_s \right\rangle^s}{\dfrac{A_{sl}}{V}L^2}\left(\dfrac{l_s}{k_s}+\dfrac{l_l}{k_l}\right) \\ \dfrac{\left\langle \Phi_s \right\rangle}{\dfrac{A_{sl}}{V}}\left(\dfrac{l_s}{k_s}+\dfrac{l_l}{k_l}\right) \end{cases}$$

For local thermal equilibrium to be valid we must require that

$$\frac{\left\langle T_s \right\rangle^s - \left\langle T_l \right\rangle^l}{\left\langle T_s \right\rangle^s} << 1$$

Which gives us three constraints for local thermal equilibrium to be valid

$$\frac{\psi_s \rho_s c_{p,s}}{\dfrac{A_{sl}}{V}\tau}\left(\frac{l_s}{k_s}+\frac{l_l}{k_l}\right) << 1$$

$$\frac{k_s \psi_s}{\dfrac{A_{sl}}{V}L^2}\left(\frac{l_s}{k_s}+\frac{l_l}{k_l}\right) << 1$$

$$\frac{\left\langle \Phi_s \right\rangle}{\Delta \left\langle T_s \right\rangle^s \dfrac{A_{sl}}{V}}\left(\frac{l_s}{k_s}+\frac{l_l}{k_l}\right) << 1$$

Repeat the process with the liquid phase thermal energy equation to calculate additional constraints on local thermal equilibrium

$$\psi_l \rho_l c_{p,l} \frac{\partial \left\langle T_l \right\rangle^l}{\partial t} + \rho_l c_{p,l} \left\langle v_l \right\rangle \cdot \nabla \left\langle T_l \right\rangle^l + \rho_l c_{p,l} \nabla \cdot \left\langle \tilde{v}_l \tilde{T}_l \right\rangle$$
$$= \nabla \cdot \left\{ k_l \left[\nabla \left(\psi_l \left\langle T_l \right\rangle^l \right) + \frac{1}{V} \int_{A_{ls}} T_l n_{ls} dA \right] \right\} - \frac{1}{V} \int_{A_{ls}} \dot{q}_l'' \cdot n_{ls} dA$$

Using the same process gives the following four constraints

$$\frac{\psi_l \rho_l c_{p,l}}{\frac{A_{ls}}{V}\tau}\left(\frac{l_s}{k_s}+\frac{l_l}{k_l}\right)<<1$$

$$\frac{\psi_l k_l}{\frac{A_{ls}}{V}L^2}\left(\frac{l_s}{k_s}+\frac{l_l}{k_l}\right)<<1$$

$$\frac{\langle \Phi_l \rangle}{\Delta\langle T_l \rangle^l \frac{A_{ls}}{V}}\left(\frac{l_s}{k_s}+\frac{l_l}{k_l}\right)<<1$$

$$\frac{\rho_l c_{p,l}\langle v_l \rangle}{L\frac{A_{ls}}{V}}\left(\frac{l_s}{k_s}+\frac{l_l}{k_l}\right)<<1$$

Where $\frac{A_{ls}}{V}$ is the specific surface area and defined by the surface area per unit volume of bulk material and it represented by A_o. If we assume that $l_l \approx l_s$, then the constraints for local thermal equilibrium for a solid – liquid system are given by the following 7 inequalities

$$\frac{\psi_s \rho_s c_{p,s} l}{A_o \tau}\left(\frac{1}{k_s}+\frac{1}{k_l}\right)<<1 \qquad \frac{\psi_l \rho_l c_{p,l} l}{A_o \tau}\left(\frac{1}{k_s}+\frac{1}{k_l}\right)<<1$$

$$\frac{\psi_s k_s l}{A_o L^2}\left(\frac{1}{k_s}+\frac{1}{k_l}\right)<<1 \qquad \frac{\psi_l k_l l}{A_o L^2}\left(\frac{1}{k_s}+\frac{1}{k_l}\right)<<1$$

$$\frac{\langle \Phi_s \rangle}{\Delta\langle T_s \rangle^s A_o}\left(\frac{1}{k_s}+\frac{1}{k_l}\right)<<1 \qquad \frac{\langle \Phi_l \rangle}{\Delta\langle T_l \rangle^l A_o}\left(\frac{1}{k_s}+\frac{1}{k_l}\right)<<1$$

$$\frac{\rho_l c_{p,l}\langle v_l \rangle}{L A_o}\left(\frac{1}{k_s}+\frac{1}{k_l}\right)<<1$$

For example, we can check if a bed of glass beads with air filling the interstitial pore spaces meets the conditions for local thermal equilibrium. Since it is a single fluid system it does not matter that it is a gas instead of a liquid. Use values for air where liquid parameters are specified. Assume bead diameters of 300 microns. In this case

$\langle \Phi_s \rangle = \langle \Phi_l \rangle = 0$. The properties of air and glass are given in the SFPE Handbook

$For\ air\ @ 293K$

$\rho_{air} = 1.21 \frac{kg}{m^3}$

$k_{air} = 0.0257 \frac{W}{mK}$

$c_{p,air} = 1.01 \frac{kJ}{kgK}$

$For\ glass\ @ 293$

$\rho_{glass} = 2700\ \frac{kg}{m^3}$

$k_{glass} = 0.78 \frac{W}{mK}$

$c_{p,glass} = 0.84 \frac{kJ}{kgK}$

Calculate an approximate value for the specific surface area based on a face centered cubic lattice structure of the glass beads.

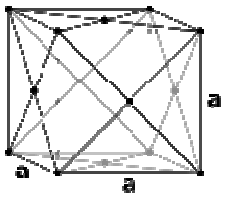

Figure 43 – Face Centered Cubic Packing of Spheres

As Figure 43 shows, a face centered cubic packing order contains 4 spheres in a box with a face diagonal of twice the diameter of the spheres. This means that the sides of the box are of length $2\sqrt{2}\,r$. The specific surface area can be calculated as

$$A = 4 \times 4\pi r^2 = 16\pi r^2$$
$$V = \left(2\sqrt{2}r\right)^3 = 16\sqrt{2}r^3$$
$$A_o = \frac{A}{V} = \frac{16\pi r^2}{16\sqrt{2}r^3} = \frac{2.22}{r} = \frac{2.22}{3\times10^{-4}m} = 7{,}400m^{-1}$$

Use the same packing order to calculate the volume fractions of solid and liquid components

$$\psi_s = \frac{V_s}{V} = \frac{4 \times \frac{4}{3}\pi r^3}{16\sqrt{2}r^3} = 0.74$$
$$\psi_g = 1 - \psi_s = 1 - 0.74 = 0.26$$

Use these values for to calculate constraints for local thermal equilibrium. The constraints are

$$\frac{\psi_{glass}\rho_{glass}c_{p,glass}l}{A_o\tau}\left(\frac{1}{k_{glass}} + \frac{1}{k_{air}}\right) << 1$$
$$\frac{\psi_{air}\rho_{air}c_{p,air}l}{A_o\tau}\left(\frac{1}{k_{glass}} + \frac{1}{k_{air}}\right) << 1$$
$$\frac{\psi_{glass}k_{glass}l}{A_oL^2}\left(\frac{1}{k_{glass}} + \frac{1}{k_{air}}\right) << 1$$
$$\frac{\psi_{air}k_{air}l}{A_oL^2}\left(\frac{1}{k_{glass}} + \frac{1}{k_{air}}\right) << 1$$
$$\frac{\rho_{air}c_{p,air}\langle v_{air}\rangle}{LA_o}\left(\frac{1}{k_{glass}} + \frac{1}{k_{air}}\right) << 1$$

So, using the values calculated for this system the inequalities become

$$\frac{(0.74)(2700)(0.84)(3\times10^{-4})}{(7400)\tau}\left(\frac{1}{0.84}+\frac{1}{0.0257}\right)<<1$$

$$\frac{(0.26)(1.21)(1.01)(3\times10^{-4})}{(7400)\tau}\left(\frac{1}{0.84}+\frac{1}{0.0257}\right)<<1$$

$$\frac{(0.74)(0.78)(3\times10^{-4})}{(7400)L^2}\left(\frac{1}{0.84}+\frac{1}{0.0257}\right)<<1$$

$$\frac{(0.26)(0.0257)(3\times10^{-4})}{(7400)L^2}\left(\frac{1}{0.84}+\frac{1}{0.0257}\right)<<1$$

$$\frac{(1.21)(1.01)\langle v_g\rangle}{L(7400)}\left(\frac{1}{0.84}+\frac{1}{0.0257}\right)<<1$$

For the above inequalities to be true, the timescale, length, and air velocity of interest must be

$$0.0273 << \tau$$

$$5.17\times10^{-7} << \tau$$

$$3.06\times10^{-4} << L$$

$$1.04\times10^{-4} << L$$

$$\langle v_g\rangle << \frac{L}{0.0662}$$

So therefore according to this analysis, as long as the timescale of interest is more than 3 seconds, the system length is more than 3cm, and the air velocity is less than 0.46m/s, the assumption of local thermal equilibrium is valid.

B.3.4. Two Phase Flow

The problem of fluid flowing through a porous material is made more complicated by the addition of another fluid. For example: water flowing into a porous material that was initially saturated with air. Interfacial surface tension forces can prevent fluid from flowing, or they can be the driving force for fluid flow. There are many factors that will affect multi phase flows in porous materials. A representative granular porous material is shown in Figure 44. Surface tension forces at the water-air interfaces will pull the water into the material if the material is hydrophilic, and oppose water entry if the material is hydrophobic. Hydrophilic/hydrophobic behavior will be determined by the contact angle which is affected by surface chemistry of the solid material and any

surface coatings and contamination.

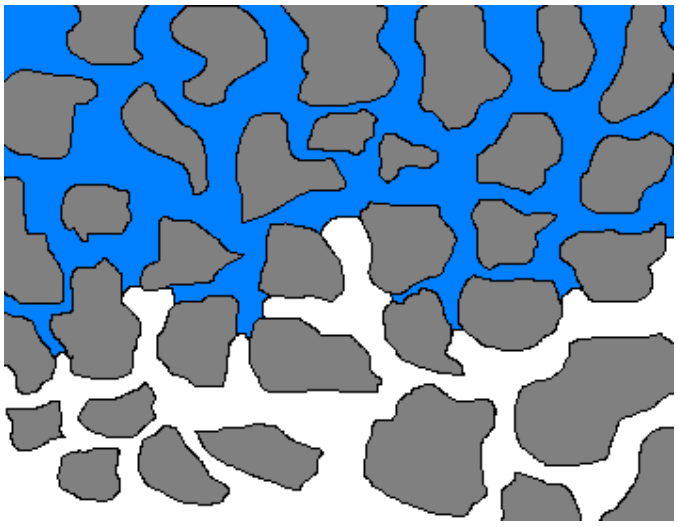

Figure 44 – Granular Porous Media Being Wetted by Water

B.3.5. Surface Tension

When two dissimilar materials are placed in contact, a surface tension force will be created at the interface. This results from asymmetric molecular bonds at the interface. Inside a volume of similar molecules, there will be symmetric intermolecular bonds pulling any given molecule in all directions which results in a net force of zero. This is shown in Figure 45. At the surface of the material, the bonds between like molecules will differ from those with the other material. This results in an interfacial surface tension force, σ, with units of N/m. Surface tensions are most apparent at liquids-liquid and liquid-gas interfaces, where they can cause curvatures, droplets, and bubbles.

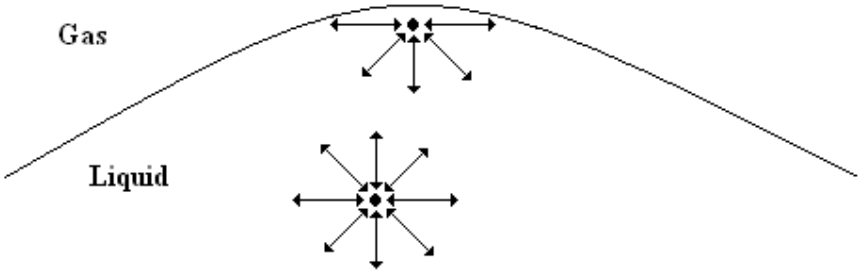

Figure 45 – Surface Tension Illustration

In general surface tension will decrease with increasing temperature. The surface tension at a water-air interface is given by the International Association for the Properties of Water and Steam as

$$\sigma = A_2 A_1^{A_4}\left(1 + A_3 A_1\right)$$

$$A_1 = 1 - \frac{T}{T_c}$$

$T = Temperature\ [K]$

$T_c = 647.096\,K$

$A_2 = 235.8\,mN/m$

$A_3 = -0.625$

$A_4 = 1.256$

This is shown graphically in Figure 46.

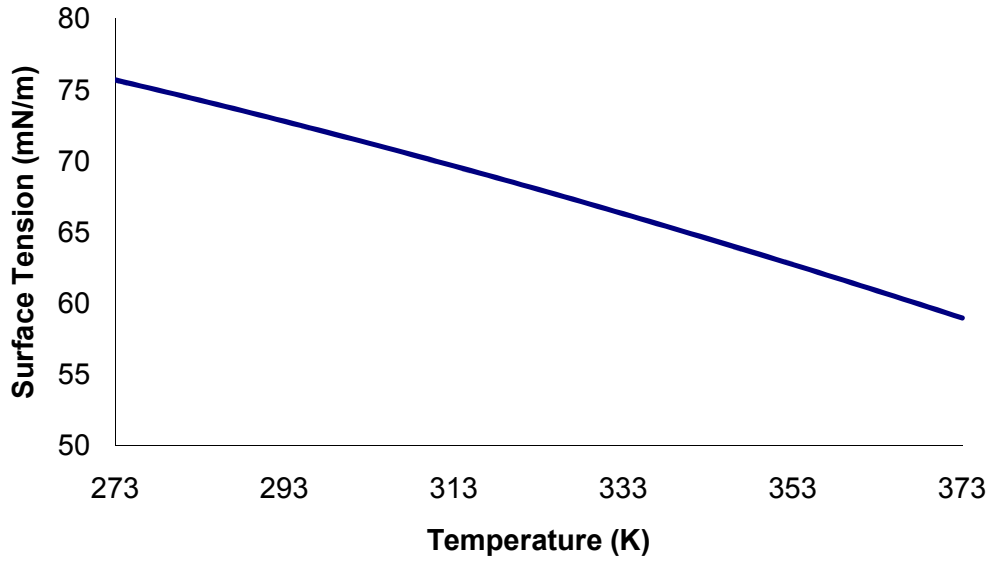

Figure 46 – Surface Tension of Water

B.3.6. Contact Angle

If two fluids are present at the surface of a material, a contact angle will be formed based on the three surface tensions present. For example consider a liquid and a gas both in contact with a solid. There will be surface tensions associated with the vapor-solid interface σ_{vs}, liquid-solid interface σ_{ls}, and vapor-liquid interface σ_{vl}.

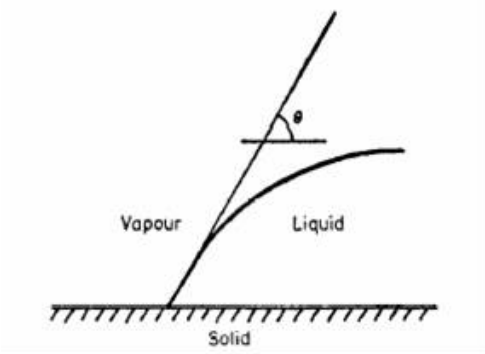

Figure 47 – Contact Angle

The contact angle θ, shown in Figure 47, is determined by Young's equation.

$$\sigma_{ls} - \sigma_{vs} + \sigma_{vl}\, cos(\theta) = 0$$

Young's equation is derived by balancing the forces at the intersection of the three interfaces. In two dimensions this is illustrated in Figure 48

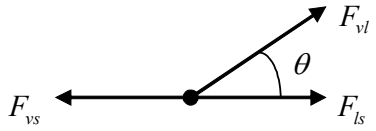

Figure 48 – Force's acting at vapor, solid, liquid interface

If we consider the static case where the interfaces are not moving, the sum of forces in the x-direction should be equal to zero.

$$\sum F_x = 0 = F_{ls} - F_{ls} + F_{vl}\, cos(\theta) = 0$$

This is essentially another form of Young's equation, since surface tension σ is a force per unit length. If the contact angle θ is less than 90 degrees, than the liquid is said to wet the solid. The contact angle is not only a function of the fluid phases present, but also the solid material. Another simplification often made is that the contact angle is constant over time. The contact angle can actually change over time and depending on the direction of fluid motion. This leads to the phenomena known as hysteresis, which will be discussed later.

B.3.7. Heat of Wetting

When a fluid displaces another fluid during the process of wetting a solid, an amount of heat is liberated from the creation and destruction of surface tensions. This is called the heat of wetting Δh_w. When the liquid in Figure 47 advances over an area A_1, energy equal to $A_1\sigma_{vs}$ is liberated and energy equal to $A_1\sigma_{ls}$ is expended. In addition, an interfacial area A_2 is created between the liquid and vapor, so energy equal to $A_2\sigma_{vl}$ is expended. The heat of wetting is therefore [25]

$$\Delta h_w = A_1\sigma_{vs} - A_1\sigma_{ls} - A_2\sigma_{vl}$$

B.3.8. Capillary Pressure

When two fluids are present in a porous material there will be a pressure drop across the interface that is a function of the interface curvature. In small pores, the curvature is much greater than in large pores and the pressure drop is therefore greater. This is called the capillary pressure, and it is a function of the surface tension, the contact angle between the fluid and the pore wall, and the pore diameter. For the simple capillary tube containing a static liquid shown in Figure 49 the pressure drop across the interface can be calculated.

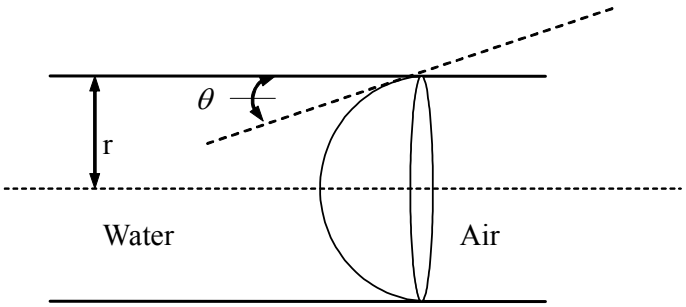

Figure 49 – Capillary Tube

Consider only the interfacial surface area, whose cross section is shown in Figure 50 along with forces arising from pressure differences across the interface and surface tension.

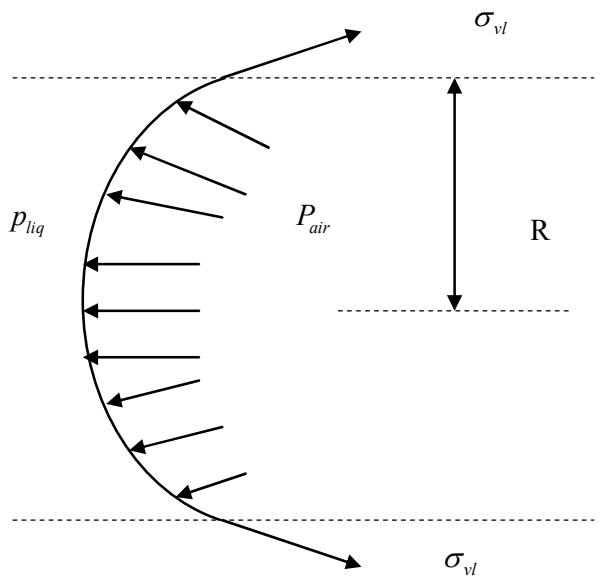

Figure 50 – Forces on Liquid - Air Interface in Capillary Tube

Summing forces in the x-direction gives

$$\sum F_x = 2\pi R\sigma\cos(\theta) - \pi R^2\left(p_{liq} - P_{air}\right) = 0$$

The pressure difference across the interface is often called the capillary pressure, P_{cap}. This is a gage pressure which is calculated to be

$$p_{cap} = -\frac{2\sigma\cos\theta}{R}$$

As a porous material is filled with water, the small pores will fill first, leaving the larger pores to fill later. As a result, the capillary pressure in an unsaturated material having a range of pore diameters is a function of the saturation of the material. The capillary pressure is defined as the pressure drop between the liquid and gas phases

$$p_{cap} = p_{liq} - P_{air}$$

Leverett showed that the capillary pressure can be predicted using a semi-empirical correlation [25]

$$p_{cap} = \left(\frac{\varphi}{K}\right)^{\frac{1}{2}} \sigma J(S)$$

Where J is a function of saturation and is dependant on the material. Leverett found that capillary pressure for a number of materials can reasonably be predicted using two different J functions, one for imbibition and one for drainage [25].

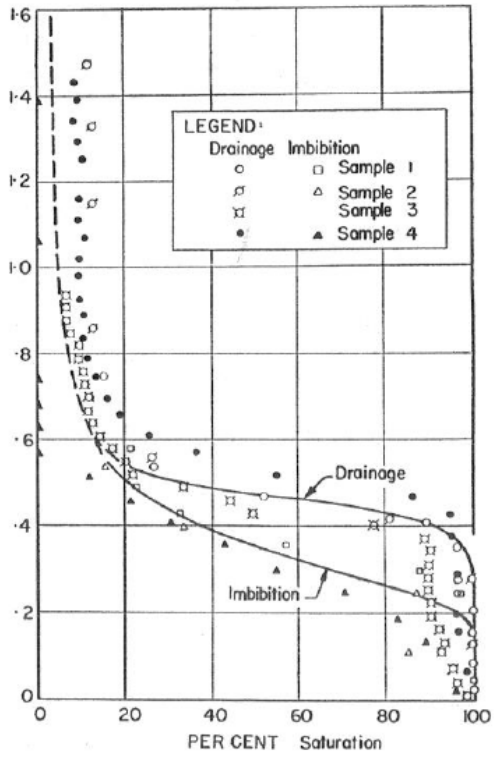

Figure 51 - Leverett's Non-Dimensional J Function (from [25])

The difference between the curves for imbibition and drainage shown in Figure 51 is due to contact angle hysteresis. The contact angle will be larger for an advancing liquid. This corresponds to the wetting process, or imbibition. The contact angle will be less for a receding liquid, corresponding to the draining or de-saturating process. Correlations for several materials are given in Table 14.

Table 14 – Capillary Pressure for Combinations of Solid and Fluid (from [23])

System	Correlation
Water – air - sand	$p_{cap} = \frac{\sigma}{\sqrt{K/\varphi}}\left[0.364\left(1-\exp\left(-40\left(1-S\right)\right)\right)+0.221\left(1-S\right)+\frac{0.005}{S-0.08}\right]$

Imbibition into non-consolidated sand – water - air	$p_{cap} = \frac{\sigma}{\sqrt{K/\varphi}}\left[1.417\left(1-S_{eff}\right)-2.120\left(1-S_{eff}\right)^2+1.263\left(1-S_{eff}\right)^3\right]$
Drainage of oil – water - sandstone	$p_{cap} = \frac{\sigma}{\sqrt{K/\varphi}}\left[0.3-0.0633\ln\left(S_l - S_{ir,l}\right)\right]$

The first correlation asymptotes to infinity as the saturation approaches zero. This equation is simply a best-fit curve which matches the experimental data for the materials specified. In reality there would be a minimum moisture content that would correspond to a maximum value for the capillary pressure. This minimum moisture content is called the irreducible saturation, and to go below it one must usually expose the material to an extremely dry environment or heat it above 100 deg C.

B.3.9. Relative Permeability

When the pore spaces of a porous material are completely filled with one fluid, the fluid velocity can be predicted with Darcy's law if the permeability K is known. When a liquid and a gas phase are present, the ability of each phase to flow will be affected. In the case of two phase flows, Darcy's Law will be modified to include a parameter K_r called the relative permeability of the material [41].

$$\vec{u}_{D,A} = -\frac{KK_r}{\mu_A}\nabla p_A$$

The relative permeability must assume values between zero and one. At a phase saturation of zero, there will be no fluid to flow, and at a saturation of one the flow will behave as a saturated material according to Darcy's Law. The relative permeability for gas or liquid of an unsaturated material is a complex function of the phase saturation, the matrix structure, the interfacial surface tension, density of the fluids, and the wetting history [23]. A simplification that is in popular usage is to reduce the relative permeability of each phase for a specific material to a function of saturation only. As either liquid or gas fills the void spaces of a porous material and displaces the fluid already there, the resistance to flow will decrease. When only a small amount of a fluid is present, it will be occupying a small cross sectional area which is available for fluid flow. If the fluid wets the solid material, it will be present in the smallest pores which were shown to have higher resistance to flow. The functional relationship of the

permeability is quite complicated and typically arrived at by curve fitting experimental data points such as those shown in Figure 52.

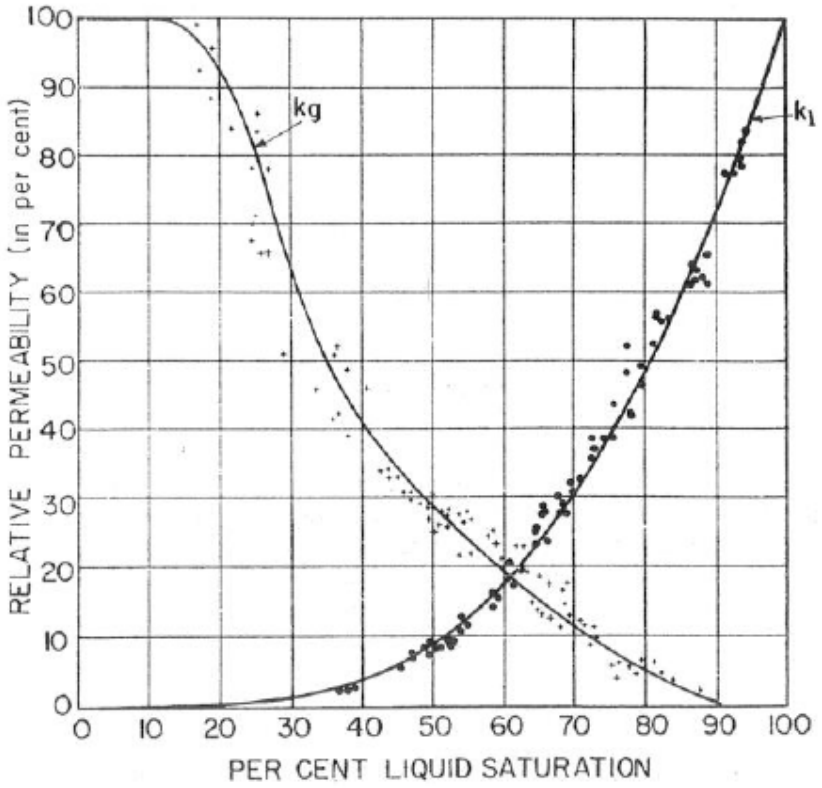

Figure 52 – Relative Permeability for Liquid and Gas (from [25])

Kaviany [23] gives empirical relationships for K_{rl} and K_{rg} for a variety of material – fluid combinations. Some of these are given in Table 15.

Table 15 – Relative Permeabilities for Several Combinations of Solid and Fluid (From [23])

Material	K_{rl}	K_{rg}
Sandstones and limestones, oil - water	S_{eff}^4	$\left(1-S_{eff}\right)^2\left(1-S_{eff}^2\right)$
Nonconsolidated sand, well sorted	S_{eff}^3	$\left(1-S_{eff}\right)^3$
Nonconsolidated sand, poorly sorted	$S_{eff}^{3.5}$	$\left(1-S_{eff}\right)^2\left(1-S_{eff}^{1.5}\right)$

Connected sandstone, limestone, rocks	S_{eff}^4	$(1-S_{eff})^2(1-S_{eff}^2)$
Sandstone, oil - water	S_{eff}^3	$1-1.1S_{eff}$
Glass Spheres - water	S_{eff}^3	$1.2984-1.9832S_{eff}^3+0.7432S_{eff}^3$

The relationships for sandstone are shown in Figure 53.

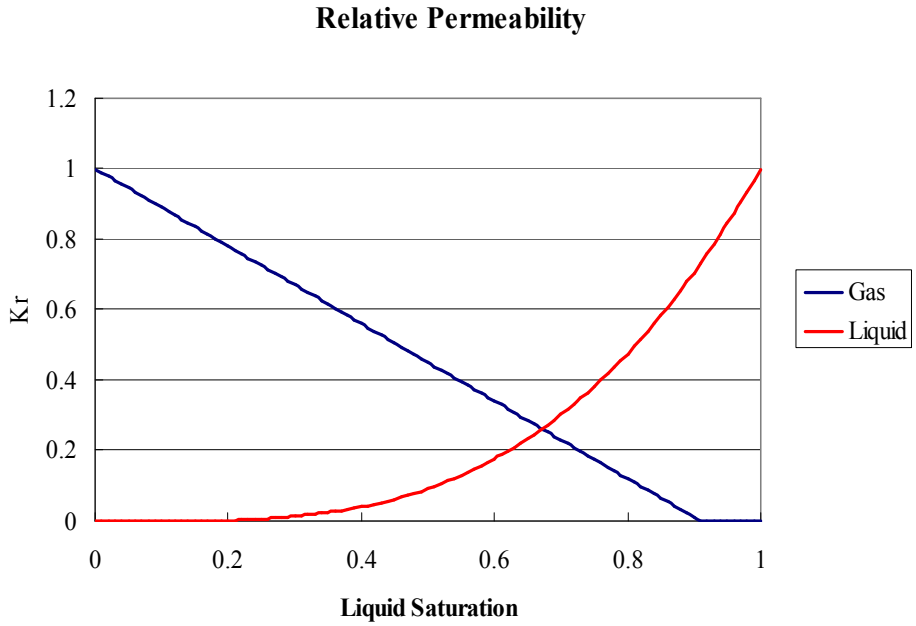

Figure 53– Relative Permeability of Liquid and Gas in Sandstone

When surface tension is the driving force for fluid flow in an unsaturated porous material, negative pressures will be formed in the water at the water-air interfaces. As was explained in the previous section, the negative pressure in the water balances the surface tension forces at the water-air interface. The negative pressure in the water causes water to flow from the surface which is at atmospheric pressure, into the material where the water is at a negative pressure from the interfacial surface tension forces. Two models for predicting such flows are capillary tube models and diffusion models.

B.3.10. Capillary Model of Unsaturated Porous Media

The porous material in Figure 44 can be roughly approximated as a bundle of parallel tubes through which the water flows. Clearly this is not the actual configuration, but we can learn much about the behavior of fluid flows in porous media with the analogy. First consider a single capillary tube. When a wetting (hydrophilic) liquid is present in a vertical capillary tube as shown in Figure 54, surface tension forces will draw the liquid into the tube.

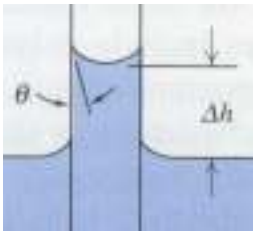

Figure 54- Capillary Rise (from [89])

The forces acting on the column of water are shown in Figure 55

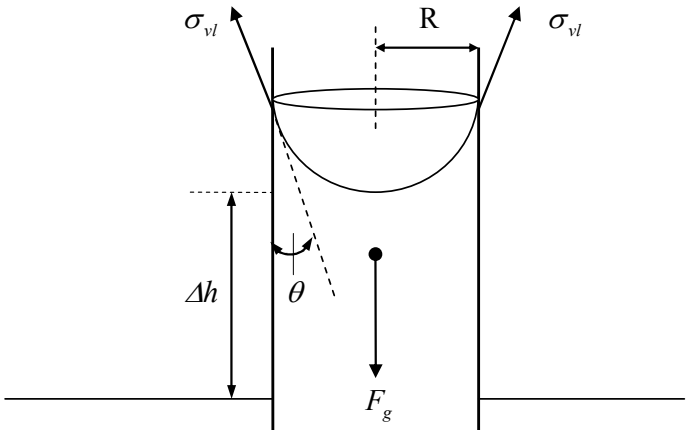

Figure 55 – Forces Acting on a Column of Water

The surface tension forces act on the perimeter of the internal cross section of the tube and are equal to

$$F_{surf\ tens} = 2\pi R\sigma\cos\theta$$

The gravity forces acting on the column of liquid are

$$F_{gravity} = \rho_l g \Delta h \pi R^2$$

Where σ is the surface tension of the liquid – gas interface, θ is the contact angle, ρ_l is the liquid density, and Δh is the capillary rise. If the capillary tube is vertical and at equilibrium as shown in Figure 54, the surface forces will balance the gravity forces acting on the column of liquid and the height of the column is

$$\Delta h = \frac{8\sigma \cos\theta}{R\rho_l g}$$

This inverse relationship between tube radius and column height shows that small tubes will have a large capillary rise. It is often of great concern how fast a liquid will travel through a capillary tube. A simplified solution to this problem can be obtained if gravity is ignored. To show that this is reasonable, consider a 10 cm high capillary tube filling with water with a radius r. The pressure drop across the liquid - air curved interface at the top of the tube is

$$\Delta p_{cap} = \frac{2\sigma \cos\theta}{R}$$

The hydrostatic pressure from gravity effects at the base of the capillary tube is

$$\Delta p_{gravity} = \rho_l g \Delta h$$

These effects are illustrated in Figure 56

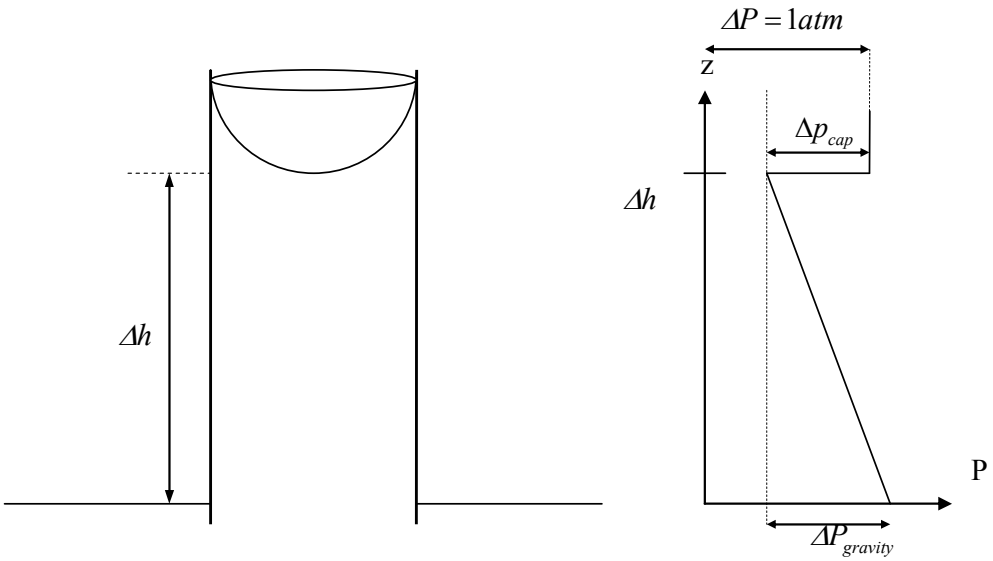

Figure 56 – Capillary Rise and Pressure

Using the following values for properties of water at 60°C to calculate the pressure differences at the top and bottom of the capillary tube

$\sigma = 0.072$ N/m [89]
$\theta \approx 0$ deg [89]
$\rho_l = 983\,\text{kg/m}^3$ [57]

If we are to neglect the effects of gravity, the pressure drop across the water – air interface should be at least an order of magnitude greater than the pressure increase due to gravity. The capillary tube radius which allows for gravity to be neglected is

$$\frac{2\sigma\cos\theta}{R} = 10\rho_l g\Delta h$$

$$R = \frac{2\sigma\cos\theta}{10\rho_l g\Delta h} = \frac{2(0.072)\cos(0)}{10(983)(9.8)(0.10)} = 1.5\times10^{-5}\,m$$

So if the capillary tube in question has a diameter of less than 15 microns, or is oriented horizontally, the rate at which water will flow into the tube can be calculated by setting the pressure drop across the water – air interface equal to the frictional pressure loss. The pressure drop in a capillary tube of length l with fully developed flow can be calculated from the Hagen-Poiseuille equation to be

$$\Delta p_{flow} = \frac{8\mu}{R^2} l \frac{dl}{dt}$$

Equating these two pressure drops produces the relationship known as the Washburn equation [90].

$$\frac{8\mu}{R^2} l \frac{dl}{dt} = \frac{2\sigma \cos\theta}{R}$$

This equation is valid when the gravity force can be neglected. The solutions to this are

$$l = \sqrt{\frac{Rt\sigma\cos\theta}{2\mu}} \quad \text{and} \quad \frac{dl}{dt} = \sqrt{\frac{R\sigma\cos\theta}{8\mu t}}$$

If the pressure at the surface is higher than atmospheric from either a depth of static water or a high velocity spray impacting the surface, then the equation relating the pressure is

$$\frac{8\mu}{R^2} l \frac{dl}{dt} = \frac{2\sigma \cos\theta}{R} + p_{surf}$$

Where P_{surf} is the pressure at the surface. This can be integrated

$$\frac{l^2}{2} = \int \frac{R\sigma\cos\theta}{4\mu} dt + \int \frac{R^2 p_{surf}}{8\mu} dt$$

The solutions to this are

$$l = \sqrt{\frac{R\sigma\cos\theta t}{2\mu}} + \sqrt{\frac{R^2 p_{surf} t}{4\mu}} \quad \textit{and} \quad \frac{dl}{dt} = \sqrt{\frac{R\sigma\cos\theta}{8\mu t}} + \sqrt{\frac{R^2 p_{surf}}{16\mu t}}$$

This indicates that the distance that a liquid has traveled into a capillary tube is proportional to the square root of time, and the velocity of the interface is inversely

proportional to the square root of time. If a porous material is approximated as a bundle of parallel capillary tubes of various diameters, water will penetrate the tubes at different rates. From the solutions to the Washburn equation we can see that the fluid velocity in a capillary tube will be proportional to the square root of radius when the capillary force is much larger than the spray impact force. This means that fluid in larger radius capillaries will have a greater velocity. This is shown qualitatively in Figure 57. Water in the larger tubes has penetrated further than water in the small tubes.

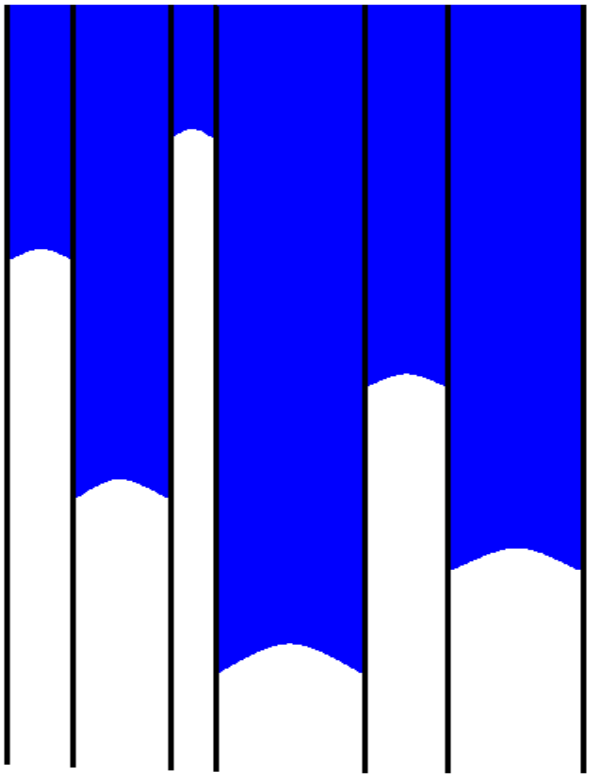

Figure 57 – Bundle of Capillary Tubes

If a positive pressure is now applied to the surface of each tube to represent a depth of static water or impact pressure from a stream of high velocity droplets, the flows will be increased. The depth of water penetration can be calculated using the modified Washburn equation. For 5 different capillary tube diameters, the pressure drop across the water-air interface and the depth of water penetration have been calculated. They are shown in Table 12.

Table 16 – Capillary Pressure and Penetration Depth for Capillary Tubes at time = 10 s, Surface Pressure = 5kPa

Radius [μm]	10	20	30	40	50
Cap Pressure [Pa]	14,400	7,200	4,800	3,600	2,880
Depth [m]	0.0612	0.0896	0.115	0.140	0.165

The pressure in each capillary tube will decrease linearly from the surface pressure to the capillary pressure at the interface located at the depth of water penetration. This is shown graphically in Figure 58.

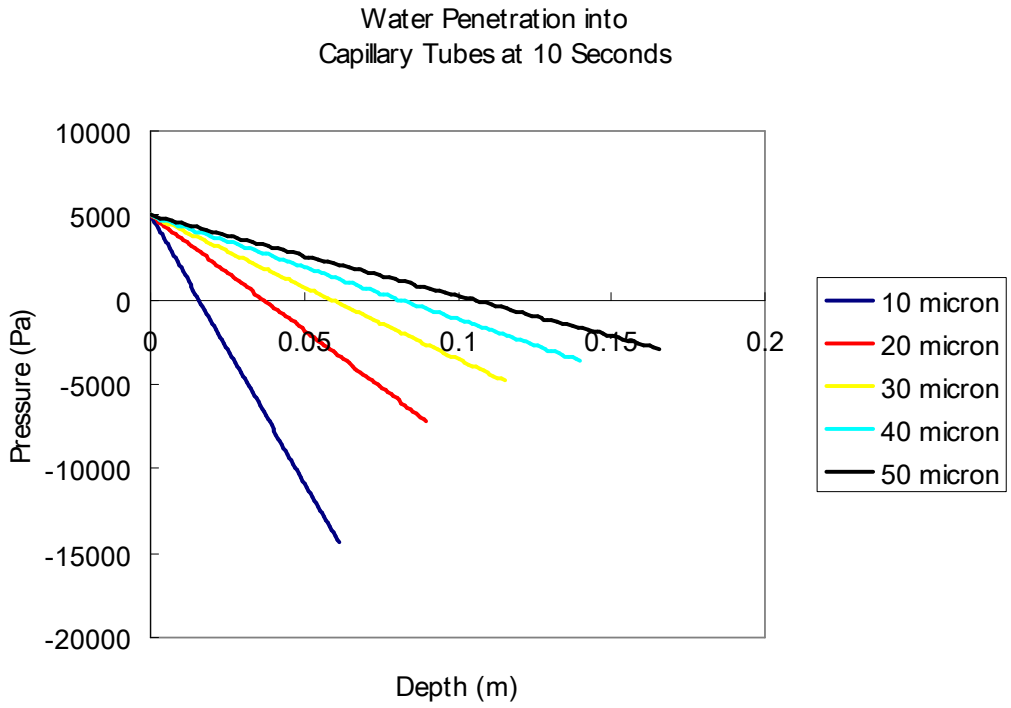

Figure 58 – Pressure in Capillary Tubes with Surface Pressure of 5 kPa

If the surface pressure were zero then the penetration depths would be as given in Table , and shown in Figure 59.

Table 17 – Capillary Pressure and Penetration Depth for Capillary Tubes at time = 10 s, Surface Pressure = 0

Radius [µm]	10	20	30	40	50
Cap Pressure [Pa]	7,200	4,800	3,600	2,880	14,400
Depth [m]	0.0600	0.0845	0.104	0.120	0.134

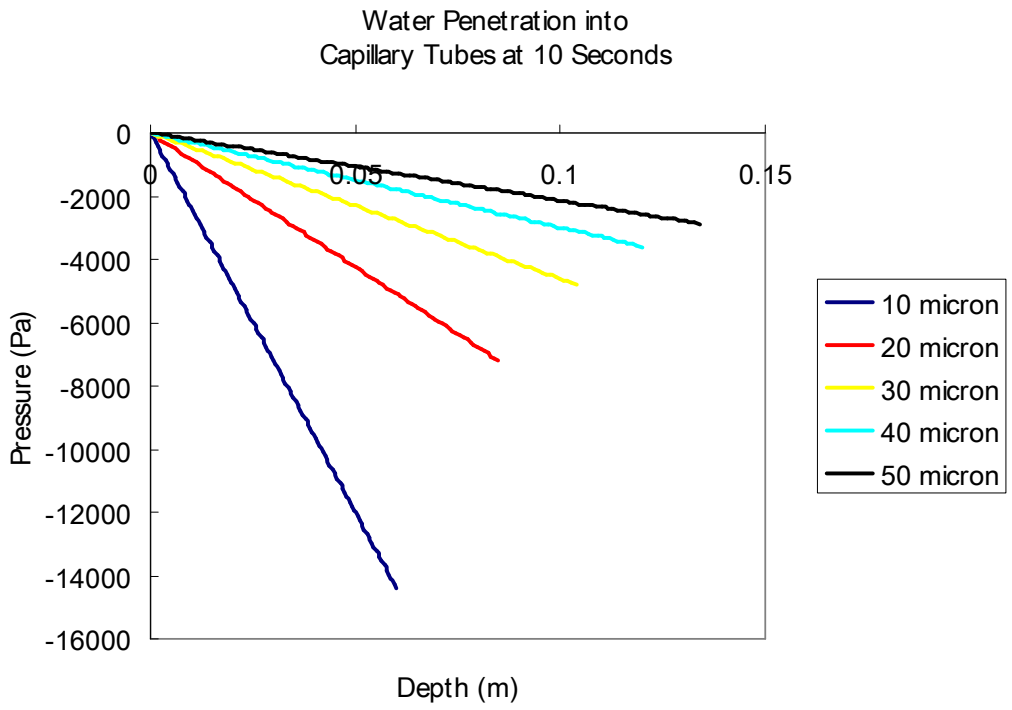

Figure 59 – Pressure in Capillary Tubes of Varying Diameter with Atmospheric Pressure at the Surface

Disadvantages of the Capillary Tube Model

The capillary tube model of a porous material has several disadvantages. It is difficult to measure the pore size distribution of a material, although it can be done using the methods discussed earlier in this document. If the distribution is known well, it is still not clear that the results will give good agreement with tests run on a porous material such as that shown in Figure 44. Pores in such materials will not have constant diameters. Another significant issue with this model is also the fact that it does not

account for horizontal movement of water between interconnected pores. Although most porous materials will have interconnected pores that constrict and expand, it has been experimentally shown that water absorption into corrugated board is roughly proportional to the square root of time [22]. This indicates some level of usefulness of the model. No measurements of depth of penetration were made during these tests however. Some sort of effective length or tortuosity would have to be introduced to account for the curved nature of the pore spaces in an actual porous material. This model also assumes steady state behavior which is not always appropriate. Early in the wetting process, the energy from surface pressure and interfacial surface tension forces will be used to accelerate the fluid from rest to an equilibrium velocity. At this velocity the pressure drop from surface pressure and interfacial surface tension forces will be balanced by viscous forces. This is the origin of the Washburn equation. Deviation from the Washburn equation will occur when the fluid is being accelerated or if the flow is turbulent. The capillary tube model is also limited to 1 dimensional flow. If phase changes are occurring, the capillary model cannot handle condensation ahead of the wetting front.

B.3.11. Diffusion Model of Unsaturated Porous Media

An alternative to the capillary tube model is to derive a diffusion equation which could then be solved using analytical or numerical methods. This method is commonly used for predicting infiltration in soil mechanics and hydrogeology, petroleum reservoir engineering, and drying of materials. In order to formulate such a model several assumptions must be made:

Assumptions:

1. Pressure in the liquid phase (capillary pressure) is caused by surface tension and can be correlated as a function of the saturation of the material.
2. Relative permeability is a function of the saturation of the material, and increases with saturation. It has a value of 1 when the material is completely wet, and zero at a critical minimum liquid saturation.
3. Contact angle is constant and does not depend on whether wetting or draining is occurring (no hyteresis effects).

While it is understood that the pressure in the water will depend on pore diameter, this model is averaging the pressure within a control volume to give an average pressure at a location. If we look at Figure 58 or Figure 59, the pressure at a certain depth is different for each pore. The diffusion model averages each of the pores to give a single

value at each depth. To derive the model start with Darcy's Law

$$\vec{u}_D = -\frac{KK_r}{\mu}\nabla P$$

Conservation of mass tells us that the total accumulation of water in a 2D differential control volume is equal to the sum of the fluxes crossing the surfaces

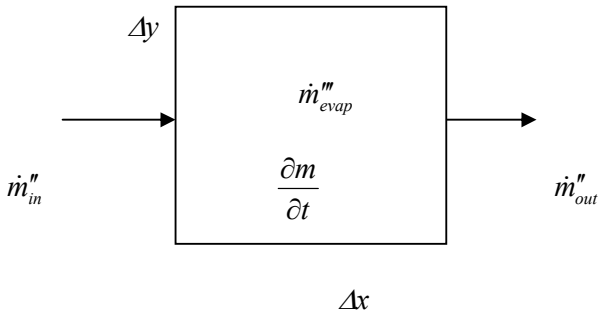

So

$$\iiint_V \left(\frac{\partial m}{\partial t} + \dot{m}''' \right) dV = -\iint_A \dot{m}'' \cdot \vec{n}\, dA = -\iint_A \left(\rho u_i \right) \cdot \vec{n}\, dA$$

Use the Divergence Theorem

$$\iiint_V \left(\frac{\partial m}{\partial t} + \dot{m}'''_{evap} \right) dV = -\iiint_V \frac{\partial \left(\rho_w u_i \right)}{\partial x_i} dV$$

Which can be written as

$$\iiint_V \left(\frac{\partial m}{\partial t} + \dot{m}''' + \frac{\partial \left(\rho_w u_i \right)}{\partial x_i} \right) dV = 0$$

Since the control volume is arbitrary

$$\frac{\partial m}{\partial t} + \dot{m}'''_{evap} = -\frac{\partial \left(\rho_w u_i \right)}{\partial x_i}$$

The mass in the control volume can be expressed as

$$m = \rho_w U$$

If the density of water is assumed to be approximately constant, then the conservation of mass can be rewritten as

$$\frac{\partial U}{\partial t} = -\frac{\partial u_i}{\partial x_i} - \frac{\dot{m}'''_{evap}}{\rho_w}$$

Substituting Darcy's Law for the velocity gives a diffusion equation for moisture content with capillary pressure as the driving force.

$$\phi \frac{\partial S}{\partial t} = \frac{\partial}{\partial x_i}\left(\frac{KK_r}{\mu}\left(\frac{\partial P_{cap}}{\partial x_i} - \rho g \right)\right) - \frac{\dot{m}'''_{evap}}{\rho_w}$$

This is sometimes called the Richards equation. In some cases the pressure gradient will be expanded

$$\phi \frac{\partial S}{\partial t} = \frac{\partial}{\partial x_i}\left(\frac{KK_r}{\mu}\left(\frac{\partial P}{\partial S}\frac{\partial S}{\partial x_i} - \rho g \right)\right) - \frac{\dot{m}'''_{evap}}{\rho_w}$$

and a moisture diffusion coefficient will be defined

$$D = \frac{KK_r}{\mu}\frac{\partial P}{\partial S}$$

so that the PDE can be rewritten as

$$\phi \frac{\partial S}{\partial t} = \frac{\partial}{\partial x_i}\left(D\frac{\partial S}{\partial x_i}\right) - \frac{\partial}{\partial x_i}\left(\rho g \frac{KK_{r,l}}{\mu_w}\right) - \frac{\dot{m}'''_{evap}}{\rho_w}$$

If the system is isothermal and gravity effects are negligible then the equation can be written as

$$\phi \frac{\partial S}{\partial t} = \frac{\partial}{\partial x_i}\left(D \frac{\partial S}{\partial x_i} \right)$$

The diffusion coefficient D is function of the saturation of the material. It is not possible to get good agreement with experimental values using a constant [33]. The diffusion coefficient for a typical soil is shown in Figure 60.

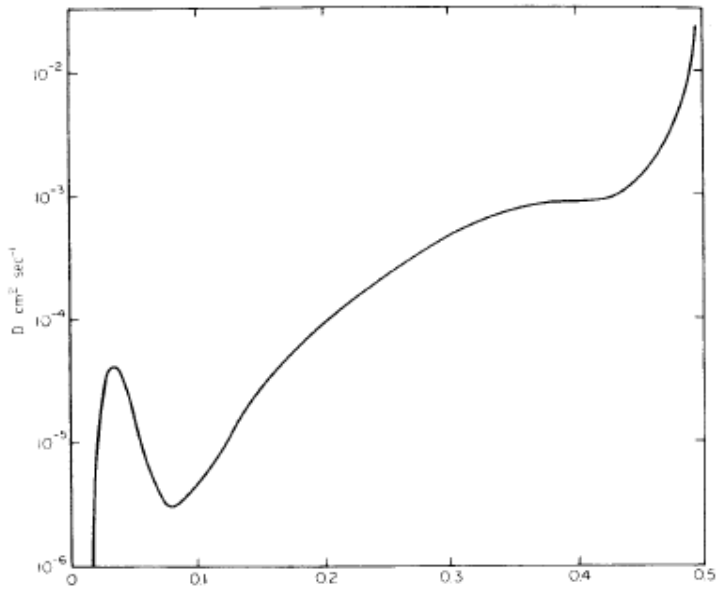

Figure 60 – Diffusion Coefficient (from Philip, 1969)

The relationship shown in Figure 60 is calculated from experimental values, and the behavior at low moisture content is due to vapor phase transport [33]. Typical results from the diffusion model are shown in Figure 61.

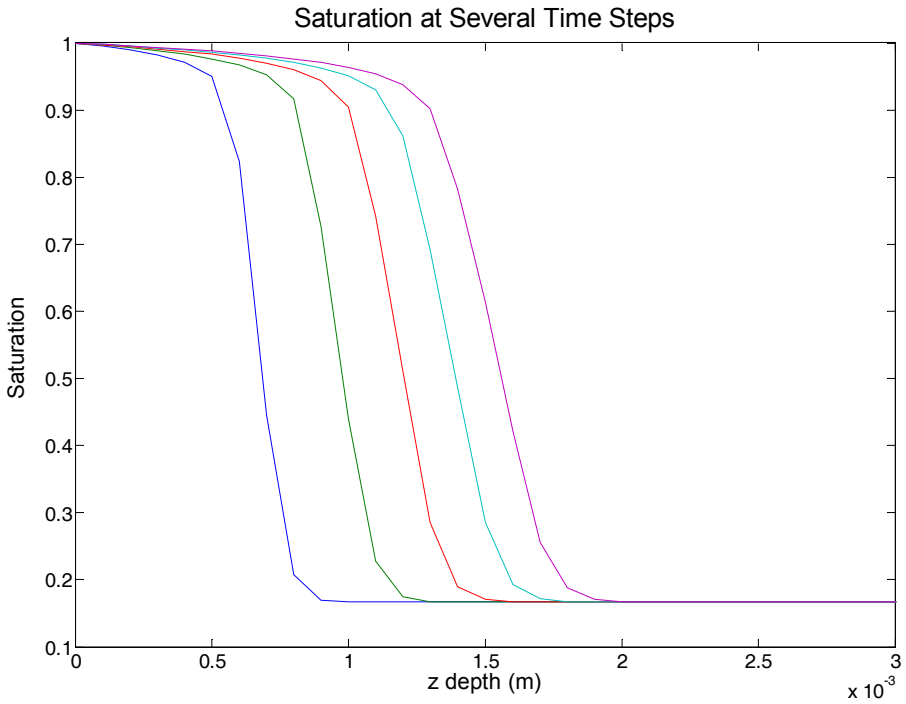

Figure 61 – Saturation Profiles in a Representative Porous Material At Several Time Steps

Disadvantages of the Diffusion Model for Porous Media Flows

The diffusion model has some of the same limitations as the capillary tube model. It cannot account for the energy used to accelerate the fluid because, strictly speaking, Darcy's law is only applicable to steady flows. It also cannot predict turbulent flows or flows where inertial effects are significant, so the Reynolds number based on pore velocity and average pore diameter must be less than 1 [23]. The diffusion model also has a serious flaw that comes from its derivation with steady state equations and relationships. The capillary tube model showed that the water will flow faster through pores with larger diameters. In the moisture profile of the diffusion model the leading edge of the wetting front will have very low saturation values, trailing off to the initial saturation. This capillary pressure that is calculated from this saturation will be quite high since the model assumes that the water is in the small pores. If the conditions were steady state, and the saturation was very low, then the water would be held in the smallest pores of the material. Since we are now dealing with a dynamic system, the water will most likely still be in the larger pores. This inconsistency of the model is

rarely discussed, but apparently does not prevent it from achieving reasonable results.

B.4. Effects of Spray Impingement on Surface

B.4.1. Impact Pressure

Until now the effects of pressure at the surface of the material have been mentioned in this paper but have not been discussed in detail. For purposes of discussion the effects of a stream of droplets have been likened to a depth of static water resting on the surface of the material. The two cases are similar, but have many fundamental differences. The pressure in a static liquid (ignoring surface tension effects) will be a function of the height only and can be calculated as [89]

$$p - p_{\infty} = \rho g h$$

Where h is the height of water above the point of interest. This case is shown in Figure 62. The pressure difference will increase from zero at the surface of the water to a value of $\rho g h$. The slope of the pressure change is

$$\frac{dp}{dz} = -\rho g$$

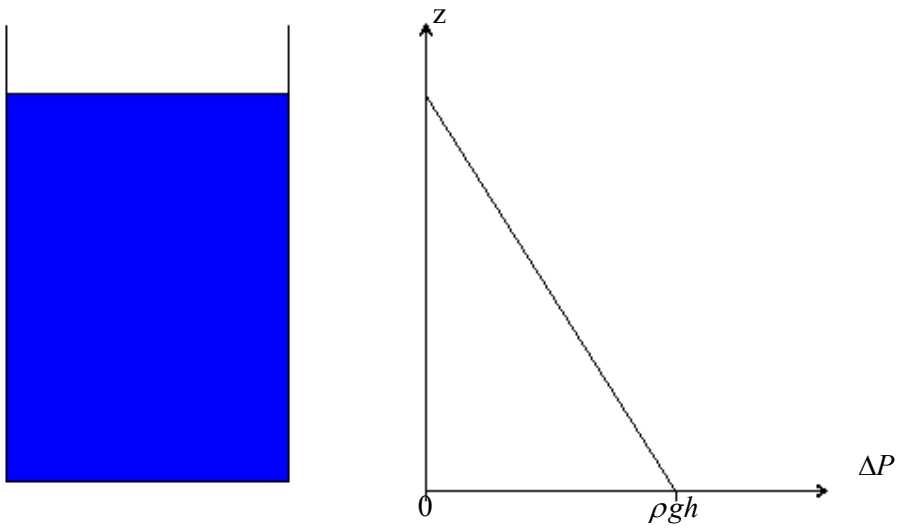

Figure 62 – Hydrostatic Pressure Variation in a Water Reservoir

In contrast to the static pressure situation, a moving droplet impinging on a solid material will produce a time varying pressure on the solid surface. A droplet impacting a solid surface will rapidly decelerate as it impacts the surface and a thin sheet will spread radially due to a rapid increase in pressure [91]. The radial jetting velocity of the liquid can be twice the impact velocity [92]. The sheet can become unstable and thin azimuthal undulations can appear [91]. If they grow enough, these 'fingers' can break up into secondary droplets. The behavior of the impinging droplet will be determined by many factors such as the droplet diameter, impact velocity, surface tension, liquid viscosity, solid surface roughness, and contact angle. If the surface is heated, the problem becomes even more complex as film boiling can occur. The impacting droplet behavior can be classified into 6 regimes as shown in Figure 63. The factors influencing which regime will occur can be grouped into several dimensionless numbers. The most important are the Reynolds number, Weber number, and Ohnesorge number [91, 93]

$$\mathrm{Re} = \frac{\rho u d}{\mu} = \left[\frac{inertial\ \ forces}{viscous\ \ forces} \right]$$

$$We = \frac{\rho d u^2}{\sigma} = \left[\frac{inertial\ \ forces}{surface tension\ \ forces} \right]$$

$$Oh = \frac{\mu}{\sqrt{\rho \sigma d}} = \frac{\sqrt{We}}{\mathrm{Re}} = \left[\frac{viscous\ \ forces}{\sqrt{inertial * surface\ tension\ \ forces}} \right]$$

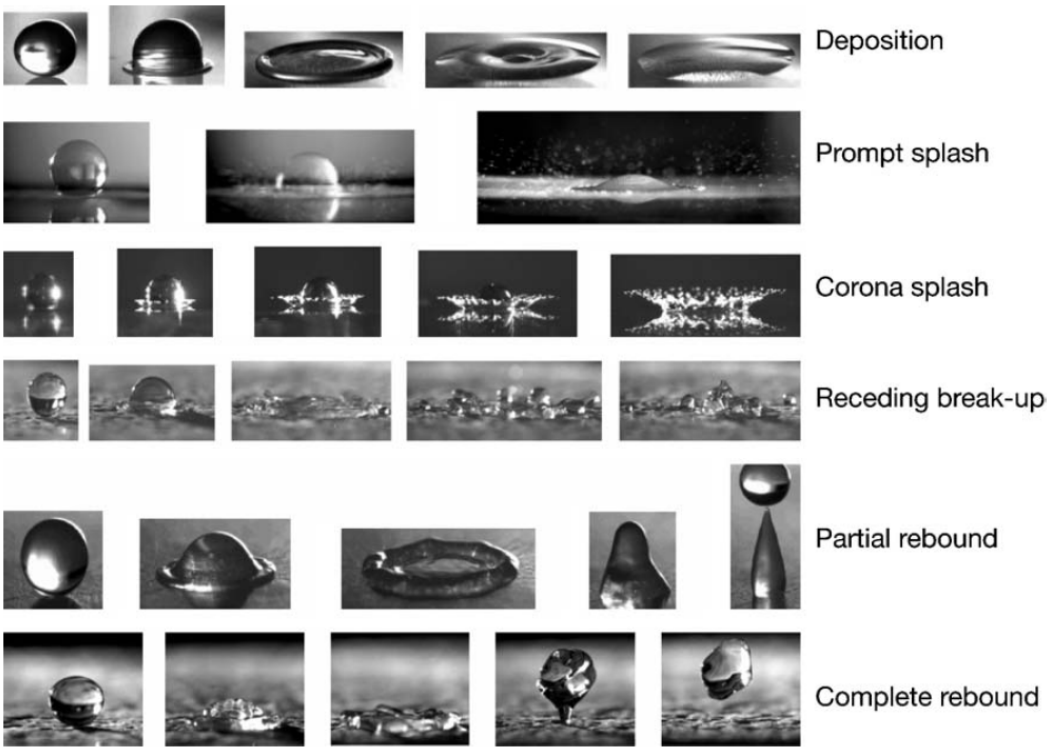

Figure 63 – Possible Regimes of Droplet Impacting Dry Solid Surface (from [93])

If the solid surface has a liquid layer on top of it, the behavior can be much different. Single droplets impacting a liquid pool can lead to a rebounding jet of water as shown in Figure 64, crater formation, crown propagation/formation/breakup as shown in Figure 65, and rolling over of the surface.

Figure 64 – Jet Rising After a Water Droplet Impact with a Pool of Milk (from [94])

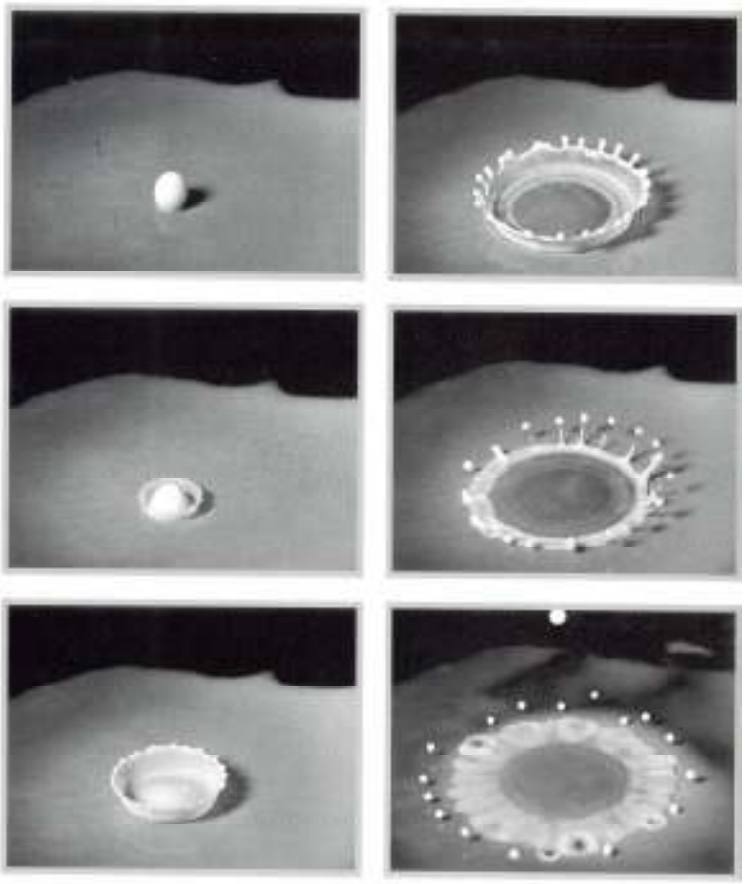

Figure 65 – Milk Droplet Impacting a Pool of Water (from [95])

Many studies have been performed on single droplet impingement on solid and liquid surfaces. Chang and Hills [96] have performed numerical studies on the impact pressure and shear stress that a 4mm droplet traveling at 5.8 and 8 m/s imparts on a solid surface. The simulations, which were performed using Flow 3D software, investigated the effect of impact angle and also of the presence of 6mm of static water on the surface of the material. Their results for a droplet traveling 8 m/s are shown in Figure 66 and Figure 67. The water on the surface of the material has the effect o smoothing the pressure curve and increasing the amount of time that the pressure is applied to the surface of the material by almost an order of magnitude. The total time that a pressure is applied to the solid surface is short, on the order of one hundredth of a second. The maximum forces applied to the solid are calculated to be less than half of a Newton in all cases. The double peaks in the case of impact on a bare surface are due to the increasing surface area of the droplet in contact with the solid. Pressure at the water-solid interface reaches a maximum at the first peak around 0.0001 seconds. After

this time the pressure drops off, but the total surface area in contact with the droplet increases considerably. This causes the second peak in total force applied to the solid. The case of a liquid film on the surface of the solid material does not exhibit this behavior and has a smoother profile.

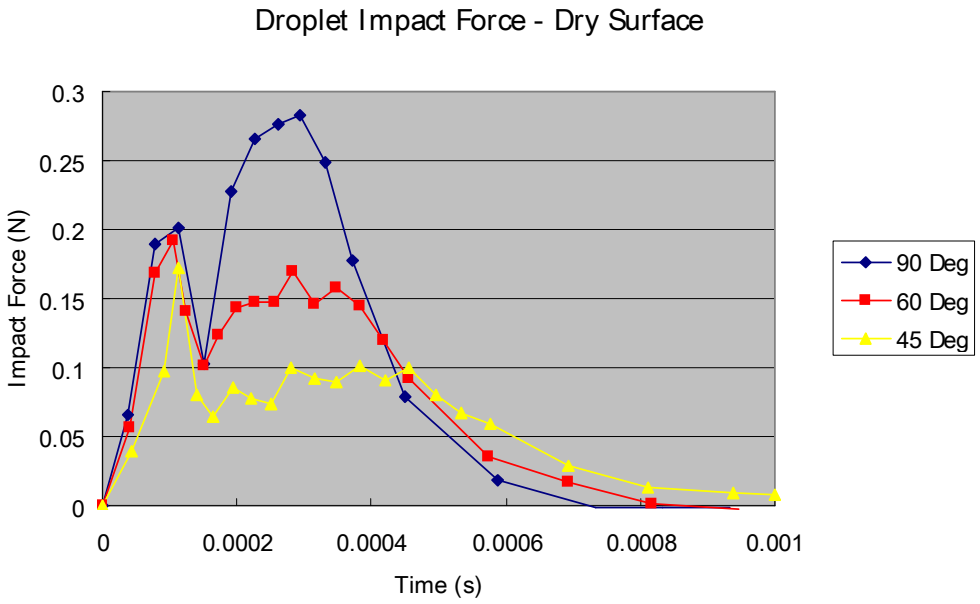

Figure 66 – Impact Force from a 4mm Droplet Impacting a Dry Surface at 8 m/s at Three Angles of Impact (data points from [96])

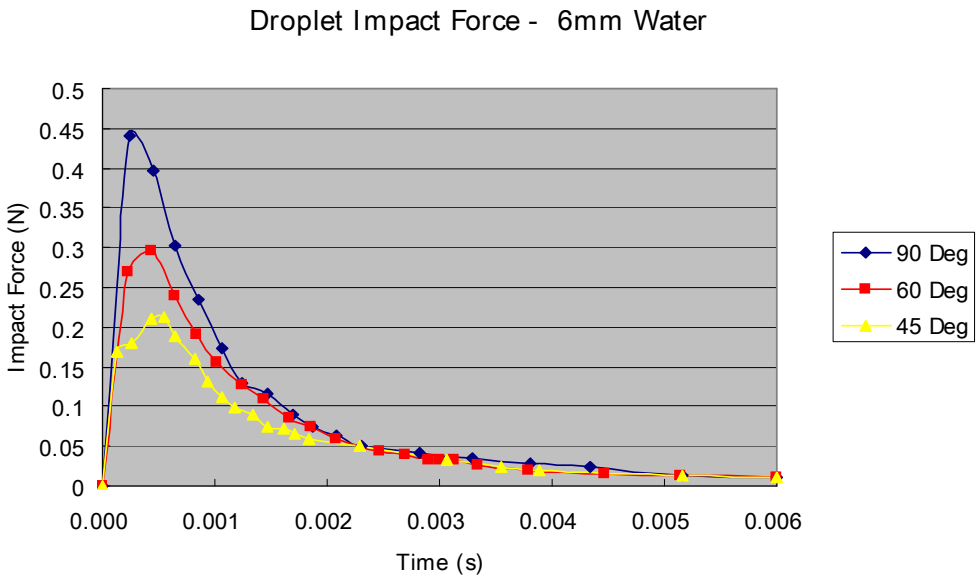

Figure 67 – Impact Force from a 4mm Droplet Impacting a Surface with 6mm of Static Water on Surface at 8 m/s at Three Angles of Impact (data points from [96])

If the solid material is porous the problem becomes more complicated. The impact pressure at the solid surface as well as capillary effects will force liquid into the pores [97]. Reis et al. developed a numerical model to predict the absorption of single drops of water into a porous material. The model was validated against experimental data obtained by dropping water drops onto beds of glass beads and measuring the location of the water using Nuclear Magnetic Resonance Imaging (MRI). The model matches the experimental data well except for cases where the beads are significantly disturbed by the droplet impact [97].

B.4.2. Interface Description

In both the case of hydrostatic pressure and a dynamic impact pressure applied to the surface of the material, there will be a positive gage pressure in the water inside the pores of the material near the surface. This pressure will be dissipated by viscous shear forces in the water as water is forced into the pores. Both the capillary model and diffusion model discussed earlier assume that the pressure in the water is negative near the liquid – air interface. In the capillary model it will be determined by the diameter of the individual tubes. In the diffusion model, the pressure in the partially saturated area will be determined by the J-Function. This means that in the models, there must be

a location where the gage pressure is zero. This can be seen for each capillary tube in Figure 58. In the capillary model it is a straightforward calculation to determine this interface location. With the diffusion model, the calculation is slightly more involved. As can be seen in Figure 61, the diffusion model predicts a saturation of slightly less than unity near the surface. This is because the model cannot predict flows when the material is saturated since pressure is calculated using the J-Function. If the material is completely saturated, the model predicts a pressure of zero. This means that the diffusion model cannot handle positive pressures or completely saturated regions near the surface of the material. We would like to modify the diffusion model to handle this scenario shown in Figure 68. Here water is forced into the pores by the impact pressure at the surface, but also pulled in by negative capillary pressure.

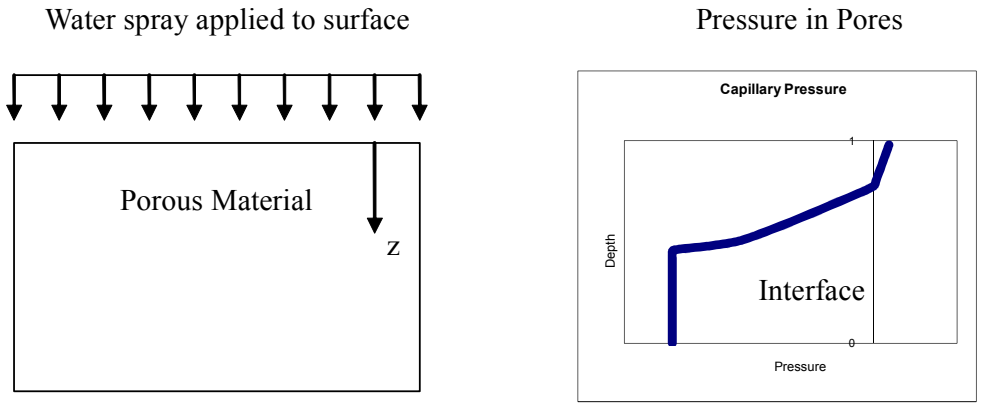

Figure 68 – Water Spray Applied to Porous Material

The saturation profile for such a situation can be seen in Figure 69.

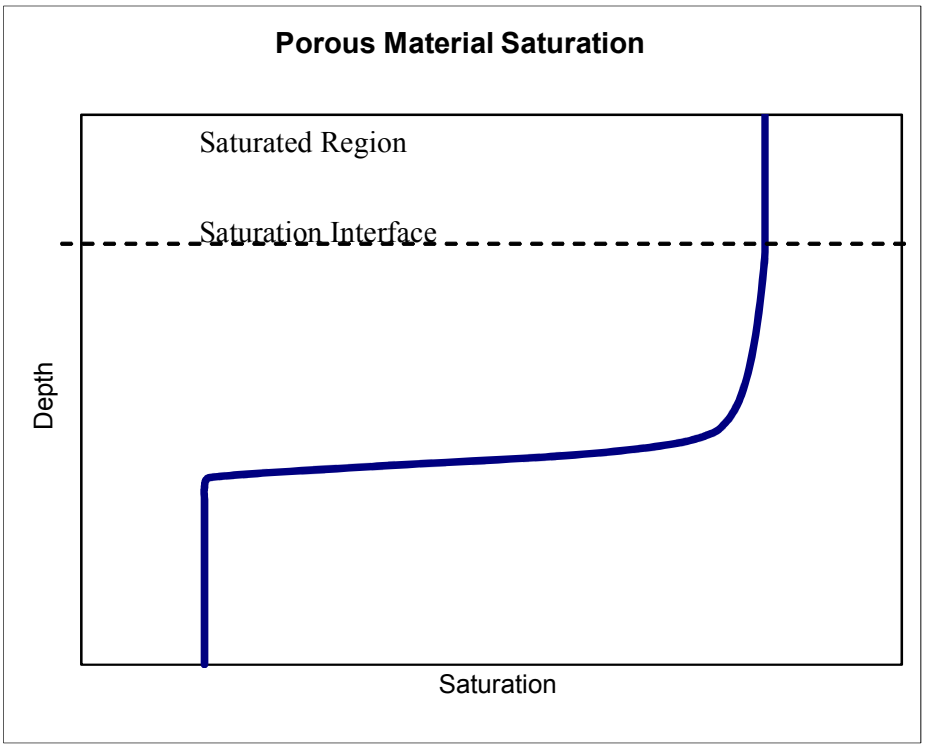

Figure 69 – Saturation Profile for Porous Material with Water Spray Applied to Surface

The impact pressure at the surface must be dissipated by the water flowing through the pores. It is therefore important to know the location of the interface if the rate of water absorption into the material is to be determined. Another method is given by Philip [32]. His method assumes that the pressure from the surface is completely dissipated according to Darcy's Law

$$v_o = \frac{K}{\mu_w}\frac{P_{surf} + \rho g z_{\text{int}}}{z_{\text{int}}}$$

Where $\frac{P_{surf} + \rho g z_{\text{int}}}{z_{\text{int}}}$ represents the pressure gradient in the completely saturated zone, v_o is the infiltration velocity, and z_{int} is the saturation interface. This equation can be rearranged to solve for z_{int}.

$$z_{\text{int}} = \frac{\frac{K}{\mu}P_{surf}}{v_o - \frac{K}{\mu}\rho g}$$

The only unknown here is the infiltration velocity v_o. This can be determined by calculating the rate of change of the total infiltration [27]. The total infiltration is the total amount of water that has been absorbed into the material which is

$$i = \int_{U_o}^{U_{sat}} z\, dU + \frac{K K_{r,l}\left(S_o\right)}{\mu_w} \rho g t$$

The first term is the summation of all moisture increase throughout the material, and the second term is a sum of the water flowing through the material under the effects of gravity. This second term is only significant if the material has a very high initial saturation. Using this equation the infiltration velocity is calculated as

$$v_o = \frac{di}{dt} = \frac{d}{dt} \int_{U_o}^{U_{sat}} x\, dU$$

If this integral can be calculated analytically or (more likely) numerically, then the interface location can be determined.

$$z_{\text{int}} = \frac{\frac{K}{\mu} P_{surf}}{\frac{d}{dt} \int_{U_o}^{U_{sat}} x\, dU - \frac{K}{\mu} \rho g}$$

In compartment fire environments a broad range of conditions can be encountered at the surface of a porous combustible material. Directly beneath a sprinkler the material will be subjected to a very high mass flux of water droplets (up to 1.1 gpm/ft^2) at high velocities. For ESFR sprinklers the water spray is required by FM Approval Standards for Class 2008 [98] and UL Listing Standard UL 1767 [99] to have a minimum center core “thrust” (their word, wrong units) of up to 2.1 lb/sqft (100 Pa). This thrust is measured over a 13.5 inch diameter plate placed 7 feet under the sprinkler while the sprinkler discharges water at a specified pressure. Under these conditions it is likely that the impact pressure at the surface will be significant. Further from the sprinkler the water flux will be much lower and the droplets will have lower velocities. In this area, it is possible for the impact pressure to play an imporatant role, but the relative significance will be determined by the characteristics of the spray and material

properties. At the edges of the sprinkler's spray pattern, the water flux will be very low, and contain many small droplets with low velocity. This scenario could also represent a water mist system. For water mist the momentum of the individual droplets would be insignificant. This would correspond to a situation with zero impact pressure at the surface of the material. Depending on the water application rate and the material properties the surface could be saturated or unsaturated. In many cases the impact pressure is much less than the capillary pressure from surface tension forces in the material. For an incident mass flux, $\dot{m}''_{spray}$, with a spray velocity, u, the spray impact pressure at the surface is assumed to be approximately the stagnation point pressure, $p_{spray} = \dot{m}''_{spray} u$. The maximum capillary pressure in the material is approximately of the order $\sigma\sqrt{\phi / K}$. For the materials used in this investigation, and the mass fluxes associated with fire sprinklers (0.271 kg/m^{2}s – 16.3mm/min) and velocities of sprinkler droplets (~20 m/s) the impact pressure is several orders of magnitude lower than the capillary pressure.

B.4.3. Water Layer on Surface of Material

If water is applied to the material at a flow rate that is greater than the absorption rate into the material plus the evaporation rate, then a layer of water will form on the surface. This layer of water is important for several reasons. The water will reflect and absorb incident radiation, and exchange heat with the solid material by conduction. The thickness of the water layer will depend on the surface area of the material. For a circular horizontal plate the film thickness can be calculated from the momentum equation if several assumptions are made. Assuming inviscid flow in the radial direction only, the film thickness is [100]

$$h_o = \frac{3}{2}\left(\frac{Q}{2\pi R\sqrt{g}}\right)^{\frac{2}{3}}$$

Where Q is the volumetric flow rate of water in $\frac{m^3}{s}$. Normal sprinkler flows are in

the range of 0.07 – 1.1 $\frac{gpm}{ft^2}$ [101]. Now calculate the layer thickness for these flow rates. Assume a flat, circular, horizontal surface 1 meter in diameter with a uniform water application. This gives an area of

$$A = \pi r^2 = \pi 0.5^2 = 0.785 m^2$$

The water application rates, volumetric water fluxes, and calculated water layer thicknesses for different NFPA hazard classifications are given in Table 18.

Table 18 – Water Layer Thickness

Hazard	$\frac{gpm}{ft^2}$	$\frac{m^3}{m^2 s} \times 10^{-5}$	$\frac{m^3}{s} \times 10^{-5}$	h_o (mm)
Light	0.07 – 0.10	4.8 – 6.8	3.7 - 5.3	0.36 – 0.46
Ordinary Group 1	0.10 – 0.15	6.8 – 1.0	5.3 – 8.0	0.46 – 0.61
Ordinary Group 2	0.15 – 0.20	1.0 – 1.4	8.0 – 11	0.61 – 0.74
Extra Group 1	0.20 – 0.30	1.4 – 2.0	11 – 16	0.74 – 0.96
Extra Group 2	0.30 – 0.40	2.0 – 2.7	16 – 21	0.96 – 1.2
Rack Storage of Plastic Commodities	1.1	7.5	58	2.3

The thickness of this water layer will strongly influence how much incident radiation it absorbs. When a radiant heat source is directed at a volume containing an absorbing medium, some energy will be absorbed and some will be transmitted through the medium. If scattering can be neglected, then the intensity of radiant energy passing through the medium is given by [102]

$$i_\lambda(L) = i_\lambda(0) \exp\left(-\int_0^L a_\lambda\left(L^*\right) dL^* \right)$$

Where i_λ is the spectral radiation intensity and a_λ is the monochromatic absorption coefficient. If it is a constant then this can be written as [102]

$$i_\lambda(L) = i_\lambda(0) \exp(-a_\lambda L)$$

The fraction of radiant energy escaping through the back face of the medium is therefore defined as [43]

$$\tau_\lambda = \frac{i_\lambda(L)}{i_\lambda(0)} = \exp(-a_\lambda L)$$

So the total transmissivity is

$$\tau = \frac{\int_{\lambda=0}^{\infty} i_\lambda(L)\partial\lambda}{\int_{\lambda=0}^{\infty} i_\lambda(0)\partial\lambda}$$

So the absorptivity of the medium is defined as [43]

$$\alpha = 1 - \tau$$

The absorption coefficient is defined as

$$a_\lambda = \frac{4\pi k_\lambda}{\lambda}$$

Where k_λ is the monochromatic extinction coefficient. The spectral or monochromatic reflectivity of water at near normal incidence is calculated from the monochromatic index of refraction n_λ and the monochromatic extinction coefficient using the Fresnel relation [103]

$$R_\lambda = \frac{(n_\lambda - 1)^2 + k_\lambda{}^2}{(n_\lambda + 1)^2 + k_\lambda{}^2}$$

The monochromatic extinction coefficient and index of refraction of water from 0.2 up to 200 microns is given by Hale and Querry [104]. Their values are used to create the absorption coefficient in Table 19 and shown in Figure 70 and the reflectivity shown in

Figure 71. For comparison the emission spectrum from a blackbody at 800, 1000, and 1200 K are also shown in Figure 70 and Figure 71. These represent typical temperatures of the electrical resistance heating element on the cone calorimeter.

Table 19 – Absorption Coefficient of Water

Wavelength $[\mu m]$	a_λ $\left[m^{-1}\right]$	Wavelength $[\mu m]$	a_λ $\left[m^{-1}\right]$
0.2	6.91	6.2	178361
0.225	2.74	6.3	113696
0.25	1.68	6.4	88161
0.275	1.07	6.5	75785
0.3	0.670	6.6	67782
0.325	0.418	6.7	63207
0.35	0.233	6.8	60429
0.375	0.117	6.9	58643
0.4	0.059	7	57446
0.425	0.038	7.1	56637
0.45	0.028	7.2	56025
0.475	0.025	7.3	55430
0.5	0.025	7.4	55020
0.525	0.032	7.5	54622
0.55	0.045	7.6	54234
0.575	0.079	7.7	54019
0.6	0.228	7.8	53971
0.625	0.279	7.9	53924
0.65	0.317	8	53878
0.675	0.415	8.2	53790
0.7	0.601	8.4	54005
0.725	1.59	8.6	54357
0.75	2.61	8.8	54978
0.775	2.40	9	55711
0.8	1.96	9.2	56685
0.825	2.77	9.4	57886
0.85	4.33	9.6	59428
0.875	5.62	9.8	61421
0.9	6.79	10	63837
0.925	14.4	10.5	74201
0.95	38.8	11	110584

0.975	44.9	11.5	155167
1	36.3	12	208392
1.2	104	12.5	260375
1.4	1239	13	294826
1.6	672	13.5	319279
1.8	803	14	332111
2	6912	14.5	336259
2.2	1651	15	336779
2.4	5006	15.5	335644
2.6	15321	16	331438
2.65	31772	16.5	325964
2.7	88430	17	317116
2.75	269606	17.5	308056
2.8	516119	18	297404
2.85	815712	18.5	285970
2.9	1161306	19	273815
2.95	1269416	19.5	260349
3	1139351	20	246929
3.05	988829	21	228588
3.1	778304	22	213057
3.15	538559	23	200516
3.2	362854	24	189019
3.25	235861	25	178945
3.3	140134	26	169163
3.35	97905	27	160105
3.4	72072	28	151694
3.45	48080	29	144297
3.5	33750	30	137392
3.6	17977	32	127235
3.7	12227	34	121598
3.8	11244	36	119730
3.9	12244	38	119381
4	14451	40	120951
4.1	17225	42	122373
4.2	20585	44	124521

4.3	24694	46	126210
4.4	29417	48	127758
4.5	37420	50	129182
4.6	40158	60	122941
4.7	41977	70	103403
4.8	39270	80	85923
4.9	35135	90	74840
5	31165	100	66853
5.1	27350	110	60661
5.2	24408	120	55083
5.3	23236	130	49685
5.4	23969	140	44880
5.5	26504	150	41469
5.6	31865	160	38956
5.7	44754	170	36738
5.8	71498	180	34837
5.9	132479	190	33136
6	224100	200	31667
6.1	269868		

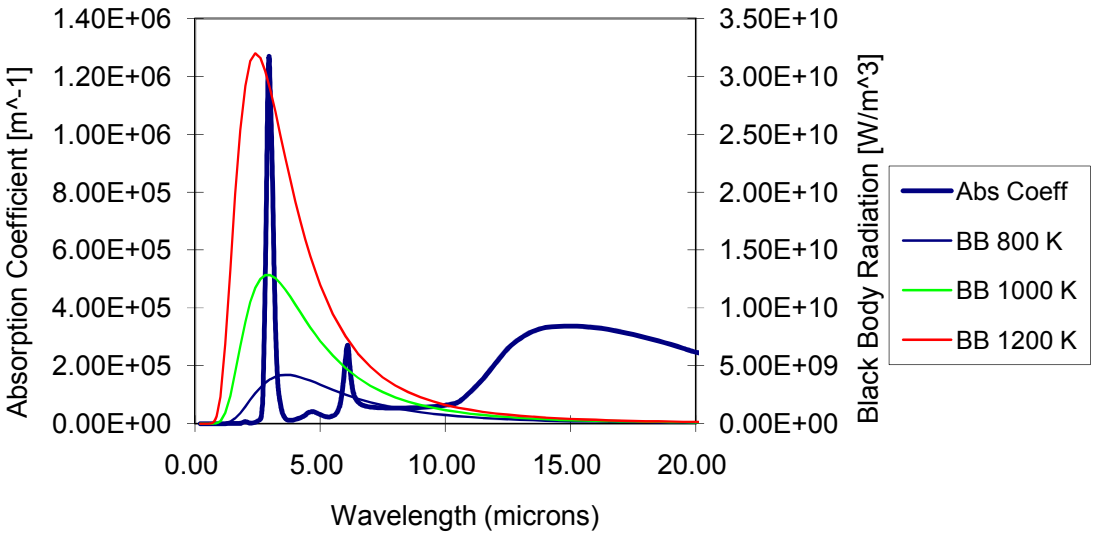

Figure 70 – Absorption Coefficient of Water 0-20 microns

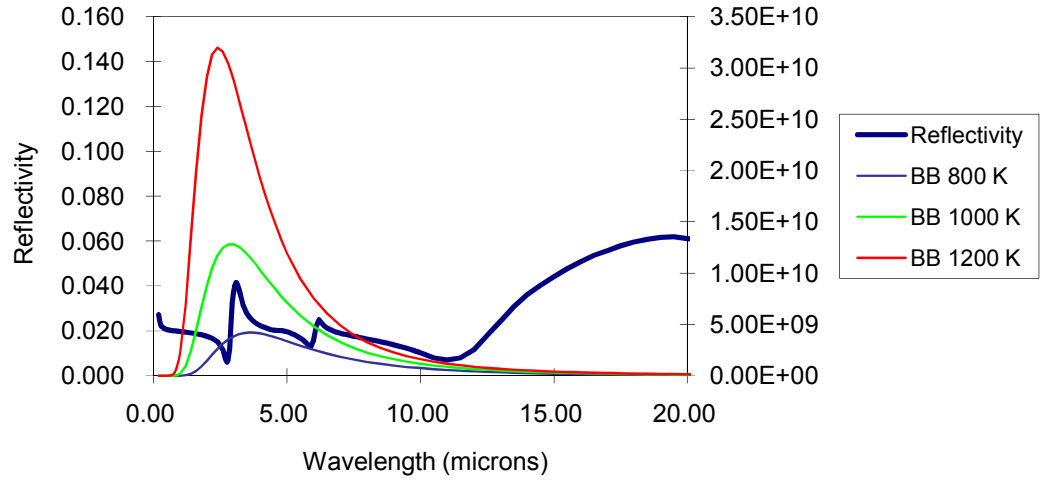

Figure 71 – Spectral Reflectivity of Water

Kondratyev [105] calculated the absorption of solar radiation into layers of water of varying depth. His data is shown in Table 20.

Table 20 – Solar Radiation Transmission Through Water

λ $[\mu m]$	Incident Solar Energy Distribution	Transmitted Energy Distribution For Water Layer Thickness [cm]							
		0.001	0.01	0.1	1	10	100	1000	100000
0.3-0.6	0.237	0.237	0.237	0.237	0.237	0.236	0.229	0.173	0.014
0.6-0.9	0.360	0.360	0.360	0.359	0.353	0.305	0.129	0.010	
0.9-1.2	0.179	0.179	0.178	0.172	0.123	0.008			
1.2-1.5	0.087	0.086	0.082	0.063	0.017				
1.5-1.8	0.080	0.078	0.064	0.027					
1.8-2.1	0.025	0.023	0.011						
2.1-2.4	0.025	0.025	0.019	0.001					
2.4-2.7	0.007	0.006	0.002						
Total	1.00	0.994	0.953	0.859	0.730	0.549	0.358	0.183	0.014

Solar radiation reaching the surface of the earth will have a much different spectral distribution than thermal radiation in a fire environment. For comparison consider the blackbody radiation in Figure 71. The monochromatic hemispherical emissive power of a black surface is

$$E_{b,\lambda} = \pi i_{b,\lambda} = \frac{C_1 \lambda^{-5}}{\exp\left(\frac{C_2}{\lambda T}\right) - 1}$$

Where

$C_1 = 2\pi hc^2 = 3.742 \times 10^{-16} Wm^2$

$C_2 = \frac{hc}{k} = 1.439 \times 10^{-2} mK$

The maximum monochromatic emissive power occurs at a wavelength determined by Wiens displacement law [43]

$\lambda T = 2.898 \times 10^{-3} mK$

Since the surface of the sun has a temperature of approximately 6000 K, the maximum monochromatic emissive power occurs at a lower wavelength. The transmissivity of a water layer exposed to blackbody radiation can be calculated using the absorption

coefficient in Table 19. The results for several temperatures integrated over all wavelengths are shown in Figure 72.

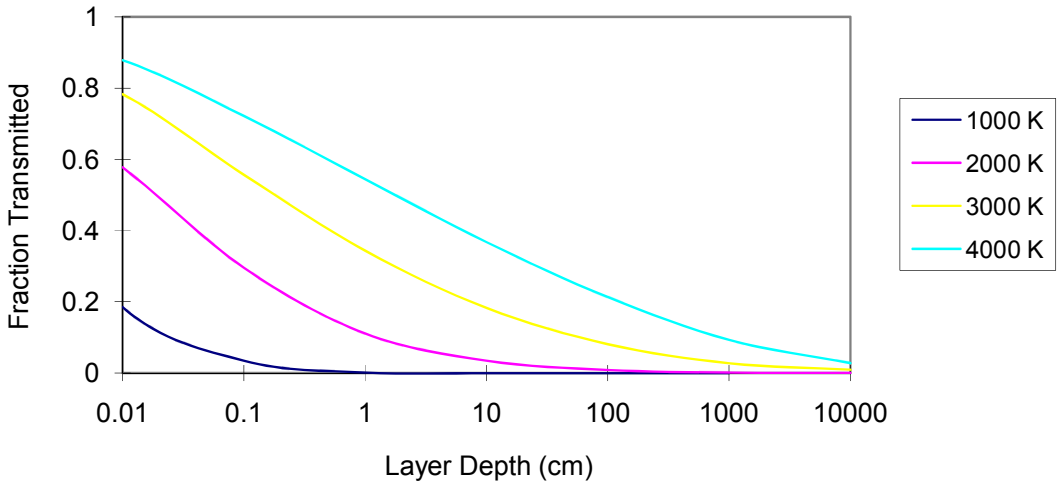

Figure 72 – Water Layer Absorption of Radiation from Blackbodies at Various Temperatures

Figure 72 shows that even a small layer of water on the surface of a material such as the layer thicknesses in Table 20 will absorb most of the thermal radiation from blackbodies with a temperature of less than 2000 K. Charts similar to Table 20 can be calculated for blackbody sources of different temperatures to show the breakdown of radiation absorption. The transmission of thermal radiation from blackbody surfaces at 800, 1000, and 1200 K through various thicknesses of water is shown in Table 21, Table 22, and Table 23.

Table 21– Transmission of Thermal Radiation from a Blackbody at 800K Through Various Thicknesses of water

λ [μm]	Incident Energy Distribution	Transmitted Energy Distribution for Water Layer Thickness [cm]				
		0.001	0.01	0.1	1	10
0.25-0.6	0.0000					
0.6-0.9	0.0000					
0.9-1.2	0.0002	0.0002	0.0002	0.0002	0.0001	
1.2-1.6	0.0038	0.0038	0.0035	0.0017	0.0001	
1.6-2.0	0.0161	0.0156	0.0122	0.0045		
2.0-2.4	0.0351	0.0338	0.0249	0.0035		
2.4-2.8	0.0534	0.0337	0.0107	0.0001		
2.8-3.2	0.0659	0.0002				
3.2-6.5	0.4833	0.3129	0.0403			
6.5-10	0.1983	0.1118	0.0007			
10- 20	0.1440	0.0266				
Total	1.000	0.539	0.093	0.010	0.000	0.000

Table 22 -Transmission of Thermal Radiation from a Blackbody at 1000K Through Various Thicknesses of water

λ [μm]	Incident Energy Distribution	Transmitted Energy Distribution For Water Layer Thickness [cm]					
		0.001	0.01	0.1	1	10	100
0.25-0.6	0.0000						
0.6-0.9	0.0001	0.0001	0.0001	0.0001	0.0001	0.0001	
0.9-1.2	0.0022	0.0022	0.0022	0.0021	0.0010		
1.2-1.6	0.0179	0.0177	0.0164	0.0079	0.0006		
1.6-2.0	0.0469	0.0456	0.0368	0.0146			
2.0-2.4	0.0732	0.0705	0.0517	0.0073			
2.4-2.8	0.0874	0.0568	0.0190	0.0001			
2.8-3.2	0.0902	0.0002	0.0000				
3.2-6.5	0.4582	0.2991	0.0406				
6.5-10	0.1379	0.0777	0.0005				
10- 20	0.0860	0.0162					
Total	1.000	0.586	0.167	0.032	0.002	0.000	0.000

Table 23 - Transmission of Thermal Radiation from a Blackbody at 1200K Through Various Thicknesses of water

λ [μm]	Incident Energy Distribution	Transmitted Energy Distribution For Water Layer Thickness [cm]					
		0.001	0.01	0.1	1	10	100
0.25-0.6	0.0000						
0.6-0.9	0.0008	0.0008	0.0008	0.0007	0.0007	0.0005	0.0001
0.9-1.2	0.0092	0.0092	0.0091	0.0085	0.0045	0.0002	
1.2-1.6	0.0453	0.0449	0.0415	0.0205	0.0021		
1.6-2.0	0.0849	0.0828	0.0681	0.0280			
2.0-2.4	0.1054	0.1015	0.0741	0.0104			
2.4-2.8	0.1070	0.0708	0.0243	0.0002			
2.8-3.2	0.0980	0.0003					
3.2-6.5	0.3972	0.2598	0.0364				
6.5-10	0.0972	0.0547	0.0003				
10- 20	0.0551	0.0105					
Total	1.000	0.635	0.255	0.068	0.007	0.001	0.000

The simplest way to model the thermal effects of a layer of water on the surface of the material is to use a lumped capacitance model. The temperature difference across a body is negligible in comparison to the temperature difference between the body and the ambient environment if the Biot number is very small [43]:

$$Bi = \frac{hl}{k} << 1$$

In the case of the water layer thicknesses in Table 18, the Biot number can be calculated. The thermal conductivity of water is 0.147 W/mK, and we can assume 10 W/mK as a typical heat transfer coefficient for natural convection [43]. For the largest layer thickness of 2.3 mm this gives a Biot number of

$$Bi = \frac{hl}{k} = \frac{10\frac{W}{m^2K}0.0023m}{0.147\frac{W}{mK}} = 0.16$$

This is about an order of magnitude less than 1, but ideally we would like it to be two orders of magnitude less than 1. The absorption of radiation in the layer can serve to smooth out the temperature profile or sharpen it. To calculate the temperature profile that could be expected when a water layer rests on the surface of a radiantly heated material, a finite difference model of the water and solid can be used. The water and solid for such a scenario are shown in Figure 73.

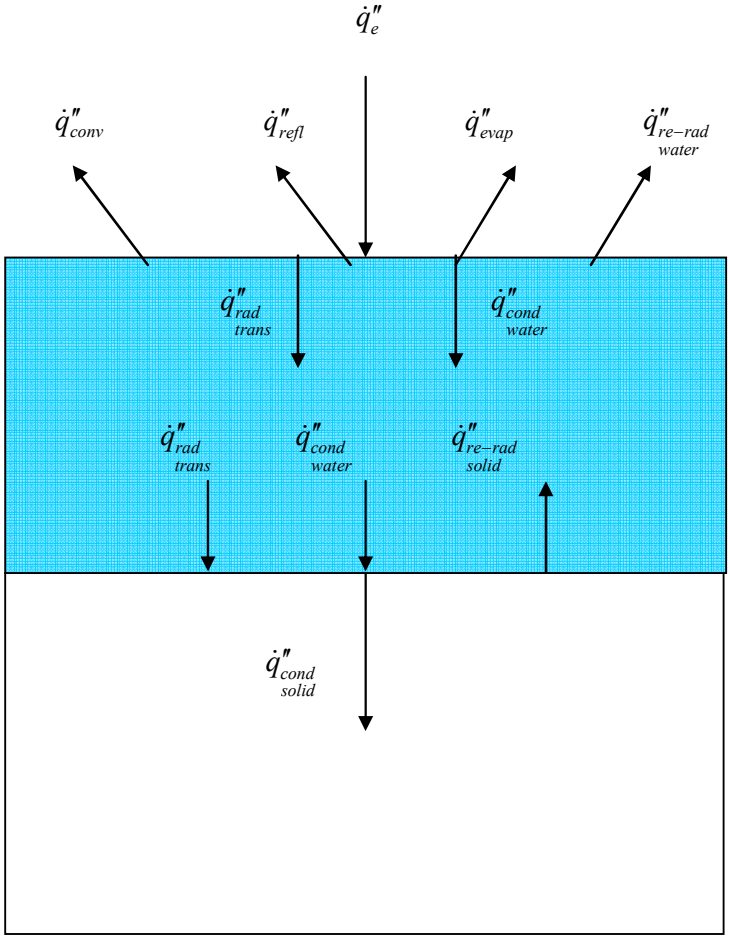

Figure 73 – Water Layer on Solid Exposed to External Heat Flux

The energy equation for an incompressible fluid with constant properties in rectangular coordinates is [102]

$$\rho C_p \frac{DT}{Dt} = k\nabla^2 T - \nabla \cdot \dot{q}_r'' + \dot{Q}''' + \Phi$$

If the water layer is unreacting and stationary the equation reduces to

$$\rho C_p \frac{\partial T}{\partial t} = k\frac{\partial^2 T}{\partial z^2} - \frac{\partial \dot{q}_{rad}''}{\partial z}$$

With the boundary conditions

$$\dot{q}_e'' = \dot{q}_{refl}'' + \dot{q}_{conv}'' + \dot{q}_{evap}'' + \dot{q}_{\substack{rerad \\ water}}'' + \dot{q}_{\substack{cond \\ water}}'' \quad @\, z = 0$$

$$k_w \frac{\partial T_w}{\partial z} + \dot{q}_{\substack{rad \\ trans}}'' - \dot{q}_{\substack{re-rad \\ solid}}'' = k_s \frac{\partial T_s}{\partial z} \qquad @ \quad z = solid\ \ surface$$

$$\dot{q}_r'' = \dot{q}_e'' \qquad @ \quad z = 0$$

And in the solid material the energy equations is simply

$$\rho C_p \frac{\partial T}{\partial t} = k\frac{\partial^2 T}{\partial x^2}$$

With the boundary conditions

$$k_w \frac{\partial T_w}{\partial z} + \dot{q}_{\substack{rad \\ trans}}'' - \dot{q}_{\substack{re-rad \\ solid}}'' = k_s \frac{\partial T_s}{\partial z} \qquad @ \quad z = solid\ \ surface$$

$$T_s = T_{init} \qquad @ \quad z = L\ \ (back\ \ face)$$

The radiant heat flux that is transmitted through the material is

$$\dot{q}_{rad}''(z) = \int_{\lambda=0}^{\infty} i_\lambda(0)\exp(-a_\lambda z)\partial\lambda$$

The energy absorption per unit volume for a single wavelength can be descried analytically by

$$\frac{\partial \dot{q}''_{\lambda}}{\partial z} = \frac{\partial i_{\lambda}(z)_{\lambda}}{\partial z} = i_{\lambda}(0)\exp(-a_{\lambda}z)(-a_{\lambda})$$

So the total energy absorption is

$$\frac{\partial \dot{q}''_{rad}(z)}{\partial z} = \int_{\lambda=0}^{\infty} \frac{\partial i_{\lambda}(z)_{\lambda}}{\partial z} \cong \int_{\lambda=0}^{\infty} i_{\lambda}(0)\exp(-a_{\lambda}z)(-a_{\lambda})\Delta\lambda$$

Or alternatively a finite difference approximation can be used

$$\frac{\partial \dot{q}''_{rad}(z)}{\partial z} \cong \frac{\dot{q}''_{rad,i+\frac{1}{2}} - \dot{q}''_{rad,i-\frac{1}{2}}}{\Delta z}$$

The re-radiation from the surface of the water will be

$$\dot{q}''_{\substack{re-rad \\ water}} = \varepsilon_w \sigma T_{surf}^4$$

For liquid water the emissivity is in the range of 0.92-0.96 for temperatures between 0-40 deg C (Bejan, 1993). Siegal and Howell [102] give a value of 0.96 for the temperature range 273-383K. The convective losses from the surface are simply

$$\dot{q}''_{conv} = h\left(T_{surf} - T_{\infty}\right)$$

The heat transfer coefficient is determined by calculating an average Nusselt number for a hot plate oriented horizontally facing upwards

$$\overline{Nu} = \frac{hl}{k}$$

For forced convection the Nusselt number is a function of the Reynolds number and Prandtl number [43]

$$\overline{Nu_x} = 0.664 \,\mathrm{Pr}^{1/3} \,\mathrm{Re}_L^{1/2}$$

For free convection the Nusselt number is a function of the Rayleight number [43]

$$\overline{Nu}_L = 0.54 Ra_L^{1/4} \quad \left(10^4 < Ra_L < 10^7\right)$$

$$\overline{Nu}_L = 0.15 Ra_L^{1/3} \quad \left(10^7 < Ra_L < 10^9\right)$$

Where

$$Ra_L = \frac{g\beta L^3 \left(T_{surf} - T_\infty\right)}{\alpha \nu}$$

The evaporative losses are

$$\dot{q}''_{evap} = \Delta h_v h_m \left(\rho_{v,surf} - \rho_{v,\infty}\right)$$

The mass transfer coefficient is calculated in an analogous fashion to the heat transfer coefficient. Instead of a Nusselt number, a Sherwood number must be calculated. For forced convection the Sherwood number is a function of the Schmidt number and Reynolds number

$$\overline{Sh_L} = 0.664 Sc^{1/3} \,\mathrm{Re}_L^{1/2}$$

The density of water vapor is determined by the partial pressure of the vapor.

$$\rho_v = \frac{p_v}{R_v T}$$

At the solid surface the air is saturated with vapor and the partial pressure is determined by the Claussius Clapeyron relation

$$p_v = \mathrm{P}_o \exp\left(-\frac{L_v}{R_v}\left(\frac{1}{T_v}-\frac{1}{T_o}\right)\right)$$

The partial pressure of vapor in the ambient air can be determined if the relative humidity is known. Relative humidity is the ratio of the partial pressure of vapor to the saturated vapor pressure as determined by the Claussius Clapeyron relation [47].

$$RH = \frac{p_{v,\infty}}{p_v}$$

The re-radiation from the solid surface can be shown to be very small, but will be included in the calculations for now. The solid surface will heat up and radiate heat through the water layer, but the radiation will be at larger wavelengths, since the surface will be at a lower temperature than the external heat source. This large wavelength radiation will fall into the high absorption region of the spectrum for water and will be more readily absorbed. Most of the radiation from the solid surface will be absorbed by the water immediately next to it. Since this water is included in the interface node, there is very little radiative loss. As an example consider a solid surface which behaves as a blackbody that is heated to 100 deg C. Assume that the grid spacing is 0.1mm thick above the solid surface. The transmissivity of the half node of water is calculated to be

$$\tau = \frac{\int_{\lambda=0}^{\infty} i_\lambda(0)\exp\left(-a_\lambda \cdot 0.05mm\right)\partial\lambda}{\int_{\lambda=0}^{\infty} i_\lambda(0)\partial\lambda}$$

$$\tau = \frac{\sum_{\lambda=0.2}^{200}\left(i_\lambda(0)\exp\left(-a_\lambda \cdot 0.05mm\right)+i_{\lambda+\Delta\lambda}(0)\exp\left(-a_{\lambda+\Delta\lambda}\cdot 0.05mm\right)\right)\Delta\lambda}{\sum_{\lambda=0.2}^{200}\left(i_\lambda(0)+i_{\lambda+\Delta\lambda}(0)\right)\Delta\lambda} = 0.045$$

The radiation emitted from the solid surface is

$$\varepsilon_s \sigma T^4 = 1\left(5.67\times10^{-8}\frac{W}{m^2K^4}\right)\left(383K^4\right) = 1.2\frac{kW}{m^2}$$

and the transmitted radiation is

$$\dot{q}''_{trans} = \int_{\lambda=0}^{\infty} i_\lambda(0)\exp(-a_\lambda \cdot 0.5mm)\partial\lambda$$

$$\dot{q}''_{trans} = 0.5\sum_{\lambda=0.2}^{200}\left(i_\lambda(0)\exp(-a_\lambda \cdot 0.5mm) + i_{\lambda+\Delta\lambda}(0)\exp(-a_{\lambda+\Delta\lambda} \cdot 0.5mm)\right)\Delta\lambda = 54\frac{W}{m^2}$$

The transmitted radiation to the second node above the water-solid interface can also be calculated

$$\int_{\lambda=0}^{\infty} i_\lambda(0)\exp(-a_\lambda \cdot 1.5mm)\partial\lambda = 3.5\frac{W}{m^2}$$

So even for the maximum possible interface node temperature and at a reasonable node spacing, the radiation that is leaving the interface node is very small, and the transmitted radiation past the next node is much smaller. As the model is developed the re-radiation from the interface node will initially be included in the calculations for completeness.

Appendix C. Model Development

The scenario that we would like to model is that of a porous material subjected to water spray cooling and radiant heating at the surface as shown in Figure 74. The governing equations will be developed for multiple dimensions for completeness, but ultimately we would like to be able to assume one dimensional behavior. Water and heat will be transported into the material from the surface. If the material is sufficiently wide in the x and y directions and the heat and water flux is uniform, it is believed that one dimensional behavior is reasonable. We would like to define two different scenarios that could be expected in the event of a fire sprinkler actuating and spraying a porous material. In the first case, the surface of the material is partially saturated by a spray with a relatively water mass flux, and gas is able to escape from the inside the material through the surface. In the second case the water mass flux is sufficiently high so that the surface is saturated and sealed so that gas cannot escape.

Case 1: Low Water Flux

This case represents a material subjected to radiant heating and water spray cooling by a sparse spray as shown in Figure 74.

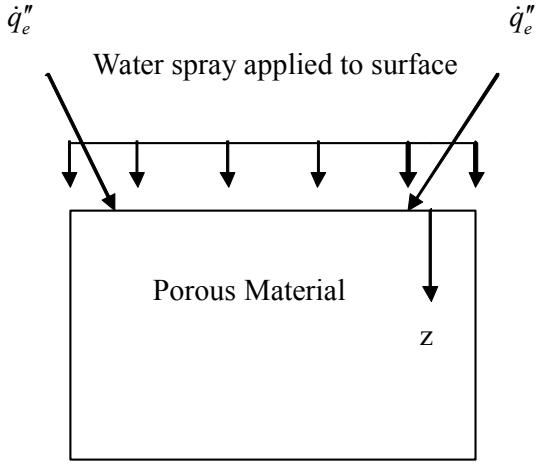

.

Figure 74 – Porous Material Subjected to Low Water Flux

If the stream of droplets impacting the surface of the porous material has a low mass flux then the surface will be wetted, but not completely saturated. We will not consider the case where the droplets have ultra high velocity, so the average impact pressure at the surface will be very small. In this case, there will be pores at the surface that contain gas, so water vapor and air will be allowed to escape from the material through the surface. A typical saturation profile for this case is shown in Figure 75.

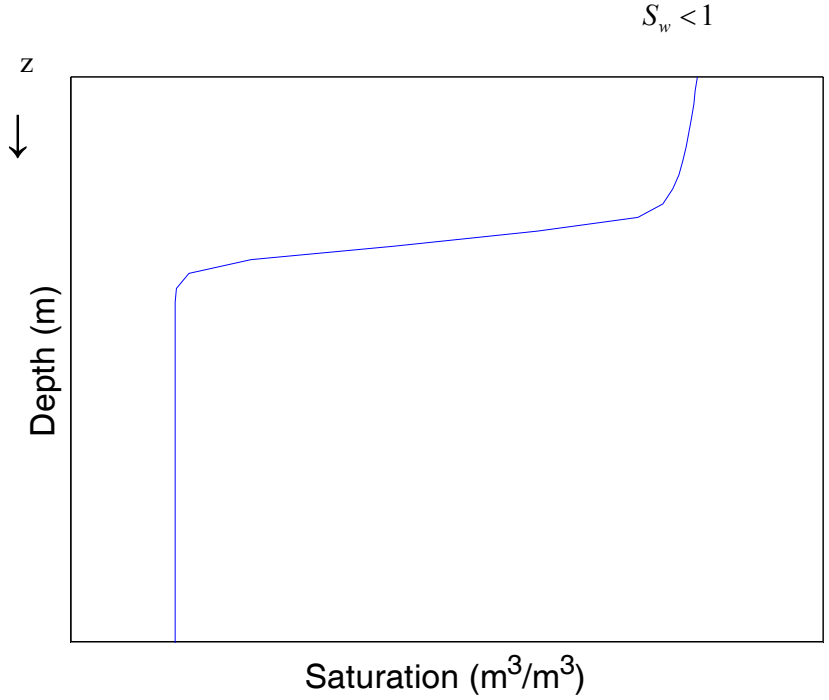

Figure 75 – Saturation Profile for Low Water Flux Case

The surface will have a saturation of less than 1 and water will be pulled into the material by surface tension forces.

Case 2; High Water Flux

This case represents a material being exposed to a radiant heating source, and also a uniform spray of droplets with a high mass flux. For liquid moisture movement, the driving forces are surface tension forces at the liquid-gas interface and impact forces from the spray at the material surface. Surface tension forces will pull the water into the material, while impact forces and gravitational forces of a water later on the surface will have the effect of pushing the water into the material. This can produce a positive gage pressure in the liquid at the surface of the material, and a negative gage pressure

at greater depths. This means that there can be a depth at which the pressure transitions from positive to negative gage pressure. This will be referred to as the saturation interface (z_{int}). This is shown in Figure 76.

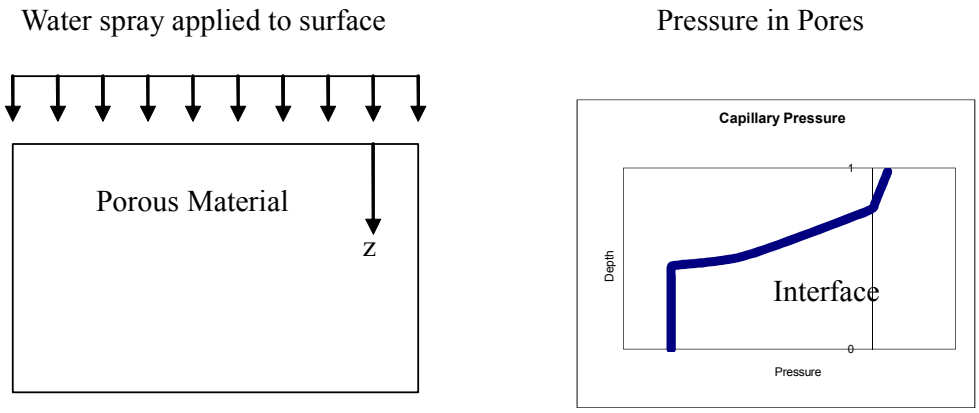

Figure 76 – Porous Slab Subjected to High Water Flux

The region on the positive pressure side of the interface is referred to as the saturated zone. The region on the negative pressure side of the interface will have a moisture content that transitions from saturated at the interface to the initial moisture content at depth. The saturation profile for this case is shown in
Figure 77.

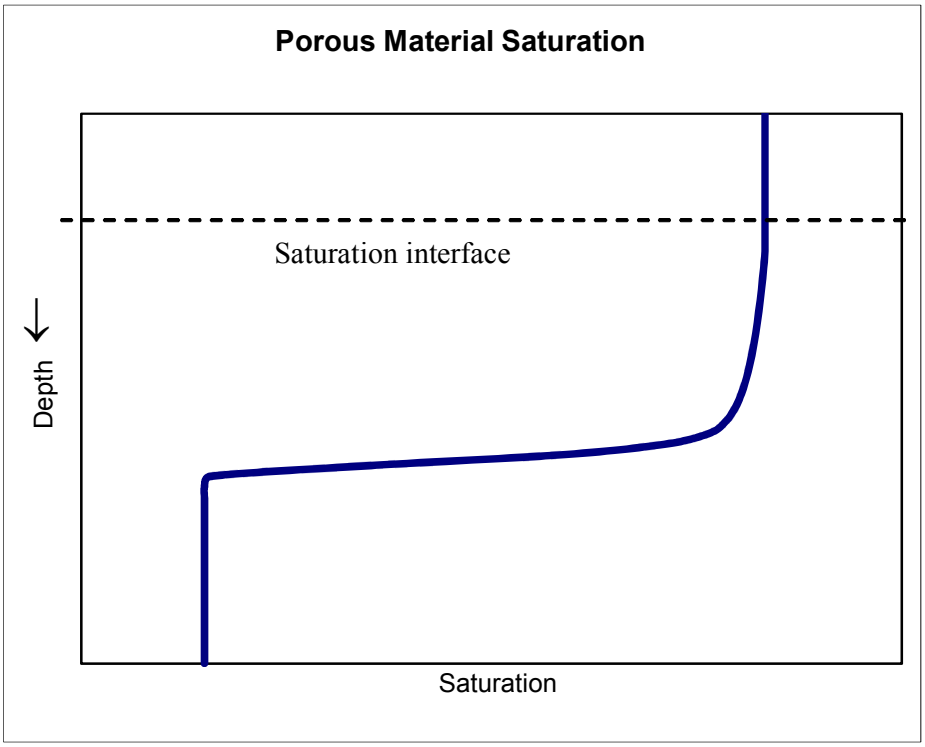

Figure 77 – Saturation Profile for High Water Flux Case

For the current model being developed we will assume that the impact force of the water spray is very low in relation to surface tension forces, and the saturation interface is at the boundary of the surface node. This means that the boundary conditions for the high water flux case will include a saturated surface node and must include the effects of a standing layer of water that will participate in the radiation absorption at the surface. This condition stipulates that the current model cannot handle significant impact pressures at the surface.

C.1. Derivation of Governing Equations

Governing equations will now be derived from principles of conservation of mass for liquid, vapor, and air, and conservation of energy. For visual simplicity, the governing equations will be derived using a two dimensional control volume and then extended to their general form in three dimensions. Finally the one dimensional form of the equations will be chosen for the current model.

First derive the equation of mass conservation for liquid water in a porous material.

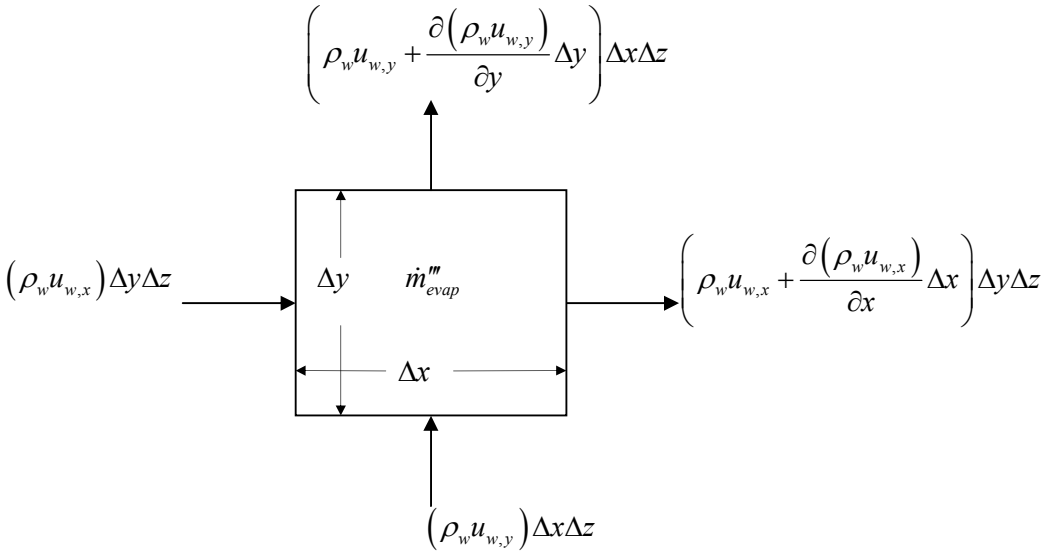

Figure 78 - Differential Control Volume in a 2D Flow Field with Liquid Water

Summing mass fluxes

$$\sum \dot{m}'' = \left(\rho_w u_{w,x}\right)\Delta y\Delta z + \left(\rho_w u_{w,y}\right)\Delta x\Delta z - \left(\rho_w u_{w,y} + \frac{\partial\left(\rho_w u_{w,y}\right)}{\partial y}\Delta y\right)\Delta x\Delta z - \left(\rho_w u_{w,x} + \frac{\partial\left(\rho_w u_{w,x}\right)}{\partial x}\Delta x\right)\Delta y\Delta z$$

$$= -\frac{\partial\left(\rho_w u_{w,y}\right)}{\partial y}\Delta x\Delta y\Delta z - \frac{\partial\left(\rho_w u_{w,x}\right)}{\partial x}\Delta x\Delta y\Delta z$$

$$= -\frac{\partial\left(\rho_w u_{w,i}\right)}{\partial x_i}$$

The rate of liquid water storage in the control including any sources (in this case evaporation) is

$$\left(\frac{\partial c_w}{\partial t} + \dot{m}'''_{evap} \right) \Delta x \Delta y \Delta z$$

Where c_w is the volumetric mass content of water [kg water/m^3] in the control volume. The total mass flow into the control volume must be equal to the increase in mass in the control volume

$$\left(\frac{\partial c_w}{\partial t} + \dot{m}'''_{evap} \right) \Delta x \Delta y \Delta z = -\frac{\partial \left(\rho_w u_{w,y} \right)}{\partial y} \Delta x \Delta y \Delta z - \frac{\partial \left(\rho_w u_{w,x} \right)}{\partial x} \Delta x \Delta y \Delta z$$

Divide by the volume of the CV

$$\frac{\partial c_w}{\partial t} + \dot{m}'''_{evap} = -\frac{\partial \left(\rho_w u_{w,y} \right)}{\partial y} - \frac{\partial \left(\rho_w u_{w,x} \right)}{\partial x}$$

Which can be written as a continuity equation for liquid water

$$\frac{\partial c_w}{\partial t} = -\nabla \cdot \left(\rho_w u_w \right) - \dot{m}'''_{evap}$$

Where the mass flux $\dot{m}''_{w,i} = \rho_w u_{w,i}$ is composed of convective and diffusive components

$u_{w,i} = u_i + V_{w,i}$ $\quad i = x, y, z$ directions

Use Darcy's Law for the convective mass flux. The pressure gradient is calculated using the capillary pressure and the contribution from gravity.

$$\dot{m}''_{w,i} = \rho_w u_{w,i} = -\rho_w \frac{KK_{r,w}}{\mu_w}\left(\nabla p_w - \rho_w \vec{g}\right)$$

Here we assume that the diffusive velocity is zero. This is reasonable since water is the only liquid present and we are assuming that the material is non-hygroscopic. Using the following relation to relate mass content to saturation

$$S_w = \frac{U_w}{\varphi} = \frac{c_w}{\rho_w \varphi}$$

allows us to write the mass conservation equation for liquid water as

$$\rho_w \phi \frac{\partial S_w}{\partial t} = \nabla \cdot \left(\rho_w \frac{KK_{r,w}}{\mu_w}\left(\nabla p_w - \rho_w \vec{g}\right)\right) - \dot{m}'''_{evap}$$

If the density of water is approximately constant we can write this as

$$\phi \frac{\partial S_w}{\partial t} = \nabla \cdot \left(\frac{KK_{r,w}}{\mu_w}\left(\nabla p_w - \rho_w \vec{g}\right)\right) - \frac{\dot{m}'''_{evap}}{\rho_w}$$

The capillary pressure is defined as the pressure difference between the water pressure and air pressure in the pore spaces

$$p_{cap} = P - p_w$$

The capillary pressure is calculated using Leverett's J-function

$$p_{cap} = \left(\frac{\varphi}{K}\right)^{\frac{1}{2}} \sigma J\left(S_w\right)$$

A typical relationship between capillary pressure and saturation (J-function) is given by

$$J(S_w) = 0.364\left(1-\exp\left(-40\left(1-S_w\right)\right)\right)+0.221\left(1-S_w\right)+\frac{0.005}{S_w-0.08}$$

and shown in

Figure 79 – Leverett J-Function

. The relative permeability for liquid is typically given by

$$K_{r,l} = S_w^{\,3}$$

The relative permeability for gas is typically described by

$$K_{r,g} = \left(1-S_w\right)^3$$

These are both shown in Figure 80.

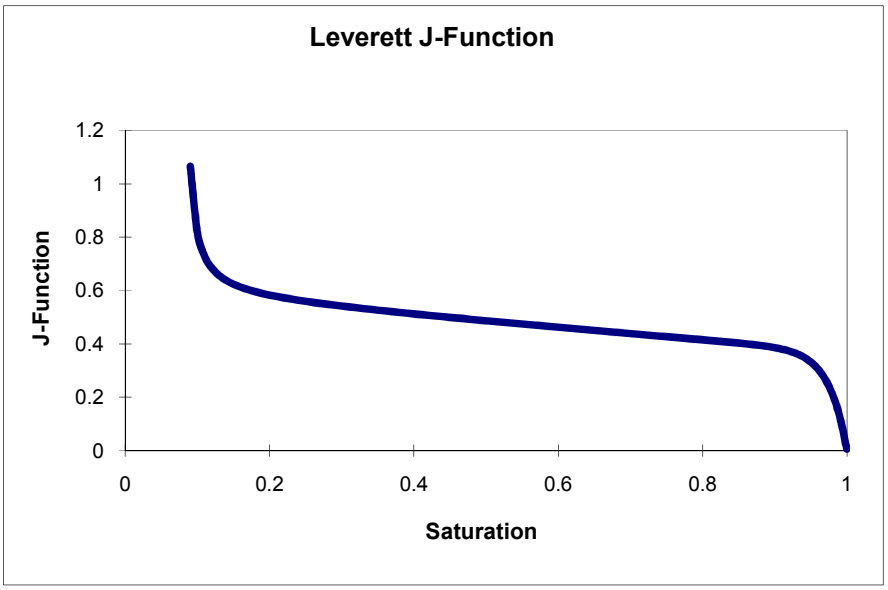

Figure 79 – Leverett J-Function

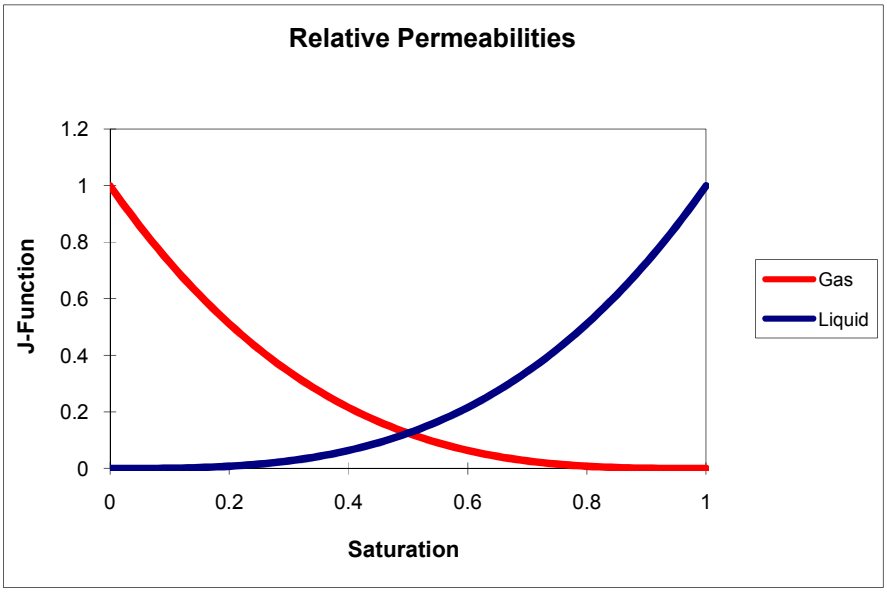

Figure 80 – Relative Permeabilities

In the case of water vapor the derivation is similar. Start with the control volume shown in Figure 81

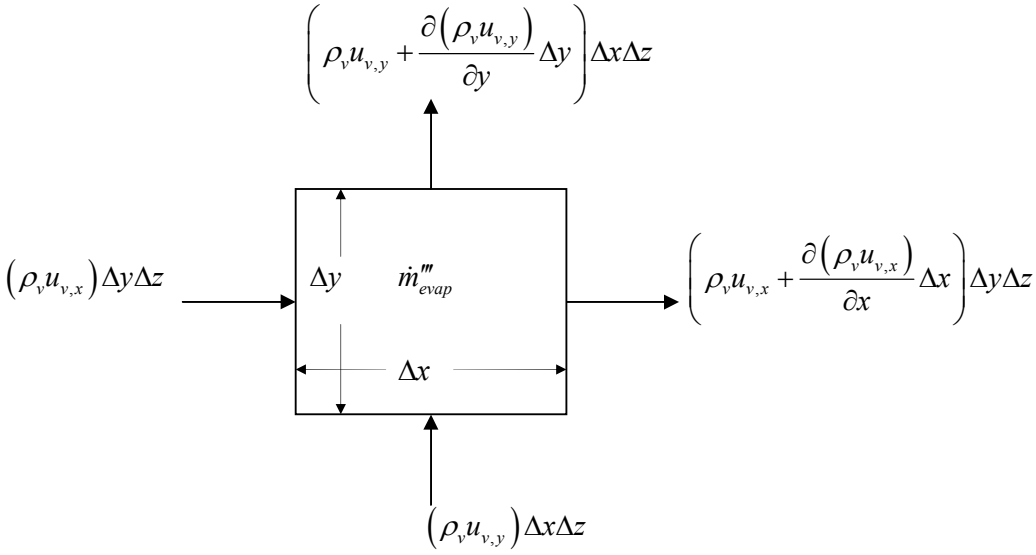

Figure 81 – Differential Control Volume in a 2D Flow Field with Water Vapor

Summing mass fluxes

$$\sum \dot{m}'' = \left(\rho_v u_{v,x}\right)\Delta y\Delta z + \left(\rho_v u_{v,y}\right)\Delta x\Delta z - \left(\rho_v u_{v,y} + \frac{\partial\left(\rho_v u_{v,y}\right)}{\partial y}\Delta y\right)\Delta x\Delta z - \left(\rho_v u_{v,x} + \frac{\partial\left(\rho_v u_{v,x}\right)}{\partial x}\Delta x\right)\Delta y\Delta z$$

$$= -\frac{\partial\left(\rho_v u_{v,y}\right)}{\partial y}\Delta x\Delta y\Delta z - \frac{\partial\left(\rho_v u_{v,x}\right)}{\partial x}\Delta x\Delta y\Delta z$$

The rate of vapor water storage in the control volume including any sources (evaporation)

$$\left(\frac{\partial c_v}{\partial t} - \dot{m}'''_{evap}\right)\Delta x\Delta y\Delta z$$

The total mass flow of water vapor into the control volume must be equal to the increase in vapor mass in the control volume

$$\left(\frac{\partial c_v}{\partial t} - \dot{m}'''_{evap}\right)\Delta x\Delta y\Delta z = -\frac{\partial\left(\rho_v u_{v,y}\right)}{\partial y}\Delta x\Delta y\Delta z - \frac{\partial\left(\rho_v u_{v,x}\right)}{\partial x}\Delta x\Delta y\Delta z$$

Divide by the volume of the CV

$$\frac{\partial c_v}{\partial t} - \dot{m}'''_{evap} = -\frac{\partial\left(\rho_v u_{v,y}\right)}{\partial y} - \frac{\partial\left(\rho_v u_{v,x}\right)}{\partial x}$$

Which can be written as

$$\frac{\partial c_v}{\partial t} = -\nabla\cdot\left(\rho_v u_v\right) + \dot{m}'''_{evap}$$

Where the water vapor mass flux is composed of convective and diffusive components

$$\dot{m}''_{v,i} = \rho_v u_{v,i} = -\rho_v \frac{KK_{r,g}}{\mu_v}\nabla P - \frac{C^2}{\rho} M_a M_v D_{eff,g}\nabla X_v$$

It should be noted that the form of Darcy's law used here ignores body forces of the

vapor which are assumed to be small. Using this relationship and the conversion from mass content to saturation allows us to write the mass conservation equation for water vapor as

$$\frac{\partial\left(S_g\rho_v\phi\right)}{\partial t} = \nabla\cdot\left(\rho_v\frac{KK_{r,v}}{\mu_v}\nabla P + \frac{C^2}{\rho}M_aM_vD_{eff,g}\nabla X_v\right) + \dot{m}'''_{evap}$$

Where the effective diffusivity $D_{eff,g}$ accounts for the reduction in cross sectional area that the vapor must diffuse through due to the presence of the solid matrix and liquid phase water, and also the tortuous path through which vapor must travel. This is represented by

$$D_{eff,g} = D_{va}\left(S_g\phi\right)^{\frac{4}{3}} = D_{va}\phi^{\frac{4}{3}}\left(\phi^2 - \phi S_w\right)^{\frac{4}{3}}$$

And the mol fraction of vapor is proportional to the vapor pressure

$$X_v = \frac{p_v}{P}$$

We will assume that the vapor pressure obeys the Clausius-Clapeyron thermodynamic relation

$$p_v = p_{ref}\exp\left[-\frac{\Delta h_{vap}}{R_v}\left(\frac{1}{T} - \frac{1}{T_{ref}}\right)\right]$$

Now repeat the derivation for air. Consider the differential control volume shown in Figure 82.

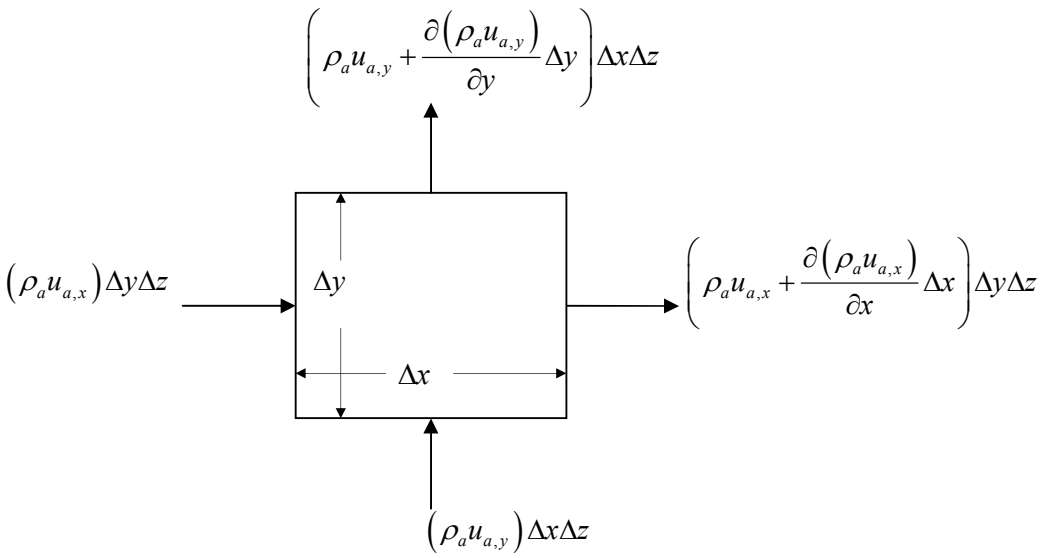

Figure 82 – Air Flow through a Differential Control Volume in a 2D Flow Field

Summing mass fluxes

$$\sum \dot{m}'' = \left(\rho_a u_{a,x}\right)\Delta y\Delta z + \left(\rho_a u_{a,y}\right)\Delta x\Delta z - \left(\rho_a u_{a,y} + \frac{\partial\left(\rho_a u_{a,y}\right)}{\partial y}\Delta y\right)\Delta x\Delta z - \left(\rho_a u_{a,x} + \frac{\partial\left(\rho_a u_{a,x}\right)}{\partial x}\Delta x\right)\Delta y\Delta z$$

$$= -\frac{\partial\left(\rho_a u_{a,y}\right)}{\partial y}\Delta x\Delta y\Delta z - \frac{\partial\left(\rho_a u_{a,x}\right)}{\partial x}\Delta x\Delta y\Delta z$$

Since there are no sinks or sources for air the rate of mass storage in the control volume is

$$\left(\frac{dc_a}{dt}\right)\Delta x\Delta y\Delta z$$

The total mass flow of air into the control volume must be equal to the increase in mass of air in the control volume

$$\left(\frac{\partial c_a}{\partial t}\right)\Delta x\Delta y\Delta z = -\frac{\partial\left(\rho_a u_{a,y}\right)}{\partial y}\Delta x\Delta y\Delta z - \frac{\partial\left(\rho_a u_{a,x}\right)}{\partial x}\Delta x\Delta y\Delta z$$

Divide by the volume of the CV

$$\frac{\partial c_a}{\partial t} = -\frac{\partial\left(\rho_a u_{a,y}\right)}{\partial y} - \frac{\partial\left(\rho_a u_{a,x}\right)}{\partial x}$$

Which can be written as

$$\frac{\partial c_a}{\partial t} = -\nabla\cdot\left(\rho_a u_a\right)$$

Where the air mass flux is composed of convective and diffusive components

$$\dot{m}''_{a,i} = \rho_a u_{a,i} = -\rho_a \frac{KK_{r,a}}{\mu_a}\nabla P - \frac{C^2}{\rho} M_v M_a D_{av} \nabla X_a$$

It should be noted that the form of Darcy's law used here ignores body forces of the air which are assumed to be small. Using this relationship and the conversion from mass content to saturation allows us to write the mass conservation equation for air as

$$\phi\frac{\partial\left(\rho_a S_g\right)}{\partial t} = \nabla\cdot\left(\rho_a \frac{KK_{r,a}}{\mu_a}\nabla P + \frac{C^2}{\rho} M_v M_a D_{av} \nabla X_a\right)$$

Now derive the energy equation in a porous material with water, vapor and air present. Consider the control volume shown in Figure 83 containing a porous material with liquid water, water vapor, and air in the pore spaces. Assume no volumetric radiation absorption or body force work. This section is based on work by Ni [41].

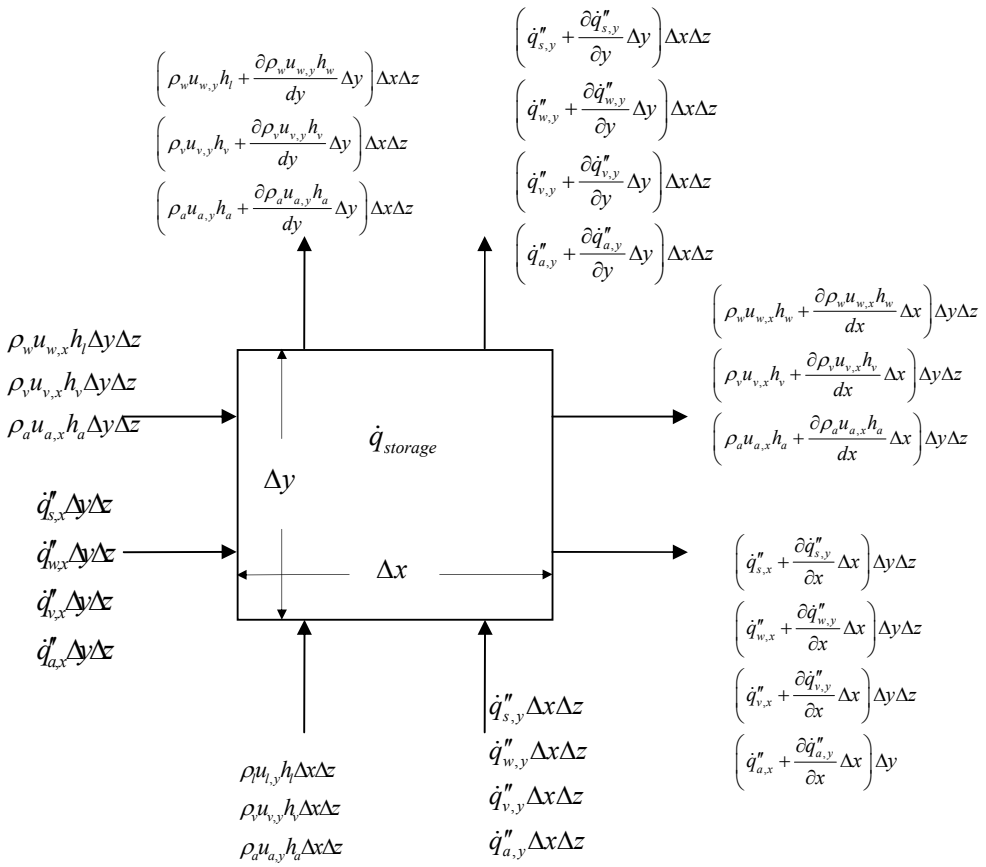

Figure 83 – Enthalpy Fluxes Through a Differential Control Volume in a Porous Media Containing Solid, Water, Vapor, and Air

The total energy storage in the control volume is equal to

$$\dot{q}_{storage} = \frac{\partial}{\partial t}\left(c_s h_s + c_w h_w + c_v h_v + c_a h_a\right)\Delta x\Delta y\Delta z$$

The energy storage must be equal to the sum of all enthalpy fluxes into and out of the control volume.

$$\frac{\partial}{\partial t}\left(c_s h_s + c_w h_w + c_v h_v + c_a h_a\right)\Delta x\Delta y\Delta z = \begin{bmatrix} -\frac{\partial}{\partial x}\left(\rho_w u_w h_w + \rho_v u_v h_v + \rho_a u_a h_a\right) - \frac{\partial}{\partial y}\left(\rho_w u_w h_w + \rho_v u_v h_v + \rho_a u_a h_a\right) \\ -\frac{\partial}{\partial x}\left(\dot{q}''_s + \dot{q}''_w + \dot{q}''_a + \dot{q}''_v\right) - \frac{\partial}{\partial y}\left(\dot{q}''_s + \dot{q}''_w + \dot{q}''_a + \dot{q}''_v\right) \end{bmatrix}\Delta x\Delta y\Delta z$$

or more generally

$$\frac{\partial}{\partial t}\left(c_s h_s + c_w h_w + c_v h_v + c_a h_a\right) = -\nabla\cdot\left(\rho_w u_w h_w + \rho_v u_v h_v + \rho_a u_a h_a\right) - \nabla\cdot\left(\dot{q}_s'' + \dot{q}_w'' + \dot{q}_a'' + \dot{q}_v''\right)$$

Rewrite this as

$$\frac{\partial}{\partial t}\left(c_w h_w\right) + \nabla\cdot\left(\rho_w u_w h_w\right) + \frac{\partial}{\partial t}\left(c_v h_v\right) + \nabla\cdot\left(\rho_v u_v h_v\right) + \frac{\partial}{\partial t}\left(c_a h_a\right) + \nabla\cdot\left(\rho_a u_a h_a\right) + \frac{\partial}{\partial t}\left(c_s h_s\right) = -\nabla\cdot\left(\dot{q}_s'' + \dot{q}_w'' + \dot{q}_a'' + \dot{q}_v''\right)$$

Expanding terms on the LHS allows us to simplify the equation using conservation of mass for water, vapor, and air.

$$\frac{\partial}{\partial t}\left(c_w h_w\right) + \nabla\cdot\left(\rho_w u_w h_w\right) = c_w\frac{\partial h_w}{\partial t} + h_w\frac{\partial c_w}{\partial t} + \rho_w u_w\nabla\cdot\left(h_w\right) + h_w\nabla\cdot\left(\rho_w u_w\right)$$
$$= c_w\frac{\partial h_w}{\partial t} + \rho_w u_w\nabla\cdot\left(h_w\right) + h_w\left(\frac{\partial c_w}{\partial t} + \nabla\cdot\left(\rho_w u_w\right)\right)$$
$$= c_w\frac{\partial h_w}{\partial t} + \rho_w u_w\nabla\cdot\left(h_w\right) - h_w\dot{m}_{evap}'''$$

$$\frac{\partial}{\partial t}\left(c_v h_v\right) + \nabla\cdot\left(\rho_v u_v h_v\right) = c_v\frac{\partial h_v}{\partial t} + h_v\frac{\partial c_v}{\partial t} + h_v\nabla\cdot\left(\rho_v u_v\right) + \rho_v u_v\nabla\cdot\left(h_v\right)$$
$$= c_v\frac{\partial h_v}{\partial t} + \rho_v u_v\nabla\cdot\left(h_v\right) + h_v\left(\frac{\partial c_v}{\partial t} + \nabla\cdot\left(\rho_v u_v\right)\right)$$
$$= c_v\frac{\partial h_v}{\partial t} + \rho_v u_v\nabla\cdot\left(h_v\right) + h_v\dot{m}_{evap}'''$$

$$\frac{\partial}{\partial t}\left(c_a h_a\right) + \nabla\cdot\left(\rho_a u_a h_a\right) = c_a\frac{\partial h_a}{\partial t} + h_a\frac{\partial c_a}{\partial t} + h_a\nabla\cdot\left(\rho_a u_a\right) + \rho_a u_a\nabla\cdot\left(h_a\right)$$
$$= c_a\frac{\partial h_a}{\partial t} + \rho_a u_a\nabla\cdot\left(h_a\right) + h_a\left(\frac{\partial c_a}{\partial t} + \nabla\cdot\left(\rho_a u_a\right)\right)$$
$$= c_a\frac{\partial h_a}{\partial t} + \rho_a u_a\nabla\cdot\left(h_a\right)$$

The energy equation can now be written as

$$c_w \frac{\partial h_w}{\partial t} + \rho_w u_w \nabla \cdot \left(h_w\right) - h_w \dot{m}'''_{evap} + c_v \frac{\partial h_v}{\partial t} + \rho_v u_v \nabla \cdot \left(h_v\right) + h_v \dot{m}'''_{evap} + c_a \frac{\partial h_a}{\partial t} + \rho_a u_a \nabla \cdot \left(h_a\right) + c_s \frac{\partial h_s}{\partial t}$$
$$= -\nabla \cdot \left(\dot{q}''_s + \dot{q}''_w + \dot{q}''_a + \dot{q}''_v\right)$$

The evaporation terms can be grouped together

$$h_v \dot{m}'''_{evap} - h_w \dot{m}'''_{evap} = \dot{m}'''_{evap}\left(h_v - h_w\right) = \dot{m}'''_{evap} \Delta h_v$$

Where Δh_v is the latent heat of vaporization. Use this and constitutive relations for enthalpy and heat flux to rewrite the combined energy equation. Use the definition of enthalpy

$$h = \Delta h_f^o + \int_{T^o}^{T} C_p dT$$

and Fourier's law of heat conduction for component n in the i-direction

$$\dot{q}''_{n,i} = k_n \frac{\partial T_n}{\partial x_i}$$

But remember that the control volume contains 4 different components, so make the assumption that the total heat flux contribution of component n is proportional to the volume fraction of component a in the control volume. Write this as

$$\dot{q}''_{n,i} = \psi_n k_n \frac{\partial T_n}{\partial x_i}$$

Where ψ_n is the volumetric content of component n. Using these relations write the energy equation as

$$c_w C_{p,w} \frac{\partial T_w}{\partial t} + c_v C_{p,v} \frac{\partial T_v}{\partial t} + c_a C_{p,a} \frac{\partial T_a}{\partial t} + c_s C_{p,s} \frac{\partial T_s}{\partial t} + \rho_v u_v C_{p,v} \nabla \cdot \left(T_v\right) + \rho_l u_l C_{p,l} \nabla \cdot \left(T_l\right) + \rho_a u_a C_{p,a} \nabla \cdot \left(T_a\right)$$
$$= -\nabla \cdot \left(\psi_a k_a \frac{\partial T_a}{\partial x_i} + \psi_v k_v \frac{\partial T_v}{\partial x_i} + \psi_w k_w \frac{\partial T_w}{\partial x_i} + \psi_s k_s \frac{\partial T_s}{\partial x_i} \right) - \dot{m}'''_{evap} \Delta h_v$$

Invoking the assumption of local thermal equilibrium allows the equation to be

simplified to

$$\left(c_w C_{p,w} + c_v C_{p,v} + c_a C_{p,a} + c_s C_{p,s}\right)\frac{\partial T}{\partial t} + \left(\rho_v u_v C_{p,v} + \rho_w u_w C_{p,w} + \rho_a u_a C_{p,a}\right)\nabla\cdot(T)$$
$$= \frac{\partial}{\partial x_i}\cdot\left(\left(\psi_a k_a + \psi_v k_v + \psi_w k_w + \psi_s k_s\right)\frac{\partial T}{\partial x_i}\right) - \dot{m}'''_{evap}\Delta h_v$$

Where the effective heat capacity is defined in terms of mass concentrations

$$\left(\rho C_p\right)_{eff} = c_w C_{p,w} + c_v C_{p,v} + c_a C_{p,a} + c_s C_{p,s}$$

or in terms of volume fractions (ψ) and densities

$$\left(\rho C_p\right)_{eff} = \psi_w \rho_w C_{p,w} + \psi_v \rho_v C_{p,v} + \psi_a \rho_a C_{p,a} + \psi_s \rho_s C_{p,s}$$

Or in terms of saturations

$$\left(\rho C_p\right)_{eff} = \phi S_w \rho_w C_{p,w} + \phi S_g \rho_v C_{p,v} + \phi S_g \rho_a C_{p,a} + (1-\phi)\rho_s C_{p,s}$$

Effective thermal conductivity is defined as

$$k_{eff} = \psi_a k_a + \psi_v k_v + \psi_w k_w + \psi_s k_s$$

Which can be written in terms of saturations

$$k_{eff} = \phi S_a k_a + \phi S_v k_v + \phi S_w k_w + (1-\phi)k_s$$

So the energy equation becomes

$$\left(\rho C_p\right)_{eff}\frac{\partial T}{\partial t}+\left(\rho_v u_{v,i}C_{p,v}+\rho_w u_{w,i}C_{p,w}+\rho_a u_{a,i}C_{p,a}\right)\frac{\partial T}{\partial x_i}=\frac{\partial}{\partial x_i}\cdot\left(k_{eff}\frac{\partial T}{\partial x_i}\right)-\dot{m}'''_{evap}\Delta h_v$$

Model Summary 1D Equations

Conservation of energy

$$\left(\rho\overline{c}_p\right)_{eff}\frac{\partial T}{\partial t}+\left[\rho_w c_{p,w}u_w+\rho_v c_{p,v}u_v+\rho_a c_{p,a}u_a\right]\frac{\partial T}{\partial z}+\Delta h_{vap}\dot{m}'''_{evap}=\frac{\partial}{\partial z}\left(k_{eff}\frac{\partial T}{\partial z}\right)$$

Conservation of mass for liquid phase water

$$\phi\frac{\partial\left(\rho_w S_w\right)}{\partial t}=\frac{\partial}{\partial z}\left(\rho_w\frac{KK_{r,l}}{\mu_w}\left(\frac{\partial\left(p_w\right)}{\partial z}-\rho g\right)\right)-\dot{m}'''_{evap}$$

Conservation of mass for vapor phase water

$$\phi\frac{\partial\left(\rho_v S_g\right)}{\partial t}=\frac{\partial}{\partial z}\left(\rho_v\frac{KK_{r,g}}{\mu_g}\frac{\partial P}{\partial z}+\frac{C^2}{\rho}M_a M_v D_{eff,g}\frac{\partial X_v}{\partial z}\right)+\dot{m}'''_{evap}$$

Conservation of mass for air

$$\phi\frac{\partial\left(\rho_a S_g\right)}{\partial t}=\frac{\partial}{\partial z}\left(\rho_a\frac{KK_{r,g}}{\mu_g}\frac{\partial P}{\partial z}+\frac{C^2}{\rho}M_v M_a D_{eff,g}\frac{\partial X_a}{\partial z}\right)$$

Ideal Gas Law

$$PV=nRT\quad\text{or}\quad\rho=\frac{n}{V}=\frac{P}{RT}\quad\text{so}\quad\rho_g=\rho_v+\rho_a=\frac{p_v}{R_v T}+\frac{p_a}{R_a T}$$

Independent variables: z, t

Dependant variables: T, P, S_w

Combine GE's

From these conservation laws and constitutive relations derive three governing equations for the three independent variables: S_w, T, and P. First add conservation of mass for water to conservation of mass for vapor to eliminate the evaporation rate term.

$$\phi\frac{\partial\left(\rho_w S_w\right)}{\partial t}+\phi\frac{\partial\left(\rho_v S_g\right)}{\partial t}=\frac{\partial}{\partial z}\left(\rho_w\frac{KK_{r,l}}{\mu}\left(\frac{\partial p_w}{\partial z}-\rho g\right)\right)+\frac{\partial}{\partial z}\left(\rho_v\frac{KK_{r,g}}{\mu_g}\frac{\partial P}{\partial z}+\frac{C^2}{\rho}M_a M_v D_{eff,g}\frac{\partial X_v}{\partial z}\right)$$

Substitute conservation of water mass to conservation of energy to eliminate the evaporation term in the energy equation

$$\left(\rho\bar{c}_p\right)_{eff}\frac{\partial T}{\partial t}+\left[\rho_w c_{p,w}u_w+\rho_v c_{p,v}u_v+\rho_a c_{p,a}u_a\right]\frac{\partial T}{\partial z}+\Delta h_{vap}\left(\frac{\partial}{\partial z}\left(\rho_w\frac{KK_{r,l}}{\mu_w}\left(\frac{\partial p_w}{\partial z}-\rho g\right)\right)-\phi\frac{\partial\left(\rho_w S_w\right)}{\partial t}\right)$$
$$=\frac{\partial}{\partial z}\left(k_{eff}\frac{\partial T}{\partial z}\right)$$

Take conservation of air as it is

$$\phi\frac{\partial\left(\rho_a S_g\right)}{\partial t}=\frac{\partial}{\partial z}\left(\rho_a\frac{KK_{r,g}}{\mu_g}\frac{\partial P}{\partial z}+\frac{C^2}{\rho}M_v M_a D_{eff,g}\frac{\partial X_a}{\partial z}\right)$$

This gives 3 equations for our three unknowns. Write these in terms of the dependant variables. Follow the method of Ni [41]. Start with water and vapor conservation equation

$$\phi\frac{\partial}{\partial t}\left(\rho_w S_w\right)+\phi\frac{\partial}{\partial t}\left(\frac{p_v}{R_v T}\left(1-S_w\right)\right)=\frac{\partial}{\partial z}\left(\rho_w\frac{KK_{r,l}}{\mu_w}\left(\frac{\partial p_w}{\partial z}-\rho g\right)\right)+\frac{\partial}{\partial z}\left(\rho_v\frac{KK_{r,v}}{\mu_v}\frac{\partial P}{\partial z}+\frac{C^2}{\rho}M_a M_v D_{eff,g}\frac{\partial X_v}{\partial z}\right)$$

The components of this equation can be written as

$$\phi\frac{\partial}{\partial t}\left(\rho_w S_w\right)=\phi\rho_w\frac{\partial}{\partial t}\left(S_w\right)$$

$$\phi\frac{\partial\left(\rho_v S_g\right)}{\partial t}=\phi\frac{\partial}{\partial t}\left(\frac{p_v}{R_v T}\left(1-S_w\right)\right)$$

$$=-\frac{\phi p_v}{R_v T}\frac{\partial S_w}{\partial t}+\frac{\phi}{R_v}\left(1-S_w\right)\frac{\partial}{\partial t}\left(\frac{p_v}{T}\right)$$

$$=-\frac{\phi p_v}{R_v T}\frac{\partial S_w}{\partial t}+\frac{\phi}{R_v}\left(1-S_w\right)\frac{\partial}{\partial T}\left(\frac{p_v}{T}\right)\frac{\partial T}{\partial t}+\frac{\phi}{R_v T}\left(1-S_w\right)\frac{\partial p_v}{\partial S_w}\frac{\partial S_w}{\partial t}$$

$$\rho_w\frac{KK_{r,l}}{\mu_w}\left(\frac{\partial p_w}{\partial z}-\rho g\right)=\rho_w\frac{KK_{r,l}}{\mu_w}\frac{\partial P}{\partial z}-\rho_w\frac{KK_{r,l}}{\mu_w}\frac{\partial p_{cap}}{\partial S_w}\frac{\partial S_w}{\partial z}-\rho_w\frac{KK_{r,l}}{\mu_w}\frac{\partial p_{cap}}{\partial T}\frac{\partial T}{\partial z}-\rho_w\frac{KK_{r,l}}{\mu_w}\rho g$$

$$\rho_v\frac{KK_{r,v}}{\mu_v}\frac{\partial P}{\partial z}=\frac{p_v}{R_v T}\frac{KK_{r,v}}{\mu_v}\frac{\partial P}{\partial z}$$

$$\frac{C^2}{\rho}M_a M_v D_{eff,g}\frac{\partial X_v}{\partial z}=\left(\frac{P}{RT}\right)^2\frac{1}{\frac{p_a}{R_a T}+\frac{p_v}{R_v T}}M_a M_v D_{eff,g}\frac{\partial}{\partial z}\left(\frac{p_v}{P}\right)$$

$$=\left(\frac{P}{RT}\right)^2\frac{1}{\frac{P-p_v}{R_a T}+\frac{p_v}{R_v T}}M_a M_v D_{eff,g}\frac{\partial}{\partial z}\left(\frac{p_v}{P}\right)$$

$$=\frac{P^2 M_a M_v D_{eff,g}}{RT\left(\left(P-p_v\right)M_a+p_v M_v\right)}\frac{\partial}{\partial z}\left(\frac{p_v}{P}\right)$$

$$=\frac{M_a M_v D_{eff,g}}{RT\left(\left(P-p_v\right)M_a+p_v M_v\right)}\left(P\frac{\partial p_v}{\partial z}-p_v\frac{\partial P}{\partial z}\right)$$

$$=\frac{M_a M_v D_{eff,g}}{RT\left(\left(P-p_v\right)M_a+p_v M_v\right)}\left(P\frac{\partial p_v}{\partial S_w}\frac{\partial S_w}{\partial z}+P\frac{\partial p_v}{\partial T}\frac{\partial T}{\partial z}-p_v\frac{\partial P}{\partial z}\right)$$

The conservation equation can now be written as

$$\left(\phi\rho_w-\frac{\phi p_v}{R_v T}+\frac{\phi}{R_v T}\left(1-S_w\right)\frac{\partial p_v}{\partial S_w}\right)\frac{\partial S_w}{\partial t}+\left(\frac{\phi}{R_v}\left(1-S_w\right)\frac{\partial}{\partial T}\left(\frac{p_v}{T}\right)\right)\frac{\partial T}{\partial t}+\left(0\right)\frac{\partial P}{\partial t}$$

$$=\frac{\partial}{\partial z}\left(\left(\rho_w\frac{KK_{r,l}}{\mu_w}\left(\frac{\partial p_w}{\partial S_w}\right)+\frac{M_a M_v D_{eff,g}}{R\left(\left(P-p_v\right)M_a+p_v M_v\right)}P\frac{\partial p_v}{\partial S_w}\right)\frac{\partial S_w}{\partial z}\right)$$

$$+\frac{\partial}{\partial z}\left(\left(\rho_w\frac{KK_{r,l}}{\mu}\frac{\partial p_w}{\partial T}+\frac{M_a M_v D_{eff,g}}{R\left(\left(P-p_v\right)M_a+p_v M_v\right)}P\frac{\partial p_v}{\partial T}\right)\frac{\partial T}{\partial z}\right)$$

$$+\frac{\partial}{\partial z}\left(\left(\frac{p_v}{R_v T}\frac{KK_{r,v}}{\mu_v}-\frac{M_a M_v D_{eff,g}}{R\left(\left(P-p_v\right)M_a+p_v M_v\right)}p_v\right)\frac{\partial P}{\partial z}\right)-\frac{\partial}{\partial z}\left(\rho_w\frac{KK_{r,l}}{\mu}\rho g\right)$$

Now take the conservation of energy equation

$$\left(\rho\bar{c}_p\right)_{eff}\frac{\partial T}{\partial t}+\left[\rho_w c_{p,w}u_w+\rho_v c_{p,v}u_v+\rho_a c_{p,a}u_a\right]\frac{\partial T}{\partial z}+\Delta h_{vap}\left(\frac{\partial}{\partial z}\left(\rho_w\frac{KK_r}{\mu}\left(\frac{\partial p_w}{\partial z}-\rho g\right)\right)-\phi\frac{\partial\left(\rho_w S_w\right)}{\partial t}\right)=\frac{\partial}{\partial z}\left(k_{eff}\frac{\partial T}{\partial z}\right)$$

Substitute with constitutive relations

$$\begin{aligned}
&\left(\phi S_l\rho_l C_{p,l}+\phi S_v\rho_v C_{p,v}+\phi S_a\rho_a C_{p,a}+\phi\rho_s C_{p,s}\right)\frac{\partial T}{\partial t}\\
&+\left[\rho_w c_{p,w}\frac{KK_{r,l}}{\mu_w}\left(\frac{\partial p_w}{\partial z}-\rho g\right)+\rho_v c_{p,v}\frac{KK_{r,g}}{\mu_g}\frac{\partial P}{\partial z}+\rho_a c_{p,a}\frac{KK_{r,g}}{\mu_g}\frac{\partial P}{\partial z}\right]\frac{\partial T}{\partial z}\\
&+\left(\frac{\partial}{\partial z}\begin{pmatrix}\Delta h_{vap}\rho_w\dfrac{KK_{r,l}}{\mu_w}\dfrac{\partial P}{\partial z}-\Delta h_{vap}\rho_w\dfrac{KK_{r,l}}{\mu}\dfrac{\partial p_w}{\partial S_w}\dfrac{\partial S_w}{\partial z}\\ -\Delta h_{vap}\rho_w\dfrac{KK_{r,l}}{\mu}\dfrac{\partial p_w}{\partial T}\dfrac{\partial T}{\partial z}-\Delta h_{vap}\rho_w\dfrac{KK_{r,l}}{\mu}\rho g\end{pmatrix}-\Delta h_{vap}\phi\rho_w\frac{\partial\left(S_w\right)}{\partial t}\right)\\
&=\frac{\partial}{\partial z}\left(\left(\phi S_a k_a+\phi S_v k_v+\phi S_l k_l+\phi k_s\right)\frac{\partial T}{\partial z}\right)
\end{aligned}$$

Now rearrange this

$$\begin{aligned}
&\left(\phi S_l\rho_l C_{p,l}+\phi S_v\rho_v C_{p,v}+\phi S_a\rho_a C_{p,a}+\phi\rho_s C_{p,s}\right)\frac{\partial T}{\partial t}-\Delta h_{vap}\phi\rho_w\frac{\partial S_w}{\partial t}+\left(0\right)\frac{\partial P}{\partial t}\\
&=-\left[\rho_w c_{p,w}\frac{KK_{r,l}}{\mu_w}\left(\frac{\partial p_w}{\partial z}-\rho g\right)+\rho_v c_{p,v}\frac{KK_{r,g}}{\mu_g}\frac{\partial P}{\partial z}+\rho_a c_{p,a}\frac{KK_{r,g}}{\mu_g}\frac{\partial P}{\partial z}\right]\frac{\partial T}{\partial z}\\
&+\frac{\partial}{\partial z}\left(\left(\phi S_a k_a+\phi S_v k_v+\phi S_l k_l+\phi k_s\right)\frac{\partial T}{\partial z}\right)+\frac{\partial}{\partial z}\left(\left(\Delta h_{vap}\rho_w\frac{KK_{r,w}}{\mu_w}\frac{\partial p_w}{\partial T}\right)\frac{\partial T}{\partial z}\right)\\
&+\frac{\partial}{\partial z}\left(\left(\Delta h_{vap}\rho_w\frac{KK_{r,l}}{\mu_w}\frac{\partial p_c}{\partial S_w}\right)\frac{\partial S_w}{\partial z}\right)+\frac{\partial}{\partial z}\left(\left(-\Delta h_{vap}\rho_w\frac{KK_{r,w}}{\mu_w}\right)\frac{\partial P}{\partial z}\right)+\frac{\partial}{\partial z}\left(\Delta h_{vap}\rho_w\frac{KK_{r,l}}{\mu_w}\rho g\right)
\end{aligned}$$

Next take the conservation of air equation

$$\phi\frac{\partial\left(\rho_a S_g\right)}{\partial t}=\frac{\partial}{\partial z}\left(\rho_a\frac{KK_{r,g}}{\mu_a}\frac{\partial P}{\partial z}+\frac{C^2}{\rho}M_v M_a D_{eff,g}\frac{\partial X_a}{\partial z}\right)$$

The components of this equation can be written as

$$\phi\frac{\partial\left(\rho_a S_g\right)}{\partial t}=\phi\frac{\partial}{\partial t}\left(\frac{p_a}{R_a T}\left(1-S_w\right)\right)$$

$$=\phi\frac{\partial}{\partial t}\left(\frac{\left(P-p_v\right)}{R_a T}\left(1-S_w\right)\right)$$

$$=-\frac{\phi}{R_a}\left(\frac{\left(P-p_v\right)}{T}+\frac{\left(1-S_w\right)}{T}\frac{\partial p_v}{\partial S_w}\right)\frac{\partial S_w}{\partial t}-\frac{\phi}{R_a}\left(\frac{P}{T^2}-\frac{PS_w}{T^2}+\left(1+S_w\right)\frac{\partial}{\partial T}\left(\frac{p_v}{T}\right)\right)\frac{\partial T}{\partial t}$$

$$+\frac{\phi\left(1-S_w\right)}{R_a T}\frac{\partial P}{\partial t}$$

$$\rho_a\frac{KK_{r,g}}{\mu_a}\frac{\partial P}{\partial z}=\frac{p_a}{R_a T}\frac{KK_{r,g}}{\mu_a}\frac{\partial P}{\partial z}$$

$$=\frac{P-p_v}{R_a T}\frac{KK_{r,g}}{\mu_a}\frac{\partial P}{\partial z}$$

$$\frac{C^2}{\rho}M_v M_a D_{eff,g}\frac{\partial X_a}{\partial z}=\left(\frac{P}{RT}\right)^2\frac{1}{\frac{p_a}{R_a T}+\frac{p_v}{R_v T}}M_v M_a D_{eff,g}\frac{\partial}{\partial z}\left(\frac{p_a}{P}\right)$$

$$=\left(\frac{P}{RT}\right)^2\frac{1}{\frac{p_a}{R_a T}+\frac{p_v}{R_v T}}M_v M_a D_{eff,g}\frac{\partial}{\partial z}\left(\frac{P-p_v}{P}\right)$$

$$=\frac{P^2}{RT\left(M_a\left(P-p_v\right)+M_v p_v\right)}M_v M_a D_{eff,g}\frac{\partial}{\partial z}\left(1-\frac{p_v}{P}\right)$$

$$=-\frac{M_v M_a D_{eff,g}}{RT\left(M_a\left(P-p_v\right)+M_v p_v\right)}\left(P\frac{\partial p_v}{\partial z}-p_v\frac{\partial P}{\partial z}\right)$$

$$=-\frac{M_v M_a D_{eff,g}}{RT\left(M_a\left(P-p_v\right)+M_v p_v\right)}\left(P\frac{\partial p_v}{\partial S_w}\frac{\partial S_w}{\partial z}+P\frac{\partial p_v}{\partial T}\frac{\partial T}{\partial z}-p_v\frac{\partial P}{\partial z}\right)$$

Now substitute into the original equation for conservation of air

$$-\frac{\phi}{R_a}\left(\frac{(P-p_v)}{T}+\frac{(1-S_w)}{T}\frac{\partial p_v}{\partial S_w}\right)\frac{\partial S_w}{\partial t}-\frac{\phi}{R_a}\left(\frac{P}{T^2}-\frac{PS_w}{T^2}+(1+S_w)\frac{\partial}{\partial T}\left(\frac{p_v}{T}\right)\right)\frac{\partial T}{\partial t}+\frac{\phi(1-S_w)}{R_aT}\frac{\partial P}{\partial t}$$
$$=\frac{\partial}{\partial z}\left(\frac{P-p_v}{R_aT}\frac{KK_{r,g}}{\mu_a}\frac{\partial P}{\partial z}+\frac{M_vM_aD_{eff,g}}{RT\left(M_a(P-p_v)+M_vp_v\right)}\left(P\frac{\partial p_v}{\partial S_w}\frac{\partial S_w}{\partial z}+P\frac{\partial p_v}{\partial T}\frac{\partial T}{\partial z}-p_v\frac{\partial P}{\partial z}\right)\right)$$

Rearrange this

$$-\frac{\phi}{R_a}\left(\frac{(P-p_v)}{T}+\frac{(1-S_w)}{T}\frac{\partial p_v}{\partial S_w}\right)\frac{\partial S_w}{\partial t}-\frac{\phi}{R_a}\left(\frac{P}{T^2}-\frac{PS_w}{T^2}+(1+S_w)\frac{\partial}{\partial T}\left(\frac{p_v}{T}\right)\right)\frac{\partial T}{\partial t}+\frac{\phi(1-S_w)}{R_aT}\frac{\partial P}{\partial t}$$
$$=\frac{\partial}{\partial z}\left(\left(\frac{P-p_v}{R_aT}\frac{KK_{r,g}}{\mu_a}-\frac{M_vM_aD_{eff,g}}{RT\left(M_a(P-p_v)+M_vp_v\right)}p_v\right)\frac{\partial P}{\partial z}\right)$$
$$+\frac{\partial}{\partial z}\left(\left(\frac{M_vM_aD_{eff,g}}{RT\left(M_a(P-p_v)+M_vp_v\right)}P\frac{\partial p_v}{\partial S_w}\right)\frac{\partial S_w}{\partial z}\right)$$
$$\frac{\partial}{\partial z}\left(\left(\frac{M_vM_aD_{eff,g}}{RT\left(M_a(P-p_v)+M_vp_v\right)}P\frac{\partial p_v}{\partial T}\right)\frac{\partial T}{\partial z}\right)$$

The three GEs can now be written as

Equation 1 (Conservation of water and vapor)

$$\left(-\phi\frac{p_v}{R_vT}+\frac{\phi(1-S_w)}{R_vT}\left(\frac{\partial p_v}{\partial S_w}\right)+\phi\rho_w\right)\frac{\partial S_w}{\partial t}+\left(\frac{\phi(1-S_w)}{R_v}\frac{\partial}{\partial T}\left(\frac{p_v}{T}\right)\right)\frac{\partial T}{\partial t}+(0)\frac{\partial P}{\partial t}$$

$$=\frac{\partial}{\partial z}\left(\left(\frac{M_aM_vD_{eff,g}}{RT\left[(P-p_v)M_a+p_vM_v\right]}P\frac{\partial p_v}{\partial S_w}-\rho_w\frac{KK_{r,w}}{\mu_w}\frac{\partial p_c}{\partial S_w}\right)\frac{\partial S_w}{\partial z}\right)$$

$$+\frac{\partial}{\partial z}\left(\left(\frac{M_aM_vD_{eff,g}}{RT\left[(P-p_v)M_a+p_vM_v\right]}P\frac{\partial p_v}{\partial T}-\rho_w\frac{KK_{r,w}}{\mu_w}\frac{\partial p_c}{\partial T}\right)\frac{\partial P}{\partial z}\right)$$

$$+\frac{\partial}{\partial z}\left(\left(\frac{p_v}{R_vT}\frac{KK_{r,g}}{\mu_g}-\frac{M_aM_vD_{eff,g}}{RT\left[(P-p_v)M_a+p_vM_v\right]}p_v+\rho_w\frac{KK_{r,w}}{\mu_w}\right)\frac{\partial P}{\partial z}\right)-\frac{\partial}{\partial z}\left(\rho_w\frac{KK_{r,l}}{\mu}\rho g\right)$$

Equation 2 (Conservation of air)

$$\left(-\frac{\phi}{R_a}\left(\frac{P-p_v}{T}+\frac{1-S_w}{T}\frac{\partial p_v}{\partial S_w}\right)\right)\frac{\partial S_w}{\partial t}+\left(-\frac{\phi}{R_a}\left(\frac{p}{T^2}-\frac{PS_w}{T^2}+(1-S_w)\frac{\partial}{\partial T}\left(\frac{p_v}{T}\right)\right)\right)\frac{\partial T}{\partial t}+\left(\frac{\phi(1-S_w)}{R_aT}\right)\frac{\partial P}{\partial t}$$

$$=\frac{\partial}{\partial z}\left(\left(-\frac{M_aM_vD_{eff,g}}{RT\left[(P-p_v)M_a+p_vM_v\right]}P\frac{\partial p_v}{\partial S_w}\right)\frac{\partial S_w}{\partial z}\right)+\frac{\partial}{\partial z}\left(\left(-\frac{M_aM_vD_{eff,g}}{RT\left[(P-p_v)M_a+p_vM_v\right]}P\frac{\partial p_v}{\partial T}\right)\frac{\partial T}{\partial z}\right)$$

$$+\frac{\partial}{\partial z}\left(\left(\frac{P-p_v}{R_aT}\frac{KK_{r,g}}{\mu_g}+\frac{M_aM_vD_{eff,g}}{RT\left[(P-p_v)M_a+p_vM_v\right]}p_v\right)\frac{\partial P}{\partial z}\right)$$

Equation 3 (Conservation of energy)

$$\left(-\Delta h_v\phi\rho_w\right)\frac{\partial S_w}{\partial t}+\left(\phi S_l\rho_lC_{p,l}+\phi S_v\rho_vC_{p,v}+\phi S_a\rho_aC_{p,a}+\phi\rho_sC_{p,s}\right)\frac{\partial T}{\partial t}+(0)\frac{\partial P}{\partial t}$$

$$=-\begin{pmatrix}C_{pv}\rho_v\frac{KK_{r,v}}{\mu_v}\frac{\partial P}{\partial z}+\frac{C^2}{\rho}M_aM_vD_{eff,g}\frac{\partial X_v}{\partial z}+C_{pa}\rho_a\frac{KK_{r,g}}{\mu_a}\frac{\partial P}{\partial z}+\frac{C^2}{\rho}M_vM_aD_{eff,g}\frac{\partial X_a}{\partial z}\\+C_{pv}\rho_w\frac{KK_{r,l}}{\mu}\left(\frac{\partial(p_w)}{\partial z}+\rho g\right)\end{pmatrix}\nabla T$$

$$+\frac{\partial}{\partial z}\left(\left(\rho_w\frac{KK_{r,l}}{\mu_w}\frac{\partial p_c}{\partial S_w}\Delta h_v\right)\frac{\partial S_w}{\partial z}\right)+\frac{\partial}{\partial z}\left(\left(\left(\phi S_ak_a+\phi S_vk_v+\phi S_lk_l+\phi k_s\right)+\rho_w\frac{KK_{r,l}}{\mu_w}\frac{\partial p_c}{\partial T}\Delta h_v\right)\frac{\partial T}{\partial z}\right)$$

$$+\frac{\partial}{\partial z}\left(\left(-\rho_w\frac{KK_{r,l}}{\mu_w}\Delta h_v\right)\frac{\partial P}{\partial z}\right)+\frac{\partial}{\partial z}\left(\Delta h_v\rho_w\frac{KK_{r,l}}{\mu_w}\rho_wg\right)$$

Following the method of Ni (1997) the conservation equations can be written as

$$K_4\frac{\partial S_w}{\partial t}+K_5\frac{\partial T}{\partial t}+K_6\frac{\partial P}{\partial t}=\nabla\left(K_1\nabla S_w\right)+\nabla\left(K_2\nabla T\right)+\nabla\left(K_3\nabla P\right)-\nabla\left(K_{19}\right)$$

$$K_{10}\frac{\partial S_w}{\partial t}+K_{11}\frac{\partial T}{\partial t}+K_{12}\frac{\partial P}{\partial t}=\nabla\left(K_7\nabla S_w\right)+\nabla\left(K_8\nabla T\right)+\nabla\left(K_9\nabla P\right)$$

$$K_{16}\frac{\partial S_w}{\partial t}+K_{17}\frac{\partial T}{\partial t}+K_{18}\frac{\partial P}{\partial t}=-\left(C_{pv}\vec{n}_v+C_{pa}\vec{n}_a+C_{pv}\vec{n}_w\right)\nabla T+\nabla\left(K_{13}\nabla S_w\right)+\nabla\left(K_{14}\nabla T\right)+\nabla\left(K_{15}\nabla P\right)+\nabla\left(K_{20}\right)$$

Where

$$K_1=\frac{M_aM_vD_{eff,g}}{RT\left[\left(P-p_v\right)M_a+p_vM_v\right]}P\frac{\partial p_v}{\partial S_w}-\rho_w\frac{KK_{r,w}}{\mu_w}\frac{\partial p_c}{\partial S_w}$$

$$K_2=\frac{M_aM_vD_{eff,g}}{RT\left[\left(P-p_v\right)M_a+p_vM_v\right]}P\frac{\partial p_v}{\partial T}-\rho_w\frac{KK_{r,w}}{\mu_w}\frac{\partial p_c}{\partial T}$$

$$K_3=\frac{p_v}{R_vT}\frac{KK_{r,g}}{\mu_g}-\frac{M_aM_vD_{eff,g}}{RT\left[\left(P-p_v\right)M_a+p_vM_v\right]}p_v+\rho_w\frac{KK_{r,w}}{\mu_w}$$

$$K_4=-\phi\frac{p_v}{R_vT}+\frac{\phi\left(1-S_w\right)}{R_vT}\left(\frac{\partial p_v}{\partial S_w}\right)+\phi\rho_w$$

$$K_5=\frac{\phi\left(1-S_w\right)}{R_v}\frac{\partial}{\partial T}\left(\frac{p_v}{T}\right)$$

$$K_6=0$$

$$K_7=-\frac{M_aM_vD_{eff,g}}{RT\left[\left(P-p_v\right)M_a+p_vM_v\right]}P\frac{\partial p_v}{\partial S_w}$$

$$K_8=-\frac{M_aM_vD_{eff,g}}{RT\left[\left(P-p_v\right)M_a+p_vM_v\right]}P\frac{\partial p_v}{\partial T}$$

$$K_9=\frac{P-p_v}{R_aT}\frac{KK_{r,g}}{\mu_g}+\frac{M_aM_vD_{eff,g}}{RT\left[\left(P-p_v\right)M_a+p_vM_v\right]}p_v$$

$$K_{10}=-\frac{\phi}{R_a}\left(\frac{P-p_v}{T}+\frac{1-S_w}{T}\frac{\partial p_v}{\partial S_w}\right)$$

$$K_{11}=-\frac{\phi}{R_a}\left(\frac{p}{T^2}-\frac{PS_w}{T^2}+\left(1-S_w\right)\frac{\partial}{\partial T}\left(\frac{p_v}{T}\right)\right)$$

$$K_{12}=\frac{\phi\left(1-S_w\right)}{R_aT}$$

$$K_{13} = \rho_w \frac{KK_{r,l}}{\mu_w} \frac{\partial p_c}{\partial S_w} \Delta h_v$$

$$K_{14} = \left(\phi S_a k_a + \phi S_v k_v + \phi S_l k_l + (1-\phi) k_s\right) + \rho_w \frac{KK_{r,l}}{\mu_w} \frac{\partial p_c}{\partial T} \Delta h_v$$

$$K_{15} = -\rho_w \frac{KK_{r,w}}{\mu_w} \Delta h_v$$

$$K_{16} = -\Delta h_v \phi \rho_w$$

$$K_{17} = \phi S_l \rho_l C_{p,l} + \phi S_v \rho_v C_{p,v} + \phi S_a \rho_a C_{p,a} + (1-\phi) \rho_s C_{p,s}$$

$$K_{18} = 0$$

$$K_{19} = \rho_w \frac{KK_{r,l}}{\mu} \rho_w g$$

$$K_{20} = \Delta h_v \rho_w \frac{KK_{r,l}}{\mu_w} \rho_w g$$

This is a system of three non-linear parabolic partial differential equations. One possible solution method involves using a banded matrix solution algorithm. Since the coefficients will also contain the dependant variables, the solution algorithm will have to iterate at each time step until the solution converges before stepping forward in time.

C.2. Boundary Conditions

The boundary conditions for this problem are complicated. The surfaces can be exposed to radiant heating, re-radiative cooling, convective cooling, evaporative cooling, and water spray impingement. Depending on the water application rate, two very different cases can be considered. If a small amount of water is applied, the surface will have a saturation of less than 1 and some surface pores will contain gas. This will allow air and water vapor in the material to escape through the surface. If the water application rate is high, then the surface will be saturated. This will seal the surface and prevent air and vapor from escaping. For this model we are not considering the case where bubbles percolate up through a saturated material. This behavior is very difficult to predict and is considered beyond the scope of this research. We will assume that when the surface becomes saturated no gases can pass through the saturated region. The boundary conditions for a saturated surface and an unsaturated surface will be described.

C.2.1. Front Face Boundary Conditions

Water Boundary Conditions at Surface

Case 1: Low Water Flux

The surface will be exposed to a specified external water mass flux $\dot{m}''_{spray}$ and experience evaporative losses $\dot{m}''_{evap}$. There will also be a water mass flux $\dot{m}''_{water}$, and a vapor mass flux of $\dot{m}''_{vapor}$ into the material. For small values of $\dot{m}''_{spray}$, the surface will be partially saturated and the water infiltration rate (amount of water entering the material) will be equal to $\dot{m}''_{spray} - \dot{m}''_{evap}$. This is shown in Figure 84. This is a type 3 (convective) boundary condition. The sign convention used for the fluxes is that fluxes in the material are positive in the positive z-direction (the downward direction as shown in figures). Surface fluxes are positive in their expected direction as shown in the figures.

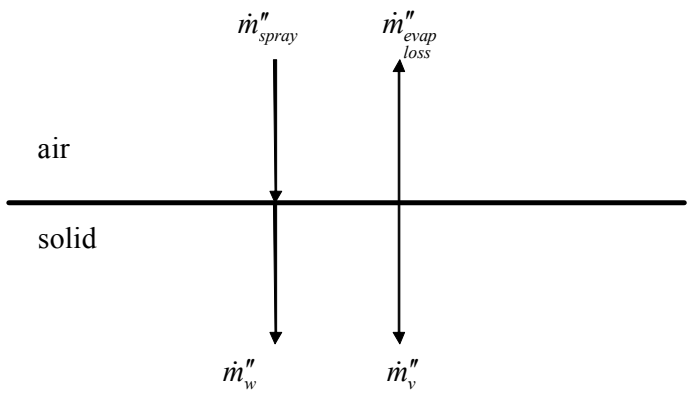

Figure 84 – Surface Saturation Boundary Condition for Small Water Flux

Where

$$\dot{m}''_{\substack{evap \\ loss}} = h_m \left(\rho_{v,surf} - \rho_{v,\infty} \right)$$

The boundary condition for the surface in this case is written as

$$\dot{m}''_{spray} = \dot{m}''_{\substack{evap \\ loss}} + \dot{m}''_{w} + \dot{m}''_{v} \qquad @\, z = 0 \quad for \;\; t > 0$$

Where

$$\dot{m}''_{v} = -\rho_v \frac{KK_{r,g}}{\mu_v} \frac{\partial P}{\partial z} - \frac{C^2}{\rho} M_a M_v D_{eff,g} \frac{\partial X_v}{\partial z}$$

$$\dot{m}''_{w} = -\rho_w \frac{KK_{r,w}}{\mu_w} \left(\frac{\partial p_w}{\partial z} - \rho_w g \right)$$

Expanding terms, these can be written as

$$\dot{m}_w'' + \dot{m}_v'' = \begin{pmatrix} -\left(\dfrac{M_a M_v D_{eff,g}}{R\left(\left(P - p_v\right)M_a + p_v M_v\right)} P \dfrac{\partial p_v}{\partial S_w} - \rho_w \dfrac{KK_{r,l}}{\mu_w} \dfrac{\partial p_{cap}}{\partial S_w} \right) \dfrac{\partial S_w}{\partial z} \\ -\left(\dfrac{M_a M_v D_{eff,g}}{R\left(\left(P - p_v\right)M_a + p_v M_v\right)} P \dfrac{\partial p_v}{\partial T} - \rho_w \dfrac{KK_{r,l}}{\mu_w} \dfrac{\partial p_{cap}}{\partial T} \right) \dfrac{\partial T}{\partial z} \\ -\left(\dfrac{p_v}{R_v T} \dfrac{KK_{r,v}}{\mu_v} - \dfrac{M_a M_v D_{eff,g}}{R\left(\left(P - p_v\right)M_a + p_v M_v\right)} p_v + \rho_w \dfrac{KK_{r,l}}{\mu_w} \right) \dfrac{\partial P}{\partial z} \\ +\rho_w \dfrac{KK_{r,l}}{\mu_w} \rho g \end{pmatrix}$$

Or using the K notation

$$\dot{m}_w'' + \dot{m}_v'' = -K_1 \frac{\partial S_w}{\partial z} - K_2 \frac{\partial T}{\partial z} - K_3 \frac{\partial P}{\partial z} + K_{19}$$

So the boundary condition can be written as

$$-K_1 \frac{\partial S_w}{\partial z} - K_2 \frac{\partial T}{\partial z} - K_3 \frac{\partial P}{\partial z} + K_{19} = \dot{m}_{spray}'' - \dot{m}_{\substack{evap \\ loss}}''$$

Case 2: High Water Flux

If $\dot{m}_{spray}'' > \dot{m}_{\substack{evap \\ loss}}'' + \dot{m}_w'' + \dot{m}_v''$ then the boundary condition at the surface is

$$S_w = 1 \quad for \quad z < z_{\text{int}} \qquad t > t_{sat}$$

There will be an initial transient period (t_{sat}) before the water can be absorbed into the material and the saturation will be less than unity. If this is very brief it can be ignored and the boundary condition becomes a type 1 boundary condition:

$$S_w = 1 \quad for \quad z < z_{\text{int}} \qquad t > 0$$

Pressure Boundary Conditions at Surface

The air mass fluxes for at the surface are shown in Figure 85.

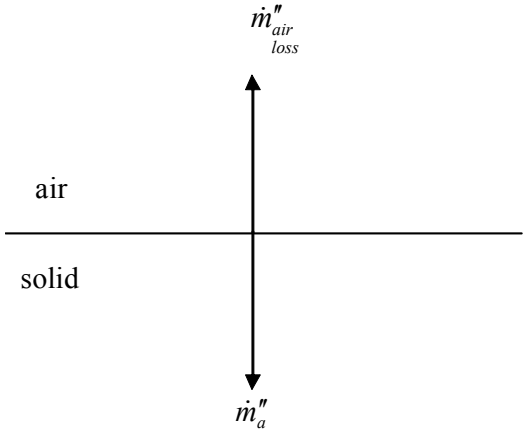

Figure 85 – Air Mass Fluxes at Surface

The pressure at the material surface will be calculated based on the saturation conditions. Different methods can be used for the low and high water flux cases.

Case 1: Low Water Flux

If the water application rate is less than the sum of the absorption plus evaporation rates, then there will be pores open to the ambient environment at the surface. Conservation of air at the surface is written as

$$-\dot{m}''_a - \dot{m}''_{air\ loss} = 0$$

Where $\dot{m}''_a$ is the air mass flux in the material. It can be written as:

$$\dot{m}''_a = -\rho_a \frac{KK_{r,a}}{\mu_a} \nabla P - \frac{C^2}{\rho} M_v M_a D_{av} \nabla X_a$$

So, conservation of air at the surface is

$$-\dot{m}_a'' - \dot{m}_{\substack{air\\loss}}'' = 0$$

Or

$$\rho_a \frac{KK_{r,a}}{\mu_a} \nabla P + \frac{C^2}{\rho} M_v M_a D_{av} \nabla X_a = \dot{m}_{\substack{air\\loss}}''$$

The terms in this equation can be expanded

$$\rho_a \frac{KK_{r,a}}{\mu_a} \nabla P = \frac{P - p_v}{R_a T} \frac{KK_{r,g}}{\mu_a} \frac{\partial P}{\partial z}$$

$$\frac{C^2}{\rho} M_v M_a D_{av} \nabla X_a = -\frac{M_v M_a D_{eff,g}}{RT\left(M_a\left(P - p_v\right) + M_v p_v\right)} \left(P \frac{\partial p_v}{\partial S_w} \frac{\partial S_w}{\partial z} + P \frac{\partial p_v}{\partial T} \frac{\partial T}{\partial z} - p_v \frac{\partial P}{\partial z} \right)$$

So the boundary condition can be written as

$$\left(-\frac{M_v M_a D_{eff,g}}{RT\left(M_a\left(P - p_v\right) + M_v p_v\right)} P \frac{\partial p_v}{\partial S_w} \right) \frac{\partial S_w}{\partial z} + \left(-\frac{M_v M_a D_{eff,g}}{RT\left(M_a\left(P - p_v\right) + M_v p_v\right)} P \frac{\partial p_v}{\partial T} \right) \frac{\partial T}{\partial z}$$

$$+ \left(\frac{P - p_v}{R_a T} \frac{KK_{r,g}}{\mu_a} + \frac{M_v M_a D_{eff,g}}{RT\left(M_a\left(P - p_v\right) + M_v p_v\right)} p_v \right) \frac{\partial P}{\partial z} = \dot{m}_{\substack{air\\loss}}''$$

Or

$$K_7 \frac{\partial S_w}{\partial z} + K_8 \frac{\partial T}{\partial z} + K_9 \frac{\partial P}{\partial z} = \dot{m}_{\substack{air\\loss}}''$$

If a no-flux boundary condition is used at the surface, then $\dot{m}_{\substack{air\\loss}}''$ is zero and

conservation of mass for air for the surface node can be written as

$$-K_7 \frac{\partial S_w}{\partial z} - K_8 \frac{\partial T}{\partial z} - K_9 \frac{\partial P}{\partial z} = 0$$

If the pores at the surface are assumed to be open to the ambient with no resistance to

convective mass transfer then the boundary condition is simply

$$P = P_{\infty} \qquad @ \qquad z = 0$$

Case 2: High Water Flux

If the water application rate is greater than the total of absorption plus evaporation rates, then a layer of water will accumulate on the surface. The Pressure at the surface is therefore the ambient pressure plus additional static pressure provided by the water layer. This is a type 1 boundary condition.

$$P = P_{\infty} + \rho_w g h_{layer} \qquad @\, z = 0 \;\; t > 0$$

This is clearly a modeling simplification. If the material is heated with the surface sealed, the internal pressure can increase above this hydrostatic value. If that should happen, air and vapor would percolate up through the water layer. This phenomenon is beyond the scope of this research, and will not be considered. Another boundary condition that will, however, be considered is a sealed surface. This will produce a no-flux condition at the surface for air. This boundary condition can be written as

$$\dot{m}''_a = 0 \;\; @\, z = 0 \quad for \;\; t > 0$$

This condition may not be appropriate for most situations being considered for this model, but it is included for completeness. It may also be useful to invoke while validating and testing the limits of the model.

Temperature Boundary Conditions at Surface

Case 1: Low Water Flux

After sprinkler activation, the surface of the material would be sprayed with water. If a small amount of water is applied to the surface, heat transfer will occur by additional mechanisms than if the material is dry. A surface boundary condition will be developed that includes convection, conduction, and radiation. Enthalpy flows at the surface that are considered in the model are external radiative heating, enthalpy carried by the water spray to the surface, enthalpy carried away by any vapor and air leaving the material, surface convective losses, re-radiative losses, internal convective fluxes into the material by water, vapor, and air, and internal conduction into the material. This is illustrated in Figure 86. This is a type 3 (convective) boundary condition. Note that evaporation is implicitly incorporated into the convective vapor enthalpy flows.

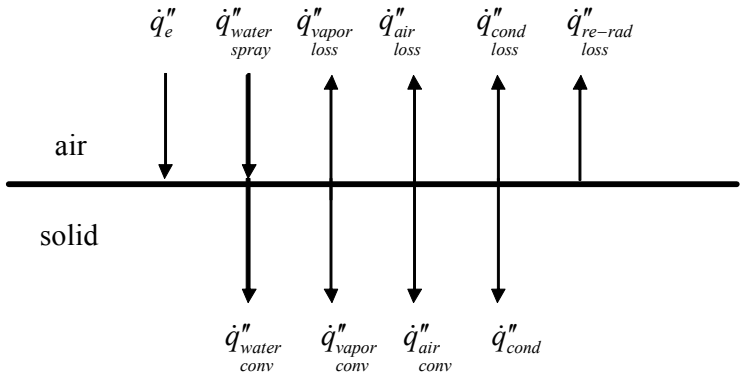

Figure 86– Thermal Energy Balance for Small Water Flux

Summing the heat fluxes at the surface gives the thermal boundary condition

$$\dot{q}''_e + \dot{q}''_{\substack{water\\spray}} - \dot{q}''_{\substack{vapor\\loss}} - \dot{q}''_{\substack{air\\loss}} - \dot{q}''_{\substack{cond\\loss}} - \dot{q}''_{\substack{re-rad\\loss}} - \dot{q}''_{\substack{water\\conv}} - \dot{q}''_{\substack{vapor\\conv}} - \dot{q}''_{\substack{air\\conv}} - \dot{q}''_{cond} = 0 \quad @\ z = 0,\ for\ \ t > 0$$

Where

$$\dot{q}''_{\substack{water\\app}} = \dot{m}''_{spray} h_w$$

$$\underset{loss}{\dot{q}''_{vapor}} = \underset{loss}{\dot{m}''_{vapor}} h_v$$

$$\underset{loss}{\dot{q}''_{air}} = \underset{loss}{\dot{m}''_{air}} h_a$$

$$\underset{loss}{\dot{q}''_{cond}} = h\left(T_s - T_\infty\right)$$

$$\underset{loss}{\dot{q}''_{re-rad}} = \varepsilon_s \sigma \left(T_s^4 - T_\infty^4\right)$$

$$\underset{conv}{\dot{q}''_{water}} = \dot{m}''_w h_w$$

$$\underset{conv}{\dot{q}''_{vapor}} = \dot{m}''_v h_v$$

$$\underset{conv}{\dot{q}''_{air}} = \dot{m}''_a h_a$$

$$\dot{q}''_{cond} = -k_{eff} \frac{\partial T}{\partial z} = -K_{14} \frac{\partial T}{\partial z}$$

This can be simplified using the relations developed previously for conservation of mass. Start with the water convection terms

$$\underset{spray}{\dot{q}''_{water}} - \underset{loss}{\dot{q}''_{vapor}} - \underset{conv}{\dot{q}''_{water}} - \underset{conv}{\dot{q}''_{vapor}}$$

$$\underset{spray}{\dot{m}''_{water}} \underset{spray}{h_{water}} - \underset{loss}{\dot{m}''_{vapor}} \underset{loss}{h_{vapor}} - \underset{conv}{\dot{m}''_{water}} \underset{conv}{h_{water}} - \underset{conv}{\dot{m}''_{vapor}} \underset{conv}{h_{vapor}}$$

Where the enthalpy of the water spray is calculated at the temperature of the incoming water spray. All other enthalpies are calculated at the surface temperature. The water enthalpy fluxes can therefore be written as

$$\underset{spray}{\dot{m}''_{water}} \underset{spray}{h_{water}} - \underset{loss}{\dot{m}''_{vapor}} h_v - \underset{conv}{\dot{m}''_{water}} h_w - \underset{conv}{\dot{m}''_{vapor}} h_v$$

Where h_v, and h_w are the enthalpy of the vapor and water at the surface temperature. It should be clarified that h_v is the enthalpy of the vapor, not to be confused with the latent heat of vaporization. These terms can be simplified as follows

$$h_{\underset{spray}{water}} = h_f^o + \int_{T_o}^{T_w} C_{p,w}\partial T + \int_{T_w}^{T_{spray}} C_{p,w}\partial T$$

$$\dot{m}''_{\underset{spray}{water}}\left(h_f^o + \int_{T_o}^{T_w} C_{p,w}\partial T + \int_{T_w}^{T_{spray}} C_{p,w}\partial T \right) - \dot{m}''_{\underset{loss}{vapor}} h_v - \dot{m}''_{\underset{conv}{water}} h_w - \dot{m}''_{\underset{conv}{vapor}} h_v$$

$$\dot{m}''_{\underset{spray}{water}}\left(h_w + \int_{T_w}^{T_{spray}} C_{p,w}\partial T \right) - \dot{m}''_{\underset{loss}{vapor}} h_v - \dot{m}''_{\underset{conv}{water}} h_w - \dot{m}''_{\underset{conv}{vapor}} h_v$$

$$\dot{m}''_{spray} C_{p,w}\left(T_{spray} - T_{surf} \right) + \left(\dot{m}''_{\underset{spray}{water}} - \dot{m}''_{\underset{conv}{water}} \right) h_w - \left(\dot{m}''_{\underset{loss}{vapor}} + \dot{m}''_{\underset{conv}{vapor}} \right) h_v$$

$$\dot{m}''_{spray} C_{p,w}\left(T_{spray} - T_{surf} \right) + \left(\dot{m}''_{evap} \right) h_w - \left(\dot{m}''_{evap} \right) h_v$$

$$\dot{m}''_{spray} C_{p,w}\left(T_{spray} - T_{surf} \right) - \dot{m}''_{evap} \Delta h_v$$

These four terms have been reduced to two. A convective enthalpy flux from the water spray, and an evaporative enthalpy flux. Next simplify the air enthalpy flows and storage

$$\begin{aligned} \dot{q}''_{\underset{conv}{air}} + \dot{q}''_{\underset{loss}{air}} &= \dot{m}''_a h_a + \dot{m}''_{\underset{loss}{air}} h_a \\ &= h_a \left(\dot{m}''_a + \dot{m}''_{\underset{loss}{air}} \right) \\ &= 0 \end{aligned}$$

Where h_a is the enthalpy of the air at the surface temperature. Thermal conduction into the material is assumed to occur by Fourier's law through each component present. ψ represents the volumetric content of air, vapor, water, and solid material present.

$$\dot{q}''_{cond} = -\psi_a k_a \frac{\partial T_a}{\partial z} - \psi_v k_v \frac{\partial T_v}{\partial z} - \psi_w k_w \frac{\partial T_w}{\partial z} - \psi_s k_s \frac{\partial T_s}{\partial z}$$

The conductive losses to the ambient and re-radiative loss terms can be defined as

$$\dot{q}''_{\underset{loss}{cond}} = h\left(T_{surf} - T_\infty \right)$$

$$\dot{q}''_{re-rad} = \varepsilon\sigma\left(T_{surf}^4 - T_\infty^4 \right)$$

The conservation of energy for the surface node can now be written as

$$\dot{q}_e'' + \dot{m}_{spray}'' C_{p,w}\left(T_{spray} - T_{surface}\right) - h\left(T_s - T_\infty\right) - \varepsilon_s \sigma\left(T_s^4 - T_\infty^4\right)$$
$$+\psi_a k_a \frac{\partial T_a}{\partial z} + \psi_v k_v \frac{\partial T_v}{\partial z} + \psi_w k_w \frac{\partial T_w}{\partial z} + \psi_s k_s \frac{\partial T_s}{\partial z} - \Delta h_v \dot{m}_{evap}'' = 0$$

Invoking the assumption of local thermal equilibrium allows this to be written as

$$\dot{q}_e'' + \dot{m}_{spray}'' C_{p,w}\left(T_{spray} - T_{surface}\right) - h\left(T_s - T_\infty\right) - \varepsilon_s \sigma\left(T_s^4 - T_\infty^4\right)$$
$$+k_{eff} \frac{\partial T}{\partial z} - \Delta h_v \dot{m}_{evap}'' = 0$$

Or

$$-K_{14} \frac{\partial T}{\partial z} = \dot{q}_e'' + \dot{m}_{spray}'' C_{p,w}\left(T_{spray} - T_{surf}\right) - h\left(T_{surf} - T_\infty\right) - \varepsilon_s \sigma\left(T_{surf}^4 - T_\infty^4\right) - \Delta h_v \dot{m}_{evap}''$$

Case 2: High Water Flux

If the water application rate is greater than the absorption rate plus evaporation rate, then a layer of water will form on the material. In this case, instead of convection to the environment, heat will transferred by conduction between the water layer and solid. Since we are focusing on the solid material, there will no longer be evaporation occurring at the surface. This new energy balance at the surface is shown in Figure 87. This is a type 3 (convective) boundary condition.

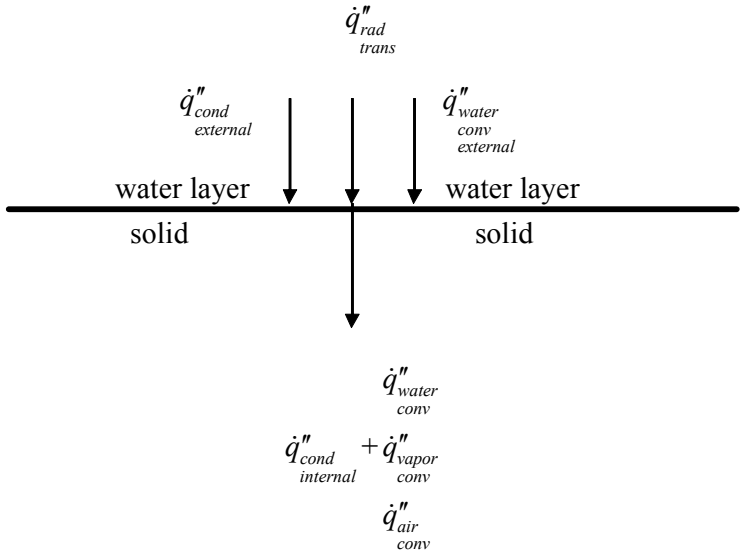

Figure 87 – Surface Energy Balance for Large Water Flux

Summing the heat fluxes at the surface gives the thermal boundary condition for the front face for the case of a high water application rate:

$$\dot{q}''_{rad\ trans} + \dot{q}''_{cond\ external} + \dot{q}''_{water\ conv\ external} = \dot{q}''_{water\ conv} + \dot{q}''_{vapor\ conv} + \dot{q}''_{air\ conv} + \dot{q}''_{cond\ internal}$$

Where the external conduction heat flux is

$$\dot{q}''_{cond\ external} = -k_w \frac{\partial T_w}{\partial z}$$

The surface in this case is below 100°C so re-radiation will not be considered.

Since the surface of the material is on contact with the water layer, the water temperature must also be considered. A model for the water layer will be developed in the next section.

C.2.2. Back Face Boundary Conditions

Saturation Boundary Conditions at Back Face

The most simple saturation boundary condition for the back face for both cases is

$$S_w = S_o \quad @\, z = L$$

This implies semi-infinite behavior. The model is therefore limited to times before the water is transported to the back face of the material if this boundary condition is used. A more realistic boundary condition is shown in Figure 88. This includes water and vapor fluxes in the material that reach the back face of the material, evaporative losses, and possible spray wetting of the back face.

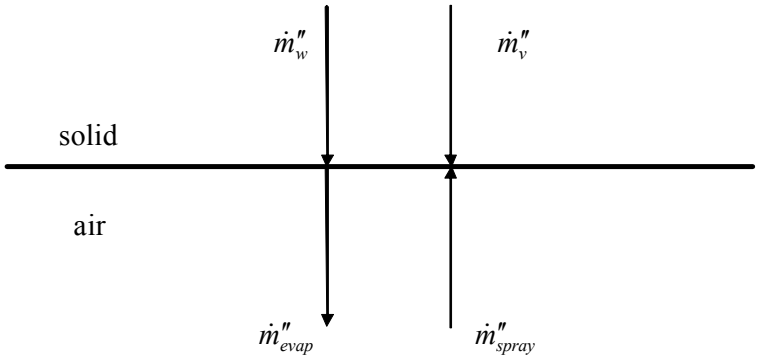

Figure 88 – Back Face Saturation Boundary Condition

This is a type 3 boundary condition (convective boundary condition) which can be written as:

$$\dot{m}''_{\substack{spray \\ back}} + \dot{m}''_v + \dot{m}''_w = \dot{m}''_{\substack{evap \\ loss}} \qquad @\, z = L \quad for\ t > 0$$

Where $\dot{m}''_w$ and $\dot{m}''_v$ are the internal water and vapor mass fluxes, $\dot{m}''_{\substack{spray \\ back}}$ is the water spray flux that is applied to the back face, and $\dot{m}''_{\substack{evap \\ back}}$, is the evaporative mass flux at

the back face. The total rate of evaporation at the back face is

$$\dot{m}''_{\substack{evap\\back\\total}} = \dot{m}''_{\substack{vapor\\loss}} - \dot{m}''_{v} = \dot{m}''_{w} + \dot{m}''_{\substack{spray\\back}}$$

The water and vapor flux terms can have convective and diffusive components

$$\dot{m}''_{w} = -\rho_{w}\frac{KK_{r,w}}{\mu_{w}}\left(\nabla p_{w} - \rho_{w}\vec{g}\right) \qquad @\, z = L$$

$$\dot{m}''_{v} = -\rho_{v}\frac{KK_{r,g}}{\mu_{v}}\nabla P - \frac{C^{2}}{\rho}M_{a}M_{v}D_{eff,g}\nabla X_{v} \qquad @\, z = L$$

Expand these terms

$$-\rho_{w}\frac{KK_{r,l}}{\mu_{w}}\left(\frac{\partial p_{w}}{\partial z} - \rho g\right) = -\rho_{w}\frac{KK_{r,l}}{\mu_{w}}\frac{\partial P}{\partial z} + \rho_{w}\frac{KK_{r,l}}{\mu_{w}}\frac{\partial p_{cap}}{\partial S_{w}}\frac{\partial S_{w}}{\partial z} + \rho_{w}\frac{KK_{r,l}}{\mu_{w}}\frac{\partial p_{cap}}{\partial T}\frac{\partial T}{\partial z} + \rho_{w}\frac{KK_{r,l}}{\mu_{w}}\rho g$$

$$-\rho_{v}\frac{KK_{r,v}}{\mu_{v}}\frac{\partial P}{\partial z} = -\frac{p_{v}}{R_{v}T}\frac{KK_{r,v}}{\mu_{v}}\frac{\partial P}{\partial z}$$

$$-\frac{C^{2}}{\rho}M_{a}M_{v}D_{eff,g}\frac{\partial X_{v}}{\partial z} = -\frac{M_{a}M_{v}D_{eff,g}}{R\left(\left(P - p_{v}\right)M_{a} + p_{v}M_{v}\right)}\left(P\frac{\partial p_{v}}{\partial S_{w}}\frac{\partial S_{w}}{\partial z} + P\frac{\partial p_{v}}{\partial T}\frac{\partial T}{\partial z} - p_{v}\frac{\partial P}{\partial z}\right)$$

The saturation boundary condition at the back face can now be written as

$$-K_{1}\frac{\partial S_{w}}{\partial z} - K_{2}\frac{\partial T}{\partial z} - K_{3}\frac{\partial P}{\partial z} + K_{19} = \dot{m}''_{\substack{evap\\loss\\back}} - \dot{m}''_{\substack{spray\\back}}$$

If the back face is sealed, a no flux boundary condition can be specified in the model by setting the back face evaporative mass flux and water spray mass flux equal to zero.

Pressure Boundary Conditions at Back Face

The air mass fluxes at the back face are shown in Figure 89.

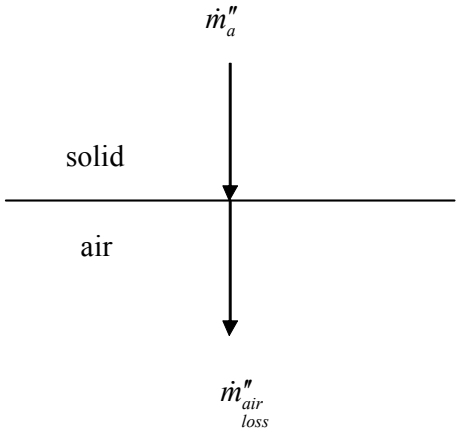

Figure 89 – Air Mass Fluxes at Back Face

Conservation of mass for the back face is expressed by summing the air fluxes into and out of the surface

$$\dot{m}''_a = \dot{m}''_{air\ loss}$$

The internal air flux term has convective and diffusive components

$$\dot{m}''_a = -\rho_a \frac{KK_{r,a}}{\mu_a} \nabla P - \frac{C^2}{\rho} M_v M_a D_{av} \nabla X_a$$

Expand these terms

$$\rho_a \frac{KK_{r,g}}{\mu_a}\frac{\partial P}{\partial z} = \frac{p_a}{R_a T}\frac{KK_{r,g}}{\mu_a}\frac{\partial P}{\partial z}$$

$$= \frac{P - p_v}{R_a T}\frac{KK_{r,g}}{\mu_a}\frac{\partial P}{\partial z}$$

$$\frac{C^2}{\rho} M_v M_a D_{eff,g}\frac{\partial X_a}{\partial z} = \left(\frac{P}{RT}\right)^2 \frac{1}{\frac{p_a}{R_a T} + \frac{p_v}{R_v T}} M_v M_a D_{eff,g}\frac{\partial}{\partial z}\left(\frac{p_a}{P}\right)$$

$$= \left(\frac{P}{RT}\right)^2 \frac{1}{\frac{p_a}{R_a T} + \frac{p_v}{R_v T}} M_v M_a D_{eff,g}\frac{\partial}{\partial z}\left(\frac{P - p_v}{P}\right)$$

$$= \frac{P^2}{RT\left(M_a\left(P - p_v\right) + M_v p_v\right)} M_v M_a D_{eff,g}\frac{\partial}{\partial z}\left(1 - \frac{p_v}{P}\right)$$

$$= -\frac{M_v M_a D_{eff,g}}{RT\left(M_a\left(P - p_v\right) + M_v p_v\right)}\left(P\frac{\partial p_v}{\partial z} - p_v\frac{\partial P}{\partial z}\right)$$

$$= -\frac{M_v M_a D_{eff,g}}{RT\left(M_a\left(P - p_v\right) + M_v p_v\right)}\left(P\frac{\partial p_v}{\partial S_w}\frac{\partial S_w}{\partial z} + P\frac{\partial p_v}{\partial T}\frac{\partial T}{\partial z} - p_v\frac{\partial P}{\partial z}\right)$$

Which can be written as

$$\dot{m}_a'' = -K_7\frac{\partial S_w}{\partial z} - K_8\frac{\partial T}{\partial z} - K_9\frac{\partial P}{\partial z}$$

So the boundary condition for conservation of air can be written as

$$-K_7\frac{\partial S_w}{\partial z} - K_8\frac{\partial T}{\partial z} - K_9\frac{\partial P}{\partial z} = \dot{m}_{\substack{air\\loss}}''$$

If the back face is assumed to be sealed, no flux boundary conditions can be applied to the model by setting $\dot{m}_{\substack{air\\loss}}''$ equal to zero. If the back face of the material is assumed to be open to the ambient environment, then a type 1 boundary condition can be used:

$$P = P_o \quad @ \;\; z = L$$

Temperature Boundary Conditions at Back Face

It is reasonable to assume that the material will act as a semi-infinite solid early in the simulation. This limits us to times before the heat and moisture reaches the back face of the material. The thermal boundary condition at the back face for this case is a type 1 boundary condition:

$$T = T_o \quad @ \; z = L$$

Later in the heating process, the back face will heat up and the material will no longer behave as a semi-infinite solid. This boundary condition is shown in Figure 90.

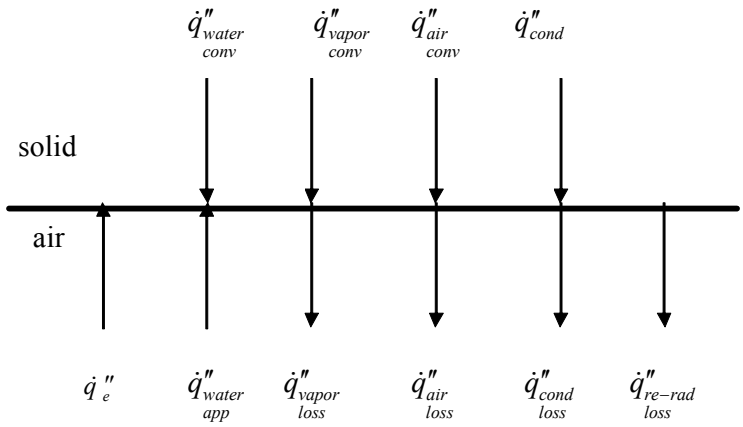

Figure 90 – Back Face Temperature Boundary Condition

This is a type 3 (convective) boundary condition:

$$\dot{q}''_{water,conv} + \dot{q}''_{vapor,conv} + \dot{q}''_{air,conv} + \dot{q}''_{cond} + \dot{q}''_{e} + \dot{q}''_{water,app} = \dot{q}''_{cond,loss} + \dot{q}''_{vapor,loss} + \dot{q}''_{air,loss} + \dot{q}''_{re-rad} \quad @ z = L \quad for \quad t > 0$$

Use conservation of mass for liquid and vapor phase water to eliminate terms. The water and vapor terms can be written as products of mass fluxes and enthalpies per unit mass

$$\dot{q}''_{water,conv} + \dot{q}''_{vapor,conv} + \dot{q}''_{water,spray} - \dot{q}''_{vapor,loss} = \dot{m}''_{water,conv} h_w + \dot{m}''_{vapor,conv} h_v + \dot{m}''_{water,spray} h_{water,spray} - \dot{m}''_{vapor,loss} h_v$$

The enthalpy of the spray can be written as

$$h_{\substack{water\\spray}} = h_f^o + \int_{T_o}^{T_w} C_{p,w}\partial T + \int_{T_w}^{T_{spray}} C_{p,w}\partial T$$

The enthalpies of the other mass fluxes are calculated at the back face surface temperature. The water and vapor terms can now be written as

$$\begin{aligned}
&\dot{m}''_{\substack{water\\conv}} h_w + \dot{m}''_{\substack{water\\spray}} h_w + \dot{m}''_{\substack{vapor\\conv}} h_v - \dot{m}''_{\substack{vapor\\loss}} h_v + \dot{m}''_{\substack{water\\spray}} C_{p,w}\left(T_{spray} - T_{surf}\right) \\
&= \left(\dot{m}''_{\substack{water\\conv}} + \dot{m}''_{\substack{water\\spray}}\right) h_w - \left(\dot{m}''_{\substack{vapor\\loss}} - \dot{m}''_{\substack{vapor\\conv}}\right) h_v + \dot{m}''_{\substack{water\\spray}} C_{p,w}\left(T_{spray} - T_{surf}\right) \\
&= \left(\dot{m}''_{\substack{evap\\back}}\right)\left(h_w - h_v\right) + \dot{m}''_{\substack{water\\spray}} C_{p,w}\left(T_{spray} - T_{surf}\right) \\
&= -\dot{m}''_{\substack{evap\\back}} \Delta h_v + \dot{m}''_{\substack{water\\spray}} C_{p,w}\left(T_{spray} - T_{surf}\right)
\end{aligned}$$

Where the enthalpies of the water and vapor fluxes are calculated at the back face temperature. Finally simplify the enthalpy flux terms associated with air

$$\begin{aligned}
\dot{q}''_{\substack{air\\loss}} - \dot{q}''_{\substack{air\\conv}} &= \dot{m}''_{\substack{air\\loss}} h_a - \dot{m}''_a h_a \\
&= \left(\dot{m}''_{\substack{air\\loss}} - \dot{m}''_a\right) h_a \\
&= 0
\end{aligned}$$

Where the enthalpy of the air fluxes is calculated at the back face temperature. This is an approximation, since the convective fluxes reaching the back face may have a slightly different temperature. This issue is addressed when the boundary conditions are discretized and solved. Thermal conduction in the material into the back face node is assumed to occur by Fourier's law through each component present. ψ represents the volumetric content of air, vapor, water, and solid material present.

$$\dot{q}''_{cond} = -\psi_a k_a \frac{\partial T_a}{\partial z} - \psi_v k_v \frac{\partial T_v}{\partial z} - \psi_w k_w \frac{\partial T_w}{\partial z} - \psi_s k_s \frac{\partial T_s}{\partial z}$$

The conductive losses to the ambient and re-radiative loss terms can be defined as

$$\dot{q}''_{\substack{cond \\ loss}} = h\left(T_{surf} - T_{\infty}\right)$$

$$\dot{q}''_{re-rad} = \varepsilon\sigma\left(T_{surf}^4 - T_{\infty}^4\right)$$

The conservation of energy for the surface node can now be written as

$$\dot{q}''_e + \dot{m}''_{spray} C_{p,w}\left(T_{spray} - T_{surface}\right) - h\left(T_s - T_{\infty}\right) - \varepsilon_s\sigma\left(T_s^4 - T_{\infty}^4\right)$$
$$-\psi_a k_a \frac{\partial T_a}{\partial z} - \psi_v k_v \frac{\partial T_v}{\partial z} - \psi_w k_w \frac{\partial T_w}{\partial z} - \psi_s k_s \frac{\partial T_s}{\partial z} - \Delta h_v \dot{m}''_{evap} = 0$$

Invoking the assumption of local thermal equilibrium allows this to be written as

$$\dot{q}''_e + \dot{m}''_{spray} C_{p,w}\left(T_{spray} - T_{surface}\right) - h\left(T_s - T_{\infty}\right) - \varepsilon_s\sigma\left(T_s^4 - T_{\infty}^4\right) - k_{eff}\frac{\partial T}{\partial z} - \Delta h_v \dot{m}''_{evap} = 0$$

Or in K notation as

$$-K_{14}\frac{\partial T}{\partial z} = -\dot{q}''_e - \dot{m}''_{spray} C_{p,w}\left(T_{spray} - T_{surface}\right) + h\left(T_s - T_{\infty}\right) + \varepsilon_s\sigma\left(T_s^4 - T_{\infty}^4\right) + \Delta h_v \dot{m}''_{evap}$$

C.2.3. Initial Conditions

The material will initially have known profiles of temperature, pressure, and saturation. In most cases the profile will assume a constant initial value.

$$T = T(z) = T_o \qquad @t = 0$$
$$S_w = S_w(z) = S_{w,o} \qquad @t = 0$$
$$P = P(z) = P_\infty \qquad @t = 0$$

C.3. Water Layer Model

If the water application rate is high, then a water layer will form on the surface of the material. This water layer will reflect and absorb some of the incident radiation and exchange heat with the solid by conduction. The energy balance on the water layer is shown in Figure 91.

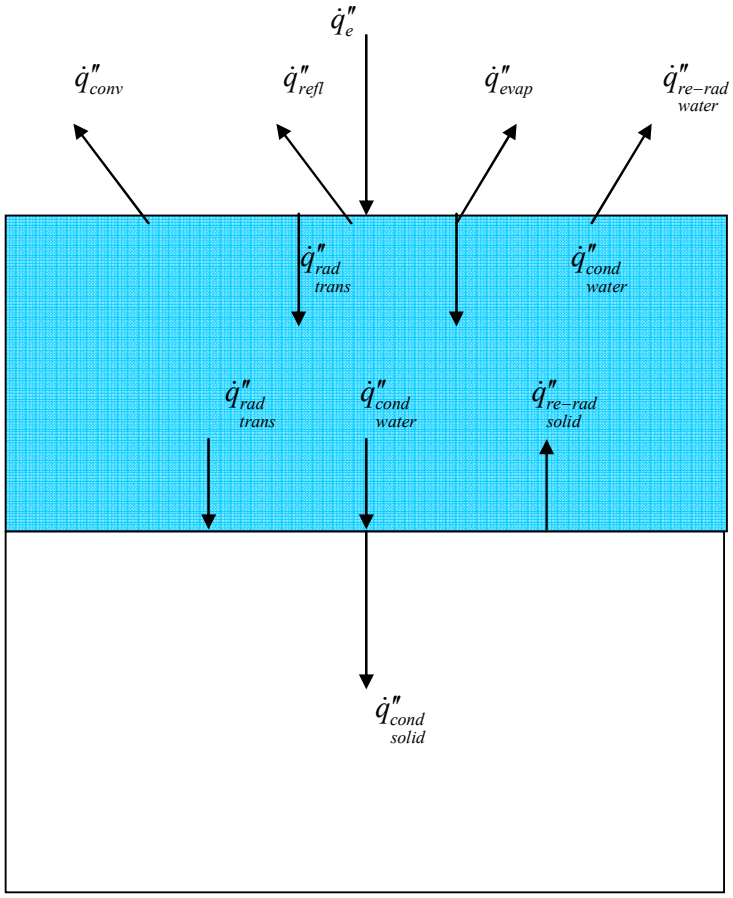

Figure 91 – Water Layer on Solid Exposed to External Heat Flux

The energy equation for an incompressible fluid with constant properties in rectangular coordinates is [102]

$$\rho C_p \frac{DT}{Dt} = k\nabla^2 T - \nabla \cdot \dot{q}''_{rad} + \dot{Q}''' + \Phi$$

If the water layer is unreacting and stationary the equation reduces to

$$\rho C_p \frac{\partial T}{\partial t} = k \frac{\partial^2 T}{\partial z^2} - \frac{\partial \dot{q}''_{rad}}{\partial z}$$

With the boundary conditions

$$\dot{q}''_e = \dot{q}''_{refl} + \dot{q}''_{conv} + \dot{q}''_{evap} + \dot{q}''_{\substack{rerad \\ water}} + \dot{q}''_{\substack{cond \\ water}} \quad @\ z = 0$$

$$k_w \frac{\partial T_w}{\partial z} + \dot{q}''_{\substack{rad \\ trans}} - \dot{q}''_{\substack{re-rad \\ solid}} = k_s \frac{\partial T_s}{\partial z} \qquad @ \quad z = solid\ \ surface$$

$$\dot{q}''_r = \dot{q}''_e \qquad @ \quad z = 0$$

The radiant heat flux that is transmitted through the material is

$$\dot{q}''_{rad}(z) = \int_{\lambda=0}^{\infty} i_\lambda(0) \exp(-a_\lambda z) \partial\lambda$$

The energy absorption per unit volume for a single wavelength can be described analytically by

$$\frac{\partial \dot{q}''_\lambda}{\partial z} = \frac{\partial i_\lambda(z)_\lambda}{\partial z} = i_\lambda(0) \exp(-a_\lambda z)(-a_\lambda)$$

So the total energy absorption is

$$\frac{\partial \dot{q}''_{rad}(z)}{\partial z} = \int_{\lambda=0}^{\infty} \frac{\partial i_\lambda(z)_\lambda}{\partial z} \cong \int_{\lambda=0}^{\infty} i_\lambda(0) \exp(-a_\lambda z)(-a_\lambda) \Delta\lambda$$

The re-radiation from the surface of the water will be

$$\dot{q}''_{\substack{re-rad \\ water}} = \varepsilon_w \sigma T^4_{surf}$$

For liquid water the emissivity is in the range of 0.92-0.96 for temperatures between 0-40 deg C [43]. Siegal and Howell [102] give a value of 0.96 for the temperature range 273-383K. The convective losses from the surface are simply

$$\dot{q}''_{conv} = h\left(T_{surf} - T_{\infty}\right)$$

The heat transfer coefficient is determined by calculating an average Nusselt number for a hot plate oriented horizontally facing upwards

$$\overline{Nu} = \frac{hL}{k}$$

For forced convection the Nusselt number is a function of the Reynolds number and Prandtl number [43]

$$\overline{Nu_x} = 0.664\,\mathrm{Pr}^{1/3}\,\mathrm{Re}_L^{1/2}$$

For free convection the Nusselt number is a function of the Rayleight number [43]

$$\overline{Nu}_L = 0.54 Ra_L^{1/4} \quad \left(10^4 < Ra_L < 10^7\right)$$

$$\overline{Nu}_L = 0.15 Ra_L^{1/3} \quad \left(10^7 < Ra_L < 10^9\right)$$

Where

$$Ra_L = \frac{g\beta L^3\left(T_{surf} - T_{\infty}\right)}{\alpha\nu}$$

The evaporative losses are

$$\dot{q}''_{evap} = \Delta h_v h_m \left(\rho_{v,surf} - \rho_{v,\infty}\right)$$

The mass transfer coefficient is calculated in an analogous fashion to the heat transfer coefficient. Instead of a Nusselt number, a Sherwood number must be calculated. For forced convection the Sherwood number is a function of the Schmidt number and Reynolds number

$$\overline{Sh_L} = 0.664 Sc^{1/3} \mathrm{Re}_L^{1/2}$$

The density of water vapor is determined by the partial pressure of the vapor.

$$\rho_v = \frac{p_v}{R_v T}$$

At the solid surface the air is saturated with vapor and the partial pressure is determined by the Claussius Clapeyron relation

$$p_v = \mathrm{P}_{ref} \exp\left(-\frac{L_v}{R_v}\left(\frac{1}{T_v} - \frac{1}{T_{ref}} \right) \right)$$

The partial pressure of vapor in the ambient air can be determined if the relative humidity is known. Relative humidity is the ratio of the partial pressure of vapor to the saturated vapor pressure as determined by the Claussius Clapeyron relation [47].

$$RH = \frac{p_{v,\infty}}{p_v}$$

The re-radiation from the solid surface can be shown to be very small, but will be included in the calculations for now. The solid surface will heat up and radiate heat through the water layer, but the radiation will be at larger wavelengths, since the surface will be at a lower temperature than the external heat source. This large wavelength radiation will fall into the high absorption region of the spectrum for water and will be more readily absorbed. Most of the radiation from the solid surface will be absorbed by the water immediately next to it. Since this water is included in the interface node, there is very little radiative loss. As an example consider a solid surface which behaves as a blackbody that is heated to 100 deg C. Assume that the grid spacing is 0.1mm thick. To calculate the radiation transmission, the absorption must be calculated over all wavelengths. Since data is only available for the absorption coefficient of water between 0.2 and 200 microns, radiation will be summed over this range which should be more than sufficient. The trapezoidal rule will be used for the

numerical integration. For example, the transmitted radiation through half of a 0.1mm cell of water is calculated as

$$\int_{\lambda=0}^{\infty} i_\lambda(0)\exp\left(-a_\lambda \cdot 0.5mm\right)\partial\lambda = 0.5\sum_{\lambda=0.2}^{200}\left(i_\lambda(0)\exp\left(-a_\lambda \cdot 0.5mm\right)+i_{\lambda+\Delta\lambda}(0)\exp\left(-a_{\lambda+\Delta\lambda}\cdot 0.5mm\right)\right)\Delta\lambda$$

So the transmissivity of the half node of water is calculated to be

$$\tau = \frac{\int_{\lambda=0}^{\infty} i_\lambda(0)\exp\left(-a_\lambda \cdot 0.5mm\right)\partial\lambda}{\int_{\lambda=0}^{\infty} i_\lambda(0)\partial\lambda}$$

$$\tau = \frac{0.5\sum_{\lambda=0.2}^{200}\left(i_\lambda(0)\exp\left(-a_\lambda \cdot 0.5mm\right)+i_{\lambda+\Delta\lambda}(0)\exp\left(-a_{\lambda+\Delta\lambda}\cdot 0.5mm\right)\right)\Delta\lambda}{\sum_{\lambda=0.2}^{200}\left(i_\lambda(0)+i_{\lambda+\Delta\lambda}(0)\right)\Delta\lambda} = 0.045$$

The radiation emitted from the solid surface is

$$\varepsilon_s\sigma T^4 = 1\left(5.67\times10^{-8}\frac{W}{m^2K^4}\right)\left(383K^4\right) = 1.2\frac{kW}{m^2}$$

and the transmitted radiation is

$$\dot{q}''_{trans} = \int_{\lambda=0}^{\infty} i_\lambda(0)\exp\left(-a_\lambda \cdot 0.5mm\right)\partial\lambda$$

$$\dot{q}''_{trans} = 0.5\sum_{\lambda=0.2}^{200}\left(i_\lambda(0)\exp\left(-a_\lambda \cdot 0.5mm\right)+i_{\lambda+\Delta\lambda}(0)\exp\left(-a_{\lambda+\Delta\lambda}\cdot 0.5mm\right)\right)\Delta\lambda = 54\frac{W}{m^2}$$

The transmitted radiation to the second node above the water-solid interface can also be calculated

$$\dot{q}''_{trans} = 0.5\sum_{\lambda=0.2}^{200}\left(i_\lambda(0)\exp\left(-a_\lambda \cdot 1.5mm\right)+i_{\lambda+\Delta\lambda}(0)\exp\left(-a_{\lambda+\Delta\lambda}\cdot 1.5mm\right)\right)\Delta\lambda = 3.5\frac{W}{m^2}$$

So even for the maximum possible interface node temperature and at a reasonable node spacing the, the radiation that is leaving the interface node is very small, and the

transmitted radiation past the next node is much smaller.

Summary of Boundary Conditions

Initial Conditions

$$S_w(z) = S_{w,o}$$
$$T(z) = T_o$$
$$P(z) = P$$

Front Face – Case 1: $\dot{m}''_{spray} < \dot{m}''_w + \dot{m}''_v + \dot{m}''_{\substack{evap \\ loss}}$

$$\left.\begin{aligned} &\dot{m}''_{spray} = \dot{m}''_{\substack{evap \\ loss}} + \dot{m}''_{water} + \dot{m}''_{vapor} \\ &\dot{q}''_e + \dot{q}''_{\substack{water \\ spray}} = \dot{q}''_{\substack{vapor \\ loss}} + \dot{q}''_{\substack{air \\ loss}} + \dot{q}''_{\substack{cond \\ loss}} + \dot{q}''_{\substack{re-rad \\ loss}} + \dot{q}''_{\substack{water \\ conv}} + \dot{q}''_{\substack{vapor \\ conv}} + \dot{q}''_{\substack{air \\ conv}} + \dot{q}''_{\substack{cond}} \\ &P = P_o \end{aligned}\right\} \quad @\, z = 0 \quad for \quad t > 0$$

or in K notation

$$@\, z = 0,\ for\ t > 0$$
$$-K_1 \frac{\partial S_w}{\partial z} - K_2 \frac{\partial T}{\partial z} - K_3 \frac{\partial P}{\partial z} + K_{19} = \dot{m}''_{spray} - \dot{m}''_{\substack{evap \\ loss}}$$
$$P_{surf} = P_\infty$$
$$-K_{14} \frac{\partial T}{\partial z} = \dot{q}''_e + \dot{m}''_{spray} C_{p,w} \left(T_{spray} - T_{surf}\right) - h\left(T_{surf} - T_\infty\right) - \varepsilon_s \sigma \left(T_{surf}^4 - T_\infty^4\right) - \Delta h_v \dot{m}''_{evap}$$

Front Face – Case 2: $\dot{m}''_{spray} > \dot{m}''_w + \dot{m}''_v + \dot{m}''_{\substack{evap \\ loss}}$

$$S_w = 1 \qquad @\, z < z_{\text{int}},\ t > 0$$
$$T = T_{surf} \qquad @\, z = 0,\quad t > 0$$
$$P = P_\infty + \rho_w g h_{layer} \qquad @\, z = 0\ \ t > 0$$

Back Face- Semi-Infinite Solid

$$\left.\begin{aligned} S_w &= S_{w,o} \\ T &= T_o \\ P &= P_o \end{aligned}\right\} @\ \ z = L$$

Back Face – Flux Conditions

$$\left.\begin{aligned} &\dot{m}''_{spray} + \dot{m}''_{v} + \dot{m}''_{w} = \dot{m}''_{\substack{evap \\ loss}} \\ &\dot{q}''_{\substack{water \\ conv}} + \dot{q}''_{\substack{vapor \\ conv}} + \dot{q}''_{\substack{air \\ conv}} + \dot{q}''_{cond} + \dot{q}''_{e} + \dot{q}''_{\substack{water \\ app}} = \dot{q}''_{\substack{cond \\ loss}} + \dot{q}''_{\substack{vapor \\ loss}} + \dot{q}''_{\substack{air \\ loss}} + \dot{q}''_{\substack{re-rad \\ loss}} \\ &P = P_o \quad or \quad \dot{m}''_{a} = 0 \end{aligned}\right\} \quad @\, z = L \quad for \quad t > 0$$

or in K notation

$$@\, z = L,\ for\ t > 0$$

$$-K_1 \frac{\partial S_w}{\partial z} - K_2 \frac{\partial T}{\partial z} - K_3 \frac{\partial P}{\partial z} + K_{19} = 0$$

$$-K_7 \frac{\partial S_w}{\partial z} - K_8 \frac{\partial T}{\partial z} - K_9 \frac{\partial P}{\partial z} = 0$$

$$-K_{14} \frac{\partial T}{\partial z} = 0$$

Appendix D. Model Solution Method

D.1. Discretize the Governing Equations

Now a discussion of the methods needed to solve the following three GEs

$$K_4\frac{\partial S_w}{\partial t}+K_5\frac{\partial T}{\partial t}+K_6\frac{\partial P}{\partial t}=\nabla\left(K_1\nabla S_w\right)+\nabla\left(K_2\nabla T\right)+\nabla\left(K_3\nabla P\right)-\nabla\left(K_{19}\right)$$

$$K_{10}\frac{\partial S_w}{\partial t}+K_{11}\frac{\partial T}{\partial t}+K_{12}\frac{\partial P}{\partial t}=\nabla\left(K_7\nabla S_w\right)+\nabla\left(K_8\nabla T\right)+\nabla\left(K_9\nabla P\right)$$

$$K_{16}\frac{\partial S_w}{\partial t}+K_{17}\frac{\partial T}{\partial t}+K_{18}\frac{\partial P}{\partial t}=-\left(C_{pv}\vec{n}_v+C_{pa}\vec{n}_a+C_{pv}\vec{n}_w\right)\nabla T+\nabla\left(K_{13}\nabla S_w\right)+\nabla\left(K_{14}\nabla T\right)+\nabla\left(K_{15}\nabla P\right)+\nabla\left(K_{20}\right)$$

subject to the boundary conditions discussed previously. Discretize the equations, starting with the first one. The LHS can be written as

$$K_4\frac{\partial S_w}{\partial t}+K_5\frac{\partial T}{\partial t}+K_6\frac{\partial P}{\partial t}\cong K4_i^{n+\frac{1}{2}}\frac{S_i^{n+1}-S_i^n}{\Delta t}+K5_i^{n+\frac{1}{2}}\frac{T_i^{n+1}-T_i^n}{\Delta t}+K6_i^{n+\frac{1}{2}}\frac{P_i^{n+1}-P_i^n}{\Delta t}$$

Note that to avoid confusion with the subscripts and finite difference index notation the w has been omitted from S_w and the subscripts of the K's are changed to full scripts. For the RHS,

$$\frac{\partial}{\partial z}\left(K_1\frac{\partial S}{\partial z}\right)+\frac{\partial}{\partial z}\left(K_2\frac{\partial T}{\partial z}\right)+\frac{\partial}{\partial z}\left(K_3\frac{\partial P}{\partial z}\right)\cong\frac{\partial}{\partial z}\left(K1^n_{i+\frac{1}{2}}\frac{S^n_{i+1}-S^n_i}{\Delta z}\right)+\frac{\partial}{\partial z}\left(K2^n_{i+\frac{1}{2}}\frac{T^n_{i+1}-T^n_i}{\Delta z}\right)+\frac{\partial}{\partial z}\left(K3^n_{i+\frac{1}{2}}\frac{P^n_{i+1}-P^n_i}{\Delta z}\right)$$

$$=\left(\frac{K1^n_{i+\frac{1}{2}}\frac{S^n_{i+1}-S^n_i}{\Delta z}-K1^n_{i-\frac{1}{2}}\frac{S^n_i-S^n_{i-1}}{\Delta z}}{\Delta z}\right)+\left(\frac{K2^n_{i+\frac{1}{2}}\frac{T^n_{i+1}-T^n_i}{\Delta z}-K2^n_{i-\frac{1}{2}}\frac{T^n_i-T^n_{i-1}}{\Delta z}}{\Delta z}\right)+\left(\frac{K3^n_{i+\frac{1}{2}}\frac{P^n_{i+1}-P^n_i}{\Delta z}-K3^n_{i-\frac{1}{2}}\frac{P^n_i-P^n_{i-1}}{\Delta z}}{\Delta z}\right)$$

$$-\frac{K19^n_{i+1}-K19^n_{i-1}}{2\Delta z}$$

$$=\frac{1}{\Delta z^2}\left[\begin{array}{l}\left(K1^n_{i+\frac{1}{2}}S^n_{i+1}-\left(K1^n_{i+\frac{1}{2}}+K1^n_{i-\frac{1}{2}}\right)S^n_i+K1^n_{i-\frac{1}{2}}S^n_{i-1}\right)\\+\left(K2^n_{i+\frac{1}{2}}T^n_{i+1}-\left(K2^n_{i+\frac{1}{2}}+K2^n_{i-\frac{1}{2}}\right)T^n_i+K2^n_{i-\frac{1}{2}}T^n_{i-1}\right)\\+\left(K3^n_{i+\frac{1}{2}}P^n_{i+1}-\left(K3^n_{i+\frac{1}{2}}+K3^n_{i-\frac{1}{2}}\right)P^n_i+K3^n_{i-\frac{1}{2}}P^n_{i-1}\right)\end{array}\right]-\frac{K19^n_{i+1}-K19^n_{i-1}}{2\Delta z}$$

For an implicit solution, which could provide better stability, the RHS can be written as

$$\frac{\partial}{\partial z}\left(K_1\frac{\partial S}{\partial z}\right)+\frac{\partial}{\partial z}\left(K_2\frac{\partial T}{\partial z}\right)+\frac{\partial}{\partial z}\left(K_3\frac{\partial P}{\partial z}\right)\cong$$

$$\frac{\theta}{\Delta z^2}\left[\begin{array}{l}\left(K1^{n+1}_{i+\frac{1}{2}}S^{n+1}_{i+1}-\left(K1^{n+1}_{i+\frac{1}{2}}+K1^{n+1}_{i-\frac{1}{2}}\right)S^{n+1}_i+K1^{n+1}_{i-\frac{1}{2}}S^{n+1}_{i-1}\right)\\+\left(K2^{n+1}_{i+\frac{1}{2}}T^{n+1}_{i+1}-\left(K2^{n+1}_{i+\frac{1}{2}}+K2^{n+1}_{i-\frac{1}{2}}\right)T^{n+1}_i+K2^{n+1}_{i-\frac{1}{2}}T^{n+1}_{i-1}\right)\\+\left(K3^{n+1}_{i+\frac{1}{2}}P^{n+1}_{i+1}-\left(K3^{n+1}_{i+\frac{1}{2}}+K3^{n+1}_{i-\frac{1}{2}}\right)P^{n+1}_i+K3^{n+1}_{i-\frac{1}{2}}P^{n+1}_{i-1}\right)\end{array}\right]-\theta\frac{K19^{n+1}_{i+1}-K19^{n+1}_{i-1}}{2\Delta z}$$

$$+\frac{(1-\theta)}{\Delta z^2}\left[\begin{array}{l}\left(K1^n_{i+\frac{1}{2}}S^n_{i+1}-\left(K1^n_{i+\frac{1}{2}}+K1^n_{i-\frac{1}{2}}\right)S^n_i+K1^n_{i-\frac{1}{2}}S^n_{i-1}\right)\\+\left(K2^n_{i+\frac{1}{2}}T^n_{i+1}-\left(K2^n_{i+\frac{1}{2}}+K2^n_{i-\frac{1}{2}}\right)T^n_i+K2^n_{i-\frac{1}{2}}T^n_{i-1}\right)\\+\left(K3^n_{i+\frac{1}{2}}P^n_{i+1}-\left(K3^n_{i+\frac{1}{2}}+K3^n_{i-\frac{1}{2}}\right)P^n_i+K3^n_{i-\frac{1}{2}}P^n_{i-1}\right)\end{array}\right]-(1-\theta)\frac{K19^n_{i+1}-K19^n_{i-1}}{2\Delta z}$$

Where the type of scheme depends on the value of theta

$\theta = 0$ Fully Explicit

$\theta = \frac{1}{2}$ Crank-Nicholson

$\theta = 1$ Fully Implicit

So the first equation can now be written as

$$K4_i^{n+\frac{1}{2}} \frac{S_i^{n+1} - S_i^n}{\Delta t} + K5_i^{n+\frac{1}{2}} \frac{T_i^{n+1} - T_i^n}{\Delta t} + K6_i^{n+\frac{1}{2}} \frac{P_i^{n+1} - P_i^n}{\Delta t}$$

$$= \frac{\theta}{\Delta z^2} \left[\begin{array}{l} \left(K1_{i+\frac{1}{2}}^{n+1} S_{i+1}^{n+1} - \left(K1_{i+\frac{1}{2}}^{n+1} + K1_{i-\frac{1}{2}}^{n+1} \right) S_i^{n+1} + K1_{i-\frac{1}{2}}^{n+1} S_{i-1}^{n+1} \right) \\ + \left(K2_{i+\frac{1}{2}}^{n+1} T_{i+1}^{n+1} - \left(K2_{i+\frac{1}{2}}^{n+1} + K2_{i-\frac{1}{2}}^{n+1} \right) T_i^{n+1} + K2_{i-\frac{1}{2}}^{n+1} T_{i-1}^{n+1} \right) \\ + \left(K3_{i+\frac{1}{2}}^{n+1} P_{i+1}^{n+1} - \left(K3_{i+\frac{1}{2}}^{n+1} + K3_{i-\frac{1}{2}}^{n+1} \right) P_i^{n+1} + K3_{i-\frac{1}{2}}^{n+1} P_{i-1}^{n+1} \right) \end{array} \right] - \theta \frac{K19_{i+1}^{n+1} - K19_{i-1}^{n+1}}{2\Delta z}$$

$$+ \frac{(1-\theta)}{\Delta z^2} \left[\begin{array}{l} \left(K1_{i+\frac{1}{2}}^{n} S_{i+1}^{n} - \left(K1_{i+\frac{1}{2}}^{n} + K1_{i-\frac{1}{2}}^{n} \right) S_i^{n} + K1_{i-\frac{1}{2}}^{n} S_{i-1}^{n} \right) \\ + \left(K2_{i+\frac{1}{2}}^{n} T_{i+1}^{n} - \left(K2_{i+\frac{1}{2}}^{n} + K2_{i-\frac{1}{2}}^{n} \right) T_i^{n} + K2_{i-\frac{1}{2}}^{n} T_{i-1}^{n} \right) \\ + \left(K3_{i+\frac{1}{2}}^{n} P_{i+1}^{n} - \left(K3_{i+\frac{1}{2}}^{n} + K3_{i-\frac{1}{2}}^{n} \right) P_i^{n} + K3_{i-\frac{1}{2}}^{n} P_{i-1}^{n} \right) \end{array} \right] - (1-\theta) \frac{K19_{i+1}^{n} - K19_{i-1}^{n}}{2\Delta z}$$

and after rearranging, it can be written in the form

$$\left(-\frac{\theta\Delta t}{\Delta z^2}K1^{n+1}_{i-\frac{1}{2}}\right)S^{n+1}_{i-1}+\left(-\frac{\theta\Delta t}{\Delta z^2}K2^{n+1}_{i-\frac{1}{2}}\right)T^{n+1}_{i-1}+\left(-\frac{\theta\Delta t}{\Delta z^2}K3^{n+1}_{i-\frac{1}{2}}\right)P^{n+1}_{i-1}$$
$$+\left(K4_i^{n+\frac{1}{2}}+\frac{\theta\Delta t}{\Delta z^2}\left(K1^{n+1}_{i+\frac{1}{2}}+K1^{n+1}_{i-\frac{1}{2}}\right)\right)S^{n+1}_i+\left(K5_i^{n+\frac{1}{2}}+\frac{\theta\Delta t}{\Delta z^2}\left(K2^{n+1}_{i+\frac{1}{2}}+K2^{n+1}_{i-\frac{1}{2}}\right)\right)T^{n+1}_i$$
$$+\left(K6_i^{n+\frac{1}{2}}+\frac{\theta\Delta t}{\Delta z^2}\left(K3^{n+1}_{i+\frac{1}{2}}+K3^{n+1}_{i-\frac{1}{2}}\right)\right)P^{n+1}_i$$
$$\left(-\frac{\theta\Delta t}{\Delta z^2}K1^{n+1}_{i+\frac{1}{2}}\right)S^{n+1}_{i+1}+\left(-\frac{\theta\Delta t}{\Delta z^2}K2^{n+1}_{i+\frac{1}{2}}\right)T^{n+1}_{i+1}+\left(-\frac{\theta\Delta t}{\Delta z^2}K3^{n+1}_{i+\frac{1}{2}}\right)P^{n+1}_{i+1}$$
$$=\left(\frac{(1-\theta)\Delta t}{\Delta z^2}K1^{n}_{i-\frac{1}{2}}\right)S^{n}_{i-1}+\left(\frac{(1-\theta)\Delta t}{\Delta z^2}K2^{n}_{i-\frac{1}{2}}\right)T^{n}_{i-1}+\left(\frac{(1-\theta)\Delta t}{\Delta z^2}K3^{n}_{i-\frac{1}{2}}\right)P^{n}_{i-1}$$
$$+\left(K4_i^{n+\frac{1}{2}}-\frac{(1-\theta)\Delta t}{\Delta z^2}\left(K1^{n}_{i+\frac{1}{2}}+K1^{n}_{i-\frac{1}{2}}\right)\right)S^{n}_i++\left(K5_i^{n+\frac{1}{2}}-\frac{(1-\theta)\Delta t}{\Delta z^2}\left(K2^{n}_{i+\frac{1}{2}}+K2^{n}_{i-\frac{1}{2}}\right)\right)T^{n}_i$$
$$+\left(K6_i^{n+\frac{1}{2}}-\frac{(1-\theta)\Delta t}{\Delta z^2}\left(K3^{n}_{i+\frac{1}{2}}+K3^{n}_{i-\frac{1}{2}}\right)\right)P^{n}_i$$
$$\left(\frac{(1-\theta)\Delta t}{\Delta z^2}K1^{n}_{i+\frac{1}{2}}\right)S^{n}_{i+1}+\left(\frac{(1-\theta)\Delta t}{\Delta z^2}K2^{n}_{i+\frac{1}{2}}\right)T^{n}_{i+1}+\left(\frac{(1-\theta)\Delta t}{\Delta z^2}K3^{n}_{i+\frac{1}{2}}\right)P^{n}_{i+1}$$
$$-\left[\theta\Delta t\frac{K19^{n+1}_{i+1}-K19^{n+1}_{i-1}}{2\Delta z}+(1-\theta)\Delta t\frac{K19^{n}_{i+1}-K19^{n}_{i-1}}{2\Delta z}\right]$$

Which is equivalent to

$$\begin{bmatrix}C_1 & C_2 & C_3 & C_4 & C_5 & C_6 & C_7 & C_8 & C_9\end{bmatrix}\begin{bmatrix}S^{n+1}_{i-1}\\T^{n+1}_{i-1}\\P^{n+1}_{i-1}\\S^{n+1}_{i}\\T^{n+1}_{i}\\P^{n+1}_{i}\\S^{n+1}_{i+1}\\T^{n+1}_{i+1}\\P^{n+1}_{i+1}\end{bmatrix}=\begin{bmatrix}RHS_1\\RHS_2\\RHS_3\end{bmatrix}$$

Where C_1 – C_9 are the coefficients which contain K_1 –K_6, θ, Δz , and Δt. Perform the same operations on the other two equations. Discretize the second equation as

$$K10_i^{n+\frac{1}{2}}\frac{S_i^{n+1}-S_i^n}{\Delta t}+K11_i^{n+\frac{1}{2}}\frac{T_i^{n+1}-T_i^n}{\Delta t}+K12_i^{n+\frac{1}{2}}\frac{P_i^{n+1}-P_i^n}{\Delta t}$$

$$=\frac{\theta}{\Delta z^2}\left[\begin{array}{l}\left(K7_{i+\frac{1}{2}}^{n+1}S_{i+1}^{n+1}-\left(K7_{i+\frac{1}{2}}^{n+1}+K7_{i-\frac{1}{2}}^{n+1}\right)S_i^{n+1}+K7_{i-\frac{1}{2}}^{n+1}S_{i-1}^{n+1}\right)\\+\left(K8_{i+\frac{1}{2}}^{n+1}T_{i+1}^{n+1}-\left(K8_{i+\frac{1}{2}}^{n+1}+K8_{i-\frac{1}{2}}^{n+1}\right)T_i^{n+1}+K8_{i-\frac{1}{2}}^{n+1}T_{i-1}^{n+1}\right)\\+\left(K9_{i+\frac{1}{2}}^{n+1}P_{i+1}^{n+1}-\left(K9_{i+\frac{1}{2}}^{n+1}+K9_{i-\frac{1}{2}}^{n+1}\right)P_i^{n+1}+K9_{i-\frac{1}{2}}^{n+1}P_{i-1}^{n+1}\right)\end{array}\right]$$

$$\frac{(1-\theta)}{\Delta z^2}\left[\begin{array}{l}\left(K7_{i+\frac{1}{2}}^{n}S_{i+1}^{n}-\left(K7_{i+\frac{1}{2}}^{n}+K7_{i-\frac{1}{2}}^{n}\right)S_i^{n}+K7_{i-\frac{1}{2}}^{n}S_{i-1}^{n}\right)\\+\left(K8_{i+\frac{1}{2}}^{n}T_{i+1}^{n}-\left(K8_{i+\frac{1}{2}}^{n}+K8_{i-\frac{1}{2}}^{n}\right)T_i^{n}+K8_{i-\frac{1}{2}}^{n}T_{i-1}^{n}\right)\\+\left(K9_{i+\frac{1}{2}}^{n}P_{i+1}^{n}-\left(K9_{i+\frac{1}{2}}^{n}+K9_{i-\frac{1}{2}}^{n}\right)P_i^{n}+K9_{i-\frac{1}{2}}^{n}P_{i-1}^{n}\right)\end{array}\right]$$

Rearrange the second equation

$$\left(-\frac{\theta\Delta t}{\Delta z^2}K7^{n+1}_{i-\frac{1}{2}}\right)S^{n+1}_{i-1}+\left(-\frac{\theta\Delta t}{\Delta z^2}K8^{n+1}_{i-\frac{1}{2}}\right)T^{n+1}_{i-1}+\left(-\frac{\theta\Delta t}{\Delta z^2}K9^{n+1}_{i-\frac{1}{2}}\right)P^{n+1}_{i-1}$$
$$+\left(K10_i^{n+\frac{1}{2}}+\frac{\theta\Delta t}{\Delta z^2}\left(K7^{n+1}_{i+\frac{1}{2}}+K7^{n+1}_{i-\frac{1}{2}}\right)\right)S^{n+1}_{i}+\left(K11_i^{n+\frac{1}{2}}+\frac{\theta\Delta t}{\Delta z^2}\left(K8^{n+1}_{i+\frac{1}{2}}+K8^{n+1}_{i-\frac{1}{2}}\right)\right)T^{n+1}_{i}$$
$$+\left(K12_i^{n+\frac{1}{2}}+\frac{\theta\Delta t}{\Delta z^2}\left(K9^{n+1}_{i+\frac{1}{2}}+K9^{n+1}_{i-\frac{1}{2}}\right)\right)P^{n+1}_{i}$$
$$\left(-\frac{\theta\Delta t}{\Delta z^2}K7^{n+1}_{i+\frac{1}{2}}\right)S^{n+1}_{i+1}++\left(-\frac{\theta\Delta t}{\Delta z^2}K8^{n+1}_{i+\frac{1}{2}}\right)T^{n+1}_{i+1}+\left(-\frac{\theta\Delta t}{\Delta z^2}K9^{n+1}_{i+\frac{1}{2}}\right)P^{n+1}_{i+1}$$
$$=\left(\frac{(1-\theta)\Delta t}{\Delta z^2}K7^{n}_{i-\frac{1}{2}}\right)S^{n}_{i-1}+\left(\frac{(1-\theta)\Delta t}{\Delta z^2}K8^{n}_{i-\frac{1}{2}}\right)T^{n}_{i-1}+\left(\frac{(1-\theta)\Delta t}{\Delta z^2}K9^{n}_{i-\frac{1}{2}}\right)P^{n}_{i-1}$$
$$+\left(K10_i^{n+\frac{1}{2}}-\frac{(1-\theta)\Delta t}{\Delta z^2}\left(K7^{n}_{i+\frac{1}{2}}+K7^{n}_{i-\frac{1}{2}}\right)\right)S^{n}_{i}+\left(K11_i^{n+\frac{1}{2}}-\frac{(1-\theta)\Delta t}{\Delta z^2}\left(K8^{n}_{i+\frac{1}{2}}+K8^{n}_{i-\frac{1}{2}}\right)\right)T^{n}_{i}$$
$$+\left(K12_i^{n+\frac{1}{2}}-\frac{(1-\theta)\Delta t}{\Delta z^2}\left(K9^{n}_{i+\frac{1}{2}}+K9^{n}_{i-\frac{1}{2}}\right)\right)P^{n}_{i}$$
$$+\left(\frac{(1-\theta)\Delta t}{\Delta z^2}K7^{n}_{i+\frac{1}{2}}\right)S^{n}_{i+1}+\left(\frac{(1-\theta)\Delta t}{\Delta z^2}K8^{n}_{i+\frac{1}{2}}\right)T^{n}_{i+1}+\left(\frac{(1-\theta)\Delta t}{\Delta z^2}K9^{n}_{i+\frac{1}{2}}\right)P^{n}_{i+1}$$

Discretize the third equation

$$K16_i^{n+\frac{1}{2}}\frac{S_i^{n+1}-S_i^n}{\Delta t}+K17_i^{n+\frac{1}{2}}\frac{T_i^{n+1}-T_i^n}{\Delta t}+K18_i^{n+\frac{1}{2}}\frac{P_i^{n+1}-P_i^n}{\Delta t}$$

$$=-\left(C_{pv}\vec{n}_v+C_{pa}\vec{n}_a+C_{pv}\vec{n}_w\right)_i^n\frac{T_{i+1}^n-T_{i-1}^n}{2\Delta z}$$

$$+\frac{\theta}{\Delta z^2}\left[\begin{array}{l}\left(K13_{i+\frac{1}{2}}^{n+1}S_{i+1}^{n+1}-\left(K13_{i+\frac{1}{2}}^{n+1}+K13_{i-\frac{1}{2}}^{n+1}\right)S_i^{n+1}+K13_{i-\frac{1}{2}}^{n+1}S_{i-1}^{n+1}\right)\\+\left(K14_{i+\frac{1}{2}}^{n+1}T_{i+1}^{n+1}-\left(K14_{i+\frac{1}{2}}^{n+1}+K14_{i-\frac{1}{2}}^{n+1}\right)T_i^{n+1}+K14_{i-\frac{1}{2}}^{n+1}T_{i-1}^{n+1}\right)\\+\left(K15_{i+\frac{1}{2}}^{n+1}P_{i+1}^{n+1}-\left(K15_{i+\frac{1}{2}}^{n+1}+K15_{i-\frac{1}{2}}^{n+1}\right)P_i^{n+1}+K15_{i-\frac{1}{2}}^{n+1}P_{i-1}^{n+1}\right)\end{array}\right]+\theta\frac{K20_{i+1}^{n+1}-K20_{i-1}^{n+1}}{2\Delta z}$$

$$\frac{(1-\theta)}{\Delta z^2}\left[\begin{array}{l}\left(K13_{i+\frac{1}{2}}^{n}S_{i+1}^{n}-\left(K13_{i+\frac{1}{2}}^{n}+K13_{i-\frac{1}{2}}^{n}\right)S_i^{n}+K13_{i-\frac{1}{2}}^{n}S_{i-1}^{n}\right)\\+\left(K14_{i+\frac{1}{2}}^{n}T_{i+1}^{n}-\left(K14_{i+\frac{1}{2}}^{n}+K14_{i-\frac{1}{2}}^{n}\right)T_i^{n}+K14_{i-\frac{1}{2}}^{n}T_{i-1}^{n}\right)\\+\left(K15_{i+\frac{1}{2}}^{n}P_{i+1}^{n}-\left(K15_{i+\frac{1}{2}}^{n}+K15_{i-\frac{1}{2}}^{n}\right)P_i^{n}+K15_{i-\frac{1}{2}}^{n}P_{i-1}^{n}\right)\end{array}\right]+(1-\theta)\frac{K20_{i+1}^{n}-K20_{i-1}^{n}}{2\Delta z}$$

Rearrange the third equation and write as

$$\left(-\frac{\theta\Delta t}{\Delta z^2}K13^{n+1}_{i-\frac{1}{2}}\right)S^{n+1}_{i-1}+\left(-\frac{\theta\Delta t}{\Delta z^2}K14^{n+1}_{i-\frac{1}{2}}\right)T^{n+1}_{i-1}+\left(-\frac{\theta\Delta t}{\Delta z^2}K15^{n+1}_{i-\frac{1}{2}}\right)P^{n+1}_{i-1}$$
$$+\left(K16_i^{n+\frac{1}{2}}+\frac{\theta\Delta t}{\Delta z^2}\left(K13^{n+1}_{i+\frac{1}{2}}+K13^{n+1}_{i-\frac{1}{2}}\right)\right)S^{n+1}_{i}+\left(K17_i^{n+\frac{1}{2}}+\frac{\theta\Delta t}{\Delta z^2}\left(K14^{n+1}_{i+\frac{1}{2}}+K14^{n+1}_{i-\frac{1}{2}}\right)\right)T^{n+1}_{i}$$
$$+\left(K18_i^{n+\frac{1}{2}}+\frac{\theta\Delta t}{\Delta z^2}\left(K15^{n+1}_{i+\frac{1}{2}}+K15^{n+1}_{i-\frac{1}{2}}\right)\right)P^{n+1}_{i}$$
$$+\left(-\frac{\theta\Delta t}{\Delta z^2}K13^{n+1}_{i+\frac{1}{2}}\right)S^{n+1}_{i+1}+\left(-\frac{\theta\Delta t}{\Delta z^2}K14^{n+1}_{i+\frac{1}{2}}\right)T^{n+1}_{i+1}+\left(-\frac{\theta\Delta t}{\Delta z^2}K15^{n+1}_{i+\frac{1}{2}}\right)P^{n+1}_{i+1}$$
$$=\left(\frac{(1-\theta)\Delta t}{\Delta z^2}K13^{n}_{i-\frac{1}{2}}\right)S^{n}_{i-1}+\left(\frac{\Delta t\left(C_{pv}\vec{n}_v+C_{pa}\vec{n}_a+C_{pv}\vec{n}_w\right)^n_i}{2\Delta z}+\frac{(1-\theta)\Delta t}{\Delta z^2}K14^{n}_{i-\frac{1}{2}}\right)T^{n}_{i-1}+\left(\frac{(1-\theta)\Delta t}{\Delta z^2}K15^{n}_{i-\frac{1}{2}}\right)P^{n}_{i-1}$$
$$+\left(K16_i^{n+\frac{1}{2}}-\frac{(1-\theta)\Delta t}{\Delta z^2}\left(K13^{n}_{i+\frac{1}{2}}+K13^{n}_{i-\frac{1}{2}}\right)\right)S^{n}_{i}+\left(K17_i^{n+\frac{1}{2}}-\frac{(1-\theta)\Delta t}{\Delta z^2}\left(K14^{n}_{i+\frac{1}{2}}+K14^{n}_{i-\frac{1}{2}}\right)\right)T^{n}_{i}$$
$$+\left(K18_i^{n+\frac{1}{2}}-\frac{(1-\theta)\Delta t}{\Delta z^2}\left(K15^{n}_{i+\frac{1}{2}}+K15^{n}_{i-\frac{1}{2}}\right)\right)P^{n}_{i}$$
$$+\left(\frac{(1-\theta)\Delta t}{\Delta z^2}K13^{n}_{i+\frac{1}{2}}\right)S^{n}_{i+1}+\left(-\frac{\Delta t\left(C_{pv}\vec{n}_v+C_{pa}\vec{n}_a+C_{pv}\vec{n}_w\right)^n_i}{2\Delta z}+\frac{(1-\theta)\Delta t}{\Delta z^2}K14^{n}_{i+\frac{1}{2}}\right)T^{n}_{i+1}+\left(\frac{(1-\theta)\Delta t}{\Delta z^2}K15^{n}_{i+\frac{1}{2}}\right)P^{n}_{i+1}$$
$$+\left[\theta\Delta t\frac{K20^{n+1}_{i+1}-K20^{n+1}_{i-1}}{2\Delta z}+(1-\theta)\Delta t\frac{K20^{n}_{i+1}-K20^{n}_{i-1}}{2\Delta z}\right]$$

The three equations can now be written in the form

$$[C][B]=[RHS]$$

Where

$[C]=3N\times 3N$ *coefficient matrix*

$[B]=3N\times 1$ *dependant* var*iable matrix*

$[RHS]=3N\times 1$ *right hand side matrix*

$$[C] = \begin{bmatrix}
 & & & & \cdots & & & & & \\
 & & & & \cdots & & & & & \\
 & & & & \cdots & & & & & \\
 & & & & \cdots & & & & & \\
\cdots & C_{3i-2,3i-5} & C_{3i-2,3i-4} & C_{3i-2,3i-3} & C_{3i-2,3i-2} & C_{3i-2,3i-1} & C_{3i-2,3i} & C_{3i-2,3i+1} & C_{3i-2,3i+2} & C_{3i-2,3i+3} & \cdots \\
\cdots & C_{3i-1,3i-5} & C_{3i-1,3i-4} & C_{3i-1,3i-3} & C_{3i-1,3i-2} & C_{3i-1,3i-1} & C_{3i-1,3i} & C_{3i-1,3i+1} & C_{3i-1,3i+2} & C_{3i-1,3i+3} & \cdots \\
\cdots & C_{3i,3i-5} & C_{3i,3i-4} & C_{3i,3i-3} & C_{3i,3i-2} & C_{3i,3i-1} & C_{3i,3i} & C_{3i,3i+1} & C_{3i,3i+2} & C_{3i,3i+3} & \cdots \\
 & & & & \cdots & & & & & \\
 & & & & \cdots & & & & & \\
 & & & & \cdots & & & & & \\
 & & & & \cdots & & & & &
\end{bmatrix}$$

$$[B] = \begin{bmatrix}
\cdots \\
B_{3i-5} = S_{i-1}^{n+1} \\
B_{3i-4} = T_{i-1}^{n+1} \\
B_{3i-3} = P_{i-1}^{n+1} \\
B_{3i-2} = S_{i}^{n+1} \\
B_{3i-1} = T_{i}^{n+1} \\
B_{3i} = P_{i}^{n+1} \\
B_{3i+1} = S_{i+1}^{n+1} \\
B_{3i+2} = T_{i+1}^{n+1} \\
B_{3i+3} = P_{i+1}^{n+1} \\
\cdots
\end{bmatrix} \qquad [RHS] = \begin{bmatrix}
RHS_1 \\
RHS_2 \\
RHS_3 \\
\cdots \\
RHS_{3i-2} \\
RHS_{3i-1} \\
RHS_{3i} \\
\cdots \\
RHS_{3N-2} \\
RHS_{3N-1} \\
RHS_{3N}
\end{bmatrix}$$

Where the coefficient matrix is

$$C_{3i-2,3i-5} = -\frac{\theta\Delta t}{\Delta z^2} K1^{n+1}_{i-\frac{1}{2}}$$

$$C_{3i-2,3i-4} = -\frac{\theta\Delta t}{\Delta z^2} K2^{n+1}_{i-\frac{1}{2}}$$

$$C_{3i-2,3i-3} = -\frac{\theta\Delta t}{\Delta z^2} K3^{n+1}_{i-\frac{1}{2}}$$

$$C_{3i-2,3i-2} = K4_i^{n+\frac{1}{2}} + \frac{\theta\Delta t}{\Delta z^2}\left(K1^{n+1}_{i+\frac{1}{2}} + K1^{n+1}_{i-\frac{1}{2}} \right)$$

$$C_{3i-2,3i-1} = K5_i^{n+\frac{1}{2}} + \frac{\theta\Delta t}{\Delta z^2}\left(K2^{n+1}_{i+\frac{1}{2}} + K2^{n+1}_{i-\frac{1}{2}} \right)$$

$$C_{3i-2,3i} = K6_i^{n+\frac{1}{2}} + \frac{\theta\Delta t}{\Delta z^2}\left(K3^{n+1}_{i+\frac{1}{2}} + K3^{n+1}_{i-\frac{1}{2}} \right)$$

$$C_{3i-2,3i+1} = -\frac{\theta\Delta t}{\Delta z^2} K1^{n+1}_{i+\frac{1}{2}}$$

$$C_{3i-2,3i+2} = -\frac{\theta\Delta t}{\Delta z^2} K2^{n+1}_{i+\frac{1}{2}}$$

$$C_{3i-2,3i+3} = -\frac{\theta\Delta t}{\Delta z^2} K3^{n+1}_{i+\frac{1}{2}}$$

$$C_{3i-1,3i-5} = -\frac{\theta\Delta t}{\Delta z^2} K7^{n+1}_{i-\frac{1}{2}}$$

$$C_{3i-1,3i-4} = -\frac{\theta\Delta t}{\Delta z^2} K8^{n+1}_{i-\frac{1}{2}}$$

$$C_{3i-1,3i-3} = -\frac{\theta\Delta t}{\Delta z^2} K9^{n+1}_{i-\frac{1}{2}}$$

$$C_{3i-1,3i-2} = K10_i^{n+\frac{1}{2}} + \frac{\theta\Delta t}{\Delta z^2}\left(K7^{n+1}_{i+\frac{1}{2}} + K7^{n+1}_{i-\frac{1}{2}} \right)$$

$$C_{3i-1,3i-1} = K11_i^{n+\frac{1}{2}} + \frac{\theta\Delta t}{\Delta z^2}\left(K8^{n+1}_{i+\frac{1}{2}} + K8^{n+1}_{i-\frac{1}{2}} \right)$$

$$C_{3i-1,3i} = K12_i^{n+\frac{1}{2}} + \frac{\theta\Delta t}{\Delta z^2}\left(K9^{n+1}_{i+\frac{1}{2}} + K9^{n+1}_{i-\frac{1}{2}} \right)$$

$$C_{3i-1,3i+1} = -\frac{\theta\Delta t}{\Delta z^2} K7^{n+1}_{i+\frac{1}{2}}$$

$$C_{3i-1,3i+2} = -\frac{\theta\Delta t}{\Delta z^2} K8^{n+1}_{i+\frac{1}{2}}$$

$$C_{3i-1,3i+3} = -\frac{\theta\Delta t}{\Delta z^2} K9^{n+1}_{i+\frac{1}{2}}$$

$$C_{3i,3i-5} = -\frac{\theta\Delta t}{\Delta z^2} K13^{n+1}_{i-\frac{1}{2}}$$

$$C_{3i,3i-4} = -\frac{\theta\Delta t}{\Delta z^2} K14^{n+1}_{i-\frac{1}{2}}$$

$$C_{3i,3i-3} = -\frac{\theta\Delta t}{\Delta z^2} K15^{n+1}_{i-\frac{1}{2}}$$

$$C_{3i,3i-2} = K16_i^{n+\frac{1}{2}} + \frac{\theta\Delta t}{\Delta z^2}\left(K13^{n+1}_{i+\frac{1}{2}} + K13^{n+1}_{i-\frac{1}{2}} \right)$$

$$C_{3i,3i-1} = K17_i^{n+\frac{1}{2}} + \frac{\theta\Delta t}{\Delta z^2}\left(K14^{n+1}_{i+\frac{1}{2}} + K14^{n+1}_{i-\frac{1}{2}} \right)$$

$$C_{3i,3i} = K18_i^{n+\frac{1}{2}} + \frac{\theta\Delta t}{\Delta z^2}\left(K15^{n+1}_{i+\frac{1}{2}} + K15^{n+1}_{i-\frac{1}{2}} \right)$$

$$C_{3i,3i+1} = -\frac{\theta\Delta t}{\Delta z^2} K13^{n+1}_{i+\frac{1}{2}}$$

$$C_{3i,3i+2} = -\frac{\theta\Delta t}{\Delta z^2} K14^{n+1}_{i+\frac{1}{2}}$$

$$C_{3i,3i+3} = -\frac{\theta\Delta t}{\Delta z^2} K15^{n+1}_{i+\frac{1}{2}}$$

The RHS matrix is

$$RHS_{3i-2} = \left(\frac{(1-\theta)\Delta t}{\Delta z^2} K1^n_{i-\frac{1}{2}} \right) S^n_{i-1} + \left(\frac{(1-\theta)\Delta t}{\Delta z^2} K2^n_{i-\frac{1}{2}} \right) T^n_{i-1} + \left(\frac{(1-\theta)\Delta t}{\Delta z^2} K3^n_{i-\frac{1}{2}} \right) P^n_{i-1}$$

$$+ \left(K4_i^{n+\frac{1}{2}} - \frac{(1-\theta)\Delta t}{\Delta z^2}\left(K1^n_{i+\frac{1}{2}} + K1^n_{i-\frac{1}{2}} \right) \right) S^n_i + \left(K5_i^{n+\frac{1}{2}} - \frac{(1-\theta)\Delta t}{\Delta z^2}\left(K2^n_{i+\frac{1}{2}} + K2^n_{i-\frac{1}{2}} \right) \right) T^n_i$$

$$+ \left(K6_i^{n+\frac{1}{2}} - \frac{(1-\theta)\Delta t}{\Delta z^2}\left(K3^n_{i+\frac{1}{2}} + K3^n_{i-\frac{1}{2}} \right) \right) P^n_i$$

$$\left(\frac{(1-\theta)\Delta t}{\Delta z^2} K1^n_{i+\frac{1}{2}} \right) S^n_{i+1} + \left(\frac{(1-\theta)\Delta t}{\Delta z^2} K2^n_{i+\frac{1}{2}} \right) T^n_{i+1} + \left(\frac{(1-\theta)\Delta t}{\Delta z^2} K3^n_{i+\frac{1}{2}} \right) P^n_{i+1}$$

$$- \left[\theta\Delta t \frac{K19^{n+1}_{i+1} - K19^{n+1}_{i-1}}{2\Delta z} + (1-\theta)\Delta t \frac{K19^n_{i+1} - K19^n_{i-1}}{2\Delta z} \right]$$

$$RHS_{3i-1} = \left(\frac{(1-\theta)\Delta t}{\Delta z^2} K7^{n}_{i-\frac{1}{2}}\right) S^{n}_{i-1} + \left(\frac{(1-\theta)\Delta t}{\Delta z^2} K8^{n}_{i-\frac{1}{2}}\right) T^{n}_{i-1} + \left(\frac{(1-\theta)\Delta t}{\Delta z^2} K9^{n}_{i-\frac{1}{2}}\right) P^{n}_{i-1}$$
$$+ \left(K10_i^{n+\frac{1}{2}} - \frac{(1-\theta)\Delta t}{\Delta z^2}\left(K7^{n}_{i+\frac{1}{2}} + K7^{n}_{i-\frac{1}{2}}\right)\right) S^{n}_{i} + \left(K11_i^{n+\frac{1}{2}} - \frac{(1-\theta)\Delta t}{\Delta z^2}\left(K8^{n}_{i+\frac{1}{2}} + K8^{n}_{i-\frac{1}{2}}\right)\right) T^{n}_{i}$$
$$+ \left(K12_i^{n+\frac{1}{2}} - \frac{(1-\theta)\Delta t}{\Delta z^2}\left(K9^{n}_{i+\frac{1}{2}} + K9^{n}_{i-\frac{1}{2}}\right)\right) P^{n}_{i}$$
$$+ \left(\frac{(1-\theta)\Delta t}{\Delta z^2} K7^{n}_{i+\frac{1}{2}}\right) S^{n}_{i+1} + \left(\frac{(1-\theta)\Delta t}{\Delta z^2} K8^{n}_{i+\frac{1}{2}}\right) T^{n}_{i+1} + \left(\frac{(1-\theta)\Delta t}{\Delta z^2} K9^{n}_{i+\frac{1}{2}}\right) P^{n}_{i+1}$$

$$RHS_{3i} = \left(\frac{(1-\theta)\Delta t}{\Delta z^2} K13^{n}_{i-\frac{1}{2}}\right) S^{n}_{i-1} + \left(\frac{\Delta t\left(C_{pv}\vec{n}_v + C_{pa}\vec{n}_a + C_{pv}\vec{n}_w\right)^{n}_{i}}{\Delta z} + \frac{(1-\theta)\Delta t}{\Delta z^2} K14^{n}_{i-\frac{1}{2}}\right) T^{n}_{i-1} + \left(\frac{(1-\theta)\Delta t}{\Delta z^2} K15^{n}_{i-\frac{1}{2}}\right) I$$
$$+ \left(K16_i^{n+\frac{1}{2}} - \frac{(1-\theta)\Delta t}{\Delta z^2}\left(K13^{n}_{i+\frac{1}{2}} + K13^{n}_{i-\frac{1}{2}}\right)\right) S^{n}_{i}$$
$$+ \left(K17_i^{n+\frac{1}{2}} - \frac{(1-\theta)\Delta t}{\Delta z^2}\left(K14^{n}_{i+\frac{1}{2}} + K14^{n}_{i-\frac{1}{2}}\right)\right) T^{n}_{i}$$
$$+ \left(K18_i^{n+\frac{1}{2}} - \frac{(1-\theta)\Delta t}{\Delta z^2}\left(K15^{n}_{i+\frac{1}{2}} + K15^{n}_{i-\frac{1}{2}}\right)\right) P^{n}_{i}$$
$$+ \left(\frac{(1-\theta)\Delta t}{\Delta z^2} K13^{n}_{i+\frac{1}{2}}\right) S^{n}_{i+1} + \left(-\frac{\Delta t\left(C_{pv}\vec{n}_v + C_{pa}\vec{n}_a + C_{pv}\vec{n}_w\right)^{n}_{i}}{\Delta z} + \frac{(1-\theta)\Delta t}{\Delta z^2} K14^{n}_{i+\frac{1}{2}}\right) T^{n}_{i+1} + \left(\frac{(1-\theta)\Delta t}{\Delta z^2} K15^{n}_{i+\frac{1}{2}}\right) P^{n}_{i+1}$$
$$+ \left[\theta\Delta t \frac{K20^{n+1}_{i+1} - K20^{n+1}_{i-1}}{2\Delta z} + (1-\theta)\Delta t \frac{K20^{n}_{i+1} - K20^{n}_{i-1}}{2\Delta z}\right]$$

We would like to solve for the dependant variable matrix [B]. In Matlab we can perform the following operation

$$[B] = [RHS][C]^{-1}$$

D.2. Discretize the Boundary Conditions

Summary of Boundary Conditions

Initial Conditions

$$S_w(z) = S_{w,o}$$
$$T(z) = T_o$$
$$P(z) = P$$

Front Face – Case 1: $\dot{m}''_{spray} < \dot{m}''_w + \dot{m}''_v + \dot{m}''_{\substack{evap \\ loss}}$

$$\left.\begin{aligned} &\dot{m}''_{spray} = \dot{m}''_{\substack{evap \\ loss}} + \dot{m}''_{water} + \dot{m}''_{vapor} \\ &\dot{q}''_e + \dot{q}''_{\substack{water \\ spray}} = \dot{q}''_{\substack{vapor \\ loss}} + \dot{q}''_{\substack{air \\ loss}} + \dot{q}''_{\substack{cond \\ loss}} + \dot{q}''_{\substack{re-rad \\ loss}} + \dot{q}''_{\substack{water \\ conv}} + \dot{q}''_{\substack{vapor \\ conv}} + \dot{q}''_{\substack{air \\ conv}} + \dot{q}''_{\substack{cond}} \\ &P = P_o \end{aligned}\right\} \quad @\, z = 0 \quad for \quad t > 0$$

Front Face – Case 2: $\dot{m}''_{spray} > \dot{m}''_w + \dot{m}''_v + \dot{m}''_{\substack{evap \\ loss}}$

$$S_w = 1 \qquad @\, z < z_{\text{int}},\ t > 0$$
$$T = T_{surf} \qquad @\, z = 0,\quad t > 0$$
$$P = P_\infty + \rho_w g h_{layer} \qquad @\, z = 0\ \ t > 0$$

Back Face- Semi-Infinite Solid

$$\left.\begin{aligned} &S_w = S_{w,o} \\ &T = T_o \\ &P = P_o \end{aligned}\right\} \ @\ \ z = L$$

Back Face – Flux Conditions

$$\left.\begin{array}{l} \dot{m}''_{spray} + \dot{m}''_{v} + \dot{m}''_{w} = \dot{m}''_{\substack{evap \\ loss}} \\ \dot{q}''_{\substack{water \\ conv}} + \dot{q}''_{\substack{vapor \\ conv}} + \dot{q}''_{\substack{air \\ conv}} + \dot{q}''_{cond} + \dot{q}''_{e} + \dot{q}''_{\substack{water \\ app}} = \dot{q}''_{\substack{cond \\ loss}} + \dot{q}''_{\substack{vapor \\ loss}} + \dot{q}''_{\substack{air \\ loss}} + \dot{q}''_{\substack{re-rad \\ loss}} \\ P = P_o \quad or \quad \dot{m}''_{a} = 0 \end{array}\right\} \quad @\, z = L \quad for \qquad t > 0$$

D.2.1 Discretized Top Surface Boundary Conditions

Case 1: Low Water Flux - $\dot{m}''_{spray} < \dot{m}''_w + \dot{m}''_v + \dot{m}''_{\substack{evap \\ loss}}$

Let the surface node have a thickness that is half that of the interior nodes. The discretized surface node is shown in Figure 92.

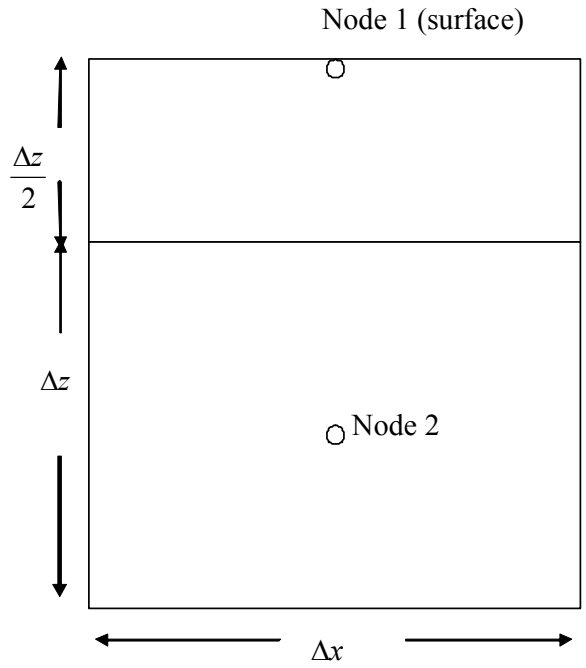

Figure 92 **– Finite Difference Representation of Surface Node**

Discretize Saturation Boundary Conditions for Top Surface

Start with the low water flux case. The boundary condition at the surface is

$$\dot{m}''_{spray} = \dot{m}''_{\substack{evap \\ loss}} + \dot{m}''_w + \dot{m}''_v$$

Where $\dot{m}''_w$ and $\dot{m}''_v$ are the water and vapor mass fluxes into the material at the surface. The water mass flows and storage associated with the surface node are shown in Figure 93. Evaporation or condensation occurs throughout the control volume, but the surface loss term $\dot{m}''_{evap}$ is the surface evaporation rate and represents vapor losses

from the control volume.

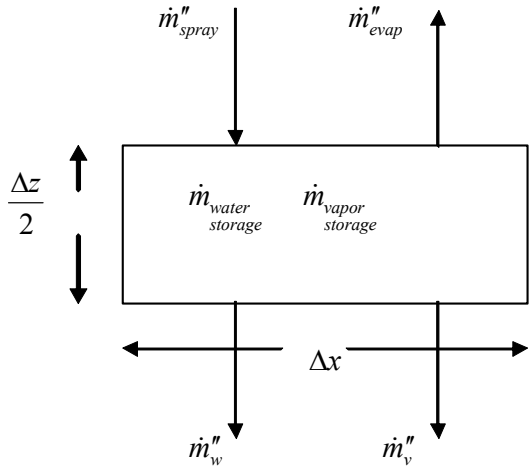

Figure 93 – Surface Node Water Fluxes

The sum of the liquid water flows into and out of the surface control volume is

$$\dot{m}_{\substack{water\\total}} = \left(\dot{m}''_{spray} - \dot{m}''_{w}\right)\Delta x \Delta y$$

The rate of storage of water in the control volume is

$$\dot{m}_{\substack{water\\storage}} \frac{\Delta x \Delta y \Delta z}{2}\left(\frac{\partial\left(\phi \rho_w S_w\right)}{\partial t} + \dot{m}'''_{evap}\right)$$

Conservation of mass for liquid water for the surface node can be expressed as

$$\frac{\Delta x \Delta y \Delta z}{2}\left(\frac{\partial\left(\phi \rho_w S_w\right)}{\partial t} + \dot{m}'''_{evap}\right) = \left(\dot{m}''_{spray} - \dot{m}''_{w}\right)\Delta x \Delta y$$

Which can be simplified to

$$\frac{\Delta z}{2}\left(\frac{\partial\left(\phi\rho_w S_w\right)}{\partial t}+\dot{m}'''_{evap}\right)=\dot{m}''_{spray}-\dot{m}''_{w}$$

The total vapor flow into the surface node control volume is

$$\dot{m}_{\substack{vapor\\total}}=\left(-\dot{m}''_{\substack{evap\\loss}}-\dot{m}''_{v}\right)\Delta x\Delta y$$

The rate of storage of vapor in the surface node control volume is

$$\dot{m}_{\substack{vapor\\storage}}=\frac{\Delta x\Delta y\Delta z}{2}\left(\frac{\partial\left(\phi\rho_g S_g\right)}{\partial t}-\dot{m}'''_{evap}\right)$$

So conservation of mass for vapor for the surface node control volume is

$$\frac{\Delta x\Delta y\Delta z}{2}\left(\frac{\partial\left(\phi\rho_g S_g\right)}{\partial t}-\dot{m}'''_{evap}\right)=\left(-\dot{m}''_{\substack{evap\\loss}}-\dot{m}''_{v}\right)\Delta x\Delta y$$

or

$$\frac{\Delta z}{2}\left(\frac{\partial\left(\phi\rho_g S_g\right)}{\partial t}-\dot{m}'''_{evap}\right)=-\dot{m}''_{\substack{evap\\loss}}-\dot{m}''_{v}$$

Adding these together eliminates the evaporation terms and gives an expression for conservation of mass for total water

$$\frac{\Delta x\Delta y\Delta z}{2}\left(\frac{\partial\left(\phi\rho_w S_w\right)}{\partial t}+\frac{\partial\left(\phi\rho_g S_g\right)}{\partial t}\right)=\left(\dot{m}''_{spray}-\dot{m}''_{w}-\dot{m}''_{v}-\dot{m}''_{\substack{evap\\loss}}\right)\Delta x\Delta y$$

Which can be written as

$$\frac{\Delta z}{2}\left(\frac{\partial\left(\phi\rho_w S_w\right)}{\partial t}+\frac{\partial\left(\phi\rho_g S_g\right)}{\partial t}\right)=\left(\dot{m}''_{spray}-\dot{m}''_w-\dot{m}''_v-\dot{m}''_{\substack{evap\\loss}}\right)\qquad @\ \ z=0\quad\ t>0$$

This derivation assumes that the density of water can be assumed to be approximately constant. Expand the temporal derivatives

$$\begin{aligned}\phi\frac{\partial\left(\rho_v S_g\right)}{\partial t}&=\phi\frac{\partial}{\partial t}\left(\frac{p_v}{R_v T}\left(1-S_w\right)\right)\\&=-\frac{\phi p_v}{R_v T}\frac{\partial S_w}{\partial t}+\frac{\phi}{R_v}\left(1-S_w\right)\frac{\partial}{\partial t}\left(\frac{p_v}{T}\right)\\&=-\frac{\phi p_v}{R_v T}\frac{\partial S_w}{\partial t}+\frac{\phi}{R_v}\left(1-S_w\right)\frac{\partial}{\partial T}\left(\frac{p_v}{T}\right)\frac{\partial T}{\partial t}+\frac{\phi}{R_v T}\left(1-S_w\right)\frac{\partial p_v}{\partial S_w}\frac{\partial S_w}{\partial t}\end{aligned}$$

So the temporal derivative can be written as

$$\frac{\Delta z}{2}\left(\left(\phi\rho_w-\frac{\phi p_v}{R_v T}+\frac{\phi}{R_v T}\left(1-S_w\right)\frac{\partial p_v}{\partial S_w}\right)\frac{\partial S_w}{\partial t}+\left(\frac{\phi}{R_v}\left(1-S_w\right)\frac{\partial}{\partial T}\left(\frac{p_v}{T}\right)\right)\frac{\partial T}{\partial t}+\left(0\right)\frac{\partial P}{\partial t}\right)$$

or

$$\frac{\Delta z}{2}\left(K_4\frac{\partial S_w}{\partial t}+K_5\frac{\partial T}{\partial t}+K_6\frac{\partial P}{\partial t}\right)$$

Define the water fluxes

$$\dot{m}''_w=-\rho_w\frac{KK_{r,w}}{\mu_w}\left(\nabla p_w-\rho_w\vec{g}\right)\qquad @\ z=0$$

$$\dot{m}''_v=-\rho_v\frac{KK_{r,g}}{\mu_v}\nabla P-\frac{C^2}{\rho}M_a M_v D_{eff,g}\nabla X_v\qquad @\ z=0$$

Expand the mass flux terms

$$-\rho_w\frac{KK_{r,l}}{\mu_w}\left(\frac{\partial p_w}{\partial z}-\rho g\right)=-\rho_w\frac{KK_{r,l}}{\mu_w}\frac{\partial P}{\partial z}+\rho_w\frac{KK_{r,l}}{\mu_w}\frac{\partial p_{cap}}{\partial S_w}\frac{\partial S_w}{\partial z}+\rho_w\frac{KK_{r,l}}{\mu_w}\frac{\partial p_{cap}}{\partial T}\frac{\partial T}{\partial z}+\rho_w\frac{KK_{r,l}}{\mu_w}\rho g$$

$$-\rho_v \frac{KK_{r,v}}{\mu_v}\frac{\partial P}{\partial z} = -\frac{p_v}{R_v T}\frac{KK_{r,v}}{\mu_v}\frac{\partial P}{\partial z}$$

$$-\frac{C^2}{\rho} M_a M_v D_{eff,g}\frac{\partial X_v}{\partial z} = -\frac{M_a M_v D_{eff,g}}{R\left(\left(P-p_v\right)M_a + p_v M_v\right)}\left(P\frac{\partial p_v}{\partial S_w}\frac{\partial S_w}{\partial z} + P\frac{\partial p_v}{\partial T}\frac{\partial T}{\partial z} - p_v\frac{\partial P}{\partial z}\right)$$

So the boundary condition is

$$\frac{\Delta z}{2}\left(\left(\phi\rho_w - \frac{\phi p_v}{R_v T} + \frac{\phi}{R_v T}\left(1-S_w\right)\frac{\partial p_v}{\partial S_w}\right)\frac{\partial S_w}{\partial t} + \left(\frac{\phi}{R_v}\left(1-S_w\right)\frac{\partial}{\partial T}\left(\frac{p_v}{T}\right)\right)\frac{\partial T}{\partial t} + \left(0\right)\frac{\partial P}{\partial t}\right)$$

$$= \left(\begin{array}{l}
\left(\frac{M_a M_v D_{eff,g}}{R\left(\left(P-p_v\right)M_a + p_v M_v\right)}P\frac{\partial p_v}{\partial S_w} - \rho_w\frac{KK_{r,l}}{\mu_w}\frac{\partial p_{cap}}{\partial S_w}\right)\frac{\partial S_w}{\partial z} \\
+\left(\frac{M_a M_v D_{eff,g}}{R\left(\left(P-p_v\right)M_a + p_v M_v\right)}P\frac{\partial p_v}{\partial T} - \rho_w\frac{KK_{r,l}}{\mu_w}\frac{\partial p_{cap}}{\partial T}\right)\frac{\partial T}{\partial z} \\
+\left(\frac{p_v}{R_v T}\frac{KK_{r,v}}{\mu_v} - \frac{M_a M_v D_{eff,g}}{R\left(\left(P-p_v\right)M_a + p_v M_v\right)}p_v + \rho_w\frac{KK_{r,l}}{\mu_w}\right)\frac{\partial P}{\partial z} \\
-\rho_w\frac{KK_{r,l}}{\mu_w}\rho g + \dot{m}''_{spray} - \dot{m}''_{\substack{evap \\ loss}}
\end{array}\right)$$

Which can be written as

$$\frac{\Delta z}{2}\left(K_4\frac{\partial S_w}{\partial t} + K_5\frac{\partial T}{\partial t} + K_6\frac{\partial P}{\partial t}\right) = \left(K_1\frac{\partial S_w}{\partial z} + K_2\frac{\partial T}{\partial z} + K_3\frac{\partial P}{\partial z} - K_{19} + \dot{m}''_{spray} - \dot{m}''_{\substack{evap \\ loss}}\right)$$

or

$$\frac{\Delta z}{2}\left(K_4\frac{\partial S_w}{\partial t} + K_5\frac{\partial T}{\partial t} + K_6\frac{\partial P}{\partial t}\right) + \dot{m}''_{\substack{evap \\ loss}} - \dot{m}''_{spray} = \left(K_1\frac{\partial S_w}{\partial z} + K_2\frac{\partial T}{\partial z} + K_3\frac{\partial P}{\partial z} - K_{19}\right)$$

Discretize the temporal derivatives. The 1 subscript indicates the 1st (surface) node)

$$\frac{\Delta z}{2}\left(K_4\frac{\partial S_w}{\partial t} + K_5\frac{\partial T}{\partial t} + K_6\frac{\partial P}{\partial t}\right) \cong \frac{\Delta z}{2}\left(K4_1^{n+\frac{1}{2}}\frac{S_1^{n+1}-S_1^n}{\Delta t} + K5_1^{n+\frac{1}{2}}\frac{T_1^{n+1}-T_1^n}{\Delta t} + K6_1^{n+\frac{1}{2}}\frac{P_1^{n+1}-P_1^n}{\Delta t}\right)$$

Since the fluxes are defined as flows out of the first node, calculate their discretized

value at the first cell boundary. Call this the $1\frac{1}{2}$ node location.

$$K_1 \frac{\partial S_w}{\partial z} + K_2 \frac{\partial T}{\partial z} + K_3 \frac{\partial P}{\partial z} - K_{19}$$
$$\cong K1^n_{1\frac{1}{2}} \frac{S_2^n - S_1^n}{\Delta z} + K2^n_{1\frac{1}{2}} \frac{T_2^n - T_1^n}{\Delta z} + K3^n_{1\frac{1}{2}} \frac{P_2^n - P_1^n}{\Delta z} - K_{19}$$

Putting it all together

$$K4_1^{n+\frac{1}{2}} \frac{S_1^{n+1} - S_1^n}{\Delta t} + K5_1^{n+\frac{1}{2}} \frac{T_1^{n+1} - T_1^n}{\Delta t} + K6_1^{n+\frac{1}{2}} \frac{P_1^{n+1} - P_1^n}{\Delta t} - \dot{m}''_{spray} + \dot{m}''_{\substack{evap \\ loss}}$$
$$= K1^n_{1\frac{1}{2}} \frac{S_2^n - S_1^n}{\Delta z} + K2^n_{1\frac{1}{2}} \frac{T_2^n - T_1^n}{\Delta z} + K3^n_{1\frac{1}{2}} \frac{P_2^n - P_1^n}{\Delta z} - K_{19}^n$$

Use a Crank Nicholson scheme

$$K4_1^{n+\frac{1}{2}} \frac{S_1^{n+1} - S_1^n}{\Delta t} + K5_1^{n+\frac{1}{2}} \frac{T_1^{n+1} - T_1^n}{\Delta t} + K6_1^{n+\frac{1}{2}} \frac{P_1^{n+1} - P_1^n}{\Delta t} - \dot{m}''_{spray} + \dot{m}''_{\substack{evap \\ loss}}$$
$$= \theta \left(K1^{n+1}_{1\frac{1}{2}} \frac{S_2^{n+1} - S_1^{n+1}}{\Delta z} + K2^{n+1}_{1\frac{1}{2}} \frac{T_2^{n+1} - T_1^{n+1}}{\Delta z} + K3^{n+1}_{1\frac{1}{2}} \frac{P_2^{n+1} - P_1^{n+1}}{\Delta z} - K19^{n+1}_{1+\frac{1}{2}} \right)$$
$$+ (1-\theta) \left(K1^n_{1\frac{1}{2}} \frac{S_2^n - S_1^n}{\Delta z} + K2^n_{1\frac{1}{2}} \frac{T_2^n - T_1^n}{\Delta z} + K3^n_{1\frac{1}{2}} \frac{P_2^n - P_1^n}{\Delta z} - K19^n_{1+\frac{1}{2}} \right)$$

This can be written as

$$\left(-\frac{\theta}{\Delta z}K1_{1\frac{1}{2}}^{n+1}-\frac{\Delta z}{2\Delta t}K4_{1}^{n+\frac{1}{2}}\right)S_1^{n+1}+\left(-\frac{\theta}{\Delta z}K2_{1\frac{1}{2}}^{n+1}-\frac{\Delta z}{2\Delta t}K5_{1}^{n+\frac{1}{2}}\right)T_1^{n+1}$$
$$+\left(-\frac{\theta}{\Delta z}K3_{1\frac{1}{2}}^{n+1}-\frac{\Delta z}{2\Delta t}K6_{1}^{n+\frac{1}{2}}\right)P_1^{n+1}$$
$$+\left(\frac{\theta}{\Delta z}K1_{1\frac{1}{2}}^{n+1}\right)S_2^{n+1}+\left(\frac{\theta}{\Delta z}K2_{1\frac{1}{2}}^{n+1}\right)T_2^{n+1}+\left(\frac{\theta}{\Delta z}K3_{1\frac{1}{2}}^{n+1}\right)P_2^{n+1}$$
$$=\left(-\frac{(1-\theta)}{\Delta z}K1_{1\frac{1}{2}}^{n}-\frac{\Delta z}{2\Delta t}K4_{1}^{n+\frac{1}{2}}\right)S_1^{n}+\left(-\frac{(1-\theta)}{\Delta z}K2_{1\frac{1}{2}}^{n}-\frac{\Delta z}{2\Delta t}K5_{1}^{n+\frac{1}{2}}\right)T_1^{n}$$
$$+\left(-\frac{(1-\theta)}{\Delta z}K3_{1\frac{1}{2}}^{n}-\frac{\Delta z}{2\Delta t}K6_{1}^{n+\frac{1}{2}}\right)P_1^{n}$$
$$+\left(\frac{(1-\theta)}{\Delta z}K1_{1\frac{1}{2}}^{n}\right)S_2^{n}+\left(\frac{(1-\theta)}{\Delta z}K2_{1\frac{1}{2}}^{n}\right)T_2^{n}+\left(\frac{(1-\theta)}{\Delta z}K3_{1\frac{1}{2}}^{n}\right)P_2^{n}+\theta K19_{1\frac{1}{2}}^{n+1}+(1-\theta)K19_{1\frac{1}{2}}^{n}$$
$$-\dot{m}''_{spray}+\dot{m}''_{\substack{evap\\loss}}$$

Discretize Pressure Boundary Condition at Top Surface

The air mass flows into the surface node control volume are shown in Figure 94. The discretized surface node will have mass storage

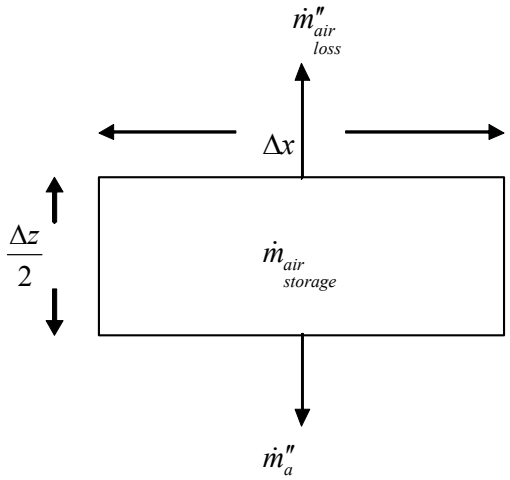

Figure 94 – Air Mass Flows in Surface Node Control Volume

If the pressure has a type 1 boundary condition, it is simply discretized as:

$$P_1^{n+1} = P_\infty$$

The total rate of mass flow into the surface node is

$$\dot{m}_{\substack{air\\total}} = \left(-\dot{m}''_a - \dot{m}''_{\substack{air\\loss}} \right) \Delta x \Delta y = \left(\rho_a \frac{KK_{r,a}}{\mu_a} \nabla P + \frac{C^2}{\rho} M_v M_a D_{av} \nabla X_a - \dot{m}''_{\substack{air\\loss}} \right) \Delta x \Delta y$$

Where $\dot{m}''_a$ is the air mass flux in the material. It can be written as:

$$\dot{m}''_a = -\rho_a \frac{KK_{r,a}}{\mu_a} \nabla P - \frac{C^2}{\rho} M_v M_a D_{av} \nabla X_a$$

$$\dot{m}_{\substack{air\\total}} = \left(-\dot{m}_a'' - \dot{m}_{\substack{air\\loss}}'' \right) \Delta x \Delta y$$

The total rate of storage of air in the surface node is

$$\dot{m}_{\substack{air\\storage}} = \left(\phi \frac{\partial \left(\rho_a S_g \right)}{\partial t} \right) \frac{\Delta x \Delta y \Delta z}{2}$$

Setting these equal gives an expression for conservation of mass for air in the surface node control volume

$$\left(\phi \frac{\partial \left(\rho_a S_g \right)}{\partial t} \right) \frac{\Delta x \Delta y \Delta z}{2} = \left(-\dot{m}_a'' - \dot{m}_{\substack{air\\loss}}'' \right) \Delta x \Delta y$$

If a no-flux boundary condition is used at the surface, then $\dot{m}_{\substack{air\\loss}}''$ is zero and

conservation of mass for air for the surface node can be written as

$$\left(\phi \frac{\partial \left(\rho_a S_g \right)}{\partial t} \right) \frac{\Delta z}{2} = \rho_a \frac{K K_{r,a}}{\mu_a} \nabla P + \frac{C^2}{\rho} M_v M_a D_{av} \nabla X_a$$

The terms in this equation can be expanded

$$\phi \frac{\partial \left(\rho_a S_g \right)}{\partial t} = -\frac{\phi}{R_a} \left(\frac{\left(P - p_v \right)}{T} + \frac{\left(1 - S_w \right)}{T} \frac{\partial p_v}{\partial S_w} \right) \frac{\partial S_w}{\partial t} - \frac{\phi}{R_a} \left(\frac{P}{T^2} - \frac{P S_w}{T^2} + \left(1 + S_w \right) \frac{\partial}{\partial T} \left(\frac{p_v}{T} \right) \right) \frac{\partial T}{\partial t} + \frac{\phi \left(1 - S_w \right)}{R_a T} \frac{\partial P}{\partial t}$$

$$\rho_a \frac{K K_{r,a}}{\mu_a} \nabla P = \frac{P - p_v}{R_a T} \frac{K K_{r,g}}{\mu_a} \frac{\partial P}{\partial z}$$

$$\frac{C^2}{\rho} M_v M_a D_{av} \nabla X_a = -\frac{M_v M_a D_{eff,g}}{R T \left(M_a \left(P - p_v \right) + M_v p_v \right)} \left(P \frac{\partial p_v}{\partial S_w} \frac{\partial S_w}{\partial z} + P \frac{\partial p_v}{\partial T} \frac{\partial T}{\partial z} - p_v \frac{\partial P}{\partial z} \right)$$

So the boundary condition can be written as

$$\frac{\Delta z}{2}\left(\begin{array}{c}-\frac{\phi}{R_a}\left(\frac{\left(P-p_v\right)}{T}+\frac{\left(1-S_w\right)}{T}\frac{\partial p_v}{\partial S_w}\right)\frac{\partial S_w}{\partial t}-\frac{\phi}{R_a}\left(\frac{P}{T^2}-\frac{PS_w}{T^2}+\left(1+S_w\right)\frac{\partial}{\partial T}\left(\frac{p_v}{T}\right)\right)\frac{\partial T}{\partial t}\\ +\frac{\phi\left(1-S_w\right)}{R_aT}\frac{\partial P}{\partial t}\end{array}\right)$$

$$=\left(-\frac{M_vM_aD_{eff,g}}{RT\left(M_a\left(P-p_v\right)+M_vp_v\right)}P\frac{\partial p_v}{\partial S_w}\right)\frac{\partial S_w}{\partial z}+\left(-\frac{M_vM_aD_{eff,g}}{RT\left(M_a\left(P-p_v\right)+M_vp_v\right)}P\frac{\partial p_v}{\partial T}\right)\frac{\partial T}{\partial z}$$

$$+\left(\frac{P-p_v}{R_aT}\frac{KK_{r,g}}{\mu_a}+\frac{M_vM_aD_{eff,g}}{RT\left(M_a\left(P-p_v\right)+M_vp_v\right)}p_v\right)\frac{\partial P}{\partial z}$$

Or

$$\frac{\Delta z}{2}\left(K_{10}\frac{\partial S_w}{\partial t}+K_{11}\frac{\partial T}{\partial t}+K_{12}\frac{\partial P}{\partial t}\right)=K_7\frac{\partial S_w}{\partial z}+K_8\frac{\partial T}{\partial z}+K_9\frac{\partial P}{\partial z}$$

Discretize this using a Crank Nicholson scheme

$$\frac{\Delta z}{2}\left(K10_1^{n+1/2}\frac{S_1^{n+1}-S_1^n}{\Delta t}+K11_1^{n+1/2}\frac{T_1^{n+1}-T_1^n}{\Delta t}+K12_1^{n+1/2}\frac{T_1^{n+1}-T_1^n}{\Delta t}\right)$$

$$=\theta\left(K7_{1/2}^{n+1}\frac{S_2^{n+1}-S_1^{n+1}}{\Delta z}+K8_{1/2}^{n+1}\frac{T_2^{n+1}-T_1^{n+1}}{\Delta z}+K9_{1/2}^{n+1}\frac{P_2^{n+1}-P_1^{n+1}}{\Delta z}\right)$$

$$+\left(1-\theta\right)\left(K7_{1/2}^{n}\frac{S_2^{n}-S_1^{n}}{\Delta z}+K8_{1/2}^{n}\frac{T_2^{n}-T_1^{n}}{\Delta z}+K9_{1/2}^{n}\frac{P_2^{n}-P_1^{n}}{\Delta z}\right)$$

Rearrange this as

$$\left(-\frac{\theta}{\Delta z}K7_{1\frac{1}{2}}^{n+1}-\frac{\Delta z}{2\Delta t}K10_{1}^{n+\frac{1}{2}}\right)S_1^{n+1}+\left(-\frac{\theta}{\Delta z}K8_{1\frac{1}{2}}^{n+1}-\frac{\Delta z}{2\Delta t}K11_{1}^{n+\frac{1}{2}}\right)T_1^{n+1}$$
$$+\left(-\frac{\theta}{\Delta z}K9_{1\frac{1}{2}}^{n+1}-\frac{\Delta z}{2\Delta t}K12_{1}^{n+\frac{1}{2}}\right)P_1^{n+1}$$
$$+\left(\frac{\theta}{\Delta z}K7_{1\frac{1}{2}}^{n+1}\right)S_2^{n+1}+\left(\frac{\theta}{\Delta z}K8_{1\frac{1}{2}}^{n+1}\right)T_2^{n+1}+\left(\frac{\theta}{\Delta z}K9_{1\frac{1}{2}}^{n+1}\right)P_2^{n+1}$$
$$=\left(-\frac{(1-\theta)}{\Delta z}K7_{1\frac{1}{2}}^{n}-\frac{\Delta z}{2\Delta t}K10_{1}^{n+\frac{1}{2}}\right)S_1^{n}+\left(-\frac{(1-\theta)}{\Delta z}K8_{1\frac{1}{2}}^{n}-\frac{\Delta z}{2\Delta t}K11_{1}^{n+\frac{1}{2}}\right)T_1^{n}$$
$$+\left(-\frac{(1-\theta)}{\Delta z}K9_{1\frac{1}{2}}^{n}-\frac{\Delta z}{2\Delta t}K12_{1}^{n+\frac{1}{2}}\right)P_1^{n}$$
$$+\left(\frac{(1-\theta)}{\Delta z}K7_{1\frac{1}{2}}^{n}\right)S_2^{n}+\left(\frac{(1-\theta)}{\Delta z}K8_{1\frac{1}{2}}^{n}\right)T_2^{n}+\left(\frac{(1-\theta)}{\Delta z}K9_{1\frac{1}{2}}^{n}\right)P_2^{n}$$

Discretize Temperature Boundary Conditions at Top Surface

Discretize the first node as shown in Figure 92. The enthalpy flows for the surface node are shown in Figure 95. The rate of vapor loss from the control volume is assumed to be equal to the surface evaporation rate. The enthalpy flow associated with the vapor leaving the surface is $\dot{q}''_{\substack{vapor \\ loss}}$. This is separate from the evaporation rate, which will be included in the energy storage term that will be calculated shortly.

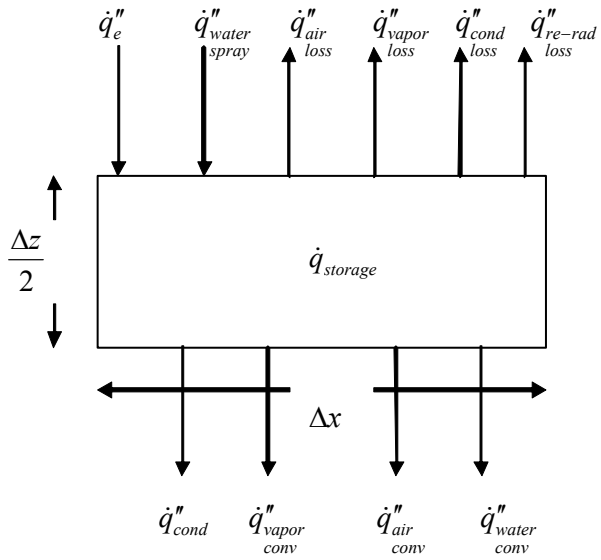

Figure 95 – Surface Node Enthalpy Fluxes

The sum of all of the fluxes into the surface node is

$$\dot{q}_{total} = \left(\dot{q}''_e + \dot{q}''_{\substack{water \\ spray}} - \dot{q}''_{\substack{air \\ loss}} - \dot{q}''_{\substack{vapor \\ loss}} - \dot{q}''_{\substack{cond \\ loss}} - \dot{q}''_{\substack{re-rad \\ loss}} - \dot{q}''_{cond} - \dot{q}''_{\substack{water \\ conv}} - \dot{q}''_{\substack{vapor \\ conv}} - \dot{q}''_{\substack{air \\ conv}} \right) \Delta x \Delta y$$

The total rate of storage of thermal energy in the surface node is

$$\dot{q}_{storage} = \frac{\Delta x \Delta y \Delta z}{2} \left(\frac{\partial}{\partial t}\left(c_s h_s\right) + \frac{\partial}{\partial t}\left(c_w h_w\right) + \frac{\partial}{\partial t}\left(c_a h_a\right) + \frac{\partial}{\partial t}\left(c_v h_v\right) \right)$$

Where c and h are the mass concentration in kg/m^3 and enthalpy in J/kg of solid, water, air, and vapor. Setting the storage equal to the total fluxes into and out of the surface

node control volume gives an expression for conservation of energy

$$\frac{\Delta x\Delta y\Delta z}{2}\left(\frac{\partial}{\partial t}\left(c_s h_s\right)+\frac{\partial}{\partial t}\left(c_w h_w\right)+\frac{\partial}{\partial t}\left(c_a h_a\right)+\frac{\partial}{\partial t}\left(c_v h_v\right)\right)$$

$$=\left(\dot{q}''_e+\underset{spray}{\dot{q}''_{water}}-\underset{loss}{\dot{q}''_{air}}-\underset{loss}{\dot{q}''_{vapor}}-\underset{loss}{\dot{q}''_{cond}}-\underset{loss}{\dot{q}''_{re-rad}}-\dot{q}''_{cond}-\underset{conv}{\dot{q}''_{water}}-\underset{conv}{\dot{q}''_{vapor}}-\underset{conv}{\dot{q}''_{air}}\right)\Delta x\Delta y$$

Rearrange and use conservation of water, vapor, and air for the surface node to simplify the enthalpy flows and storage. Start with water. Use the definition of enthalpy to simplify the water enthalpy flows and storage terms

$$\frac{\Delta z}{2}\frac{\partial}{\partial t}\left(c_w h_w\right)-\underset{spray}{\dot{q}''_{water}}+\underset{conv}{\dot{q}''_{water}}=\frac{\Delta z}{2}\left(c_w\frac{\partial h_w}{\partial t}+h_w\frac{\partial c_w}{\partial t}\right)-\dot{m}''_{spray}\underset{spray}{h_{water}}+\dot{m}''_w h_w$$

$$=\frac{\Delta z}{2}c_w\frac{\partial h_w}{\partial t}+\frac{\Delta z}{2}h_w\frac{\partial c_w}{\partial t}-\dot{m}''_{spray}\left(h_f^o+\int_{T_o}^{T_{spray}}C_{p,w}\partial T\right)+\dot{m}''_w h_w$$

$$=\frac{\Delta z}{2}c_w\frac{\partial h_w}{\partial t}+\frac{\Delta z}{2}h_w\frac{\partial c_w}{\partial t}-\dot{m}''_{spray}\left(h_f^o+\int_{T_o}^{T_w}C_{p,w}\partial T+\int_{T_w}^{T_{spray}}C_{p,w}\partial T\right)+\dot{m}''_w h_w$$

$$=\frac{\Delta z}{2}c_w\frac{\partial h_w}{\partial t}-\dot{m}''_{spray}C_{p,w}\left(T_{spray}-T_{surface}\right)+h_w\left(\frac{\Delta z}{2}\phi\frac{\partial\left(\rho_w S_w\right)}{\partial t}-\dot{m}''_{spray}+\dot{m}''_w\right)$$

$$=\frac{\Delta z}{2}c_w C_{p,w}\frac{\partial T_w}{\partial t}-\dot{m}''_{spray}C_{p,w}\left(T_{spray}-T_{surface}\right)-h_w\dot{m}'''_{evap}$$

Next simplify the vapor enthalpy flows and storage.

$$\frac{\Delta z}{2}\frac{\partial}{\partial t}\left(c_v h_v\right)+\underset{loss}{\dot{q}''_{vapor}}+\underset{conv}{\dot{q}''_{vapor}}=\frac{\Delta z}{2}\left(c_v\frac{\partial h_v}{\partial t}+h_v\frac{\partial c_v}{\partial t}\right)+h_v\dot{m}''_{evap}+h_v\dot{m}''_v$$

$$=\frac{\Delta z}{2}c_v\frac{\partial h_v}{\partial t}+h_v\left(\frac{\Delta z}{2}\phi\frac{\partial\left(\rho_g S_g\right)}{\partial t}+\dot{m}''_{evap}+\dot{m}''_v\right)$$

$$=\frac{\Delta z}{2}c_v C_{p,v}\frac{\partial T_v}{\partial t}+h_v\dot{m}'''_{evap}$$

Note that h_v is the enthalpy of the vapor leaving the surface, not the enthalpy of vaporization. The term $\underset{loss}{\dot{q}''_{vapor}}=h_v\dot{m}''_{evap}$ represents the enthalpy carried out of the control volume by vapor leaving. The rate of vapor loss is assumed to be $\dot{m}''_{evap}$, but

the evaporation is actually occurring throughout the control volume so the enthalpy storage associated with phase change is included in the volumetric term $\dot{m}'''_{evap}$. This will appear as a sink term when the conservation of energy for the surface node is reassembled.

Next simplify the air enthalpy flows and storage

$$\begin{aligned}\frac{\Delta z}{2}\frac{\partial}{\partial t}\left(c_a h_a\right)+\underset{conv}{\dot{q}''_{air}}+\underset{loss}{\dot{q}''_{air}}&=\frac{\Delta z}{2}\left(c_a\frac{\partial h_a}{\partial t}+h_a\frac{\partial c_a}{\partial t}\right)+\dot{m}''_a h_a+\underset{loss}{\dot{m}''_{air}}h_a\\&=\frac{\Delta z}{2}c_a\frac{\partial h_a}{\partial t}+h_a\left(\frac{\Delta z}{2}\phi\frac{\partial\left(\rho_a S_g\right)}{\partial t}+\dot{m}''_a+\underset{loss}{\dot{m}''_{air}}\right)\\&=\frac{\Delta z}{2}c_a C_{p,a}\frac{\partial T_a}{\partial t}\end{aligned}$$

Thermal conduction into the material is assumed to occur by Fourier's law through each component present. ψ represents the volumetric content of air, vapor, water, and solid material present.

$$\dot{q}''_{cond}=-\psi_a k_a\frac{\partial T_a}{\partial z}-\psi_v k_v\frac{\partial T_v}{\partial z}-\psi_w k_w\frac{\partial T_w}{\partial z}-\psi_s k_s\frac{\partial T_s}{\partial z}$$

The conductive losses to the ambient and re-radiative loss terms can be defined as

$$\underset{loss}{\dot{q}''_{cond}}=h\left(T_{surf}-T_\infty\right)$$

$$\dot{q}''_{re-rad}=\varepsilon\sigma\left(T_{surf}^4-T_\infty^4\right)$$

The conservation of energy for the surface node can now be written as

$$\frac{\Delta z}{2}\left(c_s C_{p,s}\frac{\partial T_s}{\partial t}+c_w C_{p,w}\frac{\partial T_w}{\partial t}+c_a C_{p,a}\frac{\partial T_a}{\partial t}+c_v C_{p,v}\frac{\partial T_v}{\partial t}+\left(h_w-h_w\right)\dot{m}'''_{evap}\right)$$
$$=\begin{pmatrix}\dot{q}''_e+\dot{m}''_{spray}C_{p,w}\left(T_{spray}-T_{surface}\right)-h\left(T_s-T_\infty\right)-\varepsilon_s\sigma\left(T_s^4-T_\infty^4\right)\\+\psi_a k_a\frac{\partial T_a}{\partial z}+\psi_v k_v\frac{\partial T_v}{\partial z}+\psi_w k_w\frac{\partial T_w}{\partial z}+\psi_s k_s\frac{\partial T_s}{\partial z}\end{pmatrix}$$

Invoking the assumption of local thermal equilibrium allows this to be written as

$$\frac{\Delta z}{2}\left(\left(\rho C_p\right)_{eff}\frac{\partial T}{\partial t}+\Delta h_v\dot{m}'''_{evap}\right)=\begin{pmatrix}\dot{q}''_e+\dot{m}''_{spray}C_{p,w}\left(T_{spray}-T_{surface}\right)-h\left(T_s-T_\infty\right)\\-\varepsilon_s\sigma\left(T_s^4-T_\infty^4\right)+k_{eff}\frac{\partial T}{\partial z}\end{pmatrix}$$

Now use conservation of mass for water to substitute for the evaporation rate. COM for water for the surface node can be written as

$$\frac{\Delta z}{2}\dot{m}'''_{evap}=\dot{m}''_{spray}+\rho_w\frac{KK_{r,l}}{\mu_w}\left(\frac{\partial\left(P-p_c\right)}{\partial z}-\rho g\right)-\frac{\Delta z}{2}\phi\frac{\partial\left(\rho_w S_w\right)}{\partial t}$$

Substituting this into the BC for conservation of energy gives

$$\frac{\Delta z}{2}\left(\rho C_p\right)_{eff}\frac{\partial T}{\partial t}+\Delta h_v\left(\dot{m}''_{spray}+\rho_w\frac{KK_{r,l}}{\mu_w}\left(\frac{\partial\left(P-p_c\right)}{\partial z}-\rho g\right)-\frac{\Delta z}{2}\phi\frac{\partial\left(\rho_w S_w\right)}{\partial t}\right)$$
$$=\begin{pmatrix}\dot{q}''_e+\dot{m}''_{spray}C_{p,w}\left(T_{spray}-T_{surface}\right)-h\left(T_s-T_\infty\right)\\-\varepsilon_s\sigma\left(T_s^4-T_\infty^4\right)+k_{eff}\frac{\partial T}{\partial z}\end{pmatrix}$$

Which can be written as

$$\frac{\Delta z}{2}K16\frac{\partial S_w}{\partial t}+\frac{\Delta z}{2}K17\frac{\partial T}{\partial t}+\frac{\Delta z}{2}K18\frac{\partial P}{\partial t}=K13\frac{\partial S_w}{\partial z}+K14\frac{\partial T}{\partial z}+K15\frac{\partial P}{\partial z}+K20$$
$$+\Delta h_v\dot{m}''_{spray}-\dot{q}''_e-\dot{m}''_{spray}C_{p,w}\left(T_{spray}-T_{surface}\right)+h\left(T_s-T_\infty\right)+\varepsilon_s\sigma\left(T_s^4-T_\infty^4\right)$$

Use a Crank Nicholson discretization scheme but use the previous time step to calculate the surface losses

$$\frac{\Delta z}{2}K16_1^{n+1}\frac{S_1^{n+1}-S_1^n}{\Delta t}+\frac{\Delta z}{2}K17_1^{n+1}\frac{T_1^{n+1}-T_1^n}{\Delta t}+\frac{\Delta z}{2}K18_1^{n+1}\frac{P_1^{n+1}-P_1^n}{\Delta t}$$
$$=\theta\left(K13^{n+1}_{1+\frac{1}{2}}\frac{S_2^{n+1}-S_1^{n+1}}{\Delta z}+K14^{n+1}_{1+\frac{1}{2}}\frac{T_2^{n+1}-T_1^{n+1}}{\Delta z}+K15^{n+1}_{1+\frac{1}{2}}\frac{P_2^{n+1}-P_1^{n+1}}{\Delta z}+K20^{n+1}_{1+\frac{1}{2}}\right)$$
$$+\left(1-\theta\right)\left(K13^{n}_{1+\frac{1}{2}}\frac{S_2^{n}-S_1^{n}}{\Delta z}+K14^{n}_{1+\frac{1}{2}}\frac{T_2^{n}-T_1^{n}}{\Delta z}+K15^{n}_{1+\frac{1}{2}}\frac{P_2^{n}-P_1^{n}}{\Delta z}+K20^{n}_{1+\frac{1}{2}}\right)$$
$$+\Delta h_v\dot{m}''_{spray}-\dot{q}''_e-\dot{m}''_{spray}C_{p,w}\left(T_{spray}-T_{surface}\right)+h\left(T_s-T_\infty\right)+\varepsilon_s\sigma\left(T_s^4-T_\infty^4\right)$$

Rearrange

$$\left(-\frac{\Delta z}{2\Delta t}K16_1^{n+1}-\frac{\theta}{\Delta z}K13^{n+1}_{1+\frac{1}{2}}\right)S_1^{n+1}+\left(-\frac{\Delta z}{2\Delta t}K17_1^{n+1}-\frac{\theta}{\Delta z}K14^{n+1}_{1+\frac{1}{2}}\right)T_1^{n+1}$$
$$+\left(-\frac{\Delta z}{2\Delta t}K18_1^{n+1}-\frac{\theta}{\Delta z}K15^{n+1}_{1+\frac{1}{2}}\right)P_1^{n+1}$$
$$+\left(\frac{\theta}{\Delta z}K13^{n+1}_{1+\frac{1}{2}}\right)S_2^{n+1}+\left(\frac{\theta}{\Delta z}K14^{n+1}_{1+\frac{1}{2}}\right)T_2^{n+1}+\left(\frac{\theta}{\Delta z}K15^{n+1}_{1+\frac{1}{2}}\right)P_2^{n+1}$$
$$=\left(\frac{\left(1-\theta\right)}{\Delta z}K13^{n}_{1+\frac{1}{2}}-\frac{\Delta z}{2\Delta t}K16_1^{n+1}\right)S_1^{n}+\left(\frac{\left(1-\theta\right)}{\Delta z}K14^{n}_{1+\frac{1}{2}}-\frac{\Delta z}{2\Delta t}K17_1^{n+1}\right)T_1^{n}$$
$$+\left(\frac{\left(1-\theta\right)}{\Delta z}K15^{n}_{1+\frac{1}{2}}-\frac{\Delta z}{2\Delta t}K18_1^{n+1}\right)P_1^{n}$$
$$+\left(-\frac{\left(1-\theta\right)}{\Delta z}K13^{n}_{1+\frac{1}{2}}\right)S_2^{n}+\left(-\frac{\left(1-\theta\right)}{\Delta z}K14^{n}_{1+\frac{1}{2}}\right)T_2^{n}+\left(-\frac{\left(1-\theta\right)}{\Delta z}K15^{n}_{1+\frac{1}{2}}\right)P_2^{n}$$
$$-\theta K20^{n+1}_{1+\frac{1}{2}}-\left(1-\theta\right)K20^{n}_{1+\frac{1}{2}}+\begin{pmatrix}\Delta h_v\dot{m}''_{spray}-\dot{q}''_e-\dot{m}''_{spray}C_{p,w}\left(T_{spray}-T_{surface}\right)\\+h\left(T_s-T_\infty\right)+\varepsilon_s\sigma\left(T_s^4-T_\infty^4\right)\end{pmatrix}$$

These boundary conditions form the top left corner of the coefficient matrix

$$\begin{bmatrix} C_{1,1} & C_{1,2} & C_{1,3} & C_{1,4} & C_{1,5} & C_{1,6} & \\ C_{2,1} & C_{2,2} & C_{2,3} & C_{2,4} & C_{2,5} & C_{2,6} & \cdots \\ C_{3,1} & C_{3,2} & C_{3,3} & C_{3,4} & C_{3,5} & C_{3,6} & \\ & & & \cdots & & & \end{bmatrix} \begin{bmatrix} B_1^{n+1} = S_1^{n+1} \\ B_2^{n+1} = T_1^{n+1} \\ B_3^{n+1} = P_1^{n+1} \\ B_4^{n+1} = S_2^{n+1} \\ B_5^{n+1} = T_2^{n+1} \\ B_6^{n+1} = P_2^{n+1} \\ \cdots \end{bmatrix} = \begin{bmatrix} RHS_1 \\ RHS_2 \\ RHS_3 \\ \cdots \end{bmatrix}$$

Where the values of the coefficient matrix are

Saturation:

$$C_{1,1} = -\frac{\theta}{\Delta z} K1_{i+\frac{1}{2}}^{n+1} - \frac{\Delta z}{2\Delta t} K4_1^{n+\frac{1}{2}}$$

$$C_{1,2} = -\frac{\theta}{\Delta z} K2_{i+\frac{1}{2}}^{n+1} - \frac{\Delta z}{2\Delta t} K5_1^{n+\frac{1}{2}}$$

$$C_{1,3} = -\frac{\theta}{\Delta z} K3_{i+\frac{1}{2}}^{n+1} - \frac{\Delta z}{2\Delta t} K6_1^{n+\frac{1}{2}}$$

$$C_{1,4} = \frac{\theta}{\Delta z} K1_{i+\frac{1}{2}}^{n+1}$$

$$C_{1,5} = \frac{\theta}{\Delta z} K2_{i+\frac{1}{2}}^{n+1}$$

$$C_{1,6} = \frac{\theta}{\Delta z} K3_{i+\frac{1}{2}}^{n+1}$$

Pressure: Type 1 BC

$$C_{2,1} = 0$$

$$C_{2,2} = 1$$

$$C_{2,3} = 0$$

$$C_{2,4} = 0$$

$$C_{2,5} = 0$$

$$C_{2,6} = 0$$

Pressure: Type 2 BC

$$C_{2,1} = -\frac{\theta}{\Delta z} K7_{i+\frac{1}{2}}^{n+1} - \frac{\Delta z}{2\Delta t} K10_{1}^{n+\frac{1}{2}}$$

$$C_{2,2} = -\frac{\theta}{\Delta z} K8_{i+\frac{1}{2}}^{n+1} - \frac{\Delta z}{2\Delta t} K11_{1}^{n+\frac{1}{2}}$$

$$C_{2,3} = -\frac{\theta}{\Delta z} K9_{i+\frac{1}{2}}^{n+1} - \frac{\Delta z}{2\Delta t} K12_{1}^{n+\frac{1}{2}}$$

$$C_{2,4} = \frac{\theta}{\Delta z} K7_{i+\frac{1}{2}}^{n+1}$$

$$C_{2,5} = \frac{\theta}{\Delta z} K8_{i+\frac{1}{2}}^{n+1}$$

$$C_{2,6} = \frac{\theta}{\Delta z} K9_{i+\frac{1}{2}}^{n+1}$$

Temperature:

$$C_{3,1} = -\frac{\theta}{\Delta z} K13_{i+\frac{1}{2}}^{n+1} - \frac{\Delta z}{2\Delta t} K16_{1}^{n+\frac{1}{2}}$$

$$C_{3,2} = -\frac{\theta}{\Delta z} K14_{i+\frac{1}{2}}^{n+1} - \frac{\Delta z}{2\Delta t} K17_{1}^{n+\frac{1}{2}}$$

$$C_{3,3} = -\frac{\theta}{\Delta z} K15_{i+\frac{1}{2}}^{n+1} - \frac{\Delta z}{2\Delta t} K18_{1}^{n+\frac{1}{2}}$$

$$C_{3,4} = \frac{\theta}{\Delta z} K13_{i+\frac{1}{2}}^{n+1}$$

$$C_{3,5} = \frac{\theta}{\Delta z} K14_{i+\frac{1}{2}}^{n+1}$$

$$C_{3,6} = \frac{\theta}{\Delta z} K15_{i+\frac{1}{2}}^{n+1}$$

Saturation:

$$RHS_1 = \left(\frac{(1-\theta)}{\Delta z} K1^{n}_{i+\frac{1}{2}} - \frac{\Delta z}{2\Delta t} K4_1^{n+\frac{1}{2}} \right) S_1^n + \left(\frac{(1-\theta)}{\Delta z} K2^{n}_{i+\frac{1}{2}} - \frac{\Delta z}{2\Delta t} K5_1^{n+\frac{1}{2}} \right) T_1^n$$
$$+ \left(\frac{(1-\theta)}{\Delta z} K3^{n}_{i+\frac{1}{2}} - \frac{\Delta z}{2\Delta t} K6_1^{n+\frac{1}{2}} \right) P_1^n$$
$$+ \left(-\frac{(1-\theta)}{\Delta z} K1^{n}_{i+\frac{1}{2}} \right) S_2^n + \left(-\frac{(1-\theta)}{\Delta z} K2^{n}_{i+\frac{1}{2}} \right) T_2^n + \left(-\frac{(1-\theta)}{\Delta z} K3^{n}_{i+\frac{1}{2}} \right) P_2^n$$
$$+\theta K19^{n+1}_{1\frac{1}{2}} + (1-\theta) K19^{n}_{1\frac{1}{2}} + h_m \left(\frac{p_v}{R_v T} - \rho_{v,o} \right) - \dot{m}''_{spray}$$

Pressure: Type 1 BC

$$RHS_2 = P_\infty$$

Pressure: Type 2 BC

$$RHS_2 = \left(\frac{(1-\theta)}{\Delta z} K7^{n}_{i+\frac{1}{2}} - \frac{\Delta z}{2\Delta t} K10_1^{n+\frac{1}{2}} \right) S_1^n + \left(\frac{(1-\theta)}{\Delta z} K11^{n}_{i+\frac{1}{2}} - \frac{\Delta z}{2\Delta t} K5_1^{n+\frac{1}{2}} \right) T_1^n$$
$$+ \left(\frac{(1-\theta)}{\Delta z} K9^{n}_{i+\frac{1}{2}} - \frac{\Delta z}{2\Delta t} K12_1^{n+\frac{1}{2}} \right) P_1^n$$
$$+ \left(-\frac{(1-\theta)}{\Delta z} K7^{n}_{i+\frac{1}{2}} \right) S_2^n + \left(-\frac{(1-\theta)}{\Delta z} K8^{n}_{i+\frac{1}{2}} \right) T_2^n + \left(-\frac{(1-\theta)}{\Delta z} K9^{n}_{i+\frac{1}{2}} \right) P_2^n$$

Temperature:

$$RHS_3 = \left(\frac{(1-\theta)}{\Delta z} K13^{n}_{i+\frac{1}{2}} - \frac{\Delta z}{2\Delta t} K16_1^{n+\frac{1}{2}} \right) S_1^n + \left(\frac{(1-\theta)}{\Delta z} K14^{n}_{i+\frac{1}{2}} - \frac{\Delta z}{2\Delta t} K17_1^{n+\frac{1}{2}} \right) T_1^n$$
$$+ \left(\frac{(1-\theta)}{\Delta z} K15^{n}_{i+\frac{1}{2}} - \frac{\Delta z}{2\Delta t} K18_1^{n+\frac{1}{2}} \right) P_1^n$$
$$+ \left(-\frac{(1-\theta)}{\Delta z} K13^{n}_{i+\frac{1}{2}} \right) S_2^n + \left(-\frac{(1-\theta)}{\Delta z} K14^{n}_{i+\frac{1}{2}} \right) T_2^n + \left(-\frac{(1-\theta)}{\Delta z} K15^{n}_{i+\frac{1}{2}} \right) P_2^n$$
$$-\theta K20^{n+1}_{1+\frac{1}{2}} - (1-\theta) K20^{n}_{1+\frac{1}{2}} + \left(\begin{array}{l} \Delta h_v \dot{m}''_{spray} - \dot{q}''_e - \dot{m}''_{spray} C_{p,w} \left(T_{spray} - T_{surface} \right) \\ + h \left(T_s - T_\infty \right) + \varepsilon_s \sigma \left(T_s^4 - T_\infty^4 \right) \end{array} \right)$$

Case 2: **High Water Flux-** $\dot{m}''_{spray} > \dot{m}''_{w} + \dot{m}''_{v} + \dot{m}''_{\substack{evap \\ loss}}$

For the case where $\dot{m}''_{spray} > \dot{m}''_{w} + \dot{m}''_{v} + \dot{m}''_{\substack{evap \\ loss}}$ the boundary conditions must account for the effects of the water layer. Since the water layer will absorb thermal radiation while allowing some to reach the surface, we must assume that there is a temperature gradient through the water which must be solved for. The water temperature profile will be solved independently as part of a sub-model and values passed to the solid model to be included in the boundary condition for the surface node. The surface node will include the back face node from the finite difference model of the water layer, as shown in Figure 96. The node spacings in the finite difference models for the water and solid may be slightly different.

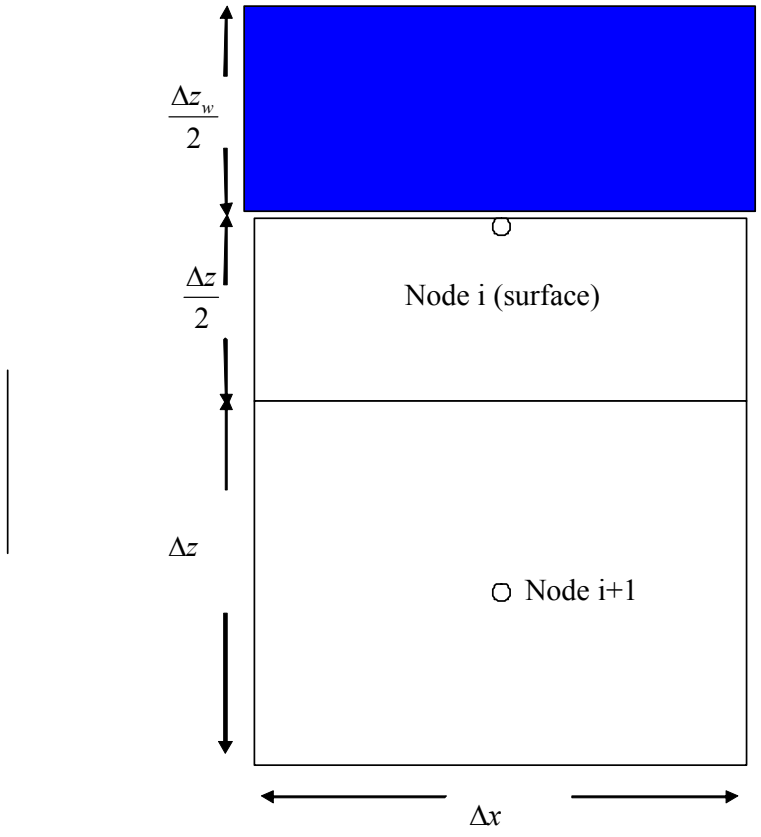

Figure 96 – Finite Difference Representation of Surface Node with Water Layer

Discretize the boundary conditions for this case

@ z = 0 t > 0

Saturation

$S_{surf}^{n+1} = 1$

and

$S_i^{n+1} = 1 \quad if \quad i\Delta z < z_{\text{int}}$

Temperature Boundary Conditions

The temperature of the surface node is calculated in the water layer sub-model and applied as a type 1 boundary condition in the model for the solid phase.

$T_1^{n+1} = T_{surf}$

Pressure Boundary Conditions

For now, assume that the interface node is the second node from the surface. If a large pressure were applied to the surface of the material, either from a large depth of standing water or a high momentum water flux, the interface could be deeper in the material. We will not consider that case, but rather only assume that the surface is completely saturated. The second node (interface node) will be partially saturated.

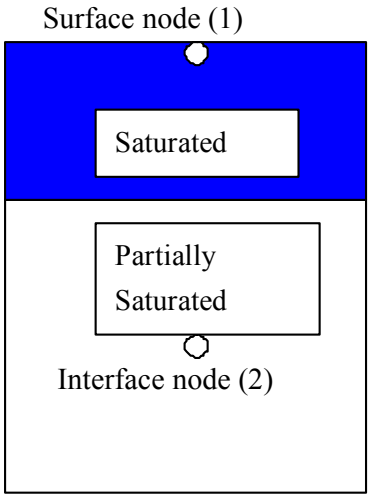

Figure 97 – Surface Node

At the surface, assume that the impact force of the water spray is negligible. The boundary pressure is simply the ambient pressure plus an additional pressure added by the water layer.

$$P = P_{\infty} + \rho_w g h_{layer} \qquad @\, z = 0$$

At the Back Face

@ z = L t > 0

$$S_N^{n+1} = S_o$$

$$T_N^{n+1} = T_o$$

$$P_N^{n+1} = P_{\infty}$$

In matrix form this is the top left hand side of the coefficient matrix.

$$\begin{bmatrix} C_{1,1} & C_{1,2} & C_{1,3} & C_{1,4} & C_{1,5} & C_{1,6} & \\ C_{2,1} & C_{2,2} & C_{2,3} & C_{2,4} & C_{2,5} & C_{2,6} & \dots \\ C_{3,1} & C_{3,2} & C_{3,3} & C_{3,4} & C_{3,5} & C_{3,6} & \\ & & \dots & & & & \end{bmatrix}$$

If the surface node is saturated, and the second node is the interface, then boundary conditions for pressure at the interface must be moved to the second node. If the interface node is past the second node, then these conditions must be moved further.

$$\begin{bmatrix} & & & & & \dots & & & & \\ \dots & C_{6,4} & C_{6,5} & C_{6,6} & C_{6,7} & C_{6,8} & C_{6,9} & C_{6,10} & C_{6,11} & C_{6,12} & \dots \\ & & & & & \dots & & & & \end{bmatrix}$$

and the bottom right corner of the coefficient matrix

$$\begin{bmatrix} & & & & & \dots & & \\ & C_{3N-2,3N-5} & C_{3N-2,3N-4} & C_{3N-2,3N-3} & C_{3N-2,3N-2} & C_{3N-2,3N-1} & C_{3N-2,3N} \\ \dots & C_{3N-1,3N-5} & C_{3N-1,3N-4} & C_{3N-1,3N-3} & C_{3N-1,3N-2} & C_{3N-1,3N-1} & C_{3N-1,3N} \\ & C_{3N,3N-5} & C_{3N,3N-4} & C_{3N,3N-3} & C_{3N,3N-2} & C_{3N,3N-1} & C_{3N,3N} \end{bmatrix}$$

and the top and bottom of the RHS matrix

$$\begin{bmatrix} RHS_1 \\ RHS_2 \\ RHS_3 \\ \dots \\ RHS_{3N-2} \\ RHS_{3N-1} \\ RHS_{3N} \end{bmatrix}$$

Where the coefficients in the upper left hand side are

$$C_{1,1} = 1$$
$$C_{1,2} = 0$$
$$C_{1,3} = 0$$

$$C_{2,1} = 0$$
$$C_{2,2} = 1$$
$$C_{2,3} = 0$$

$$C_{3,1} = 0$$
$$C_{3,2} = 0$$
$$C_{3,3} = 1$$

and the coefficients in the lower right hand side are

$$\begin{bmatrix} & & \cdots & \\ & C_{3N-2,3N-2} & C_{3N-2,3N-1} & C_{3N-2,3N} \\ \cdots & C_{3N-1,3N-2} & C_{3N-1,3N-1} & C_{3N-1,3N} \\ & C_{3N,3N-2} & C_{3N,3N-1} & C_{3N,3N} \end{bmatrix} = \begin{bmatrix} & \cdots & & \\ & 1 & 0 & 0 \\ \cdots & 0 & 1 & 0 \\ & 0 & 0 & 1 \end{bmatrix}$$

$$C_{3N-2,3N} = 0$$
$$C_{3N-2,3N-1} = 0$$
$$C_{3N-2,3N-2} = 1$$

$$C_{3N-1,3N} = 0$$
$$C_{3N-1,3N-1} = 1$$
$$C_{3N-1,3N-2} = 0$$

$$C_{3N,3N} = 1$$
$$C_{3N,3N-1} = 0$$
$$C_{3N,3N-2} = 0$$

The boundary values for the RHS matrix are

$$\begin{bmatrix} RHS_1 \\ RHS_2 \\ RHS_3 \\ \cdots \\ RHS_{3N-2} \\ RHS_{3N-1} \\ RHS_{3N} \end{bmatrix} = \begin{bmatrix} 1 \\ T_{surf} \\ P_\infty + \rho_w g h_{layer} \\ \cdots \\ S_o \\ T_o \\ P_o \end{bmatrix}$$

D.2.2. Discretized Back Face Boundary Conditions

Discretize the back face node as shown in Figure 98.

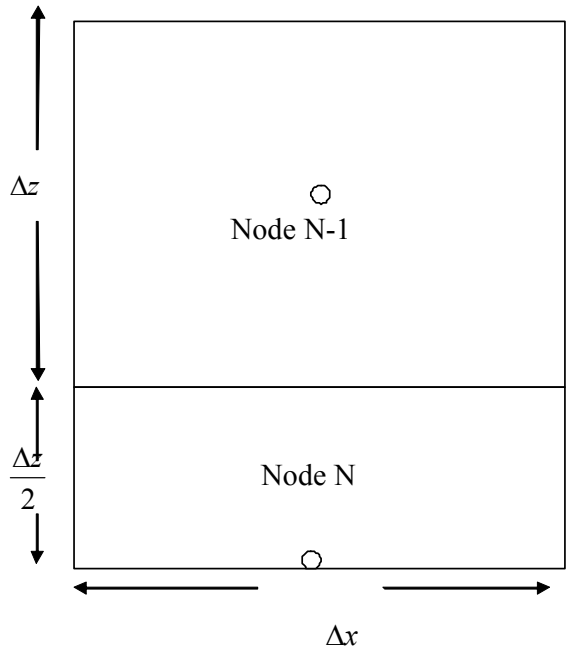

Figure 98 – Back Face Node Discretized

If the semi-infinite solid boundary condition is invoked, the boundary conditions are

$$\left.\begin{aligned} S_w &= S_{w,o} \\ T &= T_o \\ P &= P_o \end{aligned}\right\} @\ \ z = L$$

If heat or moisture reaches the back face, type 3 convective boundary conditions are given by

$$\left.\begin{aligned} &\dot{m}''_{spray} + \dot{m}''_{v} + \dot{m}''_{w} = \dot{m}''_{\substack{evap \\ loss}} \\ &\dot{q}''_{\substack{water \\ conv}} + \dot{q}''_{\substack{vapor \\ conv}} + \dot{q}''_{\substack{air \\ conv}} + \dot{q}''_{cond} + \dot{q}''_{e} + \dot{q}''_{\substack{water \\ app}} = \dot{q}''_{\substack{cond \\ loss}} + \dot{q}''_{\substack{vapor \\ loss}} + \dot{q}''_{\substack{air \\ loss}} + \dot{q}''_{\substack{re-rad \\ loss}} \\ &P = P_o \quad or \quad \dot{m}''_{a} = 0 \end{aligned}\right\} \ @ z = L \quad for \qquad t > 0$$

Discretized Back Face Saturation Boundary Condition

Discretize the back face boundary conditions. Start with COM for water. If a type 1 boundary condition is specified, the discretized form is

$$S_N^{n+1} = S_o$$

If a type 3 flux boundary condition is specified, the discretized boundary condition is much more complicated. The water and vapor flows are shown in Figure 99.

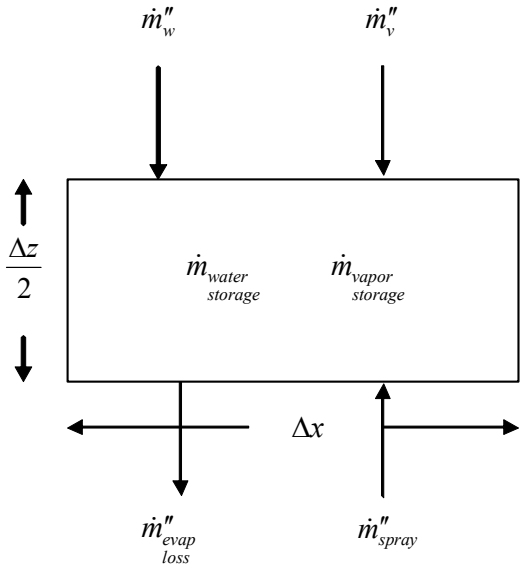

Figure 99 – Back Face Node Water and Vapor Flows

The total rate of water flow into the back face node is

$$\dot{m}_{\substack{water\\total}} = \left(\dot{m}''_w + \dot{m}''_{spray}\right)\Delta x \Delta y$$

The rate of water storage in the back face node is

$$\dot{m}_{\substack{water\\storage}} = \frac{\Delta x \Delta y \Delta z}{2}\left(\frac{\partial}{\partial t}\left(\phi \rho_w S_w\right) + \dot{m}'''_{evap}\right)$$

Setting the total flow into the control volume equal to the rate of storage gives an expression for conservation of mass for liquid water

$$\frac{\Delta z}{2}\left(\frac{\partial}{\partial t}\left(\phi\rho_w S_w\right)+\dot{m}'''_{evap}\right)=\dot{m}''_w+\dot{m}''_{spray}$$

The total rate of vapor flow into the back face node is

$$\dot{m}_{\substack{vapor\\total}}=\left(\dot{m}''_v-\dot{m}''_{\substack{evap\\loss}}\right)\Delta x\Delta y$$

The total rate of vapor storage in the back face node control volume is

$$\dot{m}_{\substack{vapor\\storage}}=\frac{\Delta x\Delta y\Delta z}{2}\left(\frac{\partial}{\partial t}\left(\phi\rho_v S_g\right)-\dot{m}'''_{evap}\right)$$

Setting the total flow into the control volume equal to the rate of storage gives an expression for conservation of mass for vapor

$$\frac{\Delta z}{2}\left(\frac{\partial}{\partial t}\left(\phi\rho_v S_g\right)-\dot{m}'''_{evap}\right)=\dot{m}''_v-\dot{m}''_{\substack{evap\\loss}}$$

Adding the conservation of mass for water and vapor together eliminates the volumetric evaporation terms and gives an expression for conservation of total water

$$\phi\frac{\Delta z}{2}\left(\frac{\partial\left(\rho_v S_g\right)}{\partial t}+\frac{\partial\left(\rho_w S_w\right)}{\partial t}\right)=\dot{m}''_w+\dot{m}''_v+\dot{m}''_{spray}-\dot{m}''_{\substack{evap\\loss}}$$

The water and vapor flux terms can have convective and diffusive components

$$\dot{m}''_w=-\rho_w\frac{KK_{r,w}}{\mu_w}\left(\nabla p_w-\rho_w\vec{g}\right)\qquad @\,z=L$$

$$\dot{m}''_v=-\rho_v\frac{KK_{r,g}}{\mu_v}\nabla P-\frac{C^2}{\rho}M_a M_v D_{eff,g}\nabla X_v\qquad @\,z=L$$

Expand these terms

$$-\rho_w \frac{KK_{r,l}}{\mu_w}\left(\frac{\partial p_w}{\partial z}-\rho g\right)=-\rho_w \frac{KK_{r,l}}{\mu_w}\frac{\partial P}{\partial z}+\rho_w \frac{KK_{r,l}}{\mu_w}\frac{\partial p_{cap}}{\partial S_w}\frac{\partial S_w}{\partial z}+\rho_w \frac{KK_{r,l}}{\mu_w}\frac{\partial p_{cap}}{\partial T}\frac{\partial T}{\partial z}+\rho_w \frac{KK_{r,l}}{\mu_w}\rho g$$

$$-\rho_v \frac{KK_{r,v}}{\mu_v}\frac{\partial P}{\partial z}=-\frac{p_v}{R_v T}\frac{KK_{r,v}}{\mu_v}\frac{\partial P}{\partial z}$$

$$-\frac{C^2}{\rho}M_a M_v D_{eff,g}\frac{\partial X_v}{\partial z}=-\frac{M_a M_v D_{eff,g}}{R\left(\left(P-p_v\right)M_a+p_v M_v\right)}\left(P\frac{\partial p_v}{\partial S_w}\frac{\partial S_w}{\partial z}+P\frac{\partial p_v}{\partial T}\frac{\partial T}{\partial z}-p_v\frac{\partial P}{\partial z}\right)$$

The total mass flow of water into the back face node can be written as

$$\dot{m}_{total}=\left(-K_1\frac{\partial S_w}{\partial z}-K_2\frac{\partial T}{\partial z}-K_3\frac{\partial P}{\partial z}+K_{19}+\dot{m}''_{spray}-\dot{m}''_{\substack{evap\\loss}}\right)\Delta x\Delta y$$

The vapor storage term can be expanded

$$\begin{aligned}\phi\frac{\partial\left(\rho_v S_g\right)}{\partial t}&=\phi\frac{\partial}{\partial t}\left(\frac{p_v}{R_v T}\left(1-S_w\right)\right)\\&=-\frac{\phi p_v}{R_v T}\frac{\partial S_w}{\partial t}+\frac{\phi}{R_v}\left(1-S_w\right)\frac{\partial}{\partial t}\left(\frac{p_v}{T}\right)\\&=-\frac{\phi p_v}{R_v T}\frac{\partial S_w}{\partial t}+\frac{\phi}{R_v}\left(1-S_w\right)\frac{\partial}{\partial T}\left(\frac{p_v}{T}\right)\frac{\partial T}{\partial t}+\frac{\phi}{R_v T}\left(1-S_w\right)\frac{\partial p_v}{\partial S_w}\frac{\partial S_w}{\partial t}\end{aligned}$$

So the total storage can be written as

$$\frac{\Delta z}{2}\left(K_4\frac{\partial S_w}{\partial t}+K_5\frac{\partial T}{\partial t}+K_6\frac{\partial P}{\partial t}\right)$$

So the back face BC for COM for water can be written as

$$\frac{\Delta z}{2}\left(K_4\frac{\partial S_w}{\partial t}+K_5\frac{\partial T}{\partial t}+K_6\frac{\partial P}{\partial t}\right)=-K_1\frac{\partial S_w}{\partial z}-K_2\frac{\partial T}{\partial z}-K_3\frac{\partial P}{\partial z}+K_{19}+\dot{m}''_{spray}-\dot{m}''_{\substack{evap\\loss}}$$

Discretized Back Face Pressure Boundary Condition

The air mass flux and storage terms associated with the back face node are shown in Figure 100.

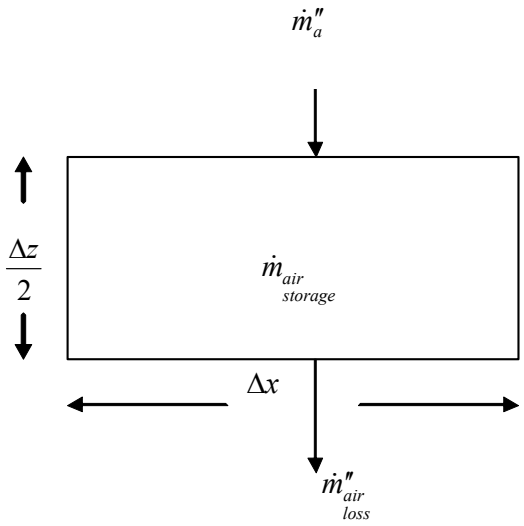

Figure 100 – Back Face Node Air Fluxes

If a type 1 boundary condition is specified, the discretized form is

$$P_N^{n+1} = P_\infty$$

If a flux boundary condition is specified, a more complicated boundary condition must be derived. The rate of mass storage of air in the back face node is

$$\dot{m}_{air\ storage} = \frac{\Delta x \Delta y \Delta z}{2} \phi \frac{\partial \left(\rho_a S_g \right)}{\partial t}$$

The total mass flow of air into the back face node is

$$\dot{m}_{air\ total} = \left(\dot{m}''_a - \dot{m}''_{air\ loss} \right) \Delta x \Delta y$$

Setting the flow equal to the rate of storage gives an expression for conservation of mass for air for the back face node

$$\frac{\Delta z}{2}\phi\frac{\partial\left(\rho_a S_g\right)}{\partial t}=\left(\dot{m}''_a-\dot{m}''_{\substack{air\\loss}}\right)$$

This condition always holds true, even if a type 1 boundary condition is specified. In that case the term $\dot{m}''_{\substack{air\\loss}}$ is assumed to adjust such that a pressure P_∞ is maintained at the surface. The surface air loss term $\dot{m}''_{\substack{air\\loss}}$ is not explicitly calculated in the model. If a no-flux boundary condition is applied to the back face, the term $\dot{m}''_{\substack{air\\loss}}$ is equal to zero and conservation of mass becomes

$$\frac{\Delta z}{2}\phi\frac{\partial\left(\rho_a S_g\right)}{\partial t}=\dot{m}''_a$$

The internal air flux term has convective and diffusive components

$$\dot{m}''_a=-\rho_a\frac{KK_{r,a}}{\mu_a}\nabla P-\frac{C^2}{\rho}M_v M_a D_{av}\nabla X_a$$

Expand these terms

$$\rho_a \frac{KK_{r,g}}{\mu_a}\frac{\partial P}{\partial z} = \frac{p_a}{R_a T}\frac{KK_{r,g}}{\mu_a}\frac{\partial P}{\partial z}$$
$$= \frac{P - p_v}{R_a T}\frac{KK_{r,g}}{\mu_a}\frac{\partial P}{\partial z}$$

$$\frac{C^2}{\rho} M_v M_a D_{eff,g}\frac{\partial X_a}{\partial z} = \left(\frac{P}{RT}\right)^2 \frac{1}{\frac{p_a}{R_a T} + \frac{p_v}{R_v T}} M_v M_a D_{eff,g}\frac{\partial}{\partial z}\left(\frac{p_a}{P}\right)$$
$$= \left(\frac{P}{RT}\right)^2 \frac{1}{\frac{p_a}{R_a T} + \frac{p_v}{R_v T}} M_v M_a D_{eff,g}\frac{\partial}{\partial z}\left(\frac{P - p_v}{P}\right)$$
$$= \frac{P^2}{RT\left(M_a\left(P - p_v\right) + M_v p_v\right)} M_v M_a D_{eff,g}\frac{\partial}{\partial z}\left(1 - \frac{p_v}{P}\right)$$
$$= -\frac{M_v M_a D_{eff,g}}{RT\left(M_a\left(P - p_v\right) + M_v p_v\right)}\left(P\frac{\partial p_v}{\partial z} - p_v\frac{\partial P}{\partial z}\right)$$
$$= -\frac{M_v M_a D_{eff,g}}{RT\left(M_a\left(P - p_v\right) + M_v p_v\right)}\left(P\frac{\partial p_v}{\partial S_w}\frac{\partial S_w}{\partial z} + P\frac{\partial p_v}{\partial T}\frac{\partial T}{\partial z} - p_v\frac{\partial P}{\partial z}\right)$$

Which can be written as

$$\dot{m}_a'' = -K_7\frac{\partial S_w}{\partial z} - K_8\frac{\partial T}{\partial z} - K_9\frac{\partial P}{\partial z}$$

The storage in the back face boundary node is

$$\phi\frac{\Delta z}{2}\frac{\partial\left(\rho_a S_g\right)}{\partial t} = \phi\frac{\Delta z}{2}\frac{\partial}{\partial t}\left(\frac{p_a}{R_a T}\left(1 - S_w\right)\right)$$
$$= \phi\frac{\Delta z}{2}\frac{\partial}{\partial t}\left(\frac{\left(P - p_v\right)}{R_a T}\left(1 - S_w\right)\right)$$
$$= -\frac{\Delta z}{2}\frac{\phi}{R_a}\left(\frac{\left(P - p_v\right)}{T} + \frac{\left(1 - S_w\right)}{T}\frac{\partial p_v}{\partial S_w}\right)\frac{\partial S_w}{\partial t} - \frac{\Delta z}{2}\frac{\phi}{R_a}\left(\frac{P}{T^2} - \frac{PS_w}{T^2} + \left(1 + S_w\right)\frac{\partial}{\partial T}\left(\frac{p_v}{T}\right)\right)\frac{\partial T}{\partial t}$$
$$+ \frac{\Delta z}{2}\frac{\phi\left(1 - S_w\right)}{R_a T}\frac{\partial P}{\partial t}$$

Which can be written as

$$\frac{\Delta z}{2}\left(K_{10}\frac{\partial S_w}{\partial t} + K_{11}\frac{\partial T}{\partial t} + K_{12}\frac{\partial P}{\partial t} \right)$$

So the boundary condition for conservation of air can be written as

$$\frac{\Delta z}{2}\left(K_{10}\frac{\partial S_w}{\partial t} + K_{11}\frac{\partial T}{\partial t} + K_{12}\frac{\partial P}{\partial t} \right) = -K_7\frac{\partial S_w}{\partial z} - K_8\frac{\partial T}{\partial z} - K_9\frac{\partial P}{\partial z}$$

Discretized Back Face Thermal Boundary Condition

The enthalpy flows into and out of the back face node are shown in

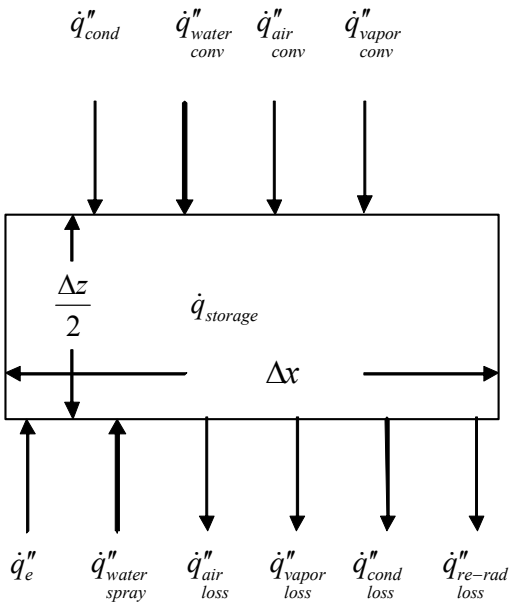

Figure 101 – Back Face Node Enthalpy Fluxes

The energy storage in the back face node is

$$\dot{q}_{storage} = \frac{\Delta x \Delta y \Delta z}{2}\left(\frac{\partial}{\partial t}\left(c_s h_s\right) + \frac{\partial}{\partial t}\left(c_w h_w\right) + \frac{\partial}{\partial t}\left(c_a h_a\right) + \frac{\partial}{\partial t}\left(c_v h_v\right)\right)$$

The total energy flow rate into the back face node is

$$\dot{q}_{total} = \left(\dot{q}''_{cond} + \dot{q}''_{\substack{water\\conv}} + \dot{q}''_{\substack{vapor\\conv}} + \dot{q}''_{\substack{air\\conv}} + \dot{q}''_{e} + \dot{q}''_{\substack{water\\spray}} - \dot{q}''_{\substack{air\\loss}} - \dot{q}''_{\substack{vapor\\loss}} - \dot{q}''_{\substack{cond\\loss}} - \dot{q}''_{\substack{re-rad\\loss}}\right)\Delta x \Delta y$$

Setting these equal gives an expression for conservation of energy for the back face node

$$\frac{\Delta x\Delta y\Delta z}{2}\left(\frac{\partial}{\partial t}\left(c_s h_s\right)+\frac{\partial}{\partial t}\left(c_w h_w\right)+\frac{\partial}{\partial t}\left(c_a h_a\right)+\frac{\partial}{\partial t}\left(c_v h_v\right)\right)$$
$$=\left(\dot{q}''_{cond}+\underset{conv}{\dot{q}''_{water}}+\underset{conv}{\dot{q}''_{vapor}}+\underset{conv}{\dot{q}''_{air}}+\dot{q}''_{e}+\underset{spray}{\dot{q}''_{water}}-\underset{loss}{\dot{q}''_{air}}-\underset{loss}{\dot{q}''_{vapor}}-\underset{loss}{\dot{q}''_{cond}}-\underset{loss}{\dot{q}''_{re-rad}}\right)\Delta x\Delta y$$

Use conservation of mass for water, vapor, and air to eliminate terms. Start with the enthalpy flux and storage terms associated with liquid water. The convective flows into the back face surface node (N) from the previous node (N-1) are assumed to be at the temperature of the N-1 node. Convective flows from the back face node to the ambient are assumed to be at the back face node temperature.

$$\frac{\Delta z}{2}\frac{\partial}{\partial t}\left(c_w h_w\right)-\underset{spray}{\dot{q}''_{water}}-\underset{conv}{\dot{q}''_{water}}=\frac{\Delta z}{2}\left(c_w\frac{\partial h_w}{\partial t}+h_w\frac{\partial c_w}{\partial t}\right)-\underset{spray}{\dot{m}''_{spray}h_{water}}-\dot{m}''_w h_w$$
$$=\frac{\Delta z}{2}c_w\frac{\partial h_w}{\partial t}+\frac{\Delta z}{2}h_w\frac{\partial c_w}{\partial t}-\dot{m}''_{spray}\left(h_f^o+\int_{T_o}^{T_{spray}}C_p\partial T\right)-\dot{m}''_w\left(h_f^o+\int_{T_o}^{T_{N-1}}C_p\partial T\right)$$
$$=\frac{\Delta z}{2}c_w\frac{\partial h_w}{\partial t}+\frac{\Delta z}{2}h_w\frac{\partial c_w}{\partial t}-\dot{m}''_{spray}\left(h_f^o+\int_{T_o}^{T_w}C_p\partial T+\int_{T_w}^{T_{spray}}C_p\partial T\right)$$
$$-\dot{m}''_w\left(h_f^o+\int_{T_o}^{T_w}C_p\partial T+\int_{T_w}^{T_{N-1}}C_p\partial T\right)$$
$$=\frac{\Delta z}{2}c_w\frac{\partial h_w}{\partial t}-\dot{m}''_{spray}C_{p,w}\left(T_{spray}-T_{surface}\right)-\dot{m}''_{spray}C_{p,w}\left(T_{N-1}-T_N\right)$$
$$+h_w\left(\frac{\Delta z}{2}\phi\frac{\partial\left(\rho_w S_w\right)}{\partial t}-\dot{m}''_{spray}-\dot{m}''_w\right)$$
$$=\frac{\Delta z}{2}c_w\frac{\partial h_w}{\partial t}-\dot{m}''_{spray}C_{p,w}\left(T_{spray}-T_{surface}\right)-\dot{m}''_w C_{p,w}\left(T_{N-1}-T_N\right)-h_w\dot{m}'''_{evap}$$

Next simplify the enthalpy flux and storage terms associated with water vapor.

$$\frac{\Delta z}{2}\frac{\partial}{\partial t}\left(c_v h_v\right)+\underset{loss}{\dot{q}''_{vapor}}-\underset{conv}{\dot{q}''_{vapor}}=\frac{\Delta z}{2}\left(c_v\frac{\partial h_v}{\partial t}+h_v\frac{\partial c_v}{\partial t}\right)+h_v\dot{m}''_{evap}-h_v\dot{m}''_v$$

$$=\frac{\Delta z}{2}\left(c_v\frac{\partial h_v}{\partial t}+h_v\frac{\partial c_v}{\partial t}\right)+h_v\dot{m}''_{evap}-\dot{m}''_v\left(h_f^o+\int_{T_o}^{T_{N-1}}C_p\partial T\right)$$

$$=\frac{\Delta z}{2}\left(c_v\frac{\partial h_v}{\partial t}+h_v\frac{\partial c_v}{\partial t}\right)+h_v\dot{m}''_{evap}-\dot{m}''_v\left(h_f^o+\int_{T_o}^{T_N}C_p\partial T+\int_{T_N}^{T_{N-1}}C_p\partial T\right)$$

$$=\frac{\Delta z}{2}c_v\frac{\partial h_v}{\partial t}-\dot{m}''C_{p,w}\left(T_{N-1}-T_N\right)+h_v\left(\frac{\Delta z}{2}\phi\frac{\partial\left(\rho_g S_g\right)}{\partial t}+\dot{m}''_{evap}-\dot{m}''_v\right)$$

$$=\frac{\Delta z}{2}c_v\frac{\partial h_v}{\partial t}-\dot{m}''C_{p,w}\left(T_{N-1}-T_N\right)+h_v\dot{m}'''_{evap}$$

Finally simplify the enthalpy flux and storage terms associated with air

$$\frac{\Delta z}{2}\frac{\partial}{\partial t}\left(c_a h_a\right)-\underset{conv}{\dot{q}''_{air}}+\underset{loss}{\dot{q}''_{air}}=\frac{\Delta z}{2}\left(c_a\frac{\partial h_a}{\partial t}+h_a\frac{\partial c_a}{\partial t}\right)-\dot{m}''_a h_a+\underset{loss}{\dot{m}''_{air}}h_a$$

$$=\frac{\Delta z}{2}\left(c_a\frac{\partial h_a}{\partial t}+h_a\frac{\partial c_a}{\partial t}\right)-\dot{m}''_a\left(h_f^o+\int_{T_o}^{T_{N-1}}C_{p,a}\partial T\right)+\underset{loss}{\dot{m}''_{air}}h_a$$

$$=\frac{\Delta z}{2}\left(c_a\frac{\partial h_a}{\partial t}+h_a\frac{\partial c_a}{\partial t}\right)-\dot{m}''_a\left(h_f^o+\int_{T_o}^{T_N}C_{p,a}\partial T+\int_{T_N}^{T_{N-1}}C_{p,a}\partial T\right)+\underset{loss}{\dot{m}''_{air}}h_a$$

$$=\frac{\Delta z}{2}c_a\frac{\partial h_a}{\partial t}-\dot{m}''_a C_{p,a}\left(T_{N-1}-T_N\right)+h_a\left(\frac{\Delta z}{2}\phi\frac{\partial\left(\rho_a S_g\right)}{\partial t}-\dot{m}''_a+\underset{loss}{\dot{m}''_{air}}\right)$$

$$=\frac{\Delta z}{2}c_a\frac{\partial h_a}{\partial t}-\dot{m}''_a C_{p,a}\left(T_{N-1}-T_N\right)$$

Thermal conduction in the material into the back face node is assumed to occur by Fourier's law through each component present. ψ represents the volumetric content of air, vapor, water, and solid material present.

$$\dot{q}''_{cond}=-\psi_a k_a\frac{\partial T_a}{\partial z}-\psi_v k_v\frac{\partial T_v}{\partial z}-\psi_w k_w\frac{\partial T_w}{\partial z}-\psi_s k_s\frac{\partial T_s}{\partial z}$$

The conductive losses to the ambient and re-radiative loss terms can be defined as

$$\dot{q}''_{\substack{cond \\ loss}} = h\left(T_{surf} - T_{\infty}\right)$$
$$\dot{q}''_{re-rad} = \varepsilon\sigma\left(T_{surf}^4 - T_{\infty}^4\right)$$

The conservation of energy for the surface node can now be written as

$$\frac{\Delta z}{2}\left(c_s C_{p,s}\frac{\partial T_s}{\partial t} + c_w C_{p,w}\frac{\partial T_w}{\partial t} + c_a C_{p,a}\frac{\partial T_a}{\partial t} + c_v C_{p,v}\frac{\partial T_v}{\partial t} + \left(h_w - h_w\right)\dot{m}'''_{evap}\right)$$
$$= \begin{pmatrix} \dot{q}''_e + \dot{m}''_{spray} C_{p,w}\left(T_{spray} - T_{surface}\right) + \dot{m}''_w C_{p,w}\left(T_{N-1} - T_N\right) + \dot{m}''_v C_{p,v}\left(T_{N-1} - T_N\right) + \dot{m}''_a C_{p,a}\left(T_{N-1} - T_N\right) \\ -h\left(T_s - T_{\infty}\right) - \varepsilon_s\sigma\left(T_s^4 - T_{\infty}^4\right) - \psi_a k_a\frac{\partial T_a}{\partial z} - \psi_v k_v\frac{\partial T_v}{\partial z} - \psi_w k_w\frac{\partial T_w}{\partial z} - \psi_s k_s\frac{\partial T_s}{\partial z} \end{pmatrix}$$

Invoking the assumption of local thermal equilibrium allows this to be written as

$$\frac{\Delta z}{2}\left(\left(\rho C_p\right)_{eff}\frac{\partial T}{\partial t} + \Delta h_v \dot{m}'''_{evap}\right) = \begin{pmatrix} \dot{q}''_e + \dot{m}''_{spray} C_{p,w}\left(T_{spray} - T_{surface}\right) \\ +\dot{m}''_w C_{p,w}\left(T_{N-1} - T_N\right) + \dot{m}''_v C_{p,v}\left(T_{N-1} - T_N\right) + \dot{m}''_a C_{p,a}\left(T_{N-1} - T_N\right) \\ -h\left(T_s - T_{\infty}\right) - \varepsilon_s\sigma\left(T_s^4 - T_{\infty}^4\right) - k_{eff}\frac{\partial T}{\partial z} \end{pmatrix}$$

Now use conservation of mass for liquid water to substitute for the evaporation rate. COM for water for the back face node can be written as

$$\frac{\Delta z}{2}\dot{m}'''_{evap} = \dot{m}''_{spray} - \rho_w\frac{KK_{r,l}}{\mu_w}\left(\frac{\partial\left(P - p_c\right)}{\partial z} - \rho g\right) - \frac{\Delta z}{2}\frac{\partial}{\partial t}\left(\phi\rho_w S_w\right)$$

Substituting this into the BC for conservation of energy gives

$$\frac{\Delta z}{2}\left(\rho C_p\right)_{eff}\frac{\partial T}{\partial t}+\Delta h_v\left(\dot{m}''_{spray}-\rho_w\frac{KK_{r,l}}{\mu_w}\left(\frac{\partial\left(P-p_c\right)}{\partial z}-\rho g\right)-\frac{\Delta z}{2}\phi\frac{\partial\left(\rho_w S_w\right)}{\partial t}\right)$$
$$=\begin{pmatrix}\dot{q}''_e+\dot{m}''_{spray}C_{p,w}\left(T_{spray}-T_{surface}\right)+\dot{m}''_w C_{p,w}\left(T_{N-1}-T_N\right)+\dot{m}''_v C_{p,v}\left(T_{N-1}-T_N\right)\\+\dot{m}''_a C_{p,a}\left(T_{N-1}-T_N\right)-h\left(T_s-T_\infty\right)-\varepsilon_s\sigma\left(T_s^4-T_\infty^4\right)-k_{eff}\frac{\partial T}{\partial z}\end{pmatrix}$$

Which can be written as

$$-\frac{\Delta z}{2}\phi\rho_w\Delta h_v\frac{\partial\left(S_w\right)}{\partial t}+\frac{\Delta z}{2}\left(\rho C_p\right)_{eff}\frac{\partial T}{\partial t}$$
$$=-\Delta h_v\rho_w\frac{KK_{r,l}}{\mu_w}\frac{\partial p_{cap}}{\partial S_w}\frac{\partial S_w}{\partial z}-k_{eff}\frac{\partial T}{\partial z}-\Delta h_v\rho_w\frac{KK_{r,l}}{\mu_w}\frac{\partial p_{cap}}{\partial T}\frac{\partial T}{\partial z}+\Delta h_v\rho_w\frac{KK_{r,l}}{\mu_w}\frac{\partial P}{\partial z}-\Delta h_v\rho_w\frac{KK_{r,l}}{\mu_w}\rho g$$
$$+\begin{pmatrix}-\Delta h_v\dot{m}''_{spray}+\dot{q}''_e+\dot{m}''_{spray}C_{p,w}\left(T_{spray}-T_{surface}\right)+\dot{m}''_w C_{p,w}\left(T_{N-1}-T_N\right)+\dot{m}''_v C_{p,v}\left(T_{N-1}-T_N\right)\\+\dot{m}''_a C_{p,a}\left(T_{N-1}-T_N\right)-h\left(T_s-T_\infty\right)-\varepsilon_s\sigma\left(T_s^4-T_\infty^4\right)\end{pmatrix}$$

Substititing for the K's

$$\frac{\Delta z}{2}\left(K_{16}\frac{\partial S_w}{\partial t}+K_{17}\frac{\partial T}{\partial t}+K_{18}\frac{\partial P}{\partial t}\right)=-K_{13}\frac{\partial S_w}{\partial z}-K_{14}\frac{\partial T}{\partial z}-K_{15}\frac{\partial P}{\partial z}-K_{20}$$
$$+\begin{pmatrix}-\Delta h_v\dot{m}''_{spray}+\dot{q}''_e+\dot{m}''_{spray}C_{p,w}\left(T_{spray}-T_{surface}\right)+\dot{m}''_w C_{p,w}\left(T_{N-1}-T_N\right)+\dot{m}''_v C_{p,v}\left(T_{N-1}-T_N\right)\\+\dot{m}''_a C_{p,a}\left(T_{N-1}-T_N\right)-h\left(T_s-T_\infty\right)-\varepsilon_s\sigma\left(T_s^4-T_\infty^4\right)\end{pmatrix}$$

So, in summary, the complete set of back face flux boundary conditions can be written

$@\, z=L \quad for \quad t>0$

$$\frac{\Delta z}{2}\left(K_4\frac{\partial S_w}{\partial t}+K_5\frac{\partial T}{\partial t}+K_6\frac{\partial P}{\partial t}\right)=-K_1\frac{\partial S_w}{\partial z}-K_2\frac{\partial T}{\partial z}-K_3\frac{\partial P}{\partial z}+K_{19}+\dot{m}''_{spray}-\dot{m}''_{evap}$$
$$\frac{\Delta z}{2}\left(K_{10}\frac{\partial S_w}{\partial t}+K_{11}\frac{\partial T}{\partial t}+K_{12}\frac{\partial P}{\partial t}\right)=-K_7\frac{\partial S_w}{\partial z}-K_8\frac{\partial T}{\partial z}-K_9\frac{\partial P}{\partial z}$$

$$\frac{\Delta z}{2}\left(K_{16}\frac{\partial S_w}{\partial t}+K_{17}\frac{\partial T}{\partial t}+K_{18}\frac{\partial T}{\partial t}\right)=-K_{13}\frac{\partial S_w}{\partial z}-K_{14}\frac{\partial T}{\partial z}K_{15}\frac{\partial P}{\partial z}-K_{20}$$
$$+\begin{pmatrix}-\Delta h_v\dot{m}''_{spray}+\dot{q}''_e+\dot{m}''_{spray}C_{p,w}\left(T_{spray}-T_{surface}\right)+\dot{m}''_w C_{p,w}\left(T_{N-1}-T_N\right)+\dot{m}''_v C_{p,v}\left(T_{N-1}-T_N\right)\\+\dot{m}''_a C_{p,a}\left(T_{N-1}-T_N\right)-h\left(T_s-T_\infty\right)-\varepsilon_s\sigma\left(T_s^4-T_\infty^4\right)\end{pmatrix}$$

Discretize the BC's using a crank Nicholson scheme

$$COM-Water$$

$$-\theta\left(K1^{n+1}_{N-\frac{1}{2}}\frac{S_N^{n+1}-S_{N-1}^{n+1}}{\Delta z}+K2^{n+1}_{N-\frac{1}{2}}\frac{T_N^{n+1}-T_{N-1}^{n+1}}{\Delta z}+K3^{n+1}_{N-\frac{1}{2}}\frac{P_N^{n+1}-P_{N-1}^{n+1}}{\Delta z}\right)+\theta K19^{n+1}_{N-\frac{1}{2}}$$

$$-(1-\theta)\left(K1^{n}_{N-\frac{1}{2}}\frac{S_N^{n}-S_{N-1}^{n}}{\Delta z}+K2^{n}_{N-\frac{1}{2}}\frac{T_N^{n}-T_{N-1}^{n}}{\Delta z}+K3^{n}_{N-\frac{1}{2}}\frac{P_N^{n}-P_{N-1}^{n}}{\Delta z}\right)+(1-\theta)K19^{n}_{N-\frac{1}{2}}$$

$$-\dot{m}''_{evap}+\dot{m}''_{spray}$$

$$=\frac{\Delta z}{2}K4^{n+\frac{1}{2}}_{N}\frac{S_N^{n+1}-S_N^{n}}{\Delta t}+\frac{\Delta z}{2}K5^{n+\frac{1}{2}}_{N}\frac{T_N^{n+1}-T_N^{n}}{\Delta t}+\frac{\Delta z}{2}K6^{n+\frac{1}{2}}_{N}\frac{P_N^{n+1}-P_N^{n}}{\Delta t}$$

$$COM-Air$$

$$-\theta\left(K7^{n+1}_{N-\frac{1}{2}}\frac{S_N^{n+1}-S_{N-1}^{n+1}}{\Delta z}+K8^{n+1}_{N-\frac{1}{2}}\frac{T_N^{n+1}-T_{N-1}^{n+1}}{\Delta z}+K9^{n+1}_{N-\frac{1}{2}}\frac{P_N^{n+1}-P_{N-1}^{n+1}}{\Delta z}\right)$$

$$-(1-\theta)\left(K7^{n}_{N-\frac{1}{2}}\frac{S_N^{n}-S_{N-1}^{n}}{\Delta z}+K8^{n}_{N-\frac{1}{2}}\frac{T_N^{n}-T_{N-1}^{n}}{\Delta z}+K9^{n}_{N-\frac{1}{2}}\frac{P_N^{n}-P_{N-1}^{n}}{\Delta z}\right)$$

$$=\frac{\Delta z}{2}K10^{n+\frac{1}{2}}_{N}\frac{S_N^{n+1}-S_N^{n}}{\Delta t}+\frac{\Delta z}{2}K11^{n+\frac{1}{2}}_{N}\frac{T_N^{n+1}-T_N^{n}}{\Delta t}+\frac{\Delta z}{2}K12^{n+\frac{1}{2}}_{N}\frac{P_N^{n+1}-P_N^{n}}{\Delta t}$$

$$COE$$

$$-\theta\left(K13^{n+1}_{N-\frac{1}{2}}\frac{S_N^{n+1}-S_{N-1}^{n+1}}{\Delta z}+K14^{n+1}_{N-\frac{1}{2}}\frac{T_N^{n+1}-T_{N-1}^{n+1}}{\Delta z}+K15^{n+1}_{N-\frac{1}{2}}\frac{P_N^{n+1}-P_{N-1}^{n+1}}{\Delta z}\right)-\theta K20^{n+1}_{N-\frac{1}{2}}$$

$$-(1-\theta)\left(K13^{n}_{N-\frac{1}{2}}\frac{S_N^{n}-S_{N-1}^{n}}{\Delta z}+K14^{n}_{N-\frac{1}{2}}\frac{T_N^{n}-T_{N-1}^{n}}{\Delta z}+K15^{n}_{N-\frac{1}{2}}\frac{P_N^{n}-P_{N-1}^{n}}{\Delta z}\right)-(1-\theta)K20^{n}_{N-\frac{1}{2}}$$

$$+\begin{pmatrix}-\Delta h_v\dot{m}''_{spray}+\dot{q}''_e+\dot{m}''_{spray}C_{p,w}\left(T_{spray}-T_{surface}\right)+\dot{m}''_wC_{p,w}\left(T_{N-1}-T_N\right)+\dot{m}''_vC_{p,v}\left(T_{N-1}-T_N\right)\\+\dot{m}''_aC_{p,a}\left(T_{N-1}-T_N\right)-h\left(T_s-T_\infty\right)-\varepsilon_s\sigma\left(T_s^4-T_\infty^4\right)\end{pmatrix}$$

$$=\frac{\Delta z}{2}K16^{n+\frac{1}{2}}_{N}\frac{S_N^{n+1}-S_N^{n}}{\Delta t}+\frac{\Delta z}{2}K17^{n+\frac{1}{2}}_{N}\frac{T_N^{n+1}-T_N^{n}}{\Delta t}+\frac{\Delta z}{2}K18^{n+\frac{1}{2}}_{N}\frac{P_N^{n+1}-P_N^{n}}{\Delta t}$$

Rearrange the discretized boundary conditions

COM – Water

$$\left(-\frac{\theta}{\Delta z}K1^{n+1}_{N-\frac{1}{2}}\right)S^{n+1}_{N-1}+\left(-\frac{\theta}{\Delta z}K2^{n+1}_{N-\frac{1}{2}}\right)T^{n+1}_{N-1}+\left(-\frac{\theta}{\Delta z}K3^{n+1}_{N-\frac{1}{2}}\right)P^{n+1}_{N-1}$$

$$+\left(\frac{\theta}{\Delta z}K1^{n+1}_{N-\frac{1}{2}}-\frac{\Delta z}{2\Delta t}K4^{n+\frac{1}{2}}_{N}\right)S^{n+1}_{N}+\left(\frac{\theta}{\Delta z}K2^{n+1}_{N-\frac{1}{2}}-\frac{\Delta z}{2\Delta t}K5^{n+\frac{1}{2}}_{N}\right)T^{n+1}_{N}+\left(\frac{\theta}{\Delta z}K3^{n+1}_{N-\frac{1}{2}}-\frac{\Delta z}{2\Delta t}K6^{n+\frac{1}{2}}_{N}\right)P^{n+1}_{N}$$

$$=\left(\frac{(1-\theta)}{\Delta z}K1^{n}_{N-\frac{1}{2}}\right)S^{n}_{N-1}+\left(\frac{(1-\theta)}{\Delta z}K2^{n}_{N-\frac{1}{2}}\right)T^{n}_{N-1}+\left(\frac{(1-\theta)}{\Delta z}K3^{n}_{N-\frac{1}{2}}\right)P^{n}_{N-1}$$

$$+\left(-\frac{\Delta z}{2\Delta t}K4^{n+\frac{1}{2}}_{N}-\frac{(1-\theta)}{\Delta z}K1^{n}_{N-\frac{1}{2}}\right)S^{n}_{N}+\left(-\frac{\Delta z}{2\Delta t}K5^{n+\frac{1}{2}}_{N}-\frac{(1-\theta)}{\Delta z}K2^{n}_{N-\frac{1}{2}}\right)T^{n}_{N}$$

$$+\left(-\frac{\Delta z}{2\Delta t}K6^{n+\frac{1}{2}}_{N}-\frac{(1-\theta)}{\Delta z}K3^{n}_{N-\frac{1}{2}}\right)P^{n}_{N}+\theta K19^{n+1}_{N-\frac{1}{2}}+(1-\theta)K19^{n}_{N-\frac{1}{2}}$$

$$-\dot{m}''_{evap}+\dot{m}''_{spray}$$

COM – Air

$$\left(-\frac{\theta}{\Delta z}K7^{n+1}_{N-\frac{1}{2}}\right)S^{n+1}_{N-1}+\left(-\frac{\theta}{\Delta z}K8^{n+1}_{N-\frac{1}{2}}\right)T^{n+1}_{N-1}+\left(-\frac{\theta}{\Delta z}K9^{n+1}_{N-\frac{1}{2}}\right)P^{n+1}_{N-1}$$

$$+\left(\frac{\theta}{\Delta z}K7^{n+1}_{N-\frac{1}{2}}-\frac{\Delta z}{2\Delta t}K10^{n+\frac{1}{2}}_{N}\right)S^{n+1}_{N}+\left(\frac{\theta}{\Delta z}K8^{n+1}_{N-\frac{1}{2}}-\frac{\Delta z}{2\Delta t}K11^{n+\frac{1}{2}}_{N}\right)T^{n+1}_{N}+\left(\frac{\theta}{\Delta z}K9^{n+1}_{N-\frac{1}{2}}-\frac{\Delta z}{2\Delta t}K12^{n+\frac{1}{2}}_{N}\right)P^{n+1}_{N}$$

$$=\left(\frac{(1-\theta)}{\Delta z}K7^{n}_{N-\frac{1}{2}}\right)S^{n}_{N-1}+\left(\frac{(1-\theta)}{\Delta z}K8^{n}_{N-\frac{1}{2}}\right)T^{n}_{N-1}+\left(\frac{(1-\theta)}{\Delta z}K9^{n}_{N-\frac{1}{2}}\right)P^{n}_{N-1}$$

$$+\left(-\frac{\Delta z}{2\Delta t}K10^{n+\frac{1}{2}}_{N}-\frac{(1-\theta)}{\Delta z}K7^{n}_{N-\frac{1}{2}}\right)S^{n}_{N}+\left(-\frac{\Delta z}{2\Delta t}K11^{n+\frac{1}{2}}_{N}-\frac{(1-\theta)}{\Delta z}K8^{n}_{N-\frac{1}{2}}\right)T^{n}_{N}$$

$$+\left(-\frac{\Delta z}{2\Delta t}K12^{n+\frac{1}{2}}_{N}-\frac{(1-\theta)}{\Delta z}K9^{n}_{N-\frac{1}{2}}\right)P^{n}_{N}$$

COE

$$\left(-\frac{\theta}{\Delta z}K13^{n+1}_{N-\frac{1}{2}}\right)S^{n+1}_{N-1}+\left(-\frac{\theta}{\Delta z}K14^{n+1}_{N-\frac{1}{2}}\right)T^{n+1}_{N-1}+\left(-\frac{\theta}{\Delta z}K15^{n+1}_{N-\frac{1}{2}}\right)P^{n+1}_{N-1}$$

$$+\left(\frac{\theta}{\Delta z}K13^{n+1}_{N-\frac{1}{2}}-\frac{\Delta z}{2\Delta t}K16^{n+\frac{1}{2}}_{N}\right)S^{n+1}_{N}+\left(\frac{\theta}{\Delta z}K14^{n+1}_{N-\frac{1}{2}}-\frac{\Delta z}{2\Delta t}K17^{n+\frac{1}{2}}_{N}\right)T^{n+1}_{N}+\left(\frac{\theta}{\Delta z}K15^{n+1}_{N-\frac{1}{2}}-\frac{\Delta z}{2\Delta t}K18^{n+\frac{1}{2}}_{N}\right)P^{n+1}_{N}$$

$$=\left(\frac{(1-\theta)}{\Delta z}K13^{n}_{N-\frac{1}{2}}\right)S^{n}_{N-1}+\left(\frac{(1-\theta)}{\Delta z}K14^{n}_{N-\frac{1}{2}}\right)T^{n}_{N-1}+\left(\frac{(1-\theta)}{\Delta z}K15^{n}_{N-\frac{1}{2}}\right)P^{n}_{N-1}$$

$$+\left(-\frac{\Delta z}{2\Delta t}K16^{n+\frac{1}{2}}_{N}-\frac{(1-\theta)}{\Delta z}K13^{n}_{N-\frac{1}{2}}\right)S^{n}_{N}+\left(-\frac{\Delta z}{2\Delta t}K17^{n+\frac{1}{2}}_{N}-\frac{(1-\theta)}{\Delta z}K14^{n}_{N-\frac{1}{2}}\right)T^{n}_{N}$$

$$+\left(-\frac{\Delta z}{2\Delta t}K18^{n+\frac{1}{2}}_{N}-\frac{(1-\theta)}{\Delta z}K15^{n}_{N-\frac{1}{2}}\right)P^{n}_{N}-\theta K20^{n+1}_{N-\frac{1}{2}}-(1-\theta)K20^{n}_{N-\frac{1}{2}}$$

$$+\begin{pmatrix}\Delta h_v\dot{m}''_{spray}-\dot{q}''_e-\dot{m}''_{spray}C_{p,w}\left(T_{spray}-T_{surface}\right)-\dot{m}''_wC_{p,w}\left(T_{N-1}-T_N\right)-\dot{m}''_vC_{p,v}\left(T_{N-1}-T_N\right)\\-\dot{m}''_aC_{p,a}\left(T_{N-1}-T_N\right)+h\left(T_s-T_\infty\right)+\varepsilon_s\sigma\left(T_s^4-T_\infty^4\right)\end{pmatrix}$$

The coefficients in the lower right hand side for the semi-infinite boundary condition are

$$\begin{bmatrix} & & \cdots & \\ & C_{3N-2,3N-2} & C_{3N-2,3N-1} & C_{3N-2,3N} \\ \cdots & C_{3N-1,3N-2} & C_{3N-1,3N-1} & C_{3N-1,3N} \\ & C_{3N,3N-2} & C_{3N,3N-1} & C_{3N,3N} \end{bmatrix} = \begin{bmatrix} & \cdots & & \\ & 1 & 0 & 0 \\ \cdots & 0 & 1 & 0 \\ & 0 & 0 & 1 \end{bmatrix}$$

$$C_{3N-2,3N} = 0$$
$$C_{3N-2,3N-1} = 0$$
$$C_{3N-2,3N-2} = 1$$

$$C_{3N-1,3N} = 0$$
$$C_{3N-1,3N-1} = 1$$
$$C_{3N-1,3N-2} = 0$$

$$C_{3N,3N} = 1$$
$$C_{3N,3N-1} = 0$$
$$C_{3N,3N-2} = 0$$

And on the right hand side

$$RHS_{3*N-2} = S_o$$
$$RHS_{3*N-1} = T_o$$
$$RHS_{3*N} = P_\infty$$

or

$$\begin{bmatrix} \cdots \\ RHS_{3N-2} \\ RHS_{3N-1} \\ RHS_{3N} \end{bmatrix} = \begin{bmatrix} \cdots \\ S_o \\ T_o \\ P_\infty \end{bmatrix}$$

For convective boundary conditions the values in the bottom right corner of the coefficient matrix and the bottom of the RHS matrix are

$$\begin{bmatrix} & & & \cdots & & & \\ & C_{3N-2,3N-5} & C_{3N-2,3N-4} & C_{3N-2,3N-3} & C_{3N-2,3N-2} & C_{3N-2,3N-1} & C_{3N-2,3N} \\ \cdots & C_{3N-1,3N-5} & C_{3N-1,3N-4} & C_{3N-1,3N-3} & C_{3N-1,3N-2} & C_{3N-1,3N-1} & C_{3N-1,3N} \\ & C_{3N,3N-5} & C_{3N,3N-4} & C_{3N,3N-3} & C_{3N,3N-2} & C_{3N,3N-1} & C_{3N,3N} \end{bmatrix} \begin{bmatrix} \cdots \\ B_{3N-5}^{n+1} = S_{N-1}^{n+1} \\ B_{3N-4}^{n+1} = T_{N-1}^{n+1} \\ B_{3N-3}^{n+1} = P_{N-1}^{n+1} \\ B_{3N-2}^{n+1} = S_{N}^{n+1} \\ B_{3N-1}^{n+1} = T_{N}^{n+1} \\ B_{3N}^{n+1} = P_{N}^{n+1} \end{bmatrix}$$

$$= \begin{bmatrix} \cdots \\ RHS_{3N-2} \\ RHS_{3N-1} \\ RHS_{3N} \end{bmatrix}$$

$$C_{3N-2,3N} = \frac{\theta}{\Delta z} K3^{n+1}_{N-\frac{1}{2}} - \frac{\Delta z}{2\Delta t} K6_N^{n+\frac{1}{2}}$$

$$C_{3N-2,3N-1} = \frac{\theta}{\Delta z} K2^{n+1}_{N-\frac{1}{2}} - \frac{\Delta z}{2\Delta t} K5_N^{n+\frac{1}{2}}$$

$$C_{3N-2,3N-2} = \frac{\theta}{\Delta z} K1^{n+1}_{N-\frac{1}{2}} - \frac{\Delta z}{2\Delta t} K4_N^{n+\frac{1}{2}}$$

$$C_{3N-2,3N-3} = -\frac{\theta}{\Delta z} K3^{n+1}_{N-\frac{1}{2}}$$

$$C_{3N-2,3N-4} = -\frac{\theta}{\Delta z} K2^{n+1}_{N-\frac{1}{2}}$$

$$C_{3N-2,3N-5} = -\frac{\theta}{\Delta z} K1^{n+1}_{N-\frac{1}{2}}$$

$$C_{3N-1,3N} = \frac{\theta}{\Delta z} K9^{n+1}_{N-\frac{1}{2}} - \frac{\Delta z}{2\Delta t} K12_N^{n+\frac{1}{2}}$$

$$C_{3N-1,3N-1} = \frac{\theta}{\Delta z} K8^{n+1}_{N-\frac{1}{2}} - \frac{\Delta z}{2\Delta t} K11_N^{n+\frac{1}{2}}$$

$$C_{3N-1,3N-2} = \frac{\theta}{\Delta z} K7^{n+1}_{N-\frac{1}{2}} - \frac{\Delta z}{2\Delta t} K10_N^{n+\frac{1}{2}}$$

$$C_{3N-1,3N-3} = -\frac{\theta}{\Delta z} K9^{n+1}_{N-\frac{1}{2}}$$

$$C_{3N-1,3N-4} = -\frac{\theta}{\Delta z} K8^{n+1}_{N-\frac{1}{2}}$$

$$C_{3N-1,3N-5} = -\frac{\theta}{\Delta z} K7^{n+1}_{N-\frac{1}{2}}$$

$$C_{3N,3N} = \frac{\theta}{\Delta z} K15^{n+1}_{N-\frac{1}{2}} - \frac{\Delta z}{2\Delta t} K18_N^{n+\frac{1}{2}}$$

$$C_{3N,3N-1} = \frac{\theta}{\Delta z} K14^{n+1}_{N-\frac{1}{2}} - \frac{\Delta z}{2\Delta t} K17_N^{n+\frac{1}{2}}$$

$$C_{3N,3N-2} = \frac{\theta}{\Delta z} K13^{n+1}_{N-\frac{1}{2}} - \frac{\Delta z}{2\Delta t} K16_N^{n+\frac{1}{2}}$$

$$C_{3N,3N-3} = -\frac{\theta}{\Delta z} K15^{n+1}_{N-\frac{1}{2}}$$

$$C_{3N,3N-4} = -\frac{\theta}{\Delta z} K14^{n+1}_{N-\frac{1}{2}}$$

$$C_{3N,3N-5} = -\frac{\theta}{\Delta z} K13^{n+1}_{N-\frac{1}{2}}$$

And the bottom of the RHS matrix is

$$RHS_{3N-2}=\left(\frac{(1-\theta)}{\Delta z}K1^{n}_{N-\frac{1}{2}}\right)S^{n}_{N-1}+\left(\frac{(1-\theta)}{\Delta z}K2^{n}_{N-\frac{1}{2}}\right)T^{n}_{N-1}+\left(\frac{(1-\theta)}{\Delta z}K3^{n}_{N-\frac{1}{2}}\right)P^{n}_{N-1}$$
$$+\left(-\frac{\Delta z}{2\Delta t}K4^{n+\frac{1}{2}}_{N}-\frac{(1-\theta)}{\Delta z}K1^{n}_{N-\frac{1}{2}}\right)S^{n}_{N}+\left(-\frac{\Delta z}{2\Delta t}K5^{n+\frac{1}{2}}_{N}-\frac{(1-\theta)}{\Delta z}K2^{n}_{N-\frac{1}{2}}\right)T^{n}_{N}$$
$$+\left(-\frac{\Delta z}{2\Delta t}K6^{n+\frac{1}{2}}_{N}-\frac{(1-\theta)}{\Delta z}K3^{n}_{N-\frac{1}{2}}\right)P^{n}_{N}+\theta K19^{n+1}_{N-\frac{1}{2}}+(1-\theta)K19^{n}_{N-\frac{1}{2}}-\dot{m}''_{evap}+\dot{m}''_{spray}$$
$$RHS_{3N-1}=\left(\frac{(1-\theta)}{\Delta z}K7^{n}_{N-\frac{1}{2}}\right)S^{n}_{N-1}+\left(\frac{(1-\theta)}{\Delta z}K8^{n}_{N-\frac{1}{2}}\right)T^{n}_{N-1}+\left(\frac{(1-\theta)}{\Delta z}K9^{n}_{N-\frac{1}{2}}\right)P^{n}_{N-1}$$
$$+\left(-\frac{\Delta z}{2\Delta t}K10^{n+\frac{1}{2}}_{N}-\frac{(1-\theta)}{\Delta z}K7^{n}_{N-\frac{1}{2}}\right)S^{n}_{N}+\left(-\frac{\Delta z}{2\Delta t}K11^{n+\frac{1}{2}}_{N}-\frac{(1-\theta)}{\Delta z}K8^{n}_{N-\frac{1}{2}}\right)T^{n}_{N}$$
$$+\left(-\frac{\Delta z}{2\Delta t}K12^{n+\frac{1}{2}}_{N}-\frac{(1-\theta)}{\Delta z}K9^{n}_{N-\frac{1}{2}}\right)P^{n}_{N}$$
$$RHS_{3N}=\left(\frac{(1-\theta)}{\Delta z}K13^{n}_{N-\frac{1}{2}}\right)S^{n}_{N-1}+\left(\frac{(1-\theta)}{\Delta z}K14^{n}_{N-\frac{1}{2}}\right)T^{n}_{N-1}+\left(\frac{(1-\theta)}{\Delta z}K15^{n}_{N-\frac{1}{2}}\right)P^{n}_{N-1}$$
$$+\left(-\frac{\Delta z}{2\Delta t}K16^{n+\frac{1}{2}}_{N}-\frac{(1-\theta)}{\Delta z}K13^{n}_{N-\frac{1}{2}}\right)S^{n}_{N}+\left(-\frac{\Delta z}{2\Delta t}K17^{n+\frac{1}{2}}_{N}-\frac{(1-\theta)}{\Delta z}K14^{n}_{N-\frac{1}{2}}\right)T^{n}_{N}$$
$$+\left(-\frac{\Delta z}{2\Delta t}K18^{n+\frac{1}{2}}_{N}-\frac{(1-\theta)}{\Delta z}K15^{n}_{N-\frac{1}{2}}\right)P^{n}_{N}-\theta K20^{n+1}_{N-\frac{1}{2}}-(1-\theta)K20^{n}_{N-\frac{1}{2}}$$
$$+\begin{pmatrix}\Delta h_v\dot{m}''_{spray}-\dot{q}''_e-\dot{m}''_{spray}C_{p,w}\left(T_{spray}-T_{surface}\right)-\dot{m}''_wC_{p,w}\left(T_{N-1}-T_N\right)-\dot{m}''_vC_{p,v}\left(T_{N-1}-T_N\right)\\-\dot{m}''_aC_{p,a}\left(T_{N-1}-T_N\right)+h\left(T_s-T_\infty\right)+\varepsilon_s\sigma\left(T_s^4-T_\infty^4\right)\end{pmatrix}$$

C.3 Discretize the Water Layer Model

To calculate the surface temperature the model will call on a sub model to calculate the temperature in the water layer. To develop a finite difference model of the water later, start with the energy equation for a static, unreacting liquid.

$$\rho C_p \frac{\partial T}{\partial t} = k \frac{\partial^2 T}{\partial z^2} - \frac{\partial \dot{q}''_{rad}}{\partial z}$$

For the control volume shown in Figure 102 the radiation entering and exiting the control volume can be calculated exactly at the cell boundaries. This is exactly halfway between two nodes and will be labeled as location i-1/2 and i+1/2.

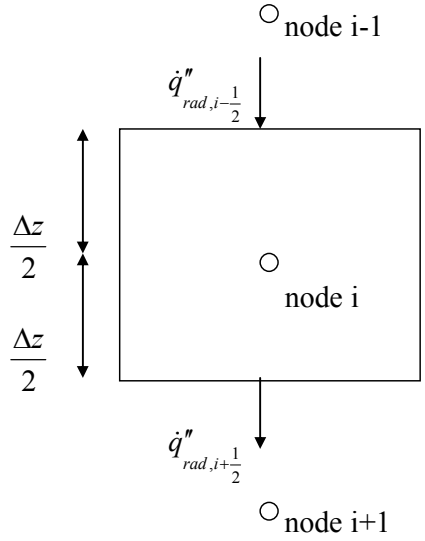

Figure 102 – Control Volume for Radiation Calculations

The total accumulation of energy in the cell from radiation absorption is therefore

$$\frac{\partial \dot{q}''_{rad}(z)}{\partial z} \cong \frac{\dot{q}''_{rad,i+\frac{1}{2}} - \dot{q}''_{rad,i-\frac{1}{2}}}{\Delta z}$$

The discretized governing equation for the liquid is

$$\frac{T_i^{n+1}-T_i^n}{\Delta t}=\alpha\frac{T_{i+1}^n-2T_i^n+T_{i-1}^n}{\Delta x^2}-\frac{1}{\rho C_p}\frac{\dot{q}''_{rad,i+\frac{1}{2}}-\dot{q}''_{rad,i-\frac{1}{2}}}{\Delta z}$$

Solve for T_i^{n+1}

$$T_i^{n+1}=T_i^n+\frac{\Delta t\alpha}{\Delta x^2}\left(T_{i+1}^n-2T_i^n+T_{i-1}^n\right)-\frac{\Delta t}{\rho C_p}\frac{\dot{q}''_{rad,i+\frac{1}{2}}-\dot{q}''_{rad,i-\frac{1}{2}}}{\Delta z}$$

The discretized governing equation for the solid material is simply

$$T_i^{n+1}=T_i^n+\frac{\Delta t\alpha}{\Delta x^2}\left(T_{i+1}^n-2T_i^n+T_{i-1}^n\right)$$

Next discretize the boundary conditions. The surface node boundary condition is

$$\dot{q}''_e=\dot{q}''_{refl}+\dot{q}''_{conv}+\dot{q}''_{evap}+\dot{q}''_{\substack{rerad\\water}}+\dot{q}''_{\substack{cond\\water}}\quad @z=0$$

The surface node has a thickness of $\frac{\Delta z}{2}$ as shown in Figure 103.

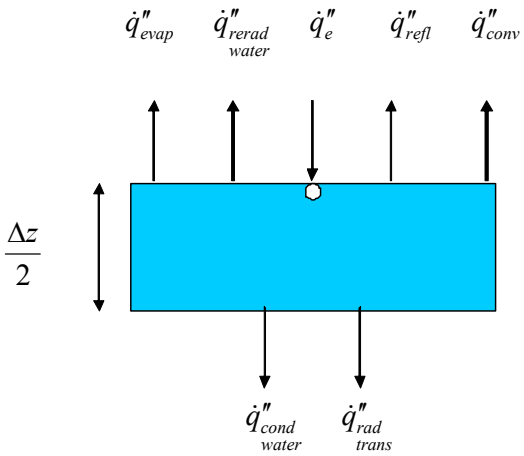

Figure 103 – Water Surface Node

The energy balance on the surface node is

$$\frac{\Delta x \Delta y \Delta z}{2} \rho_w C_{p,w} \frac{\partial T}{\partial t} = \left(\dot{q}''_e - \dot{q}''_{refl} - \dot{q}''_{conv} - \dot{q}''_{evap} - \dot{q}''_{rerad,\ water} - \dot{q}''_{cond,\ water} - \dot{q}''_{rad,\ trans} \right) \Delta x \Delta y$$

Which can be written as

$$\frac{T^{n+1}_{surf} - T^{n}_{surf}}{\Delta t} = \frac{2}{\Delta z \rho_w C_{p,w}} \left(\begin{array}{l} \dot{q}''_e - \dot{q}''_{refl} - h\left(T^{n}_{surf} - T^{n}_{\infty}\right) - \Delta h_v h_m \left(\rho_{surf} - \rho_{\infty}\right) - \varepsilon_w \sigma T^{4}_{surf} \\ + k_w \dfrac{T^{n}_{surf+1} - T^{n}_{surf}}{\Delta z} - \dot{q}''_{rad,\ trans} \end{array} \right)$$

Solving for T^{n+1}_{surf}

$$T^{n+1}_{surf} = T^{n}_{surf} + \frac{2\Delta t}{\Delta z \rho_w C_{p,w}} \left(\begin{array}{l} \dot{q}''_e - \dot{q}''_{refl} - h\left(T^{n}_{surf} - T^{n}_{\infty}\right) - \Delta h_v h_m \left(\rho_{surf} - \rho_{\infty}\right) - \varepsilon_w \sigma T^{4}_{surf} \\ + k_w \dfrac{T^{n}_{surf+1} - T^{n}_{surf}}{\Delta z} - \dot{q}''_{rad,\ trans} \end{array} \right)$$

Where the radiation transmitted through the first node is equal to

$$\dot{q}''_{\substack{rad\\trans}} = 0.5\sum_{\lambda=0.2}^{200}\left(i_\lambda(0)\exp\left(-a_\lambda\cdot\frac{\Delta z}{2}\right)+i_{\lambda+\Delta\lambda}(0)\exp\left(-a_{\lambda+\Delta\lambda}\cdot\frac{\Delta z}{2}\right)\right)\Delta\lambda$$

Discretize the interface node boundary condition, shown in Figure 104.

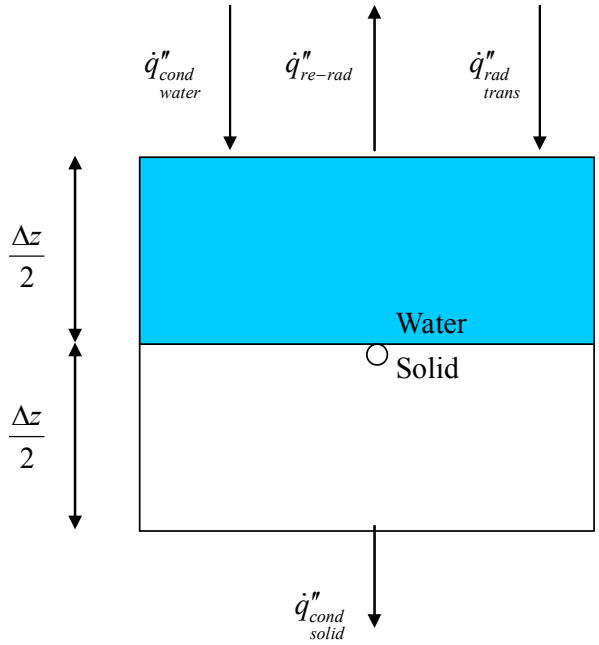

Figure 104 – Water – Solid Interface Node

The water – solid interface node is half water and half solid by volume. The solid is assumed to radiate upward through the water. The radiation that escapes from the interface node must therefore pass through a length of water equal to $0.5\Delta z$. This is equal to

$$\dot{q}''_{re-rad} = \int_{\lambda=0}^{\infty} i_\lambda(0)\exp\left(-a_\lambda 0.5\Delta z\right)\partial\lambda$$

The re-radiation can be calculated to be

$$\dot{q}''_{re-rad} = 0.5\sum_{\lambda=0.2}^{200}\left(i_\lambda(0)\exp\left(-a_\lambda 0.5\Delta z\right)+i_{\lambda+\Delta\lambda}(0)\exp\left(-a_{\lambda+\Delta\lambda}0.5\Delta z\right)\right)\Delta\lambda$$

The discretized boundary condition is

$$\frac{\Delta x\Delta y\Delta z}{2}\left(\rho_w C_{p,w}+\rho_s C_{p,s}\right)\frac{T_{\text{int}}^{n+1}-T_{\text{int}}^{n}}{\Delta t}=\left(-k_w\frac{T_{\text{int}}^{n}-T_{\text{int}-1}^{n}}{\Delta z}+k_s\frac{T_{\text{int}+1}^{n}-T_{\text{int}}^{n}}{\Delta z}+\dot{q}''_{\substack{rad\\trans}}-\dot{q}''_{re-rad}\right)\Delta x\Delta y$$

Solve for T_{int}^{n+1}

$$T_{\text{int}}^{n+1}=T_{\text{int}}^{n}-2\frac{k_w\Delta t}{\left(\rho_w C_{p,w}+\rho_s C_{p,s}\right)}\frac{T_{\text{int}}^{n}-T_{\text{int}-1}^{n}}{\Delta z^2}+2\frac{k_s\Delta t}{\left(\rho_w C_{p,w}+\rho_s C_{p,s}\right)}\frac{T_{\text{int}+1}^{n}-T_{\text{int}}^{n}}{\Delta z^2}+2\Delta t\frac{\dot{q}''_{\substack{rad\\trans}}-\dot{q}''_{re-rad}}{\left(\rho_w C_{p,w}+\rho_s C_{p,s}\right)\Delta z}$$

If the node spacing in the water and solid is not the same, then the equation for the interface node is

$$\frac{\Delta x\Delta y}{2}\left(\Delta z_w\rho_w C_{p,w}+\Delta z_s\rho_s C_{p,s}\right)\frac{T_{\text{int}}^{n+1}-T_{\text{int}}^{n}}{\Delta t}=\left(-k_w\frac{T_{\text{int}}^{n}-T_{\text{int}-1}^{n}}{\Delta z_w}+k_s\frac{T_{\text{int}+1}^{n}-T_{\text{int}}^{n}}{\Delta z_s}+\dot{q}''_{\substack{rad\\trans}}-\dot{q}''_{re-rad}\right)\Delta x\Delta y$$

Solve for T_{int}^{n+1}

$$T_{\text{int}}^{n+1}=T_{\text{int}}^{n}-\frac{2\Delta t k_w}{\left(\Delta z_w\rho_w C_{p,w}+\Delta z_s\rho_s C_{p,s}\right)}\frac{T_{\text{int}}^{n}-T_{\text{int}-1}^{n}}{\Delta z_w}+\frac{2\Delta t k_s}{\left(\Delta z_w\rho_w C_{p,w}+\Delta z_s\rho_s C_{p,s}\right)}\frac{T_{\text{int}+1}^{n}-T_{\text{int}}^{n}}{\Delta z_s}$$
$$+\frac{2\Delta t}{\left(\Delta z_w\rho_w C_{p,w}+\Delta z_s\rho_s C_{p,s}\right)}\left(\dot{q}''_{\substack{rad\\trans}}-\dot{q}''_{re-rad}\right)$$

or

$$T_{\text{int}}^{n+1}=T_{\text{int}}^{n}-\frac{2\Delta t k_w}{\left(\Delta z_w\rho_w C_{p,w}+\Delta z_s K17_{\text{int}}^{n}\right)}\frac{T_{\text{int}}^{n}-T_{\text{int}-1}^{n}}{\Delta z_w}+\frac{2\Delta t K17_{\text{int}}^{n}}{\left(\Delta z_w\rho_w C_{p,w}+\Delta z_s K17_{\text{int}}^{n}\right)}\frac{T_{\text{int}+1}^{n}-T_{\text{int}}^{n}}{\Delta z_s}$$
$$+\frac{2\Delta t}{\left(\Delta z_w\rho_w C_{p,w}+\Delta z_s K17_{\text{int}}^{n}\right)}\left(\dot{q}''_{\substack{rad\\trans}}-\dot{q}''_{re-rad}\right)$$

This interface temperature will be the surface temperature in the model for the solid material.

Solution Algorithm in Matlab

1. Load inputs
2. Set Initial Conditions (B_{old})
3. Iterate
   A. Apply Boundary Conditions
   B. Calculate K matrix
      i. Kold uses old values of S, T, P
      ii. Knew uses new values of S, T, P. First use old values
   C. Calculate C matrix from K values
   D. Calculate RHS matrix
   E. Solve for B_{new} matrix

$$[B] = [RHS][C]^{-1}$$

4. If the change between iterations is greater than a specified tolerance, repeat 3
5. Set B_{old}=B_{new}

D.3. Define Inputs

Now Define K's

$$K_1 = \frac{M_a M_v D_{eff,g}}{RT\left[\left(P - p_v\right)M_a + p_v M_v\right]} P \frac{\partial p_v}{\partial S_w} - \rho_w \frac{KK_{r,w}}{\mu_w} \frac{\partial p_c}{\partial S_w}$$

$$\frac{\partial p_v}{\partial S_w} = 0$$

So

$$K_1 = -\rho_w \frac{KK_{r,w}}{\mu_w} \frac{\partial p_c}{\partial S_w}$$

Where

$$\frac{\partial p_w}{\partial S_w} = \frac{\partial}{\partial S_w}\left(p_c\right) = \left(\frac{\varphi}{K}\right)^{\frac{1}{2}} \sigma \frac{\partial}{\partial S_w}\left(J\left(S_w\right)\right)$$

Where

$$J\left(S_w\right) = 0.364\left(1 - \exp\left(-40\left(1 - S_w\right)\right)\right) + 0.221\left(1 - S_w\right) + \frac{0.005}{S_w - 0.08}$$

or

$$J\left(S_w\right) = 0.364 - 0.364\exp\left(40S_w - 40\right) + 0.221 - 0.221S_w + 0.005\left(S_w - 0.08\right)^{-1}$$

so

$$\frac{\partial}{\partial S_w}\left(J\left(S_w\right)\right) = -0.364\left(40\right)\exp\left(40S_w - 40\right) - 0.221 - 0.005\left(S_w - 0.08\right)^{-2}$$

$$K_2 = \frac{M_a M_v D_{eff,g}}{RT\left[\left(P - p_v\right)M_a + p_v M_v\right]} P \frac{\partial p_v}{\partial T} - \rho_w \frac{KK_{r,w}}{\mu_w} \frac{\partial p_c}{\partial T}$$

Since

$$\frac{\partial p_c}{\partial T} = 0$$

We can write

$$K_2 = \frac{M_a M_v D_{eff,g}}{RT\left[\left(P - p_v\right)M_a + p_v M_v\right]} P \frac{\partial p_v}{\partial T}$$

Where

$$M_a = 8,314 \frac{J}{kmol\,K} \times \frac{1}{28.8 \frac{kg}{kmol}} = 288.7 \frac{J}{kgK}$$

$$M_v = 8,314 \frac{J}{kmol\,K} \times \frac{1}{18 \frac{kg}{kmol}} = 461.8 \frac{J}{kgK}$$

$$D_{eff,g} = D_{va} \phi^{\frac{4}{3}} \left(\phi^2 - \phi S_w \right)^{\frac{4}{3}}$$

$$D_{va} = 2.2 \times 10^{-5} \frac{m^2}{s} \quad (from\ \ Turns)$$

So

$$D_{eff,g} = \left(2.2 \times 10^{-5} \right) \phi^{\frac{4}{3}} \left(\phi^2 - \phi S_w \right)^{\frac{4}{3}}$$

$$R = 8314 \frac{J}{kmol\,K}$$

$$p_v = p_{ref} \exp\left[-\frac{\Delta h_{vap}}{R_v} \left(\frac{1}{T} - \frac{1}{T_{ref}} \right) \right]$$

where

$$\Delta h_{vap} = 2600 \frac{kJ}{kg}$$

$$p_{ref} = 101,300 kPa$$

$$T_{ref} = 100^o C$$

So

$$\frac{\partial p_v}{\partial T} = p_{ref} \exp\left[-\frac{\Delta h_{vap}}{R_v} \left(\frac{1}{T} - \frac{1}{T_{ref}} \right) \right] \frac{\Delta h_{vap}}{R_v} T^{-2}$$

$$K_3 = \frac{p_v}{R_v T}\frac{KK_{r,g}}{\mu_g} - \frac{M_a M_v D_{eff,g}}{RT\left[\left(P-p_v\right)M_a + p_v M_v\right]}p_v + \rho_w \frac{KK_{r,l}}{\mu_w}$$

where

$$K_{r,g} = \left(1-S_w\right)^3$$

$$K_{r,l} = S_w{}^3$$

$$\mu_g = 2\times 10^{-5}\,\frac{kg}{ms}\ (air\ @300K, SFPE\ HB-this\ can\ be\ changed\ later)$$

$$\rho_w = 1000\,\frac{kg}{m^3}$$

$$\mu_w = 8.6\times 10^{-4}\,\frac{kg}{ms}\ (water@300K, SFPE\ HB-this\ can\ be\ changed\ later)$$

$$K_4 = -\phi\frac{p_v}{R_v T} + \frac{\phi\left(1-S_w\right)}{R_v T}\left(\frac{\partial p_v}{\partial S_w}\right) + \phi\rho_w$$

$$\frac{\partial p_v}{\partial S_w} = 0$$

so

$$K_4 = -\phi\frac{p_v}{R_v T} + \phi\rho_w$$

$$K_5 = \frac{\phi\left(1-S_w\right)}{R_v}\frac{\partial}{\partial T}\left(\frac{p_v}{T}\right)$$

Use the quotient rule

$$\frac{\partial}{\partial T}\left(\frac{p_v}{T}\right) = \frac{T\frac{\partial p_v}{\partial T} - p_v\frac{\partial T}{\partial T}}{T^2} = \frac{1}{T^2}\left[Tp_{ref}\exp\left[-\frac{\Delta h_{vap}}{R_v}\left(\frac{1}{T}-\frac{1}{T_{ref}}\right)\right]\frac{\Delta h_{vap}}{R_v}T^{-2} - p_v\right]$$

$$K_6 = 0$$

$$K_7 = -\frac{M_a M_v D_{eff,g}}{RT\left[\left(P-p_v\right)M_a + p_v M_v\right]}P\frac{\partial p_v}{\partial S_w}$$

$$\frac{\partial p_v}{\partial S_w} = 0$$

so

$$K_7 = 0$$

$$K_8 = -\frac{M_a M_v D_{eff,g}}{RT\left[\left(P-p_v\right)M_a + p_v M_v\right]} P \frac{\partial p_v}{\partial T}$$

$$K_9 = \frac{P-p_v}{R_a T}\frac{KK_{r,g}}{\mu_g} + \frac{M_a M_v D_{eff,g}}{RT\left[\left(P-p_v\right)M_a + p_v M_v\right]} p_v$$

$$K_{10} = -\frac{\phi}{R_a}\left(\frac{P-p_v}{T} + \frac{1-S_w}{T}\frac{\partial p_v}{\partial S_w}\right)$$

$$\frac{\partial p_v}{\partial S_w} = 0$$

so

$$K_{10} = -\frac{\phi}{R_a}\left(\frac{P-p_v}{T}\right)$$

$$K_{11} = -\frac{\phi}{R_a}\left(\frac{p}{T^2} - \frac{PS_w}{T^2} + \left(1-S_w\right)\frac{\partial}{\partial T}\left(\frac{p_v}{T}\right)\right)$$

$$K_{12} = \frac{\phi\left(1-S_w\right)}{R_a T}$$

$$K_{13} = -\rho_w \frac{KK_{r,l}}{\mu_w}\frac{\partial p_c}{\partial S_w}\Delta h_v$$

$$K_{14} = \left(\phi S_a k_a + \phi S_v k_v + \phi S_l k_l + \left(1-\phi\right)k_s\right) - \rho_w \frac{KK_{r,g}}{\mu_w}\frac{\partial p_c}{\partial T}\Delta h_v$$

$$\frac{\partial p_c}{\partial T} = 0$$

So

$$K_{14} = \left(\phi S_a k_a + \phi S_v k_v + \phi S_l k_l + \left(1-\phi\right)k_s\right)$$

$$K_{15} = -\rho_w \frac{KK_{r,w}}{\mu_w}\Delta h_v$$

$$K_{16} = -\Delta h_v \phi \rho_w$$

$$K_{17} = \phi S_l \rho_l C_{p,l} + \phi S_v \rho_v C_{p,v} + \phi S_a \rho_a C_{p,a} + \left(1-\phi\right) \rho_s C_{p,s}$$

$$S_v = X_v S_g = \frac{p_v}{P} S_g = \frac{p_v}{P}\left(1 - S_w\right)$$

$$S_a = 1 - S_w - S_v$$

$$K_{18} = 0$$

$$K_{19} = \rho_w \frac{KK_{r,l}}{\mu_w} \rho_w g$$

$$K_{20} = \Delta h_v \rho_w \frac{KK_{r,l}}{\mu_w}$$

Appendix E. Verification

E.1. Saturation Verification

In order to verify that the moisture transport processes are being modeled correctly, comparisons with analytical solutions are needed. Start with the conservation of mass for liquid water

$$\phi \frac{\partial \left(\rho_w S_w \right)}{\partial t} = \frac{\partial}{\partial z} \left(\rho_w \frac{KK_{r,l}}{\mu_w} \left(\frac{\partial \left(p_w \right)}{\partial z} - \rho_w g \right) \right) - \dot{m}'''_{evap}$$

If we assume isothermal conditions and convert pressure to units of head

$$\dot{m}'''_{evap} = 0$$

$$\psi = \frac{p_w}{\rho_w g}$$

and define hydraulic conductivity as

$$K_h = \frac{KK_{r,l} \rho_w g}{\phi \mu_w}$$

The equation is now

$$\frac{\partial S_w}{\partial t} = \frac{\partial}{\partial z} \left(K_h \left(\frac{\partial \psi}{\partial z} - 1 \right) \right)$$

Define moisture diffusivity as

$$D_w = K_h \frac{\partial \psi}{\partial S_w}$$

The equation for conservation of mass for liquid water can now be written as

$$\frac{\partial S_w}{\partial t} = \frac{\partial}{\partial z}\left[D_w\left(S_w\right)\frac{\partial S_w}{\partial z} \right] - \frac{\partial K\left(S_w\right)}{\partial z}$$

With the boundary conditions

$$S_w\left(z=0,t\right) = S_{surface}$$
$$S_w\left(z,t=0\right) = S_w\left(z=\infty,t\right) = S_o$$

E.1.1. Moisture Diffusion Verification

If we assume that the gravitational forces acting on the water in the material are negligible (such as in the case of horizontal infiltration, or materials with very small pores) then an analytical solution is possible. The conservation of mass equation for water becomes

$$\frac{\partial S_w}{\partial t} = \frac{\partial}{\partial z}\left[D_w\left(S_w\right)\frac{\partial S_w}{\partial z} \right]$$
$$S_w\left(z=0,t\right) = S_{surface}$$
$$S_w\left(z,t=0\right) = S_w\left(z=\infty,t\right) = S_o$$

Introduce the Boltzmann transform variable:

$$\lambda = \frac{z}{\sqrt{t}}$$

Define derivatives

$$\frac{\partial z}{\partial \lambda} = \sqrt{t} \qquad \partial z = \sqrt{t}\,\partial\lambda$$
$$\frac{\partial t}{\partial \lambda} = \frac{-2z^2}{\lambda^3} \qquad \partial t = \frac{-2z^2}{\lambda^3}\partial\lambda$$

Substituting into the Richards equation transforms the partial differential equation into an ordinary differential equation

$$-\frac{\lambda}{2}\frac{dS_w}{d\lambda}=\frac{d}{d\lambda}\left[D_w\left(S_w\right)\frac{dS_w}{d\lambda}\right]$$

With the boundary conditions

$$S_w\left(\lambda=0\right)=S_{surface}$$
$$S_w\left(\lambda=\infty\right)=S_o$$

Multiply each side by $d\lambda$

$$-\frac{\lambda}{2}dS_w=d\left[D_w\left(S_w\right)\frac{\partial S_w}{\partial\lambda}\right]$$

Integrate from S_o *to* S_w

$$-\int_{S_o}^{S_w}\frac{\lambda}{2}\partial S_w=D_w\left(S_w\right)\frac{\partial S_w}{\partial\lambda}$$

Which can be written as

$$D_w\left(S_w\right)=-\frac{1}{2}\frac{\partial\lambda}{\partial S_w}\int_{S_o}^{S_w}\lambda\partial S_w$$

This is known as the Bruce and Klute equation. Certain expressions for the moisture diffusivity allow for analytical solutions of this equation. If the diffusivity is given by

$$D\left(S_w\right)=\frac{D_{w,sat}}{n}\left(n+1\right)S_w{}^n\left[1-\frac{S_w{}^n}{n+1}\right]$$

Then one possible solution to the Bruce and Klute equation is

$$\lambda = \left(1 - S_w^{\ n}\right)\left(\frac{2D_{w,sat}\left(n+1\right)}{n^2}\right)^{\frac{1}{2}}$$

The variable n represents a measure of the pore size distribution. Higher values of n indicate a more narrow pore size distribution. The solution is shown in Figure 105.

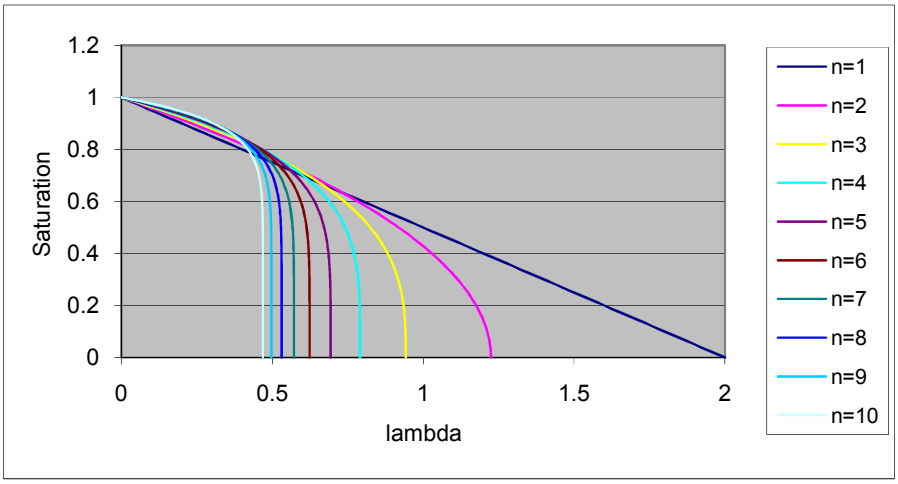

Figure 105 – Analytical Solution to the Moisture Diffusion Equation

We cannot compare this to the model results yet however, since the relation for diffusivity is not the same. The current model is set up to use units of $\frac{m^3 s}{kg}$ for $\frac{KK_{r,l}}{\mu}$ and Pa for water pressure, p_w. The relationships between these parameters are

$$K_h = \rho_w g \frac{KK_{r,l}}{\phi \mu_w}$$

$$\psi = \frac{p_{cap}}{\rho_w g}$$

Care must be taken when converting these parameters for these two applications. For the model we are using the following constitutive relationships

$$p_{cap} = \frac{\sigma}{\sqrt{K/\varphi}}\left[0.364\left(1-\exp\left(-40\left(1-S_w\right)\right)\right)+0.221\left(1-S_w\right)+\frac{0.005}{S_w-0.08}\right]$$

$$K_{r,l} = S_w^3$$

In order to use the analytical solution for comparison, we need to change these parameters to match those used to obtain a solution to the Richards equation. The moisture diffusivity is defined as

$$D_w\left(S_w\right) = K_h\left(S_w\right)\frac{\partial \psi}{\partial S_w}$$

Assume that the relative permeability is the same as previously stated for the model. In order to compare the model results to the analytical results we need to calculate $\frac{\partial p_c}{\partial S_w}$ for K_1.

$$\frac{\partial p_c}{\partial S_w} = \frac{\rho_w g D_w\left(S_w\right)}{K_h\left(S_w\right)} = \frac{\rho_w g \frac{D_{w,sat}}{n}\left(n+1\right)S_w{}^n\left[1-\frac{S_w{}^n}{n+1}\right]}{\rho_w g \frac{KK_{r,l}}{\phi\mu}}$$

For the saturated value of moisture diffusivity use an arbitrary value of

$$D_{w,sat} = 1\times10^{-4}\,\frac{m^2}{s}$$

If this value for $\frac{\partial p_c}{\partial S_w}$ is used in the model, then the results can be compared to the analytical solution. The following initial and boundary conditions will be used

Initial Conditions:

$$S_w(z,t=0) = 1\times10^{-6}$$
$$T(z,t=0) = 283K$$
$$P(z,t=0) = P_{atm}$$

Boundary Conditions

$$S_w\left(z=0,t>0\right)=0.999$$
$$T\left(z=0,t>0\right)=283K$$
$$P\left(z=0,t>0\right)=P_{atm}$$

$$S_w\left(z=L,t>0\right)=1\times10^{-6}$$
$$T\left(z=L,t>0\right)=283K$$
$$P\left(z=L,t>0\right)=P_{atm}$$

The small value for initial saturation is to avoid numerical errors associated with a value of zero for saturation. The value of gravitational acceleration will be set to zero so that surface tension forces are the only force acting on the water. The model and analytical results are shown in Figure 106 for a simulation time of 100 seconds. This simulation used 101 grid points and a time step of 0.1 seconds.

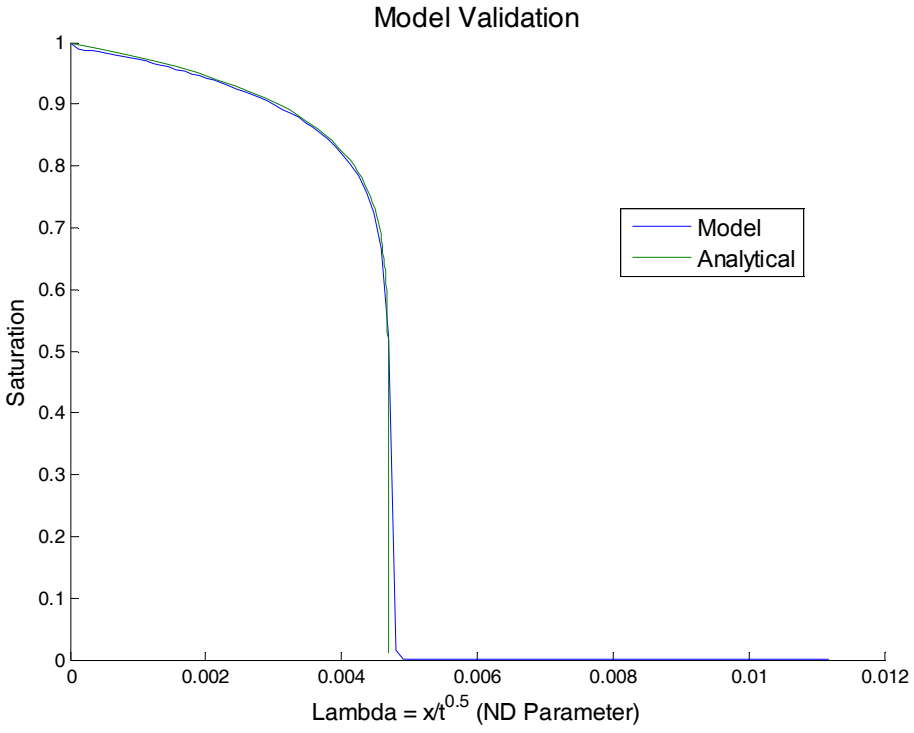

Figure 106 – Saturation Verification – No Gravity

E.1.2. Traveling Wave Solution

If the gravity forces can not be ignored, the conservation of mass equation for liquid water is

$$\frac{\partial S_w}{\partial t} = \frac{\partial}{\partial z}\left[D_w\left(S_w\right)\frac{\partial S_w}{\partial z} \right] - \frac{\partial K\left(S_w\right)}{\partial z}$$

In order to solve the equation, use the following transform

$$\eta = z - \frac{\left[K\left(S_{surf}\right) - K\left(S_o\right) \right] t}{S_{surf} - S_o}$$

So that the infiltration equation can be written as

$$\frac{K\left(S_{surf}\right) - K\left(S_o\right)}{S_{surf} - S_o}\frac{\partial S_w}{\partial \eta} = \frac{\partial}{\partial \eta}\left[D_w\left(S_w\right)\frac{\partial S_w}{\partial \eta} \right] - \frac{\partial K\left(S_w\right)}{\partial \eta}$$

If an infinite soil profile is considered, the boundary conditions can be defined as

$$S_w\left(\eta = -\infty\right) = S_{surf}$$
$$S_w\left(\eta = \infty\right) = S_o$$
$$\left.\frac{\partial S_w}{\partial \eta}\right|_{-\infty} = \left.\frac{\partial S_w}{\partial \eta}\right|_{\infty} = 0$$

Integrating the transformed infiltration equation with these boundary conditions yields

$$\Delta\eta = \eta\left(S_w\right) - \eta\left(S_a\right) = \left(S_{surf} - S_o\right)\int_{S_w}^{S_a} \frac{D_w\left(S_w\right) dS_w}{\left[K\left(S_{surf}\right) - K\left(S_o\right) \right]\left(S_w - S_o\right) - \left[K\left(S_w\right) - K\left(S_o\right) \right]\left(S_{surf} - S_o\right)}$$

This is what is known as a traveling wave solution. Since we are assuming the boundaries are far enough away to not significantly influence the solution, the

saturation profile has reached a steady shape. S_a is reference saturation, and S_w is the saturation at a distance z from the reference saturation. The results for three different times are shown in Figure 107.

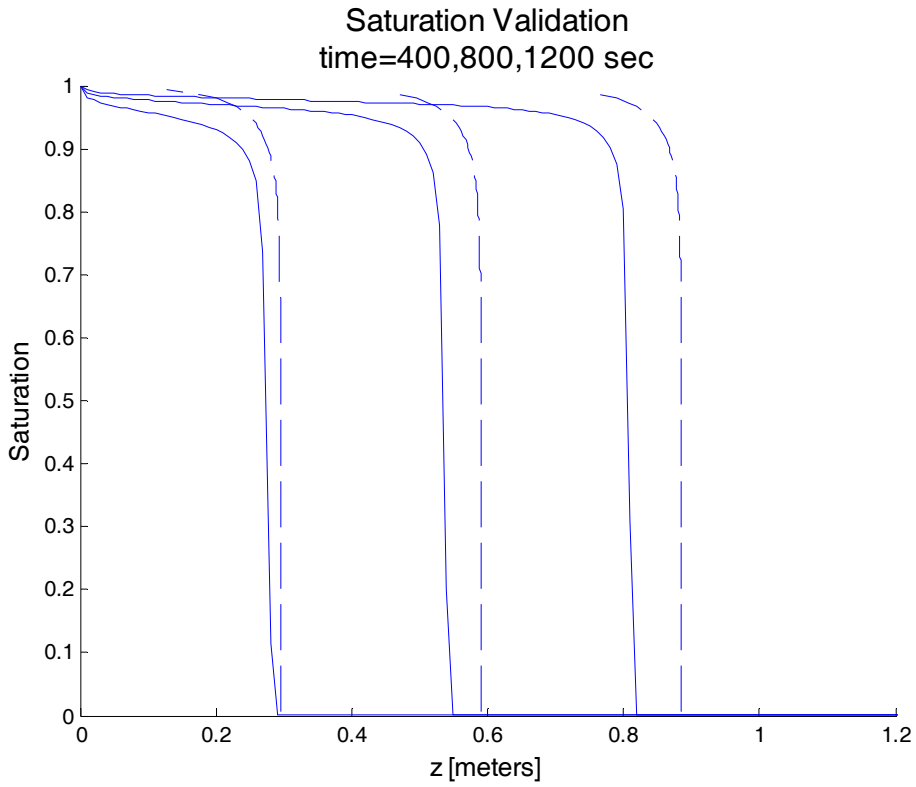

Figure 107 – Saturation Verification - Gravity Included

From Figure 107 it can be seen that there is a significant difference between the model and analytical solutions at each time plotted. The dashed lines represent the analytical solutions. The difference is likely caused by a rise in pressure in the pores of the material that is calculated by the model as air is displaced by water. The analytical solution does not account for this internal pressure in the material. If the pressure in the model is set to ambient and not allowed to rise, the model solution is much closer to the analytical solution. This is shown in Figure 108.

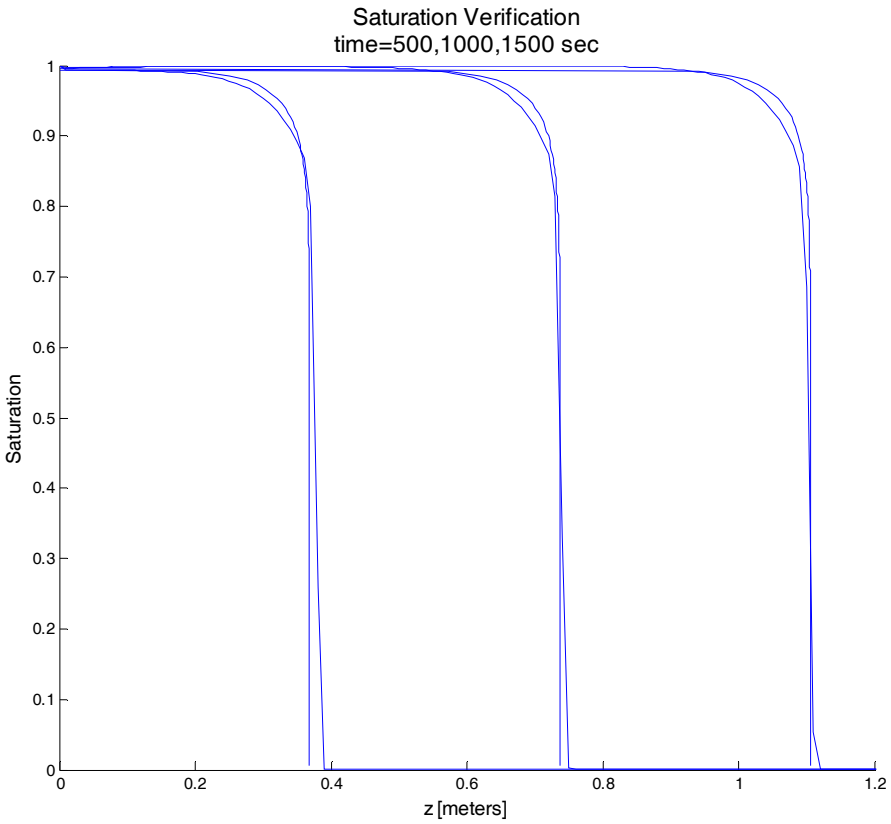

Figure 108 – Saturation Verification – Gravity Included, Fixed Pressure at P_{∞}

E.2. Temperature Verification

E.2.1. Type 1 Boundary Condition

To verify that the heat transfer is being correctly modeled, the initial saturation of the material was set to 0.001, and a surface temperature of 363 K boundary condition was imposed. The complete boundary conditions for this simulation are

$$For\ z = 0,\ t > 0$$
$$S_w = S_o = 0.001$$
$$T = T_s = 363K$$
$$P = P_\infty = 101,300Pa$$

$$For\ z = L = 0.25m,\ t > 0$$
$$S_w = S_o = 0.001$$
$$T = T_o = 283K$$
$$P = P_\infty = 101,300Pa$$

And the initial conditions are

$$For\ 0 \le Z \le L,\ t = 0$$
$$S_w = S_o = 0.001$$
$$T = T_o = 283K$$
$$P = P_\infty = 101,300Pa$$

The thermal properties used for the simulation are

$Solid\ (\mathrm{Pr}operties\ of\ Wood)$	Air
$\rho_s = 640\ \frac{kg}{m^3}$	$\rho_a = 1.17\ \frac{kg}{m^3}$
$C_{p,s} = 2800\ \frac{J}{kgK}$	$C_{p,a} = 1.0057\ \frac{J}{kgK}$
$k_{t,s} = 0.147\frac{W}{m^2K}$	$k_{t,a} = 0.02624\frac{W}{m^2K}$

Water	*Vapor*
$\rho_w = 995\ \frac{kg}{m^3}$	$\rho_v = 0.5863\ \frac{kg}{m^3}$
$C_{p,w} = 4180\ \frac{J}{kgK}$	$C_{p,v} = 2.6\ \frac{J}{kgK}$
$k_{t,w} = 0.597\ \frac{W}{m^2K}$	$k_{t,v} = 0.0246\ \frac{W}{m^2K}$

The analytical solution to this problem is given by Bejan [43]

$$\frac{T - T_s}{T_o - T_s} = erf\left(\frac{z}{2\sqrt{\alpha t}}\right)$$

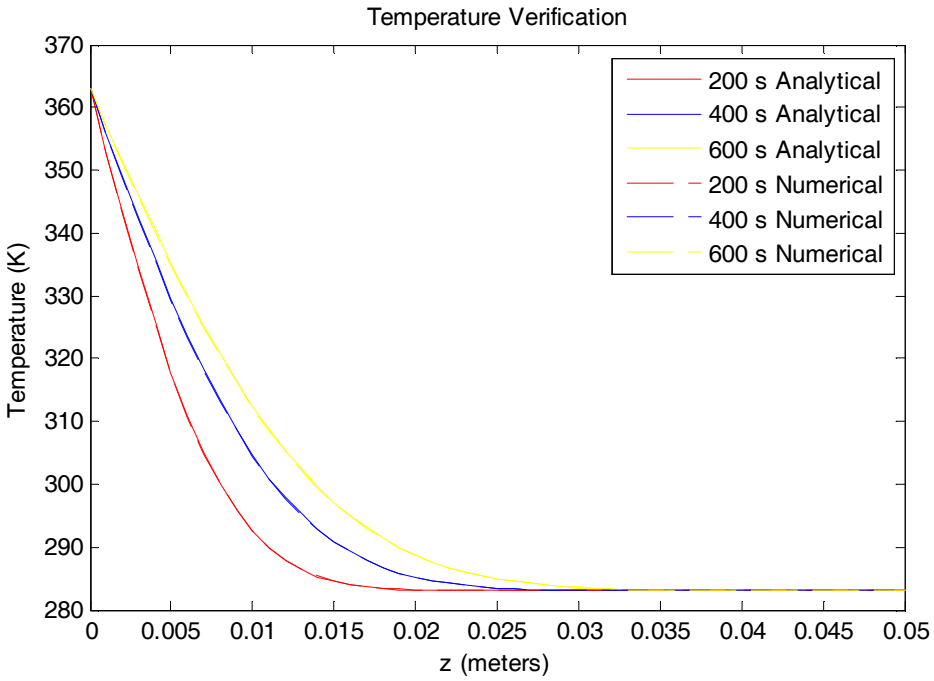

The numerical data matches the analytical solution very well, so the model is correctly handling the conduction heat transfer.

E.2.2 Type 2 Boundary Condition

To verify the external heat flux boundary condition, analytical solutions can be used. Consider the one dimensional conduction equation, written in flux formulation [106] with a prescribed heat flux at the surface.

$$\frac{1}{\alpha}\frac{\partial \dot{q}''}{\partial t} = \frac{\partial^2 \dot{q}''}{\partial x^2} \qquad in \qquad 0 < x < \infty, \quad t > 0$$
$$\dot{q}'' = \dot{q}_o'' \qquad @ \qquad x = 0, \; t > 0$$
$$\dot{q}''(x,t) = 0 \qquad @ \qquad t = 0$$

The solution to this problem is [106]

$$T(x,t) = \frac{2\dot{q}_o''}{k}\left[\left(\frac{\alpha t}{\pi}\right)^{\frac{1}{2}} e^{-\frac{x^2}{4\alpha t}} - \frac{x}{2} erfc\left(\frac{x}{\sqrt{4\alpha t}}\right)\right]$$

For an incident heat flux of 2 kW/m^2 the numerical and analytical results match up as shown in Figure 109. The heat and mass transfer coefficients were set to zero for this simulation.

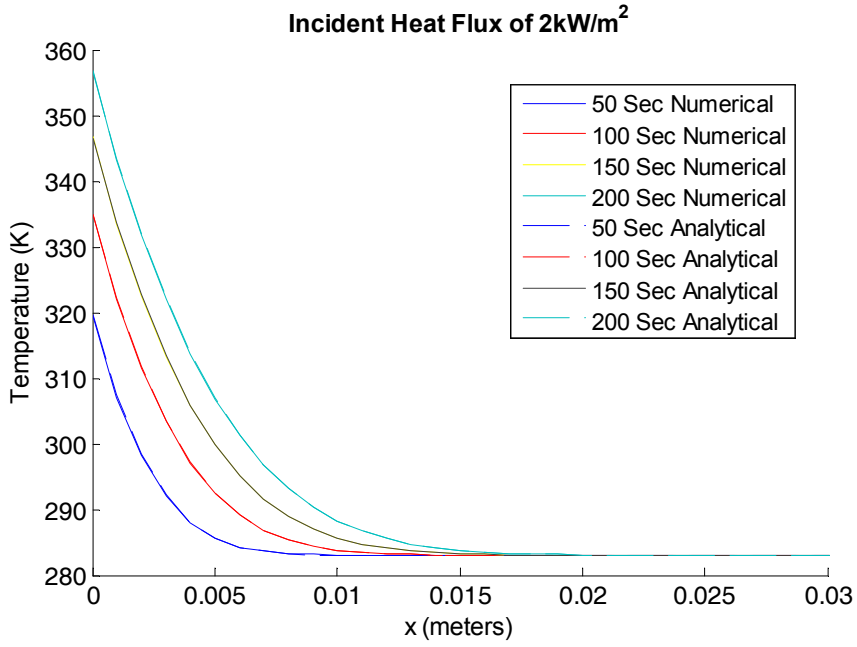

Figure 109 – Verification of Heat Flux Boundary Condition

The agreement is very good, so the heat flux boundary condition is being modeled correctly.

E.3. Pressure Verification

Next the pressure equation will be verified to show that gas phase pressure is being calculated correctly. Total gas pressure is comprised of the partial pressure of air and water vapor

$$P = p_a + p_v$$

As temperature and moisture content change, the gas pressure will change due to heating/cooling effects, compression, and evaporation.

To verify the pressure equation is working correctly, use the ideal gas law for air pressure

$$\frac{p_a V}{nRT} = \text{constant}$$

Where

p_a = air pressure
V = volume
n = number of moles of air
R = universal gas constant
T = absolute temberature

Consider the differential control volume shown in Figure 110.

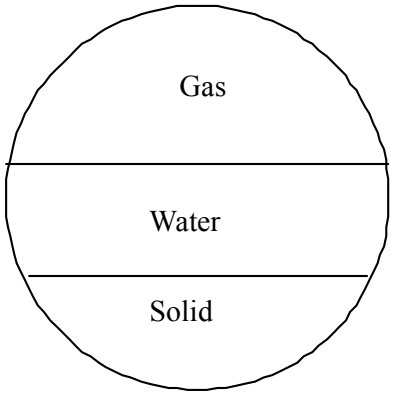

Figure 110 – Porous Media Control Volume

The volume fractions of gas, U_g is

$$U_g = \phi\left(1 - S_w\right)$$

If we consider the control volume at two discrete points in time, t_1 and t_2, the ideal gas law states that

$$\frac{p_{a1}V_1}{nRT_1} = \frac{p_{a2}V_2}{nRT_2}$$

If we assume that no air enters or exits the control volume, the ideal gas law reduces to

$$\frac{p_{a1}V_1}{T_1} = \frac{p_{a2}V_2}{T_2}$$

or

$$p_{a2} = p_{a1}\frac{V_1}{V_2}\frac{T_2}{T_1}$$

The ratio of volumes can be calculated from the change in saturation.

$$\frac{V_1}{V_2} = \frac{\left(1 - S_{w,1}\right)}{\left(1 - S_{w,2}\right)}$$

Use this to verify the change in pressure in the model. The total pressure is calculated by adding the air pressure to the vapor pressure. Apply the following boundary and initial conditions to run the model:

$at\ z = 0,\ t > 0$
$S_w = 0.8$
$T = 293K$
$P = P_\infty$

$at\ z = L = 0.01m,\ t > 0$
$S_w = 0.2$
$T = 293K$
$P = P_\infty$

$at\ t = 0$
$S_w = 0.2$
$T = 293K$
$P = P_\infty$

The viscosity of water as a function of temperarure given by [57] is used. Use thermal properties of wood from section 5.2. For the moisture transport, use properties of wood from Spolek and Plumb [45], and Plumb et al. [56]

$K = 1 \times 10^{-16}\ \left[m^2\right]$
$p_c = 1.24 \times 10^{-5} S_w^{-0.61}\ \left[Pa\right]$

For liquid relative permeability use a cubic function

$K_{rl} = S_w^3$

To ensure that no mass transfer of air or vapor occurs, set gas relative permeability and binary diffusivity of vapor in air equal to zero.

$$K_{rg} = 0$$
$$D_{va} = 0$$

The model was run a mesh of 61 grid points, time step of 1 second, and a total simulation time of 100 min. The model prediction for pressure and the ideal gas prediction are shown in Figure 111.

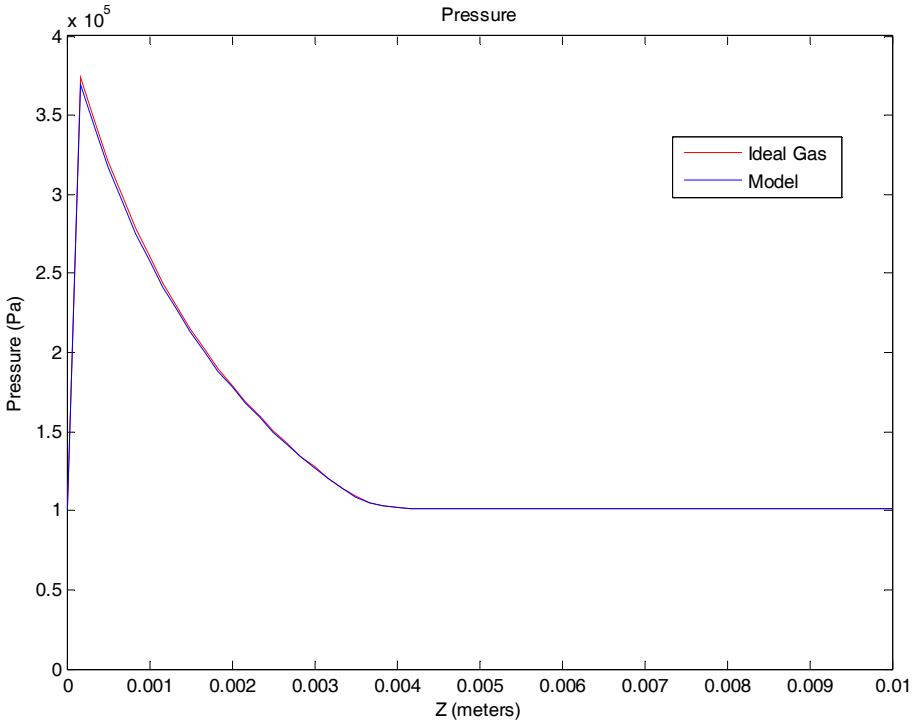

Figure 111 – Pressure Verification for Increase in Saturation

The pressure rise shown in Figure 111 represents the simulation of compression caused by water entering the material. The model predicted pressure rise and analytically predicted ideal gas pressure rise never differ by more than 1.6%.

Next, check to make sure that the model responds to an increase in temperature. Apply a constant temperature surface boundary condition to heat the material. Use the

following boundary and initial conditions.

$at\ z = 0,\ t > 0$
$S_w = 0.2$
$T = 333K$
$P = P_\infty$

$at\ z = L = 0.01m,\ t > 0$
$S_w = 0.2$
$T = 293K$
$P = P_\infty$

$at\ t = 0$
$S_w = 0.2$
$T = 293K$
$P = P_\infty$

Once again the model was run a mesh of 61 grid points, time step of 1 second, and a total simulation time of 100 seconds. The model pressure and ideal gas pressure are shown in Figure 112.

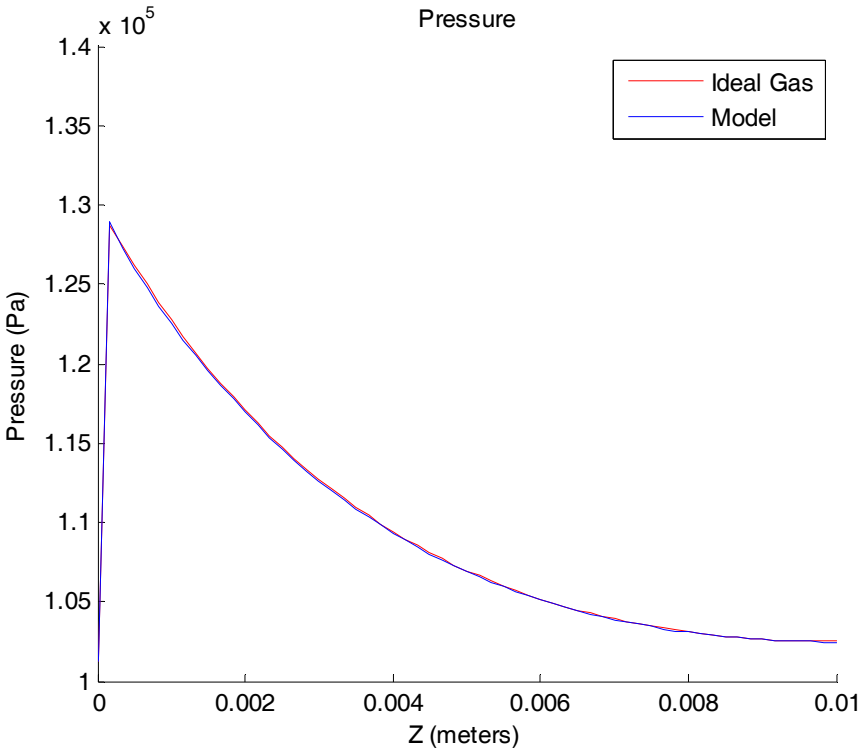

Figure 112 – Pressure Verification for Increase in Temperature

The model pressure rise and expected ideal gas pressure rise never differ by more than 1.2%.

In the course of verifying the model, it was observed that cases of simultaneous heating and convective mass transfer boundary conditions at the surface, the gas phase pressure initially decreased to below ambient pressure, and later increased as the material heated up further and dried out. This has also been observed in numerical model results by Ni [41], Wei et al. [107], and Nasrallah and Perre [38]. Initially this phenomenon was assumed to be caused by the expansion of air gaps in pores as water was drawn out of the material by surface tension and transported towards the surface as it was dried. This behavior has been observed in the model, but it is not the only cause of negative pressures. While testing the current model it was observed that a drop in pressure also occurred during heating when the mass transfer coefficient was set to zero. A model simulation of convective heating of a wet slab of brick 5cm thick, with no convective mass loss at the surface was conducted. Convective heating boundary conditions are applied to the surface, and no-flux boundary conditions are applied to the back face. The results are shown in Figure 113.

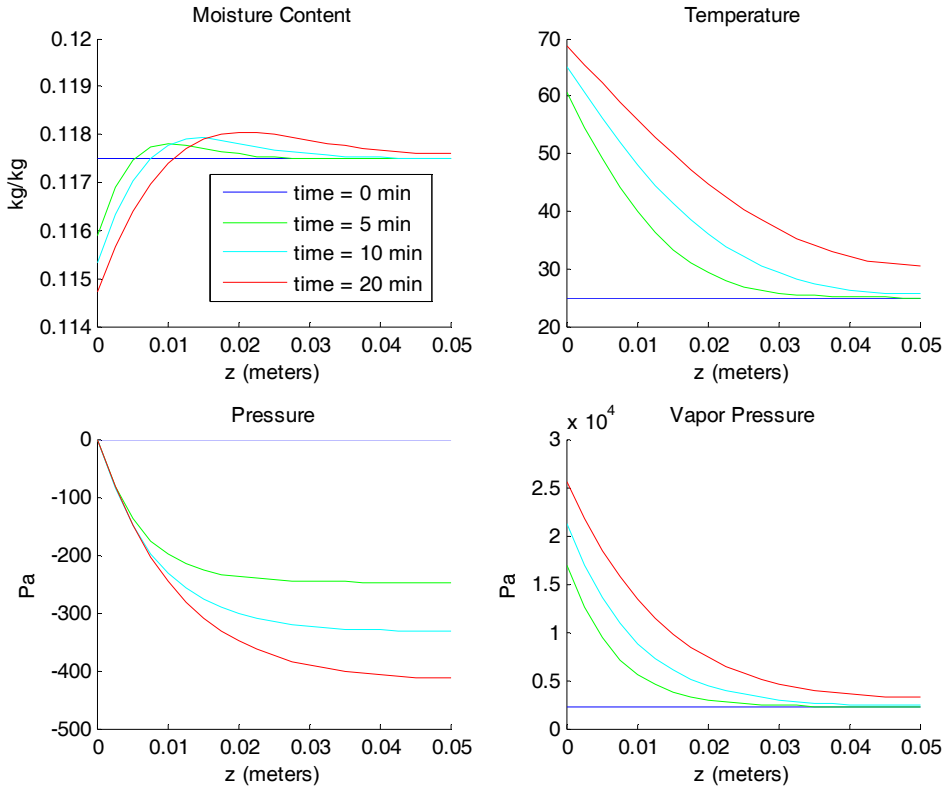

Figure 113 – Brick Heating Model Results – h=75 W/m^2K, h_m=0 m/s T_{amb}=80 degC, L=5cm

The total moisture content of the slab remains constant, but the pressure gradient draws the liquid away from the surface and into the material. The temperature increases at the surface as would be expected. The pressure drop was unexpected, and at first was suspected to be caused by a bug in the code. The vapor pressure increases as temperature increases as would be expected. After closer inspection the gas phase pressure drop phenomenon appears to be caused by the diffusive component of the air mass fluxes which transports air towards the surface of the material. The diffusive component of the air mass flux is proportional to the air mol fraction, while the vapor diffusive mass flux is proportional to the vapor mol fraction. These are shown in Figure 114.

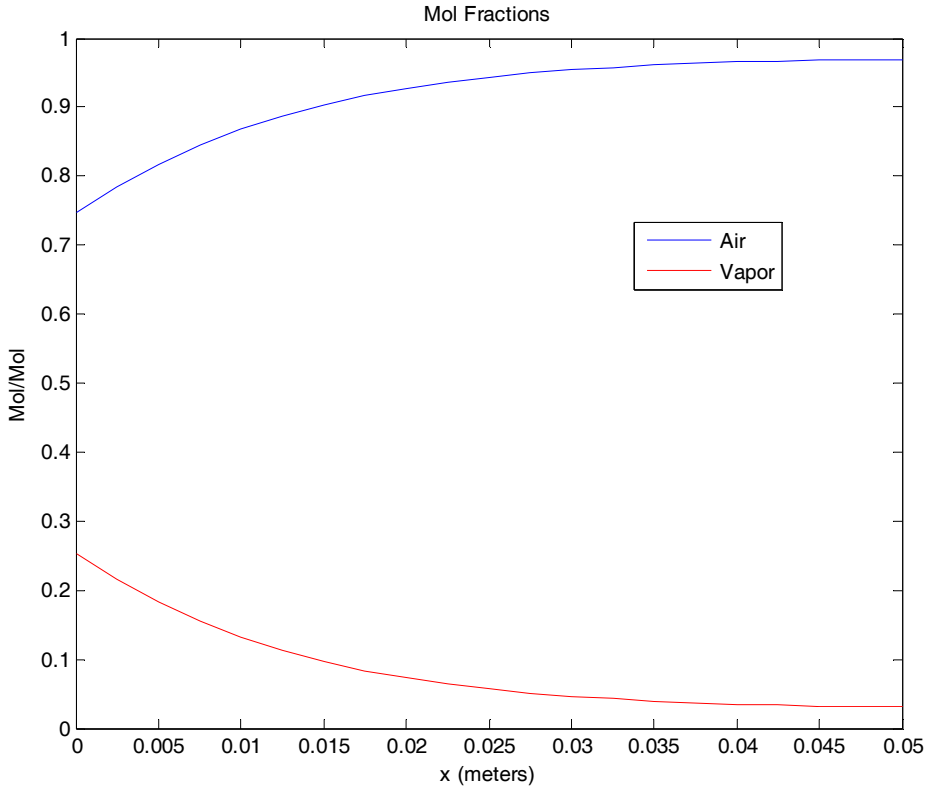

Figure 114 – Mol Fractions of Air and Water Vapor

The resulting mass fluxes are shown in Figure 115.

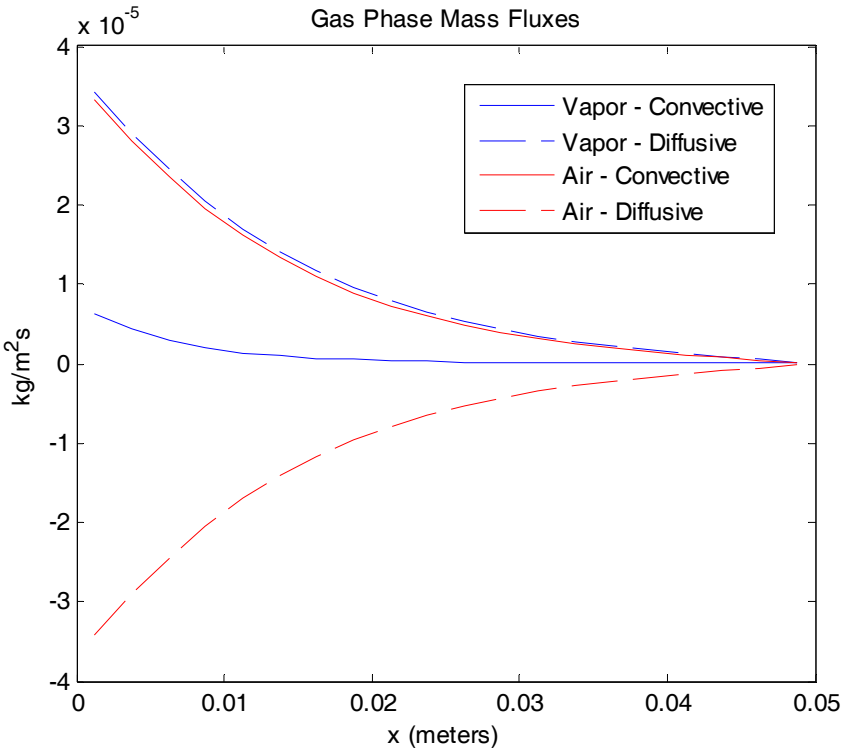

Figure 115 – Mass Fluxes of Air and Water Vapor

The sign convention for the mass fluxes is that negative fluxes are directed out of the material, and positive fluxes are directed into the material. The diffusive mass fluxes of air and vapor are equal in magnitude and opposite in direction as would be expected. Air diffuses to the surface, vapor diffuses into the material. The convective fluxes are driven by the same pressure gradients and will always have the same sign. Their magnitudes are unequal as a reflection of the difference in mol fractions. The total (convective plus diffusive) mass flux of vapor is positive and much larger than the total mass flux of air. The vapor diffusive flux does not have an impact on the total gas pressure however, since local thermal equilibrium dictates that the excess vapor instantly condenses and the vapor content is solely a function of temperature. So, as air is diffusing to the surface, vapor is diffusing into the material and immediately condensing where the material is cooler. This produces a net mass flux to the surface, where the pressure is fixed at ambient. Essentially all of the air that is transported to the surface is lost. This causes the pressure to drop in the material. Since gas phase pressure in the pores is not commonly measured, the pressure that is predicted by the model is difficult to validate. Validation of porous media models is often performed

against more easily measured quantities like mass loss and temperature. The previously mentioned models were able to produce reasonable results, despite having questionable pressure outputs. The difficulties associated with predicting internal pressures are prevalent in other areas of study as well. The pyrolysis model of Henderson and Wicek which was developed for expanding phenolic foam predicted internal overpressures of 40 atm in the pore spaces of the material [108]. To further demonstrate that the mechanism described is responsible for the decrease in pressure, the surface was sealed in the model with no flux boundary conditions for the pressure equation (conservation of air). The gas phase pressure in the pores increased as the material heated up, as shown in Figure 116.

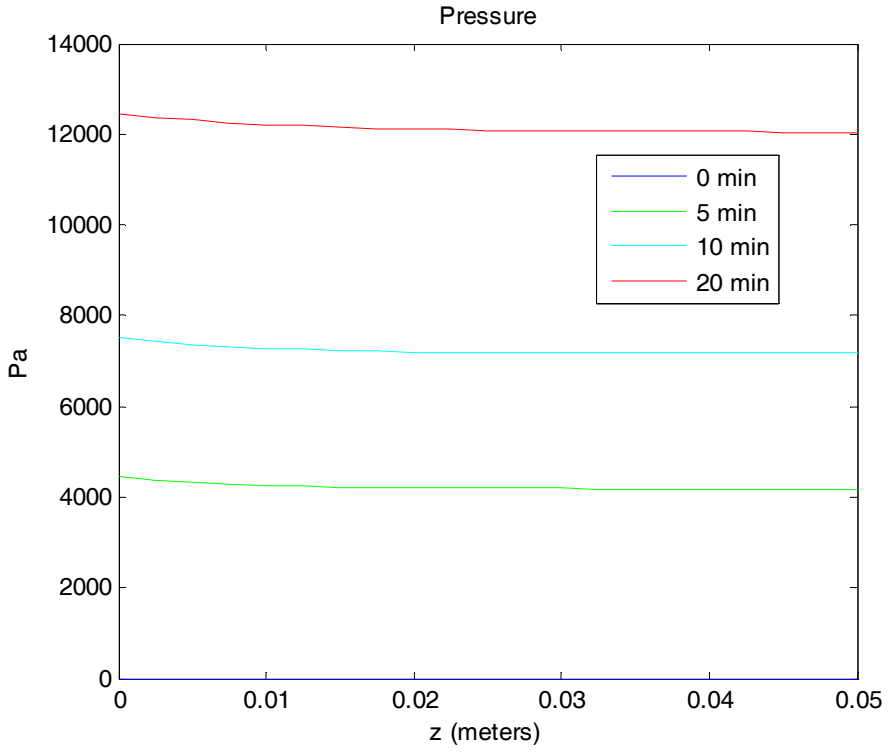

Figure 116 – Pressure Increase with No-Flux Pressure Condition at Surface

E.4. Model Results

E.4.1. Results for Glass Beads With Low Flux Water Spray

Now apply the model to a bed of glass beads. Use the correlation of Rumpf and Gupte [82] to calculate the permeability of the bed. Assume 300 micron beads in a face centered cubic packing order which produces a porosity of 0.26

$$K = \frac{\varphi^{5.5}}{5.6} d^2 = \frac{(0.26)^{5.5}}{5.6}\left(300\times10^{-6}\right)^2 = 9.74\times10^{-12}$$

Calculate the capillary pressure using Leverett's J-function.

$$p_{cap} = \left(\frac{\varphi}{K}\right)^{\frac{1}{2}} \sigma J(S)$$

Where the surface tension of water is 0.07 N/m and the J-function is

$$J(S) = 0.364\left(1-\exp\left(-40\left(1-S\right)\right)\right) + 0.221\left(1-S\right) + \frac{0.005}{S-0.08}$$

Expose the bed of beads to a water flux of 0.0478 kg/m^2 (light hazard group 1 water flux) and a heat flux of 10 kW/m^2. For a simulation time of 400 seconds, a time step of 1 second, and 51 grid points the saturation, temperature, air pressure, and mass conservation are shown in Figure 117.

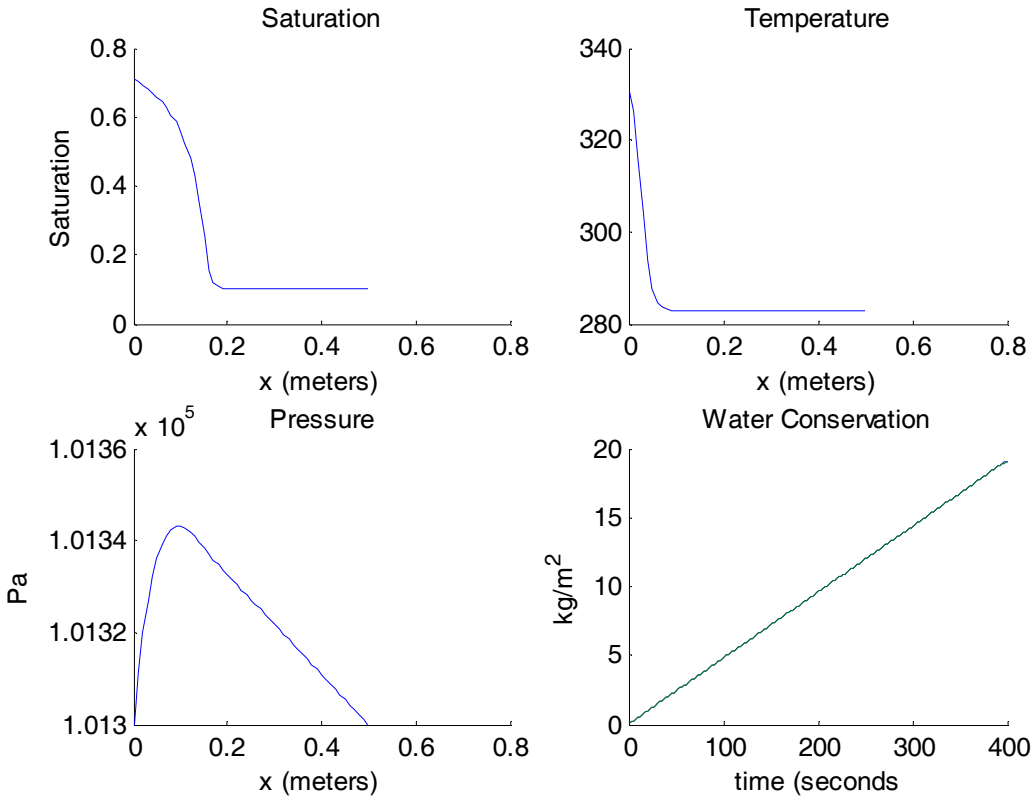

Figure 117 – Model Results for 300 Micron Glass Beads Exposed to 10 kW/m^2 and 0.0478 kg/m^2 Water Spray

In this case the water is being transported into the glass beads at a faster rate than the heat. There is a slight rise in pressure inside the bed, which peaks at just over 40 Pa. The water conservation in the fourth subplot is showing that the model is conserving mass. Here the water that has been sprayed on the material is plotted along with the total amount of water that has been absorbed as calculated by a simple numerical integration. The two plots are indistinguishable, so water is being conserved.

E.4.2. Model Results for Wood with Water Layer on the Surface

Now model the situation where a layer of water has formed on the surface of a solid material. In this case use thermal properties of wood for the solid. Use the following values for other input parameters

$$K = 1 \times 10^{-14} \ m^2$$
$$\phi = 0.1$$
$$h = 10 \frac{W}{m^2 K}$$
$$h_m = 0.03 \frac{m}{s}$$
$$\dot{q}'' = 10 \frac{kW}{m^2}$$

The results at a time of 300 seconds for a length of material 0.02m thick and containing 31 grid points, and a 0.001m thick water layer containing 11 grid points, a time step of 0.1 seconds, and a incident heat flux of 10 kW/m^2 are shown in Figure 118.

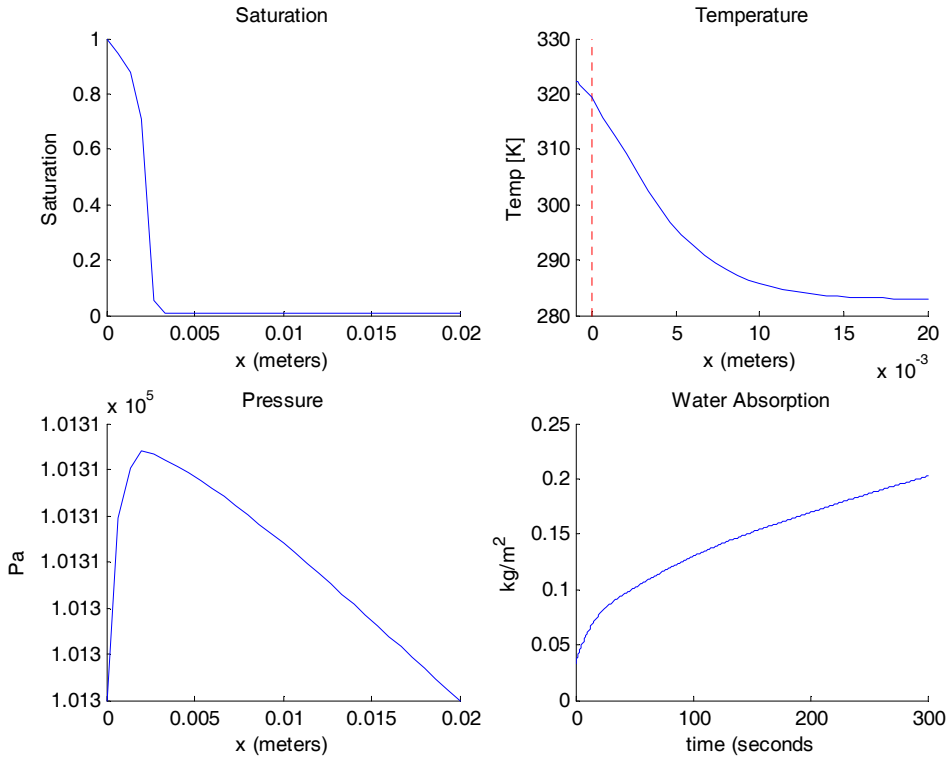

Figure 118 – Water Layer on Wood with a Heat Flux of 10 kW/m^2

The temperature at several time steps is shown in Figure 119. The dashed orange vertical line represents the material surface. The water temperature profiles are to the left of the dashed line and are beginning to flatten out as the surface heats up and

begins to lose heat by convection and evaporation.

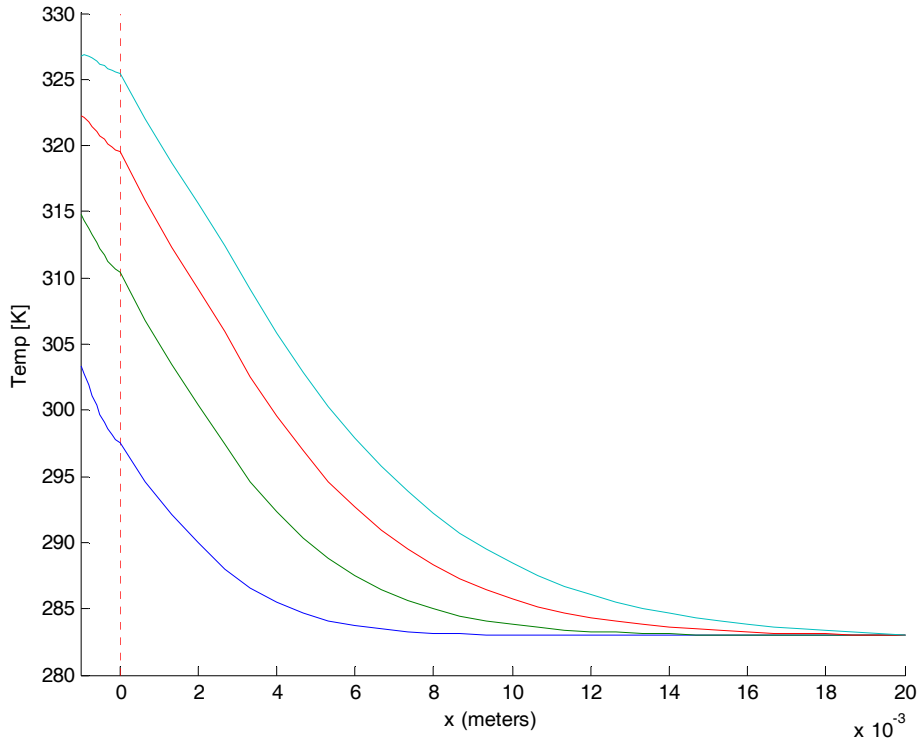

Figure 119 – Temperature of Wood with a Water Layer Exposed to 10 kW/m^2 at 100, 200, 300, and 400 Seconds

Appendix F. Validation

F.1. CFB Wetting

Ceramic fiberboard (CFB) was chosen for a representative test material. CFB is a hydrophilic material, it is inert, and on the macro level it is isotropic and homogeneous. Before the model can be used with ceramic fiberboard samples, several input parameters must be estimated.

F.1.1. CFB Parameter Measurement

Porosity measurement

The porosity of the fiberboard was measured by weighing a sample completely dry and completely saturated with water. A sample measuring $6" \times 6" \times 2"$ was used. The porosity
is calculated as follows:

$$Width = 6" \pm 1/16" = 0.1524m \pm 0.003175m$$
$$Length = 6" \pm 1/16" = 0.1524m \pm 0.003175m$$
$$Thickness = 2" \pm 1/16" = 0.0508m \pm 0.003175m$$
$$Volume = 0.0012m^3$$
$$Mass\left(dry\right) = 340g \pm 0.1g$$
$$Mass\left(wet\right) = 1281 \pm 10g$$
$$Mass\ of\ water\ absorbed = 941 \pm 10g$$
$$Volume\ of\ water\ absorbed = 0.941kg \frac{1m^3}{1000kg} = 9.41 \times 10^{-4} m^3$$
$$Porosity = \frac{0.000941}{0.0012} = 0.80 \pm 0.05$$

The CFB is calculated to be 80% porous. A representative from Thermal Ceramics indicated in a personal communication that he had performed tests which concluded that the porosity is 83%, which is very close to the value determined here. Since the details of his test were not provided, the value of 80% will be used. This porosity value can be used to calculate the properties of the solid fibers.

Capillary Pressure Measurement

In order to predict the movement of moisture through the fiberboard, constitutive relationships are needed for capillary pressure and the relative permeabilities. These are not available for ceramic fiberboard, so suitable relations must be found from the literature or experiment. The capillary pressure for several material-fluid combinations are given by Kaviany [23]. Each correlation has the form

$$p_{cap} = \sigma\sqrt{\frac{\phi}{K}}J(S)$$

Where

$\sigma = surface\ tension\ \left[\frac{N}{m}\right]$

$K = permeability\ \left[m^2\right]$

$\phi = porosity$

$J(S) = J - function$

Kaviany [23] gives an empirical J-function for particulate media (from [44]):

$$J(S) = \left[0.364\left(1-\exp\left(-40\left(1-S\right)\right)\right) + 0.221\left(1-S\right) + \frac{0.005}{S-0.08}\right]$$

Kaviany [23] also gives relative permeability data for particulate media:

$$K_{rl} = S_{eff}^3$$

$$K_{rg} = \left(1-S_{eff}\right)^3$$

Where $S_{eff} = \frac{S_w - S_{ir}}{1-S_{ir}}$

These relations are shown in Figure 120 and Figure 121.

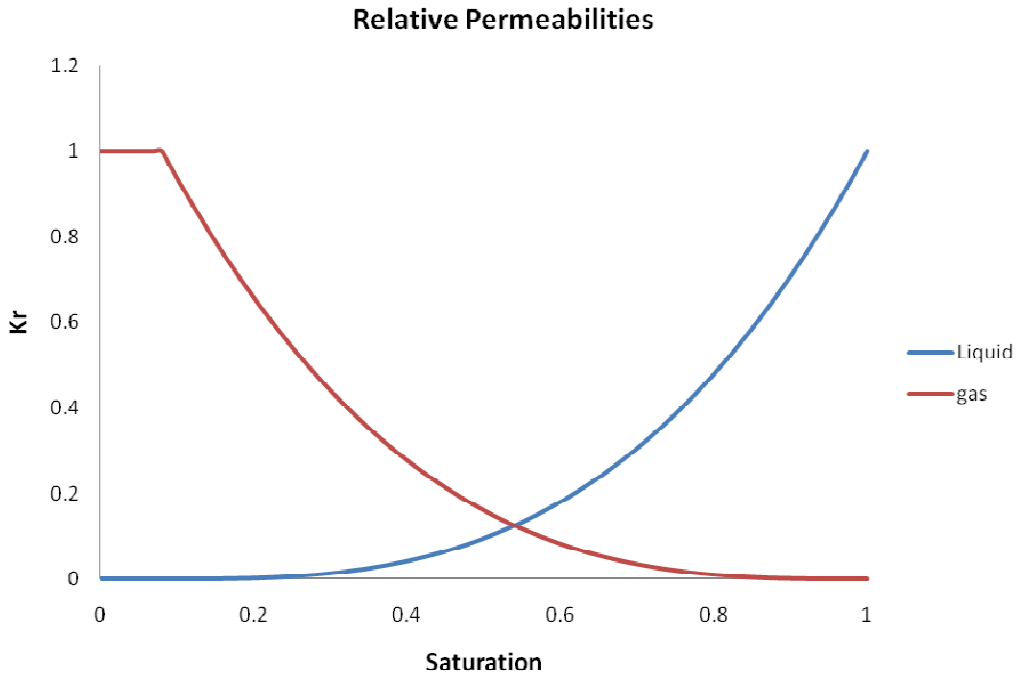

Figure 120 – Relative Permeabilities

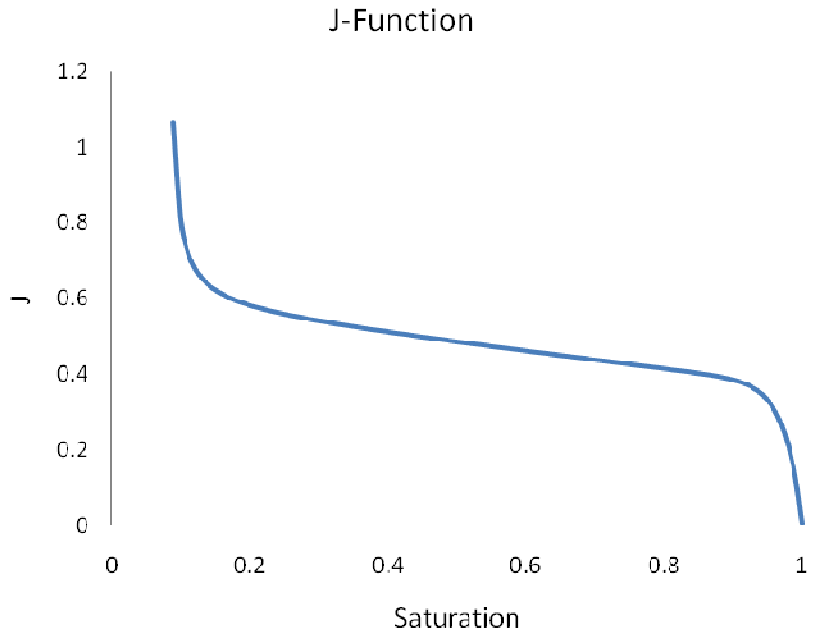

Figure 121 J-Function from Literature

It should be emphasized that these relations were developed from experiments on particulate media, but they are widely used to characterize solid materials. In order to determine an appropriate J-function that is specific to ceramic fiberboard several capillary wetting tests were conducted. Wetting tests were conducted using initially dry samples of CFB. Three samples were used for the tests. Two samples measured 2” by 3” by 12” tall and the third measured 2” by 3” and 24” tall. The samples were cut into smaller slabs each measuring 1” by 2” by 3”. These slabs were stacked in the same orientation as before they were cut to form good contact along the cuts. This is shown in Figure 122.

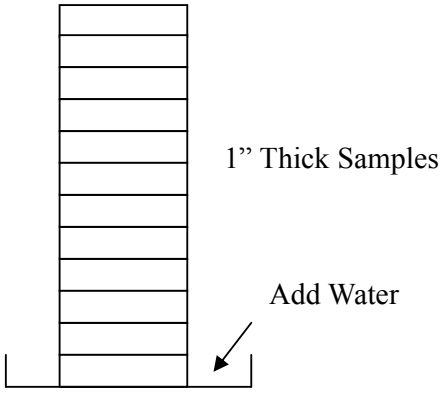

Figure 122 - CFB Sample Used For Capillary Pressure Test

Three wetting tests were carried out as follows: Water was applied to the base of the CFB stack and allowed to be absorbed into the material. Water was added at 4 hour intervals times to maintain a 1cm depth and allowed to soak in for 24 hours. The stack was wrapped in plastic to minimize evaporative losses. The interfaces between the slabs introduced a resistance to water flow, but given the amount of time allowed for the test, the effects from interfacial resistance should be minimal. After 24 hours, the individual slabs were weighed to determine how much water each has absorbed. From the mass of water absorbed, the saturation of each block could be calculated. This data was used to determine the J function of the CFB. The results are shown in Figure 123.

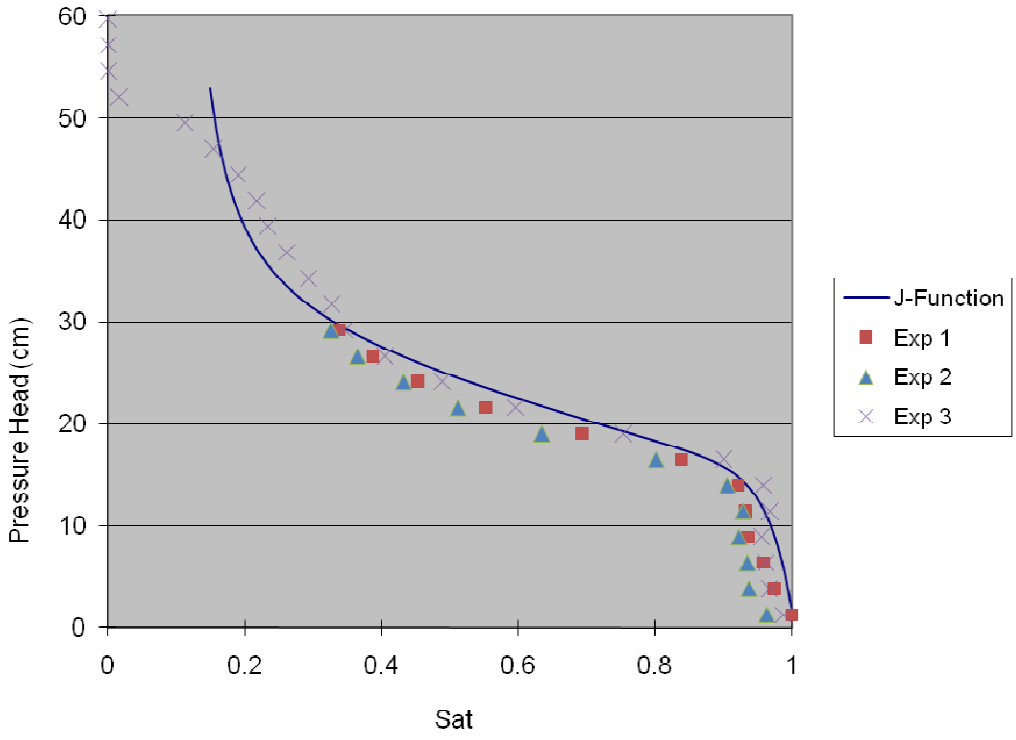

Figure 123 – J Function for CFB

The J function shown in Figure 123 is obtained by curve fitting to the experimental data points. The equation is

$$J(S) = 0.4\left[0.364\left(1-\exp\left(-30\left(1-S\right)\right)\right)+0.471\left(1-S\right)+\frac{0.035}{S-0.1}\right]$$

So therefore

$$\frac{\partial p_{cap}}{\partial S} = \sigma\sqrt{\frac{\phi}{K}}\frac{\partial J(S)}{\partial S} = \sigma\sqrt{\frac{\phi}{K}}0.4\left(\left(-30\right)0.364\exp\left(\left(-30+30S\right)\right)\right)-0.471-0.035\left(S-0.1\right)^{-2}$$

This equation contains a singularity at S=0.1. From the experimental data it can be seen that water absorption by capillary action breaks down around a saturation of 15%. At this value, the water is no longer continuously connected, and cannot flow.

Therefore below S=0.15 the relative permeability for liquid must be zero and the singularity is not problematic. The absolute permeability is estimated to be

$$K = 5 \times 10^{-11} m^2$$

The value of K that was determined falls in the range of values given for sand, concrete, and fiberglass by Sheidegger [25]. The relative permeabilities are assumed to follow a cubic relationship with saturation as given in the literature for particulate media.

Vapor Pressure

The vapor pressure in the ceramic fiberboard is assumed to obey the same relationship as brick.

$$S_w = \frac{(1-\phi)\rho_s}{\phi \rho_w}\left(0.0105\left(\frac{p_v}{p_{vs}}\right)^{0.2} + 0.0125\exp\left(20\frac{p_v}{p_{vs}} - 20\right)\right)$$

Where

$$p_v = vapor\ \ pressure\ in\ \ pore\ space\ \left[Pa\right]$$
$$p_{vs} = vapor\ \ pressure\, above\ a\ \ flat\ \ liquid\ \ surface\ at\ \ equilibrium\ \left[Pa\right]$$

This correlation was determined to be appropriate for CFB even though it was measured for brick. To test this, 4 samples of CFB measuring 3" by 2" by 1" were placed in sealed 3.25 quart plastic containers and exposed to environments of varying relative humidity. The laboratory conditions for these tests were 72 deg F and 60% RH. The relative humidity in the containers was measured using an Omega RH411 Thermo-Hygrometer. The relative humidity in the containers was adjusted using one of the following methods.

1. RH =100% was achieved by placing a pan of water in the container with the CDB sample.
2. 100% > RH > 60% was achieved by placing slightly damp paper towel in the container with the CDB sample.
3. 60% > RH > 0% was achieved by placing a 3" diameter pan with a small

amount of dri-rite in the container with the CDB sample.

4. 0% RH was achieved by placing a 3" diameter pan full of dri-rite in the container with the CFB sample.

The experimental results and the brick correlation are shown in Figure 124.

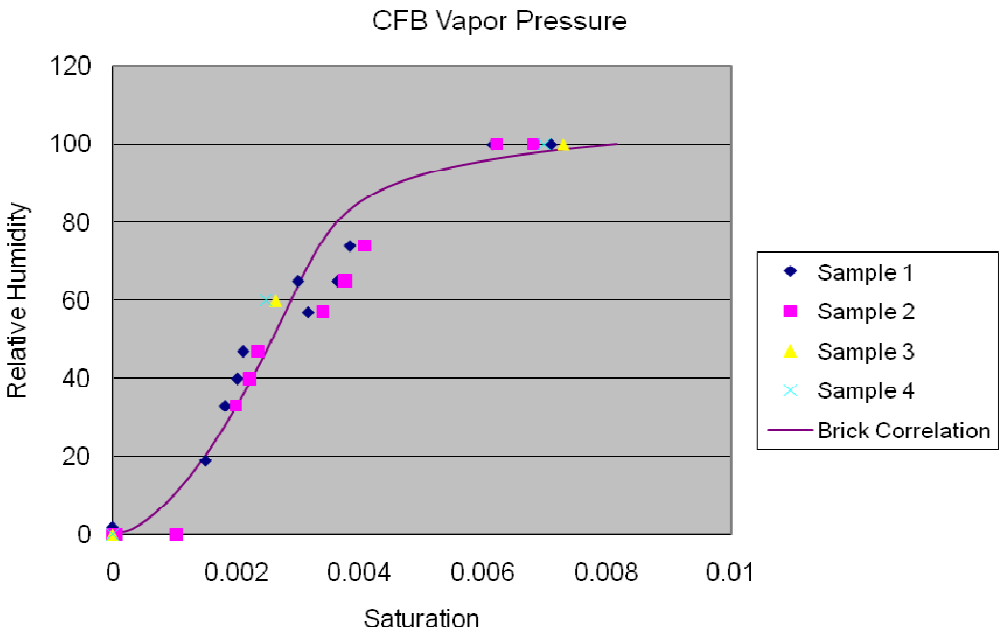

Figure 124 – Measured Vapor Pressure in CFB

F.1.2. Type 1 Boundary Condition Wetting

Wetting tests were carried out in the WPI Fire Science Lab with ceramic fiberboard. Blocks of fiberboard were placed in contact with a reservoir of water, and the depth of water penetration was measured over time. The water levels were maintained by manually adding water. Two sets of tests were carried out: wetting the blocks from the top and bottom. The two geometries are shown in Figure 125 and Figure 126.

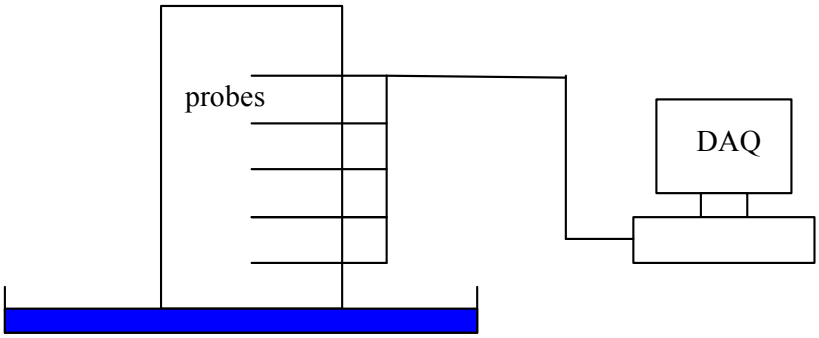

Figure 125 – Experimental Bottom-Wetting Set-Up for CFB

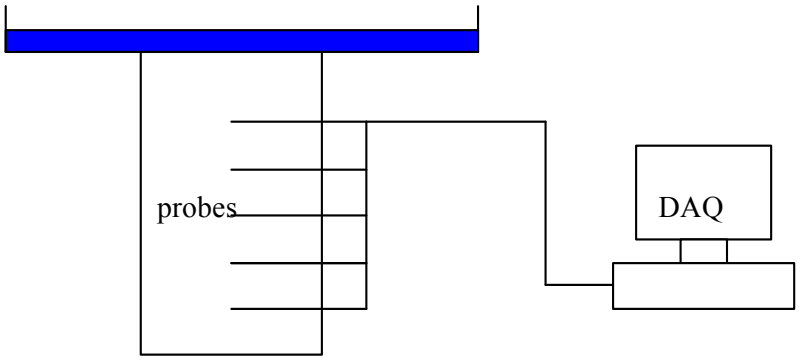

Figure 126 – Experimental Top-Wetting Set-Up for CFB

The edges of the ceramic fiberboard blocks were sealed with silicone caulking. For the top-wetting scenario, a pan was built to rest on top of the block. Water was poured into the pan and formed a reservoir that kept the surface of the block saturated. The depth of water penetration was measured by 5 probes spaced 1" apart. The probes each consisted of two thin gauge nails which were inserted into the ceramic fiberboard at a distance of ½ inch apart. The resistance between the nails was measured using data

acquisition hardware and software from National Instruments. The resistance between the two nails decreases significantly when water reaches that point. The signal recorded by the data acquisition system is shown in Figure 127.

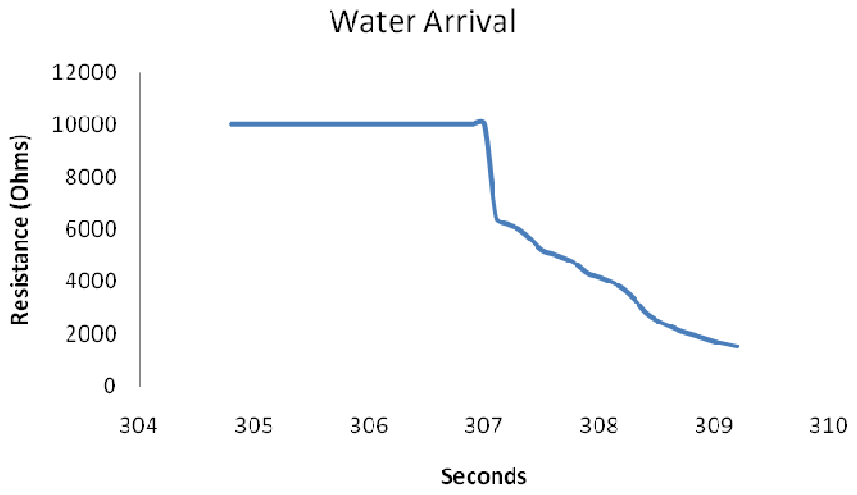

Figure 127 - Water Arrival Electrical Signal from Probe

The signal is out of range initially, meaning that the resistance is very high, until 307.1 seconds into this particular test. The value of 10,000 ohms, indicates an out of range signal. When the material is very dry, its resistance is extremely high. In this case the resistance between the nails is much greater than 10k ohms. Once the water arrives at the probes, the resistance drops to around 6 k-ohms. This is seen as a step function in the probe signal.

It was observed that the water travels much faster when the block is wetted from the top than the bottom. This demonstrates that the effects of gravity are significant in ceramic fiberboard. The model was used to simulate these conditions. The value of K that was determined in the first experiment was used for this set of model simulations. The surface that is being wetted (either the top or bottom), has the following boundary conditions

$$S = 0.99$$
$$T = T_{\infty} \qquad @z = 0$$
$$P = P_{\infty}$$

The surface that is not being wetted has the following boundary conditions

$$S_w = S_o$$
$$T = T_\infty \qquad @\, z = L$$
$$P = P_\infty$$

The hydrostatic pressure at the surface is small and is ignored. The surface saturation value is chosen to be 0.99 due to the inability of a wetting fluid to displace all of the non-wetting fluid from the very small pores of the material. This residual amount of non-wetting fluid (in this case: air) is called the irreducible non-wetting phase saturation and can vary between 0.75 and 0.98 [23]. For the CFB it is assumed to be 0.99, meaning that completely saturating the material only fills it 99 percent. It will later be shown that the model is sensitive to this surface saturation boundary condition. For surface saturation values between 0.98 and 0.999 the model gives good agreement with the experimental results. A value of S=1 cannot practically be used because it causes the model to crash due to numerical issues. The model and experimental results for $S_{surf} = 0.99$ are shown in Figure 128. The circular data points represent top wetting tests, and the "plus" data points represent bottom wetting tests. The different colors represent different tests, and there is some scatter between the tests. It can be clearly seen that the water penetrated the ceramic fiberboard much faster when assisted by gravity in the top wetting scenario.

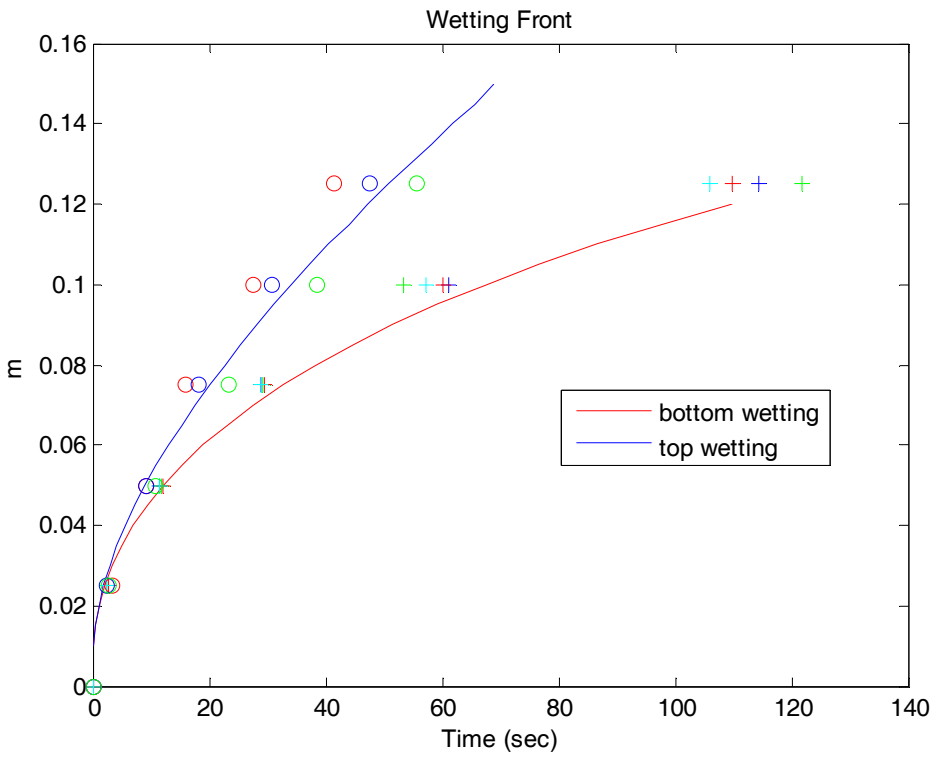

Figure 128 – Wetting of Ceramic Fiberboard and Model Prediction

F.1.3. Spray Wetting Boundary Condition

A third set of experiments was conducted using a spray wetting boundary condition. To provide the water spray a water delivery apparatus was designed in the WPI Fire Science Laboratory. A solid cone water mist nozzle was used to provide the spray. Water to the nozzle was piped from the building's water supply and regulated via a valve. Pressure was monitored with a pressure gauge located close to the nozzle. This way the water flow rate could be measured at various nozzle pressures and a measure of repeatability is provided. Since we are concerned with the water mass flux reaching the surface of the material, a water collection apparatus was designed to measure this flux over a plane where the sample would sit. The measurement apparatus consisted of 36 individual 6" sections of 1" by 1" square polycarbonate tubing. One end of each tube was sealed and they were all placed in a square array. This allowed the water reaching the plane of the open ends of the tubes to be collected and later measured. This data provides a map of the water flux reaching the sample surface. The water delivery system and measurement apparatus is shown in Figure 129 and Figure 130.

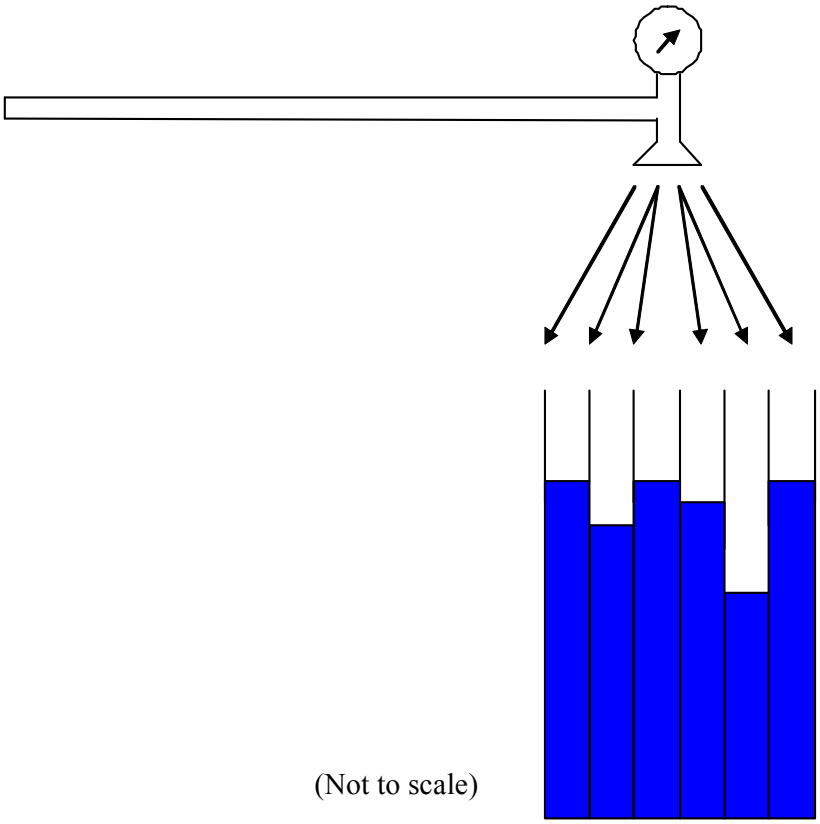

Figure 129 – Water Delivery System and Collection Tubes

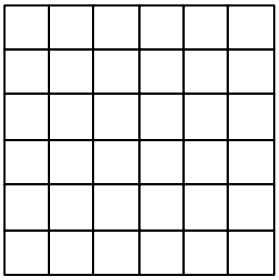

Figure 130 - Water Collection Tubes - Top View

After collecting water from the nozzle at a specific pressure for several minutes, the water flow was shut off, and the water in each tube was measured. The mass fluxes that were measured in the center 16 tubes forming a 4” by 4” square at the center of the array were fairly uniform. The average mass flux measured in the center 16 tubes is shown in Figure 131.

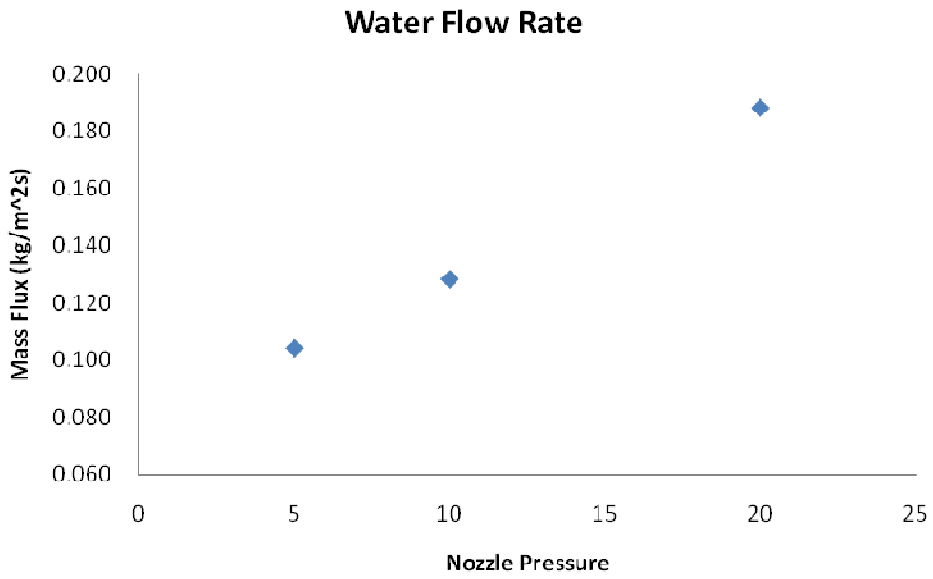

Figure 131 - Measured Water Flux at Sample Surface

Samples of CFB were sealed at the longest edges in the same manner as the previous wetting experiments. The location of a wetting front was measured using the same probes as well. The only difference for these experiments was that the water is now applied using the water spray apparatus discussed here. This experimental set up is shown in Figure 132.

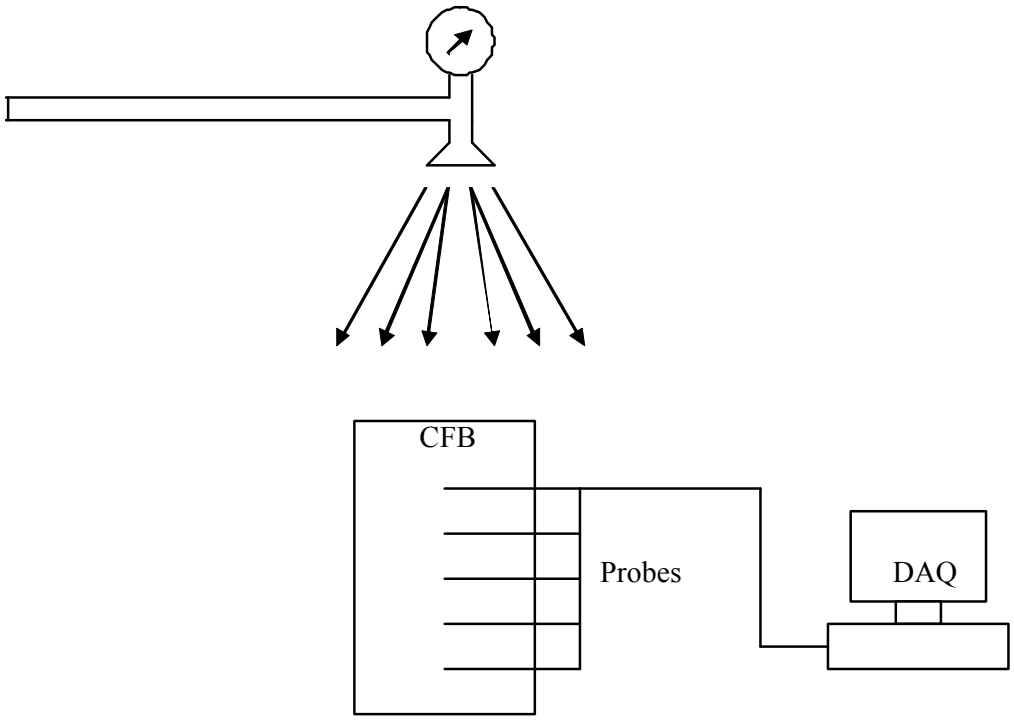

Figure 132 - Spray Wetting Experimental Set Up

Simulations were run using the properties of CFB discussed previously. The surface boundary conditions are now as follows: The top surface has the following boundary conditions:

$$\dot{m}''_w + \dot{m}''_v = \dot{m}''_{spray}$$
$$T = T_\infty$$
$$P = P_\infty$$

No overflow was observed from the exposed surface, so all of the water applied is assumed to be absorbed into the material. The surface evaporation rate is much smaller the water application rate, so it is left out. The surface that is not being wetted has the following boundary conditions:

$S_w = S_o$

$T = T_\infty$

$P = P_\infty$

The results of the simulations are shown in Figure 133.

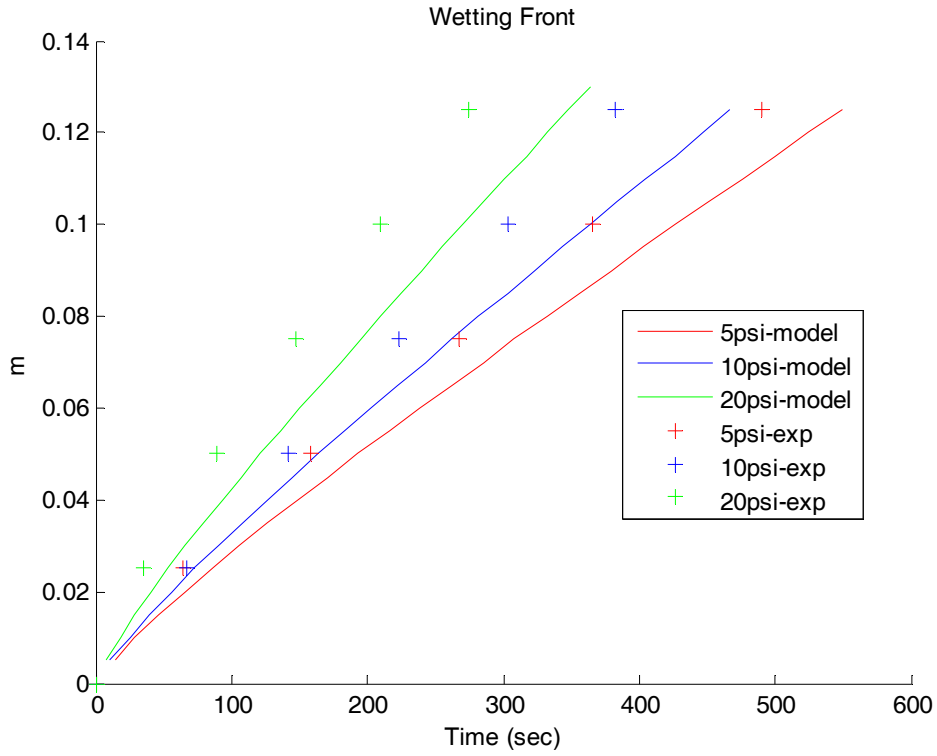

Figure 133 - Spray Wetting at Three Water Mass Fluxes

Time Dependant Sorption Test

To validate the vapor transport aspects of the model, tests were conducted to measure the rate of water vapor absorption from the ambient by dry samples of CFB. A sample measuring 2” by 3” by 1” was placed in a sealed container with a 3” diameter pan of dri-rite for 24 hours to remove all water. Prior to conditioning the sample, its edges were sealed, leaving only the 2” by 3” sides open.

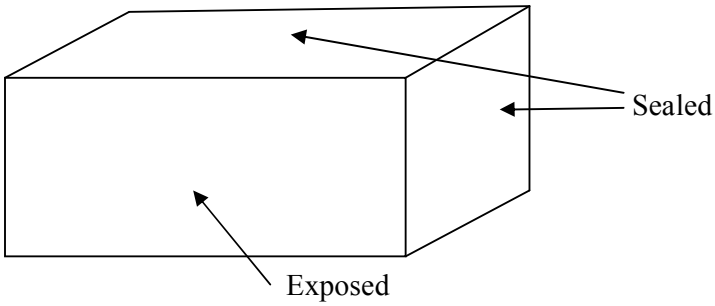

The sample was removed from the conditioning chamber, and placed on an extremely accurate scale with a sensitivity of 0.0001 g and the mass was observed and recorded by hand over time. The scale is a model HR 120 manufactured by A&D. The sample was placed so that both exposed sides were vertical. The ambient conditions for the tests were 72 deg F and 60% relative humidity. The model predictions and experimental data are shown in Figure 134. The model agrees very well with the experimental data for the first 25 min, then begins to deviate slightly. The experimental data exhibits a smooth parabolic shape, while the model has slight “kink” around 35 min. This is believed to be due to the function used in the model to represent the relation between vapor pressure and saturation.

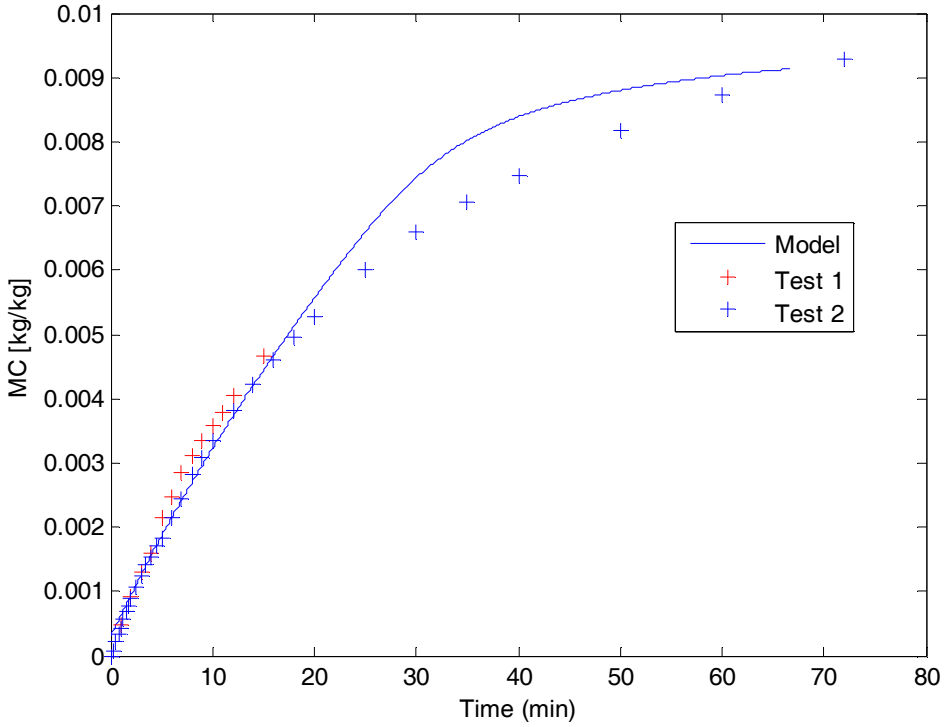

Figure 134 – Vapor Absorption from Ambient

F.2. Particulate Media Heating

Drying Experiments were conducted by Lu et al. [53] on a packed bed of particulate material. The experimental apparatus is shown in Figure 135.

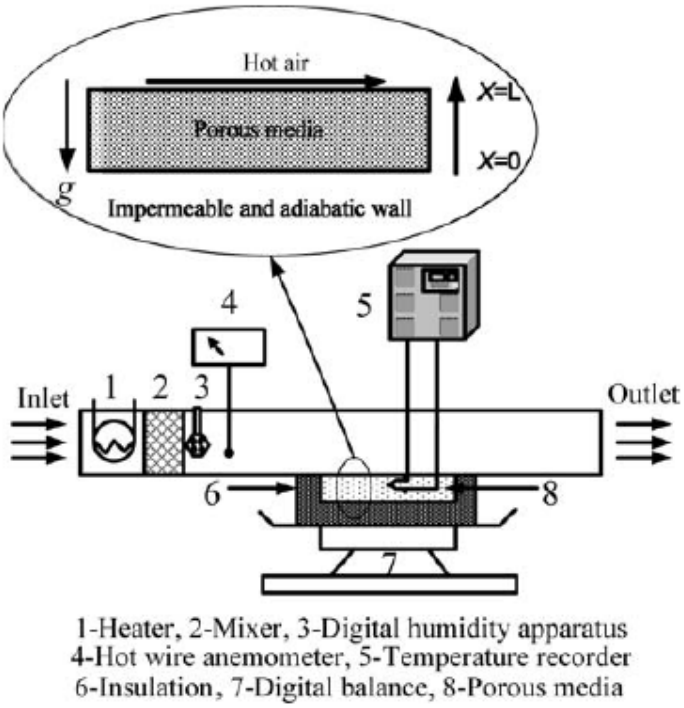

Figure 135 – Drying Apparatus (from [53])

The porous media used was a bed of 1-1.5mm diameter quartz particles. The bed was cylindrical in shape and 45mm in diameter, and 15 mm deep. The sample was initially at a temperature of 298K, and the stream of hot air had a temp 321K a velocity of 1.89 m/s, and a relative humidity of 33+/-2%. The sample was initially saturated and had a moisture content of 0.226 kg/kg. The total mass loss rate was measured as well as temperature at 5 locations. Thermocouples were placed 0, 6, 8, 10, and 12 mm from the bottom surface.

The properties of quartz are given by Bejan [43]

$$\rho_s = 2100 - 2500\, kg/m^3 \left(Lu\ et.\ al\ use\ 2610\right)$$
$$C_p = 780\, J/kgK$$
$$k_s = 1.4\, W/mK$$

The permeability of the bed can be calculated from the quasi-analytical Carmen-Kozeny equation [23]

$$K = \frac{\phi^3 d^2}{180\left(1-\phi\right)^2}$$

or the empirical correlation of Rumpf and Gupte [82]

$$K = \frac{\phi^{5.5}}{5.6} d^2$$

The permeability can be calculated to be in the range of $1.9 - 5.6 \times 10^{-11} m^2$. For this modeling exercise a value of $3.75 \times 10^{-11} m^2$ was used.

The capillary pressure and relative permeabilities given by Kaviany [23] for sand will be used

$$p_{cap} = \frac{\sigma}{\sqrt{K/\varphi}}\left[0.364\left(1-\exp\left(-40\left(1-S\right)\right)\right) + 0.221\left(1-S\right) + \frac{0.005}{S-0.08}\right]$$
$$K_{rl} = S_{eff}^3$$
$$K_{rg} = \left(1-S_{eff}\right)^3$$

This correlation has a singularity at S=0.08 which leads to unreasonable values of the capillary pressure as the saturation approaches this value. Below a saturation of 0.09 the relative permeability is zero, so this is not significant.

Lu et al. state that bound water exists on the surface of the particles, but we will assume that this is very small. For the purpose of this analysis, it will be assumed that the quartz particles are non-hygroscopic and do not absorb water into the solid phase. The correlations used to calculate the surface heat and mass transfer coefficients

are given by Lu et al., but the dryer geometry is not given. We will attempt to estimate their inputs from their results. From 40 min until 280 min, their model predicted that the entire material remained at the wet bulb temperature of 303+/-2K. The temperature profile was flat during this period, so the evaporative heat losses were equal to the convective heating rate. This is expressed as

$$h\left(T_\infty - T_s\right) = \Delta h_{vap} h_m \left(\rho_{v,s} - \rho_{v,\infty}\right)$$

From the graphical scaled model output given by Lu et al. (2005), the moisture content throughout the material was 0.0648 and the surface temperature was 304.5K. The instantaneous mass loss rate at was calculated by digitizing their non-dimensional mass loss plot. The calculated value is

$$\frac{dMC}{dt} = 8.5\times10^{-4}\ \text{min}^{-1}$$

Lu et al. calculate the moisture content on a wet material basis

$$MC = \frac{\psi_l \rho_l + \psi_b \rho_b}{\psi_l \rho_l + \psi_b \rho_b + \psi_s \rho_s}$$

Where ψ_i represents the volume fraction of the ith component, and the subscripts l, b, s represent liquid water, bound water, and solid. This differs from the "dry basis" definition of moisture content used by others, where the ratio represents the mass of water to the mass of dry material (solid + air). Since bound water is not considered in this analysis, it will be left out of the calculations. Using this definition, the saturation at 240 min is calculated to be

$$S_w = \frac{\left(1-\phi\right)\rho_s MC}{\left(\phi\rho_l MC + \phi\rho_l\right)} = \frac{\left(1-0.46\right)2500\left(0.0648\right)}{0.46\left(1000\right)0.0648 + 0.46\left(1000\right)} = 0.179$$

Use the scaled model output from Lu et al. (2005)[53] to calculate a dimensional total mass loss rate

$$\dot{m} = L\left[\phi S_w \rho_l + (1-\phi)\rho_s\right]\frac{dMC}{dt}$$

so the dimensional mass loss rate is

$$\dot{m} = 0.015\left[0.46(0.179)1000 + (1-0.46)2300\right]\left(8.5\times10^{-4}\right) = 0.0169\ \frac{kg}{m^2\ \min} = 2.82\times10^{-4}\ \frac{kg}{m^2 s}$$

The surface temperature at 240 min is 304K. So the vapor pressures and densities can be calculated

$$\rho_{v,surf} = \frac{P_{v,surf}}{R_v T_{surf}},\ \ \rho_{v,\infty} = \frac{P_{v,\infty}}{R_v T_\infty}$$

$$P_{v,surf} = P_o \exp\left(-\frac{M_v \Delta h_v}{R}\left(\frac{1}{T_{surf}} - \frac{1}{T_o}\right)\right) = 101300\exp\left(-\frac{(0.018)2600000}{8.314}\left(\frac{1}{304.5} - \frac{1}{373}\right)\right)$$

$$P_{v,surf} = 3294Pa$$

$$P_{v,\infty} = RH \times P_o \exp\left(-\frac{M_v \Delta h_v}{R}\left(\frac{1}{T_\infty} - \frac{1}{T_o}\right)\right) = 101300\exp\left(-\frac{(0.018)2600000}{8.314}\left(\frac{1}{321} - \frac{1}{373}\right)\right)$$

$$P_{v,\infty} = 0.33\times8784Pa$$

$$P_{v,\infty} = 2898Pa$$

$$\rho_{v,surf} = \frac{3500}{461.8(305)} = 0.0241 kg/m^3$$

$$\rho_{v,\infty} = \frac{2899}{461.8(321)} = 0.0196\ \ kg/m^3$$

The mass transfer coefficient can be calculated to be

$$\dot{m}''_{evap} = h_m\left(\rho_s - \rho_\infty\right)$$

$$h_m = \frac{\dot{m}''_{evap}}{\left(\rho_s - \rho_\infty\right)} = \frac{2.82\times10^{-4}}{0.0235 - 0.0196} = 0.0626\frac{m}{s}$$

Lu et al. [53] calculate the mass transfer coefficient using the following relationship from Bird et al. [109]

$$h_m = \frac{h}{\left(\rho C_p\right)_{air}} Le^{-2/3}$$

Where the Lewis number is defined as the ratio of thermal diffusivity to mass diffusivity. Calculate the Lewis number for air at a film temperature of 312K

$$for\ water\ vapor\ in\ air\ @T = 312K, P = 101300Pa\ \left(Ni, 1997\right)$$

$$D = 2.3\times10^{-5}\frac{101300}{P}\left(\frac{T}{256}\right)^{1.81} = 3.29\times10^{-5}\,m^2/s$$

$$for\ pure\ air\ @312K\ \left(SFPE\ HB, 2002\right)$$

$$\alpha = 2.4\times10^{-5}\,m^2/s$$

$$\rho_a = 1.13\ kg/m^3$$

$$C_{p,a} = 1.0065\ kJ/kgK$$

$$so$$

$$Le = \frac{\alpha}{D} = \frac{2.4\times10^{-5}}{3.29\times10^{-5}} = 0.729$$

Calculating the heat transfer coefficient from the relation from Bird et al. [109] using the mass transfer coefficient calculated previously gives $57.7\ W/m^2K$.

Using the input parameters and constitutive relations described above, the convective drying experiments of Lu et al. [53] were modeled. The initial conditions are

$$T_o = 289.8K$$

$$P_o = P_\infty$$

$$\frac{\partial P_w}{\partial z} = \rho_w g$$

The drying rate is shown in Figure 136.

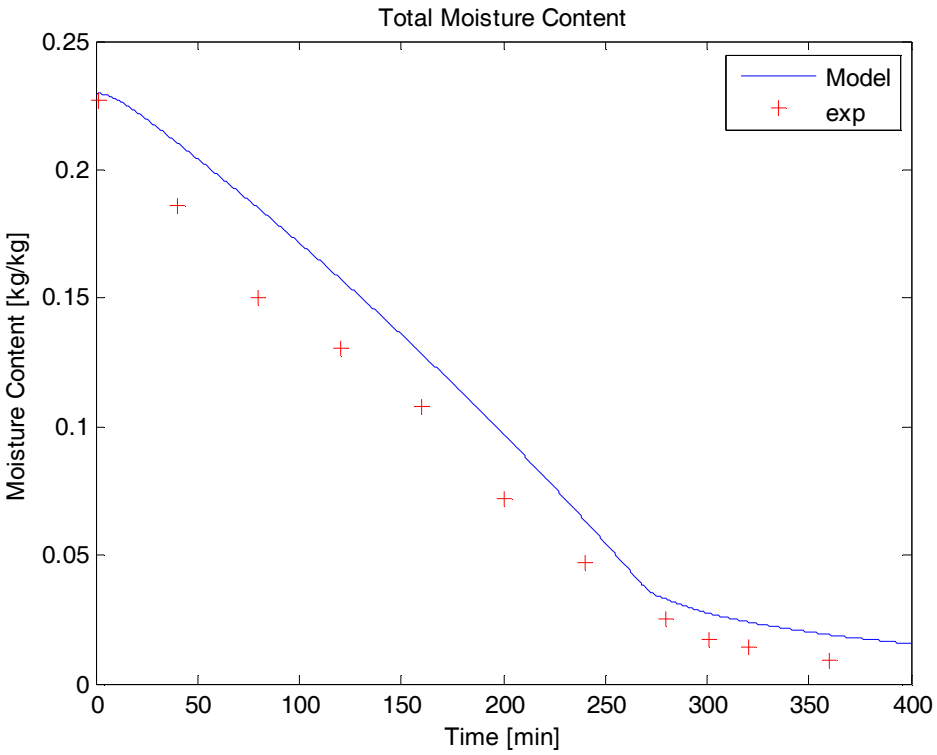

Figure 136 – Total Moisture Content of Bed of Quartz Particles

The temperature at thermocouples placed at 2mm and 5mm beneath the surface are shown in
Figure 137 and Figure 138. The model is able to predict the general behavior fairly well. From 50 until 270 min, the entire material is approximately at the wet bulb temperature of 305K. The model slightly over-predicts the temperature early in the experiment. This could be caused by the assumption of adiabatic conditions at the back face, which is not exactly correct. It was observed that the temperature increased rapidly throughout the material late in the experiment after most of the water was removed. The temperatures predicted by the model display this behavior as well.

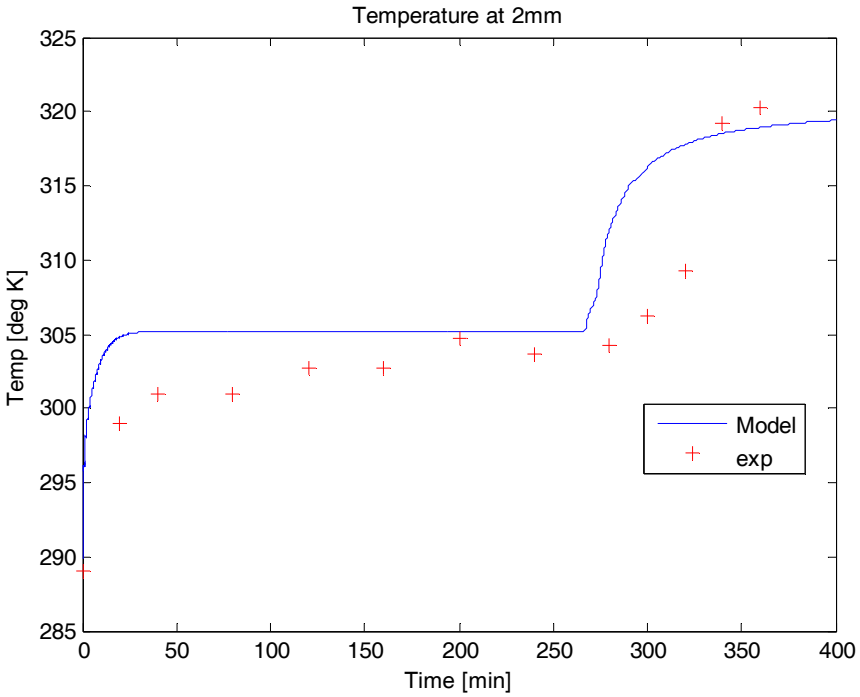

Figure 137 – Temperature History at 2mm Beneath Surface

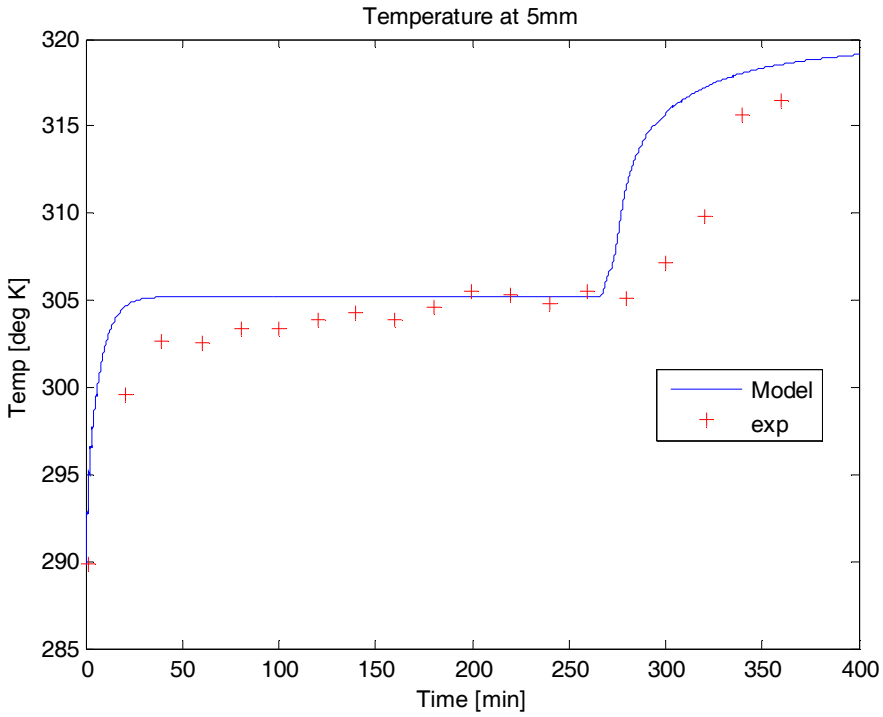

Figure 138 – Temperature History at 5mm Beneath Surface

F.3. Brick Drying Validation

The model was validated against experimental data from the drying of brick slabs by Przesmycki and Strumillo [54]. Data for the experimental conditions of brick drying tests run by Przesmycki and Strumillo is given by Chen and Pei [39]

$$\text{Properties of Brick}$$
$$\phi = 0.435 \ \left(porosity\right)$$
$$\rho_{eff} = 1450 \frac{kg}{m^3}$$
$$C_p = 0.75 \frac{kJ}{kgK}$$
$$k_{eff} = 0.50 \frac{W}{mK}$$

The back face of the brick is sealed and insulated, so no-flux boundary conditions are applied to the back face. The initial density of the brick is given, but this value includes the air and water in the pore spaces. To calculate the density of the solid material, use the values of total effective density and porosity

$$\rho_s = \frac{\rho_{eff}}{1-\phi} = \frac{1450}{1-0.435} = 2566 \frac{kg}{m^3}$$

The thermal conductivity of the solid phase is calculated in the same manner.

$$k_s = \frac{k_{eff}}{1-\phi} = \frac{0.5}{1-0.435} = 0.885 \frac{W}{mK}$$

Using the initial moisture content of 0.168 kg/kg, the initial saturation is calculated to be

$$S_o = \frac{M_o \left(1-\phi\right) \rho_s}{\phi \rho_w} = \frac{0.168\left(1-0.435\right)2566}{0.435\left(1000\right)} = 0.56$$

Drying conditions

$$u = 5\frac{m}{s}$$

$$T_\infty = 80^o C$$

$$\text{Re}\,lative\ humidity = 9.3\%$$

Chen and Pei [39] use the following empirical correlations for heat and mass transfer coefficients which are fit to data for brick drying

$$h = 75\left(0.8 + 0.2\frac{M_{surf} - 0.015}{0.09 - 0.015}\right)\left[\frac{W}{m^2 K}\right]$$

$$h_m = 0.083\left(0.1 + 0.9\frac{M_{surf} - 0.015}{0.09 - 0.015}\right)\left[\frac{m}{s}\right]$$

The sorption isotherm (relationship between moisture content and vapor pressure) for brick is correlated by Chen and Pei [39] from the data given by Haertling [48] as

$$M = 0.0105\left(RH\right)^{0.2} + 0.0125\exp\left(20 \cdot RH - 20\right)$$

Where M is the moisture content on a mass basis relative to the dry weight, and RH is the relative humidity. This is shown in Figure 139.

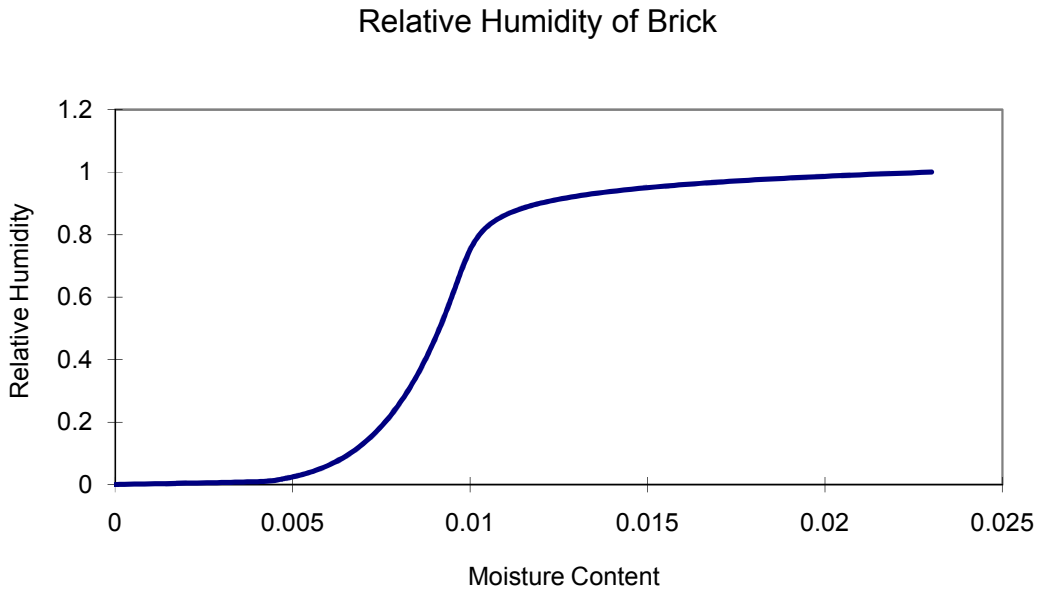

Figure 139 – Relative Humidity of Brick

It can also be written as

$$S = \frac{(1-\phi)\rho_s}{\phi\rho_w}\left(0.0105\left(\frac{p_v}{p_{vs}}\right)^{0.2} + 0.0125\exp\left(20\frac{p_v}{p_{vs}} - 20\right)\right)$$

Where S, p_v, and p_{vs} are: saturation, vapor pressure, and saturated vapor pressure. Saturated vapor pressure is the value observed above a flat liquid surface at equilibrium at a given temperature. Since the maximum sorption moisture content (maximum amount of water absorbed into the solid matrix from moisture in the atmosphere) is low, brick can be considered a non-hygroscopic material [39]. Above a moisture content of 0.023 the vapor pressure in the material can be calculated by the Claussius Clapeyron relation.

The model requires as inputs the following terms

$$\frac{\partial p_v}{\partial T}, \frac{\partial}{\partial T}\left(\frac{p_v}{T}\right), and \ \frac{\partial p_v}{\partial S_w}$$

The exponential term prevents inverting the function to solve for relative humidity in terms of saturation, so these quantities must be calculated numerically.
Since

$$p_v = p_{v,sat} RH$$

The derivatives can be calculated as

$$\frac{\partial p_v}{\partial T} = RH \frac{\partial p_{v,sat}}{\partial T}$$

$$\frac{\partial}{\partial T}\left(\frac{p_v}{T}\right) = \frac{T \cdot RH \frac{\partial p_{v,sat}}{\partial T} - p_{v,sat} RH}{T^2}$$

$$\frac{\partial p_v}{\partial S_w} = p_{v,sat} \frac{\partial RH}{\partial S_w}$$

In order to calculate the relative humidity from water saturation values, the following method was used. The relative humidity at 100 saturation values was calculated. To calculate the relative humidity for any saturation value in between those 100 discrete values, a linear interpolation scheme in MATLAB was used.

The capillary pressure and relative permeability for brick are calculated using the following correlations for sandstone from Kaviany [23]

$$p_c = P - p_w = \frac{\sigma}{\sqrt{K/\phi}}\left[0.3 - 0.0663 \ln\left(S_w - S_{ir}\right)\right]$$

$$K_{rl} = S_{eff}^4$$

$$K_{rg} = \frac{\left(1 - S_{eff}\right)^2}{\left(1 - S_{eff}^2\right)}$$

The model also requires as an input the derivative of capillary pressure with respect to water saturation

$$\frac{\partial p_c}{\partial S} = -\frac{\sigma}{\sqrt{K/\phi}} 0.0663 \frac{1}{\left(S_w - S_{ir}\right)}$$

The only parameter that is not known for brick is the permeability. Nasrallah and Perre [38] use a value in their model for brick of

$$K = 2.5 \times 10^{-14} m^2$$

but they give no source for this value. Sheidegger [25] gives values for permeability of brick in the range of

$$4.8 \times 10^{-15} < K < 2.2 \times 10^{-13} m^2$$

A value of $K = 5 \times 10^{-14} m^2$ gives good agreement with the drying rate data from Przesmycki and Strumillo as shown in Figure 140.

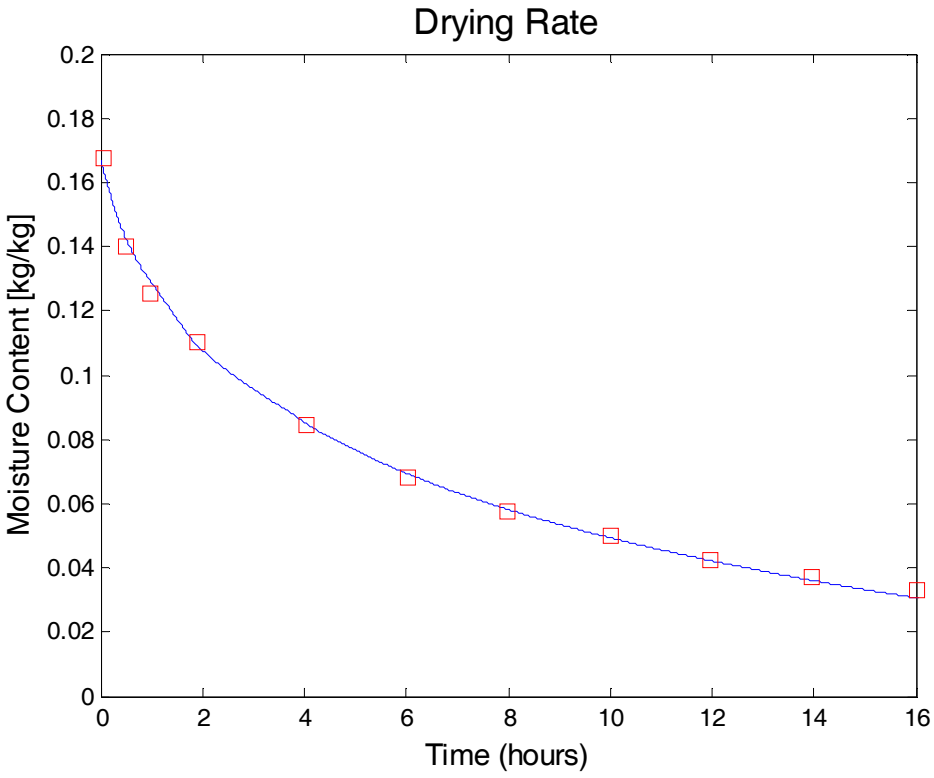

Figure 140 – Drying Data for Brick

The agreement between temperature predictions and experimental data is shown in Figure 141 for 0.5, 1, 3.5, and 9.5 hours. Temperatures near the back face are under-

predicted, and the surface temperatures are slightly over-predicted as compared with the experimental results.

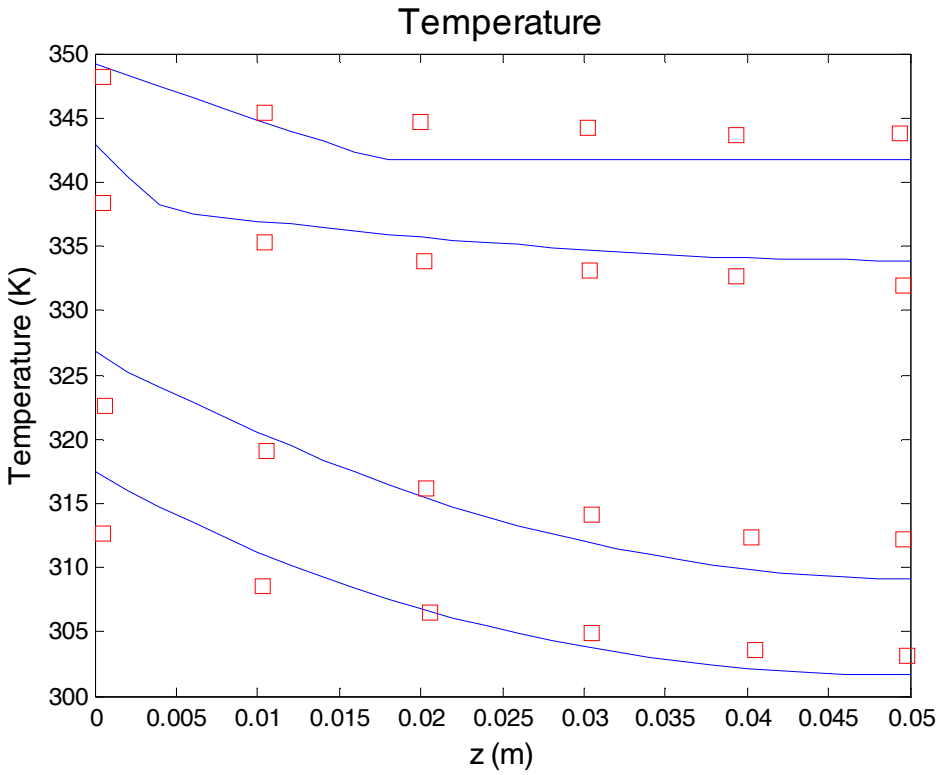

Figure 141 – Temperature of Brick During Drying

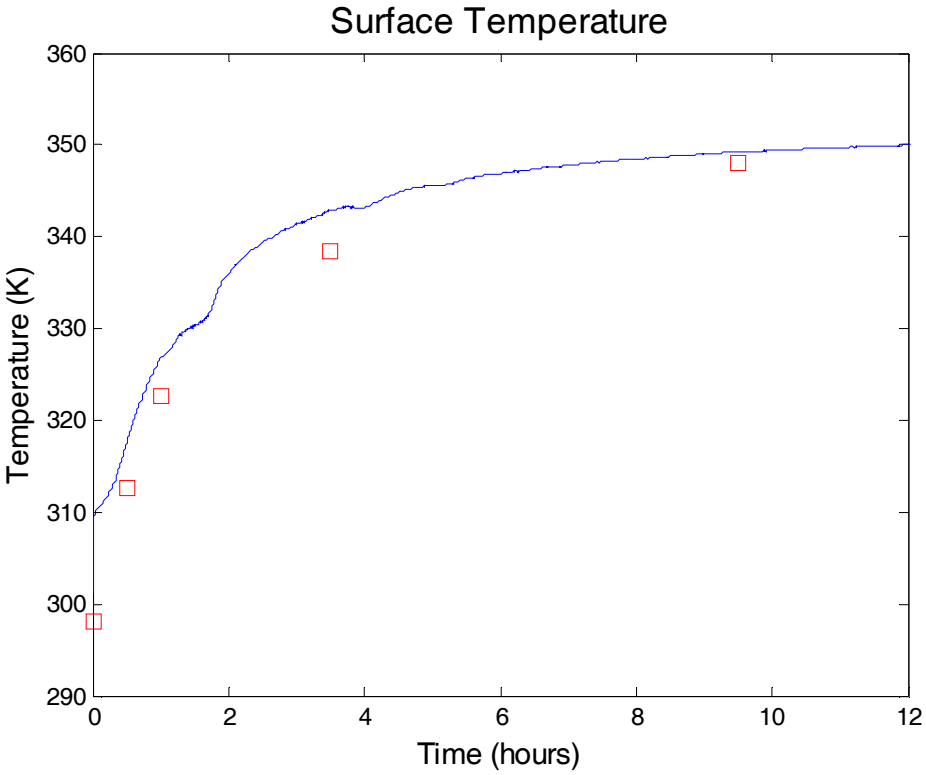

Figure 142 – Surface Temperature of Brick During Drying

F.4. Wood

The model was validated against experimental data for the convective drying of wood from Plumb et al. [55, 56] and Spolek and Plumb [45]. In their experiments, temperature and moisture content were measured at various locations in the material during the drying process.

Capillary pressure in wood can be modeled as [45]

$$p_c = BS_w^{\ n}$$

Based on experimental testing, Spolek and Plumb determine the average values for the coefficients B and n for softwoods are [45]

$$B = 1.24\times10^5 \frac{dynes}{cm^2} = 1.24\times10^4 \frac{N}{m^2}$$
$$n = -0.61$$

So

$$p_c = 1.24\times10^4 S^{-0.61}$$
$$and$$
$$\frac{\partial p_c}{\partial S_w} = -0.756\times10^4 S^{-1.61}$$

The range of permeabilities for the wood tested was determined by Plumb and Spolek [56] by matching their model to the experimental data. The two samples examined fell in the following range:

$$K = 1-5\times10^{-16} m^2$$

The experimentally measured permeabilities of different woods are given by Comstock [59]. He gives experimentally measured values of permeability in the tangential and radial direction

$K = 4.9 - 29 \times 10^{-17} m^2$ tangential

$K = 2.56 - 11 \times 10^{-15} m^2$ radial

For thermal properties, use data for yellow pine from [57].

$$\rho_s = 640 \frac{kg}{m^3}$$

$$C_{p,s} = 2800 \frac{J}{kg}$$

$$k_s = 0.147 \frac{W}{mK}$$

This value of density is an average value for the wood, including void spaces and any moisture contained. The model requires a value representative of the wood fibers alone. Siau [60] gives a value of 1500 kg/m^3 for the cell walls in wood. When the average value of wood density is calculated using this value for the solid matrix, and a reasonable amount of moisture present (30% by mass) the volume averaged density is close to the value in the SFPE Handbook. For the model, a value of 1500 kg/m^3 will be used.

The porosity of the wood must also be calculated. Use the saturated moisture content of 134% to calculate the porosity. Water in is present in wood as a liquid and as bound water.

$$M = \frac{mass\ liquid + bound\ water}{mass\ dry\ solid} = \frac{\phi S_w \rho_w + bound\ water}{(1-\phi)\rho_s}$$

Wood is a hygroscopic material, which means that it contains significant amounts of bound water in the solid matrix. The bound water in wood is approximately 0.3 kg/kg at the fiber saturation point [60]. This water is chemically bound to the hydroxyl groups of the cellulose [61]. Since the current model is not intended for hygroscopic materials, it cannot simulate moisture contents below 0.3 kg/kg. The experimental data up until the wood was dried to this point will be used for validation.

The porosity can be calculated to be

$$\phi = \frac{(1.34-0.3)\rho_s}{\left((1.34-0.3)\rho_s + S\rho_w\right)} = \frac{(1.34-0.3)1500}{\left((1.34-0.3)1500+1000\right)} = 0.61$$

The thermal conductivity for the solid phase is also calculated from the porosity

$$k_s = \frac{k_{eff}}{1-\phi} = \frac{0.147}{1-0.61} = 0.377\ W/mK$$

The vapor pressure in wood is given by Nasrallah and Perre [38]

$$p_v = p_{vs} \exp\left(\left(17.884 - 0.1423T + 0.0002363T^2\right)\left(1.0327 - 0.000674T\right)^{92M}\right)$$

This relationship is known as a sorption isotherm and is shown for three temperatures in Figure 143. Below a moisture content of 0.3 the vapor pressure drops off sharply. As the surface moisture content approaches this range, vapor pressure will drop, and gas phase diffusion will draw vapor to the surface. For this reason it is important to know the sorption isotherm for a material being dried.

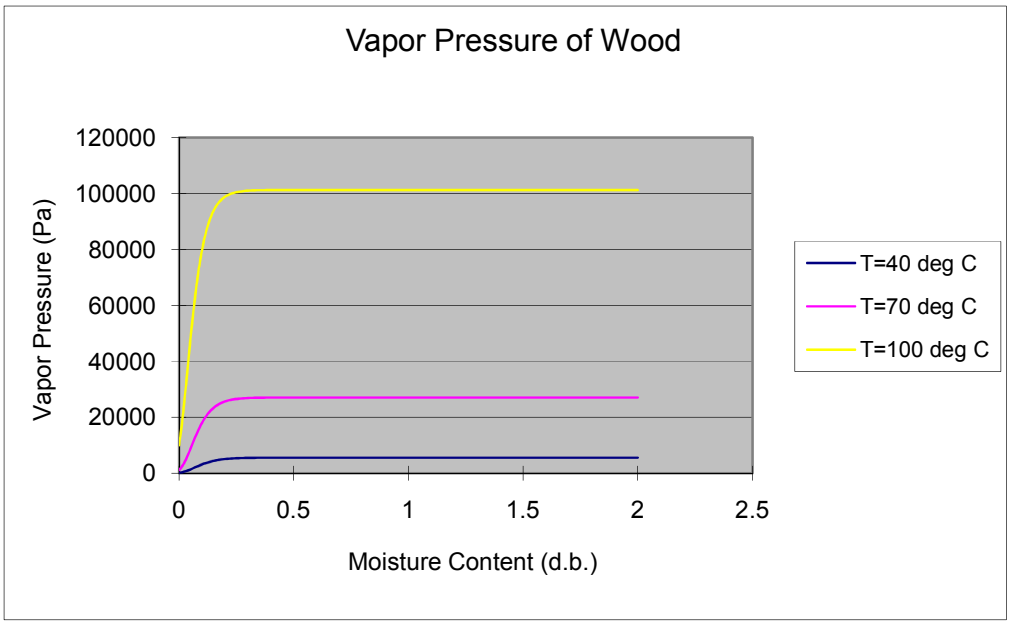

Figure 143 – Vapor Pressure in Wood

Define vapor pressure partial derivatives for model inputs. Need to calculate

$$\frac{\partial p_v}{\partial T},\ \frac{\partial}{\partial T}\left(\frac{p_v}{T}\right), and\ \frac{\partial p_v}{\partial S_w}$$

The relationship for vapor pressure contains moisture content as an input. This can be re-written using the definition of moisture content so that the relationship is in terms of saturation. The vapor pressure is therefore

$$p_v = p_{vs}\exp\left(\left(17.884-0.1423T+0.0002363T^2\right)\left(1.0327-0.000674T\right)^{92\left(\frac{\phi S\rho_w}{(1-\phi)\rho_s}+0.3\right)}\right)$$

$$\frac{\partial p_v}{\partial T} = p_{vs} \exp\left(\left(17.884 - 0.1423T + 0.0002363T^2\right)\left(1.0327 - 0.000674T\right)^{92\left(\frac{\phi S \rho_w}{(1-\phi)\rho_s}+0.3\right)} \right) \cdot$$

$$\left(\begin{array}{l} \left(17.884 - 0.1423T + 0.0002363T^2\right) 92 \left(\dfrac{\phi S \rho_w}{(1-\phi)\rho_s} + 0.3 \right) (-0.000674)\left(1.0327 - 0.000674T\right)^{92\left(\frac{\phi S \rho_w}{(1-\phi)\rho_s}+0.3\right)-1} \\ + \left(-0.1423 + (2)0.0002363T\right)\left(1.0327 - 0.000674T\right)^{92\left(\frac{\phi S \rho_w}{(1-\phi)\rho_s}+0.3\right)} \end{array} \right)$$

$$+ \frac{\partial p_{vs}}{\partial T} \exp\left(\left(17.884 - 0.1423T + 0.0002363T^2\right)\left(1.0327 - 0.000674T\right)^{92\left(\frac{\phi S \rho_w}{(1-\phi)\rho_s}+0.3\right)} \right)$$

$$\frac{\partial p_v}{\partial S_w} = p_{vs} \frac{\partial}{\partial S_w} \exp\left(\left(17.884 - 0.1423T + 0.0002363T^2\right)\left(1.0327 - 0.000674T\right)^{92\left(\frac{\phi S \rho_w}{(1-\phi)\rho_s}+0.3\right)} \right)$$

$$= p_{vs} \exp\left(\left(17.884 - 0.1423T + 0.0002363T^2\right)\left(1.0327 - 0.000674T\right)^{92\left(\frac{\phi S \rho_w}{(1-\phi)\rho_s}+0.3\right)} \right)$$

$$\left(\begin{array}{l} \left(17.884 - 0.1423T + 0.0002363T^2\right) \dfrac{92\phi\rho_w}{(1-\phi)\rho_s} \left(1.0327 - 0.000674T\right)(92 \cdot 0.3) \\ \cdot \left(1.0327 - 0.000674T\right)^{92\left(\frac{\phi \rho_w}{(1-\phi)\rho_s} S+0.3\right)} \ln\left(1.0327 - 0.000674T\right) \end{array} \right)$$

$$\frac{\partial}{\partial T}\left(\frac{p_v}{T}\right) = \frac{T\dfrac{\partial p_v}{\partial T} - p_v}{T^2}$$

For relative permeabilities, use a linear relationship. Plumb et al. suggest that relative permeabilities for gas and liquid in wood are weakly nonlinear functions of water saturation. They use linear relationships in their model with reasonable results. For gas phase flow, the relative permeability is often assumed to be very low. Spolek assumes it is zero in his wood drying model [61], while Nasrallah and Perre [38] and Plumb et al. [56] assume a linear relationship that is 0.05 when the material is dry, and zero when it is saturated. All of these researchers cite a study by Meyer [110], who observes that as a wood is being dried, 95% of the small pores which connect the lumens (larger pores) become aspirated (blocked), which makes gas flow difficult.

$$K_{rl} = S_{eff}$$
$$K_{rg} = 0.05\left(1 - S_{eff}\right)$$

These are shown in Figure 144

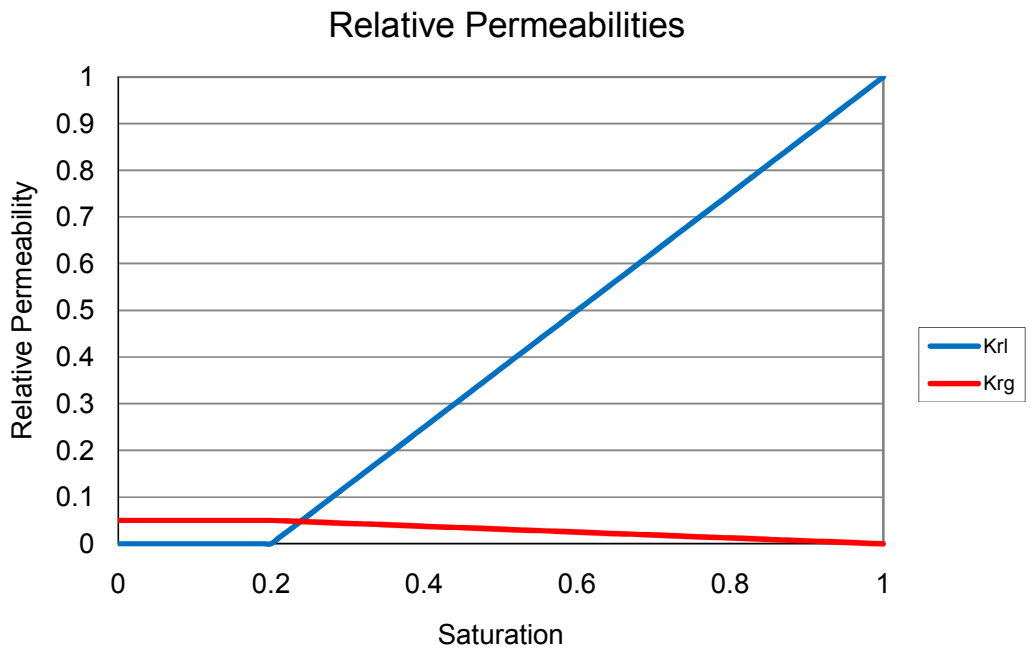

Figure 144 – Relative Permeabilities of Wood

To account for the tortuous path through which gas phase molecular diffusion must take place, the effective gas diffusivity can be modeled as [60]

$$D_{eff} = D_{va}\frac{K_{rg}}{45}$$

The experimental set up used by Spolek and Plumb is shown in Figure 145.

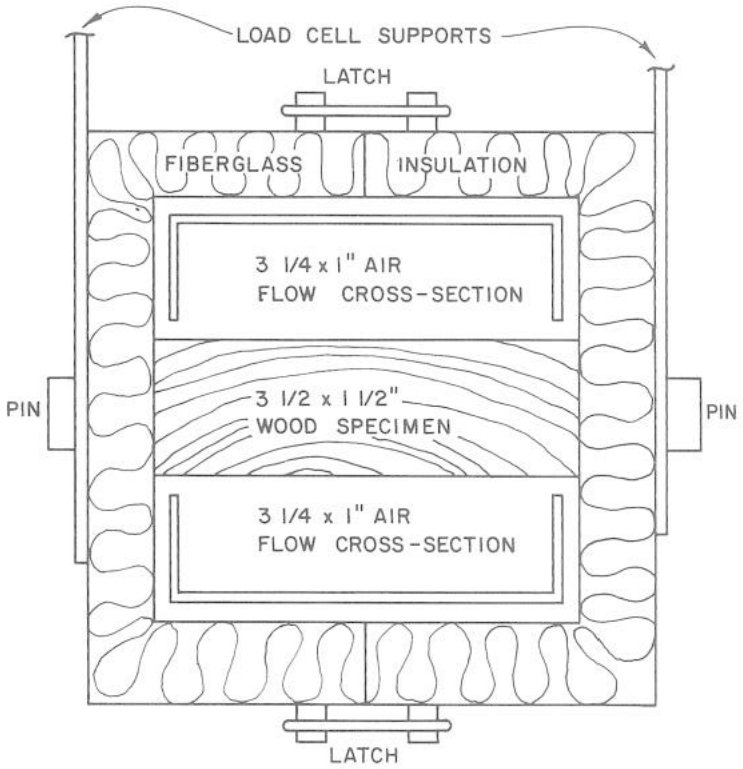

Figure 145 – Experimental Apparatus for Wood Drying (from [56])

Both the top and bottom faces of the wood are heated with a flow of hot dry air at 40 deg C. The specific velocity and relative humidity of the drying air is not given. Plumb et al. [55] conducted multiple wood drying experiments with air velocities between 8.52 and 26.24 m/s and relative humidity's between 0.9 and 10%. Test 113 and other low temperature drying tests were conducted at "relatively high air velocities". For this modeling exercise, assume an air velocity of 26 m/s and a relative humidity of 5%.

The surface heat transfer coefficient can be calculated using the following correlation for turbulent flow in a duct [55]

$$Nu = \frac{hD_h}{k} = 0.023\,\mathrm{Re}^{0.8}\,\mathrm{Pr}^{0.33}$$

where

$$\mathrm{Re} = \frac{\bar{u}D_h}{\nu}$$

$$ambient\ air @ 40^o C$$

$$wood\ initially\ @ 10^o C$$

$$film\ temp = \frac{40+10}{2} = 25^o C$$

$$k = 0.02608\frac{W}{mK}\left(from\ SFPE\ HB\right)$$

$$\nu = 16.68\times10^{-6}\frac{m^2}{s}\ \left(from\ SFPE\ HB\right)$$

$$for\ specimen\ 123$$

$$\bar{u} = 26\frac{m}{s}$$

$$D_h = \frac{4A}{P} = \frac{4\left(0.002097\right)}{0.2159} = 0.0389m$$

$$\mathrm{Re} = \frac{26\left(0.0389\right)}{16.68\times10^{-6}} = 60,635$$

$$Nu = 0.023\left(60,635\right)^{0.8}\left(0.7\right)^{0.33} = 138$$

$$h = \frac{Nu\,k}{D_h} = \frac{138\left(0.02608\right)}{\left(0.0389\right)} = 92.5\frac{W}{m^2K}$$

The mass transfer coefficient can be calculated by analogy to heat transfer [56]

$$Sh = \frac{h_m D_h}{D_{va}} = 0.023\,\mathrm{Re}^{0.8}\,Sc^{0.33}$$

$$D_{va} = 2.3\times10^{-5}\frac{P_o}{P}\left(\frac{T}{T_o}\right)^{1.81} = 2.3\times10^{-5}\left(\frac{298}{256}\right)^{1.81} = 3.03\times10^{-5}\frac{m^2}{s}$$

$$Sc = \frac{\nu}{D_{va}} = \frac{16.68\times10^{-6}\frac{m^2}{s}}{3.03\times10^{-5}} = 0.55$$

$$Sh = 0.023\left(60,635\right)^{0.8}\left(0.55\right)^{0.33} = 127$$

$$h_m = \frac{ShD_{va}}{D_h} = \frac{127\left(3.03\times10^{-5}\right)}{0.0389} = 0.099\frac{m}{s}$$

Plumb et al. [56], ran tests to determine the effect of surface saturation on mass transfer

rate. As the surface becomes dry, the evaporation rate will drop below that of a flat liquid surface. Drying experiments were conducted by Plumb et al. [56] on southern pine to determine the effect of surface saturation on drying rate. They found the mass transfer rate at the surface can be approximated for dry air as

$$\dot{m}''_{evap} = \beta^3 h_m \left(\rho_{v,surf} - \rho_{v,\infty} \right)$$

where

$$\beta = \frac{M - EMC}{M_{\max} - EMC}$$

Where M is the moisture content in kg/kg, and EMC is the moisture content of the wood at equilibrium with the ambient relative humidity. This is calculated from the sorption isotherm. This correlation was used in the model to determine the drying rate. It was determined by comparing model results that gravity has a negligible effect on the model predictions for wood. As such it is appropriate to model half of the wood slab, and use no flux boundary conditions at the center. This would not be appropriate if gravity were significant, since the upper and lower halves of the slab would not behave identically. Gravity would draw water into the lower half across the plane of symmetry. Using the input parameters calculated for wood, model predictions for moisture content as a function of depth, total drying rate, and surface temperature were calculated for a drying test labeled Sample 113 by the authors. Sample 113 was determined by Spolek and Plumb to have a permeability of $5 \times 10^{-16} m^2$. The best agreement with the current model was realized with a permeability of $2 \times 10^{-16} m^2$ The air flow past the wood slab was 40 deg C. The simulations for moisture content for 0 min, 180 min, and 780 min for sample 113 are shown in Figure 146. Drying rate and surface temperature for sample 113 are shown in Figure 147 and Figure 148.

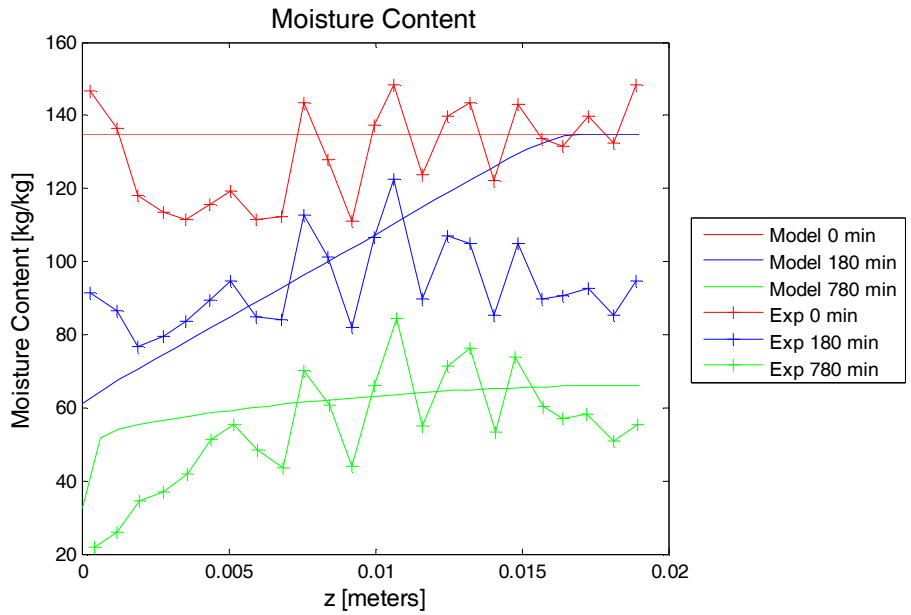

Figure 146 – Moisture Content for Wood Sample 113

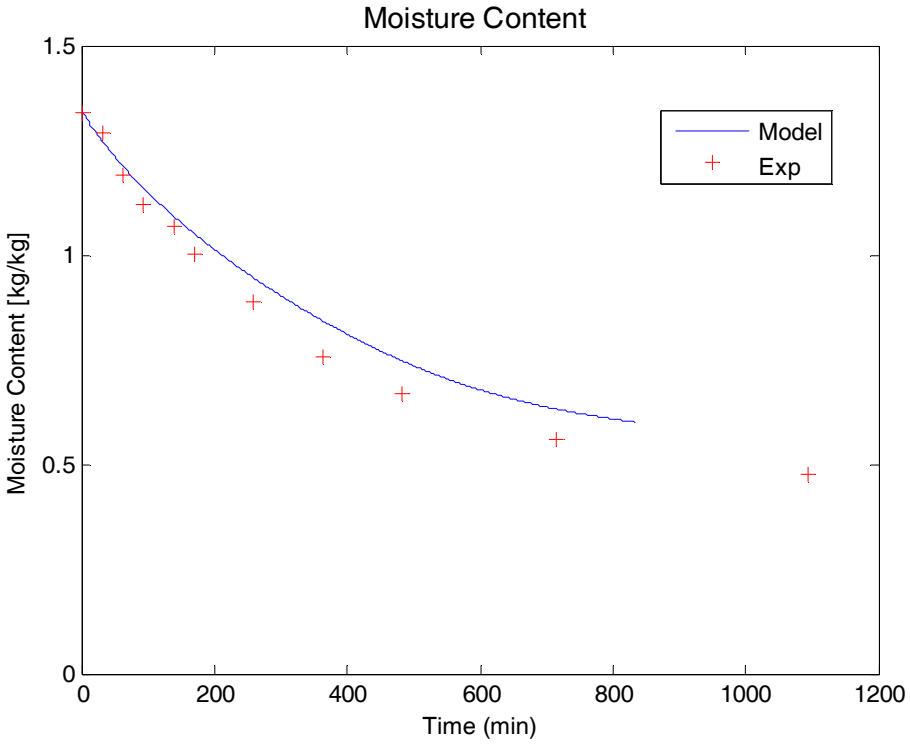

Figure 147 – Total Moisture Content for Wood Sample 113

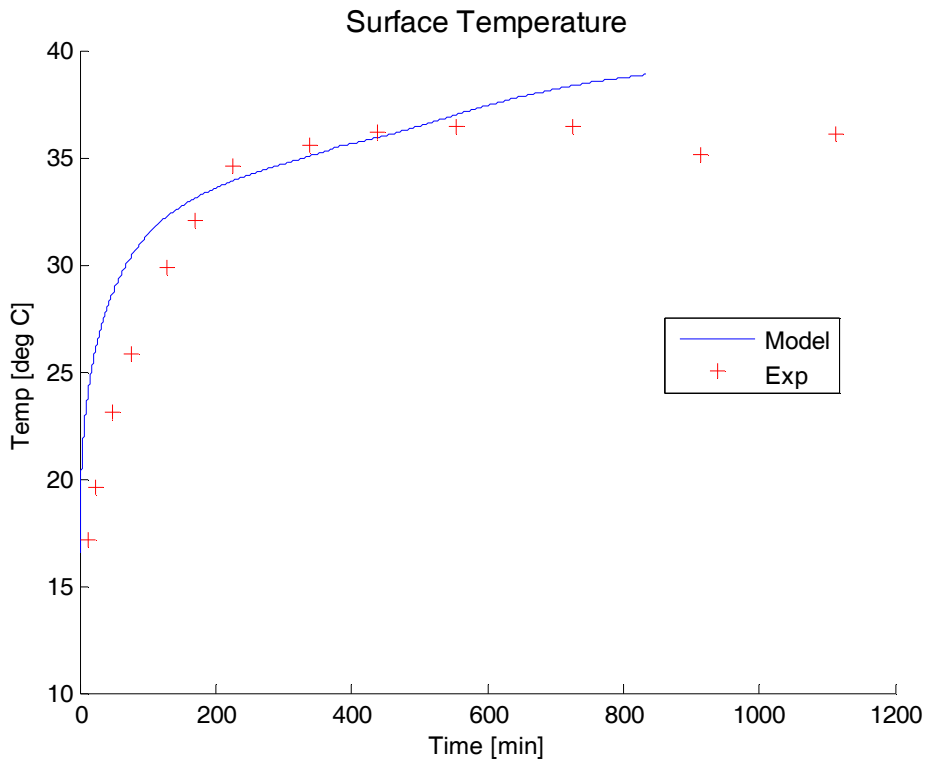

Figure 148 – Surface Temperature for Wood Sample 113

The irregular nature of the spatial moisture content distribution in the experimental data is due to differences in density and porosity between the annular growth rings of the wood. The calculated moisture content profiles show reasonable agreement with the experimental data. The model is able to give a reasonable approximation of the mass loss, and does a good job predicting surface temperature. The model appears to be under-predicting the internal rate of moisture transfer, as shown in Figure 146. Two likely causes of this are the lack of bound water transfer in the model AND the gas relative permeability correlation. In wood approximately 30% of the moisture is chemically bound to the wood fibers. This moisture will diffuse to the surface by means not included in the model. The relative permeability correlation is much lower for wood than other materials used for model validation. There is very little validation data to support this correlation. If the gas relative permeability is changed to

$$K_{rg} = 1 - S_{eff}$$

then the internal moisture profiles are as shown in Figure 149. It is unclear if this correlation is more appropriate, or if the discrepancy is caused by bound moisture or other factors.

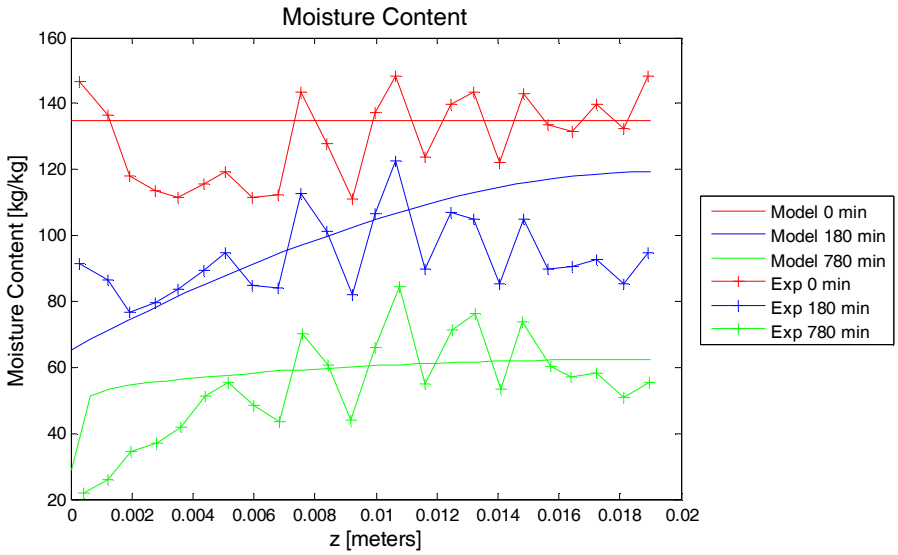

Figure 149 - Moisture Content for Wood Sample 113 – New K_{rg}

F.5. CFB Radiant Heating Tests

Test Description

Tests were carried out in the cone calorimeter in the WPI Fire Science Laboratory for model validation purposes. Six test samples were used for the tests. The test samples were 4” by 4” and 1” thick. The edges were sealed with two coats of primer to prevent moisture loss. The samples were wrapped in 1” thick Kaowool blanket to minimize heat losses. The evaporation rate was measured with the cone load cell, and temperatures were measured using surface thermocouples and a 40 gauge thermocouple probe that was inserted into the sample from the edge at a depth of ½” ± 1/32”. The sample is diagramed in Figure 150.

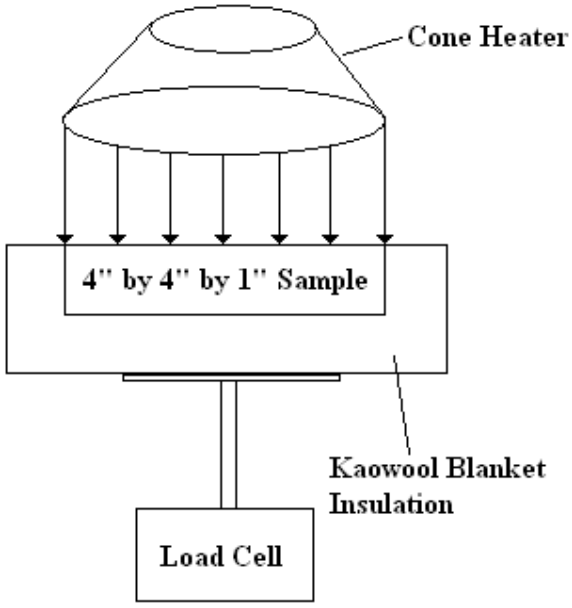

Figure 150 – Cone Sample Diagram – Side View

Thermocouples were inserted into the surface of the material for each test. The bead of the thermocouple was bent at a 90 deg angle and pressed gently into the surface of the material. The thermocouple bead is diagrammed in Figure 151. The bent portion of the thermocouple wire was 1.6 mm. It should be noted that the thermocouple bead was not inserted this full depth. The bead was inserted only far enough to remain in place at the surface.. For one test the surface thermocouple became detached from the surface. Some of the variation in experimental data is due to slight variations in the

thermocouple bead depth.

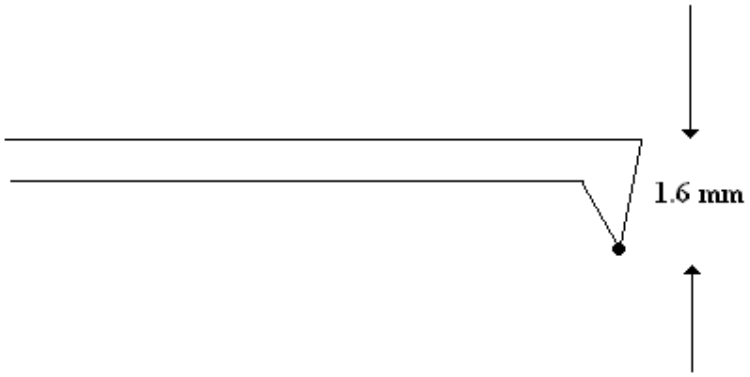

Figure 151 – Thermocouple Bead Design

Three rounds of tests were conducted on the 6 samples of CFB at 20 kW/m2. The saturation of the samples was adjusted for the three rounds of tests to 0.3, 0.5, and 0.7. The results of the tests and the model predictions are shown in
Figure 152 through Figure 160. A saturation of 0.3 was achieved by adding 63 grams of water to the samples. A saturation of 0.5 was achieved by adding 105 grams of water to the samples. A saturation of 0.7 was achieved by adding 147 grams of water. The water was poured onto the surface of the material using a glass beaker. The sample was placed on a load cell to measure how much water had been applied. The water was allowed to soak in for 15 minutes for the tests conducted at an initial saturation of 0.7 and 0.5. For the initial saturation of 0.3, there was concern that the water was not completely soaking through to the back face of the material, so the samples were left to soak overnight wrapped in plastic to prevent them from drying out.

Model Inputs

Material parameters

The ceramic fiberboard was Kaowool M Board manufactured by Thermal Ceramics. The manufacturer gives the following material thermal properties:

$$\rho = 272 \frac{kg}{m^3}$$

$$C_p = 0.25 \frac{Btu}{lb\,^oF} = 1046 \frac{J}{kgK}$$

Chemical composition: 42% alumina $\left(Al_2O_3\right)$, 56% silica $\left(SiO_2\right)$, 2% other

The thermal conductivity is a function of temperature of the material. Thermal Ceramics provides the values for thermal conductivity shown in Table .

Table 24 - Thermal Conductivity of M-Board

Temperature [deg C]	Thermal Conductivity [W/mK]
37.8	0.047289
93.3	0.052103
148.9	0.057075
204.4	0.062293
260	0.067828
315.6	0.073722
371.1	0.080064
426.7	0.086867
482.2	0.094175
537.8	0.10203
593.3	0.110432
648.9	0.119441
704.4	0.129083
760	0.139388
815.6	0.150414
871.1	0.162233
926.7	0.174902

The values given for thermal conductivity and density are the effective properties which include contributions from the solid, air and any vapor that is present. The effective values can be used to calculate the properties of the solid material.

$$k_{eff} = \phi S_w k_w + \phi S_v k_v + \phi S_a k_a + \left(1-\phi\right) k_s$$

$$\rho_{eff} = \phi S_w \rho_w + \phi S_v \rho_v + \phi S_a \rho_a + (1-\phi)\rho_s$$

Calculate the thermal conductivity of the solid at low temperatures since at higher temperatures the increased value of thermal conductivity is partially due to internal radiation. Ignore the contributions from water and vapor, since these properties are measured when the material is dry.

$$@T = 38^o C$$
$$k_s = \frac{k_{eff} - \phi S_a k_a}{1-\phi} = \frac{0.04732 - 0.8(1)0.0298}{1-0.8} = 0.117 \frac{W}{mK}$$

$$\rho_s = \frac{\rho_{eff} - \phi S_a \rho_a}{(1-\phi)} = \frac{272 - 0.8(1.17)}{1-0.8} = 1355 \frac{kg}{m^3}$$

The specific heat is calculated on a mass basis so the contribution from the air is very small due to the relatively small mass of the air in the pore space. For this reason, use the effective specific heat value given by Thermal Ceramics.

Use the following values for the solid

$$\rho_s = 1355 \frac{kg}{m^3}$$
$$C_{p,s} = 1046 \frac{J}{kgK}$$
$$k_s = 0.117$$

The surface emissivity was assumed to be that of asbestos mineral fiber board. The emissivity of asbestos is given as 0.96 by Luikov [62]. The molecular diffusivity of water vapor in air was previously assumed to be a constant value of $2.6 \times 10^{-5} m^2 / s$. This simplification is not always appropriate, particularly when large differences in temperature are observed. For the case of radiant heating of CFB, very high surface temperatures are expected, so the model was modified to include a variable diffusion coefficient. Temperature and pressure dependence of the diffusion coefficient was added by using the correlation

$$D = D_o \left(\frac{T}{T_o} \right)^{1.75} \frac{P_o}{P}$$

Where D_o is the diffusivity at the temperature T_o and pressure P_o.

Heat and Mass Transfer Coefficients

The heat and mass transfer coefficients were calculated by combining the driving forces for heat and mass transfer that are calculated separately. This approach is discussed by Gebhardt et al. [63]. For a heated isothermal plate the heat transfer coefficient can be calculated from the average Nusselt number using a correlation for free convection conditions [57]

$$\overline{Nu} = 0.54 Ra_h^{1/4} \qquad for\ 10^5 < Ra_h < 10^7$$
$$\overline{Nu} = 0.15 Ra_h^{1/3} \qquad for\ 10^7 < Ra_h < 10^{10}$$

The heat transfer Rayleigh number is defined using the heat transfer Grashof number and Prandtl number

$$Ra_h = Gr_h \Pr = \frac{g\beta(T_s - T_\infty)L^3}{\nu^2} \frac{\nu}{\alpha} = \frac{g\beta(T_s - T_\infty)L_c^{\ 3}}{\nu\alpha}$$

From the Nusselt number, calculate the heat transfer coefficient

$$\overline{Nu} = \frac{\bar{h}L}{k}$$
$$\bar{h} = \frac{k\overline{Nu}}{L}$$

The mass transfer coefficient for a wet surface can be calculated by observing the analogy between heat and mass transfer and calculating an average Sherwood number. The Sherwood number can be calculated from a correlation with the mass transfer Rayleigh number

$$\overline{Sh} = 0.54 Ra_m^{1/4} \ \ for\ 10^5 < Ra_m < 10^7$$
$$\overline{Sh} = 0.15 Ra_m^{1/3} \ \ for\ 10^7 < Ra_m < 10^{10}$$

The mass transfer Rayleigh number is defined as [43]

$$Ra_m = \frac{g\beta_c\left(\rho_s - \rho_\infty\right)L^3}{\nu D}$$

Which can be written as the product of a mass transfer Grashof number and Schmidt number

$$Ra_m = Gr_m Sc = \frac{g\beta_c\left(\rho_s - \rho_\infty\right)L^3}{\nu^2}\frac{\nu}{D}$$

For both of these correlations, the characteristic length L_c is

$$L_c = \frac{surface\ area}{perimeter} = \frac{\left(0.1016m\right)^2}{4\left(0.1016m\right)} = 0.0254m$$

And the properties are evaluated at the film temperature

$$T_{film} = \frac{T_s + T_\infty}{2}$$

For water vapor in air the composition expansion coefficient is defined by Bejan [43] as

$$\beta_c = 0.61$$

These two sets of correlations have been developed for situations in which a single buoyancy effect dominates. In the case of heat transfer, buoyancy is caused by thermal diffusion effects. In the case of mass transfer, buoyancy is caused by species diffusion effects. The case of a wet heated slab being considered here contains both driving forces. The Rayleigh number should account for this. If the Schmidt number is equal to the Prandtl number $Sc = \Pr = \frac{\nu}{D} = \frac{\nu}{\alpha}$ then the problem reduces to a single buoyancy effect [63] and the total Grashof number is

$$Gr = Gr_h + Gr_m$$

In this case the Rayleigh number is calculated from total Grashof number

$$Ra = Gr \,\mathrm{Pr}$$
$$Ra = \left(Gr_h + Gr_m\right)\mathrm{Pr}$$

This method is implemented in the model. Temperature dependant properties of air are used for the fluid properties at the surface. In the model these are implemented using second order polynomials that are curve fit to the properties of air from the SFPE HB [57].

Boundary Conditions

Using these transfer coefficients, the boundary condition at the front face is

$$\dot{m}''_{\substack{evap \\ loss}} + \dot{m}''_w + \dot{m}''_v = 0$$
$$\dot{q}''_e = h\left(T_{surf} - T_\infty\right) + \varepsilon\sigma\left(T_{surf}^4 - T_\infty^4\right) + \dot{m}''_{evap}\Delta h_v - k_{eff}\frac{\partial T}{\partial z} \qquad @\ z = 0$$
$$P_{surf} = P_\infty$$

The back face of the material is assumed to be perfectly insulated, and sealed so that

$$\dot{m}''_w + \dot{m}''_v = 0$$
$$k_{eff}\frac{\partial T}{\partial z} = 0 \qquad @ z = L$$
$$\dot{m}''_a = 0$$

Initial Conditions

The initial conditions are

$S_o = 0.3,\ 0.5,\ or\ 0.7$
$T_o = 297\,K$
$P_o = 101300\,Pa$

Solution Details

The CFB heating was modeled using the material properties and boundary conditions outlined here and the solutions techniques discussed earlier. The one modification to the solution technique involved the numerical scheme. When the surface of the material approached zero saturation, the vapor pressure at the surface of the material began to drop rapidly. Once the surface vapor pressure dropped below the saturated value, the surface temperature "jumped" in temperature rapidly. At this point, a very small tim estep is needed to prevent the model from crashing. For the purpose of efficiency, a time step of 1 second was used up until the surface reached a saturation of 0.15, and then the time step was decreased to 0.001 seconds.

Results

Six cone tests were conducted with an initial saturation of 0.3 and a heat flux was 20 kW/m^2. The results from these tests are shown in Figure 152 through Figure 154. Six different samples were tested. They were each tested once and are labeled sample 11 through sample 16. T1 indicates that it was the first test of the day using this sample. For sample 12 (yellow line) the surface thermocouple malfunctioned and data was not collected. The variation in the data is possibly due to incomplete wetting of the sample at this low value of initial saturation. If the water was unable to be evenly distributed throughout the material, then more water would rest close to the surface, and explain in part the discrepancy between the model predictions and experimental results. The general behavior is predicted fairly well by the model. The model predicts the surface temperature jumping rather early however. The model also predicts a sudden drop in the rate of temperature rise at all subsurface locations when the surface dries out. This is due to vapor diffusion effects. A discussion of this will be given later. The model over-predicted the mass loss rate as compared to the experimental data for experiments with this initial saturation. The general trend is approximately accurate however. A relatively linear mass loss rate is observed as the surface is at the wet bulb temperature. After some amount of time, the surface dries out, the surface temperature jumps dramatically, and the mass decreases at a much lower rate. The humps in the predicted

surface temperature are related to the changes in the vapor pressure at the surface.

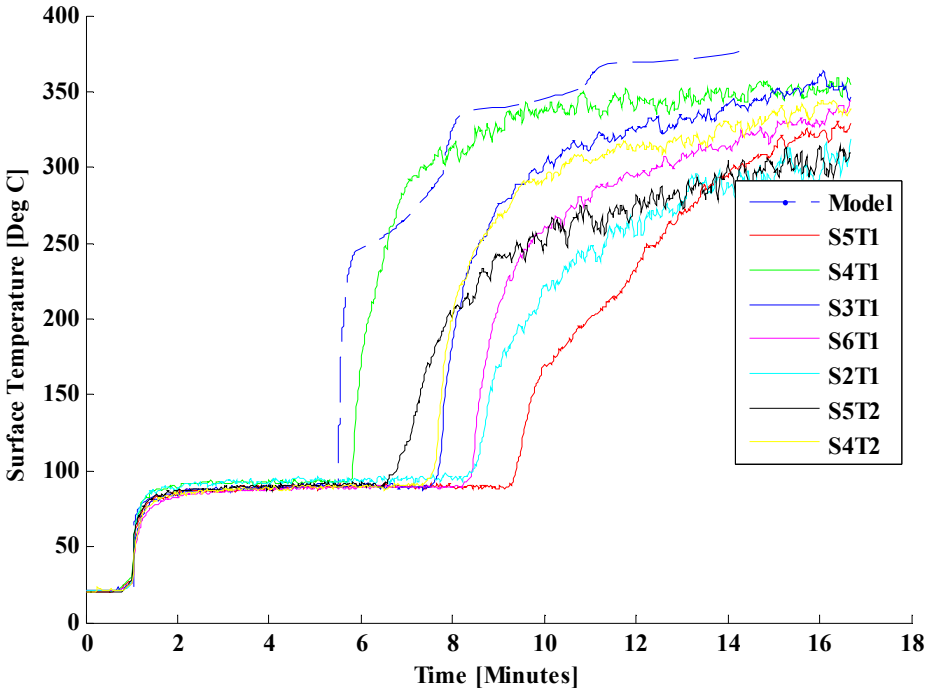

Figure 152 – CFB Surface Temperature for Initial Saturation of 0.3

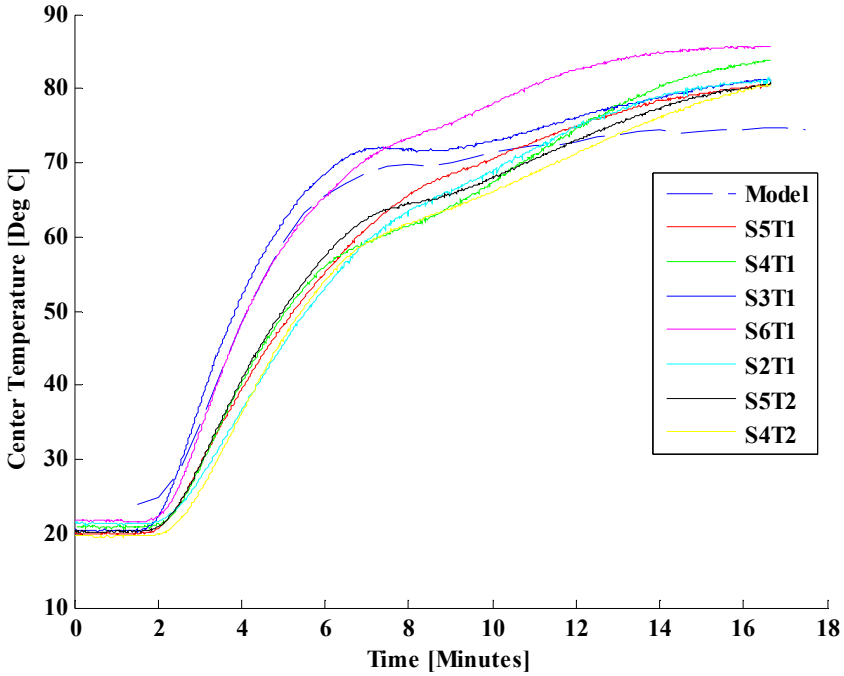

Figure 153 – CFB Center Temperature for Initial Saturation of 0.3

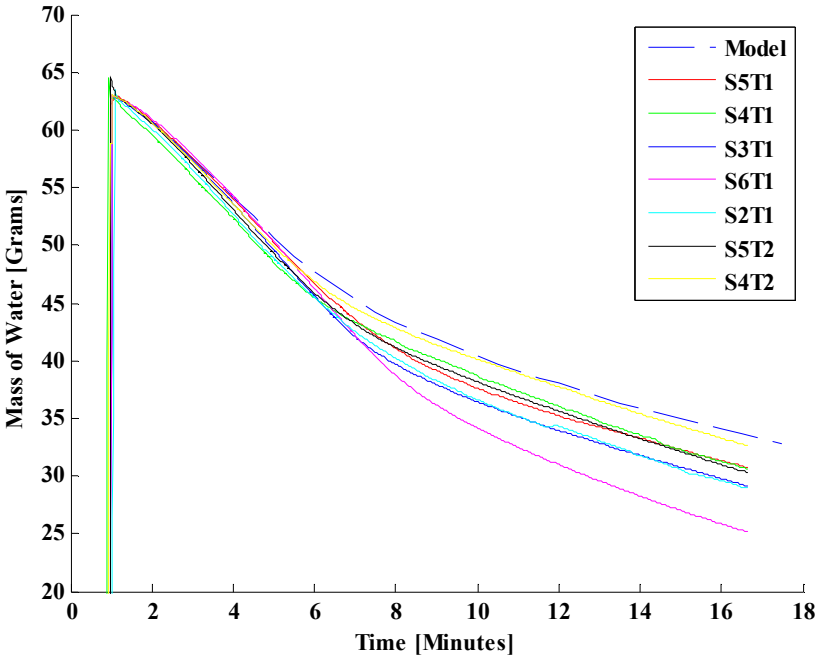

Figure 154 – CFB Mass for Initial Saturation of 0.3

Seven tests were conducted at an initial saturation of 0.5 and a heat flux of 20 kW/m^2. Four CFB samples were tested and are labeled samples 1, 2, 3, and 4. Samples 1, 2, and 3 were tested twice, with several hours in between for the samples to cool down. The results for these tests are shown in Figure 155 through Figure 157. The predicted surface temperature matches well with the experimental data, as shown in Figure 155. The predicted center temperature matches well with the experimental data. When the surface dries out at 1020 seconds, the internal rate of temperature rise slows due to vapor diffusion effects, as shown in Figure 156. The predicted rate of mass loss is very close to what is observed in the experiments, as is shown in Figure 157.

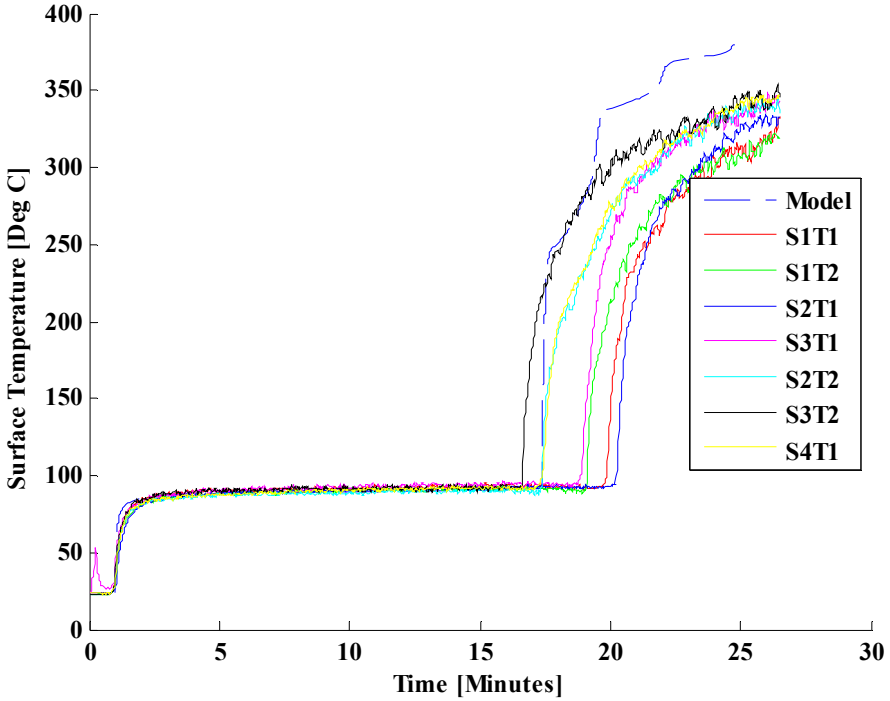

Figure 155 – CFB Surface Temperature for Initial Saturation of 0.5

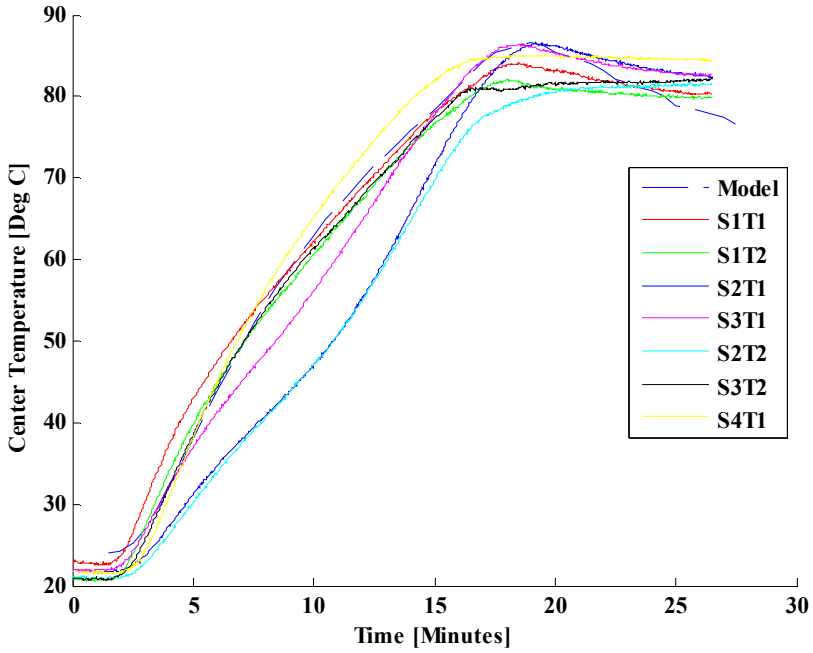

Figure 156 – CFB Center Temperature for Initial Saturation of 0.5

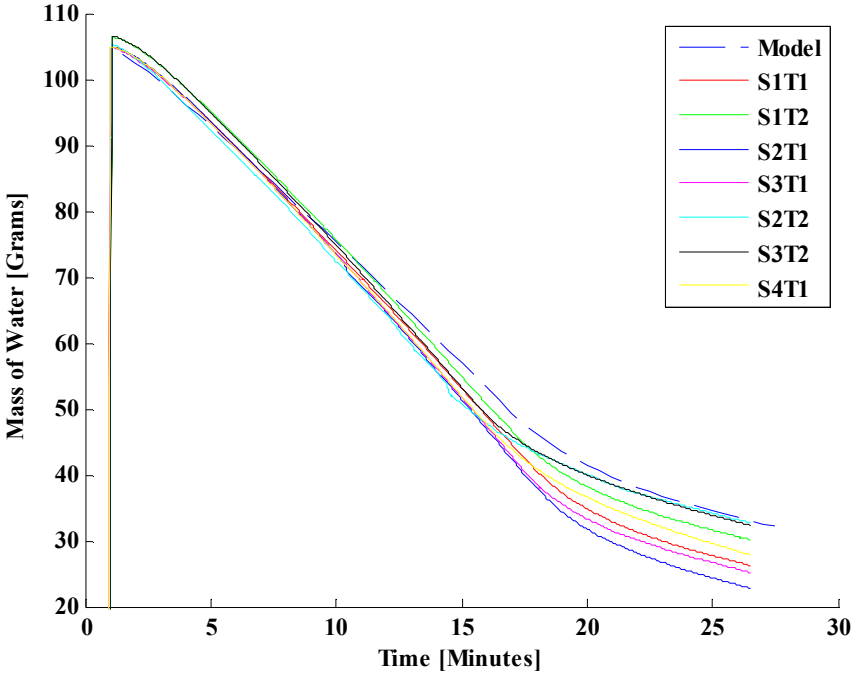

Figure 157 – CFB Mass Loss for Initial Saturation of 0.5

Four tests were conducted with an initial saturation of 0.7 and a heat flux of 20 kW/m2. The samples were labeled 11, 12, 13 and 14. Each one was tested once. The results are shown in Figure 158 through Figure 160. When sample 11 was tested, the surface thermocouple became detached from the surface of the CFB around 820 seconds. The three tests with functioning surface thermocouples show very little scatter in the "jump time". These tests probably had the most even water distribution at the start of the test due to the higher initial saturation. The jump time is slightly over-predicted, as shown in Figure 158. The predicted center temperature matches experimental data very well, up until the surface dries out, as shown in Figure 159. The center temperature drops slightly after the surface dries out, around 1700 seconds. This predicted temperature drop is observed in the experimental data. The predicted rate of mass loss is slightly less than that which is observed in experiment, as shown in Figure 160.

.

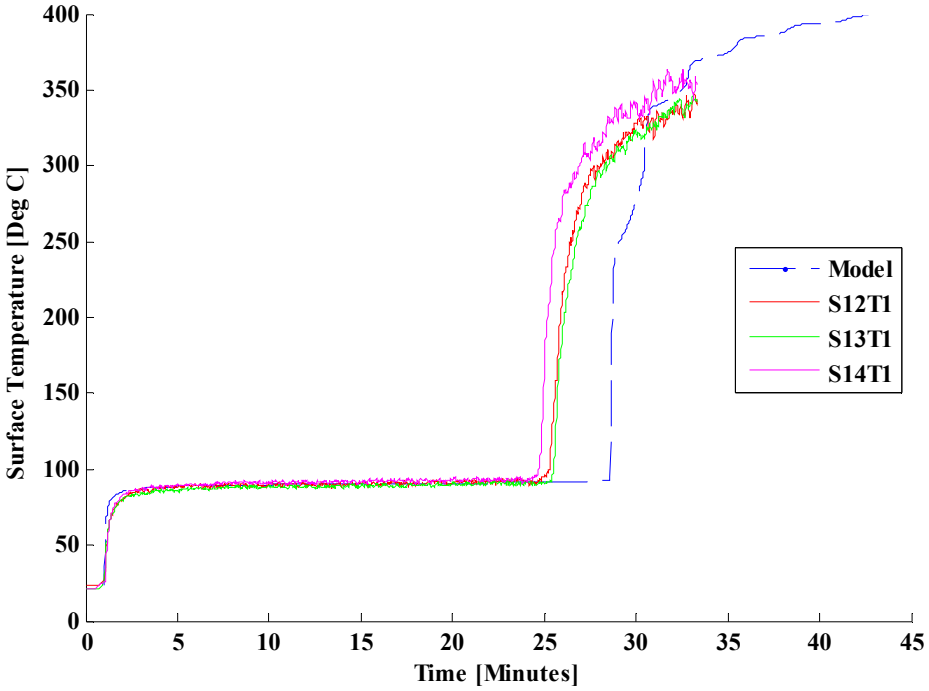

Figure 158 – CFB Surface Temp for Initial Saturation of 0.7

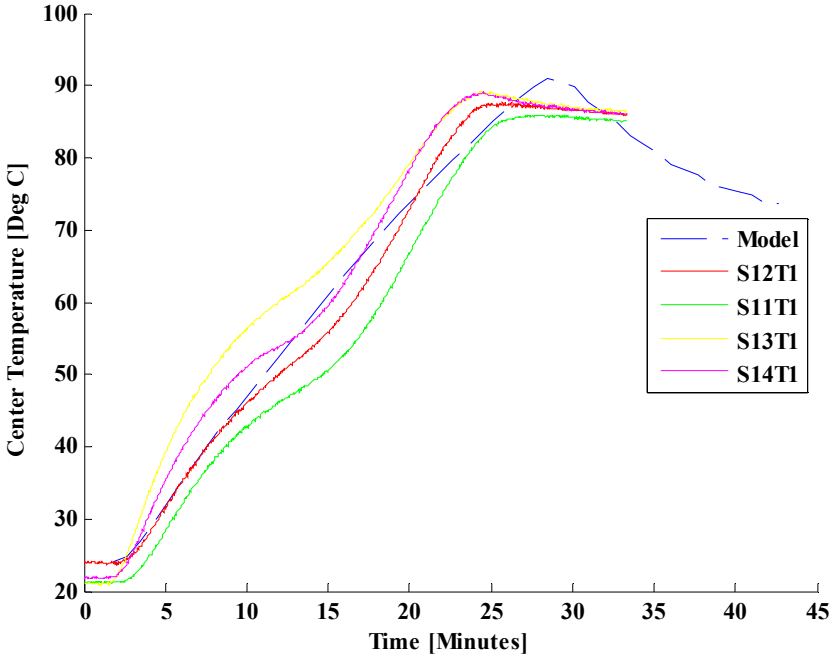

Figure 159 – CFB Center Temperature for Initial Saturation of 0.7

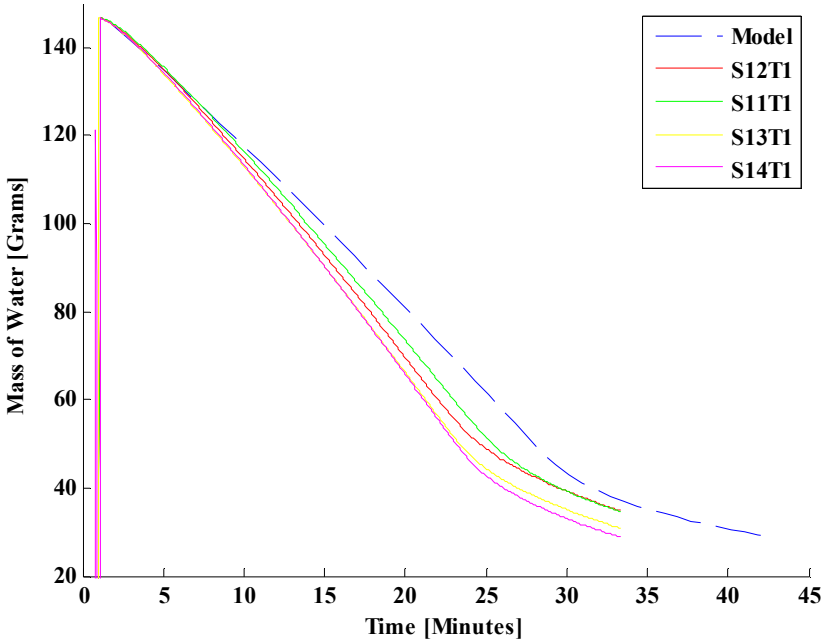

Figure 160 – CFB Mass for Initial Saturation of 0.7

Discussion

The process that is being modeled, and which is supported by these experiments in the cone, is described in detail here. The CFB material is at an initial saturation when the simulation starts. As the surface heats up there is a temperature gradient into the material. For example, the predicted temperature in the material at several times for the cone test with an initial saturation of 0.5 is shown in Figure 161.

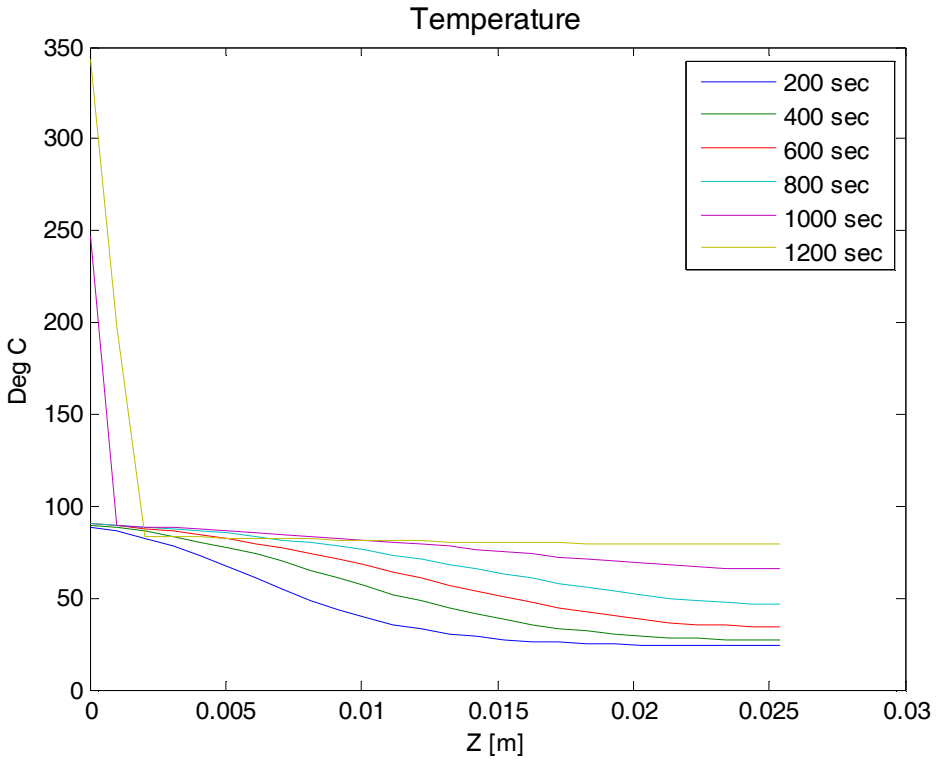

Figure 161 – Temperature in Cone Sample over Time – So = 0.5

The saturation in the material drops as evaporation occurs at the surface. As the surface dries out, surface tension forces draw liquid water to the surface. The saturation at several times is shown in Figure 162.

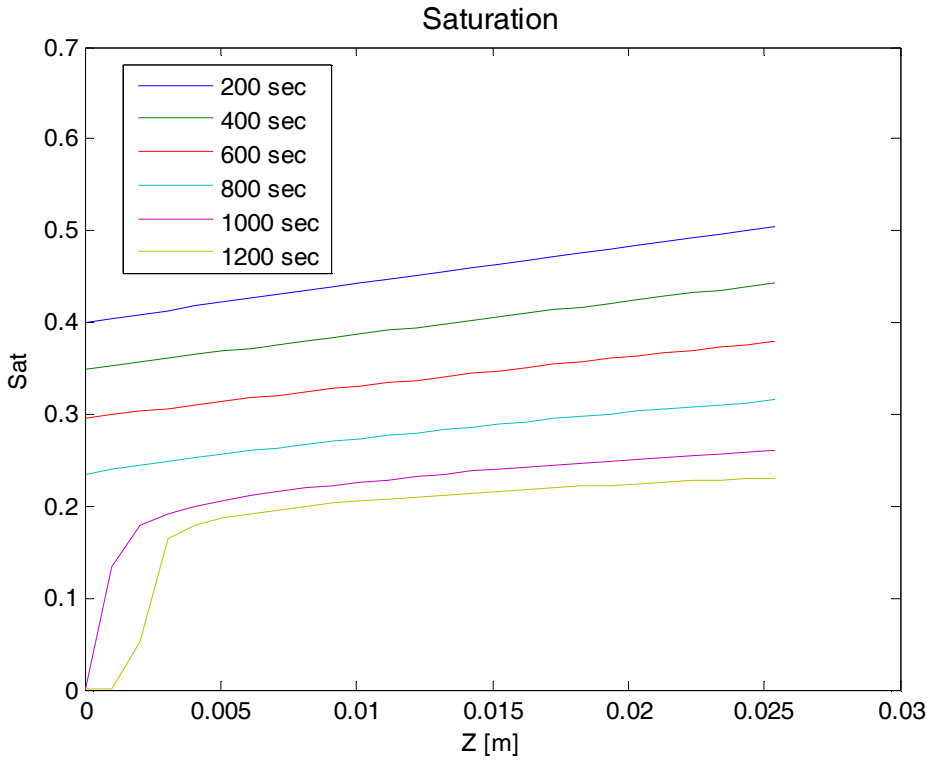

Figure 162 – Saturation in Cone Sample over Time – So = 0.5

As liquid water is being drawn to the surface and evaporated, water vapor is being transferred into the material. This is driven by a vapor pressure gradient into the material. The vapor pressure at several times is shown in Figure 163. This vapor diffuses into the material and condenses where the material is cooler, transferring heat and water into the material. When the surface of the material drops below the irreducible saturation of 0.15, water in the pores is assumed to be non-continuous, and cannot flow to the surface. In the model, this is accounted for by the correlation for relative permeability dropping off to zero at a saturation of 0.15. Once the surface reaches this saturation, liquid water cannot flow to the surface and it dries out rapidly. Once the surface saturation drops below 0.008, the vapor pressure correlation causes the vapor pressure to drop. The surface vapor pressure is the driving force for surface evaporation in the model, so when it drops, the rate of evaporative cooling drops as well. At this time, when the vapor pressure at the surface drops the temperature jumps rapidly. The surface vapor pressure variation over the entire simulation is shown in Figure 164.

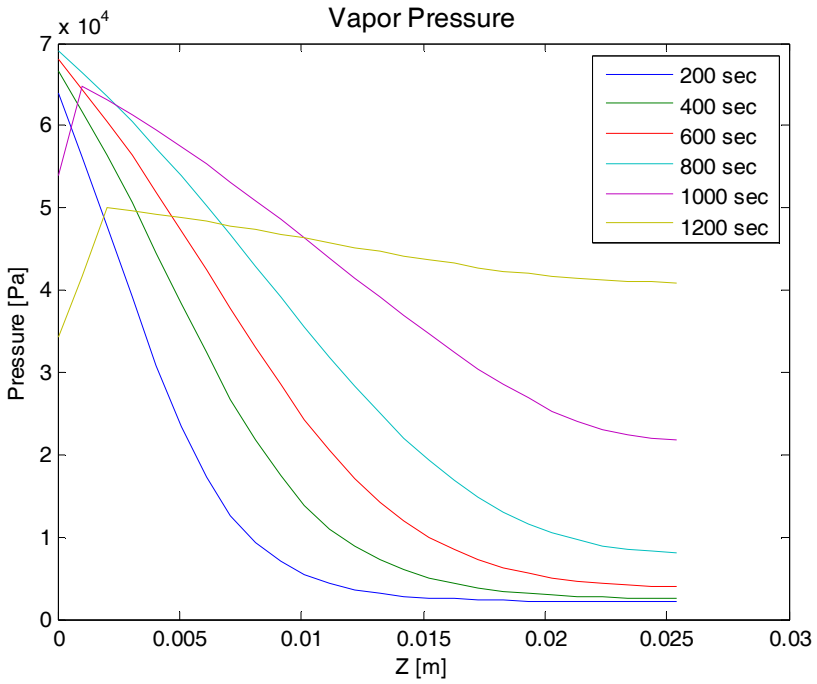

Figure 163 – Vapor Pressure in Cone Sample over Time – So = 0.5

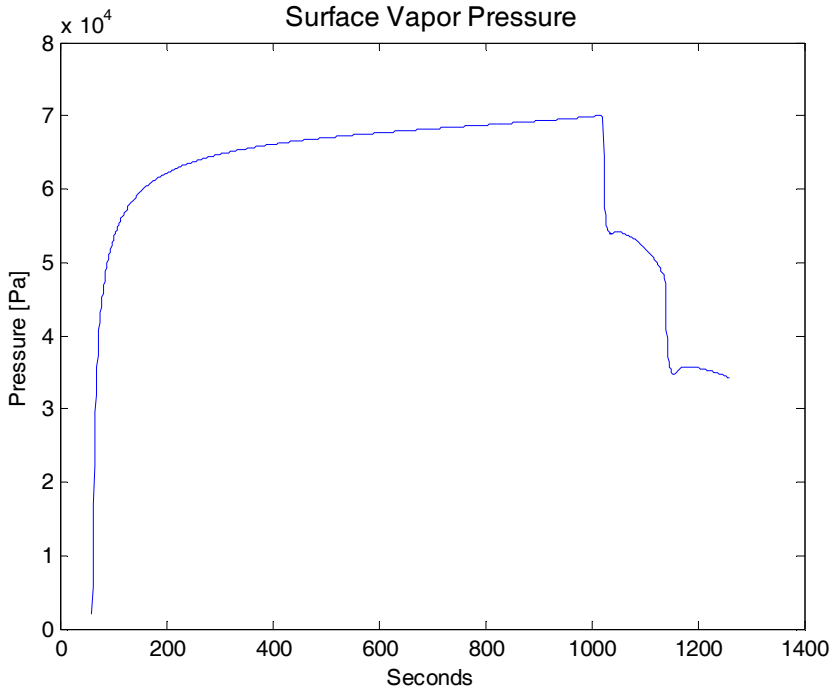

Figure 164 – Surface Vapor Pressure over Time – So = 0.5

Appendix G. Sensitivity Analysis

Overview

A sensitivity analysis was conducted on the model for each of the 6 validation cases considered. A one factor at a time local sensitivity analysis was chosen for low computational effort. This method consists of measuring the effect on the model output when one single input parameter is adjusted and all others are held constant. The measure of the sensitivity of the model output, y, to a single parameter x_i is given by a sensitivity coefficient S_i [50]

$$S_i = \frac{x_i}{y}\frac{\partial y}{\partial x_i}$$

Since we are not dealing with an analytical model, this is approximated numerically as

$$S_i = \frac{x_i}{y}\frac{\Delta y}{\Delta x_i}$$

Tests were conducted for each validation scenario where the input parameters were adjusted individually, and a sensitivity coefficient was calculated for the model output. The sensitivity coefficient for the input parameters was used to create sensitivity rankings of the input parameters.

Wetting Tests

A sensitivity analysis was conducted on the two wetting validation tests using CFB described earlier. The first parameters that were adjusted are the surface saturation, water spray flux, initial saturation, irreducible saturation, permeability, porosity, diffusivity, sample depth, number of nodes, and time step. The values of these parameters are shown in Table 25.

Table 25 – Basic Parameters Used for Sensitivity Analysis of CFB Wetting

Parameter	Units	Base Value	"High" Value	"Low Value
Surface Saturation – S_{surf}	-	0.99	0.999 (+1%)	0.98 (-1%)
Water Spray Flux - $\dot{m}''_{spray}$	kg/m^2s	0.128	0.1408	0.1152
Initial Saturation - S_o	-	0.004	0.0044 (+10%)	0.0036 (-10%)
Irreducible Saturation - S_{ir}	-	0.15	0.165 (+10%)	0.135 (-10%)
Permeability - K	m^2	5×10^{-11}	5.5×10^{-11} (+10%)	4.5×10^{-11} (-10%)
Porosity - ϕ	-	0.80	0.88 (+10%)	0.72 (-10%)
Diffusivity - D	m^2/s	2.6E-5	2.86E-5 (+10%)	2.34E-6 (-10%)
Depth of Sample - L	m	0.15	0.165(+10%)	0.135 (-10%)
Number of Nodes - n	-	31	36	26
Time Step - Δt	seconds	1	0.1	10

Additionally the sensitivity of the model to other constitutive relations was tested. The relative permeabilities for liquid and gas were adjusted from their base case cubic function. A square function was used as the "high" value and a fourth order function was used as the "low" value. These correlations are shown in Figure 165.

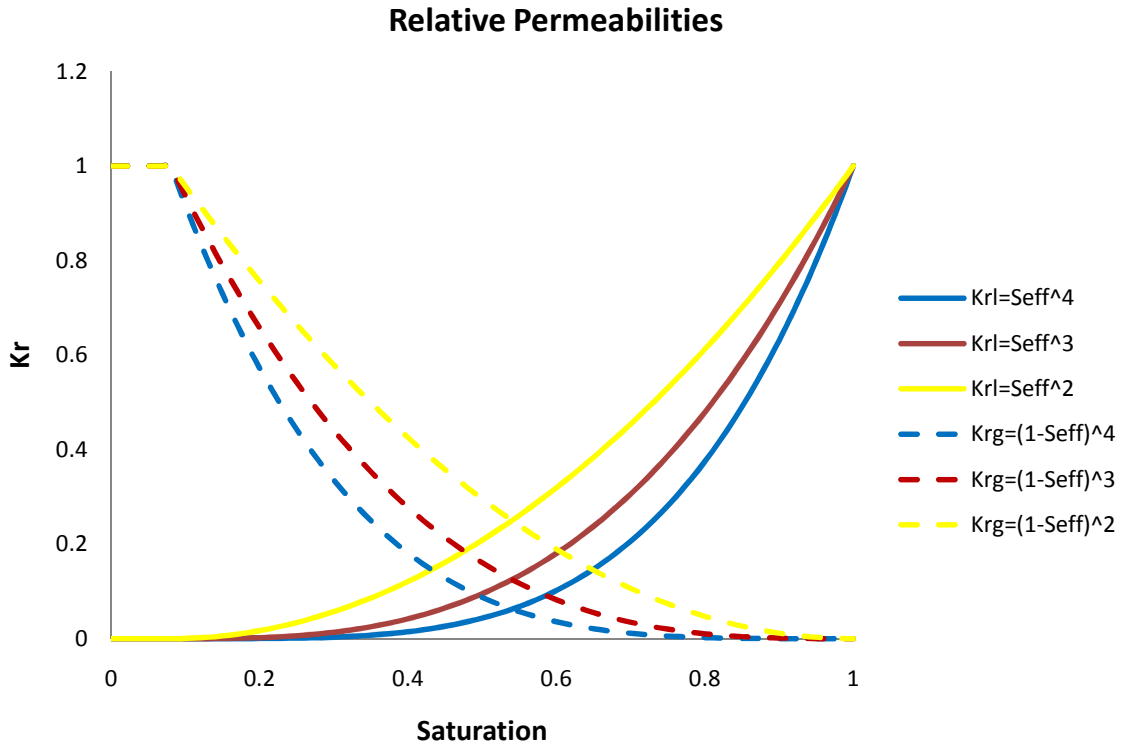

Figure 165 – Relative permeabilities used in sensitivity Analysis

The J-function correlation used for capillary pressure in the CFB was determined from capillary rise tests to be

$$J(S) = 0.4\left[0.364\left(1-\exp\left(-30\left(1-S\right)\right)\right)+0.471\left(1-S\right)+\frac{0.035}{S-0.1}\right]$$

The sensitivity of the model to each of the coefficients in this correlation was tested. The values used for the sensitivity analysis are shown in Table 26.

Table 26 – Capillary Pressure Parameters for Sensitivity Analysis of CFB Wetting

Parameter	Base Value	+10%	-10%
1	0.4	0.44	0.36
2	0.364	0.4004	0.3276
3	-30	-33	-27
4	0.471	0.5181	0.4239
5	0.035	0.0385	0.0315
6	0.1	0.11	0.09

The base cases on which the sensitivity analysis was performed for type 1BC conditions, and spray wetting conditions are shown in Figure 166 and Figure 167 respectively.

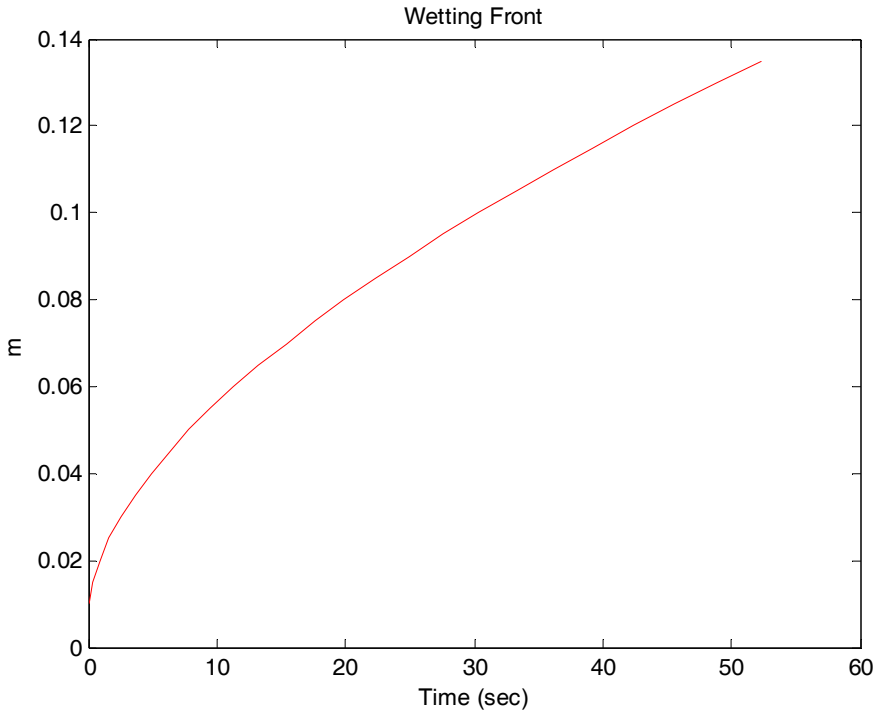

Figure 166 – Base Case for Sensitivity Analysis of Type 1 BC Wetting of CFB

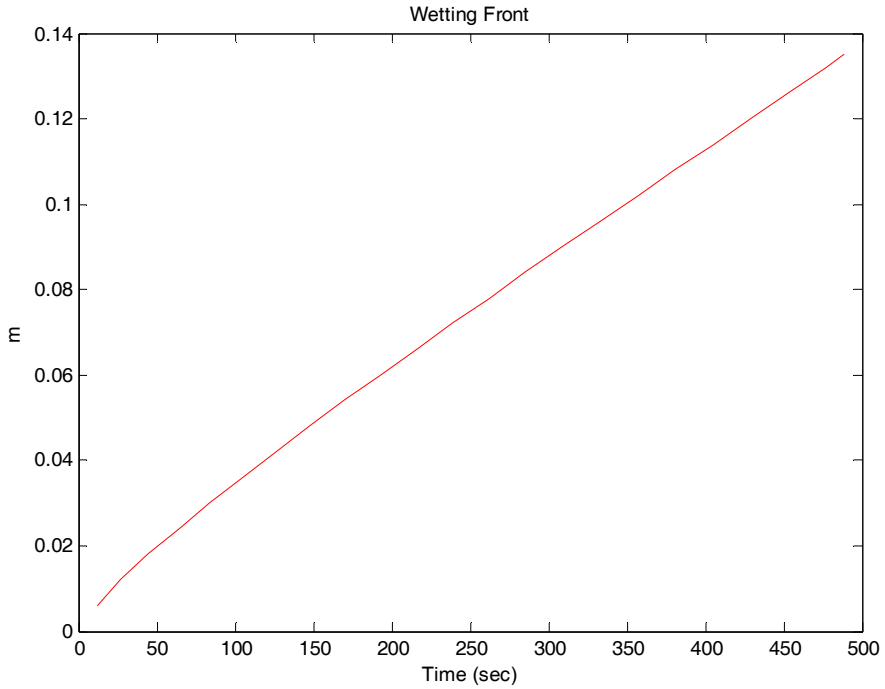

Figure 167 –Base Case for Sensitivity Analysis of Spray Wetting of CFB

The total area to the left of the water penetration depth curve was integrated to give a quantitative measure of the effect of changing each parameter. This was done numerically using the trapezoidal rule.

$$Z_{sum} = \sum_{i=1}^{nt} \left(t_i + t_{i+1} \right) \Delta z \qquad \text{(units: meter * seconds)}$$

Where z_i is the depth of water penetration at timestep i. The depth – time curve was integrated up to a depth of 0.135m. This is shown in Figure 168. The area to the left of the curve was chosen because the model output gives the time at which the water reaches each node, so a consistent upper bound was readily available for integration. This is not the case for the area under the curve, which would require a consistent upper bound in time.

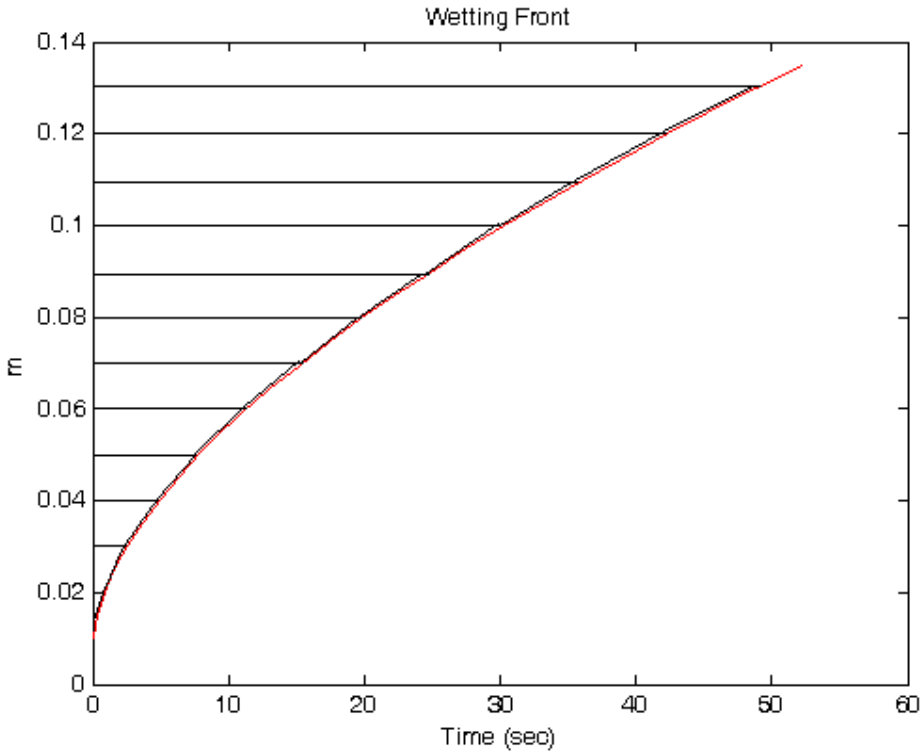

Figure 168 – Integration Method for Sensitivity Analysis of CFB Wetting

The integrated value was used to calculate a sensitivity coefficient for each parameter x_i

$$S_i = \frac{x_i}{Z_{sum}} \frac{\Delta Z_{sum}}{\Delta x_i}$$

The sensitivity coefficient was calculated for each parameter for the cases of Type 1 BC wetting, and spray wetting. The total integrated area to the left of the penetration depth curve was calculated for the "high" and "low" cases of each parameter. For the case of Type 1 BC wetting the total integrated area under the infiltration depth/time curve is shown for the base case of type 1 BC wetting is 2.88 meter-seconds. The integrated area for each adjusted parameter is shown in Table 27.

Table 27 – Sensitivity Analysis Results for CFB Wetting – Type 1 BC

Parameter	Total (high)	Change	Total (low)	Change
Surface Saturation	2.4568	-0.42802	3.3816	0.49678
Initial Saturation	2.8809	-0.00393	2.8976	0.012825
Permeability	2.7197	-0.16512	3.0777	0.19288
Porosity	3.0596	0.1748	2.703	-0.18185
Liq Rel Permeability	3.2783	0.3935	2.3527	-0.53215
Gas Rel Permeability	2.9543	0.0695	2.796	-0.0888
Cap Press Coeff 1	2.6803	-0.20455	3.1236	0.23875
Cap Press Coeff 2	2.7512	-0.1336	3.0331	0.14825
Cap Press Coeff 3	2.9103	0.025475	2.862	-0.02278
Cap Press Coeff 4	2.8191	-0.06575	2.9533	0.0685
Cap Press Coeff 5	2.872	-0.01278	2.8976	0.01275
Cap Press Coeff 6	2.8799	-0.00495	2.8895	0.004725
Irreducible Saturation	2.9117	0.026925	2.8576	-0.02723
Sample Length	2.8617	-0.02307	2.9058	0.020963
Number of Nodes	2.6846	-0.20025	2.9857	0.10091
Time step	2.8786	-0.0062	2.8862	0.0014
Diffusivity	2.8847	-0.00013	2.8851	0.00025

For the spray wetting tests, the base case integrated value of the penetration depth curve is 30.8 ms. The value for each of the adjusted parameters is shown in Table 28. The parameter “surface saturation” is only applicable to the type 1 BC wetting case, and does not show up in Table 28. Likewise, the parameter “water flux” is only applicable to the spray wetting case, and does now show up in Table 27. The calculated values of the sensitivity coefficient for each parameter were calculated based on the absolute value of the maximum change from the “high” and “low” cases. The sensitivity coefficients for each parameter for both wetting cases are shown in Table 29.

Table 28 – Integrated Water Absorption for Spray Wetting of CFB

Parameter	Total (high)	Change	Total (low)	Change
Water flux	28.648	-2.185	33.455	2.6225
Initial Saturation	30.825	-0.0075	30.848	0.015
Permeability	30.363	-0.47	31.35	0.5175
Porosity	33.708	2.875	27.948	-2.885
Liq Rel Permeability	35.903	5.07	22.75	-8.0825
Gas Rel Permeability	30.825	-0.0075	30.833	0
Diffusivity	30.828	-0.005	30.833	0
Depth of Sample	30.753	-0.07925	30.886	0.05325
Number of Nodes	30.702	-0.1305	30.935	0.10229
Time Step	30.756	-0.07671	31.725	0.8925
Cap Press Coeff 1	30.448	-0.385	31.23	0.3975
Cap Press Coeff 2	30.833	0	30.833	0
Cap Press Coeff 3	30.833	0	30.833	0
Cap Press Coeff 4	30.585	-0.2475	31.095	0.2625
Cap Press Coeff 5	30.665	-0.1675	30.975	0.1425
Cap Press Coeff 6	30.725	-0.1075	30.93	0.0975
Irreducible Saturation	31.418	0.585	30.203	-0.63

Table 29 – Sensitivity Coefficient Ranking for Wetting of CFB

	Type 1 BC		Spray Wetting	
Rank	**Parameter**	**S_i**	**Parameter**	**S_i**
1	Surface Saturation	17.05	Porosity	0.9357
2	Cap Press Coeff 1	0.82761	Water flux	0.85056
3	Permeability	0.66859	Liq Rel Perm.	0.79437
4	Porosity	0.63037	Irreducible Saturation	0.20433
5	Liq Rel Permeability	0.55899	Permeability	0.16784
6	Cap Press Coeff 2	0.5139	Cap Press Coeff 1	0.12892
7	Cap Press Coeff 4	0.23745	Cap Press Coeff 4	0.085137
8	Number of Nodes	0.21491	Cap Press Coeff 5	0.054326
9	Irreducible Saturation	0.094374	Cap Press Coeff 6	0.034866
10	Gas Rel Permeability	0.093279	Number of Nodes	0.026289
11	Cap Press Coeff 3	0.088308	Depth of Sample	0.025703
12	Sample Length	0.07998	Time Step	0.024881
13	Initial Saturation	0.044457	Initial Saturation	0.004865
14	Cap Press Coeff 5	0.044284	Diffusivity	0.001622
15	Cap Press Coeff 6	0.017159	Gas Rel Permeability	0.000737
16	Time step	0.002387	Cap Press Coeff 2	0
17	Diffusivity	0.000867	Cap Press Coeff 3	0

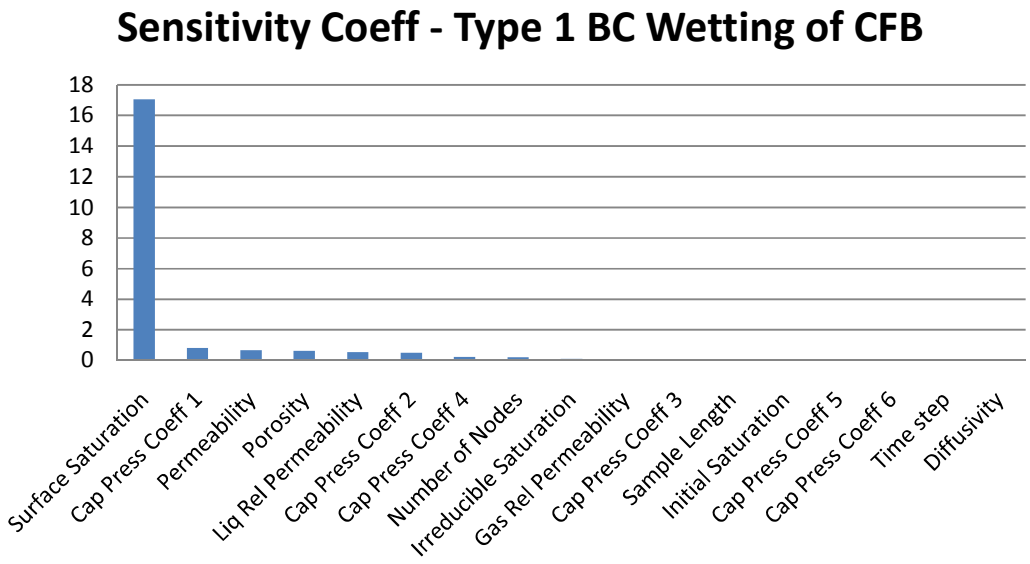

Figure 169 – Sensitivity Analysis Results for Type 1 BC CFB Wetting

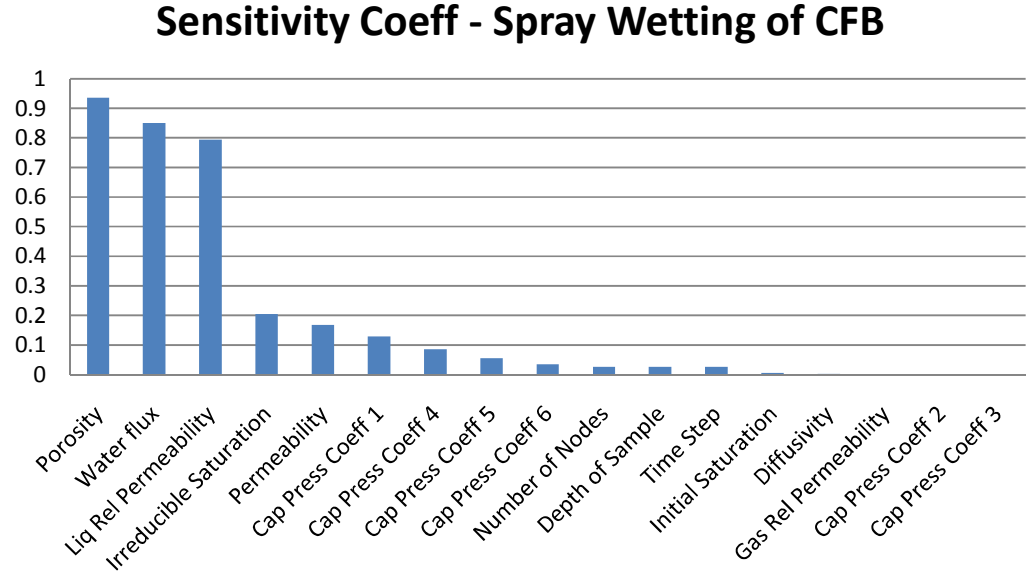

Figure 170 – Sensitivity Analysis Results for Spray Wetting of CFB

The type 1 BC wetting case was extremely sensitive to the surface saturation value. A change of only 1% had a significant effect on the model output. The model was also sensitive to the Capillary Pressure Coefficient 1, permeability, porosity, liquid relative permeability, and Capillary Pressure Coefficient 2. All other input parameters had a sensitivity coefficient of less than 0.5. The spray wetting case was most sensitive to the porosity, water flux, and liquid relative permeability. All other input parameters have a sensitivity coefficient of less than 0.5.

Heating Tests

The sensitivity of the model was tested for each of the 4 heating validation cases. For each case, a set of basic parameters was chosen to be adjusted first. The basic parameters that were adjusted for particulate media, brick, wood, and CFB are shown in Table 30, Table 31, Table 32, and Table 33.

Table 30 –Parameters used for Sensitivity Analysis of Particulate Media Drying

Parameter	Units	Base Value	High Value	Low Value
Permeability	m^2	3.75E-11	4.13E-11 (+10%)	3.38E-11 (-10%)
Porosity	-	0.460	0.506 (+10%)	0.414 (-10%)
Specific Heat	J/kgK	780	858 (+10%)	702 (-10%)
Thermal Cond	W/mK	1.4	1.54 (+10%)	1.26 (-10%)
Density	kg/m^3	2500	2750 (+10%)	2250 (-10%)
Diffusivity	m^2/s	2.6E-5	2.86E-6 (+10%)	2.34E-6 (-10%)
Heat Trans Coeff	W/m^2K	43.0	47.3 (+10%)	38.7 (-10%)
Mass Trans Coeff	m/s	0.0723	0.0795 (+10%)	0.0651 (-10%)
Relative Humidity	%	33%	36.6% (+10%)	29.7% (-10%)
Initial Temp	K	289.8	291.8 (+2^{o}C)	287.8 (-2^{o}C)
Ambient Temp	K	321	323 (+2^{o}C)	319 (-2^{o}C)
Length	m	0.015	0.016 (+6.6%)	0.014 (-6.6%)
Initial Saturation	-	0.915	0.961 (+5%)	0.869 (-5%)
Number of Nodes	-	31	41	21
Time Step	seconds	1	2	0.1
Irr. Saturation	-	0.09	0.099 (+10%)	0.081 (-10%)

Table 31 – Parameters used for Sensitivity Analysis of Brick Drying

Parameter	Units	Base Value	High Value	Low Value
Permeability	m^2	5E-14	5.5E-14 (+10%)	4.5E-14 (-10%)
Porosity	-	0.435	0.4785 (+10%)	0.3915 (-10%)
Specific Heat	J/kgK	750	825 (+10%)	675 (-10%)
Thermal Conductivity	W/Mk	0.885	0.9735 (+10%)	0.7965 (-10%)
Density	kg/m^3	2566	2823 (+10%)	2309 (-10%)
Diffusivity	m^2/s	2.6E-5	2.86E-5 (+10%)	2.34E-5 (-10%)
Heat Trans Coeff	W/m^2K	f(S,T)	+10%	-10%
Mass Trans Coeff	m/s	f(S,T)	+10%	-10%
Relative Humidity	%	9.3	10.23 (+10%)	8.37 (-10%)
Initial Temp	K	298	300 (+2^{o}C)	296 (-2^{o}C)
Ambient Temp	K	353	355 (+2^{o}C)	351 (-2^{o}C)
Length	M	0.05	0.055 (+10%)	0.045 (+10%)
Initial Saturation	-	0.56	0.616 (+10%)	0.504 (-10%)
Number of Nodes	-	31	41	21
Time Step	seconds	1	10	0.1
Irreducible Saturation	-	0.09	0.099 (+10%)	0.081(-10%)

Table 32 – Parameters used for Sensitivity Analysis of Wood Drying

Parameter	Units	Base Value	High Value	Low Value
Permeability	m^2	2E-16	2.2-16 (+10%)	1.8E-16 (-10%)
Porosity	-	0.615	0.6765 (+10%)	0.5535 (-10%)
Specific Heat	J/kgK	2800	3080 (+10%)	2520 (-10%)
Thermal Conductivity	W/Mk	0.377	0.4147 (+10%)	0.3397 (-10%)
Density	kg/m^3	1500	1650 (+10%)	1350 (-10%)
Diffusivity	m^2/s	2.6E-5	2.86E-5 (+10%)	2.34E-5 (-10%)
Heat Trans Coeff	W/m^2K	92.5	101.75 (+10%)	83.25 (-10%)
Mass Trans Coeff	m/s	0.099	0.1089 (+10%)	0.0891 (-10%)
Relative Humidity	%	5	5.5 (+10%)	4.5 (-10%)
Initial Temp	K	289	291 (+2^{o}C)	287 (-2^{o}C)
Ambient Temp	K	313	315 (+2^{o}C)	311 (-2^{o}C)
Length	m	0.019	0.0209 (+10%)	0.0171 (-10%)
Initial Saturation	-	0.99	0.90 (-10%)	0.80 (-20%)
Number of Nodes	-	31	41	21
Time Step	seconds	5	10	1
Irreducible saturation	-	0.2	0.22 (+10%)	0.18 (-10%)

Table 33 - Parameters used for Sensitivity Analysis of CFB Drying

Parameter	Units	Base Value	High Value	Low Value
Permeability	m^2	5E-11	5.5E-11 (+10%)	4.5E-11 (-10%)
Porosity	-	0.8	0.88 (+10%)	0.82 (-10%)
Specific Heat	J/kgK	1046	1151 (+10%)	941.4 (-10%)
Thermal Conductivity	W/mK	0.133	0.1463 (+10%)	0.1197 (-10%)
Density	kg/m^3	1360	1496 (+10%)	1224 (-10%)
Diffusivity	m^2/s	2.6E-5	2.86E-5 (+10%)	2.34E-6 (-10%)
Heat Trans Coeff	W/m^2K	$f(T_{surf})$	+10%	-10%
Mass Trans Coeff	m/s	$f(T_{surf})$	+10%	-10%
Relative Humidity	%	20	22 (+10%)	18 (-10%)
Initial Temp	K	24	26 (+10%)	22 (-10%)
Ambient Temp	K	24	26 (+10%)	22 (-10%)
Length	m	0.0254	0.0279 (+10%)	0.0229 (-10%)
Initial Saturation	-	0.5	0.55 (+10%)	0.45 (-10%)
Number of Nodes	-	25	30	20
Time Step	seconds	1	1.5	0.5
S_{ir}	-	0.15	0.165 (+10%)	0.135 (-10%)
Radiant Heat Flux	W/m^2	20,000	22,000 (+10%)	18,000 (-10%)
Surface Emissivity	-	0.96	1.0 (+4.2%)	0.92 (-4.2%)

In addition to these basic parameters, constitutive relations for the capillary pressure, liquid relative permeability, gas relative permeability, and relative humidity were adjusted. The capillary pressure for each material was calculated using empirical correlations. The calculated value of the capillary pressure was adjusted ±10% for each drying case. The base case capillary pressure correlations used for the 4 drying cases are given in Table 34.

Table 34 – Capillary Pressure Correlations for Sensitivity Analysis of Heating Tests

Material	Capillary Pressure
Particulate Media	$p_c = \frac{\sigma}{\sqrt{K/\varphi}}\left[0.364\left(1-\exp\left(-40\left(1-S\right)\right)\right)+0.221\left(1-S\right)+\frac{0.005}{S-0.08}\right]$
Brick	$p_c = \frac{\sigma}{\sqrt{K/\phi}}\left[0.3-0.0663\ln\left(S-S_{ir}\right)\right]$
Wood	$p_c = 1.24\times10^4 S^{-0.61}$
Ceramic Fiberboard	$p_c = \sigma\sqrt{\frac{\phi}{K}}0.4\left[0.364\left(1-\exp\left(-30\left(1-S\right)\right)\right)+0.471\left(1-S\right)+\frac{0.035}{S-0.1}\right]$

The relative permeability was calculated as a function of saturation. The correlations used for liquid and gas permeabilities are shown in Table 35 and Table 36.

Table 35 – Liquid Relative Permeability for Sensitivity Analysis of Heating Tests

Material	Base Case	High Case	Low Case
Particulate Media	$K_{rl} = S_{eff}^3$	$K_{rl} = S_{eff}^2$	$K_{rl} = S_{eff}^4$
Brick	$K_{rl} = S_{eff}^4$	$K_{rl} = S_{eff}^3$	$K_{rl} = S_{eff}^5$
Wood	$K_{rl} = S_{eff}$	$K_{rl} = S_{eff}^2$	$K_{rl} = S_{eff}^3$
Ceramic Fiberboard	$K_{rl} = S_{eff}^3$	$K_{rl} = S_{eff}^2$	$K_{rl} = S_{eff}^4$

Table 36 – Gas Relative Permeability for Sensitivity Analysis of Heating Tests

Material	Base Case	High Case	Low Case
Particulate Media	$K_{rg} = \left(1 - S_{eff}\right)^3$	$K_{rg} = \left(1 - S_{eff}\right)^2$	$K_{rg} = \left(1 - S_{eff}\right)^4$
Brick	$K_{rg} = \frac{\left(1 - S_{eff}\right)^2}{\left(1 - S_{eff}^2\right)}$	$K_{rg} = \frac{\left(1 - S_{eff}\right)^{1.5}}{\left(1 - S_{eff}^{1.5}\right)}$	$K_{rg} = \frac{\left(1 - S_{eff}\right)^{2.5}}{\left(1 - S_{eff}^{2.5}\right)}$
Wood	$K_{rg} = 0.05\left(1 - S_{eff}\right)$	$K_{rg} = 0.05\left(1 - S_{eff}\right)^2$	$K_{rg} = 0.05\left(1 - S_{eff}\right)^3$
Ceramic Fiberboard	$K_{rg} = \left(1 - S_{eff}\right)^3$	$K_{rg} = \left(1 - S_{eff}\right)^2$	$K_{rg} = \left(1 - S_{eff}\right)^4$

The relative humidity in the materials is calculated using the empirical correlations shown in Table 37. The relative humidity calculated from these correlations was adjusted $\pm 10\%$ for each heating case.

Table 37 – Relative Humidity Correlations for Sensitivity Analysis of Heating Tests

Material	Relative Humidity Correlation
Particulate Media	$S = \frac{(1-\phi)\rho_s}{\phi\rho_w}\left(0.0105\left(RH\right)^{0.2} + 0.0125\exp\left(20RH - 20\right)\right)$
Brick	$S = \frac{(1-\phi)\rho_s}{\phi\rho_w}\left(0.0105\left(RH\right)^{0.2} + 0.0125\exp\left(20RH - 20\right)\right)$
Wood	$RH = \exp\left(\left(17.884 - 0.1423T + 0.0002363T^2\right)\left(1.0327 - 0.00067^{4}\right)\right.$
Ceramic Fiberboard	$S = \frac{(1-\phi)\rho_s}{\phi\rho_w}\left(0.0105\left(RH\right)^{0.2} + 0.0125\exp\left(20RH - 20\right)\right)$

A sensitivity coefficient was calculated based on the model predicted temperature for each case. The base case scenario model outputs for the 4 drying cases are shown in Figure 171, Figure 172, Figure 173, and Figure 174.

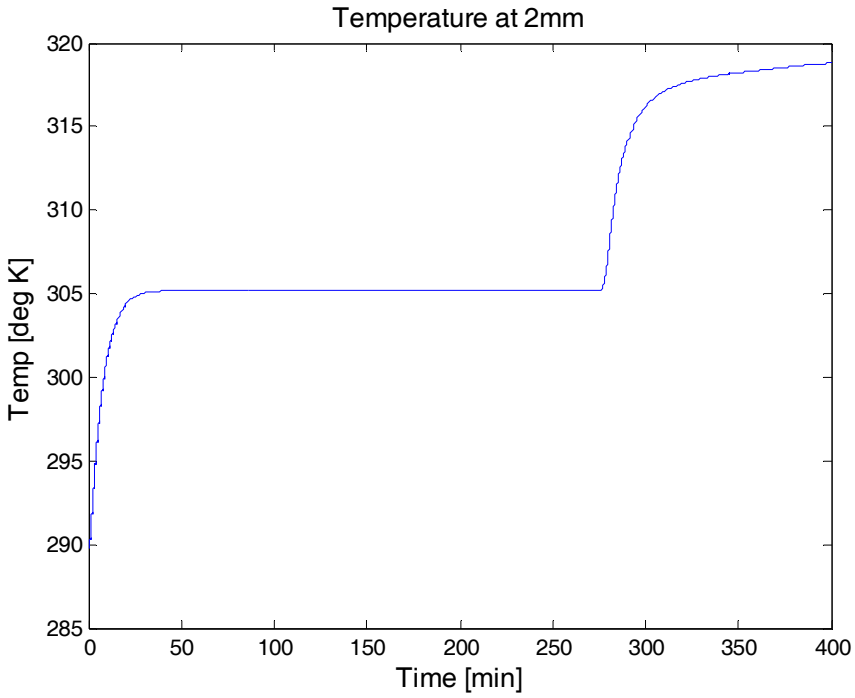

Figure 171 – Base Case for Sensitivity Analysis of Drying of Particulate Media

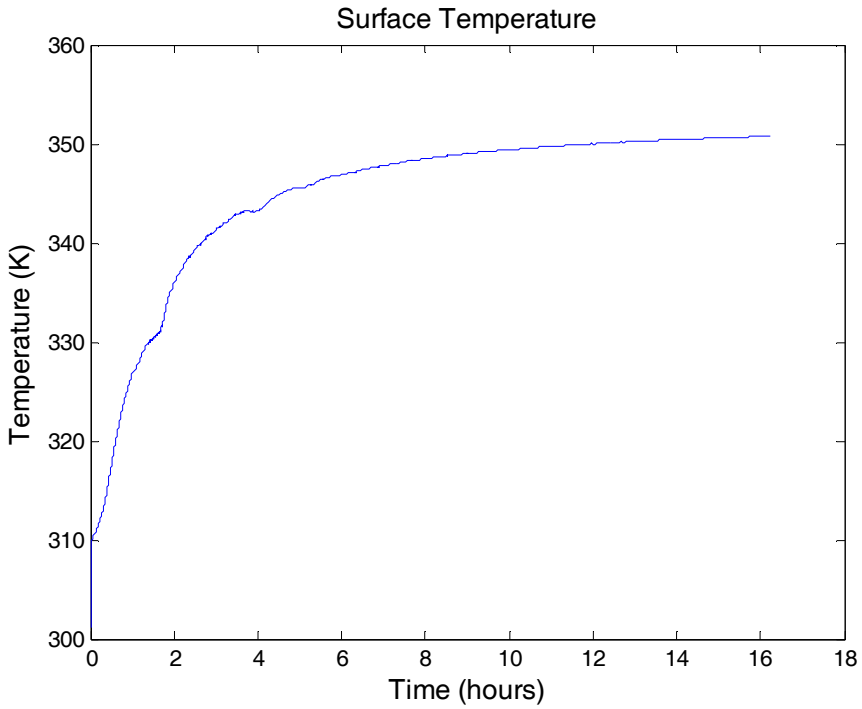

Figure 172 – Base Case for Sensitivity Analysis of the Drying of Brick

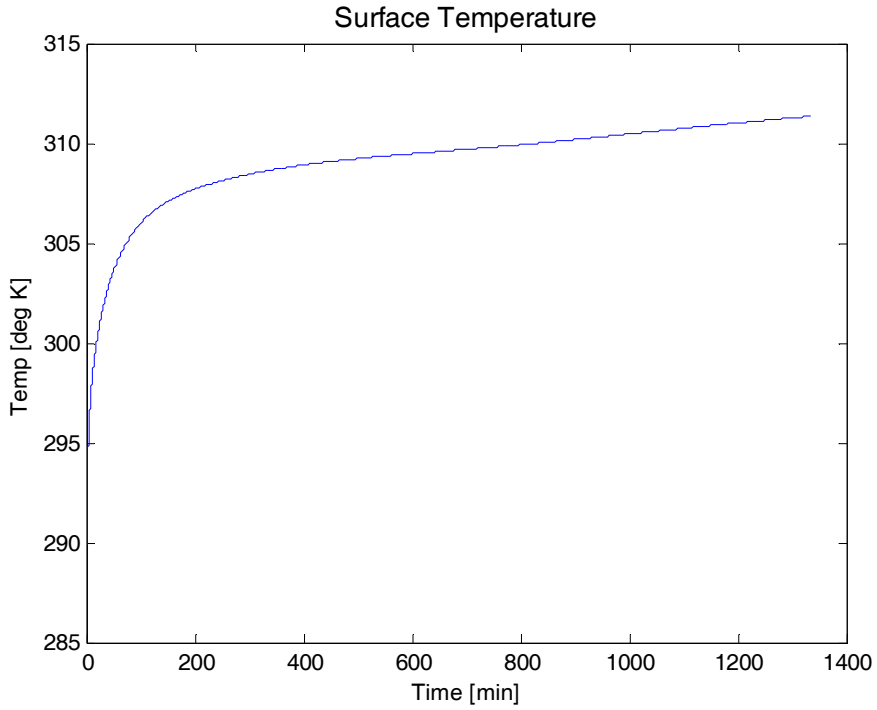

Figure 173 – Base Case for Sensitivity Analysis of the Drying of Wood

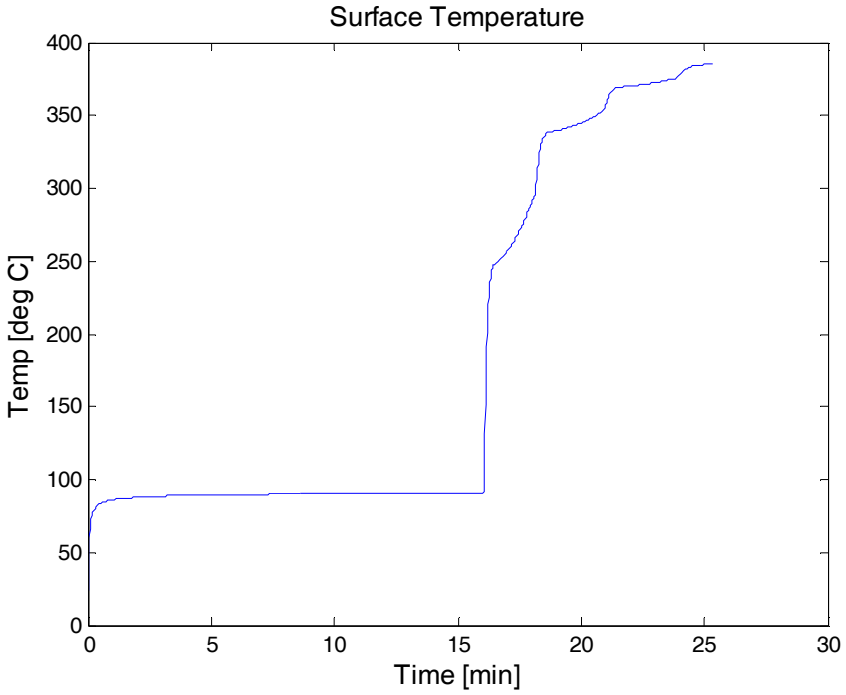

Figure 174 – Base Case for Sensitivity Analysis of the Drying of CFB

For the particulate media and CFB cases, the time at which the temperature jumped dramatically was used as the quantitative measure of the effect of adjusting each parameter. For the cases of brick and wood drying, the area under the temperature – time curve was integrated numerically using the trapezoidal rule.

$$T_{sum} = \sum_{i=1}^{nt} \left(T_i + T_{i+1} \right) \Delta t \qquad \text{(units Kelvin * seconds)}$$

Where T_i is the temperature at the i^{th} time step. This is illustrated in Figure 45.

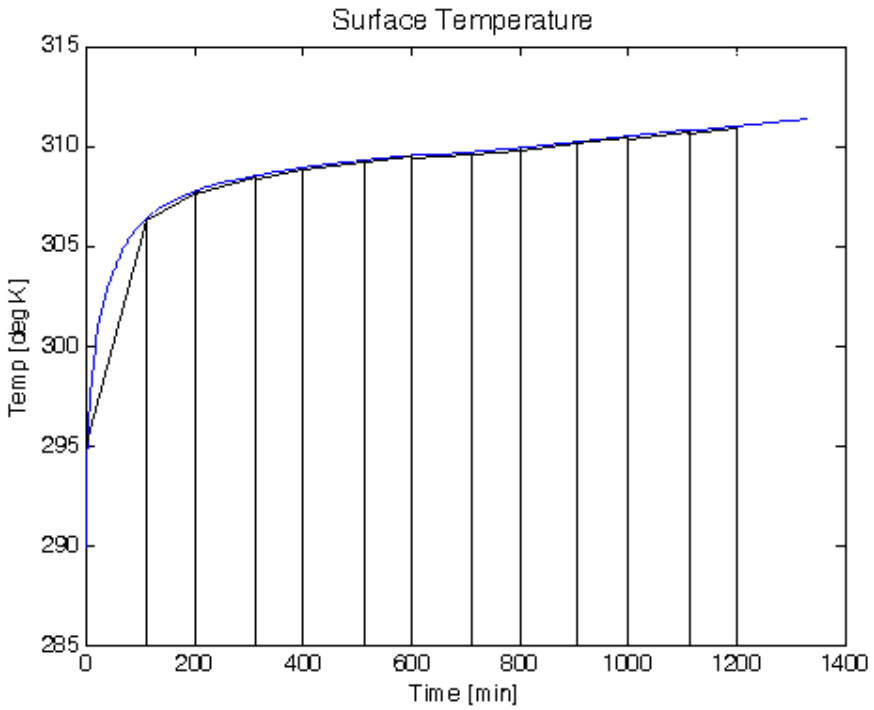

Figure 175 – Numerical Method for Integrating Heating Temperature Curve for Sensitivity Analysis of Brick and Wood

The model outputs for the drying of particulate media, brick, wood, and ceramic fiberboard are shown in Table 38 through Table 39.

Table 38 – Jump Times for Particulate Media Drying

Parameter	"High" Value	Change	"Low" Value	Change
Permeability	16024	17	15989	-18
Porosity	15871	-136	16159	152
Specific Heat	16030	23	15983	-24
Thermal Cond	16003	-4	16010	3
Density	16030	23	15983	-24
Diffusivity	16007	0	16006	-1
Heat Trans Coeff	14801	-1206	17457	1450
Mass Trans Coeff	15710	-297	16372	365
Relative Humidity	17255	1248	14861	-1146
Initial Temp	15934	-73	16079	72
Ambient Temp	14512	-1495	17824	1817
Length	15861	-146	16167	160
Initial Saturation	16945	938	15082	-925
Number of Nodes	16064	57	15973	-34
Time Step	16056	49	15993	-14.5
Liquid Relative Permeability	14704	-1303	16683	676
Gas Relative Permeability	16008	1	15999	-8
Relative Humidity Correlation	15959	-48	16043	36
Capillary Pressure Correlation	16044	37	15962	-45
Irr. Saturation	15727	-280	16339	332

Table 39 – Integrated Area Under Surface Temperature Curve for Brick Drying

Parameter	"High" Value	Change	"Low" Value	Change
Permeability	1561900	-1060.3	1564200	1219.4
Porosity	1576500	13553	1551500	-11444
Specific Heat	1559700	-3261.3	1566200	3271.3
Thermal Cond	1560800	-2162.3	1565500	2535.6
Density	1559700	-3242.6	1566200	3294.3
Diffusivity	1560300	-2617.2	1565800	2893.7
Heat Trans Coeff	1597000	34059	1522200	-40688
Mass Trans Coeff	1562200	-755.83	1563900	944.45
Relative Humidity	1564300	1364.5	1561600	-1319.4
Initial Temp	1565500	2558.4	1560400	-2554.2
Ambient Temp	1626400	63453	1499500	-63401
Length	1583100	20139	1548900	-14038
Initial Saturation	1526100	-36870	1603200	40230
Number of Nodes	1562000	-944.33	1565400	2488.2
Time Step	1563200	251.58	1609400	46439
Liquid Relative Permeability	1604000	41110	1526800	-36169
Gas Relative Permeability	1563900	965.32	1563900	925.31
Relative Humidity Correlation	1565400	2455.8	1558100	-4809.9
Capillary Pressure Correlation	1560700	-2221.9	1565600	2697
Irreducible Sat.	1566100	3142	1559800	-3124

Table 40 – Integrated Area Under Surface Temperature Curve for Wood Drying

Parameter	"High" Value	Change	"Low" Value	Change
Permeability	947130	-3703	955530	4702
Porosity	946870	-3963	943790	-7042
Specific Heat	950130	-704	951540	704
Thermal Cond	950810	-22	950860	23
Density	959730	8894	970290	19460
Diffusivity	950840	2	950830	-4
Heat Trans Coeff	972640	21812	924380	-26453
Mass Trans Coeff	950290	-542	951560	729
Relative Humidity	951400	572	950370	-462
Initial Temp	952440	1608	949220	-1609
Ambient Temp	1047100	96270	854870	-95960
Length	971600	20766	992200	41370
Initial Saturation	976630	25793	1006400	55571
Number of Nodes	949540	-1289	950830	0
Timestep	949440	-1394	951940	1112
Liq. Rel. Perm.	1015200	64402	1057500	106700
Gas Rel. Perm.	956500	5670	965070	14234
Rel. Hum. Corr.	950250	-583	951640	804
Cap. Press. Corr.	947140	-3697	955530	4699
Irr. Saturation	958690	7857	942980	-7850
Beta Power	949560	-1270	952730	1893

Table 41 – Jump Times for CFB Drying

Parameter	"High" Value	Change	"Low" Value	Change
Permeability	968	3	962	-3
Porosity	898	-67	1031	66
Specific Heat	966	1	964	-1
Thermal Conductivity	965	0	965	0
Density	966	1	964	-1
Diffusivity	969	4	961	-4
Heat Trans Coeff	969	4	960	-5
Mass Trans Coeff	949	-16	984	19
Relative Humidity	965	0	965	0
Initial Temp	962	-3	968	3
Ambient Temp	963	-2	967	2
Length	867	-98	1058	93
Initial Saturation	1136	171	792	-173
Number of Nodes	975	10	958	-7
Time Step	965.5	0.5	962	-3
S_{ir}	1039	74	895	-70
Radiant Heat Flux	872	-93	1081	116
Surface Emissivity	925	-40	1009	44

The sensitivity coefficient rankings for the parameters are given for particulate media, brick, wood, and ceramic fiberboard in Table 42 through Table 45.

Table 42 – Sensitivity Coefficients for Input Parameters for Particulate Media Drying

Rank	Parameter	Sensitivity Coefficient
1	Ambient Temp	16.451
2	Initial Saturation	1.172
3	Heat Trans Coeff	0.90585
4	Relative Humidity	0.77966
5	Initial Temp	0.66094
6	Liquid Relative Permeability	0.24667
7	Mass Trans Coeff	0.22803
8	Irreducible Saturation	0.20741
9	Length	0.19991
10	Porosity	0.18992
11	Cap. Press. Correlation	0.028113
12	Relative Humidity Correlation	0.014993
13	Specific Heat	0.014993
14	Density	0.014993
15	Number of Nodes	0.013387
16	Permeability	0.011245
17	Thermal Cond	0.002499
18	Gas Relative Permeability	0.001515
19	Time Step	0.001007
20	Diffusivity	0.000625

Table 43 – Sensitivity Coefficients for Input Parameters for Brick Drying

Rank	Parameter	Sensitivity Coefficient
1	Ambient Temp	6.05
2	Initial Temp	0.289
3	Heat Trans Coeff	0.260
4	Initial Saturation	0.257
5	Length	0.129
6	Liquid Relative Permeability	0.105
7	Porosity	0.0867
8	Density	0.0211
9	Specific Heat	0.0209
10	Irreducible Saturation	0.0201
11	Diffusivity	0.0185
12	Capillary Pressure Correlation	0.0173
13	Thermal Cond	0.0162
14	Relative Humidity Correlation	0.0154
15	Relative Humidity	0.00873
16	Permeability	0.00780
17	Mass Trans Coeff	0.00604
18	Number of Nodes	0.00493
19	Time Step	0.00330
20	Gas Relative Permeability	0.00186

Table 44 – Sensitivity Coefficients for Input Parameters for Wood Drying

Rank	Parameter	Sensitivity Coefficient
1	Ambient Temp	15.845
2	Initial Saturation	0.29222
3	Heat Trans Coeff	0.2782
4	Initial Temp	0.24451
5	Length	0.2184
6	Density	0.10233
7	Irr. Saturation	0.082629
8	Liquid Relative Permeability	0.067732
9	Permeability	0.049451
10	Cap. Press. Correlation	0.04942
11	Porosity	0.041683
12	Beta Power	0.019908
13	Relative Humidity Correlation	0.008456
14	Mass Trans Coeff	0.007662
15	Gas Relative Permeability	0.007485
16	Specific Heat	0.007407
17	Number of Nodes	0.004198
18	Time Step	0.001466
19	Relative Humidity	0.000602
20	Thermal Cond	0.000237
21	Diffusivity	0.0000410

Table 45 – Sensitivity Coefficients for Input Parameters for CFB Drying

Rank	Parameter	Sensitivity Coefficient
1	Initial Saturation	2.1843
2	Radiant Heat Flux	1.0731
3	Surface Emissivity	1.0457
4	Length	0.87902
5	S_{ir}	0.78212
6	Porosity	0.64016
7	Liq. Rel. Perm.	0.50723
8	Initial Temp	0.4605
9	Ambient Temp	0.30732
10	Mass Trans Coeff	0.19309
11	Cap. Pressure	0.1686
12	Heat Trans Coeff	0.052083
13	Diffusivity	0.041623
14	Number of Nodes	0.036534
15	Permeability	0.031185
16	Specific Heat	0.010373
17	Density	0.010373
18	Time Step	0.00312
19	Thermal Cond.	0
20	Relative Humidity	0
21	Gas Rel. Perm.	0
22	Rel. Hum. Corr.	0

The sensitivity coefficients from Table 42 through and Table 45 are shown graphically in Figure 176 through Figure 179.

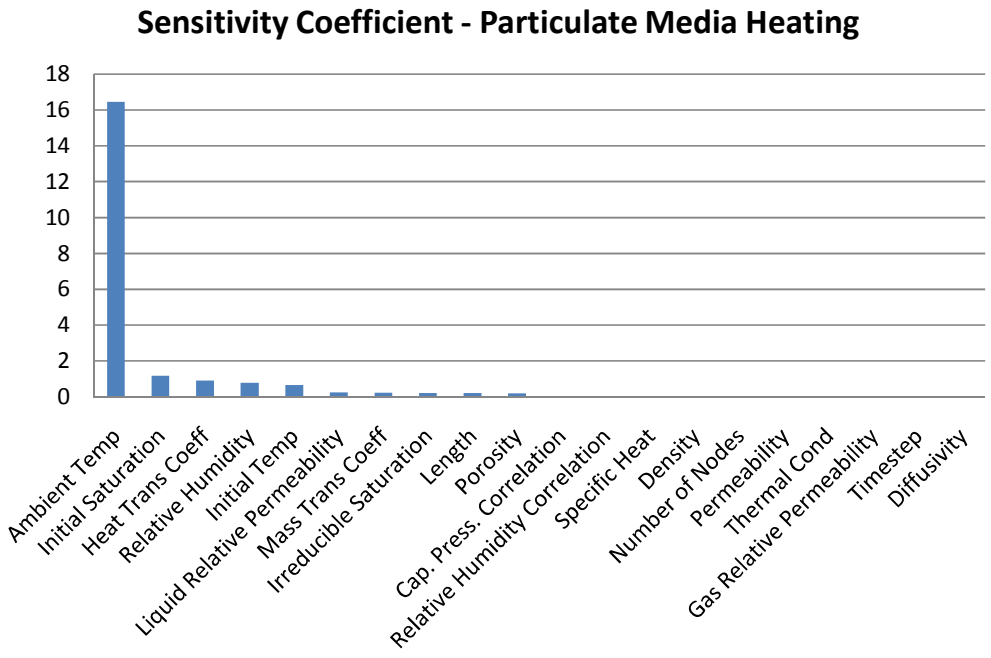

Figure 176 – Sensitivity Coefficients for Input Parameters for Particulate Media Drying

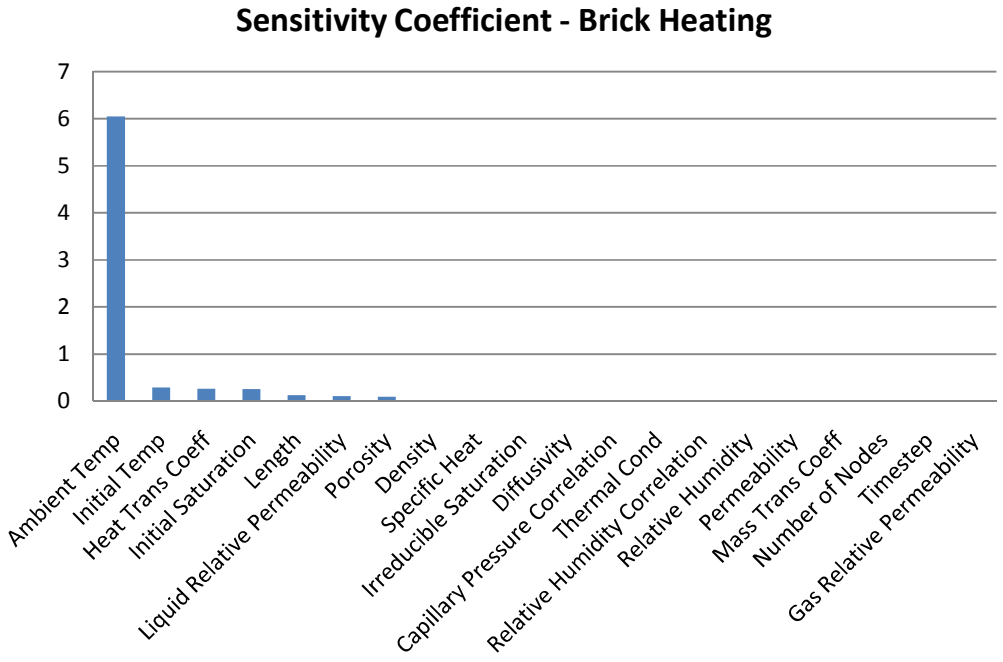

Figure 177 – Sensitivity Coefficients for Input Parameters for Brick Drying

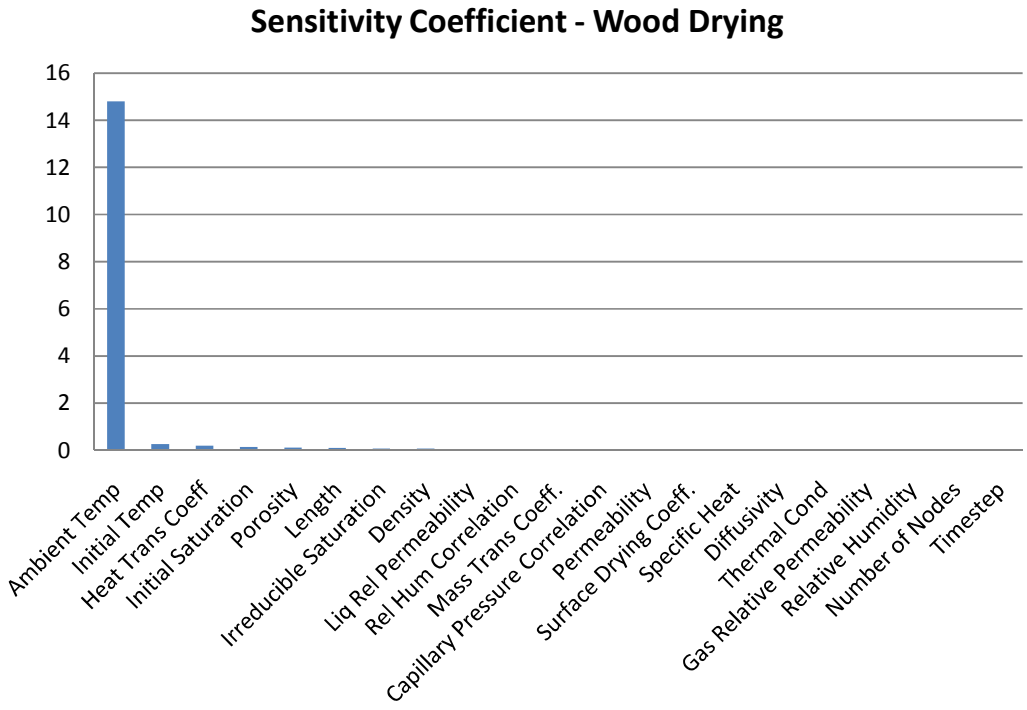

Figure 178 – Sensitivity Coefficients for Input Parameters for Wood Drying

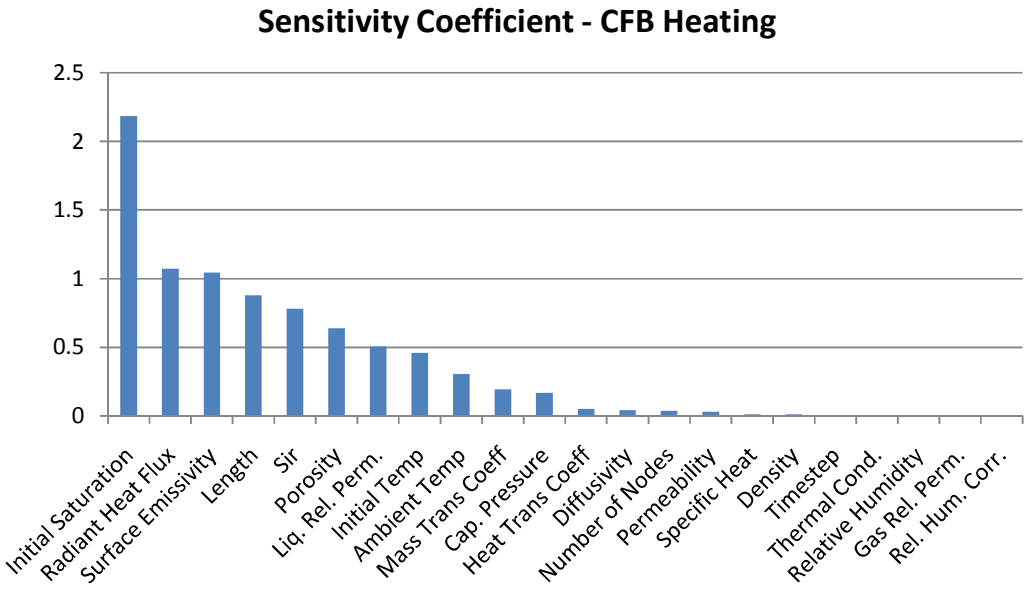

Figure 179 – Sensitivity Coefficients for CFB Drying

G.1. Details of CFB Wetting Sensitivity Analysis

The sensitivity of the model was tested for the case of wetting ceramic fiberboard. Two scenarios were tested. The first was for a type 1 boundary condition, where the surface was wetted completely. The second situation was for a spray wetting boundary condition.

G.1.1. Type 1 BC Wetting

In order to test the model sensitivity in a situation where the surface saturation boundary condition is specified, the following parameters were adjusted.

$S_{surf} - Surface\ saturation$

$S_o - Initial\ saturation$

$S_{ir} - Irreducible\ saturation$

$K - Permeability\left[m^2\right]$

$\phi - Porosity$

$L - Depth\ of\ sample\left[m\right]$

$n - Number\ of\ nodes$

$\Delta t - Timestep$

When possible, these parameters were adjusted by $\pm 10\%$ from their base value. Some parameters were adjusted by different amounts. The surface saturation was already close to 1 and could not be increased by very much, so it was adjusted by $\pm 1\%$. The values used are given in Table 46.

Table 46 – Parameters used for Type 1 Wetting Sensitivity Analysis

Parameter	Base Value	High Value	Low Value
Surface Saturation	0.99	0.999 (+1%)	0.98 (-1%)
Initial Saturation	0.004	0.0044 (+10%)	0.0036 (-10%)
Irreducible Saturation	0.15	0.165 (+10%)	0.135 (-10%)
Permeability	5×10^{-11}	5.5×10^{-11} (+10%)	4.5×10^{-11} (-10%)
Porosity	0.80	0.88 (+10%)	0.72 (-10%)
Diffusivity	2.6E-5	2.86E-5 (+10%)	2.34E-6 (-10%)
Depth of Sample	0.15	0.165(+10%)	0.135 (-10%)
Number of Nodes	31	36	26
Time Step	1	0.1	10

Other Parameters Tested

To determine the sensitivity of the model to several other constitutive relations, several of the correlations used in the model were tested as well. The correlations for relative permeabilities and capillary pressure were tested.

Relative Permeabilities

To determine the sensitivity of the model to the relative permeability correlation, two other correlations were used for both the liquid and gas relative permeabilities. The base case for each was a cubic function. A square function was used as the "high" value and a fourth order function was used as the "low" value. These correlations are shown in Figure 165. For the case of wetting CFB using a type 1 boundary condition at the surface, the model is shown to be very sensitive to the surface saturation, and liquid relative permeability. The model is also sensitive to the permeability, porosity, and gas relative permeability. This simulation is not very sensitive to the initial saturation, irreducible saturation, or depth of sample.

Capillary Pressure

The J-function correlation used for capillary pressure in the CFB is

$$J(S) = 0.4\left[0.364\left(1-\exp\left(-30\left(1-S\right)\right)\right)+0.471\left(1-S\right)+\frac{0.035}{S-0.1}\right]$$

The sensitivity of the model to each of the coefficients in this correlation was tested.

Table 47 – Capillary Pressure Coefficients for Sensitivity Analysis of CFB Wetting

Parameter	Base Value	+10%	-10%
1	0.4	0.44	0.36
2	0.364	0.4004	0.3276
3	-30	-33	-27
4	0.471	0.5181	0.4239
5	0.035	0.0385	0.0315
6	0.1	0.11	0.09

The results are shown in Figure 192 through Figure 197. The model results for CFB wetting with a type 1 BC are most sensitive parameters 1 and 2, and to a lesser degree, parameters 3 and 4. Adjusting parameters 5 and 6 did not have a significant effect.

Sensitivity Coefficient

The total area to the left of the water penetration depth curve was integrated to give a quantitative measure of the effect of changing each parameter. This was done numerically using the trapezoidal rule.

$$Z_{sum} = \sum_{i=1}^{nt} \left(t_i + t_{i+1} \right) \Delta z \qquad \text{(units meter * seconds)}$$

Where z_i is the depth of water penetration at time step i. The integrated value was used to calculate a sensitivity coefficient for each parameter x_i

$$S_i = \frac{x_i}{Z_{sum}} \frac{\Delta Z_{sum}}{\Delta x_i}$$

The sensitivity coefficient was calculated for each parameter for the cases of Type 1 BC wetting, and spray wetting. It was calculated for the “high” and “low” cases of each parameter. The total integrated area under the infiltration depth/time curve for each adjusted parameter is shown in Table 48.

Table 48 – Results of Sensitivity Analysis of CFB Wetting

Parameter	Total (high)	Change	Total (low)	Change
Surface Saturation	2.4568	-0.42802	3.3816	0.49678
Initial Saturation	2.8809	-0.00393	2.8976	0.012825
Permeability	2.7197	-0.16512	3.0777	0.19288
Porosity	3.0596	0.1748	2.703	-0.18185
Liq Rel Permeability	3.2783	0.3935	2.3527	-0.53215
Gas Rel Permeability	2.9543	0.0695	2.796	-0.0888
Cap Press Coeff 1	2.6803	-0.20455	3.1236	0.23875
Cap Press Coeff 2	2.7512	-0.1336	3.0331	0.14825
Cap Press Coeff 3	2.9103	0.025475	2.862	-0.02278
Cap Press Coeff 4	2.8191	-0.06575	2.9533	0.0685
Cap Press Coeff 5	2.872	-0.01278	2.8976	0.01275
Cap Press Coeff 6	2.8799	-0.00495	2.8895	0.004725
Irreducible Saturation	2.9117	0.026925	2.8576	-0.02723
Sample Length	2.8617	-0.02307	2.9058	0.020963
Number of Nodes	2.6846	-0.20025	2.9857	0.10091
Time step	2.8786	-0.0062	2.8862	0.0014
Diffusivity	2.8847	-0.00013	2.8851	0.00025

Table 49 – Sensitivity Coefficient Rankings for CFB Wetting

Rank	Parameter	Sensitivity Coefficient
1	Surface Saturation	17.05
2	Cap Press Coeff 1	0.82761
3	Permeability	0.66859
4	Porosity	0.63037
5	Liq Rel Permeability	0.55899
6	Cap Press Coeff 2	0.5139
7	Cap Press Coeff 4	0.23745
8	Number of Nodes	0.21491
9	Irreducible Saturation	0.094374
10	Gas Rel Permeability	0.093279
11	Cap Press Coeff 3	0.088308
12	Sample Length	0.07998
13	Initial Saturation	0.044457
14	Cap Press Coeff 5	0.044284
15	Cap Press Coeff 6	0.017159
16	Time step	0.002387
17	Diffusivity	0.000867

Surface Saturation

The surface saturation was initially 0.99 for the base case. This is due to the fact that the wetting fluid (water) will not penetrate all of the very small pores and displace all of the non-wetting fluid (air). Adjusting this value, even a small amount, had a significant effect on the rate of infiltration. The results are shown in Figure 180.

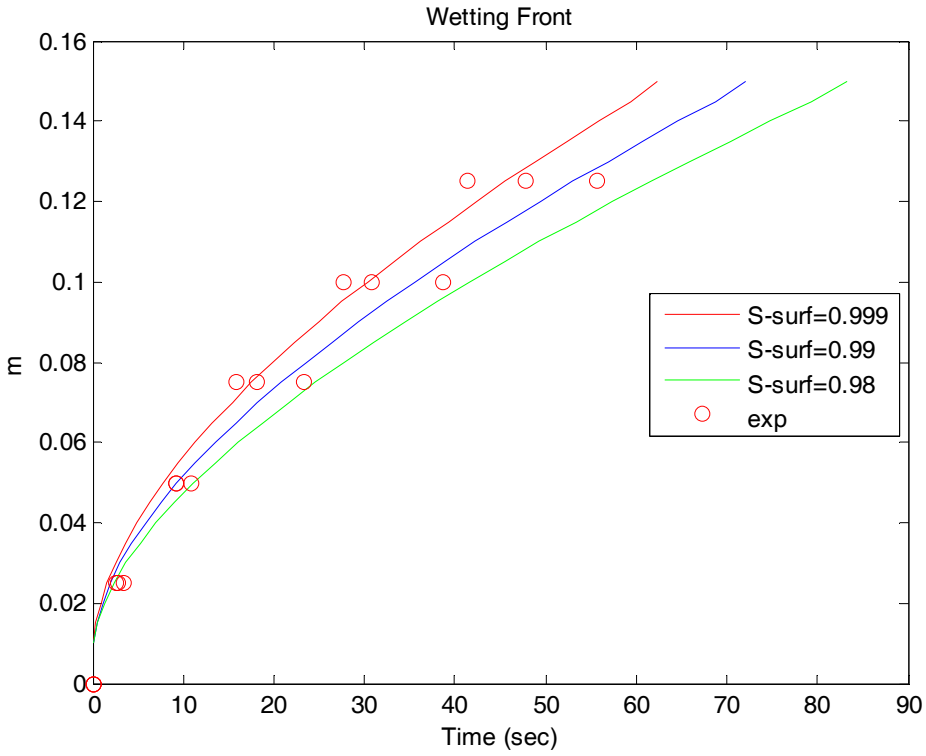

Figure 180 – Effect of Surface Saturation Value on Infiltration

Initial Saturation

The initial water saturation was calculated to be 0.004 from the vapor pressure correlation. Adjusting this value did not seem to have a significant effect on the depth of water penetration. The results are shown in Figure 181.

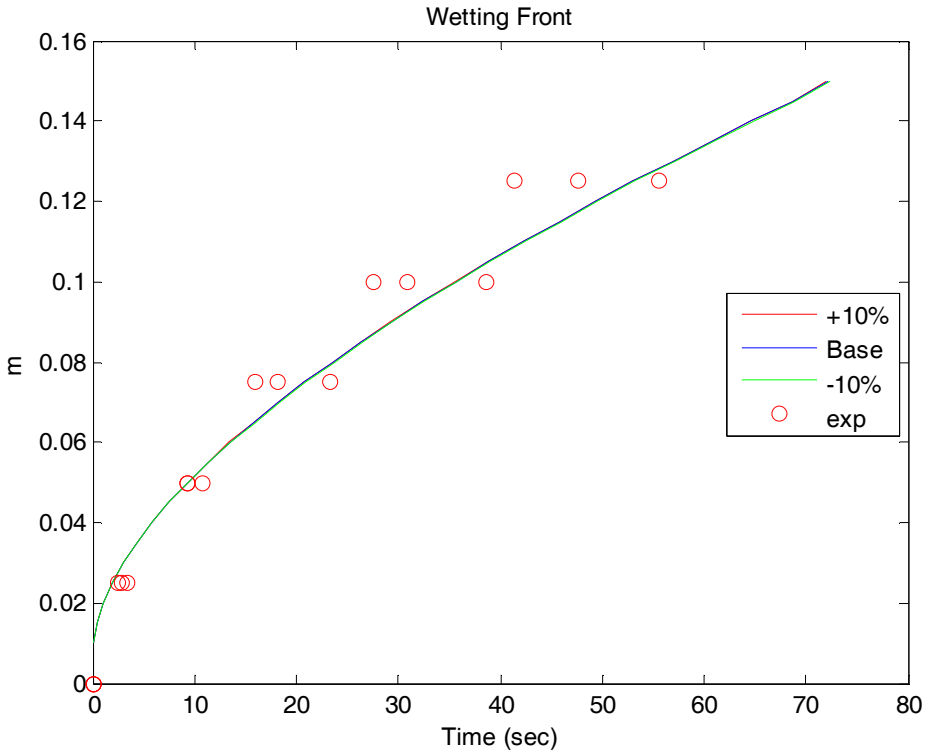

Figure 181 - Effect of Adjusting the Initial Saturation

Irreducible Saturation

The irreducible saturation was adjusted by ±10% from its base value of 0.15. This did not have a significant effect on the rate of water absorption, as shown in Figure 182.

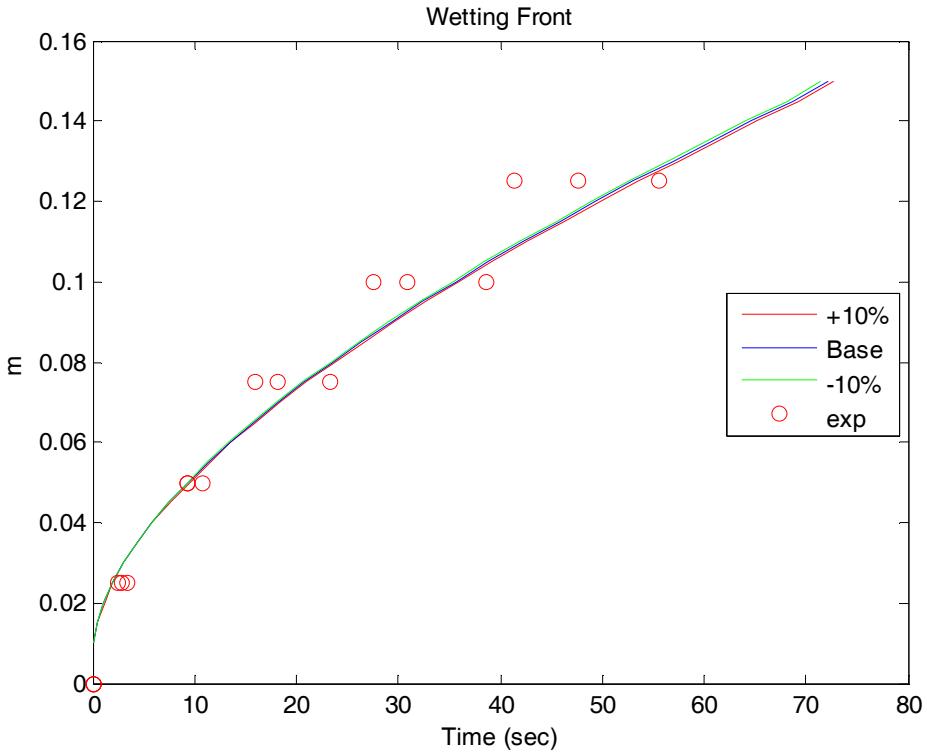

Figure 182 – Effect of Irreducible Saturation on Water Absorption into CFB

Permeability

The permeability was adjusted by ±10%. This had a significant effect on the depth of water penetration. The results are shown in Figure 183. Increasing the permeability had the effect of increasing the depth of water penetration into the material.

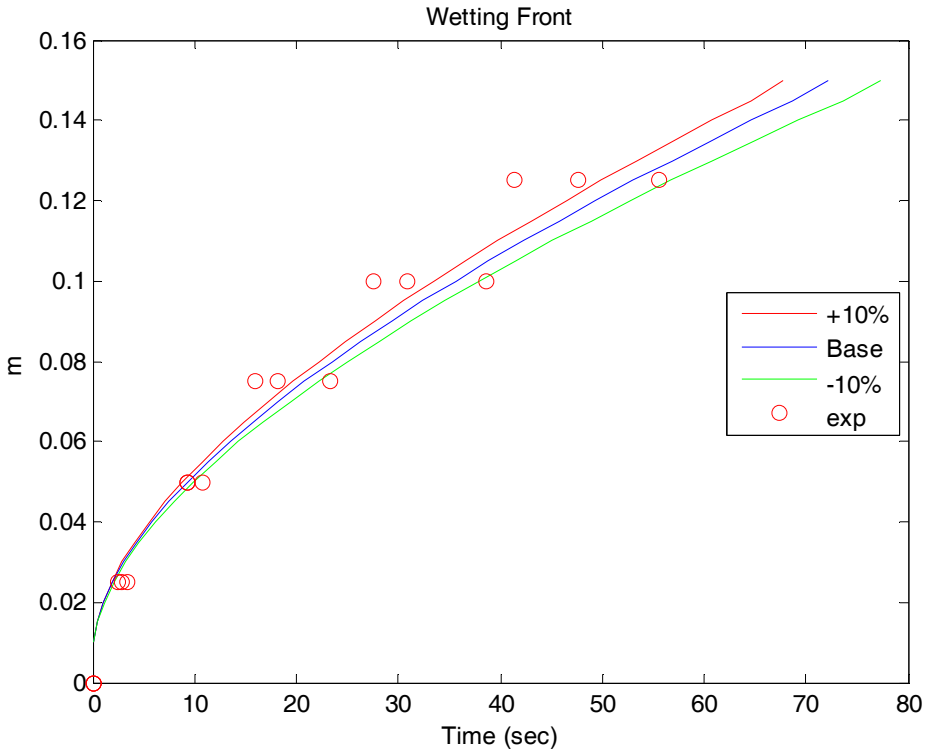

Figure 183 – Effect of Permeability on Infiltration

Porosity

The porosity was adjusted by ±10%. This had a significant effect on the depth of penetration. The results are shown in Figure 184. Increasing the porosity had the effect of decreasing the depth of water penetration.

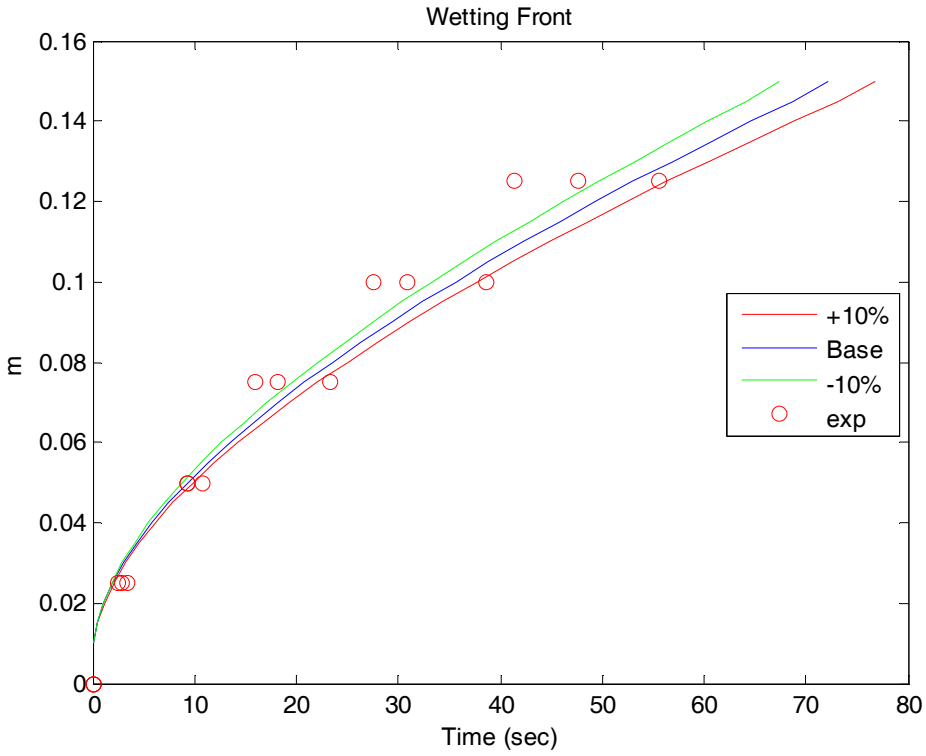

Figure 184 - Effect of Porosity on Infiltration

It can be shown that this also has an effect on the total mass of water absorbed, as shown in Figure 185. Increasing the porosity increased the total mass of water absorbed into the material, while decreasing the porosity decreased the total mass of water absorbed.

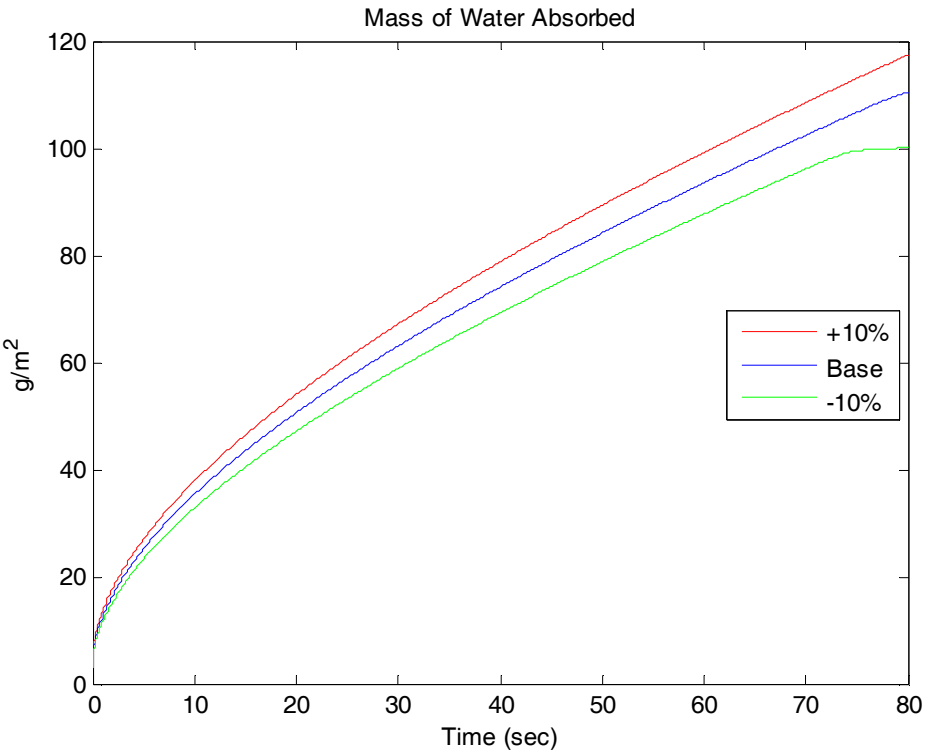

Figure 185 – Effect of Porosity on Total Mass of Water Absorbed into CFB – Type 1 BC

Diffusivity

The gas diffusivity was adjusted $\pm 10\%$ from its base value of $2.6\times10^{-5} m^2 / s$. This did not have a significant effect on the rate of water absorption into CFB, as shown in Figure 186.

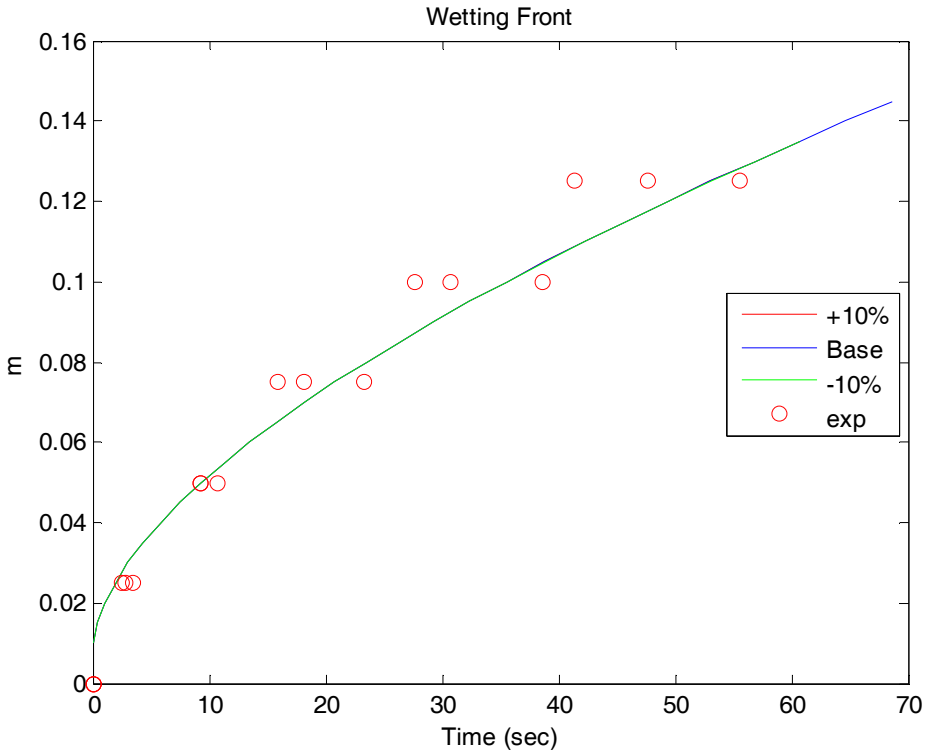

Figure 186 – Effect of Diffusivity on CFB Wetting

Depth of Sample

The depth of the sample was adjusted ±10% from its base value of 0.15 m. This had very little effect on the depth of water penetration, as shown in Figure 187.

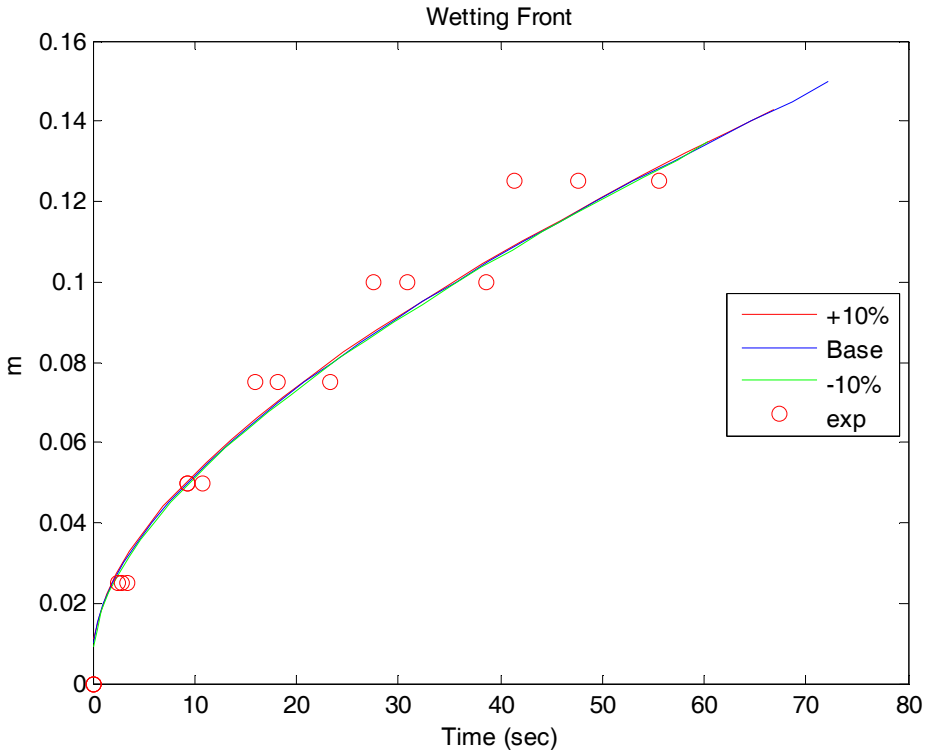

Figure 187 – Effect of Sample Depth on CFB Wetting

Number of Nodes

The number of nodes was adjusted from its base value of 31, up to a "high" value of 41, and down to a "low" value of 21. This had a small effect, as shown in Figure 188.

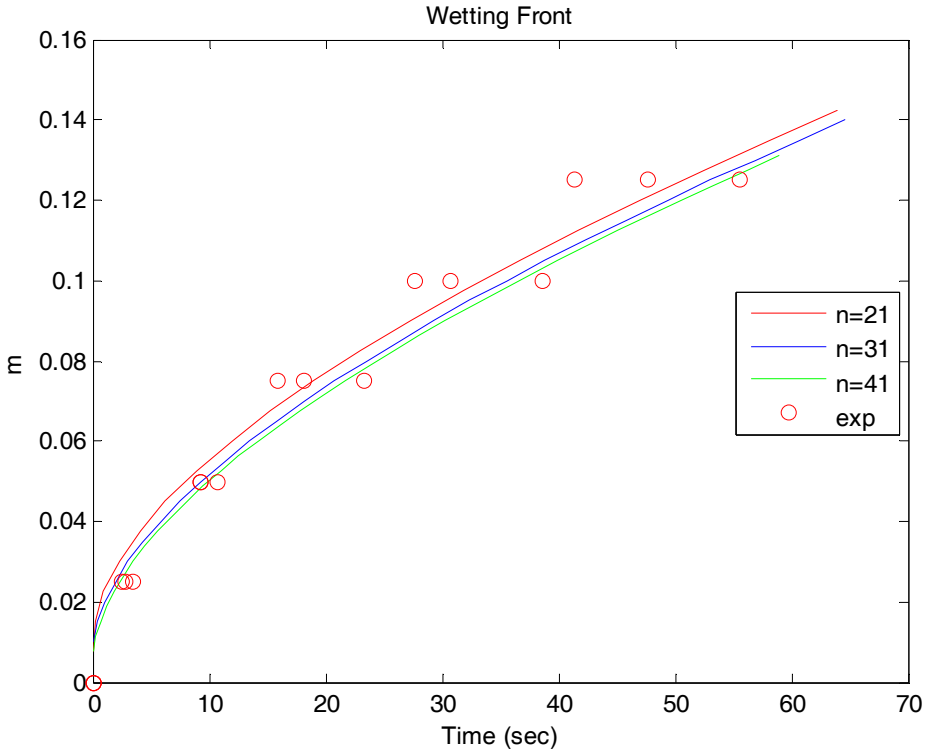

Figure 188 – Effect of Number of Nodes on CFB Wetting

Time Step

The time step was adjusted from its base value of 0.01 seconds to a "high" value of 0.04 seconds and down to a "low" value of 0.001 seconds. Increasing the time step above 0.04 seconds caused the model to crash. Aside from the stability issue associated with the time step, adjusting it did not have a noticeable effect on the model predictions, as shown in Figure 189.

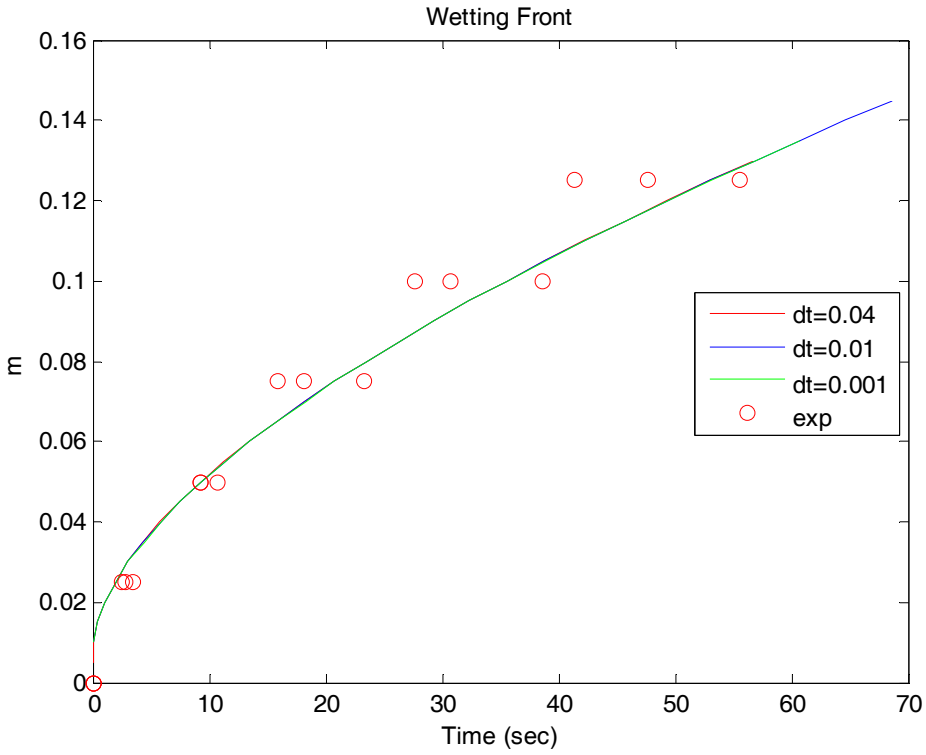

Figure 189 – Effect of Timestep on CFB Wetting

Liquid Relative Permeability

Adjusting the liquid relative permeability had a significant effect on the depth of water penetration. The results are shown in Figure 190. This shows that higher order power law functions have lower rates of water penetration.

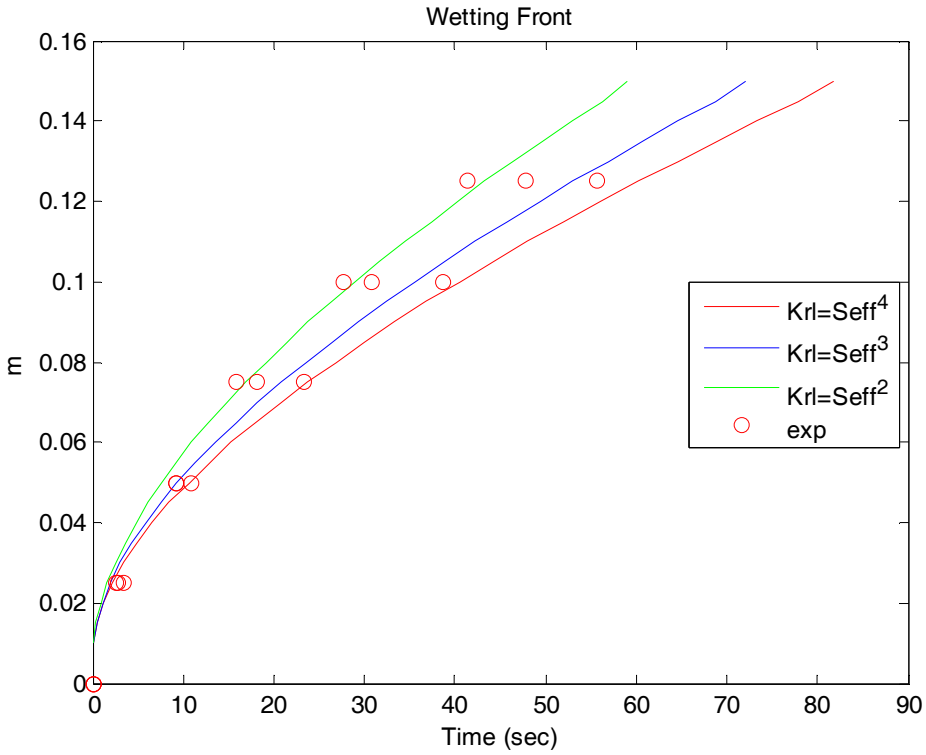

Figure 190 - Effect of Liquid Relative Permeability on CFB Wetting

Gas Relative Permeability

Adjusting the gas relative permeability had a significant effect on the rate of water penetration. The results are shown in Figure 191. The same trend was observed as in the liquid relative permeability. Higher order power law functions tend to decrease the rate of water penetration.

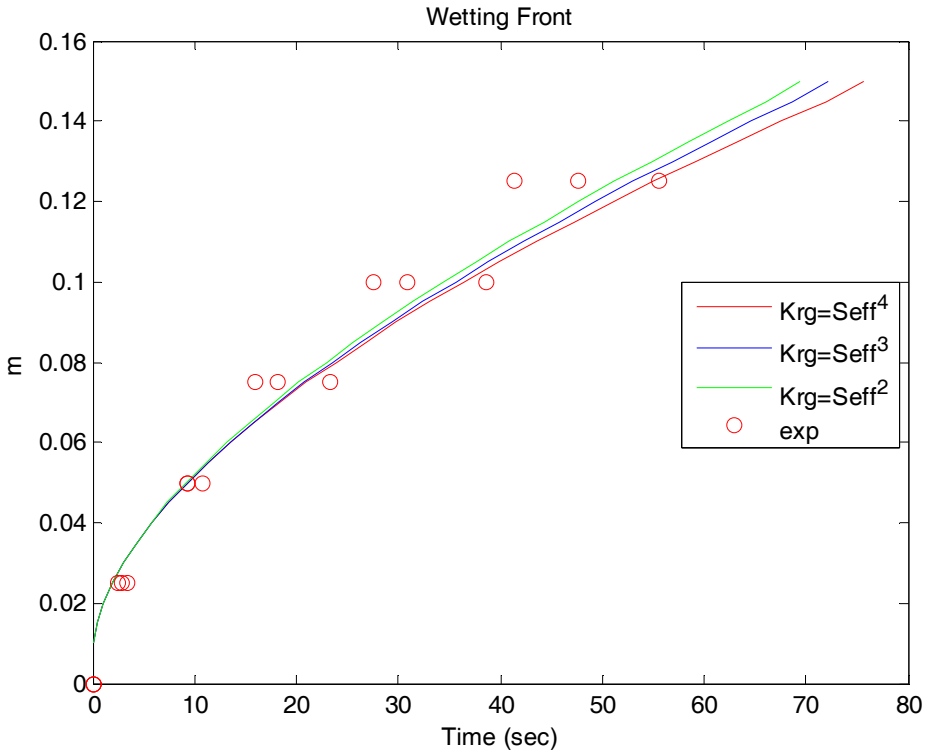

Figure 191 – Effect of Gas Relative Permeability on CFB Wetting

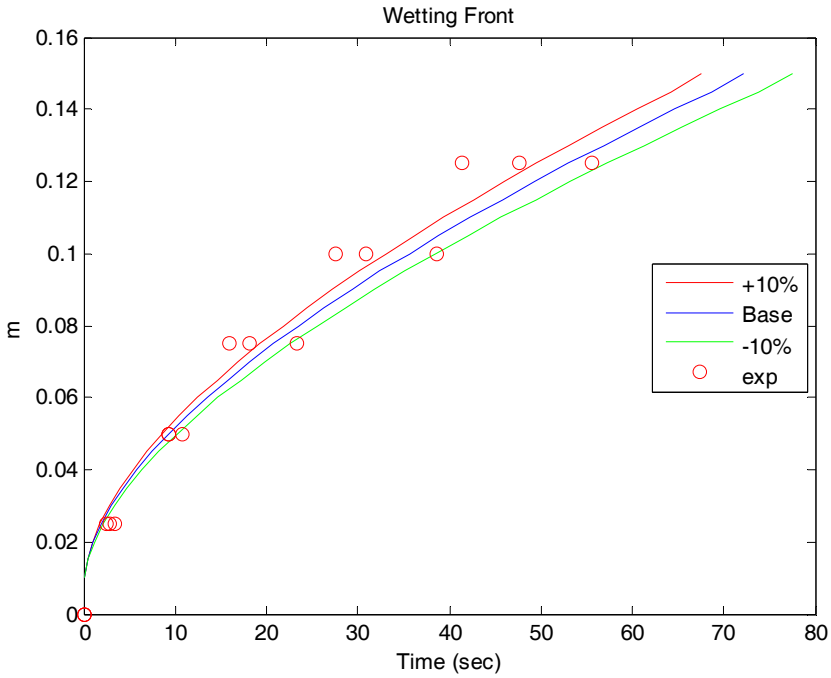

Figure 192 – Effect of J-Function Coefficient 1

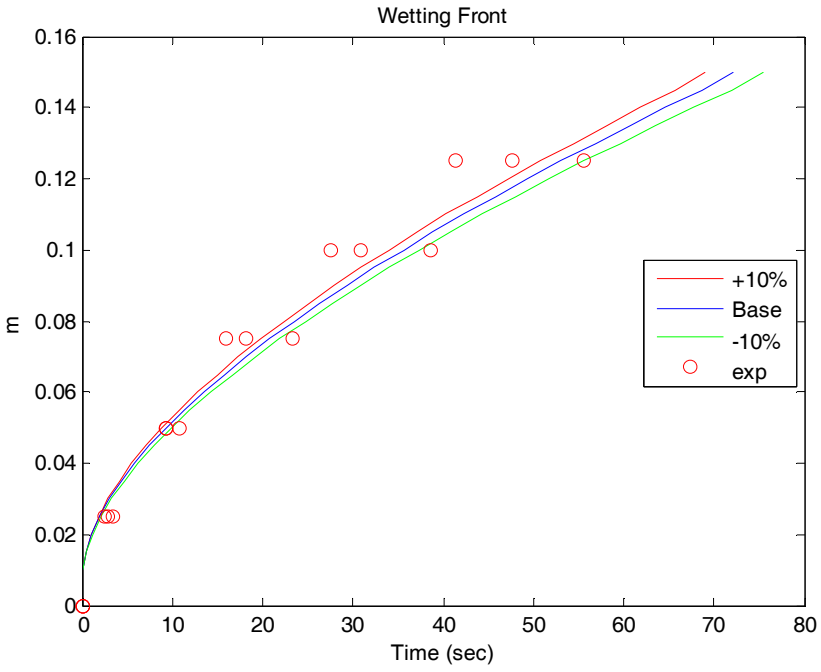

Figure 193 - Effect of J-Function Coefficient 2

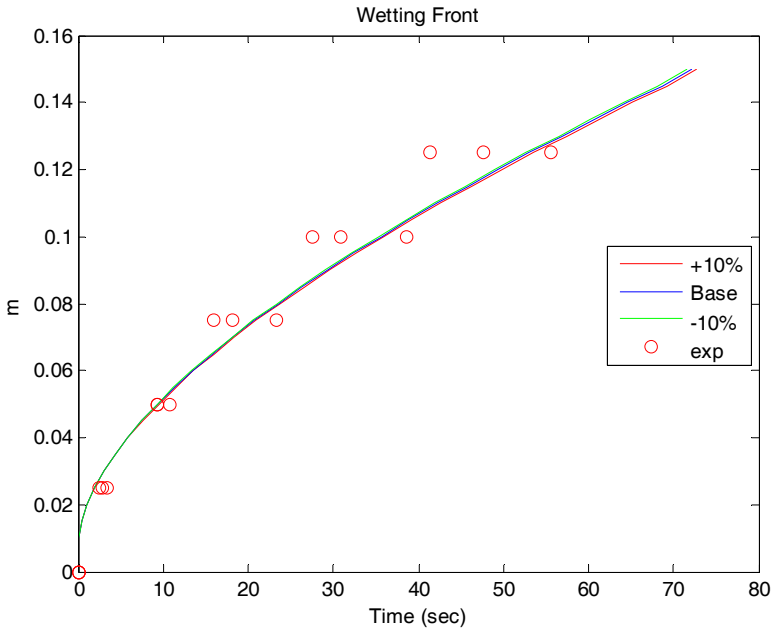

Figure 194 - Effect of J-Function Coefficient 3

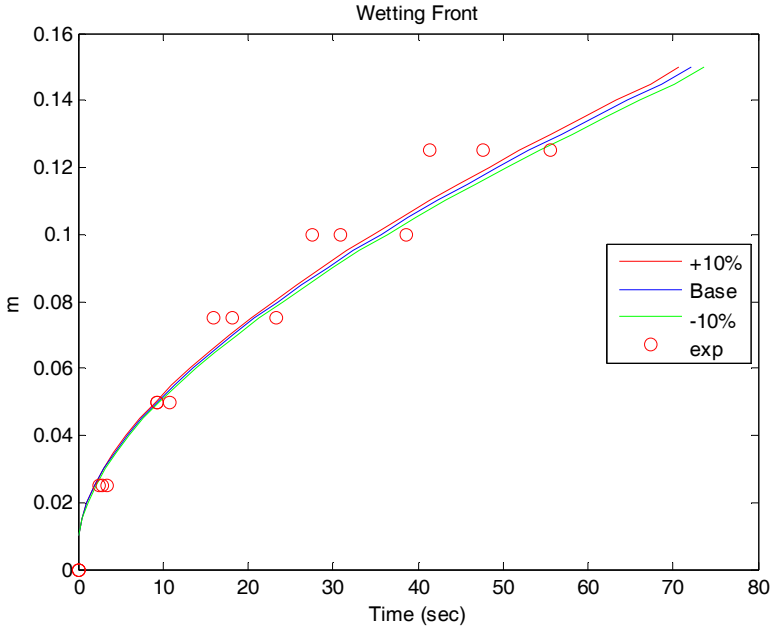

Figure 195 - Effect of J-Function Coefficient 4

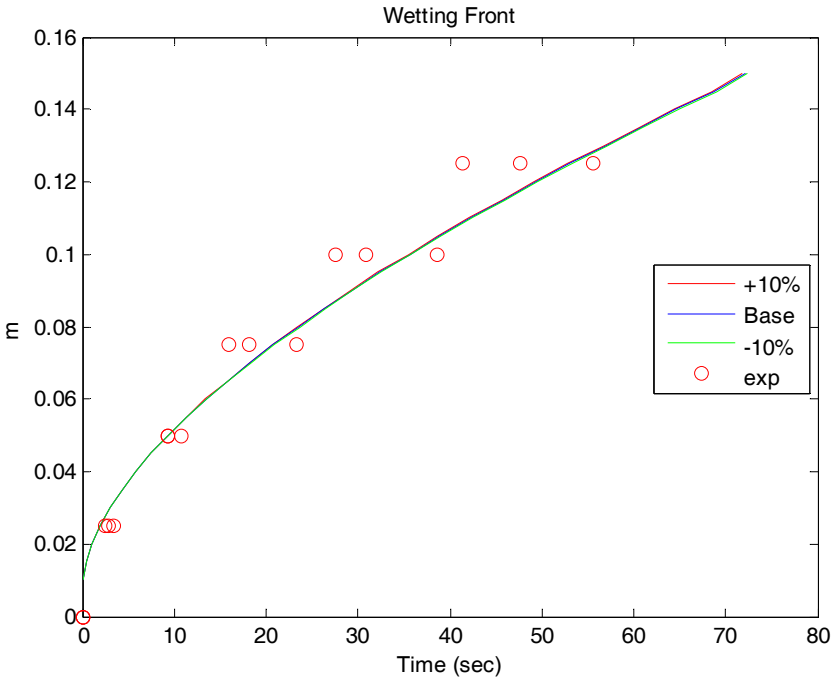

Figure 196 - Effect of J-Function Coefficient 5

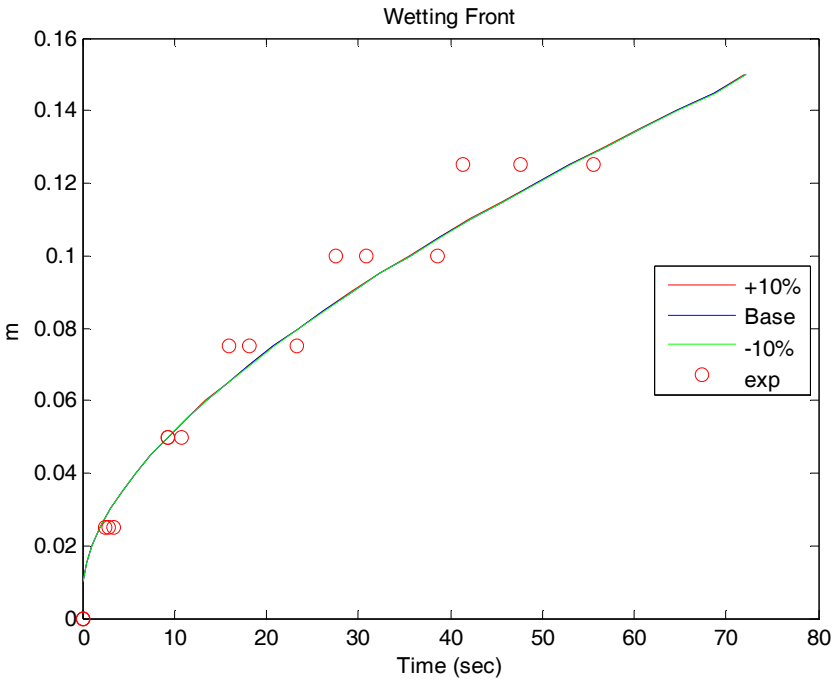

Figure 197 - Effect of J-Function Coefficient 6

G.1.2. Spray Wetting Sensitivity Analysis

Flux Boundary Condition

To test the sensitivity of the model during a spray wetting scenario, several parameters were adjusted one at a time. The parameters that were adjusted are

$\dot{m}''_{spray} - Water\ mass\ flux \left[\frac{kg}{m^2 s} \right]$

$S_o - Initial\ saturation$

$S_{ir} = Irreducible\ saturation$

$K - Permeability \left[m^2 \right]$

$\phi - Porosity$

$D_{va} = Vapor\ mass\ diffusivity\ in\ air \left[\frac{m^2}{s} \right]$

$L - Depth\ of\ sample \left[m \right]$

$n = number\ of\ nodes$

$\Delta t = time\ step$

Thermal properties were found to have very little effect on the infiltration process. When possible values chosen for examination were adjusted $\pm 10\%$. To investigate the effect of numerical parameters, the time step and node spacing were adjusted as well. The values of the parameters are shown in Table 25. In addition to these parameters, three additional correlations were tested. The relative permeability for liquid and gas, and the capillary pressure were adjusted in the same manner as for the CFB wetting using a Type 1 BC . The results of adjusting the parameters in Table 25 and the three additional correlations are shown in Figure 198 through Figure 214. The model showed the greatest sensitivity to the water mass flux, porosity, and liquid relative permeability. To a much lesser degree the model exhibited some sensitivity to permeability. The model did not exhibit a significant sensitivity to the initial saturation, diffusivity, depth of sample, number of nodes, and time step.

Sensitivity Coefficient

The baseline value for the case of spray wetting was 35.4 ms. The values of this quantity for each of the cases where an input parameter was adjusted are shown in

Table 28. The sensitivity coefficients for the parameters adjusted are shown in Table 29 in order of most sensitive to least sensitive. The maximum absolute value of the change from the “high” and “low” cases was chosen to represent each parameter.

Water Flux

The water flux was adjusted ±10% from its base value. This has a significant effect on the depth of water penetration, as shown in Figure 198.

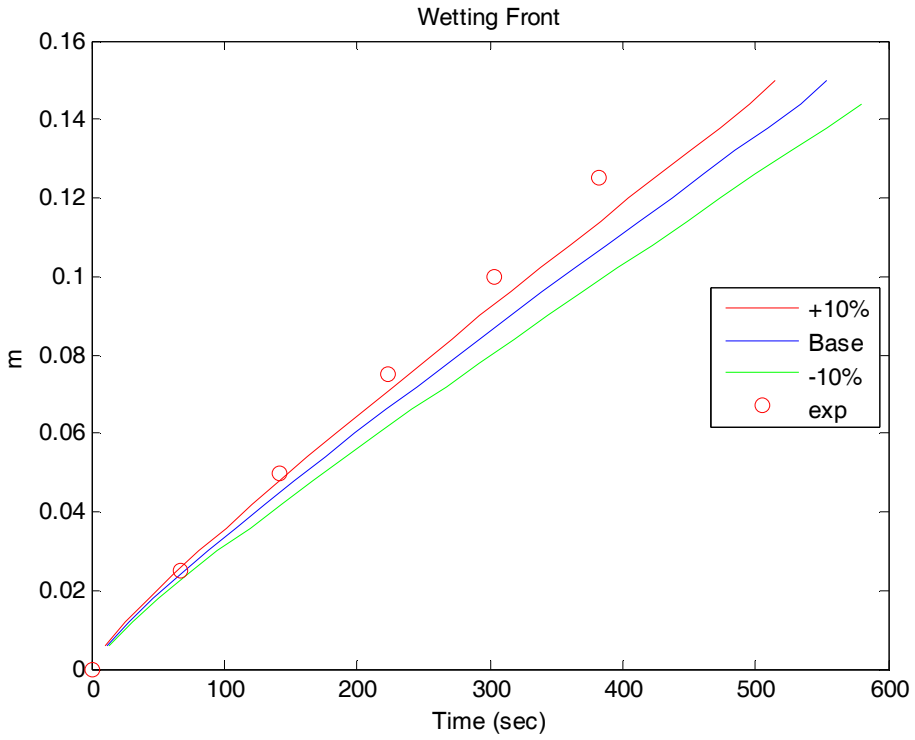

Figure 198 - Effect of Adjusting the Water Flux on Spray Wetting

Initial Saturation

The initial water saturation was adjusted ±10% from its base value. This did not have a significant effect on the depth of water penetration, as shown in Figure 199.

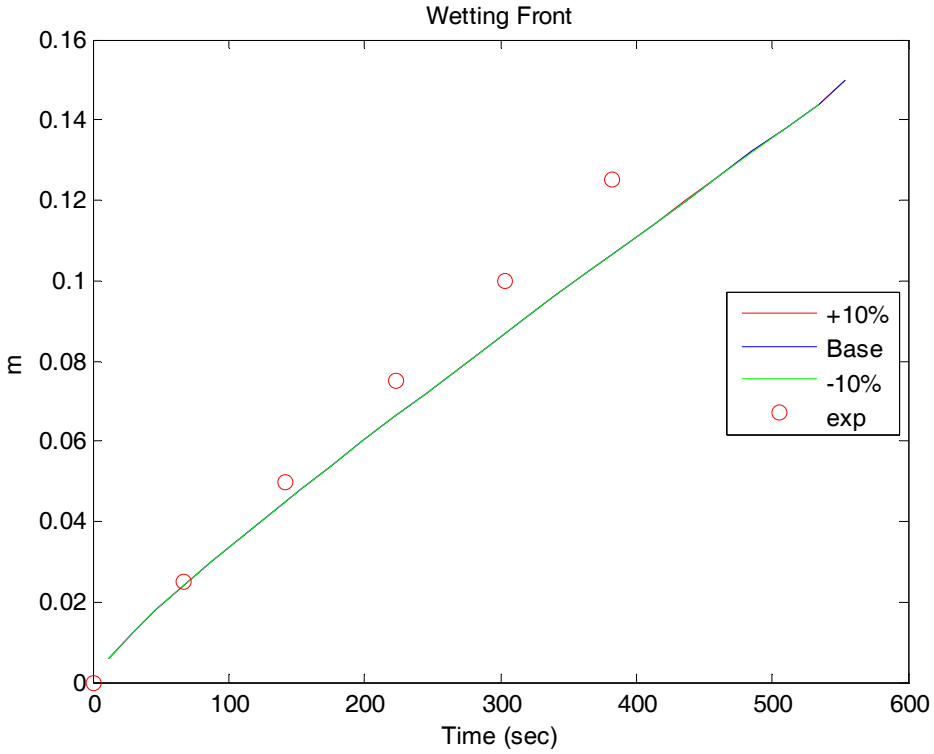

Figure 199 - Effect of Adjusting the Initial Saturation on Spray Wetting

Permeability

The permeability was adjusted ±10% from its base value. This had a slight effect on the depth of water penetration, as shown in Figure 200.

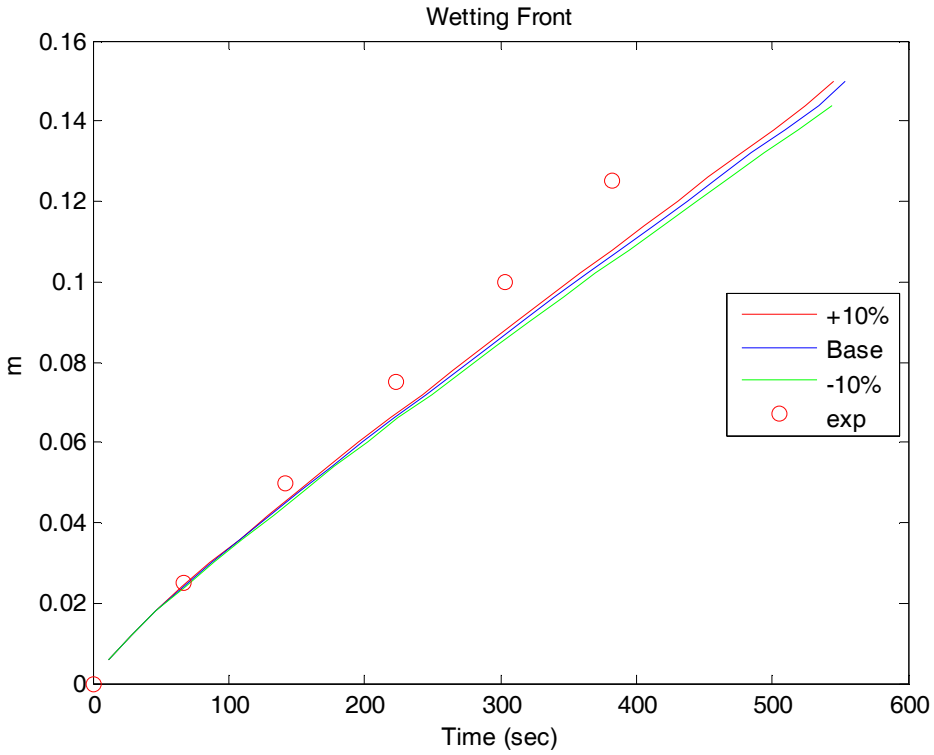

Figure 200 - Effect of Adjusting the Permeability on Spray Wetting

Porosity

The porosity was adjusted ±10% from its base value. This had a very significant effect on the depth of water penetration, as shown in Figure 201. Increasing the porosity decreased the depth of water penetration, while decreasing the porosity increased the depth of water penetration.

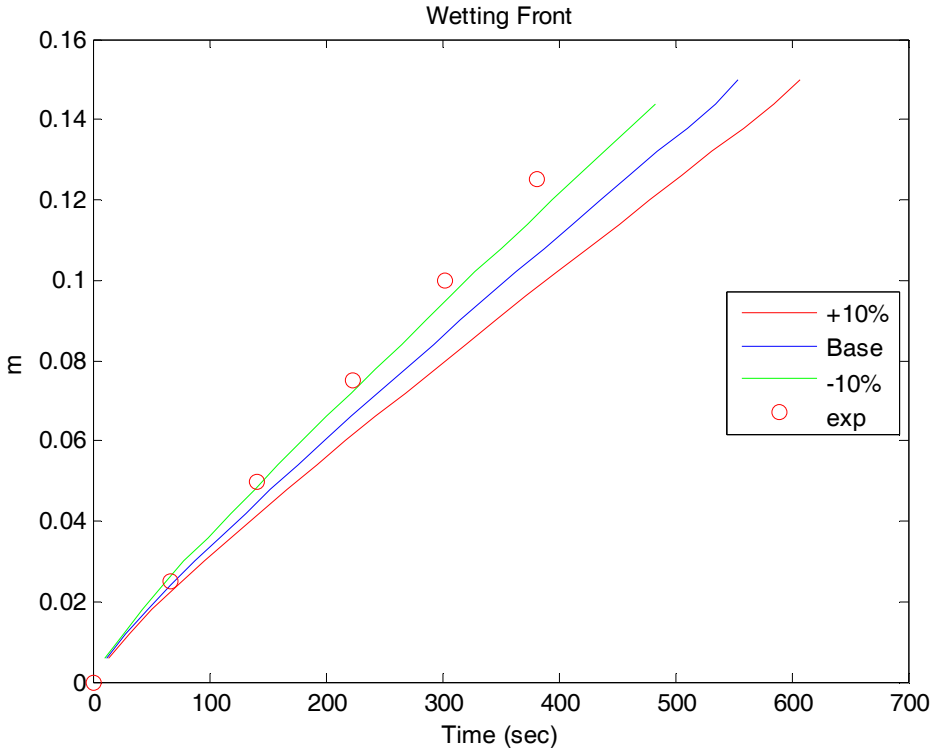

Figure 201 – Effect of Adjusting the Porosity on Spray Wetting

Irreducible Saturation

The irreducible saturation was adjusted ±10% from its baseline value of 0.15. This had a significant effect on the depth of water penetration as shown in Figure 202.

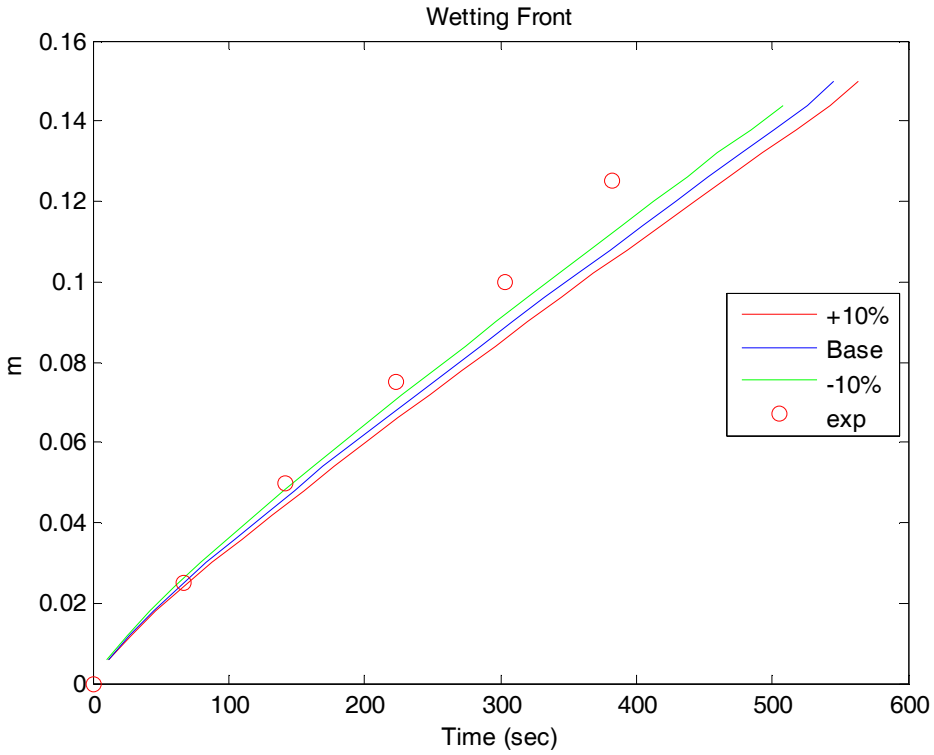

Figure 202 – Effect of Adjusting the Irreducible Saturation on Spray Wetting

Sample Depth

The sample depth was adjusted ±10% from its base value. This did not have a significant effect on the depth of water penetration, as shown in Figure 203.

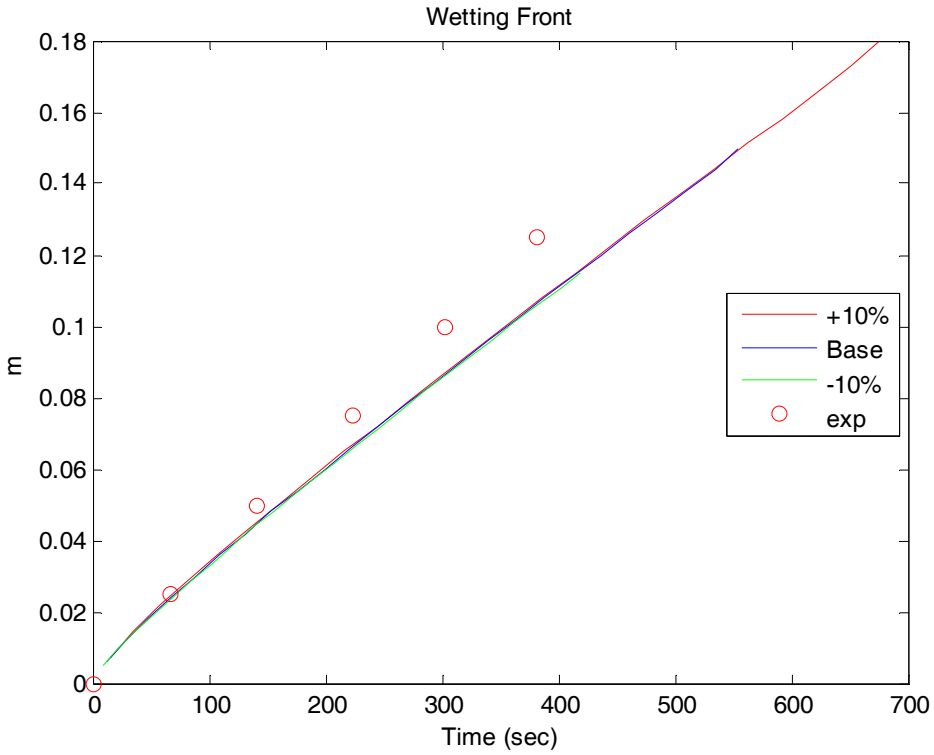

Figure 203 - Effect of Adjusting the Depth of the Sample on Spray Wetting

Diffusivity

The diffusivity was adjusted ±10% from its base value. This did not have a significant effect on the depth of water penetration, as shown in Figure 204.

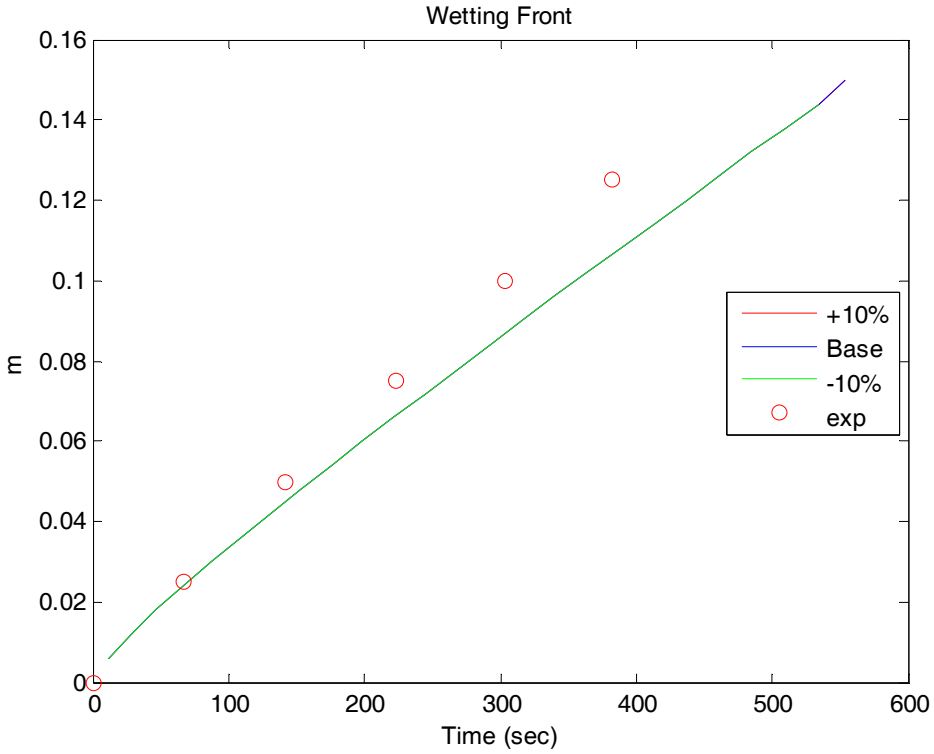

Figure 204 – Effect of Adjusting the Gas Phase Diffusivity on Spray Wetting

Number of Nodes

The number of nodes was adjusted from its base value of 31 to a high value of 36 and a low value of 26. This did not have a significant effect on the depth of water penetration, as shown in Figure 205.

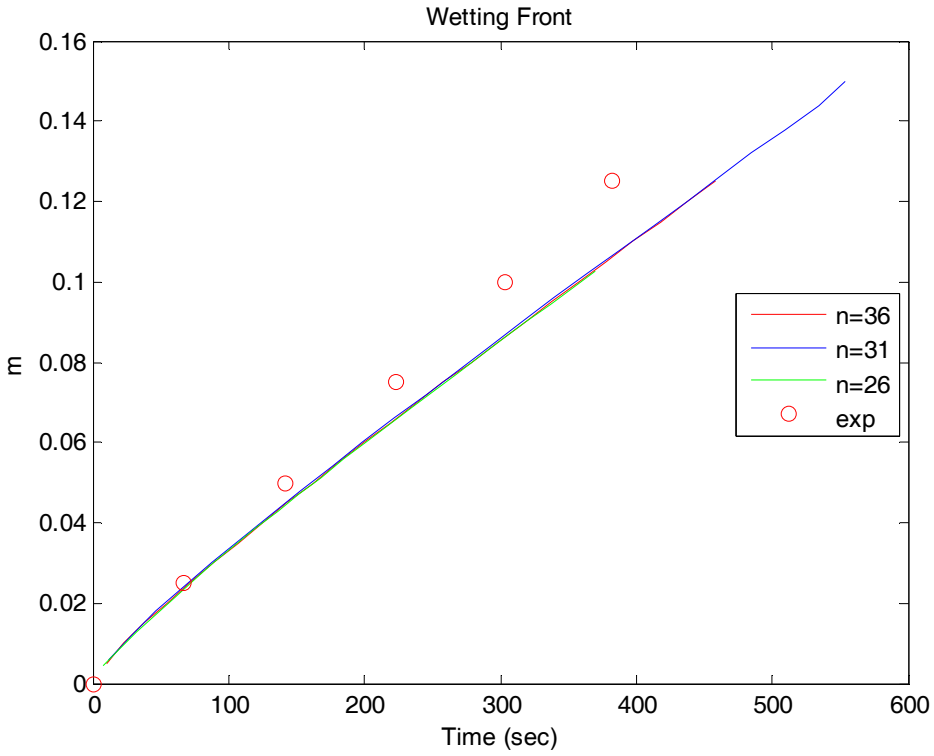

Figure 205 – Effect of Number of Nodes on Spray Wetting

Time Step

The time step was adjusted from its base value of 1 second, to a high value of 10 seconds and a low value of 0.1 seconds. This did not have a significant effect on the predicted depth of water penetration, as shown in Figure 206.

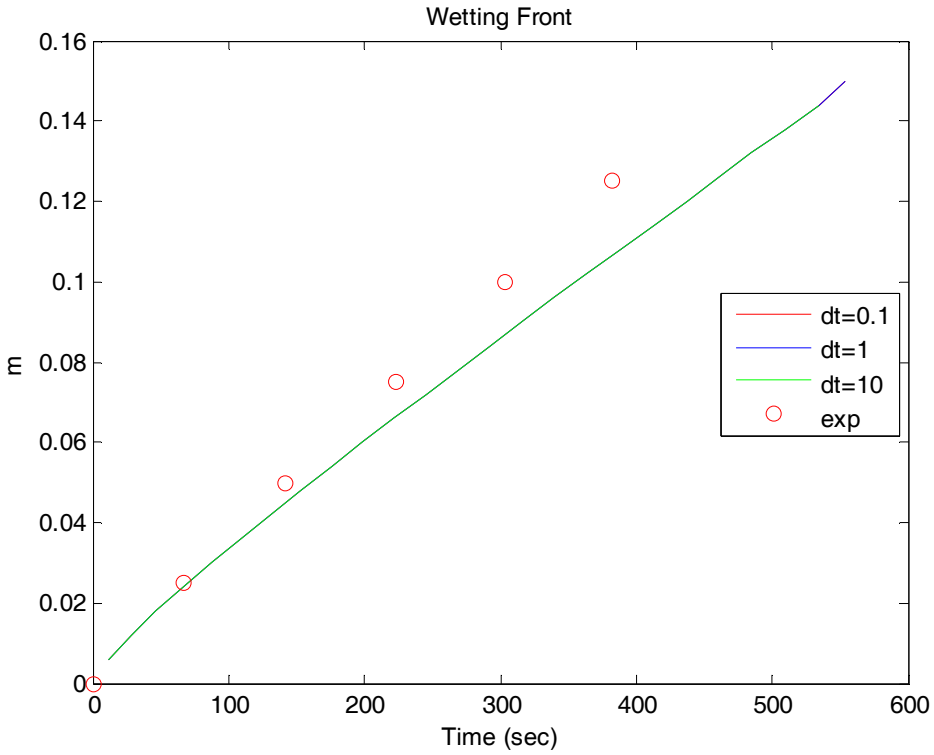

Figure 206 - Effect of Adjusting the Timestep on Spray Wetting

Liquid Relative Permeability

Using different correlations for relative permeability had a significant effect on the depth of water penetration into the material. Using a square function increased the rate of water penetration significantly, while using a fourth power function decreased the rate of water penetration. The results are shown in Figure 207.

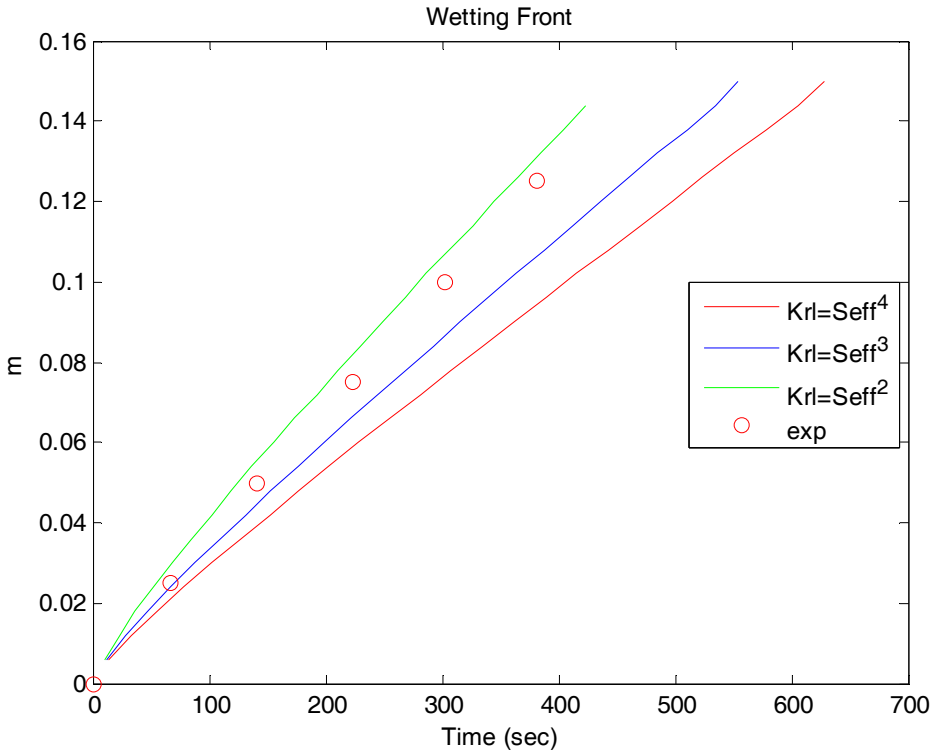

Figure 207 - Effect of Adjusting the Liquid Relative Permeability

Gas Relative Permeability

Using different correlations for gas relative permeability did not have a significant effect on the spray wetting process. The results are shown in Figure 208.

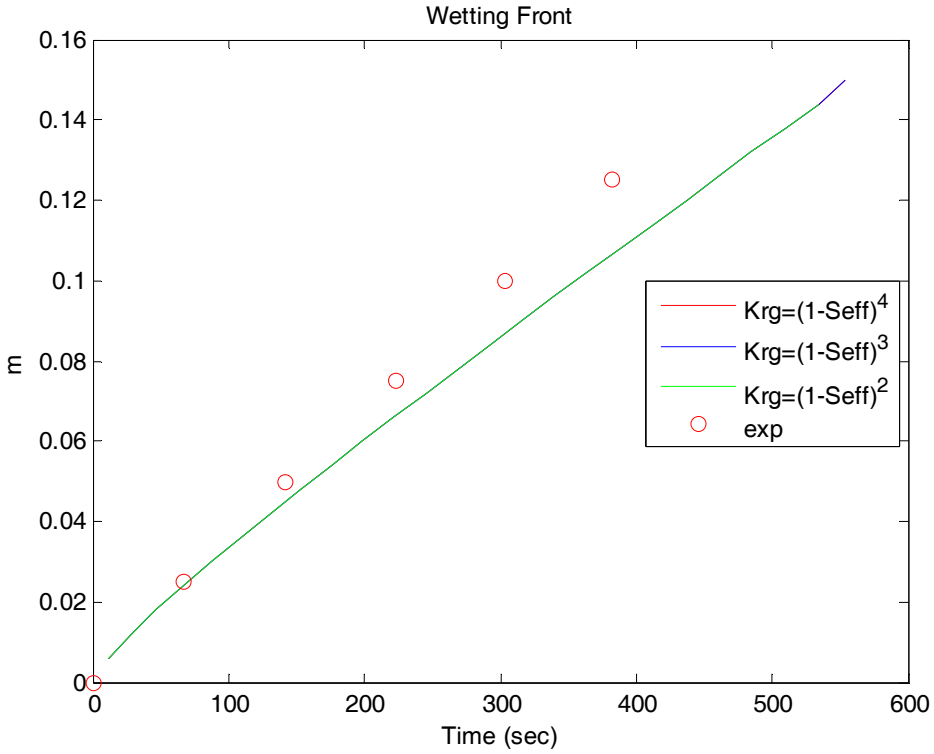

Figure 208 - Effect of Adjusting the Gas Relative Permeability

Capillary Pressure

The same 6 coefficients of the J-Function that were adjusted in the first wetting sensitivity analysis were adjusted for the spray wetting scenario. Each coefficient was adjusted $\pm 10\%$. The results are shown in Figure 209 through Figure 214. The model exhibited a slight sensitivity to coefficients 1 and 4, and very little sensitivity to coefficients 2, 3, 5, and 6. Overall, the model does not appear to be nearly as sensitive to the J-Function correlation as it is to the water mass flux, porosity, and liquid relative permeability.

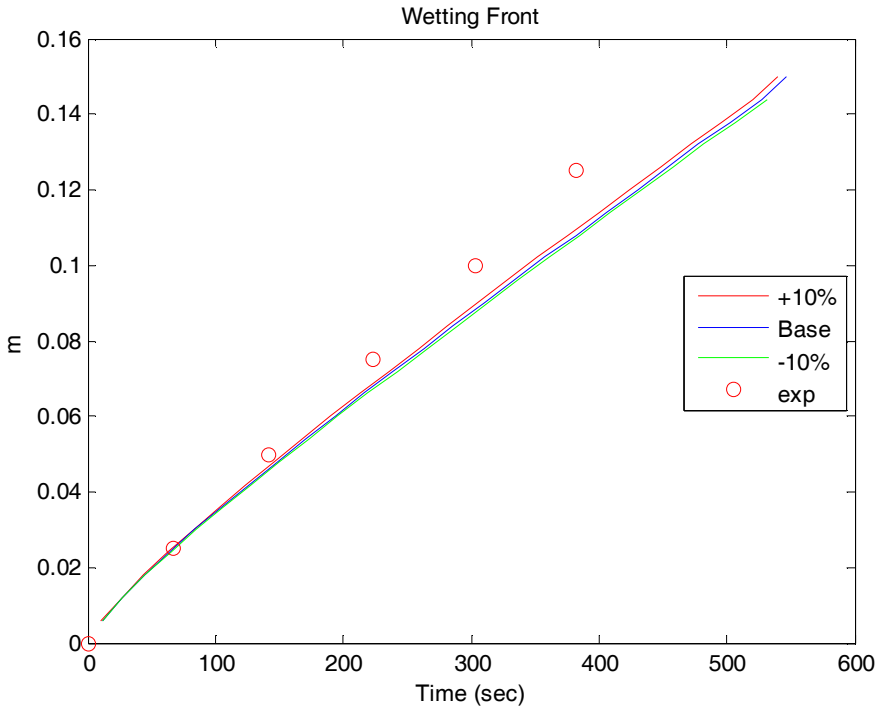

Figure 209 – Effect of J-Function Coefficient 1 on Spray Wetting of CFB

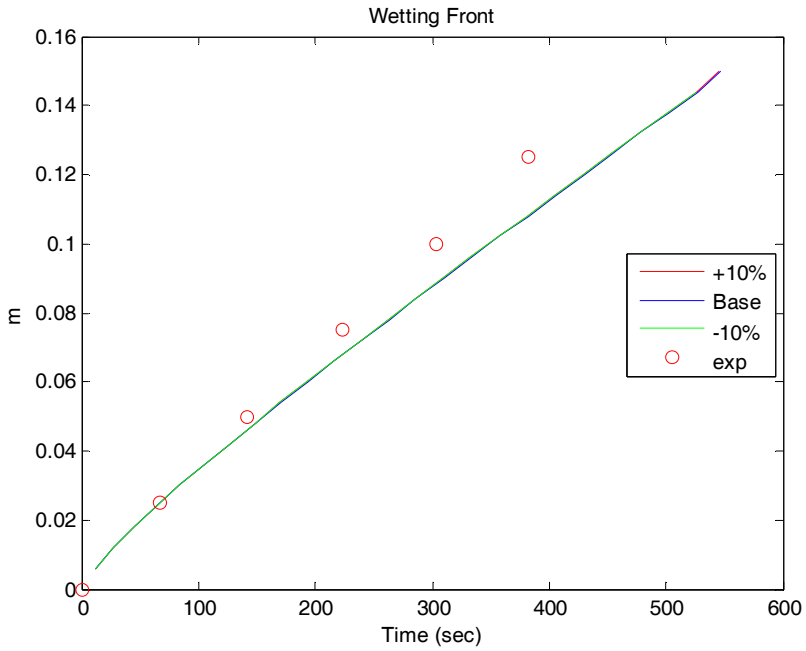

Figure 210 – Effect of J-Function Coefficient 2 on Spray Wetting of CFB

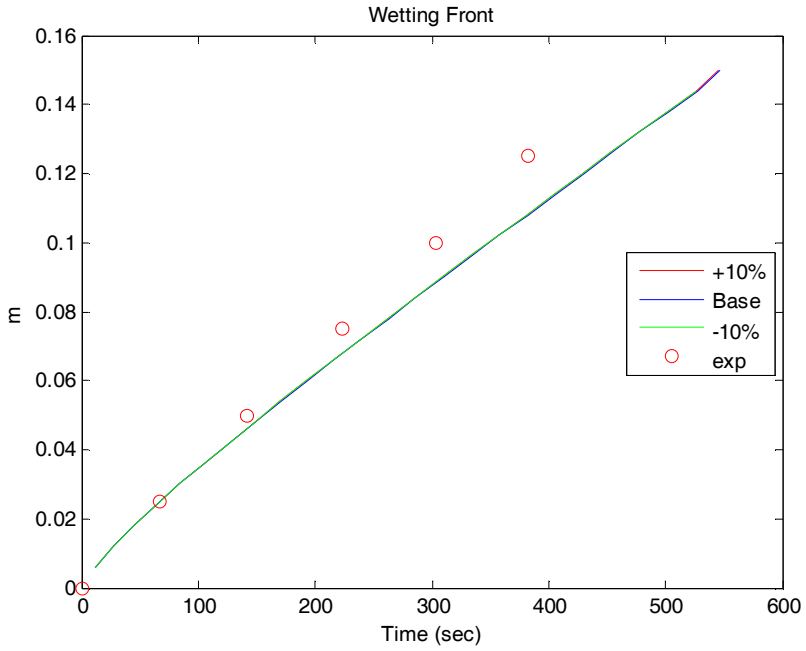

Figure 211 – Effect of J-Function Coefficient 3 on Spray Wetting of CFB

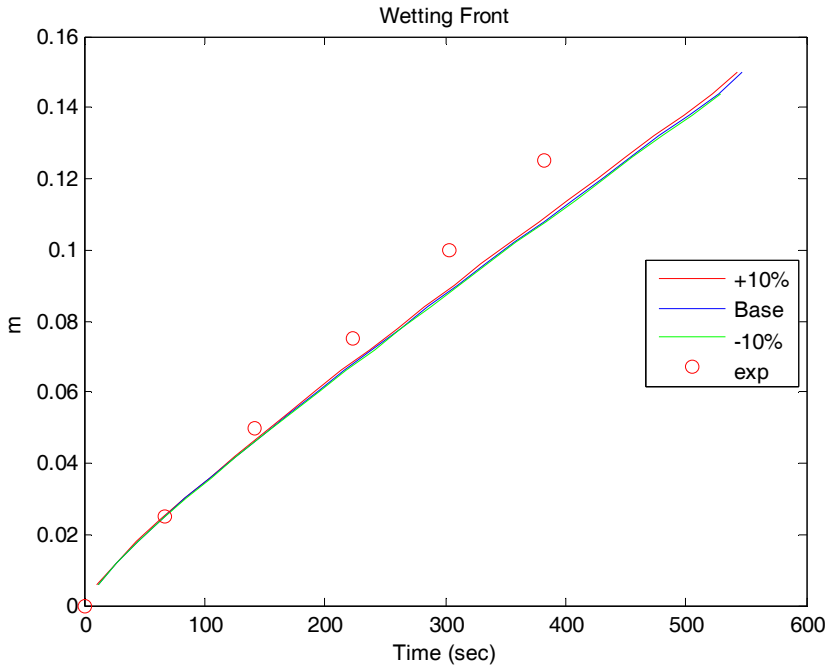

Figure 212 – Effect of J-Function Coefficient 4 on Spray Wetting of CFB

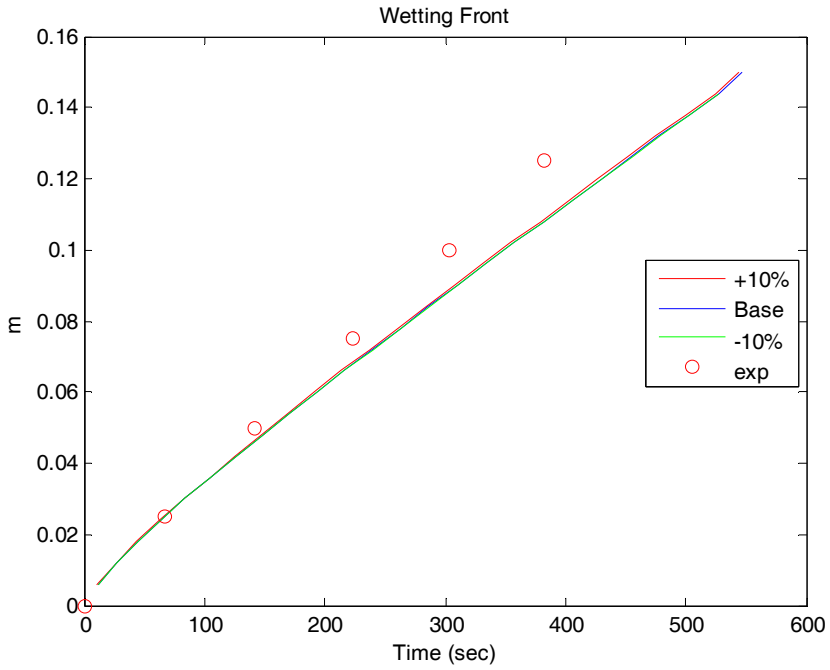

Figure 213 – Effect of J-Function Coefficient 5 on Spray Wetting of CFB

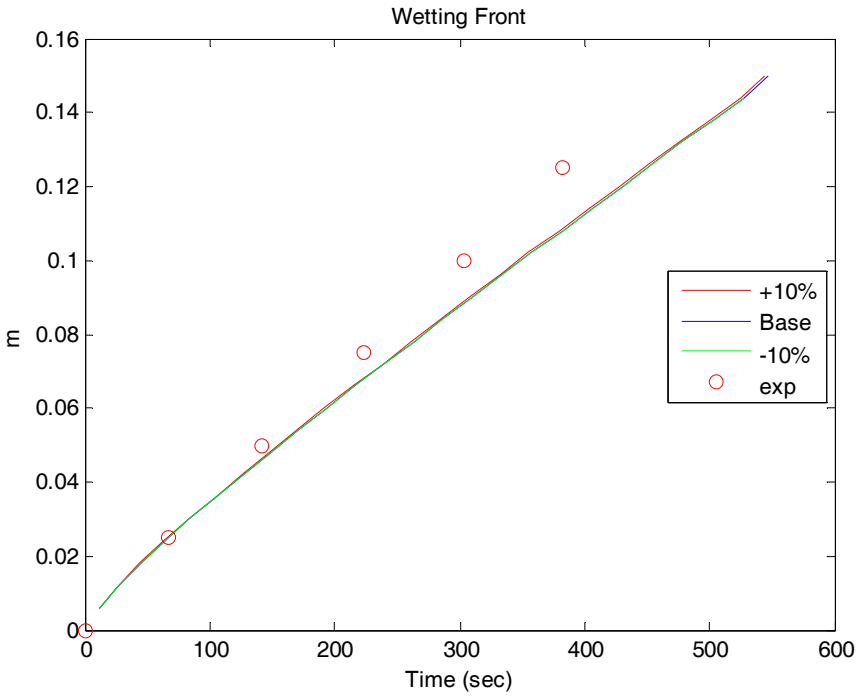

Figure 214 – Effect of J-Function Coefficient 6 on Spray Wetting of CFB

G.2. Details of Particulate Media Drying Sensitivity Analysis

A sensitivity analysis was conducted on the drying of particulate media discussed in the validation section. The inputs are those given in the validation section. Several of the inputs were each adjusted by adding and subtracting 10% of their base value. The effects of these changes on the total mass of the sample, and the temperature at a depth of 5mm beneath the surface of the material are observed. Other inputs were adjusted by other amounts when 10% was not reasonable, such as the initial and ambient temperatures. The values of the parameters used for this screening exercise are given in Table 30.

Other Parameters Tested

In addition to the testing the sensitivity of the model to the input parameters in Table 30, several additional constitutive relations were also tested. The correlations tested were those for relative permeabilities for liquid and gas, capillary pressure, and relative humidity.

Relative Permeabilities

The effect of the liquid and gas relative permeability correlation was tested by adjusting the power that the saturation is raised to. The correlations used were

For liquid relative permeability

$K_{rl} = S_{eff}^{3} \; - Baseline\ case$

$K_{rl} = S_{eff}^{2} \; - "High"\ case$

$K_{rl} = S_{eff}^{4} \; - "Low"\ case$

For gas relative permeability

$K_{rl} = \left(1 - S_{eff}\right)^{3} \; - Baseline\ case$

$K_{rl} = \left(1 - S_{eff}\right)^{2} \; - "High"\ case$

$K_{rl} = \left(1 - S_{eff}\right)^{4} \; - "Low"\ case$

Capillary Pressure Correlation

The sensitivity of the model to the correlation for capillary pressure was tested by adjusting the J-Function. The correlations used for the J-Function are shown in Figure 215. The results are shown in Figure 241.

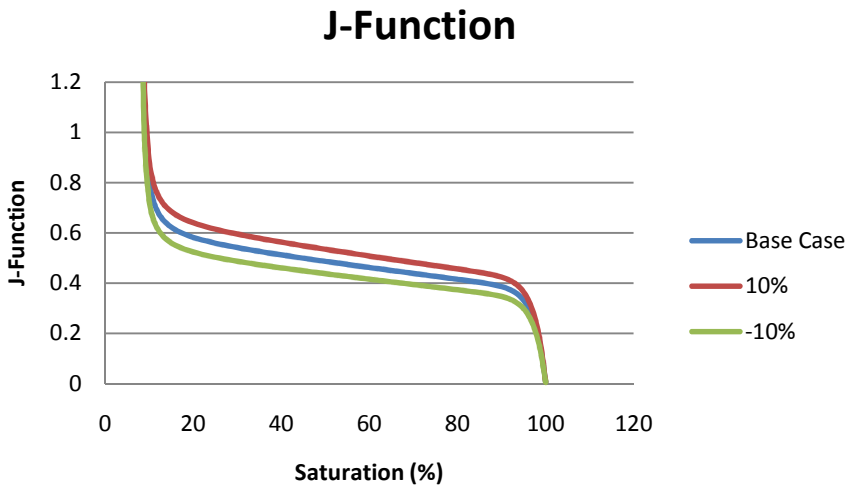

Figure 215 – J-Function Curves used for Sensitivity Analysis of Particulate Media Drying

Relative Humidity Correlation

The sensitivity of the model to the form of the relative humidity correlation used was tested. The three correlations used are shown in Figure 216.

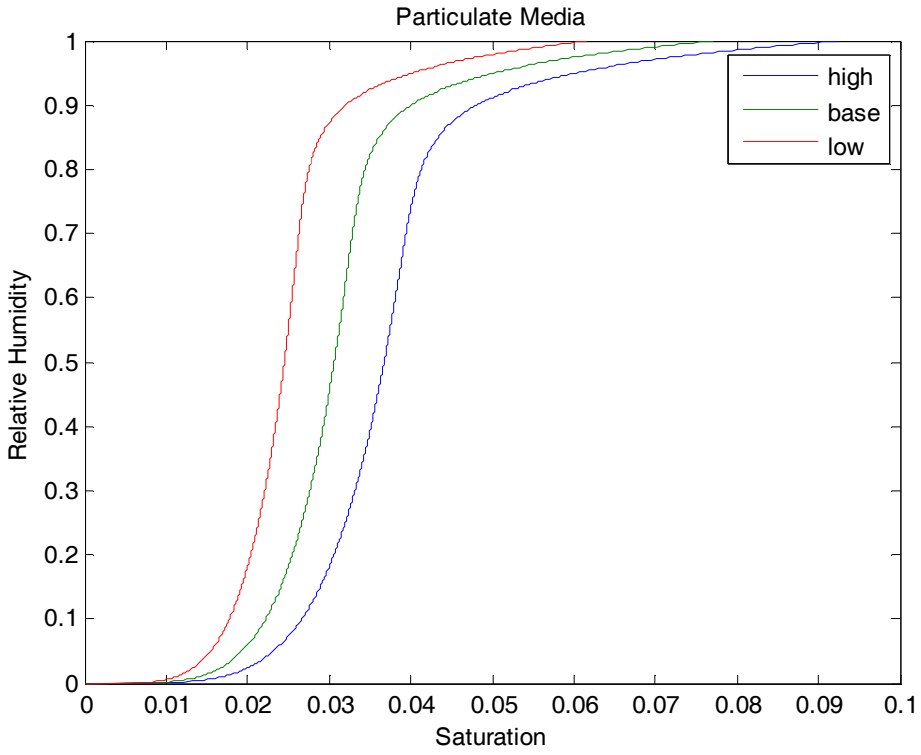

Figure 216 – Relative Humidity Correlations used for Sensitivity Analysis of Particulate Media Drying

The results of adjusting the 15 input parameters from Table 30 and the 4 constitutive relations are shown in Figure 217 through Figure 241. The model showed the greatest sensitivity to adjusting the heat and mass transfer coefficients, ambient relative humidity, ambient temperature, and initial saturation. The model did not exhibit significant sensitivity to the permeability, porosity, specific heat, thermal conductivity, density, diffusivity, liquid or gas relative permeabilities, relative humidity correlation, or capillary pressure. Of the parameters that did have an significant effect, they can be broken down into two groups: factors that affect the surface heat and mass transfer rates, and factors that affect the initial dimensional water content. Adjusting the porosity and density of the solid phase had a significant effect on the model results, but

this was determined to be caused by the associated change in the initial mass of water and the mass of solid materials. What this indicates is that the process that is being observed is one where a mass of water is being evaporated, and once enough of the water is evaporated, the surface evaporative cooling will drop rapidly, and the temperature of the material will jump rapidly. Any change in the initial mass of water in the sample will have a significant impact on the time until the jump occurs. Since there is very little internal resistance to fluid flow (as measured by the large permeability), this is essentially a surface transfer controlled process. Internal transfer mechanisms are not limiting the drying process in any significant way until the material becomes very dry.

Temperature Jump

The temperature of the sample was observed both experimentally and in the model to exhibit a dramatic "jump" once the saturation at the surface became sufficiently low and the evaporative cooling decreased rapidly. The time at which this jump occurred is of interest, and provides a definitive location in time that can be quantitatively compared when adjusting input parameters. The effect on the jump time when adjusting the model inputs described previously is shown in Table 38. The baseline jump time was 16,007 seconds. The rankings of the calculated sensitivity coefficients of the input parameters for particulate media drying are shown in Table 42

Permeability

Adjusting the permeability did not appear to make a noticeable difference in the predicted temperature history or mass loss outputs, shown in Figure 217.

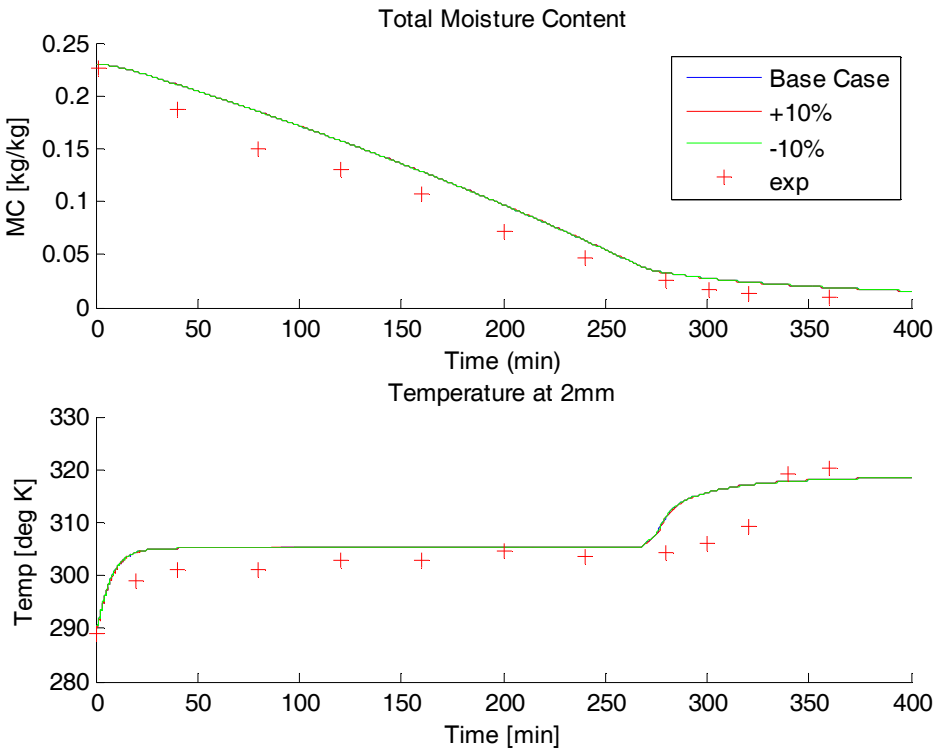

Figure 217 – Effect of Permeability on Drying of Quartz Particles

Porosity

Adjusting the porosity did not seem to affect the evaporation rate significantly, but it did change the initial moisture content, and the predicted time needed to evaporate all of the water, as seen in Figure 218. This is due to the significant initial moisture content change. Since the model calculates the moisture content from saturation, if the initial saturation is not changed as an input, the initial moisture content will be changed as the porosity is changed. Essentially the pores are being made larger, but the fraction of pores filled with water is constant, so there is more water in the material for a larger value of porosity. If the initial moisture content is held constant and the initial saturation is changed, the result is seen in Figure 219. For that analysis, the porosity was only increased by +10% and +20%. To determine if this is caused by the porosity or the corresponding increase in the initial mass of water in the sample, the following condition was applied to keep the initial mass of water in the material constant

$$S_2 = \frac{S_1 \phi_1}{\phi_2}$$

From Figure 220 it can be seen that changing the porosity in the range of 5% has very little effect on the dimensional drying rate at the surface, as evidenced by the results in Figure 220. This indicates that the porosity itself has little effect on the drying rate or rate of heat transfer. Instead, this demonstrates that the initial mass of water in the material (which is related to the porosity) does have a significant effect on the rate of drying, and therefore the time at which the surface temperature jumps.

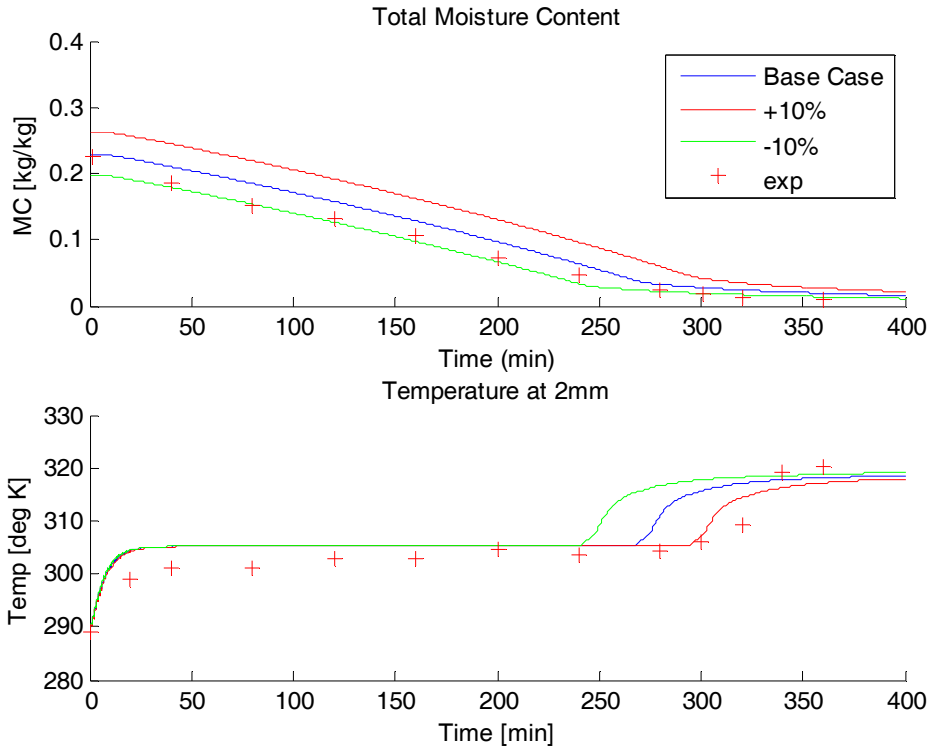

Figure 218 - Effect of Porosity on Drying of Quartz Particles - S_o Held Constant

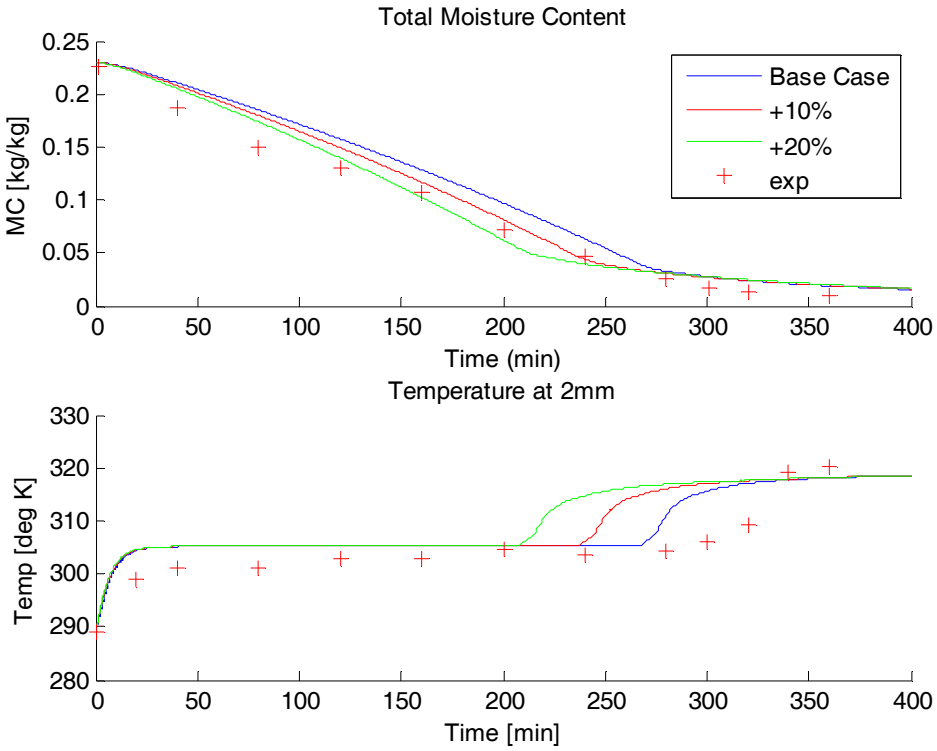

Figure 219 - Effect of Porosity on Drying of Quartz Particles - MC_o Held Constant

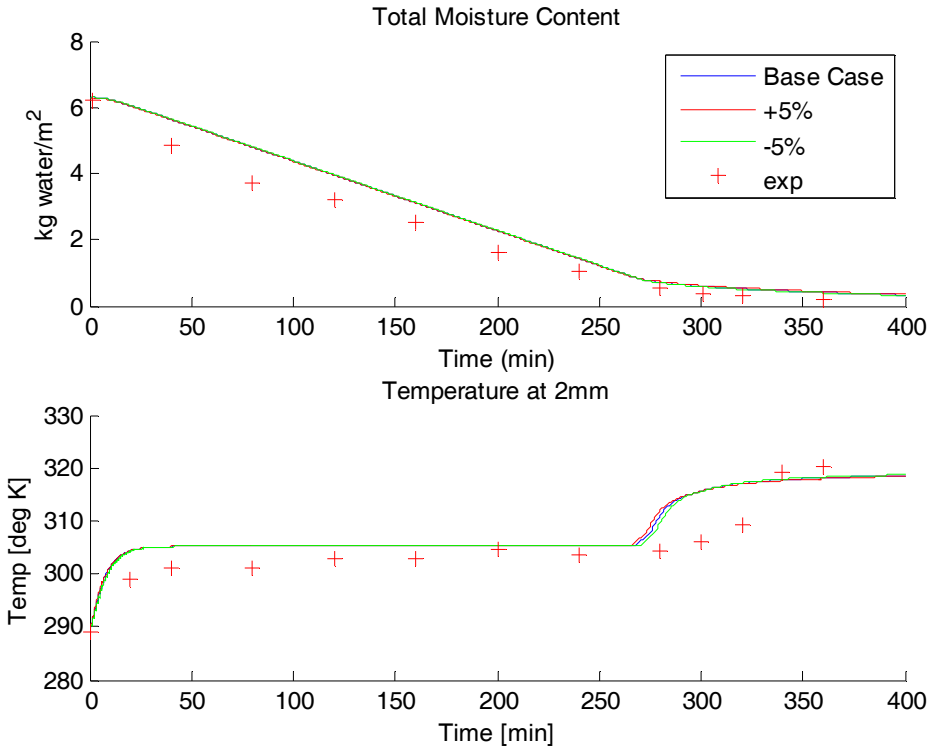

Figure 220 - Effect of Adjusting the Porosity - Initial Mass of Water Held Constant

Specific Heat of Solid Phase

The specific heat of the solid phase was adjusted by ±10%. This had very little effect on the predicted temperature history, or the drying rate of the quartz particles, as shown in Figure 221.

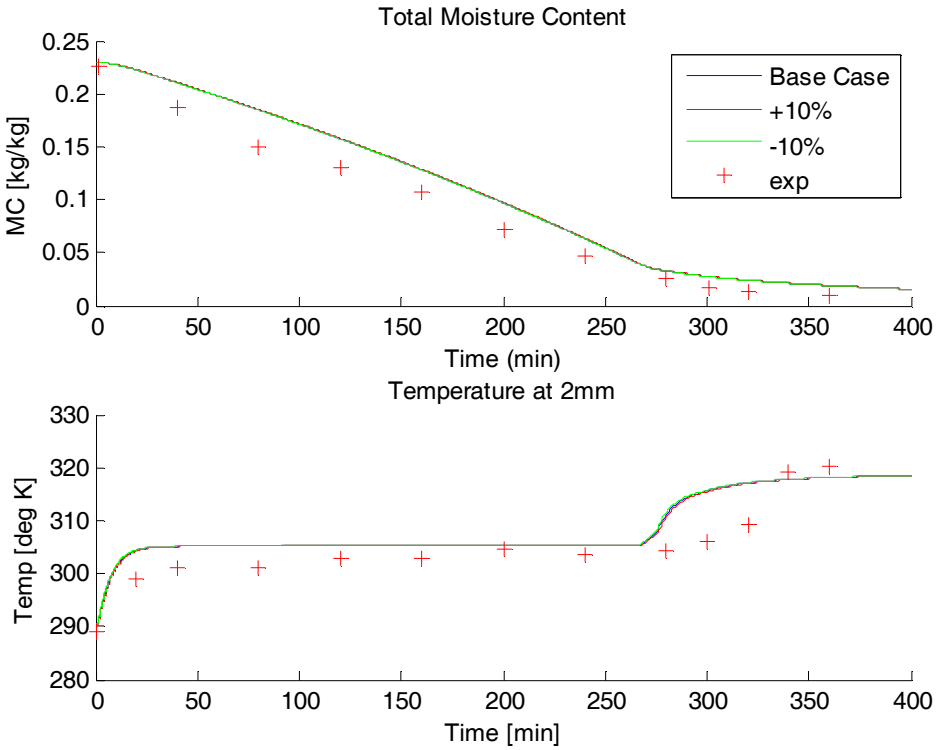

Figure 221 - Effect of Specific Heat on Drying of Quartz Particles

Thermal Conductivity of Solid Phase

Adjusting the thermal conductivity of the solid phase had little effect on the predicted temperature history of drying rate of the quartz particles, as seen in Figure 222.

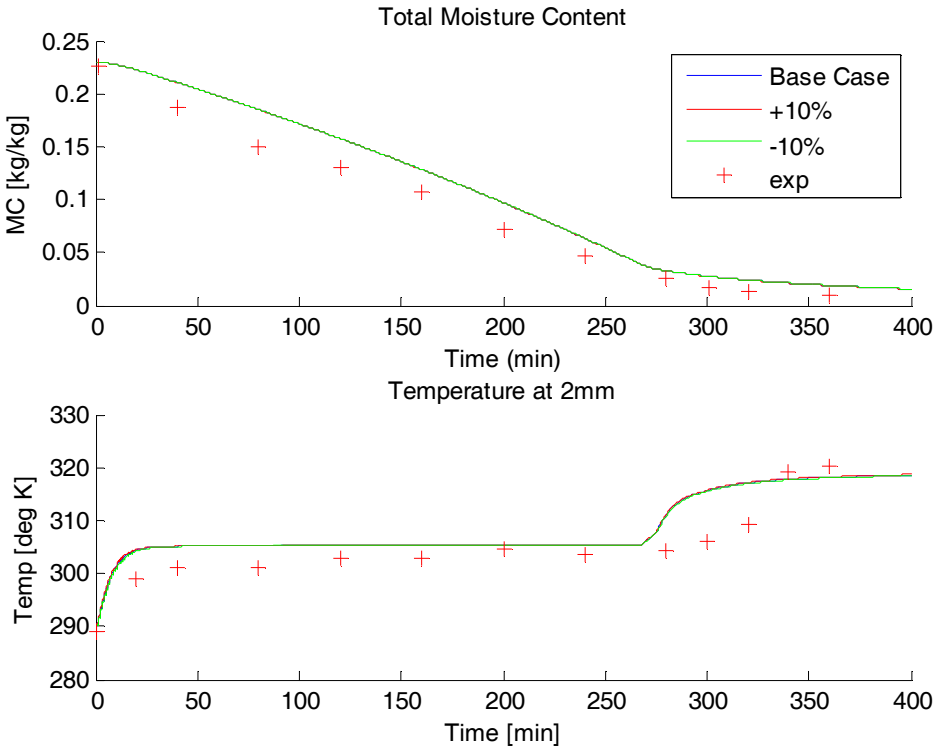

Figure 222 - Effect of Thermal Conductivity on Drying of Quartz Particles

Density of Solid Phase

Adjusting the density of the solid phase while leaving the initial water saturation constant had only a very slight effect on the predicted temperature history, but a more pronounced effect on the predicted drying rate as seen in Figure 223. In this case, by adjusting the density of the solid, the moisture content is changed, but the amount of water in the material remains unchanged. The dimensional drying rate is therefore approximately the same in each case as shown in Figure 224. For that reason, each case reached the dry state at approximately the same time. If the initial moisture content is held constant and the initial saturation is adjusted, the results are shown in Figure 225. For that analysis, the moisture content was only able to be increased by 5%. In this case however it is the increase in the mass of water in the material that is responsible for the significant changes.

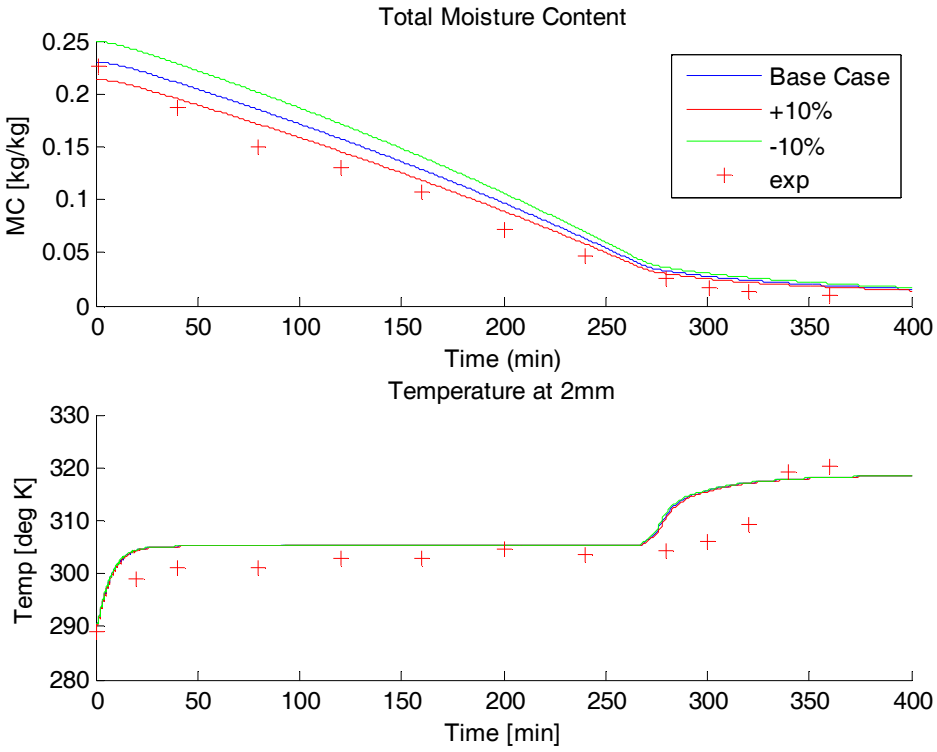

Figure 223 - Effect of Solid Phase Density on Drying of Quartz Particles - S_o Held Constant

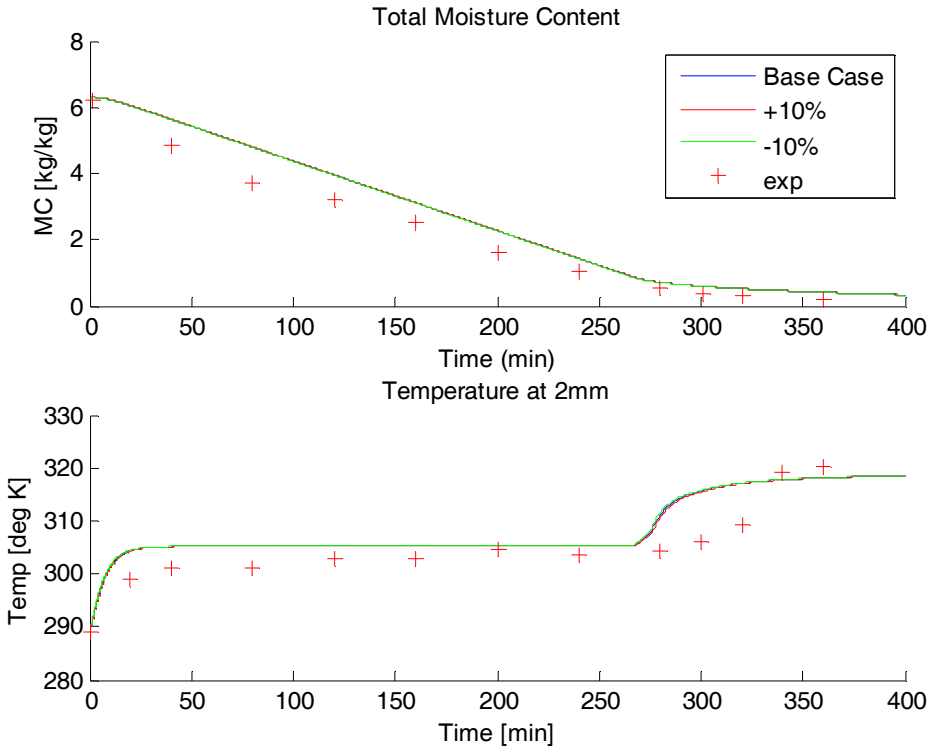

Figure 224 – Effect of Solid Phase Density on Dimensional Drying Rate

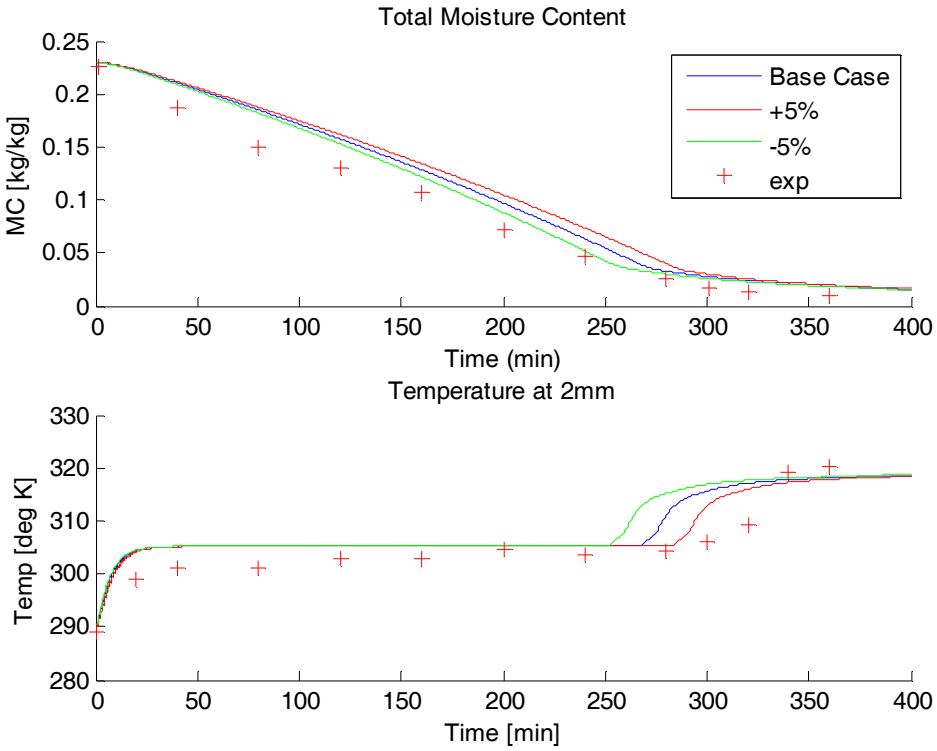

Figure 225- Effect of Solid Phase Density on Drying of Quartz Particles – MC_o Held Contant

Diffusivity of Vapor in Air

Adjusting the diffusivity of vapor in air had little effect on the predicted temperature or mass loss histories of the quartz particles.

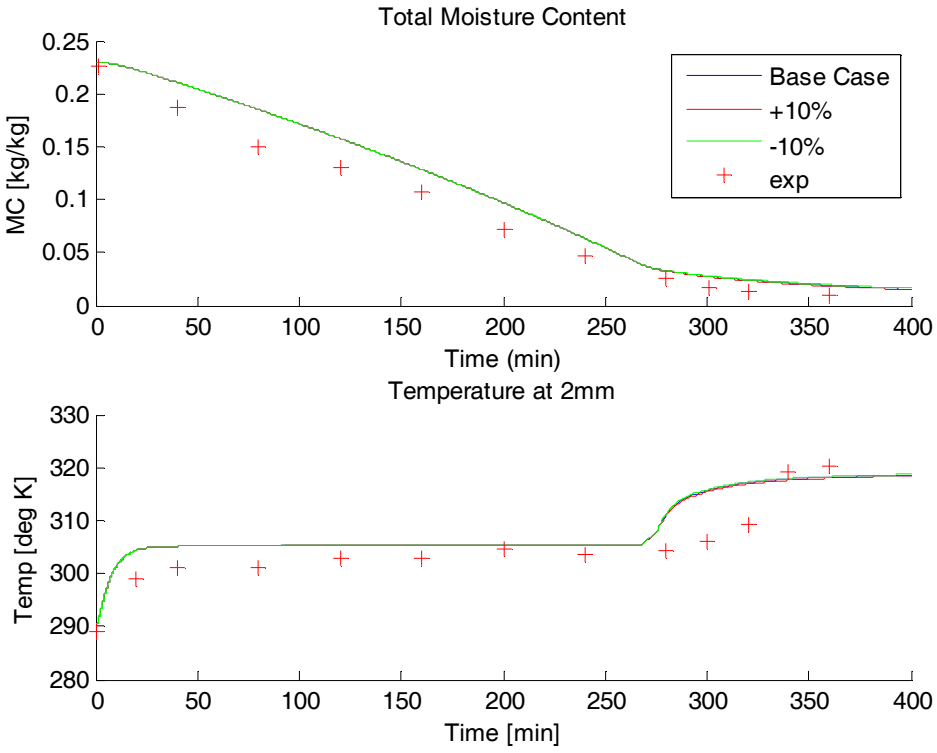

Figure 226 - Effect of Diffusivity on Drying of Quartz Particles

Heat Transfer Coefficient

Adjusting the heat transfer coefficient had a significant effect on the predicted mass loss rate during the drying of the quartz particles. Increasing the heat transfer coefficient produced a slightly higher surface temperature, which in turn produced a greater drying rate. Once the material reached it's nearly dry state, the temperature jumped up significantly.

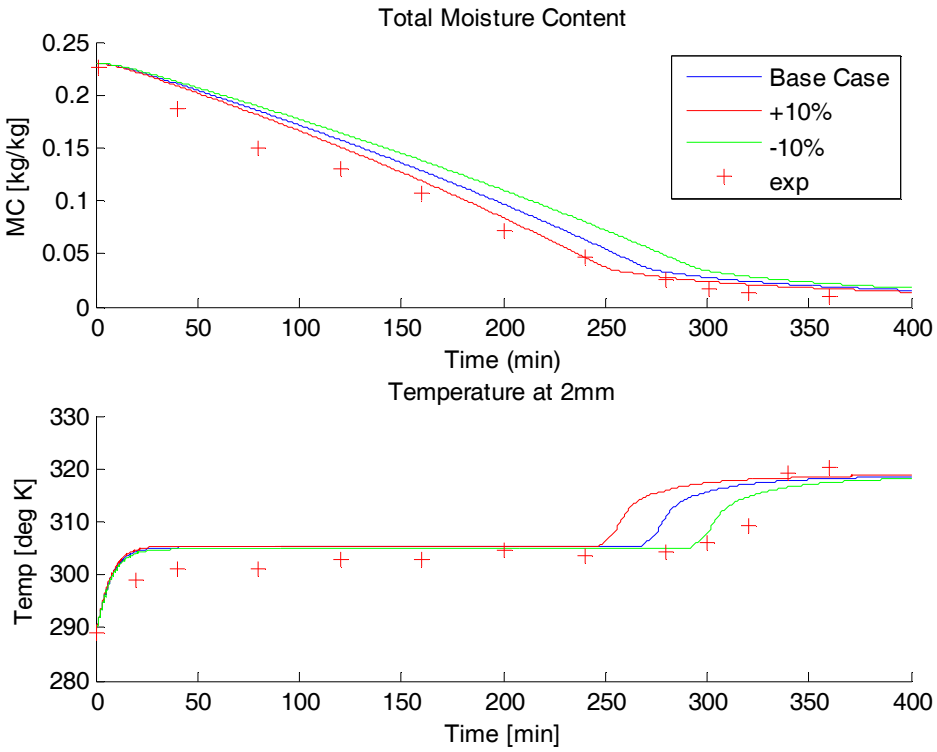

Figure 227 - Effect of Heat Transfer Coefficient on Drying of Quartz Particles

Mass Transfer Coefficient

The choice of mass transfer coefficient had a much less significant effect on the predicted temperature and moisture content histories than did the heat transfer coefficient. Increasing the mass transfer coefficient initially lowered the surface temperature very slightly but increased the evaporation rate. This caused the material to dry out slightly faster, and once the material was dry the temperature jumped up slightly sooner. The opposite was true for the lower mass transfer coefficient case.

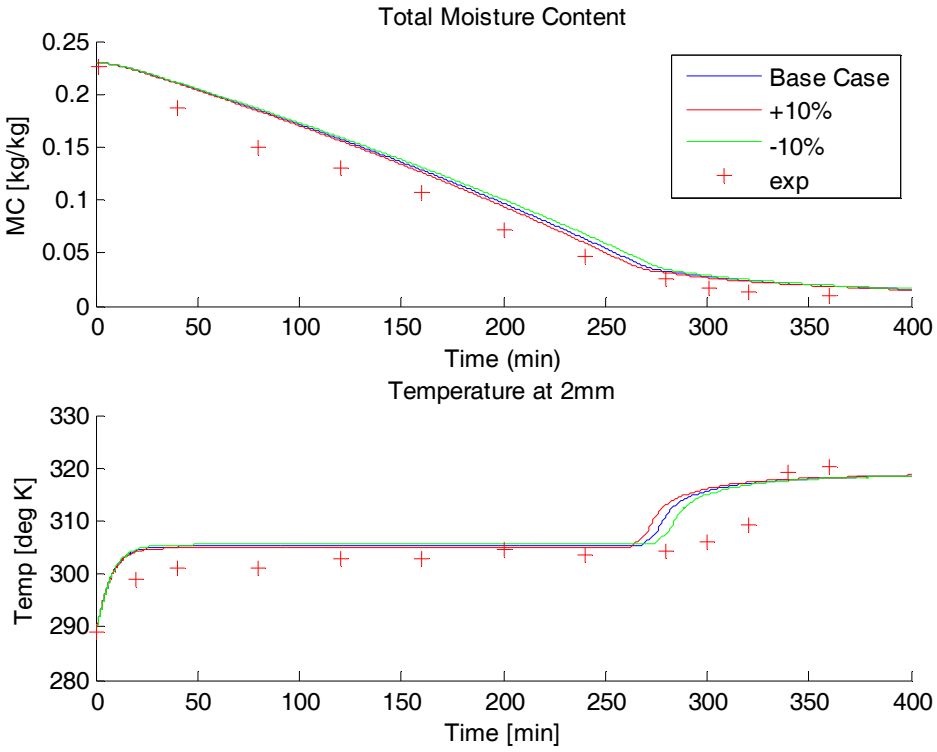

Figure 228 - Effect of Mass Transfer Coefficient on Drying of Quartz Particles

Relative Humidity

The relative humidity has a significant effect on both the temperature and moisture content histories as shown in Figure 229. Increasing the relative humidity lowers the evaporation rate, and increases the surface temperature, since the evaporative heat losses at the surface are less. This delays the point at which the material becomes nearly dry and the temperature jumps up. The opposite is true for decreasing the relative humidity. In that case, the evaporation rate is increased, thereby increasing the evaporative heat losses, and lowering the surface temperature. The material dries out faster and the temperature jumps up sooner.

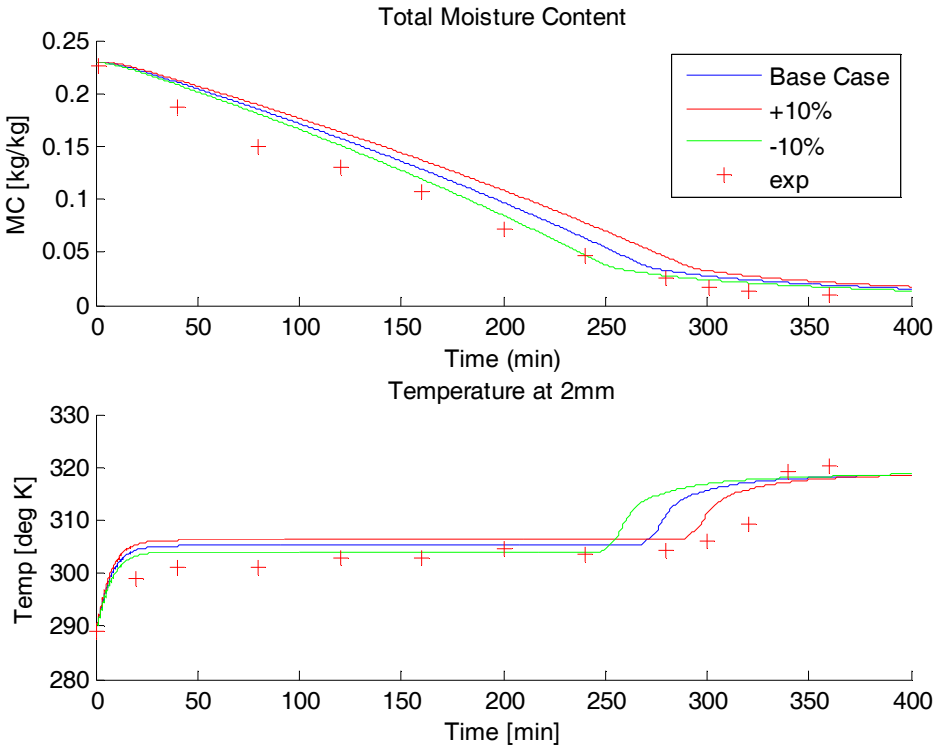

Figure 229 - Effect of Relative Humidity on Drying of Quartz Particles

Initial Temperature

Changing the initial temperature by $\pm 2^{o}$ did not have a significant effect on this simulation. The results are shown in Figure 230.

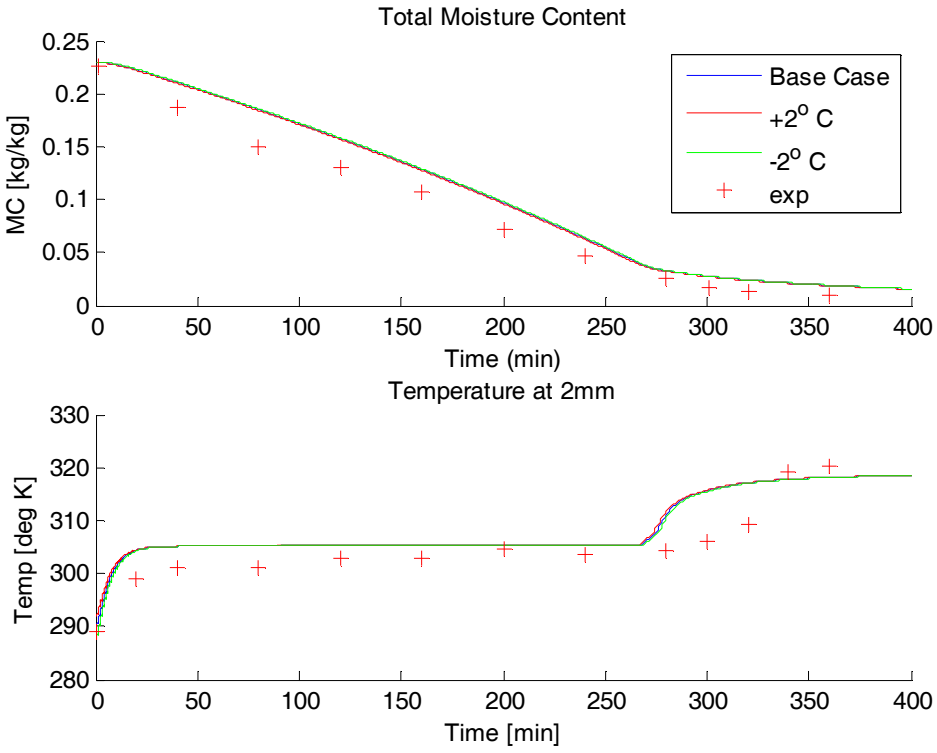

Figure 230 - Effect of Adjusting the Initial Temperature

Ambient Temperature

Adjusting the ambient temperature by $\pm 2^{o}$ had a significant effect on this simulation. The effect was an increase or decrease in the rate of heat transfer into the material from the ambient. The rate of mass loss and the time that the surface temperature jumped were both affected. The results are shown in Figure 231.

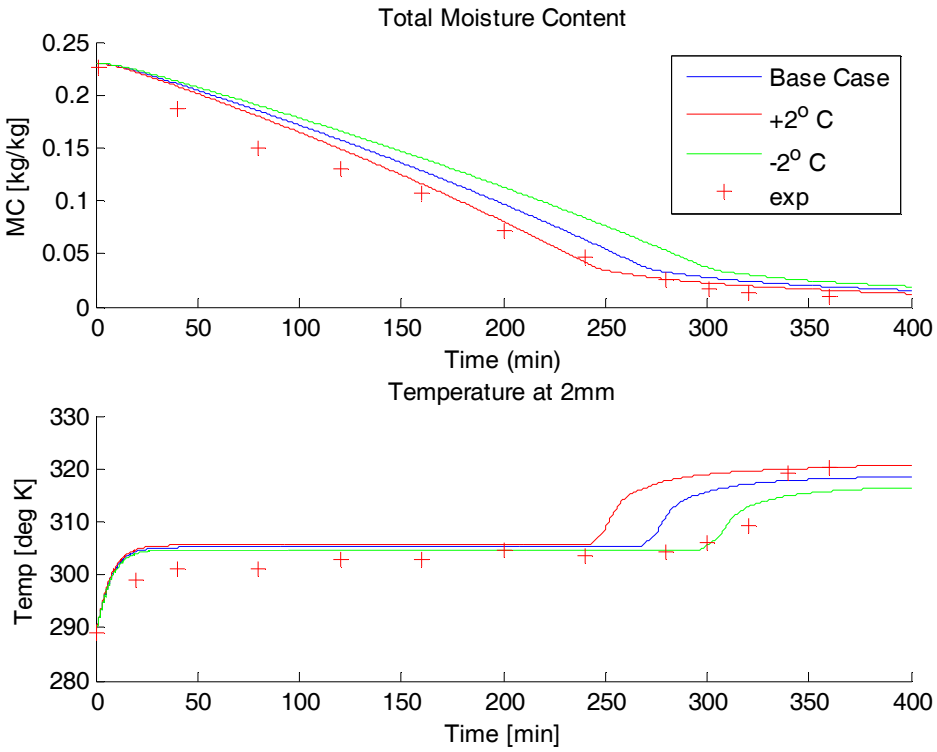

Figure 231 - Effect of Changing the Ambient Temperature

Depth of Sample

Adjusting the depth of the sample by $\pm 1.5mm$ (10%) had a significant effect on the rate of change of the moisture content. This is because the moisture content is scaled with the total mass of the sample. The time at which the temperature jumps is significantly affected, since the total amount of water to be removed is changed. This is shown in Figure 232. The dimensional mass loss rate does not seem to be affected. This is shown in Figure 233.

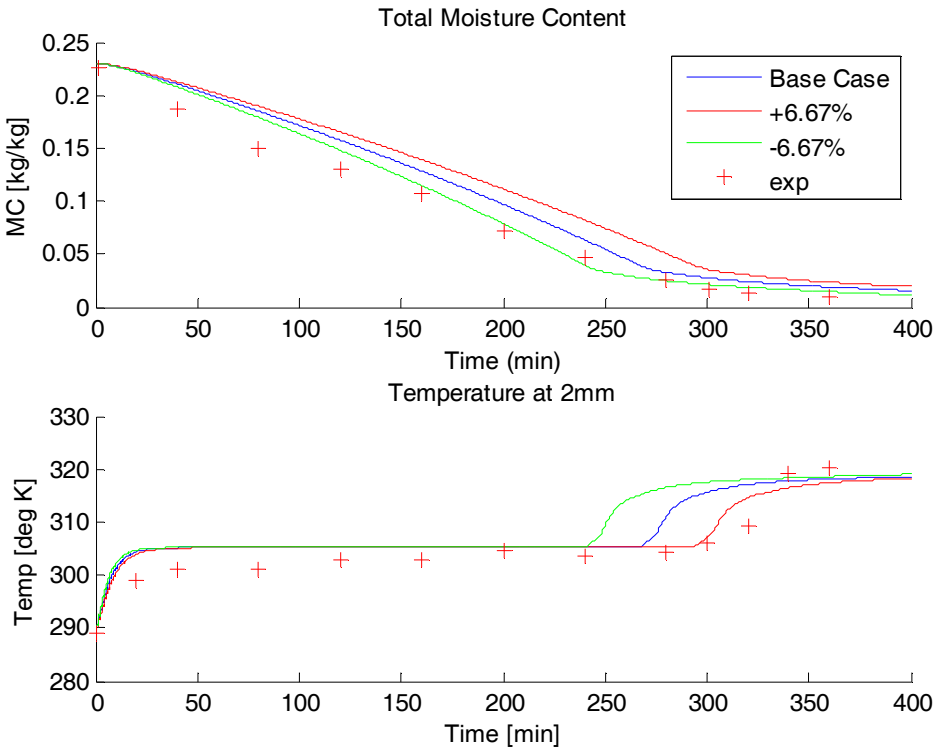

Figure 232 – Effect of Adjusting the Depth of the Sample

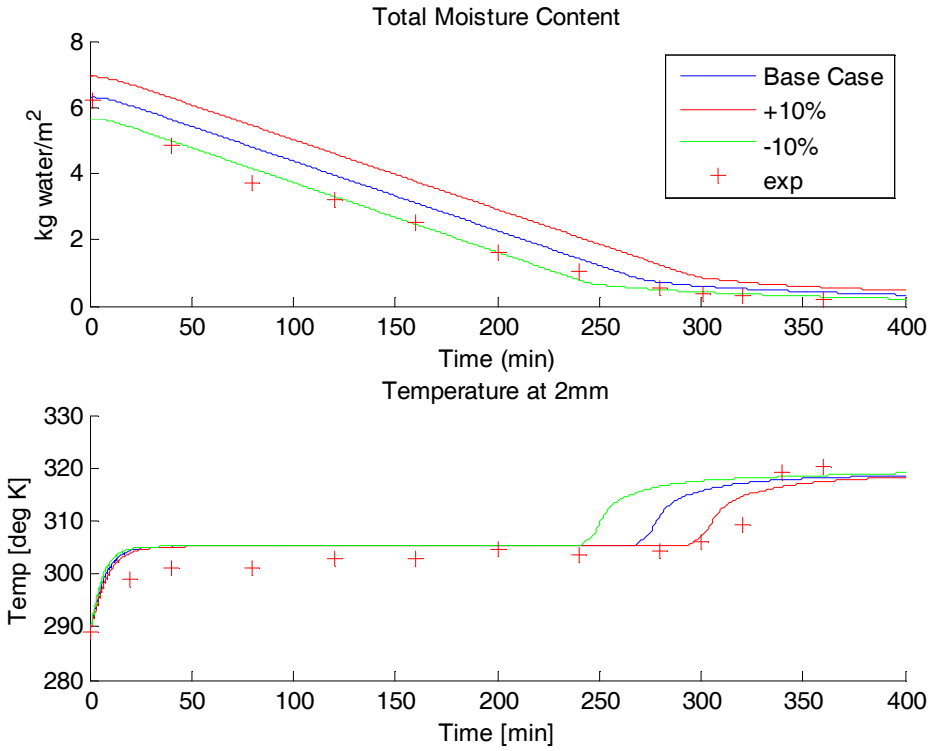

Figure 233 – Effect of Adjusting the Depth of the Sample – Dimensional Mass Loss Rate

If the depth is adjusted and the initial mass of water in the sample is held constant using the following constraint

$$S_2 = \frac{S_1 L_1}{L_2}$$

It can be shown that the model is not sensitive to the length of the sample when the initial mass of water is held constant, as shown in Figure 234. For this simulation, the length was only adjusted by $\pm 5\%$ to avoid saturations above 1.

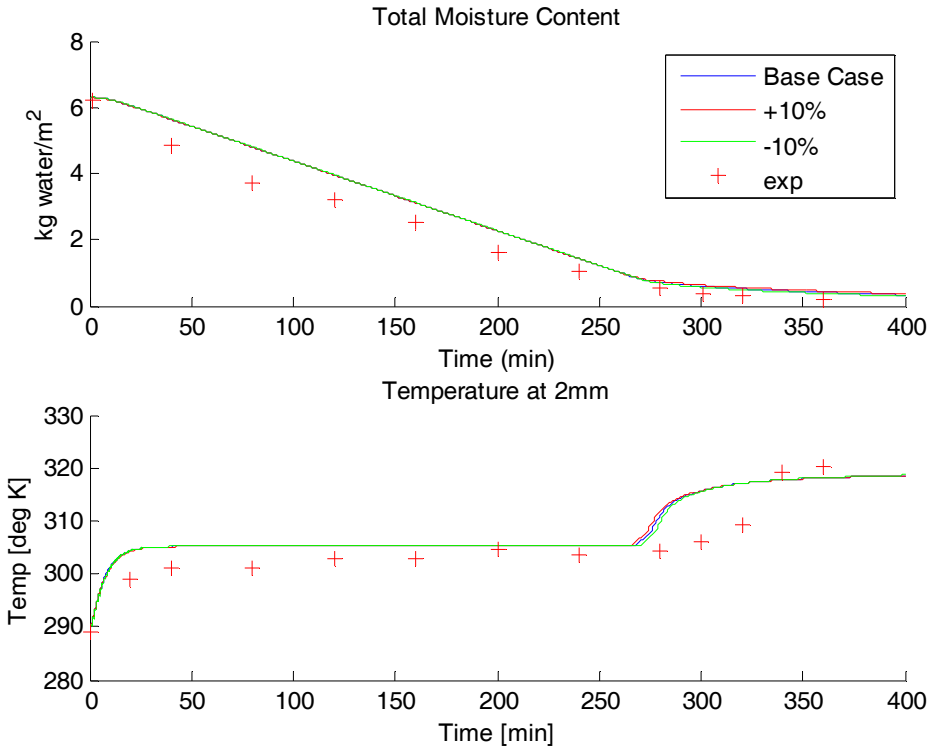

Figure 234 – Effect of Depth of Sample on Drying of Particulate Media – Initial Mass of Water Held Constant

Initial Saturation

The initial water saturation was adjusted ±5% from its base value. This had a significant effect on the time at which the surface temperature jumped, as shown in Figure 235. Increasing the initial saturation increased the mass of water that had to be evaporated before the temperature could jump, and therefore increased the time at which the jump occurred.

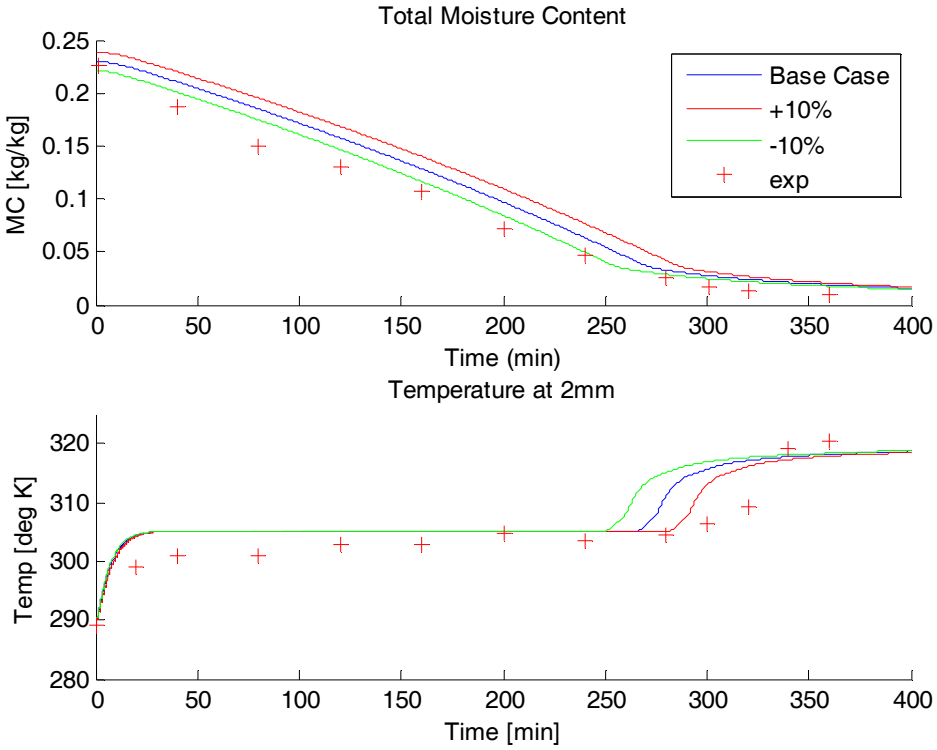

Figure 235 – Effect of Initial Saturation on Drying of Particulate Media

Number of Nodes

The number of nodes was adjusted from its base value of 16 to a "low" value of 11 and a "high" value of 21. This did not have a significant effect on the mass loss rate or temperature.

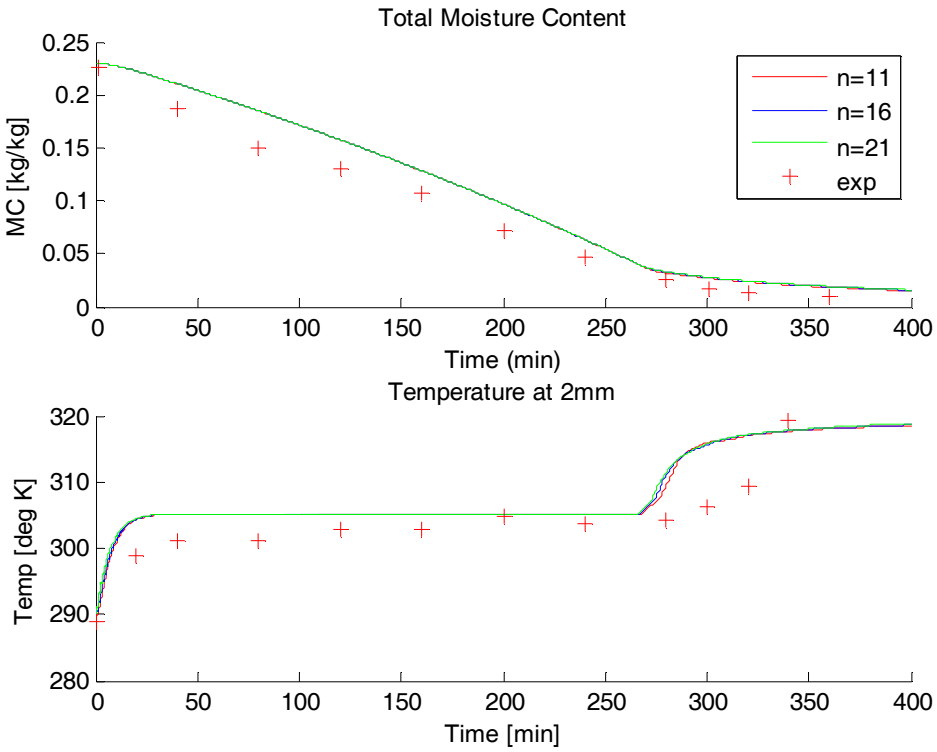

Figure 236 – Effect of Adjusting the Number of Nodes

Time Step

The time step was adjusted from its base value of 1 second, to a "high" value of 2 seconds and a "low" value of 0.5 seconds. Adjusting the time step had no significant effect on the mass loss rate or temperature.

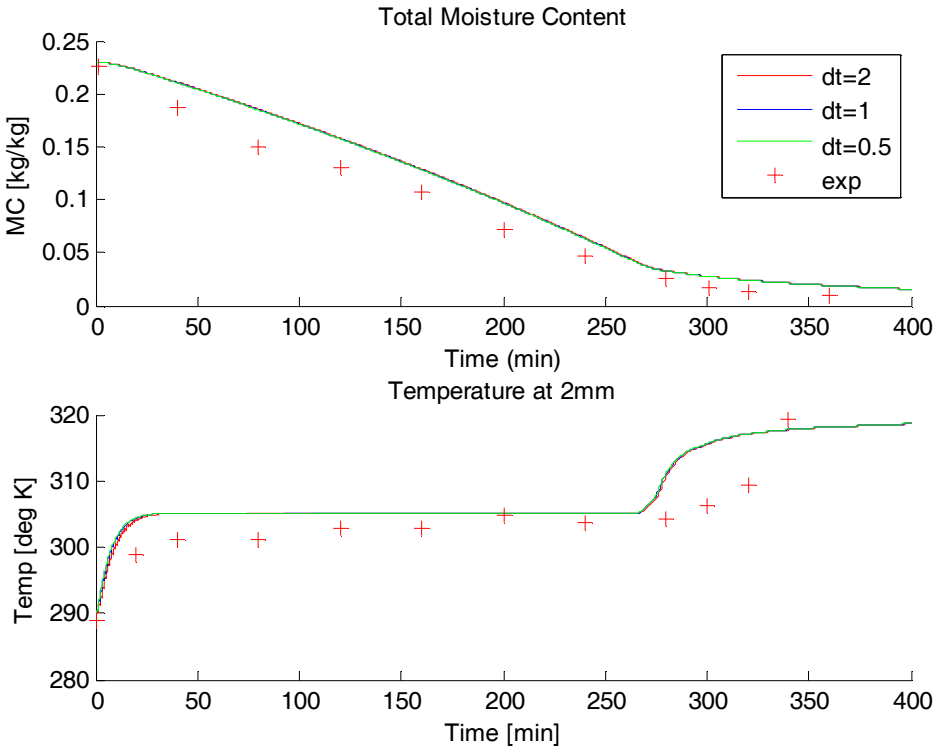

Figure 237 – Effect of Adjusting the Timestep

Liquid Relative Permeability

The liquid relative permeability was changed from its base case of a cubic function of saturation, to a fourth order function and a square function. This had an effect on the mass loss rate or temperature, as is shown in Figure 238.

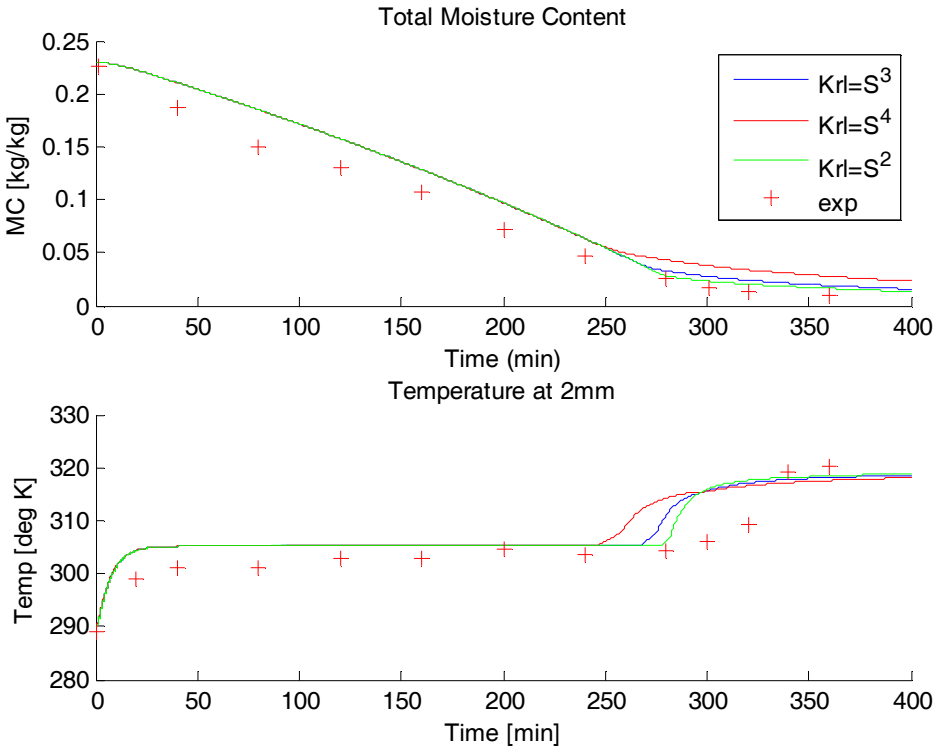

Figure 238 – Effect of the Liquid Relative Permeability Correlation

Gas Relative Permeability

The gas relative permeability was changed from its base case of a cubic function of saturation, to a fourth order function and a square function. This did not have a significant effect on the mass loss rate or temperature, as is shown in Figure 239.

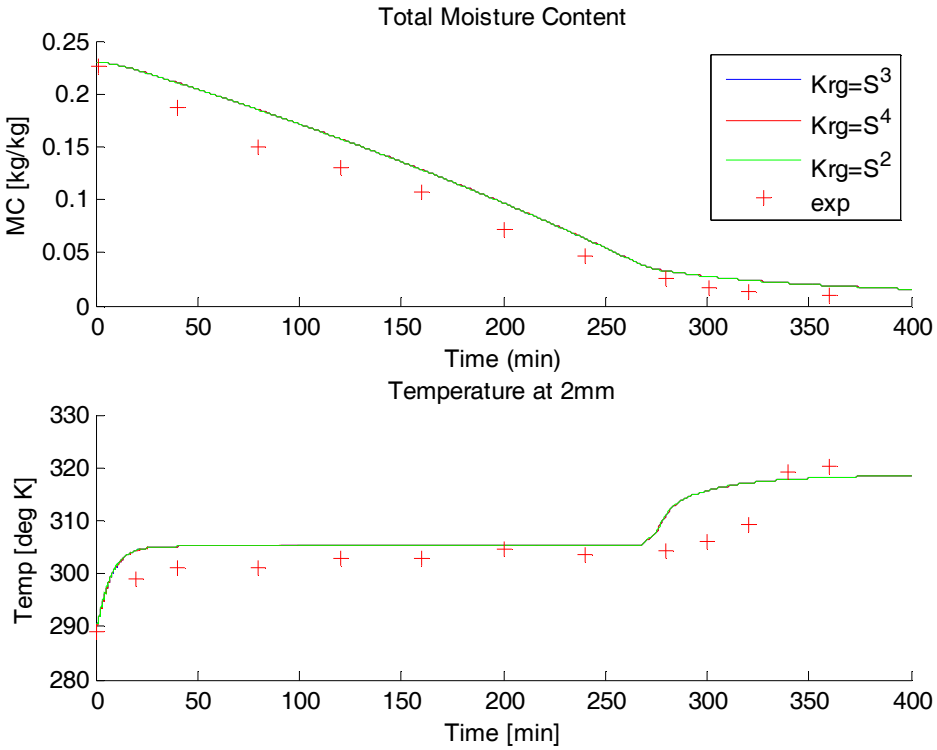

Figure 239 – Effect of Gas Relative Permeability

Relative Humidity

The relative humidity correlation was adjusted as shown in Figure 216. This did not have a significant effect on the mass loss rate or temperature as shown in Figure 240.

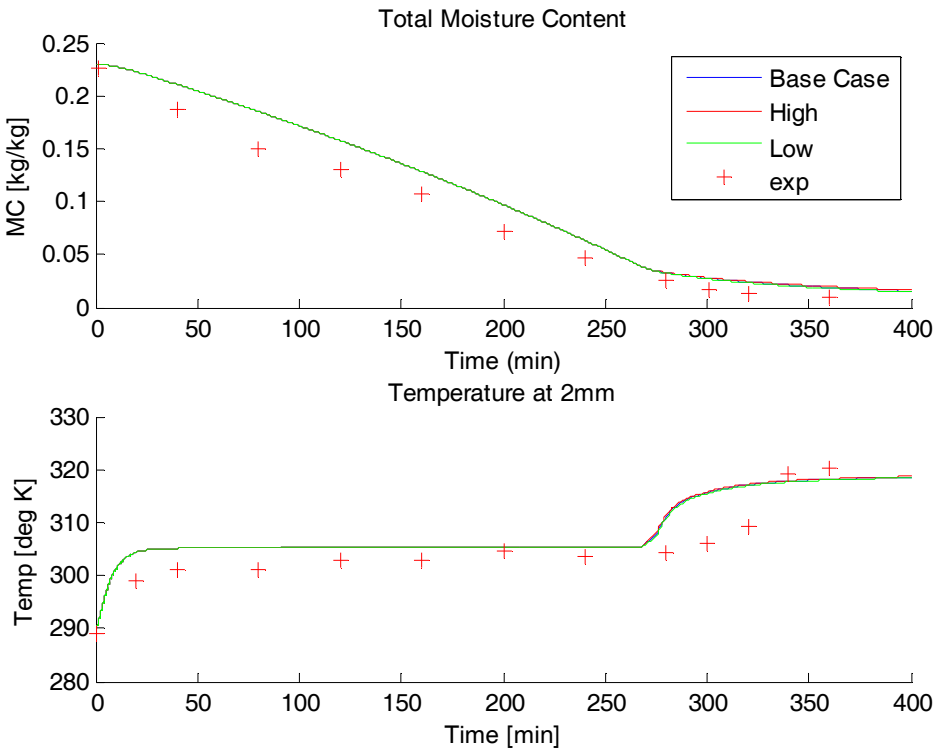

Figure 240 – Effect of Relative Humidity Correlation on Drying of Particulate Media

Capillary Pressure Correlation

The capillary pressure was adjusted from its base correlation, to the "high" and "low" values shown in Figure 215. This did not have a significant effect on the mass loss rate or temperature as shown in Figure 241.

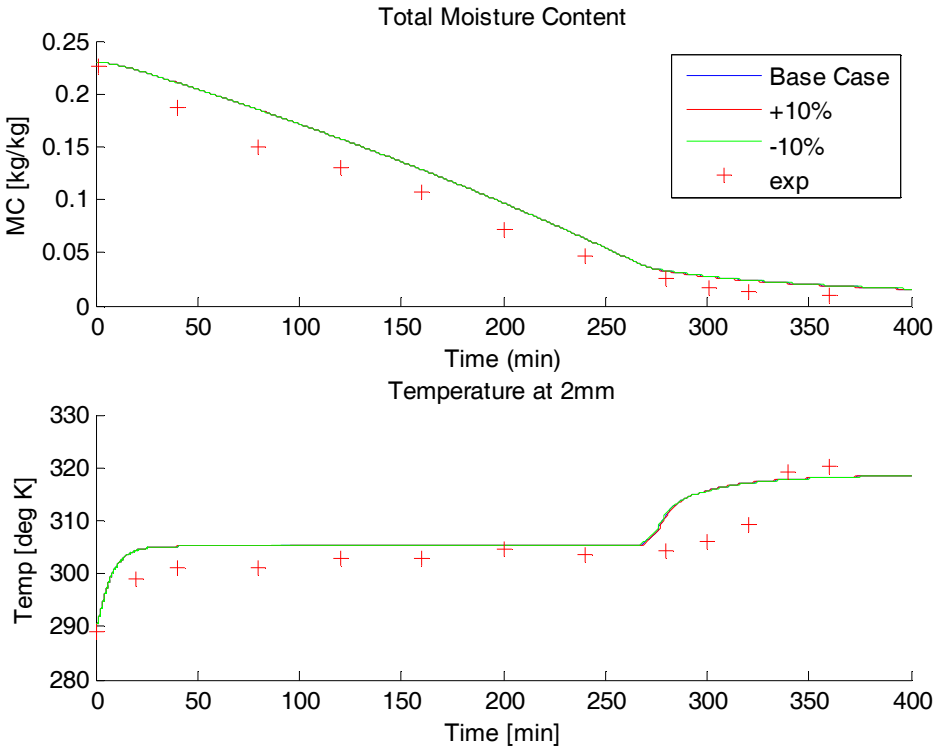

Figure 241 – Effect of Capillary Pressure Correlation on Particulate Media Drying

Irreducible Saturation

The irreducible saturation was adjusted ±10% from its base value of 0.09. This had a slight effect on the temperature and mass loss rate, as shown in Figure 242.

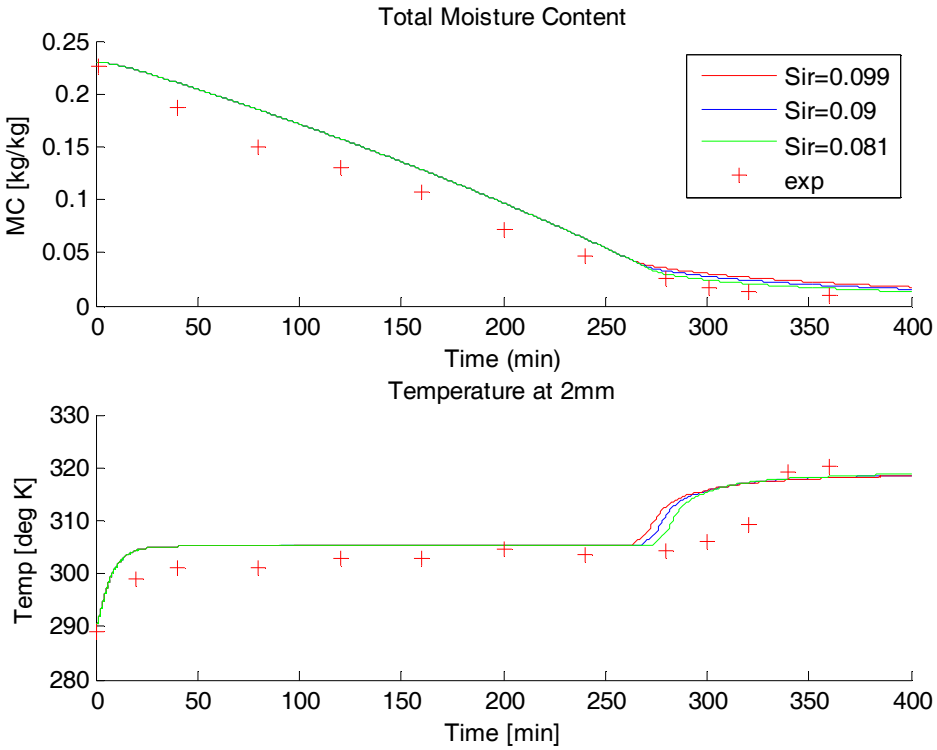

Figure 242 - Effect of Irreducible Saturation on Particulate Media Drying

G.3. Details of Brick Drying Sensitivity Analysis

The sensitivity of the model was tested for the case of convective drying of brick. The parameters tested and their values are shown in Table 31. Additionally, the correlations used for relative permeabilities, relative humidity, and capillary pressure were tested.

Capillary Pressure

The capillary pressure of brick is assumed to be that of sandstone, which is given by Kaviany [23] to be

$$p_c = P - p_w = \frac{\sigma}{\sqrt{K/\phi}}\left[0.3 - 0.0663\ln\left(S_w - S_{ir}\right)\right]$$

The capillarty pressure calculated using relationship was adjusted ±10% as shown in Figure 243.

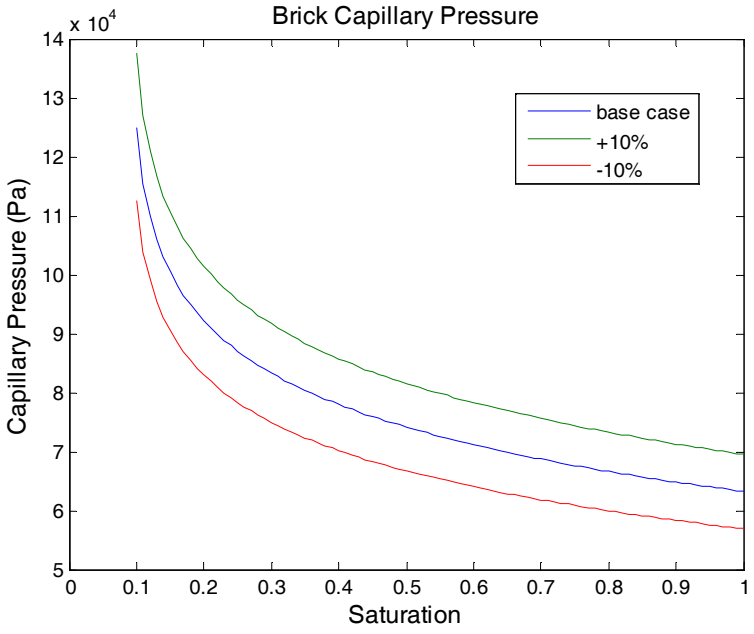

Figure 243 – Capillary Pressure Correlations Used for Sensitivity Analysis of Brick Drying

Relative Permeabilities

The gas and liquid relative permeabilities for brick are assumed to be that of sandstone which is given by Kaviany [23] as

$$K_{rl} = S_{eff}^4$$

$$K_{rg} = \frac{\left(1 - S_{eff}\right)^2}{\left(1 - S_{eff}^2\right)}$$

These correlations were adjusted to the following high and low cases

High Case

$$K_{rl} = S_{eff}^3$$

$$K_{rg} = \frac{\left(1 - S_{eff}\right)^{1.5}}{\left(1 - S_{eff}^{1.5}\right)}$$

Low Case

$$K_{rl} = S_{eff}^5$$

$$K_{rg} = \frac{\left(1 - S_{eff}\right)^{2.5}}{\left(1 - S_{eff}^{2.5}\right)}$$

These correlations are shown in Figure 244.

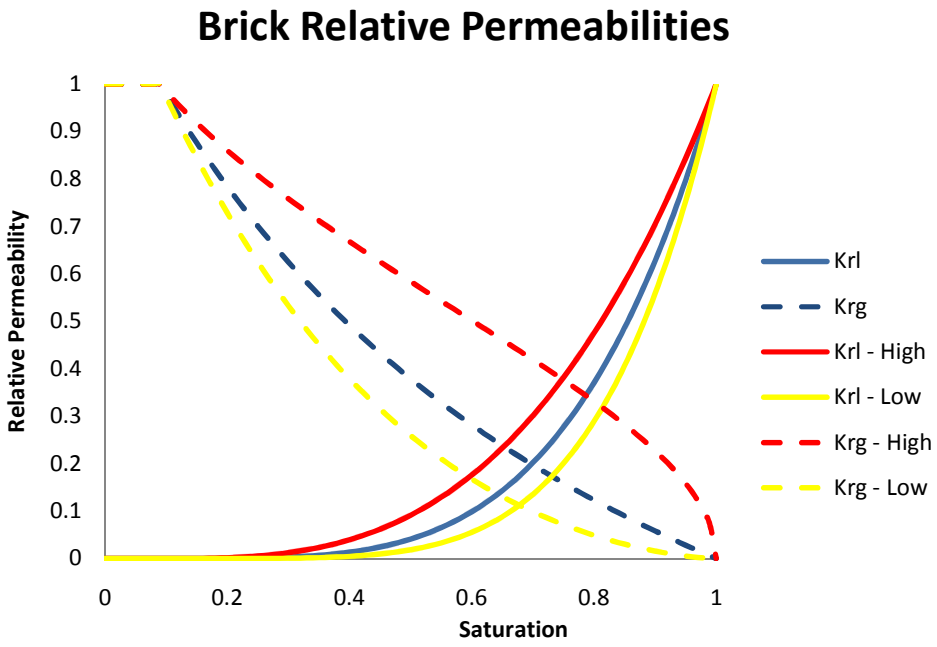

Figure 244 – Relative Permeabilities used in Sensitivity Analysis of Brick Drying

Relative Humidity

The sensitivity of the model to the relative humidity correlation was tested. The base case the correlation was adjusted as shown in Figure 245. The saturation at a given relative humidity was adjusted by ±20%.

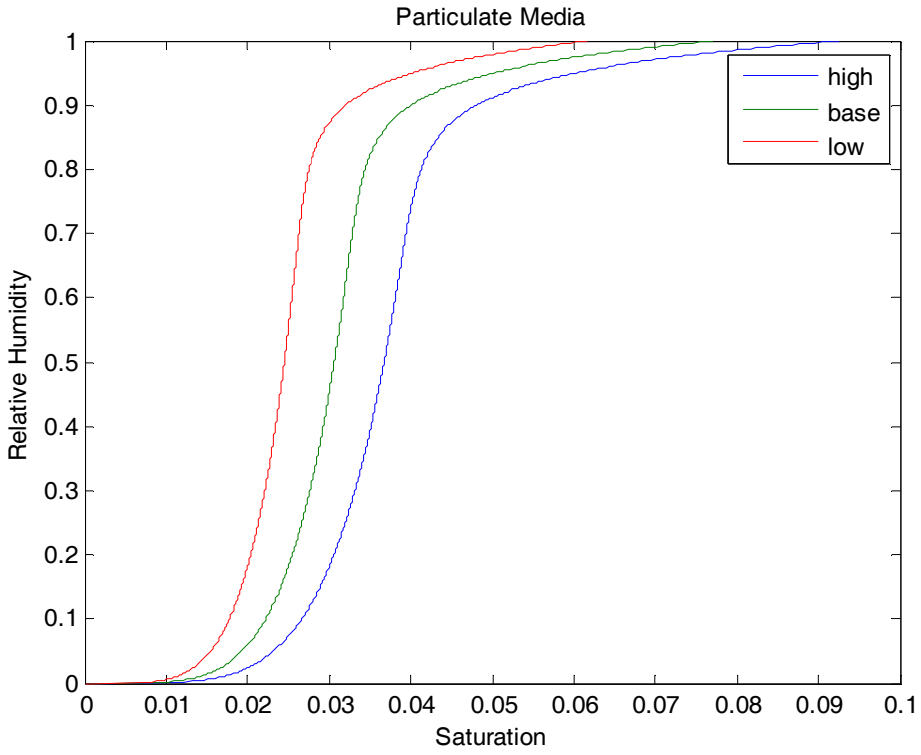

Figure 245 - Relative Humidity Relations Used for Sensitivity Analysis of Brick Drying

Results

From this analysis it was shown that for the case of brick drying, the model is sensitive to the porosity, heat transfer coefficient, ambient temperature, depth of sample, initial saturation, and liquid relative permeability. The model is not sensitive to the permeability, specific heat, thermal conductivity, density, diffusivity, mass transfer coefficient, relative humidity, initial temperature, gas relative permeability, relative humidity correlation, or capillary pressure correlation. This indicates that the process of brick drying is sensitive to the amount of water in the brick, the surface heat transfer heat transfer, and the internal liquid transport mechanisms.

Sensitivity Coefficient

The model-predicted surface temperature was used to measure the model's sensitivity to the adjusted inputs. The area under the surface temperature curve was integrated using the trapezoidal rule

$$T_{sum} = \sum_{i=1}^{nt} \left(T_{surf,i} + T_{surf,i+1} \right) \Delta t \qquad \text{(units Kelvin * seconds)}$$

This value was used to calculate a sensitivity coefficient for each parameter x_i

$$S_i = \frac{x_i}{T_{sum}} \frac{\Delta T_{sum}}{\Delta x_i}$$

The baseline value for T_{sum} is 20,170,000 Ksec. This quantity was calculated for each of the 19 parameters that were adjusted. These values are shown in Table 39. The calculated sensitivity coefficients for the adjusted input parameters are shown in Table 43.

Permeability

The permeability was adjusted by ±10%. This had a very small effect on the mass loss rate and surface temperature.

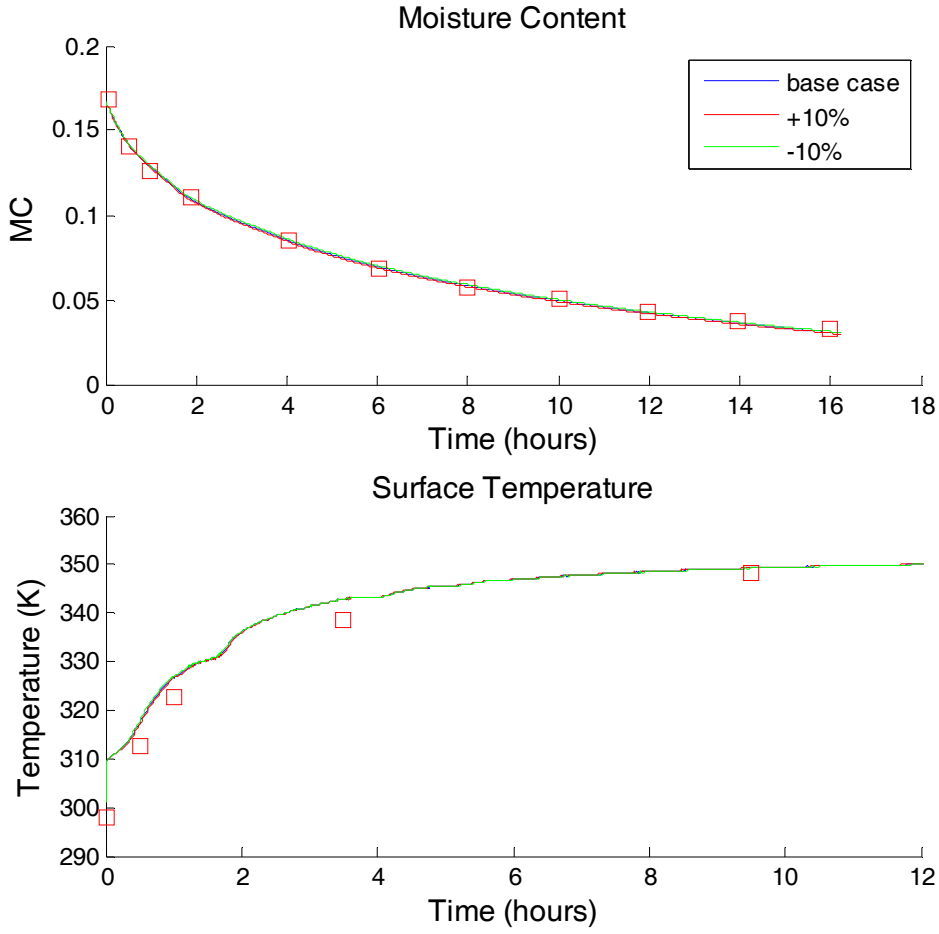

Figure 246 – Effect of Permeability on Convective Drying of Brick

Porosity

The porosity was adjusted by ±10%. This had a significant effect on the mass loss rate and surface temperature as shown in Figure 247. Increasing the porosity lowered the surface temperature, and lowering the porosity increased the surface temperature. The difference in mass loss rates is partially due to the fact that adjusting the porosity while keeping the saturation constant affects the moisture content. To investigate this further two alternative cases were considered; 1) adjusting the porosity while keeping the initial moisture content constant, and 2) adjusting the porosity while keeping the initial mass of water in the sample constant.

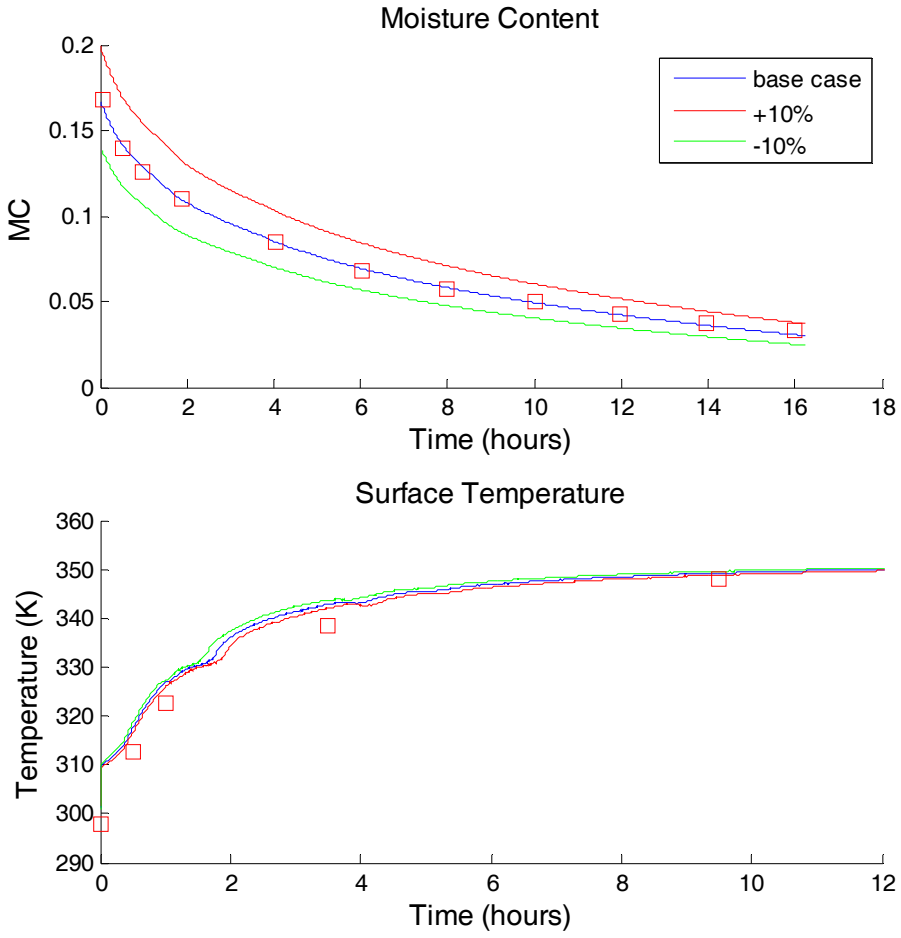

Figure 247 – Effect of Porosity on Convective Drying of Brick

The moisture content in brick is defined as

$$MC = \frac{\phi S_w \rho_w V}{(1-\phi)\rho_s V}\left[=\right]\frac{mass\ water}{mass\ solid}$$

Where V is the volume of the sample. The initial moisture content is held constant by the following constraint

$$S_{w,2} = \frac{\phi_1 S_{w,1}\rho_w}{(1-\phi_1)\rho_s}\frac{(1-\phi_2)\rho_s}{\phi_2 \rho_w}$$

The result of using this constraint while adjusting the porosity is shown in Figure 248. The mass of water in the sample is

$$m_{water} = \phi S_w \rho_w V$$
$$or$$
$$m''_{water} = \phi S_w \rho_w L$$

So the initial mass of water in the material is held constant with the following constraint

$$S_{w,2} = \frac{\phi_1 S_{w,1}}{\phi_2}$$

The results of using this constraint while adjusting the porosity are shown in Figure 249.

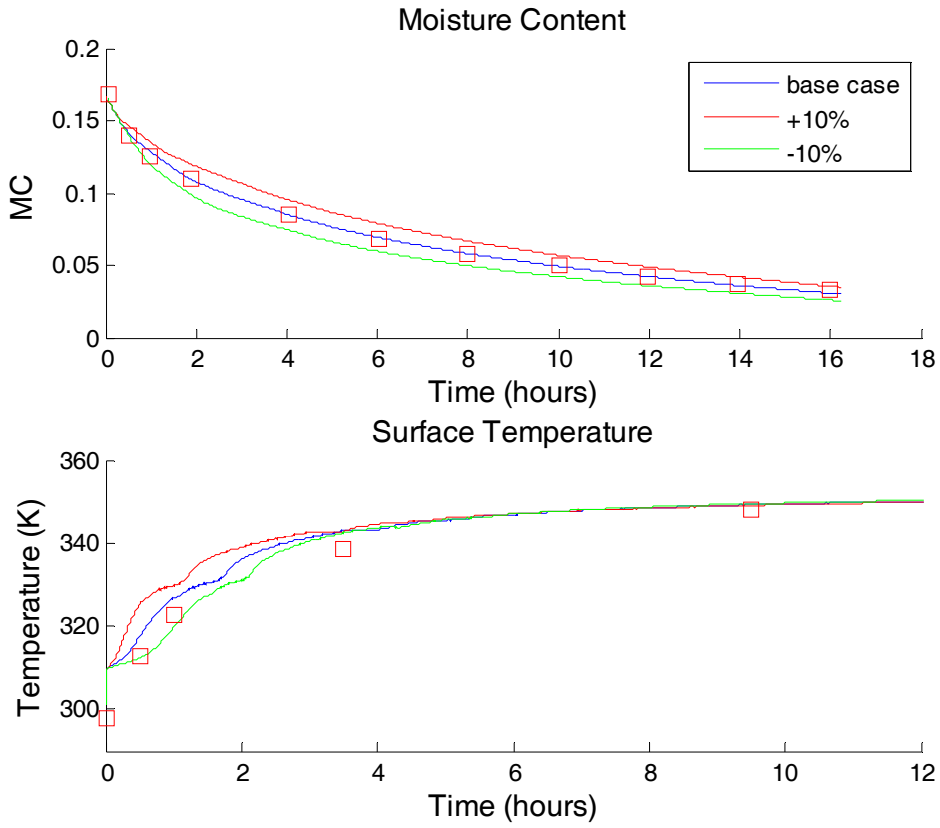

Figure 248 – Effect of Porosity on Convective Drying of Brick – MC_o Held Constant

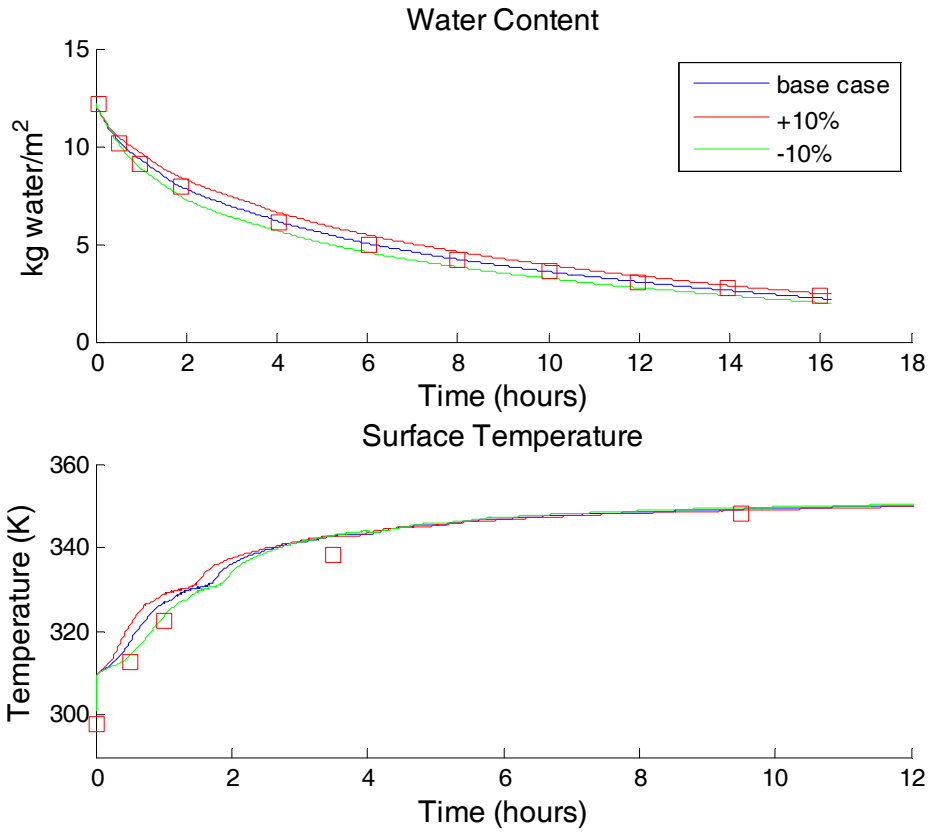

Figure 249 – Effect of Porosity on Convective Drying of Brick – Initial Mass of Water Held Constant

From these results it can be seen that the porosity has a significant effect on the drying rate and the surface temperature is relatively independent from initial moisture content effects. In order to determine if this is a porosity effect, or if it is related to the moisture content dependence of the heat and mass transfer coefficients, an additional test was performed. The porosity was adjusted, while the surface heat and mass transfer coefficients were maintained constant values

$$h = 37.5 \frac{W}{m^2 K}$$

$$h_m = 0.0415 \frac{m}{s}$$

The results are shown in Figure 250 for the case where the initial water mass in the brick is constant. Adjusting the porosity is shown to have a significant effect that is separate from the associated change in the initial mass of water in the material or its

effect on surface heat and mass transfer coefficients.

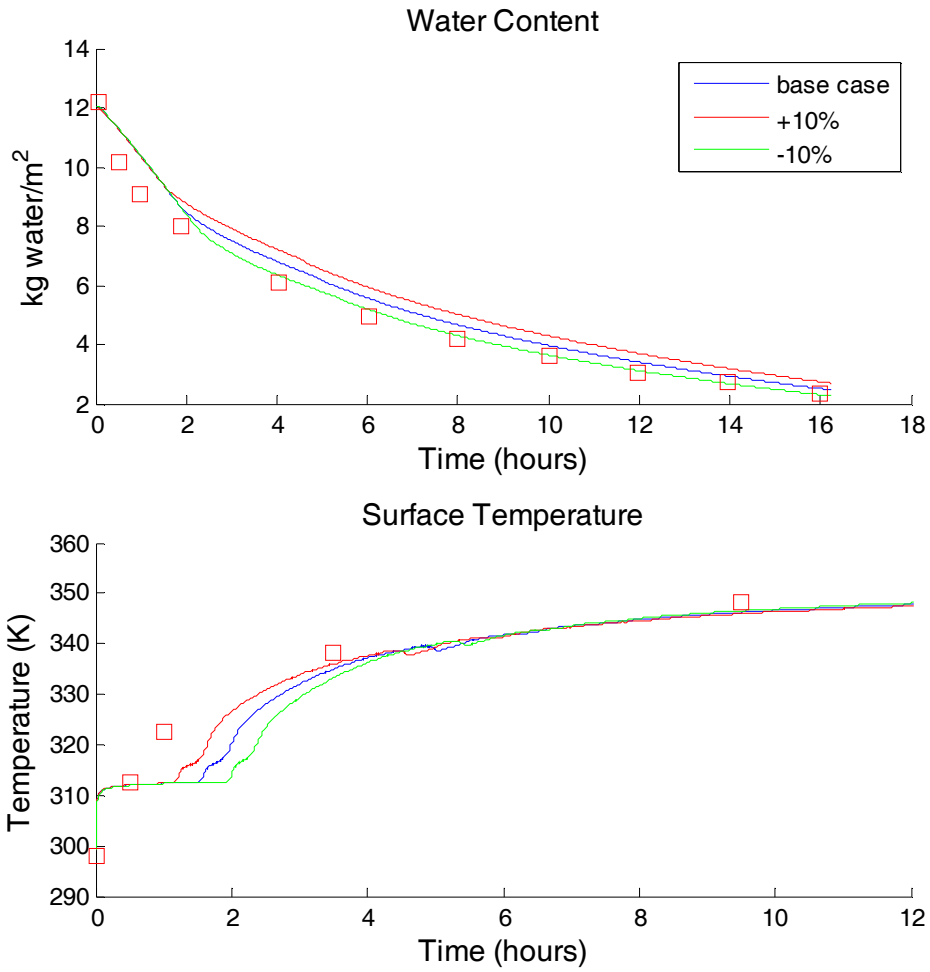

Figure 250 – Effect of Adjusting the Porosity on Convective Drying of Brick – Constant Initial Mass of water and Constant Heat and Mass Transfer Coefficients

Specific Heat of Solid Phase

The specific heat was adjusted by ±10%. This did not have a significant effect on the mass loss rate or surface temperature, as shown in Figure 251.

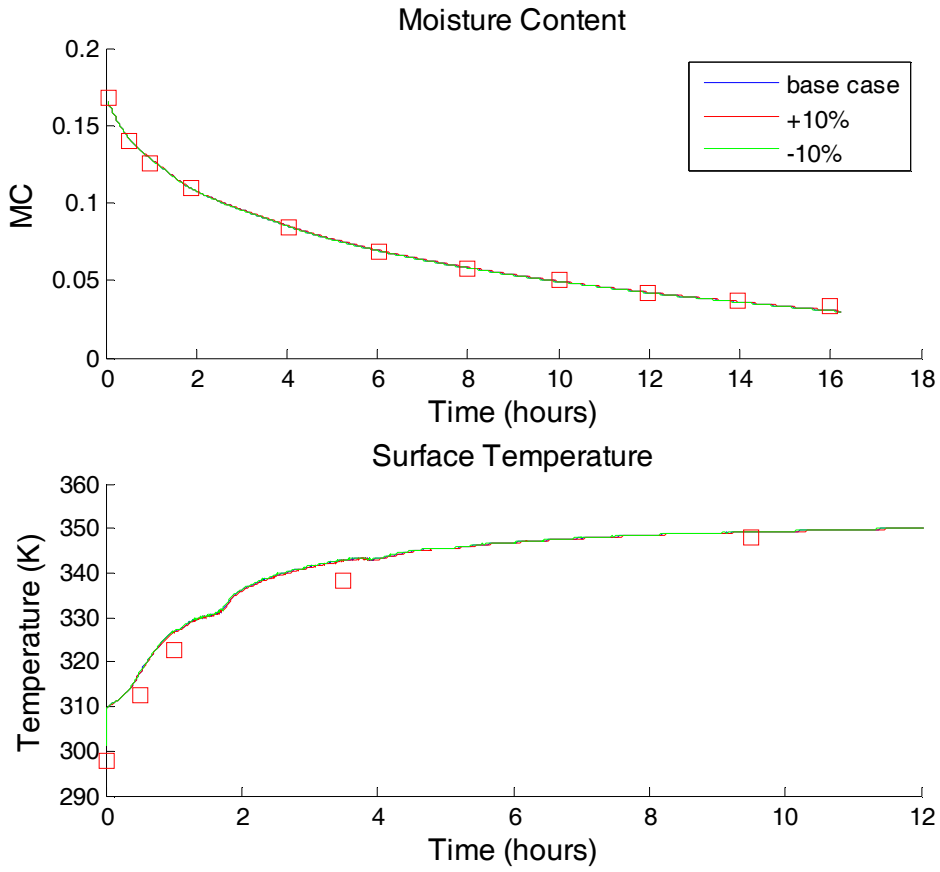

Figure 251 - Effect of Specific Heat of Solid on Convective Drying of Brick

Thermal Conductivity of Solid Phase

The thermal conductivity of the solid phase was adjusted by ±10%. This did not have a significant effect on the mass loss rate or surface temperature, as shown in Figure 252.

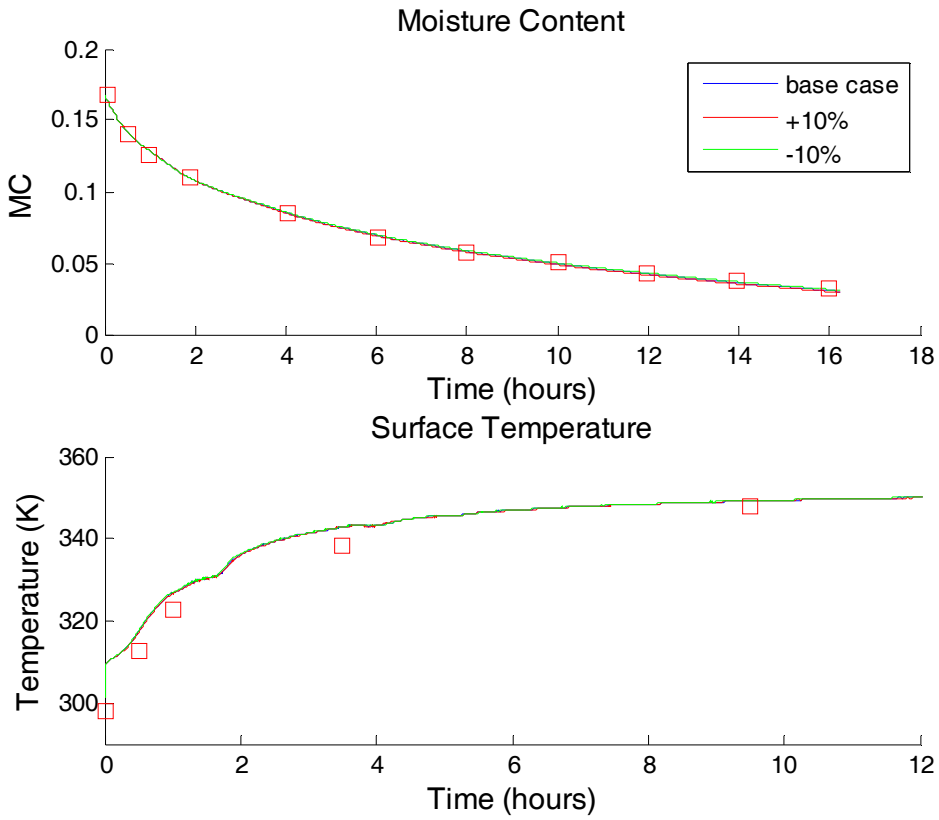

Figure 252 - Effect of Thermal Conductivity of Solid on Convective Drying of Brick

Density of Solid Phase

The density of the solid phase was adjusted by $\pm 10\%$. This had a significant effect on the non-dimensional mass loss rate, but very little effect on the surface temperature, as shown in Figure 253. This is partially due to the fact that adjusting the solid phase density changes the moisture content, which is calculated on a per unit solid mass basis. If the dimensional mass loss rate is plotted with kg of water/m^2 on the y-axis it can be seen in Figure 254 that the dimensional drying rate is not significantly affected by changing the solid density. To investigate this further the density of the solid phase was adjusted with the initial moisture content held constant with the following constraint.

$$S_{w,2} = S_{w,1} \frac{\rho_{s,2}}{\rho_{s,1}}$$

The results from this test are shown in Figure 255.

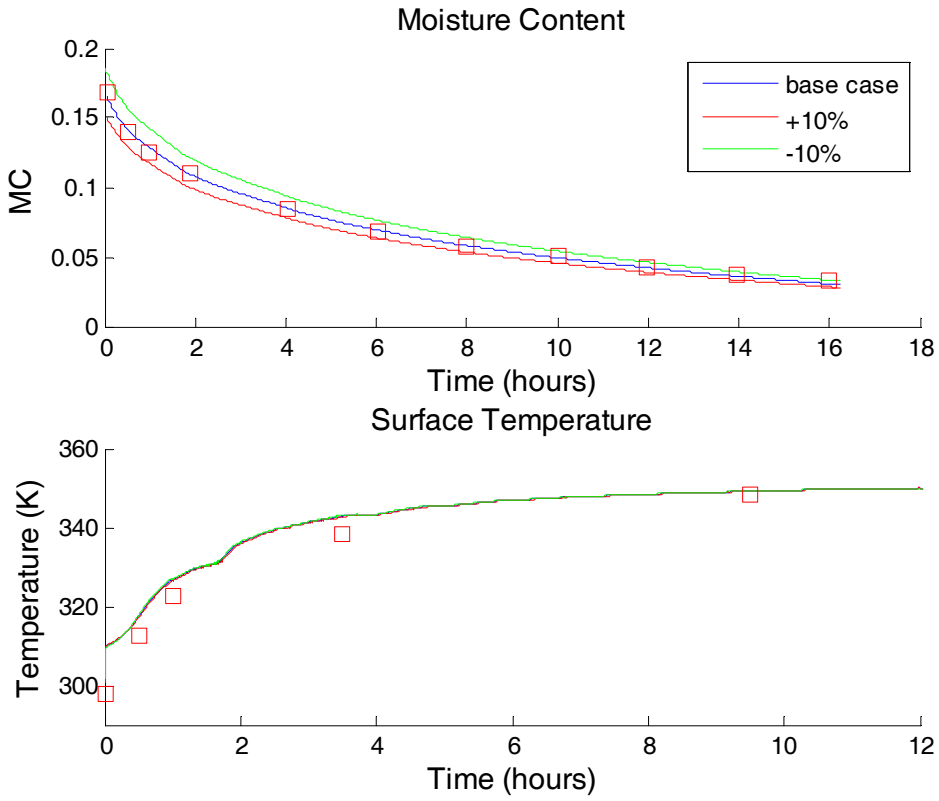

Figure 253 - Effect of Density of Solid Phase on Convective Drying of Brick

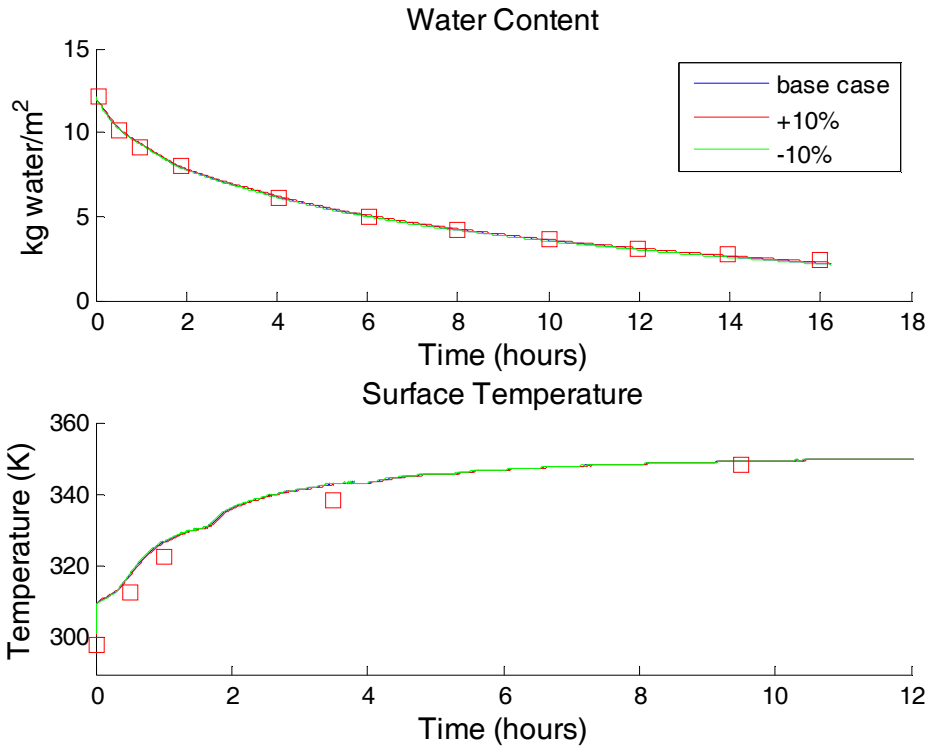

Figure 254 – Effect of Density of Solid Phase on Dimensional Mass Loss Rate

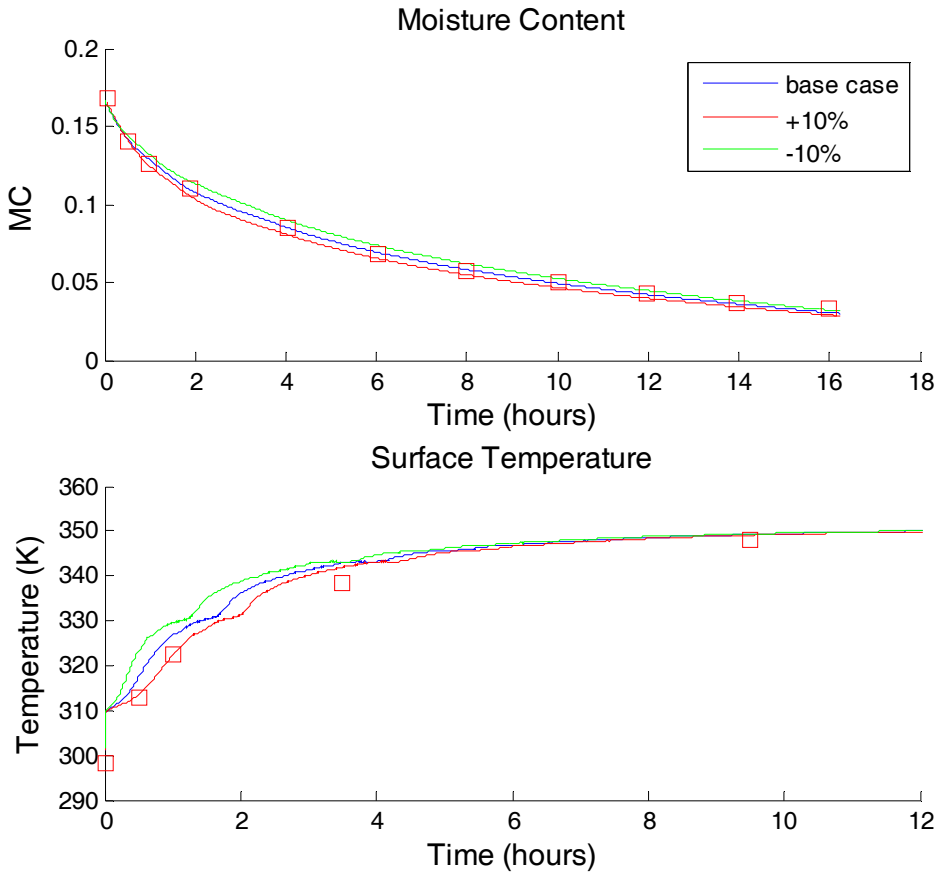

Figure 255 – Effect of Density of Solid Phase on Convective Drying of Brick – MC_o Held Constant

Diffusivity

The vapor diffusivity was adjusted by $\pm 10\%$. This had a very slight effect on the moisture content and surface temperature, as shown in Figure 256. Increasing the diffusivity allowed slightly more water vapor to diffuse to the surface, thereby increasing the evaporation rate, and lowering the surface temperature. Decreasing the diffusivity had the opposite effect.

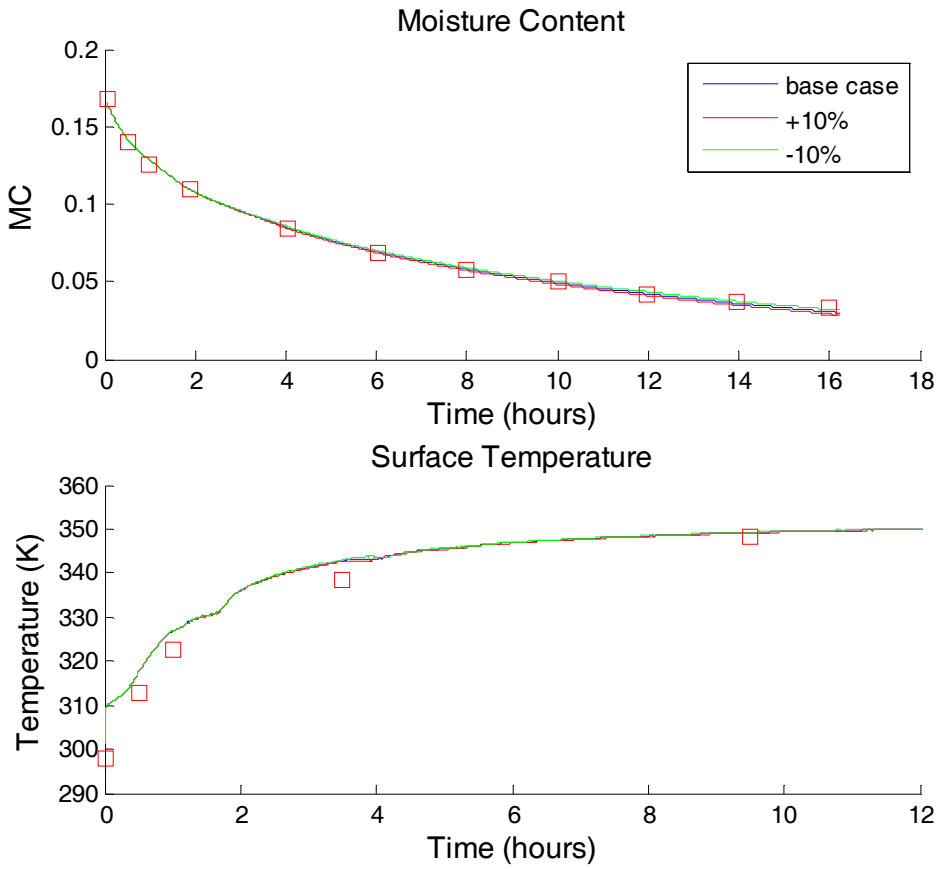

Figure 256 - Effect of Diffusivity on Convective Drying of Brick

Heat Transfer Coefficient

The surface heat transfer coefficient is calculated in the model using the correlation of Chen and Pei (1988) for forced convection

$$h = 75\left(0.8 + 0.2\frac{MC_{surf} - 0.015}{0.09 - 0.015}\right) \quad [\mathrm{W/m^2K}]$$

This value of h that was calculated for each iteration in the model was adjusted ±10%. This had a slight effect on the mass loss rate, and a much more significant effect on the surface temperature, as shown in Figure 257.

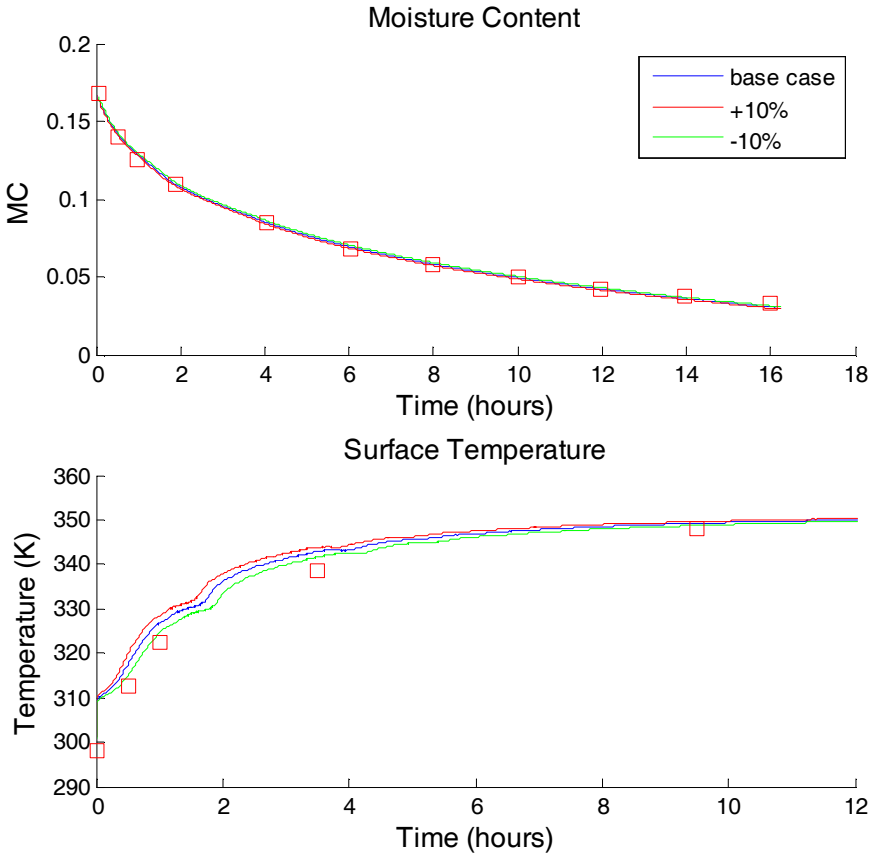

Figure 257 - Effect of Heat Transfer Coefficient on Convective Drying of Brick

Mass Transfer Coefficient

The mass transfer coefficient was calculated using the correlation of Chen and Pei [39] for forced convection

$$h_m = 0.083\left(0.1 + 0.9\frac{M_{surf} - 0.015}{0.09 - 0.015}\right) \quad [\text{m/s}]$$

This value that was calculated every iteration in the mode was adjusted $\pm 10\%$. This had almost no effect on the mass loss rate and a very small effect on the surface temperature.

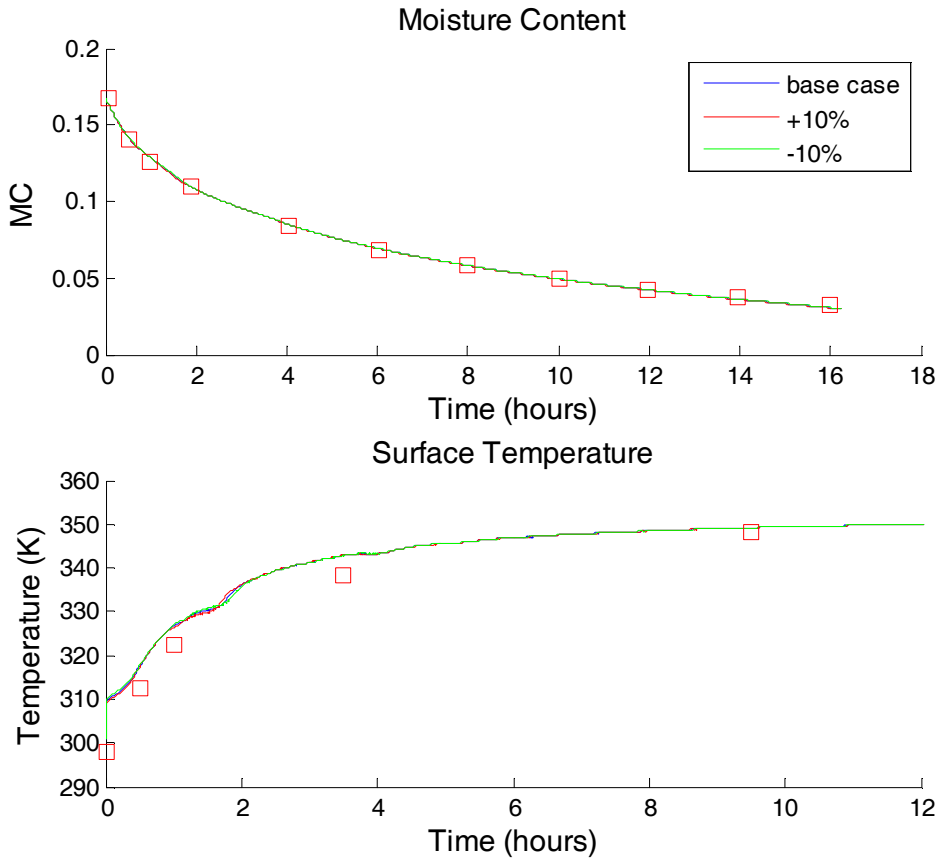

Figure 258 - Effect of Mass Transfer Coefficient on Convective Drying of Brick

Relative Humidity

The relative humidity was adjusted by $\pm 10\%$. This had a very slight effect on the mass loss rate and surface temperature as shown in Figure 259. Since the expected uncertainty in the relative humidity is most likely more than 10% of 9.3% (0.93% RH), the sensitivity to larger changes was tested. Values of 0%, 9.3% (base case), and 20% were tested and shown in Figure 260.

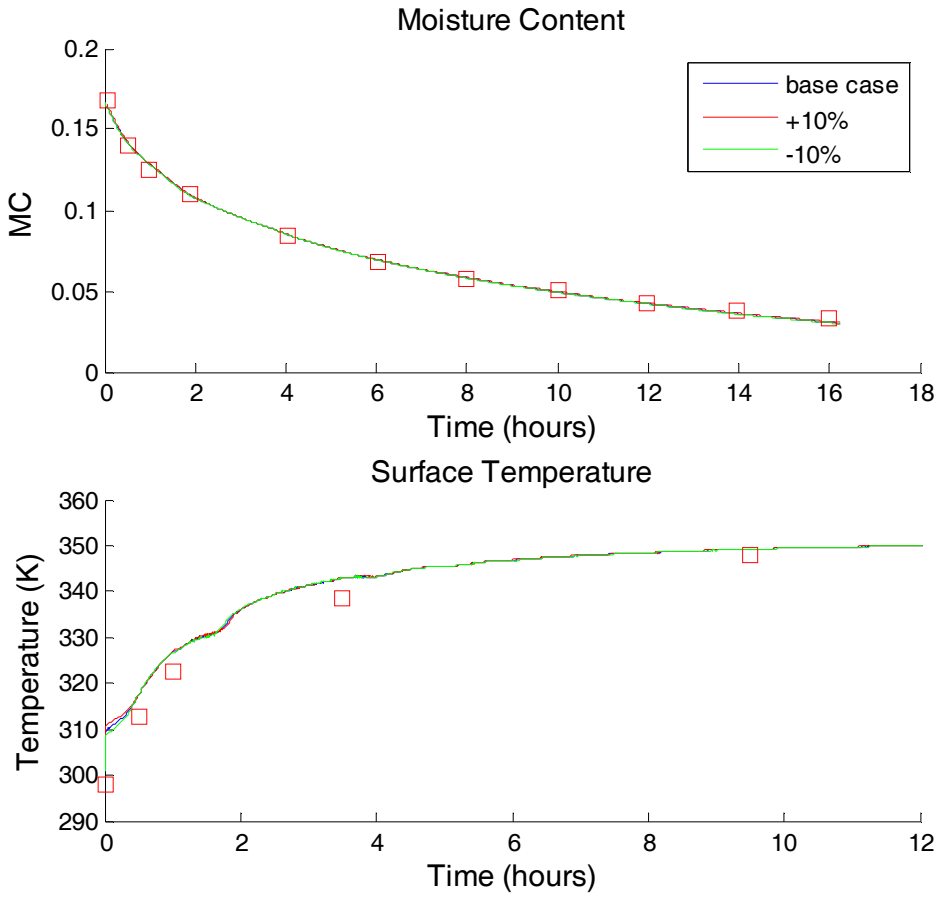

Figure 259 - Effect of Relative Humidity on Convective Drying of Brick

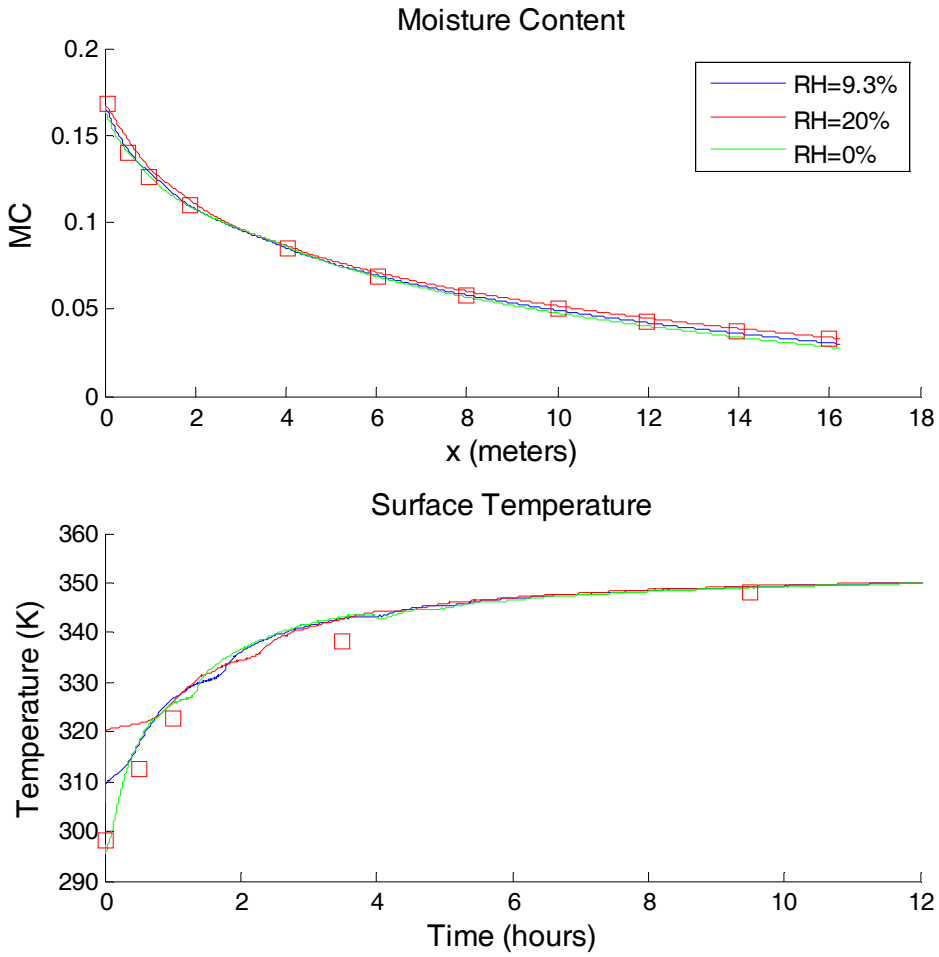

Figure 260 – Effect of Larger Changes in Relative Humidity on Drying of Brick

From Figure 260 it can be seen that larger changes in the relative humidity can have a significant effect on the surface temperature and drying rate.

Initial Temperature

The initial temperature of the brick was adjusted $\pm 2^{o} C$. This did not have a significant effect on the surface temperature history or the mass loss rate as shown in Figure 261.

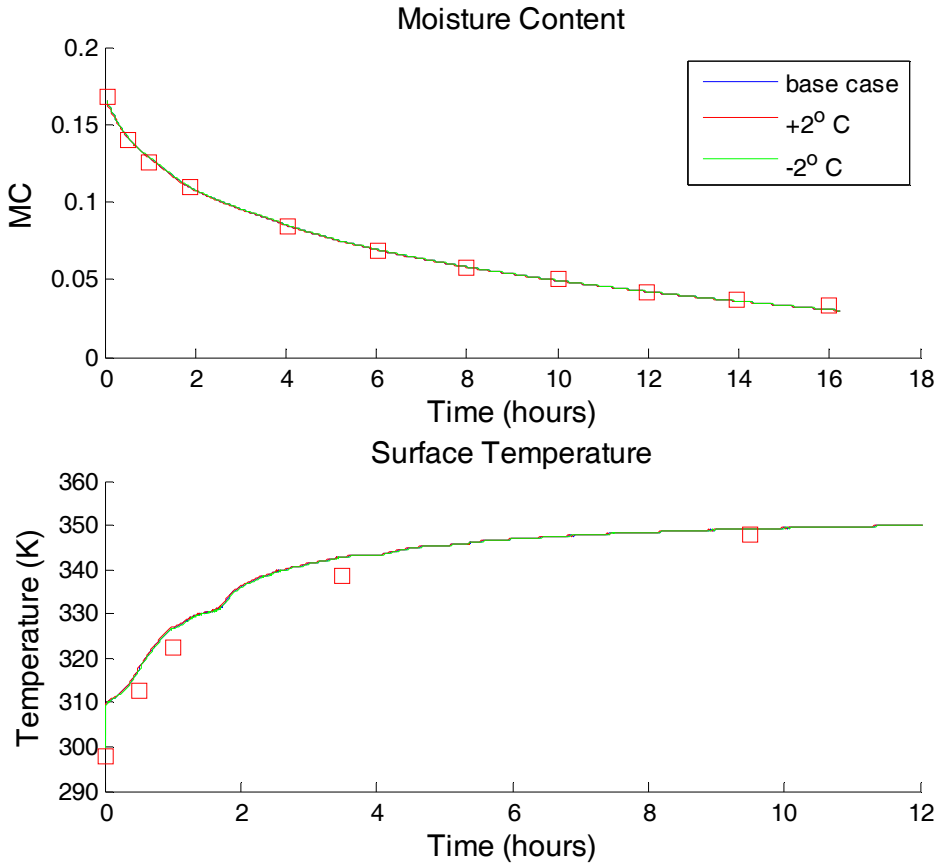

Figure 261 - Effect of Initial Temperature on Convective Drying of Brick

Ambient Temperature

The ambient temperature was adjusted by $\pm 2^{o}C$. This had a significant impact on the surface temperature as shown in Figure 262.

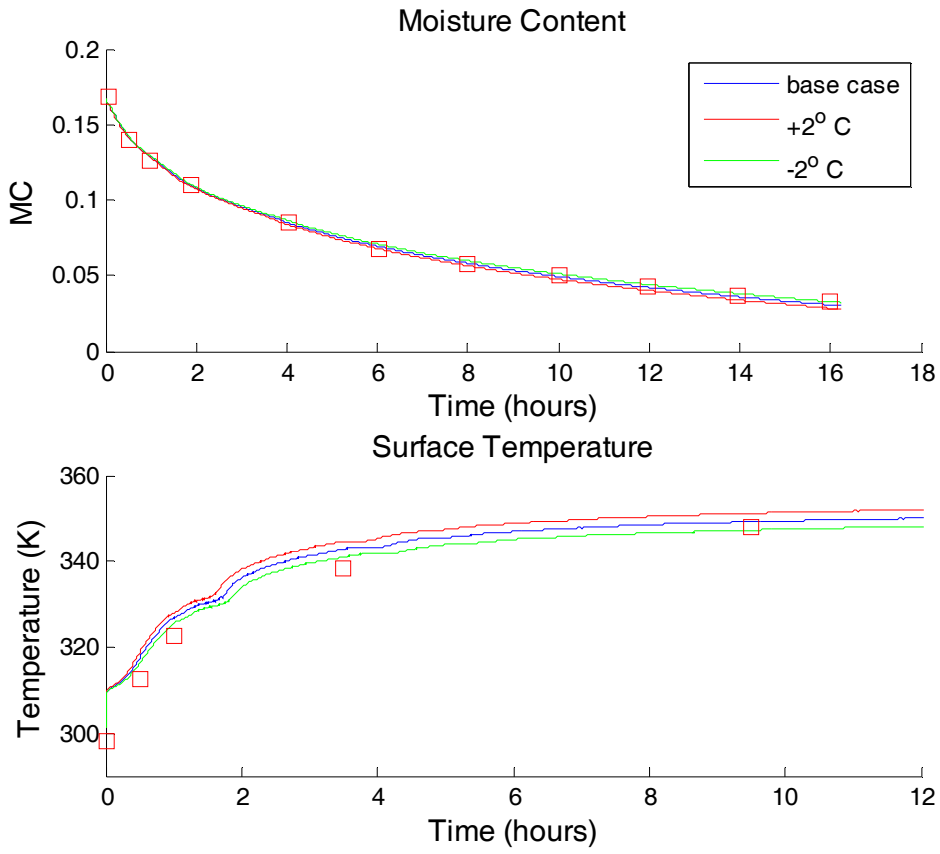

Figure 262 - Effect of Ambient Temperature on Convective Drying of Brick

Sample Depth

The depth of the brick sample was adjusted by $\pm 10\%$. This had a significant effect on the drying rate and surface temperature as shown in Figure 263. This is partially due to the fact that increasing the length while holding the initial moisture content constant will increase the total mass of water in the sample.

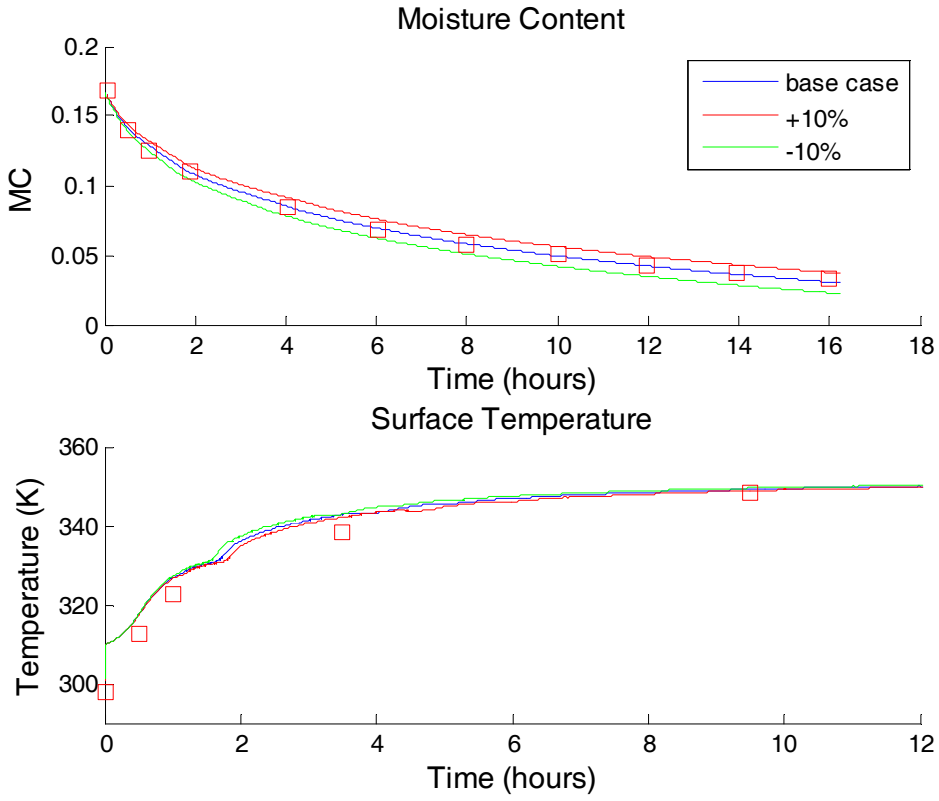

Figure 263 - Effect of Sample Depth on Convective Drying of Brick

To separate the effects of changes in sample depth from the effects of the associated increase in mass of water in the sample, the initial mass in the sample was held constant by using the following constraint while changing the sample depth.

$$S_1 = S_2 \frac{L_2}{L_1}$$

The results of this change are shown in Figure 264. Adjusting the depth of the sample has a significant effect on the drying rate and surface temperature. Increasing the depth of the sample increases the distance that water must travel in order to reach the surface and evaporate. This increases the resistance to water flowing to the surface, lowers the

evaporation rate, and increases the surface temperature. Decreasing the sample depth has the opposite effect.

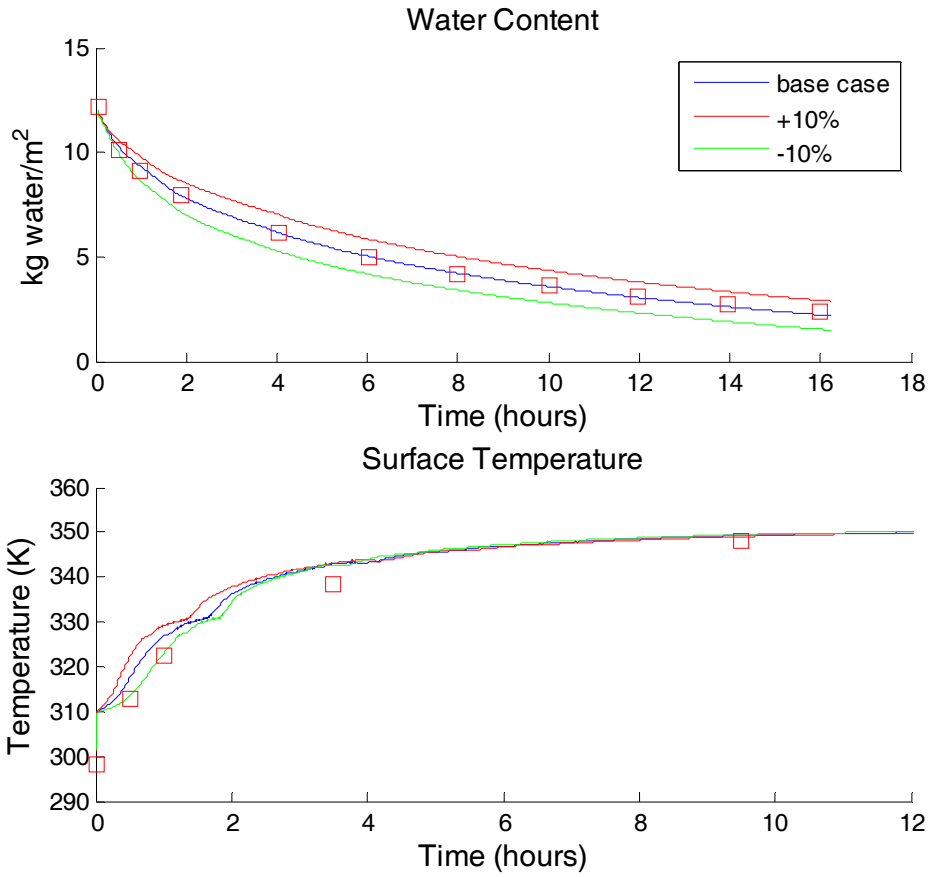

Figure 264 – Effect of Sample Depth on Dimensional Drying Rate for Convective Drying of Brick

Initial Water Saturation

The initial saturation was adjusted ±10% from its base value. This had a significant effect on the mass loss rate and surface temperature, as shown in Figure 265.

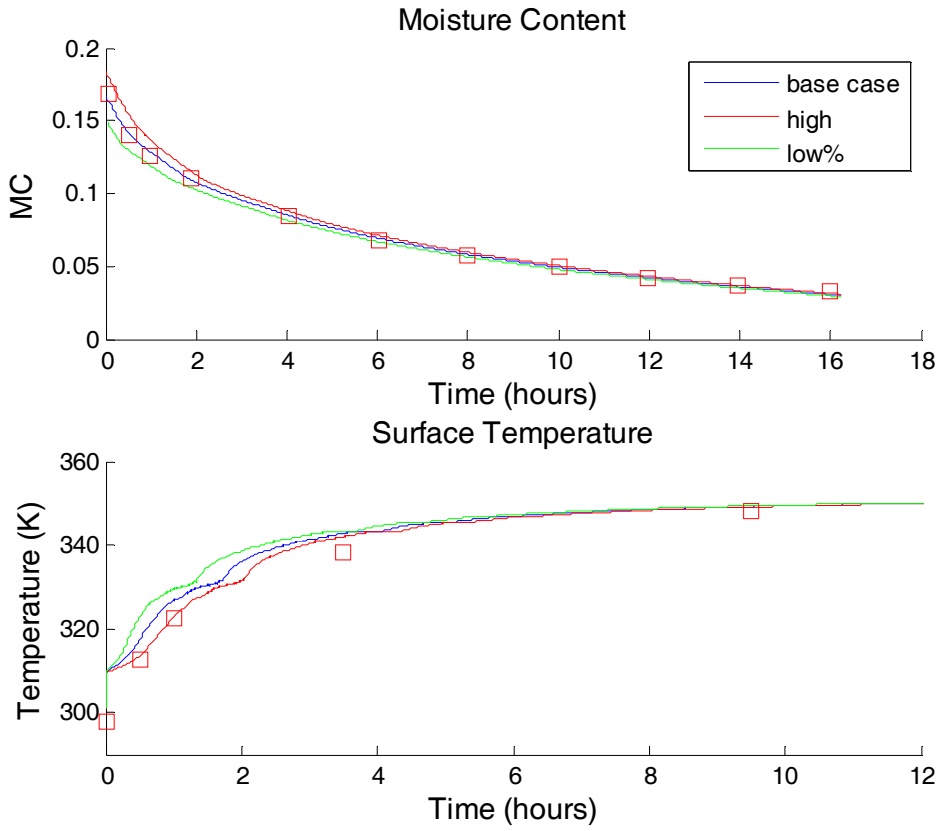

Figure 265 – Effect of Initial Saturation on Convective Drying of Brick

Number of Nodes

The number of nodes was adjusted from the base value of 31, to a "high" value of 41 and a "low" value of 21. This had a very slight effect on the model result, as shown in Figure 266. Increasing the number of nodes increased the mass loss rate slightly.

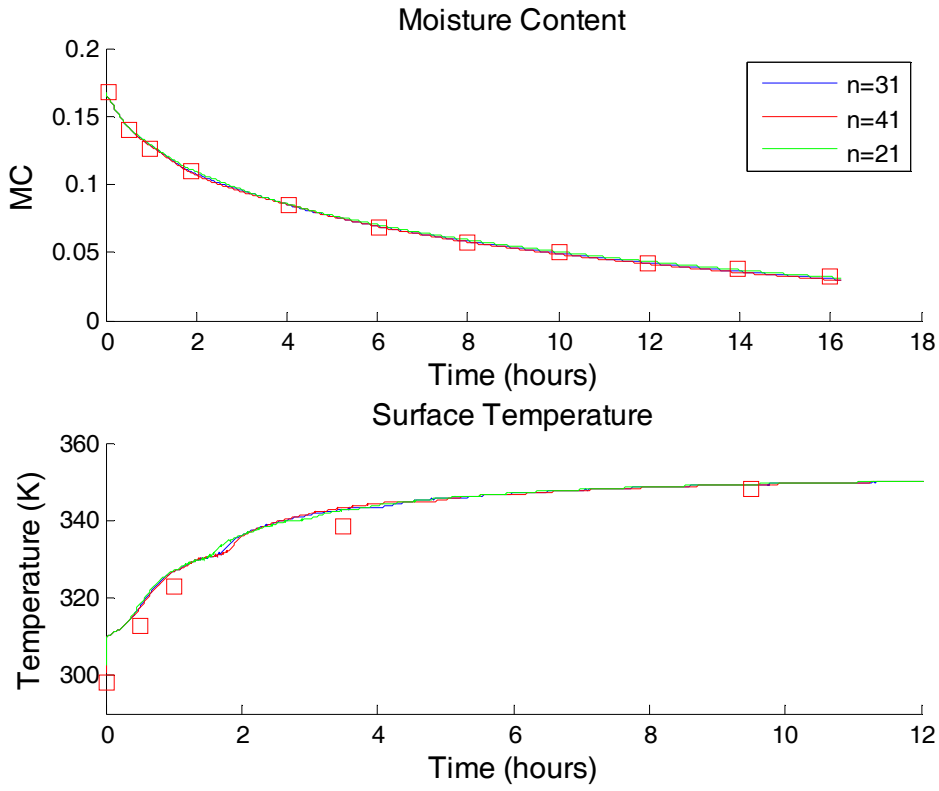

Figure 266 – Effect of Number of Nodes on Convective Drying of Brick

Timestep

The time step was adjusted from its base value of 1 second, to a "high" value of 10 seconds and a "low" value of 0.1 second. The smaller time step did not have any observable effect on the temperature or mass loss rate, as shown in Figure 266. The larger time step produced a lower mass loss rate, and severe oscillations in the surface temperature.

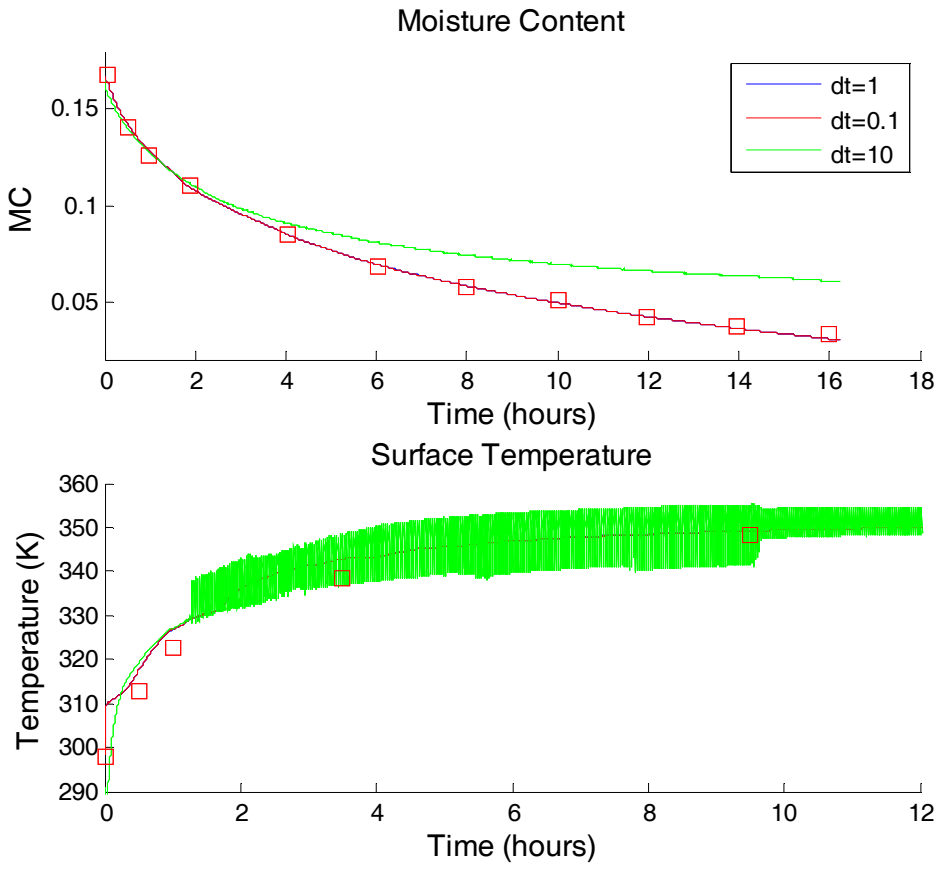

Figure 267 – Effect of Timestep on Convective Drying of Brick

Liquid Relative Permeability

The sensitivity of the model to the liquid relative permeability correlation was tested. A fourth power function of saturation is the base case. A fifth power and cubic function were used as the 'low' and 'high' cases. This had a very significant effect on the drying rate and surface temperature.

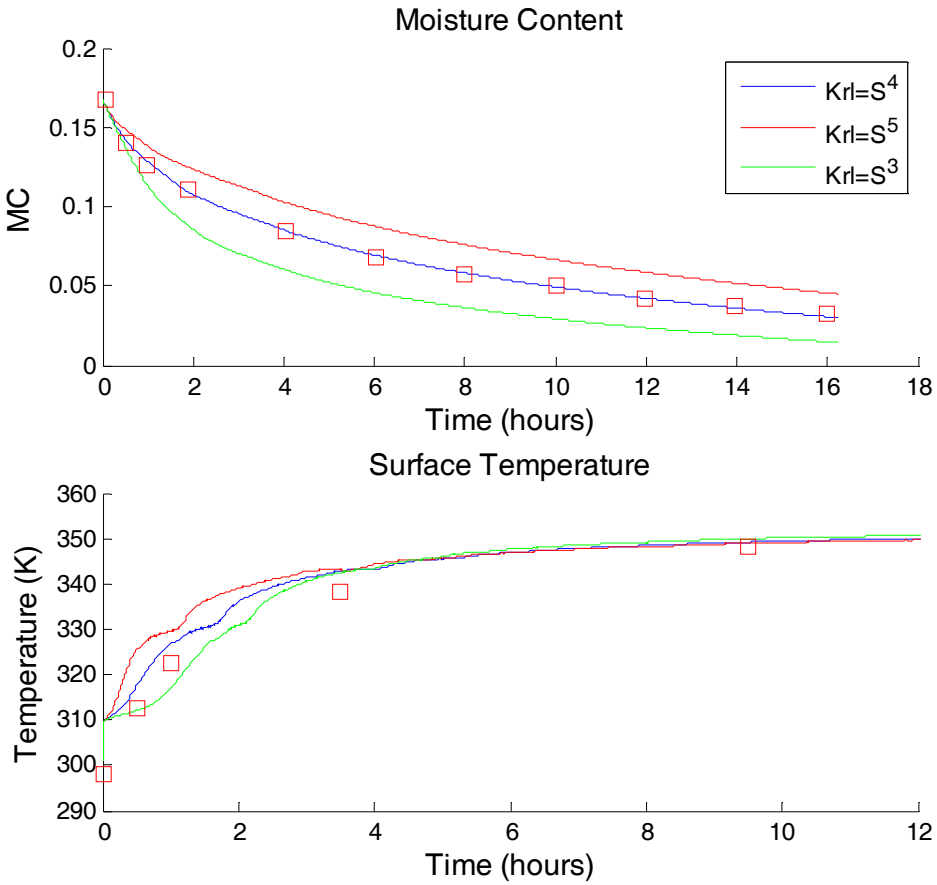

Figure 268 - Effect of Liquid Relative Permeability on Convective Drying of Brick

Gas Relative Permeability

The sensitivity of the model to the gas relative permeability correlation was tested by adjusting the correlation from the base case to the high and low correlations shown in Figure 244. The results are shown in Figure 269. This did not have a significant effect on the surface temperature or drying rate.

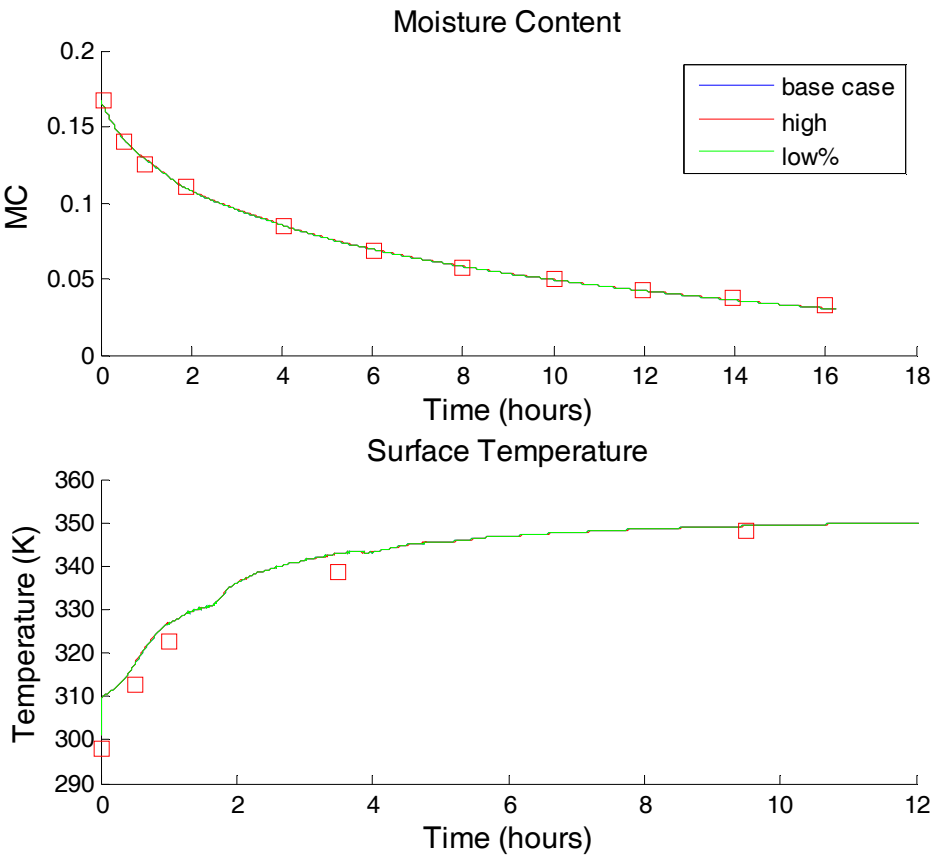

Figure 269 - Effect of Gas Relative Permeability on Convective Drying of Brick

Relative Humidity Correlation

The relative humidity correlation was adjusted from its base case correlation to the "high" and "low" correlations as shown in Figure 245. This had a slight effect on the surface temperature and mass loss rates as shown in Figure 270.

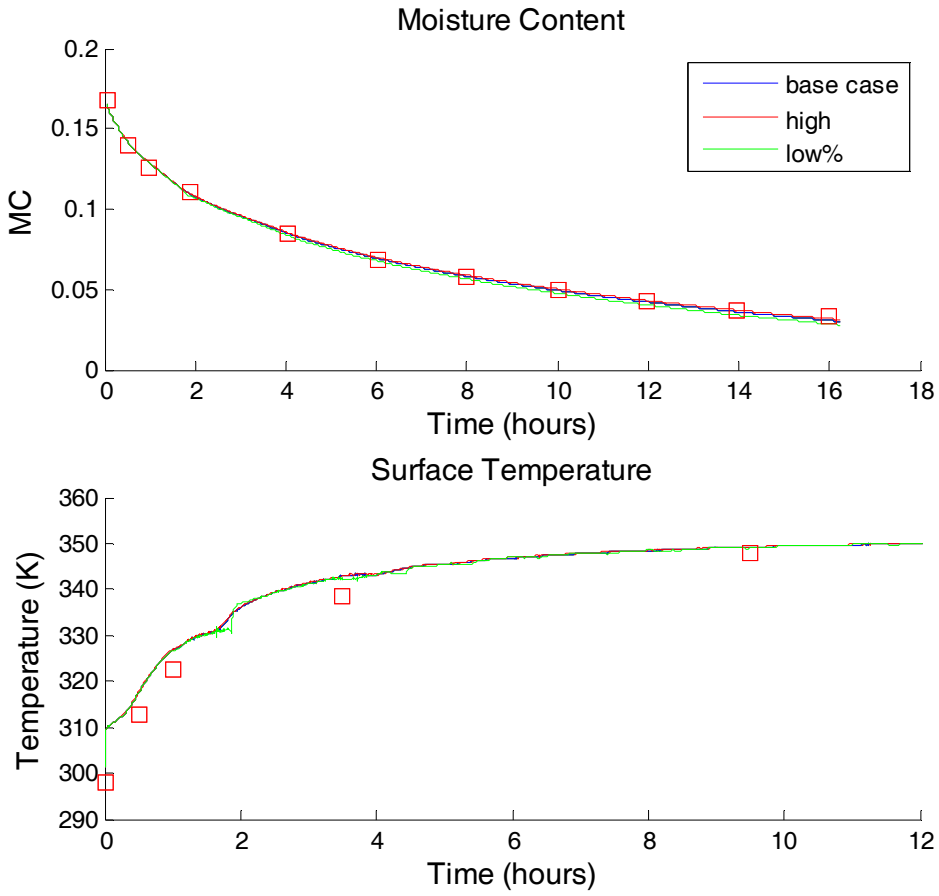

Figure 270 – Effect of Relative Humidity Correlation on Convective Drying of Brick

Capillary Pressure

The sensitivity of the model to the capillary pressure correlation was tested. The base case capillary pressure was adjusted ±10% as shown in Figure 243. The results are shown in Figure 271. Increasing the capillary pressure increased the mass loss rate and lowered the surface temperature. Presumably this means that the increased capillary pressure drew more water to the surface, thus allowing for a greater evaporation rate, which increased the evaporative cooling, and led to a cooler surface temperature. Decreasing the capillary pressure had the opposite effect.

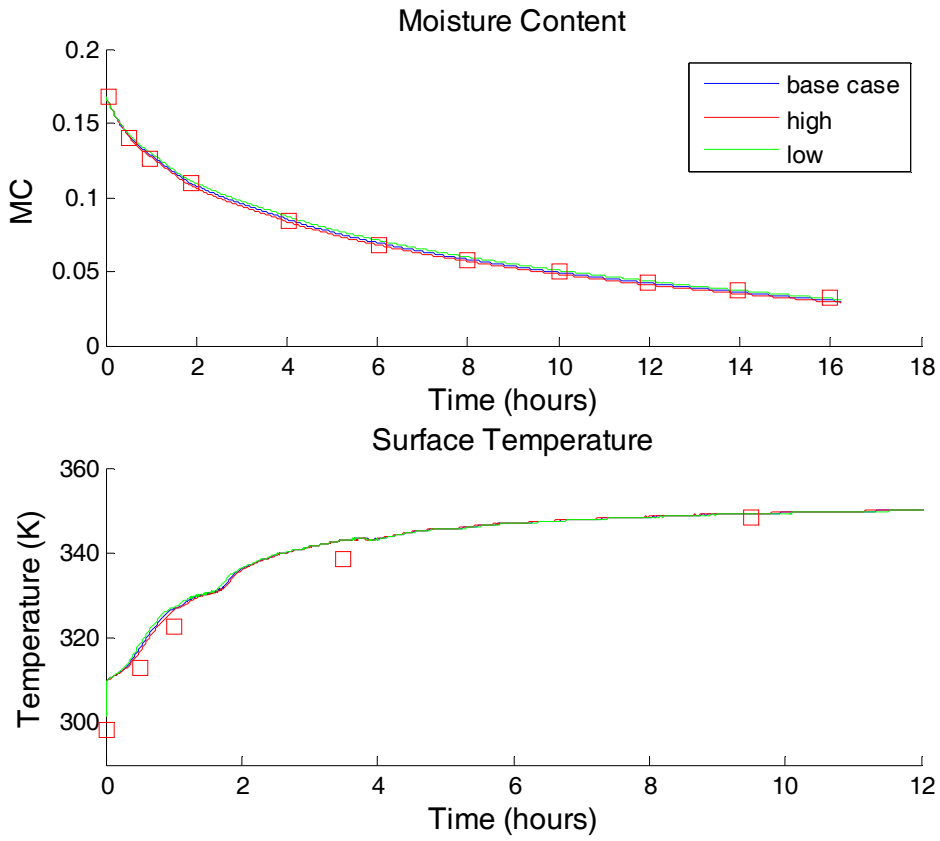

Figure 271 – Effect of Capillary Pressure Correlation on Brick Drying

Irreducible Saturation

The irreducible saturation was adjusted $\pm 10\%$ from its base value of 0.09. The results are shown in Figure 272.

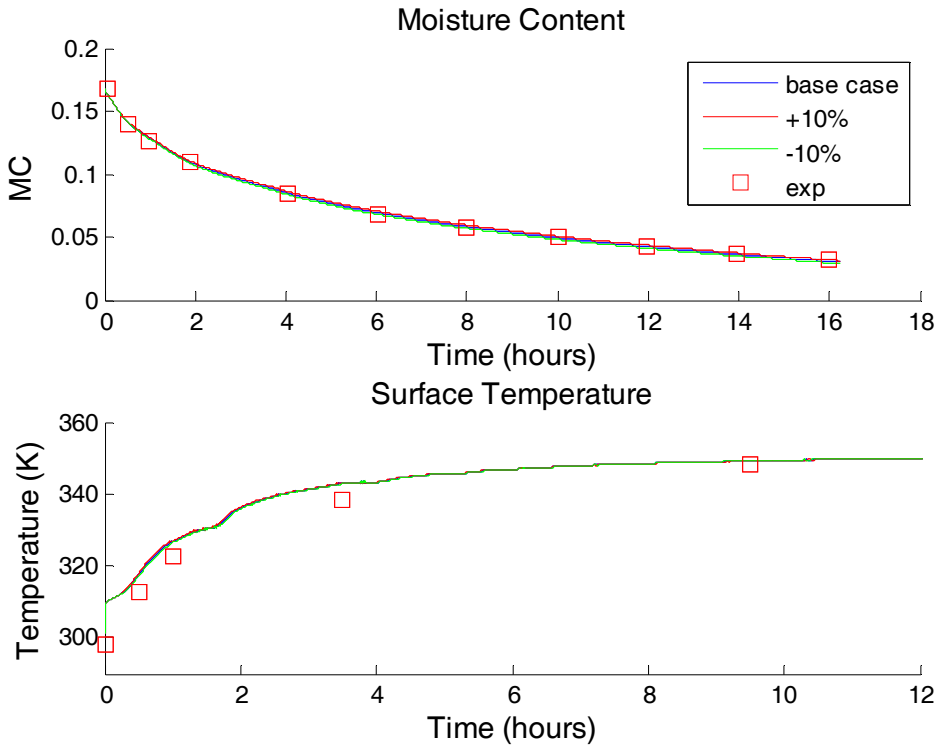

Figure 272 – Effect of Irreducible Saturation on Brick Drying

G.4. Convective Drying of Wood Sensitivity Analysis

The sensitivity of the model was tested for the case of wood drying. The values of the simple parameters that were adjusted are shown in Table 32. Whenever possible these were adjusted by $\pm 10\%$. In some cases this was not possible or practical. For example the initial temperature and ambient temperature were adjusted by 2 degrees C because that is a reasonable uncertainty to associate with temperature measurements made with thermocouples. The material was initially completely saturated, so the initial saturation could only be decreased. It was decreased by approximately 10% and 20%.

Constitutive Relations Tested

To determine if the form of other constitutive relations have a significant effect on the model, tests were conducted on the correlations for liquid and gas relative permeability, relative humidity, capillary pressure, and surface drying coefficient.

Relative Permeability

The relative permeabilities of wood are assumed to be linear in the model. To test the sensitivity of the model to this assumption, non-linear correlations were used. The liquid relative permeability was tested as a square and cubic function of saturation

$$K_{rl} = S_{eff}^2 \quad (case\ 1)$$
$$K_{rl} = S_{eff}^3 \quad (case\ 2)$$

The gas relative permeability was tested as square and cubic functions of gas saturation

$$K_{rg} = 0.05\left(1 - S_{eff}\right)^2 \quad (case\ 1)$$
$$K_{rg} = 0.05\left(1 - S_{eff}\right)^3 \quad (case\ 2)$$

These correlations are shown in Figure 273. The results of adjusting the gas and liquid relative permeability correlations are shown in Figure 296 and Figure 297.

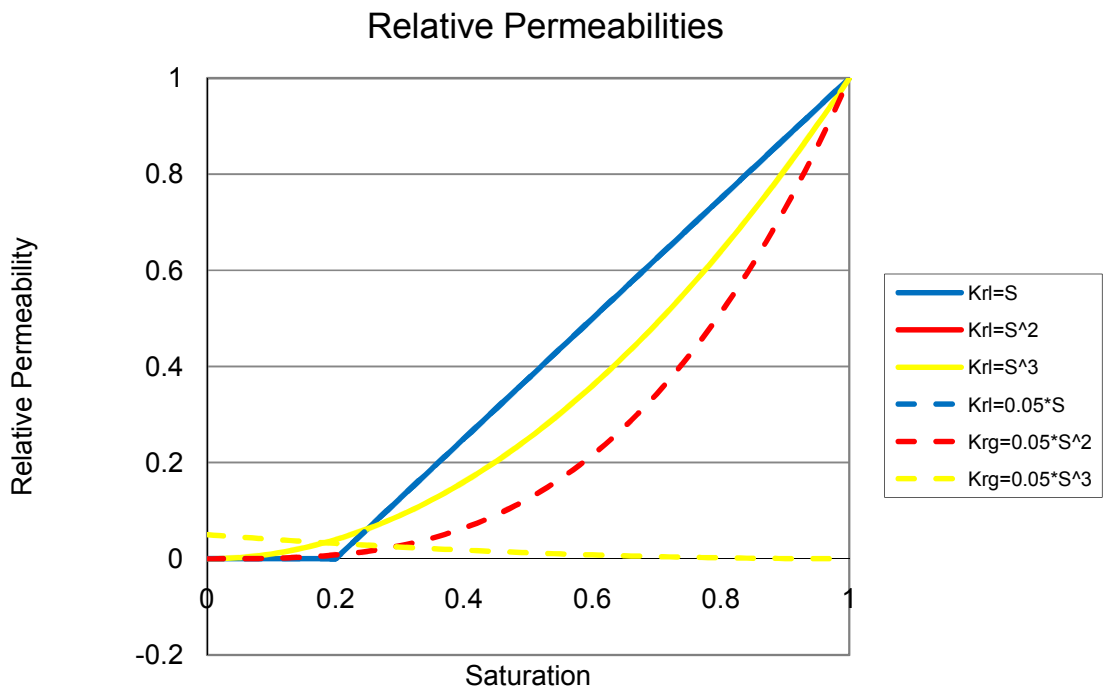

Figure 273 – Relative Permeabilities used in Sensitivity Analysis

Relative Humidity

The relative humidity for wood is calculated from the vapor pressure correlation given by Nasrallah and Perre [38]

$$p_v = p_{vs} \exp\left(\left(17.884 - 0.1423T + 0.0002363T^2\right)\left(1.0327 - 0.000674T\right)^{92M}\right)$$

The value obtained from this correlation was adjusted $\pm 10\%$. The results are shown in Figure 298.

Capillary Pressure

The correlation used for the capillary pressure in wood was measured by Spolek and Plumb [45]. They found a wide variation between the different samples tested. Their average correlation was used in the model

$$p_c = 1.24 \times 10^4 S^{-0.61}$$

To test the sensitivity of the model to this correlation, it was adjusted ±10% as shown in Figure 274.

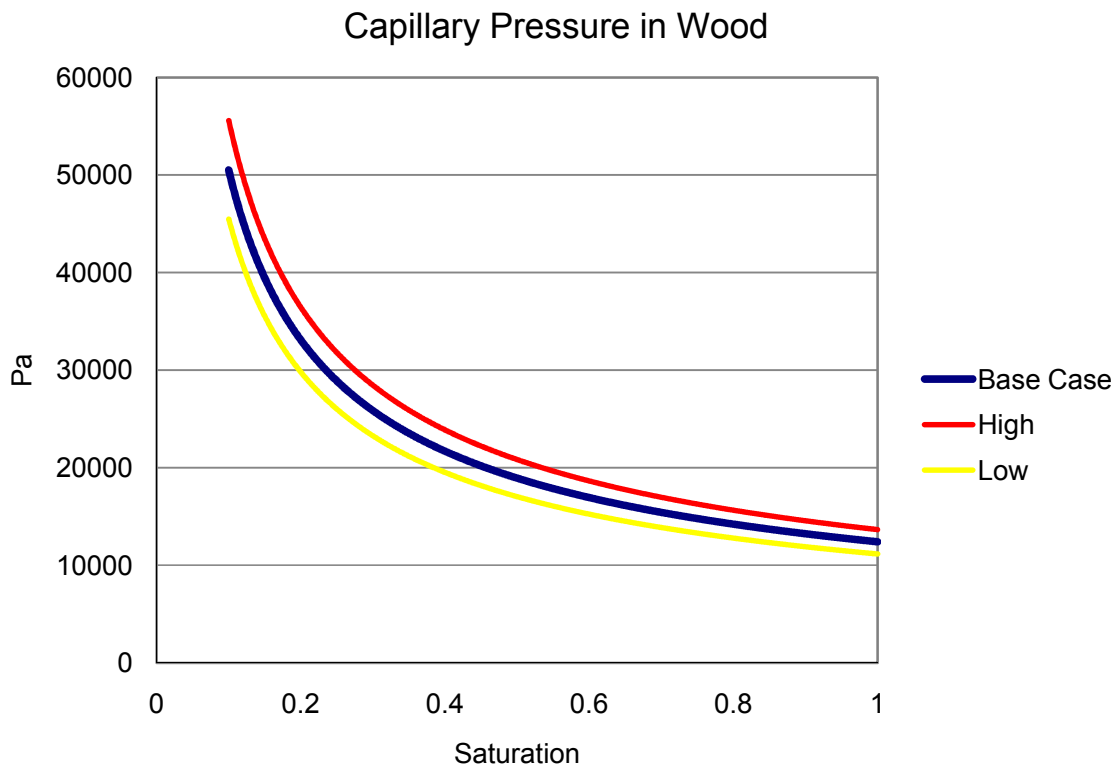

Figure 274 – Capillary Pressure Used for Sensitivity Analysis of Wood

The results of adjusting the capillary pressure are shown in Figure 299.

Surface Drying Coefficient

The surface mass loss rate for wood is calculated as

$$\dot{m}''_{evap} = \beta h_m \left(\rho_{v,surf} - \rho_{v,\infty} \right)$$

Where the surface drying coefficient, beta, is the surface saturation to the third power:

$$\beta = S_w^{\,3}$$

The power of this function was adjusted $\pm 10\%$. The results are shown in Figure 300.

Results

Adjusting the parameters in Table 32 and the 5 constitutive relations discussed showed that for convective drying of wood, the model is the most sensitive to the ambient temperature and liquid relative permeability. The model is also is sensitive, to a lesser degree, to the pemeability, porosity, density, heat and mass transfer coefficients, length of the sample, initial saturation, gas relative permeability, relative humidity correlation, capillary pressure, and drying coefficient. The model did not exhibit significant sensitivity to the specific heat, thermal conductivity, diffusivity, relative humidity, or initial temperature. This indicates that both surface transfer phenonemon as well as internal heat and mass transfer is important to the drying process when modeling the convective drying wood.

Sensitivity Coefficient

The model predicted surface temperature was used to measure the models sensitivity to the adjusted inputs. The area under the surface temperature curve was integrated using the trapezoidal rule

$$T_{sum} = \sum_{i=1}^{nt} \left(T_{surf,i} + T_{surf,i+1} \right) \Delta t \qquad \text{(units Kelvin * seconds)}$$

This value was used to calculate a sensitivity coefficient for each parameter x_i

$$S_i = \frac{x_i}{T_{sum}} \frac{\Delta T_{sum}}{\Delta x_i}$$

The baseline value for T_{sum} is 24,720,000 Ksec. This quantity was calculated for each of the 19 parameters that were adjusted. These values are shown in Table 40. The calculated sensitivity coefficients for the adjusted input parameters are shown in Table 44.

Permeability

The permeability of wood was adjusted by $\pm 10\%$. This did not have a significant effect on the drying rate and surface temperature as shown in Figure 275. Increasing the permeability allowed slightly more water to be transported to the surface, thus increasing the mass loss rate, and decreasing the surface temperature by a small amount.

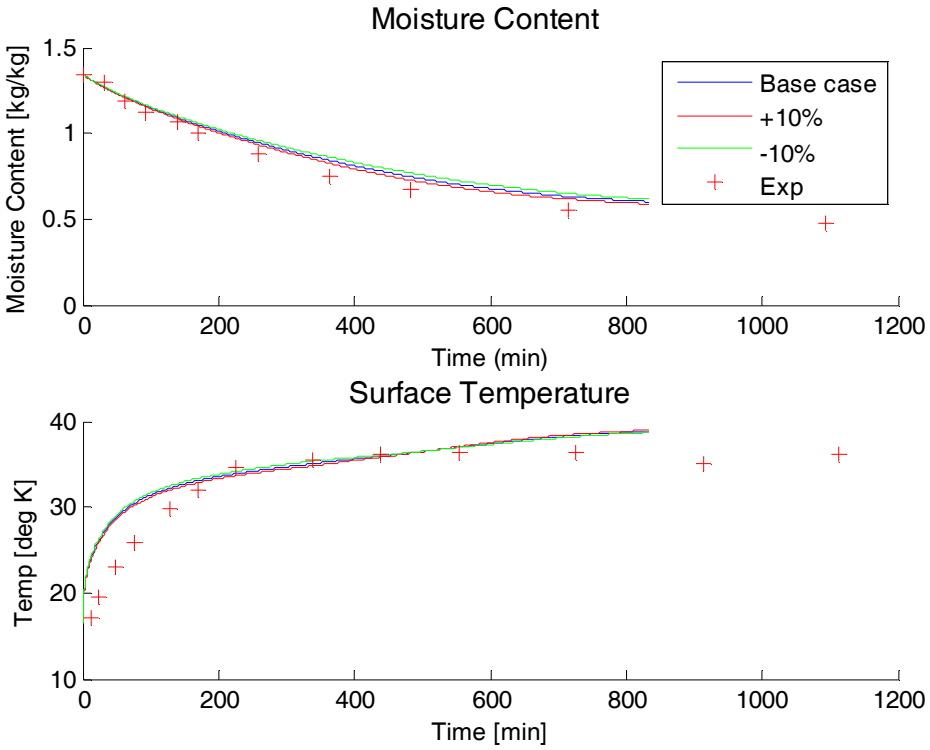

Figure 275 -Effect of Permeability on Convective Drying of Wood

Porosity

The porosity of wood was adjusted by $\pm 10\%$. This had a significant effect on the drying rate and surface temperature as shown in Figure 276. By adjusting the porosity, the amount of water in the material is also changed. To investigate this further, two more cases were considered: 1) adjusting the porosity and the initial water saturation while keeping the initial moisture content constant, and 2) adjusting the porosity and the initial water saturation while keeping the total initial mass of water in the wood constant. Since the initial saturation was already 0.99 for the base case, it cannot be increased significantly. For the second and third cases considered the porosity was increased the saturation decreased to give the desired initial conditions. The results of these tests are shown in Figure 277 and Figure 278.

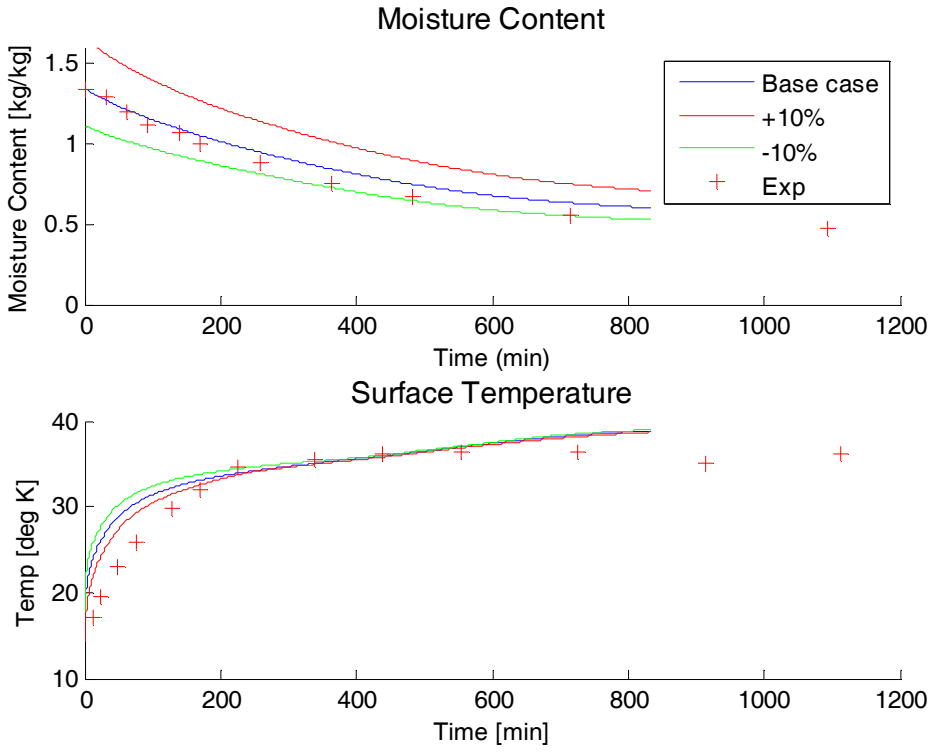

Figure 276 - Effect of Porosity on Convective Drying of Wood

To keep the initial mass of water in the material constant, the following method was used. Since we are assuming that wood has 30% moisture content that is chemically bonded to the solid matrix, the moisture content is

$$MC = \frac{\phi S_w \rho_w}{(1-\phi)\rho_s} + 0.3 = \frac{\phi S_w \rho_w + 0.3(1-\phi)\rho_s}{(1-\phi)\rho_s} \left[=\right] \frac{\frac{kg\ water}{m^3}}{\frac{kg\ solid}{m^3}}$$

The total mass of water in the sample is

$$m_{water} = MC(1-\phi)\rho_s V$$

or

$$m''_{water} = MC(1-\phi)\rho_s L$$

Where V and L are the volume and the thickness of the sample being dried. To keep the initial water content of the material constant while changing the porosity, the following constraint was used

$$S_{w,2} = \frac{\phi_1 S_{w,1}\rho_w + 0.3(1-\phi_1)\rho_{s,1} - 0.3(1-\phi_2)\rho_{s,2}}{\phi_2 \rho_w}$$

This constraint was used to adjust the initial saturation while also adjusting the porosity. By keeping the initial mass of water in the material constant, it was shown that adjusting the porosity alone increased the evaporation rate and decreased the surface temperature. This is shown in Figure 278. Note that the y-axis units for mass loss are kg water/m^2.

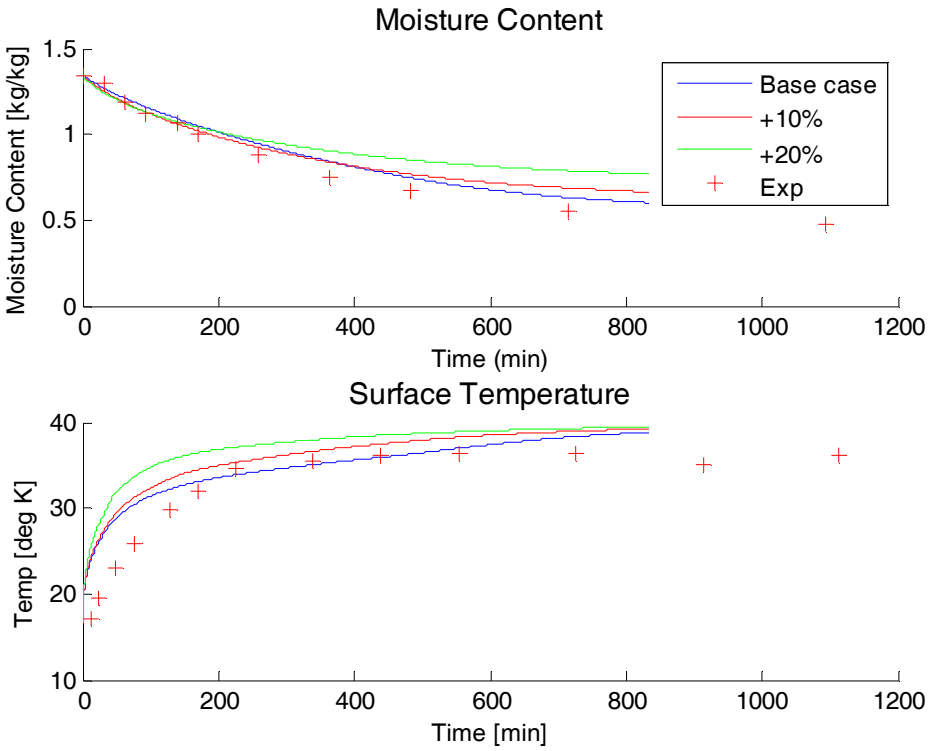

Figure 277 –Effect of Porosity on Drying of Wood – MC_o Held Constant

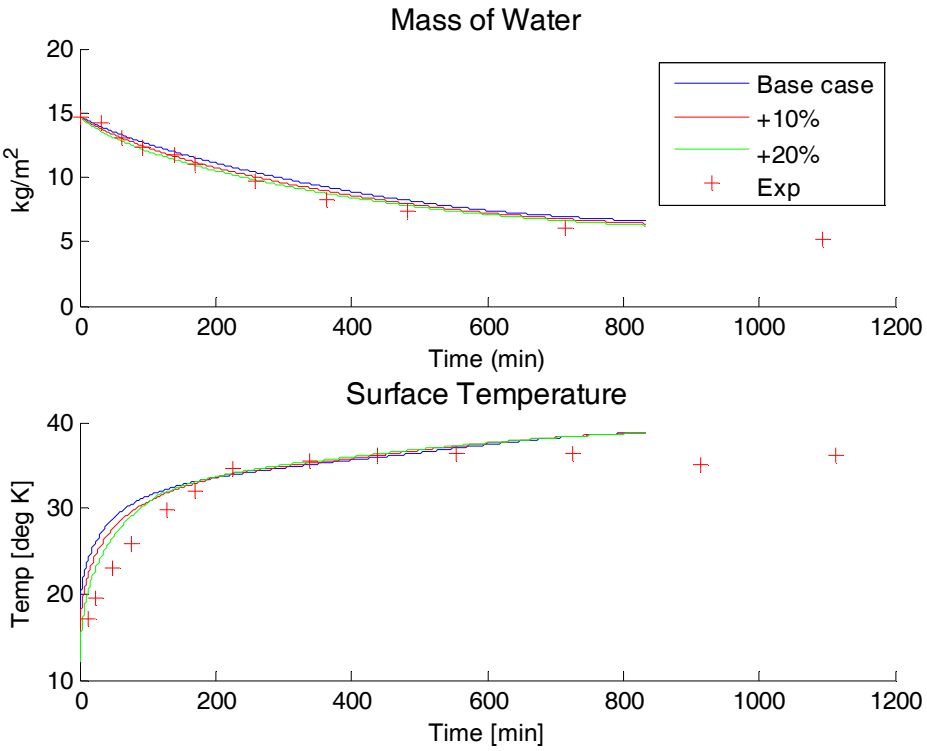

Figure 278 – Effect of Porosity on Drying of Wood – Initial Mass of Water Held Constant

From these tests it can be seen that increasing the porosity increases the mass loss rate, and decreases the surface temperature. It is unclear how much of this is caused by internal transport and how much is surface effects arising from the dependence of the mass transfer coefficient on the surface moisture content. The results from Figure 278 will be used to calculate the sensitivity coefficient for porosity.

Specific Heat of Solid

The specific heat of the solid phase of wood was adjusted by $\pm 10\%$. This did not a significant effect on the drying rate and surface temperature as shown in Figure 279.

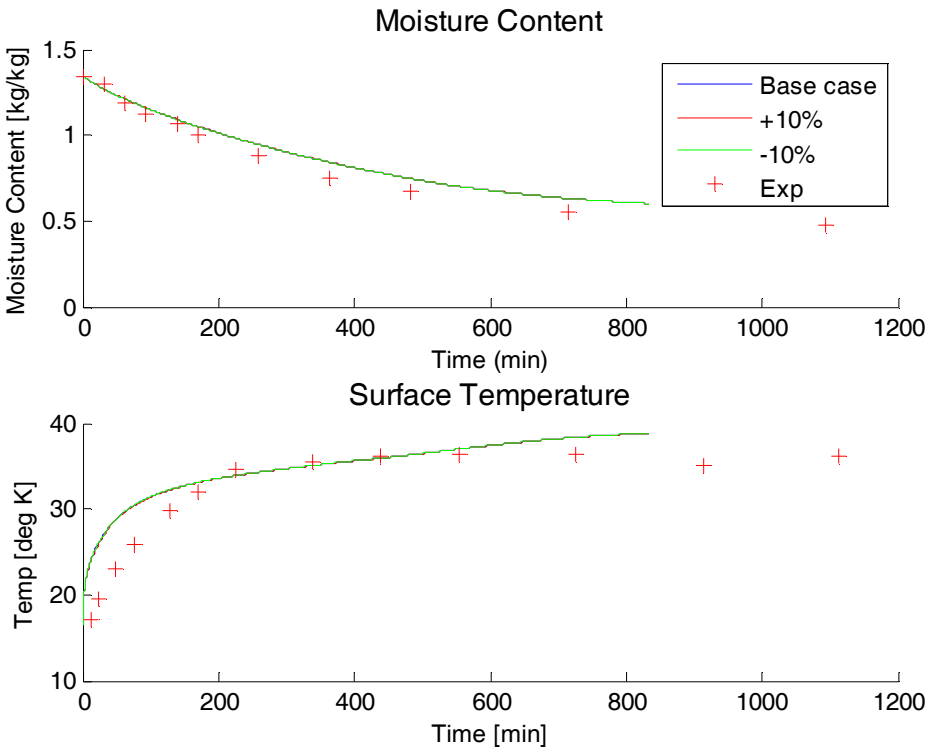

Figure 279- Effect of Specific Heat of Solid on Convective Drying of Wood

Thermal Conductivity of Solid

The specific thermal conductivity of the solid phase of wood was adjusted by $\pm 10\%$. This did not a significant effect on the drying rate and surface temperature as shown in Figure 280.

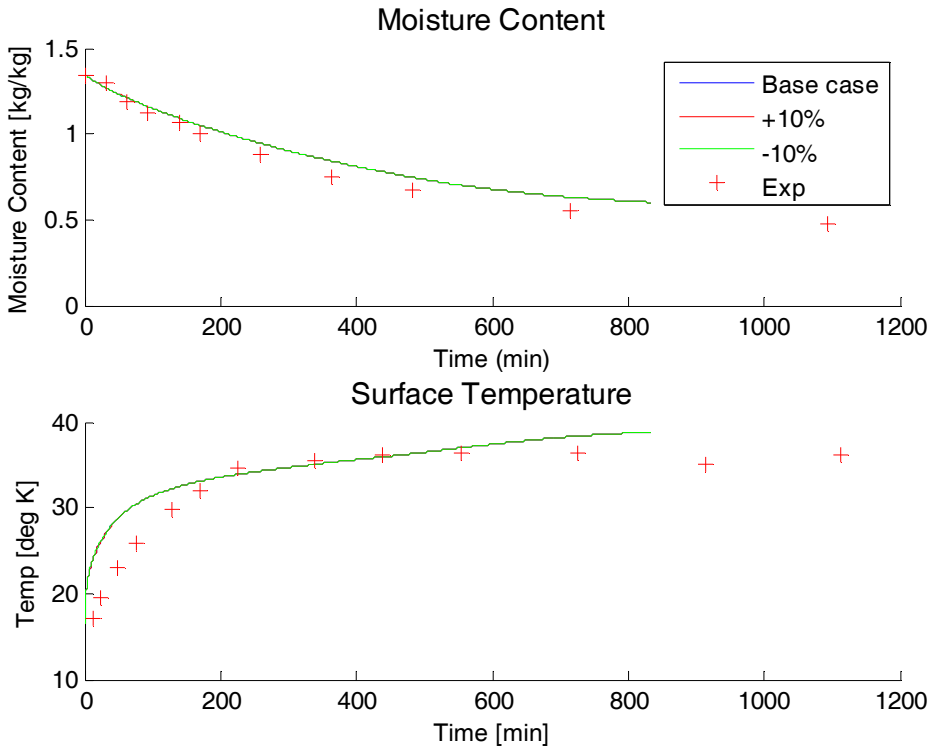

Figure 280 – Effect of Thermal Conductivity of Solid on Convective Drying of Wood

Density of Solid Phase

The density of the solid phase of wood was adjusted by $\pm 10\%$. This had a significant effect on the drying rate and a much less significant effect on surface temperature as shown in Figure 281. This is due to the fact that adjusting the density of the solid phase affects the moisture content (mass of water per unit mass of solid) by changing the mass of solid material without changing the mass of water. To investigate this effect further, two more cases were considered: 1) adjusting the density of the solid phase while keeping the initial moisture content constant, and 2) adjusting the density of the solid phase while keeping the initial mass of water in the wood constant.

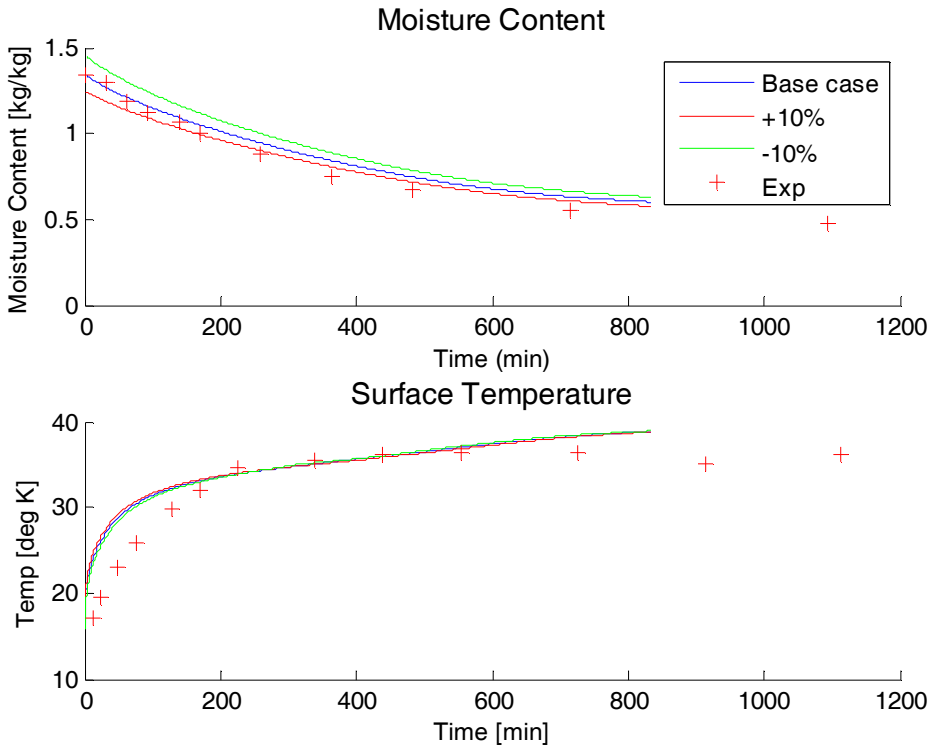

Figure 281 - Effect of Density of Solid Phase on Convective Drying of Wood

In order to adjust the density while keeping the initial moisture content constant and the saturation less than 1, the density could only be decreased. The results of this test are shown in Figure 282.

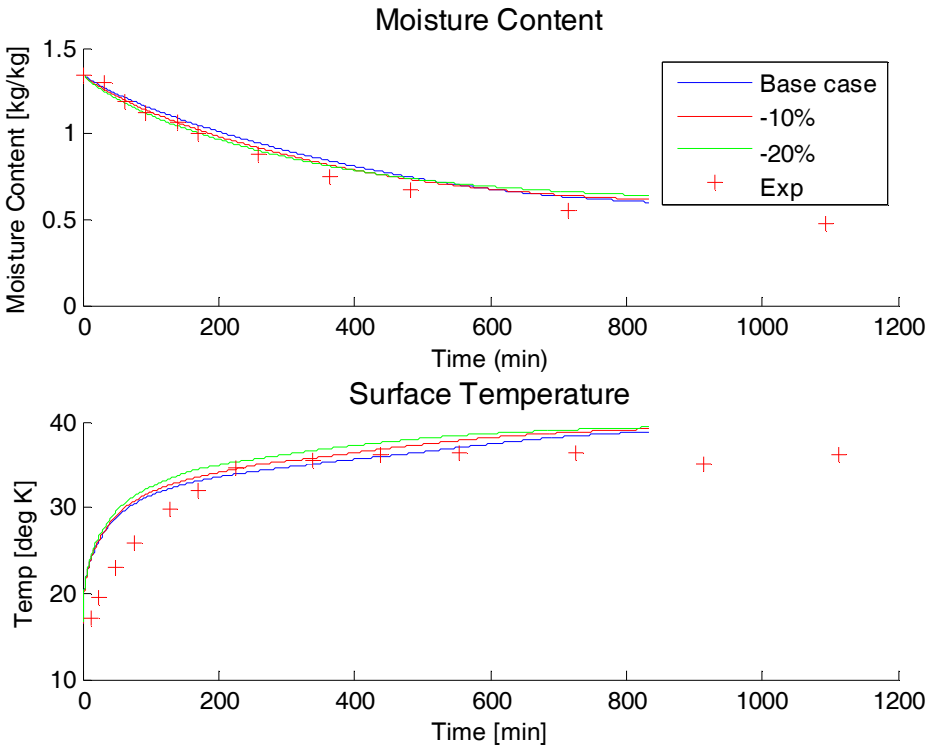

Figure 282 - Effect of Density of Solid Phase on Convective Drying of Wood – MC_o Held Constant

In order to adjust the density while keeping the initial mass of water constant and the saturation less than 1, the density could only be increased. This is due to the fact that 30% of the total mass of water is bound to the solid matrix. The results of this test are shown in Figure 283. The dimensional mass loss rate is decreased when the density is increased. From these three cases it can be seen that changing the density had a significant effect on both the dimensional and non-dimensional mass loss rates. It is unclear if this is due to heating effects or surface mass transfer coefficient dependence on surface moisture content. The results from Figure 283 will be used to calculate a sensitivity coefficient for density.

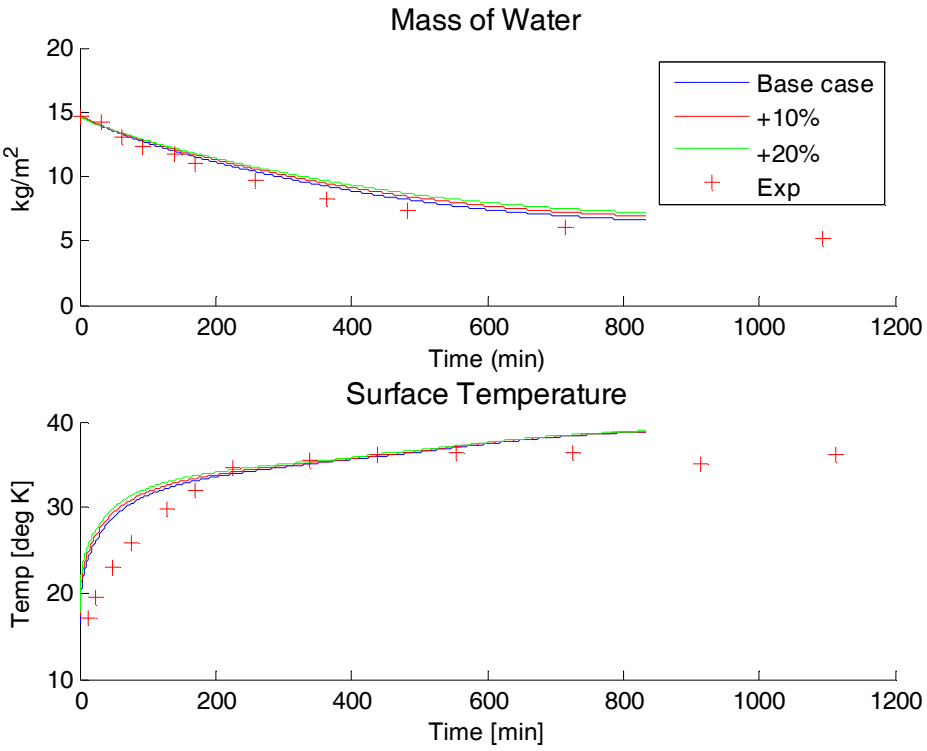

Figure 283 - Effect of Density of Solid Phase on Convective Drying of Wood – Initial Mass of Water Held Constant

Diffusivity

The diffusivity was adjusted by $\pm 10\%$. This did not have a significant effect on the mass loss rate or surface temperature as shown in Figure 284.

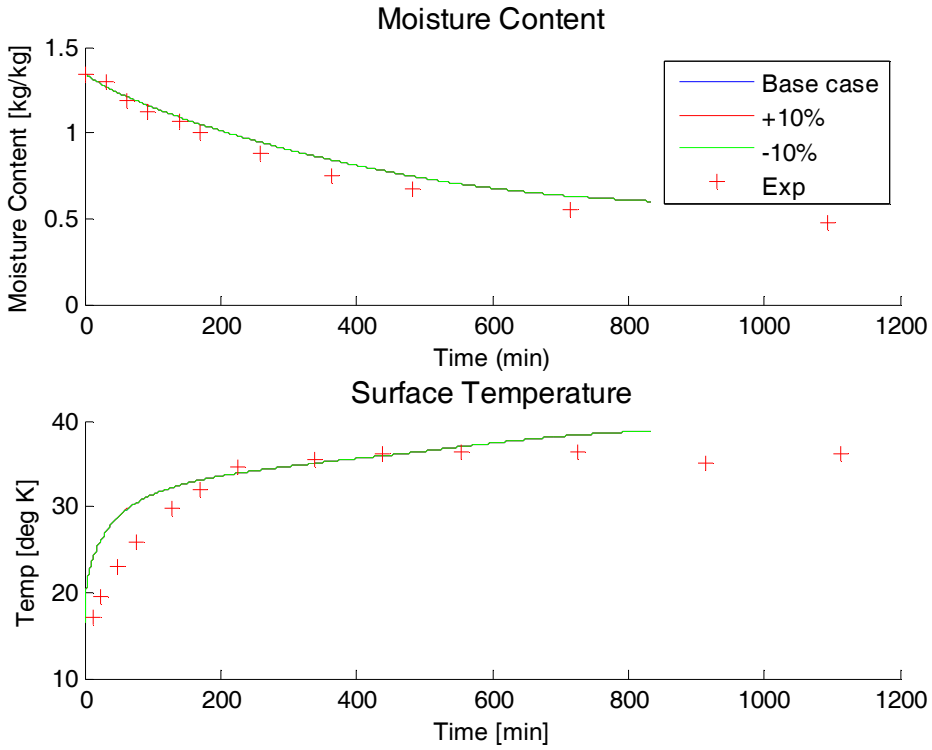

Figure 284 - Effect of Diffusivity on Convective Drying of Wood

Heat Transfer Coefficient

The heat transfer coefficient was adjusted by $\pm 10\%$. This had a significant effect surface temperature and a very small effect on the mass loss rate as shown in Figure 285.

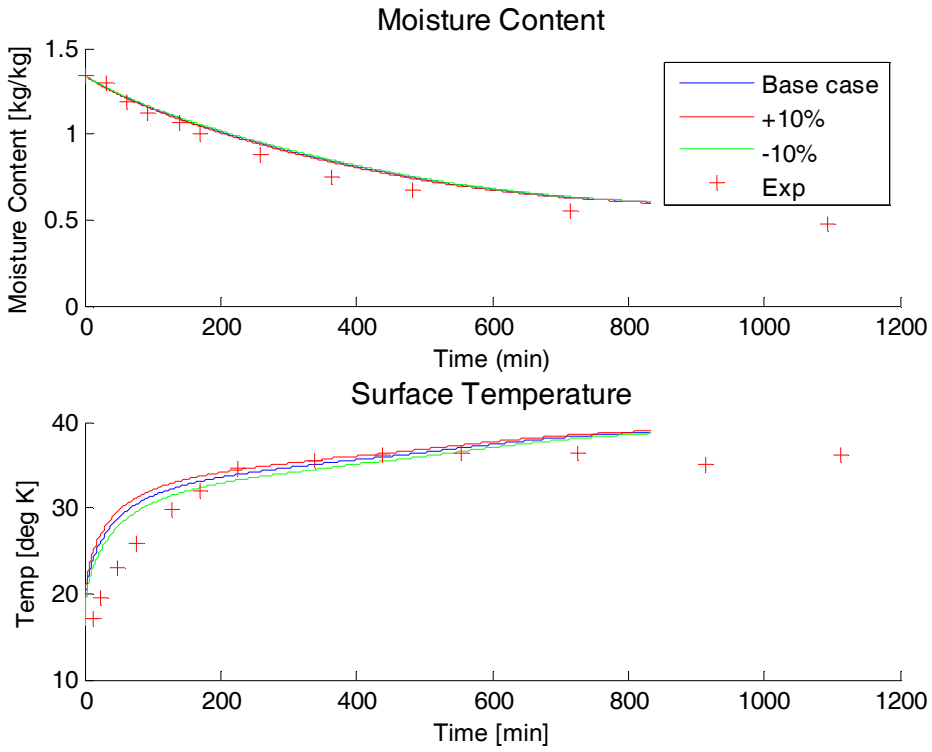

Figure 285 - Effect of Heat Transfer Coefficient on Convective Drying of Wood

Mass Transfer Coefficient

The mass transfer coefficient was adjusted by $\pm 10\%$. This did not had a significant effect on the mass loss rate or the surface temperature as shown in Figure 286. Increasing the mass transfer coefficient lowered the surface temperature and increased the mass loss rate a very small amount. Decreasing the mass transfer coefficient increased the surface temperature and lowered the mass loss rate a very small amount.

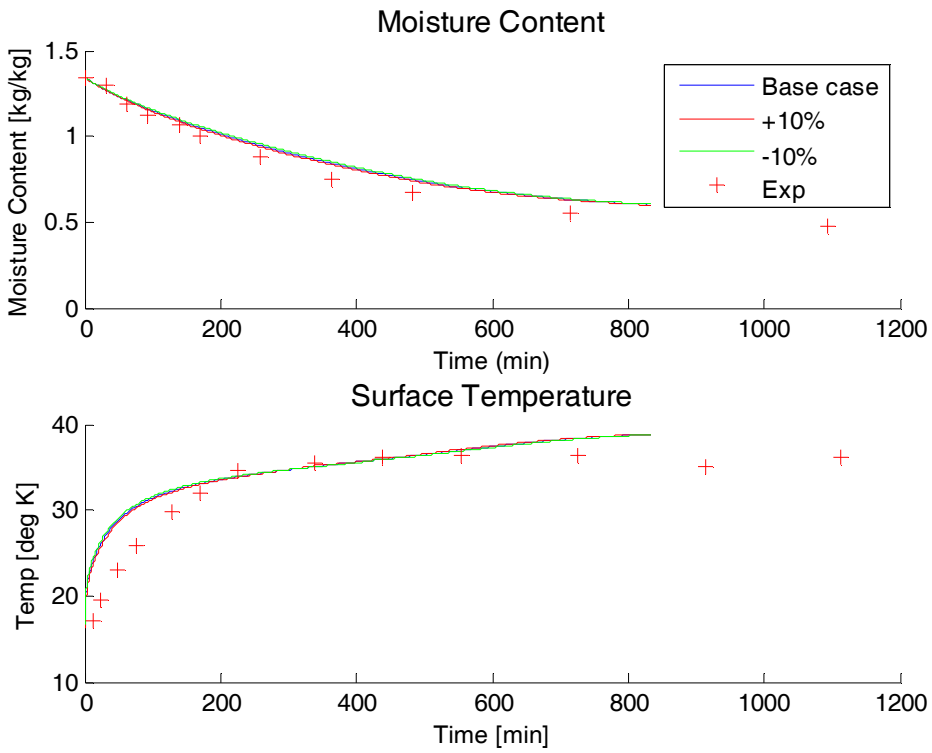

Figure 286 - Effect of Mass Transfer Coefficient on Convective Drying of Wood

Relative Humidity

The relative humidity was adjusted by $\pm 10\%$. This had almost no effect on the mass loss rate or surface temperature as shown in Figure 287. To test whether further changes in the relative humidity would have significant effects, simulations were run at RH=0% and RH=10%. These are shown in Figure 287.

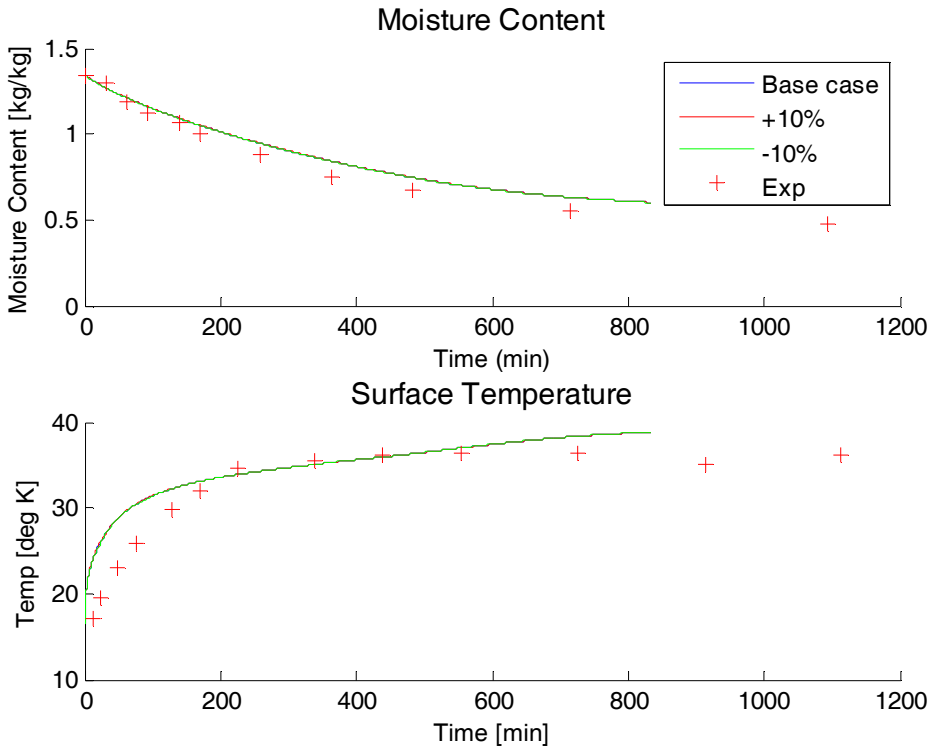

Figure 287 - Effect of Relative Humidity on Convective Drying of Wood

Adjusting the relative humidity from 5% up to 10% and down to 0% had a slight effect on the mass loss rate and surface temperature.

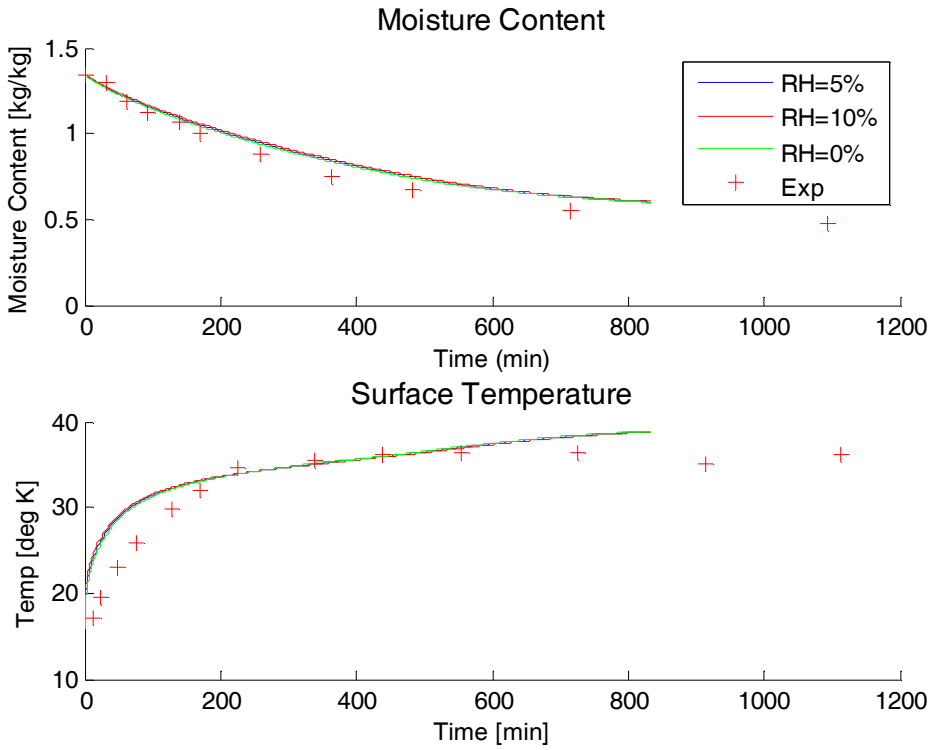

Figure 288 – Effect of Relative Humidity on Drying of Wood – Large Changes

Initial Temperature

The initial temperature was adjusted by $\pm 2^{o} C$. This did not have a significant effect on the mass loss rate or surface temperature as shown in Figure 289.

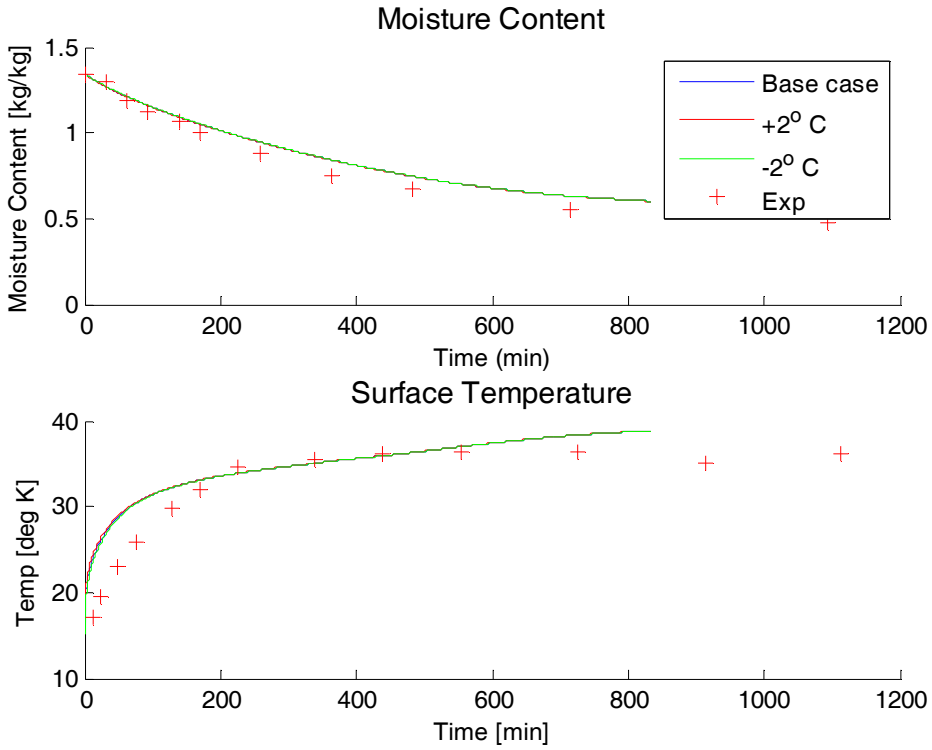

Figure 289 - Effect of Initial Temperature on Convective Drying of Wood

Ambient Temperature

The ambient temperature was adjusted by $\pm 2^{o}C$. This had a very small effect on the mass loss rate and a very significant effect on the surface temperature as shown in Figure 290.

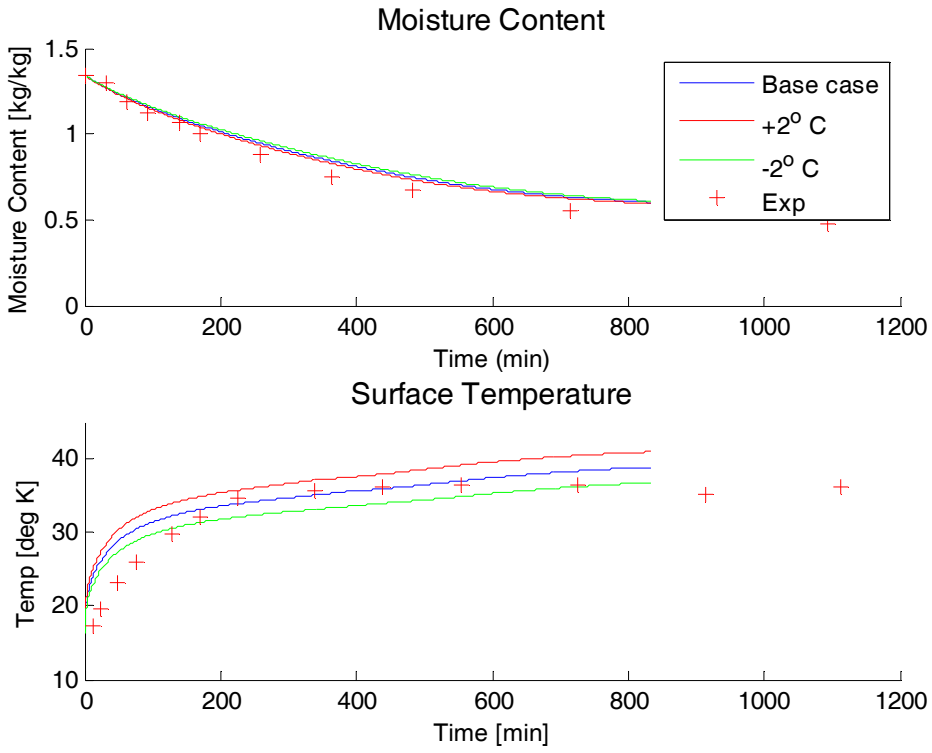

Figure 290 - Effect of Ambient Temperature on Convective Drying of Wood

Sample Length

The length of the sample was adjusted by $\pm 10\%$. This had a significant effect on the mass loss rate and surface temperature as shown in Figure 291. Adjusting the length of the sample increases the total mass of water in the material. To investigate this effect, the sample length was adjusted by $\pm 10\%$ while keeping the total amount of water in the sample constant.

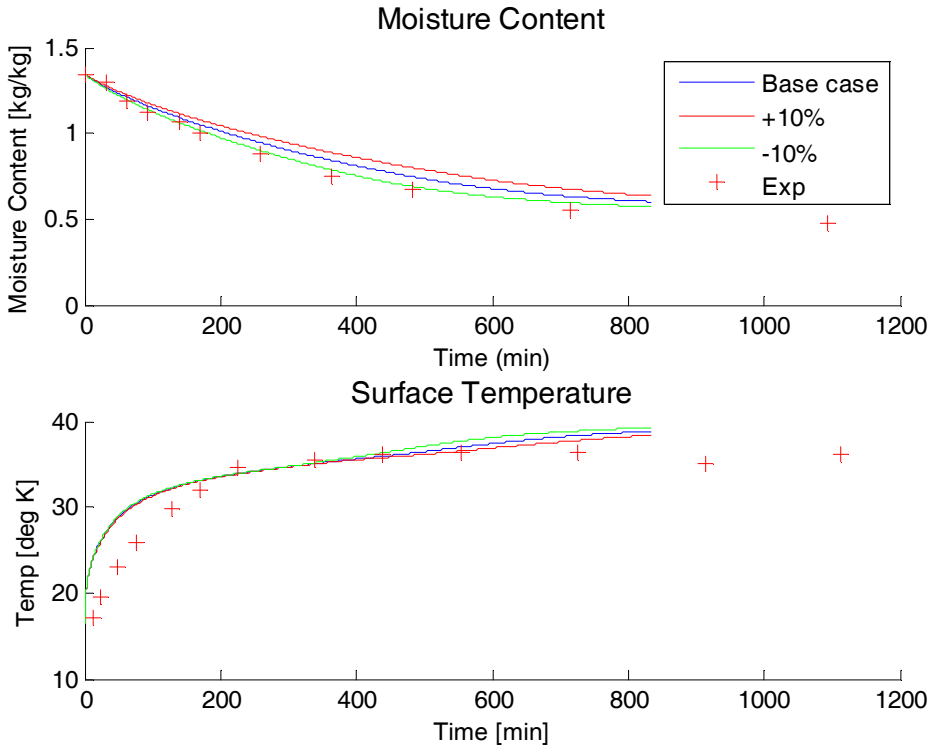

Figure 291 - Effect of Sample Length on Convective Drying of Wood

To keep the initial mass of water in the material constant, the following method was used. Since we are assuming that wood has 30% moisture content that is chemically bonded to the solid matrix, the moisture content is

$$MC = \frac{\phi S_w \rho_w}{(1-\phi)\rho_s} + 0.3 = \frac{(\phi S_w \rho_w + 0.3(1-\phi)\rho_s)V}{(1-\phi)\rho_s V} [=] \frac{kg\ water}{kg\ solid}$$

To keep the initial water content of the material constant while changing the porosity, the following constraint was used

$$S_{w,2} = \frac{\left(\phi_1 S_{w,1}\rho_w + 0.3\left(1-\phi_1\right)\rho_s\right)L_1 - 0.3\left(1-\phi_2\right)\rho_s L_2}{\phi_2 \rho_w L_2}$$

This constraint was used to adjust the initial saturation while also adjusting the sample length therefore keeping the initial mass of water in the sample constant. By keeping the initial mass of water in the material constant, it was shown that increasing the sample length by 10% increased the surface temperature yet decreased the mass loss rate. Increasing the sample rate by 20% increased the surface temperature further, and decreased the mass loss rate further. The results are shown in Figure 292. It is unclear how much of these effects are due to length effects alone, and how much are due to the surface mass transfer coefficient dependency on surface moisture content. The results from Figure 292 will be used to calculate a sensitivity coefficient for length.

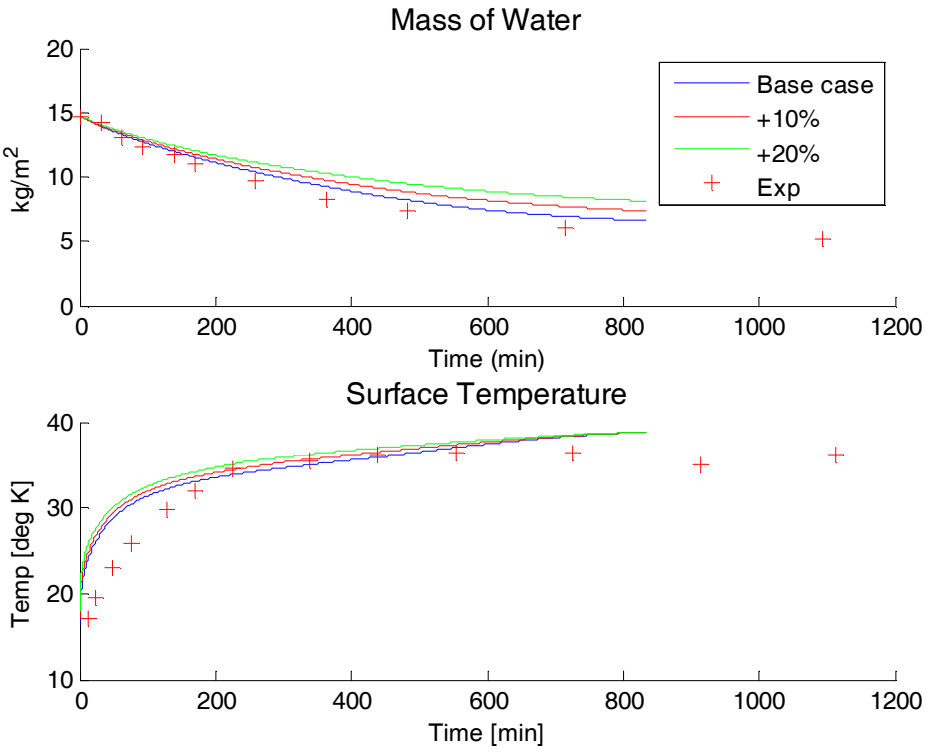

Figure 292- Effect of Sample Length on Convective Drying of Wood – Initial Mass of Water Held Constant

Initial Saturation

The initial saturation was decreased from its base value of 0.99, to 0.9 and 0.8. This had an effect on the mass loss rate and surface as shown in Figure 293. Decreasing the initial saturation tended to decrease the mass loss rate and increase the surface temperature.

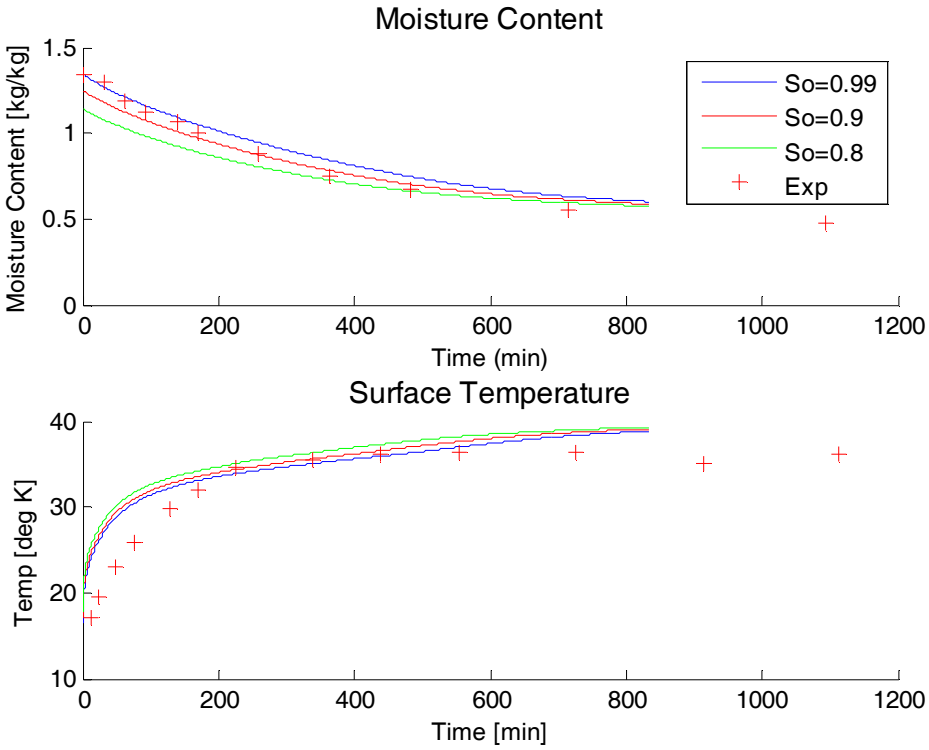

Figure 293 – Effect of Initial Saturation on Drying of Wood

Number of Nodes

The number of nodes was adjusted from its base value of 31 to a "high" value of 41, and down to a "low" value of 21. This did not have any significant effect on the mass loss rate or surface temperature.

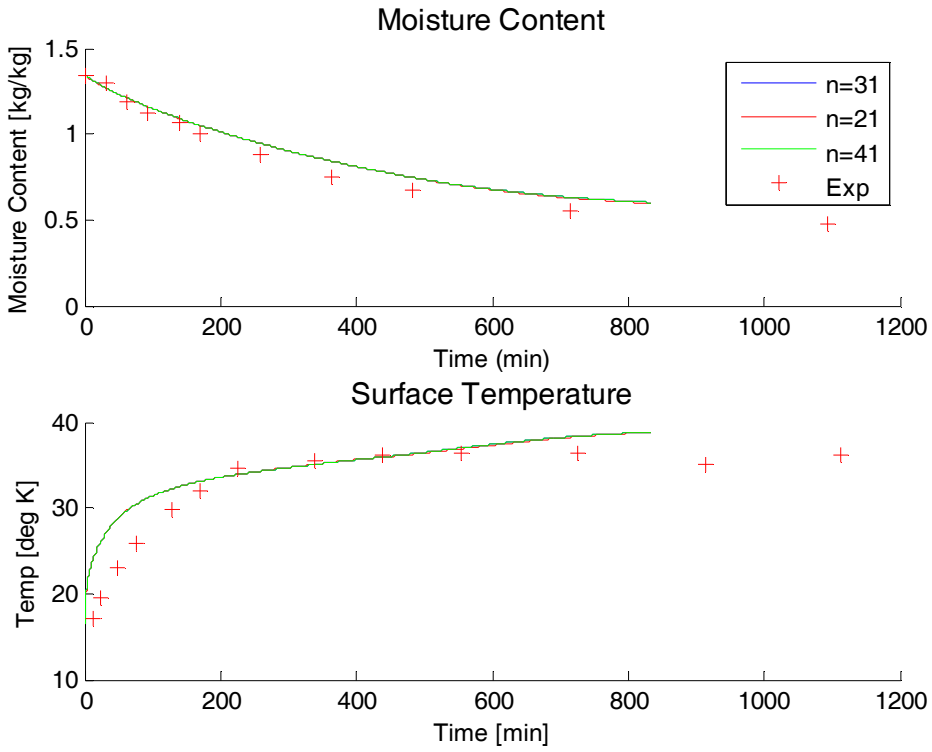

Figure 294 – Effect of Number of Nodes on Drying of Wood

Time Step

The time step was adjusted from its base value of 5 seconds up to a "high" value of 10 seconds, and down to a "low" value of 1 second. This did not have a significant effect on the rate of mass loss or the surface temperature, as shown in Figure 295.

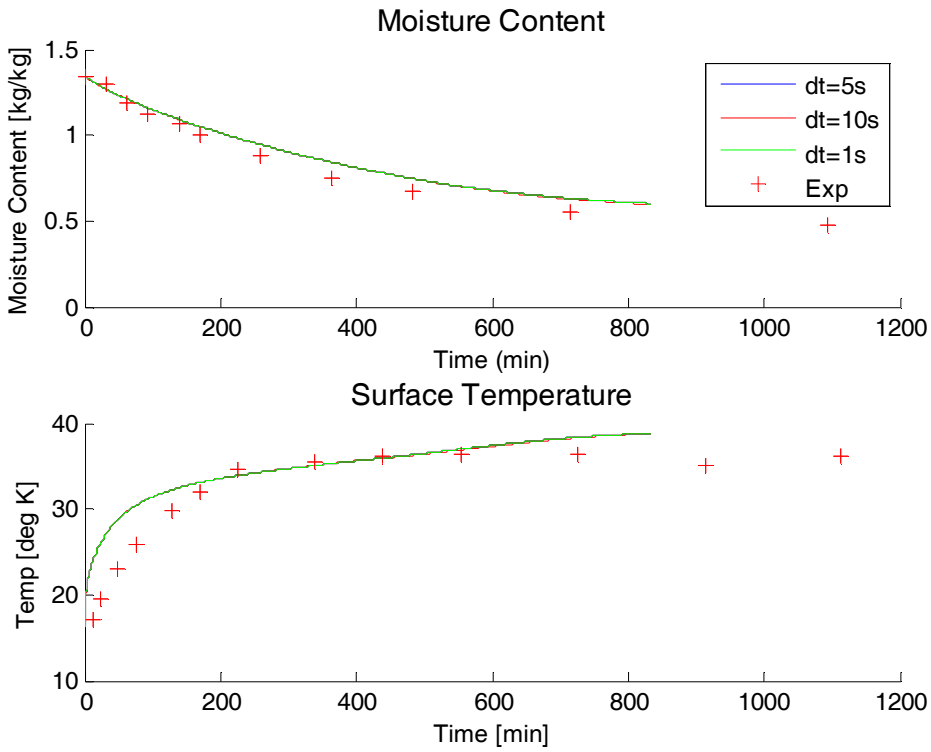

Figure 295 – Effect of Adjusting the Timestep on Drying of Wood

Liquid Relative Permeability

The liquid relative permeability was adjusted from its linear base correlation, to a square function of saturation (high case), and a cubic function of saturation (low case). Increasing the power of the function lowered the rate of mass loss, and increased the surface temperature, as shown in Figure 296.

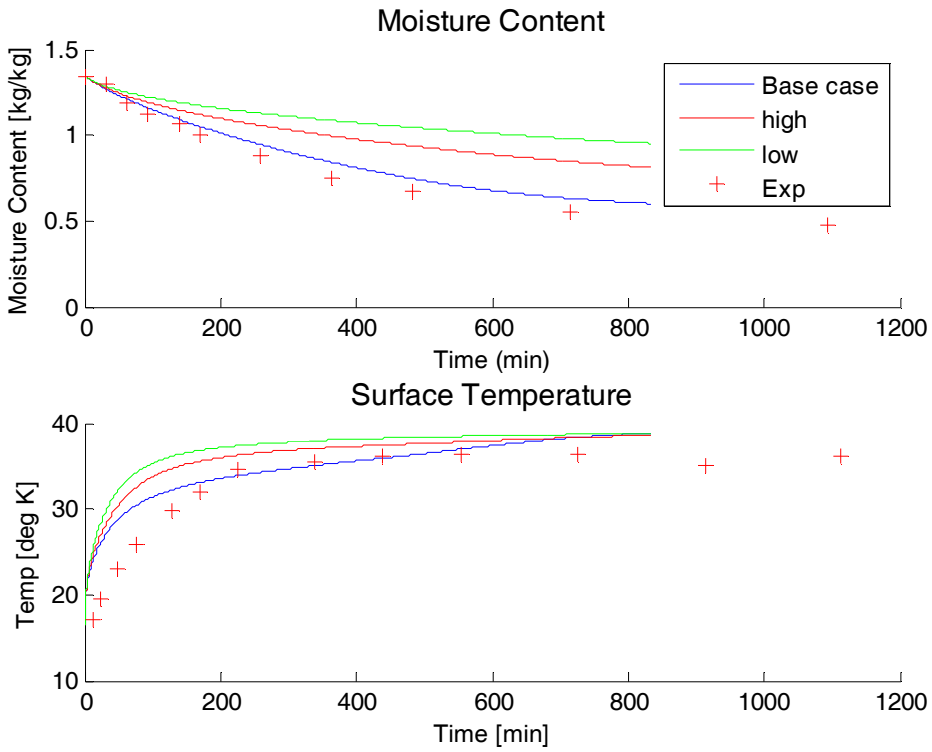

Figure 296 – Effect of Liquid Relative Permeability Correlation on Drying of Wood

Gas Relative Permeability

The gas relative permeability was adjusted from its linear correlation base case to a square (high case) and cubic function (low case) of saturation as shown in Figure 273. This had a significant effect on the mass loss rate, and surface temperature as shown in Figure 297. Increasing the power dependence of the correlation lowered the rate of mass loss and increased the surface temperature.

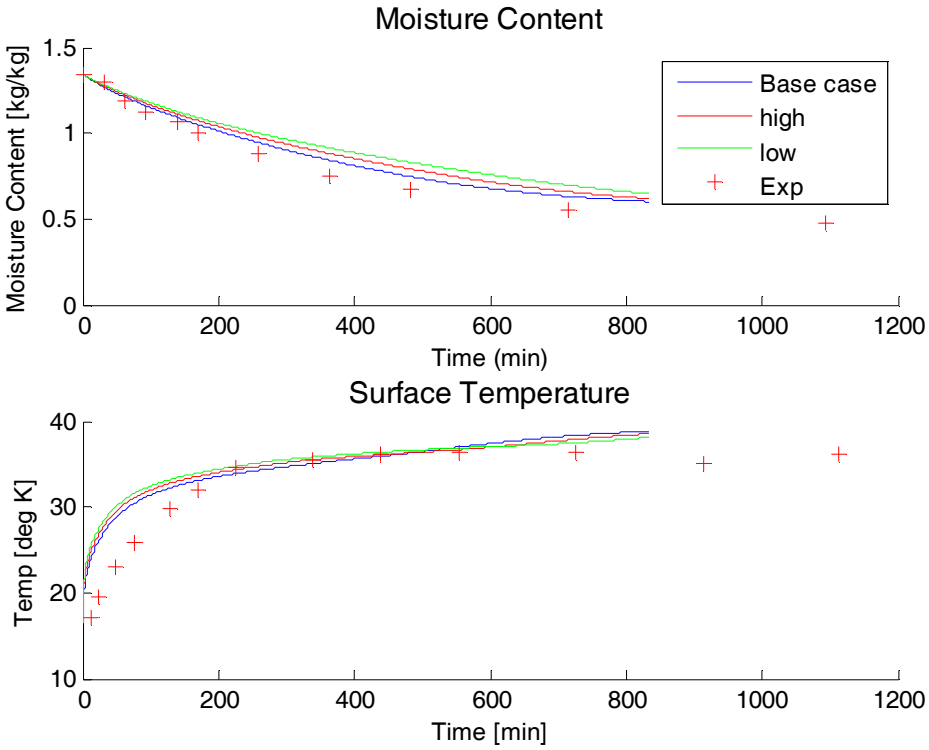

Figure 297 –Effect of Gas Relative Permeability Correlation on Drying of Wood

Relative Humidity Correlation

The relative humidity correlation was adjusted $\pm 10\%$. The results are shown in Figure 298. Increasing the relative humidity correlation drew more water to the surface by vapor phase diffusion. This increased the mass loss rate and decreased the surface temperature.

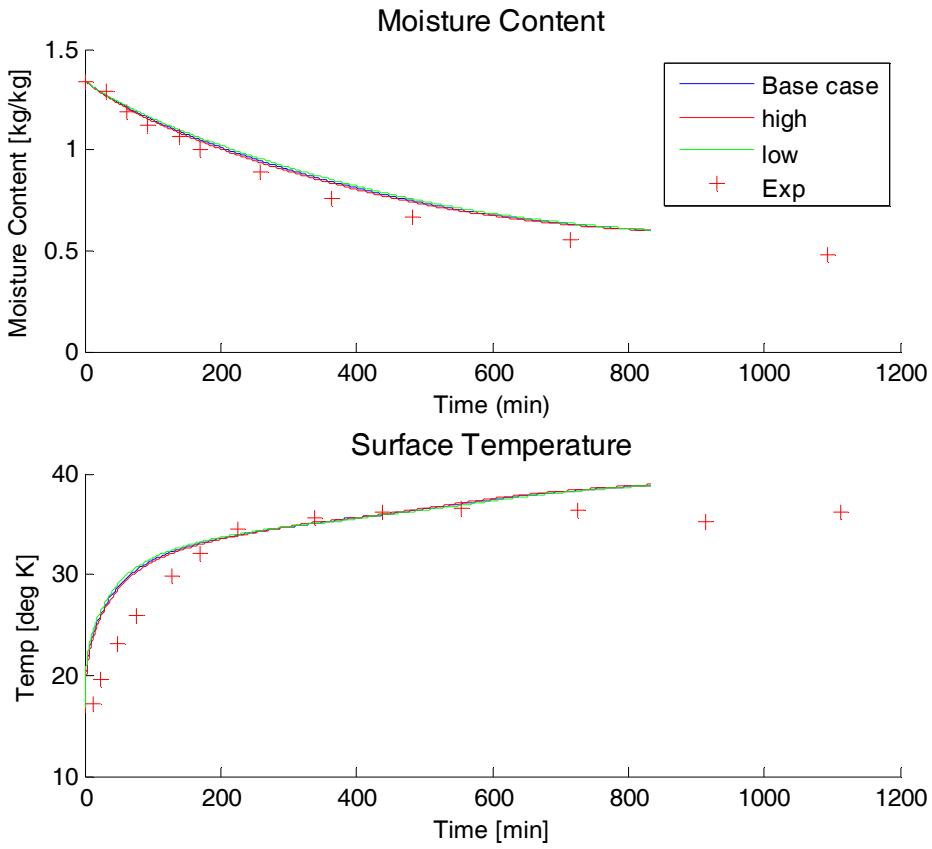

Figure 298 – Effect of Relative Humidity Correlation on Drying of Wood

Capillary Pressure

The capillary pressure of wood was adjusted from its base correlation to the "high" and "low" correlations in Figure 274. This had a slight effect on the mass loss rate and surface temperature as shown in Figure 299. Increasing the capillary pressure had the effect of drawing more water to the surface, increasing the mass loss rate and decreasing the surface temperature. Decreasing the capillary pressure correlation had the opposite effects.

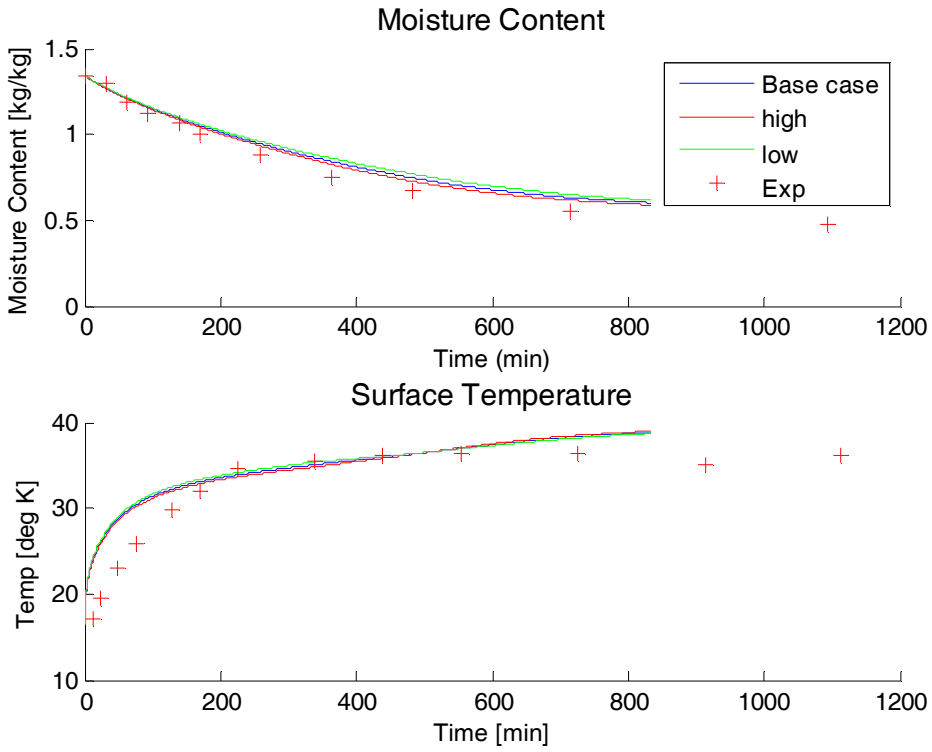

Figure 299 – Effect of Capillary Pressure on Drying of Wood

Surface Drying Coefficient

The surface drying coefficient was adjusted from its cubic function base case. The power of the function was increased to a "high" value of 3.3, and decreased to a "low" value of 2.7. This had a slight effect on the mass loss rate and surface temperature, as shown in Figure 300. Increasing the power had the effect of decreasing the evaporation rate, thereby increasing the surface temperature. Decreasing the power had the opposite effect.

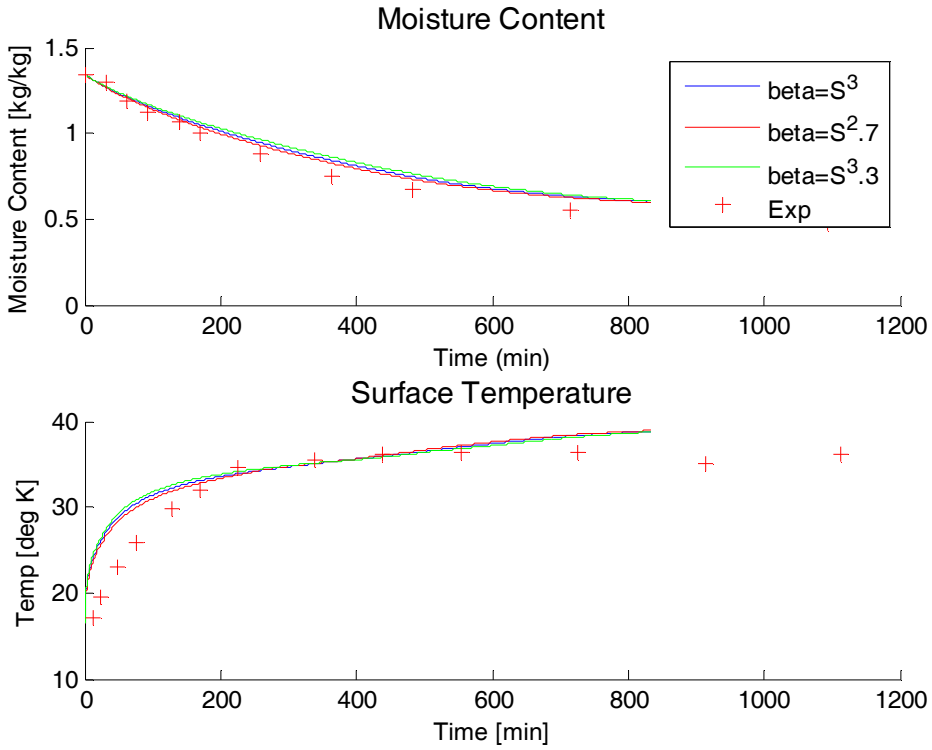

Figure 300 – Effect of Surface Drying Coefficient (Beta) on Drying of Wood

Irreducible Saturation

The irreducible saturation was adjusted ±10% from its base value of 0.2. This had a slight effect on the surface temperature and sample mass. The results are shown in Figure 301.

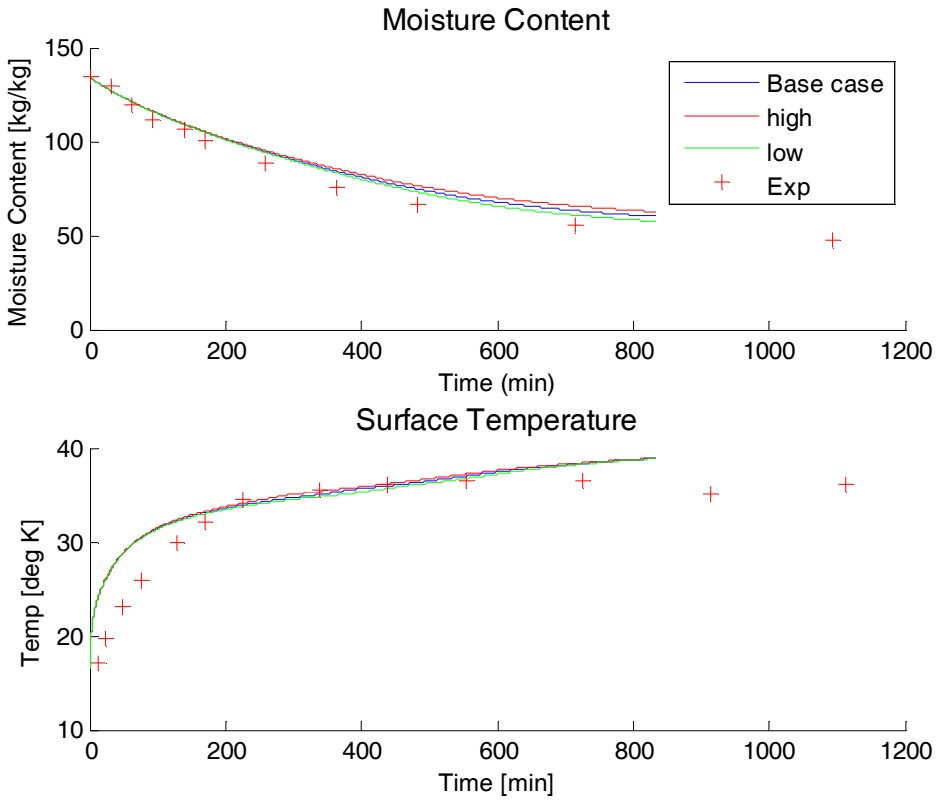

Figure 301 – Effect of Irreducible Saturation on Drying of Wood

G.5. Radiant Heating of CFB Sensitivity Analysis

The sensitivity of the model was tested for the case of radiant heating of wet samples of ceramic fiberboard. The case selected for this exercise was the heating of samples with an initial saturation of 0.5 at a heat flux of 20 kW/m^2. The values of the parameters adjusted are shown in Table 33. The results of adjusting these 18 parameters are shown in Figure 305 through Figure 376.

Other Input Parameters

The sensitivity of the model to several other constitutive relations was tested. The sensitivity of the model to the correlations used for liquid relative permeability, gas relative permeability, capillary pressure, and relative humidity was tested by adjusting the correlations as described in the following sections.

Relative Permeability

The correlations for gas and liquid relative permeability used in the model for CFB are taken from Kaviany [23]

$$K_{rl} = S_{eff}^3$$
$$K_{rg} = \left(1 - S_{eff}\right)^3$$

Where $S_{eff} = \frac{S_w - S_{ir}}{1 - S_{ir}}$

To test the sensitivity of the model to these correlations, a second order function was used as the “high” case, and a fourth order function was used as the “low” case. These correlations are shown in Figure 302.

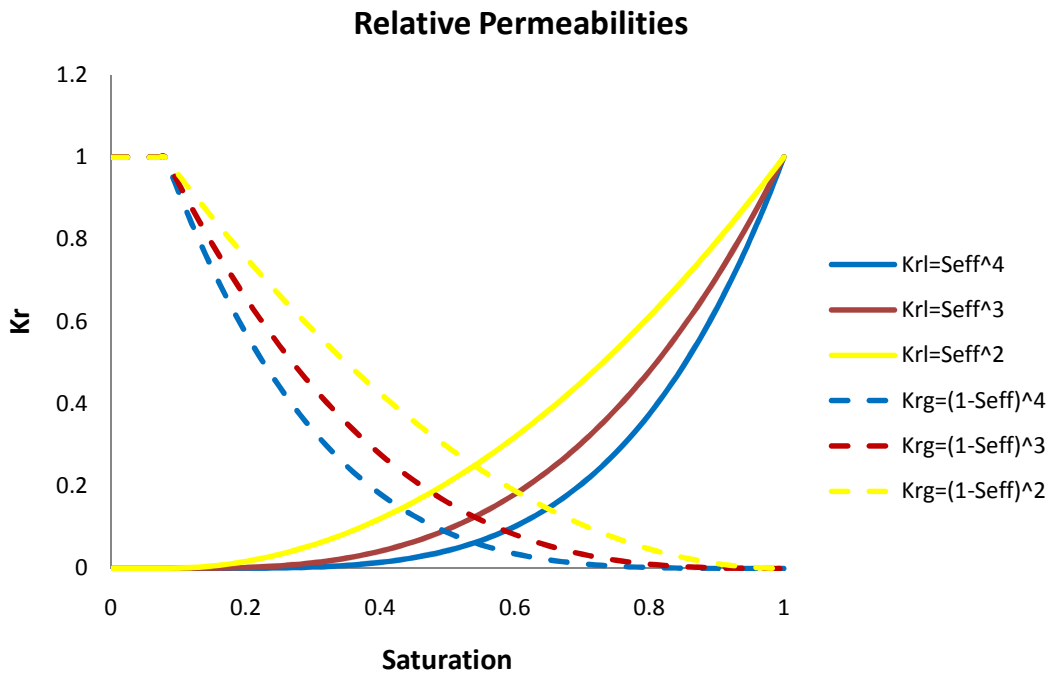

Figure 302 – Correlations used for Liquid and Gas Relative Permeability

Capillary Pressure

The correlation for capillary pressure that is used for CFB was determined from experiments to be

$$p_{cap} = \sigma\sqrt{\frac{\phi}{K}}J(S)$$

where

$$J(S) = 0.4\left[0.364\left(1-\exp\left(-30\left(1-S\right)\right)\right)+0.471\left(1-S\right)+\frac{0.035}{S-0.1}\right]$$

The value calculated from this correlation was adjusted $\pm 10\%$, as shown in Figure 303.

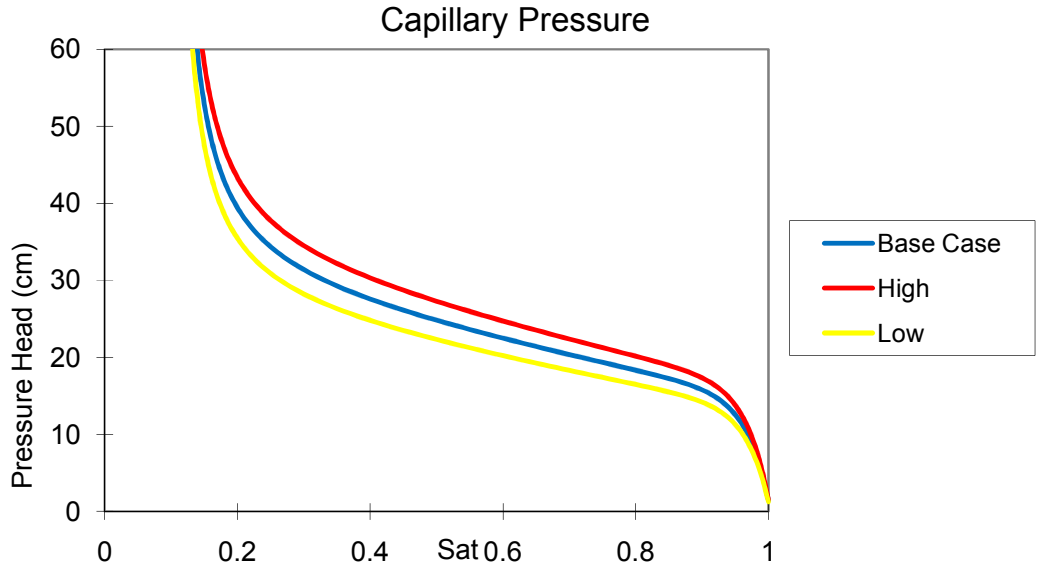

Figure 303 – Capillary Pressure Correlations used for Sensitivity Analysis

Relative Humidity

The relative humidity of CFB is assumed to be similar to that of brick, which is given by the following correlation

$$S = \frac{(1-\phi)\rho_s}{\phi\rho_w}\left(0.0105\left(\frac{p_v}{p_{vs}}\right)^{0.2} + 0.0125\exp\left(20\frac{p_v}{p_{vs}} - 20\right)\right)$$

The value calculated from this correlation was adjusted $\pm 10\%$, as shown in Figure 304.

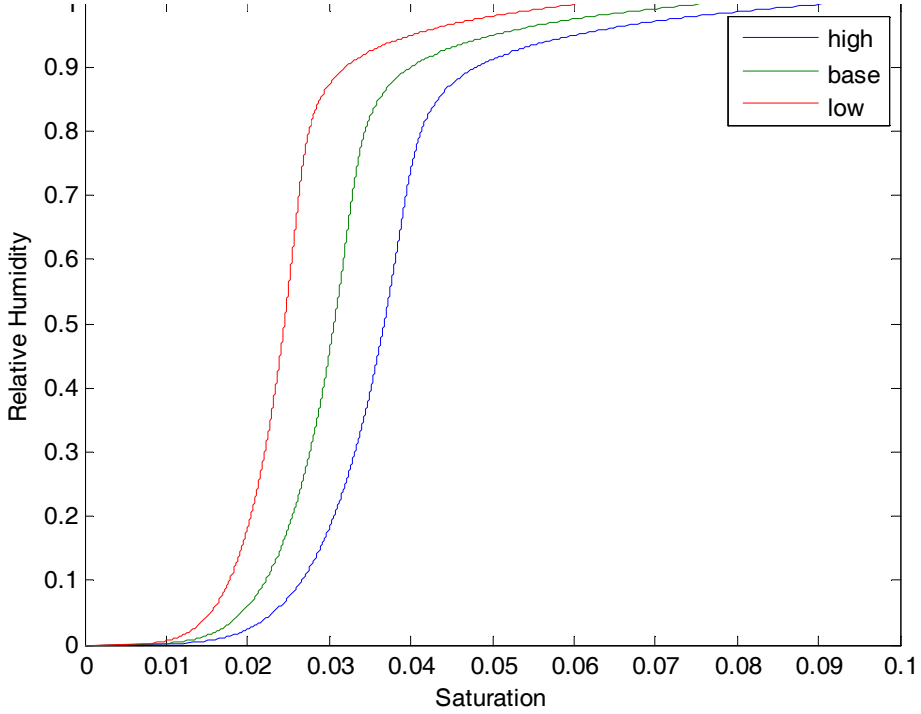

Figure 304 – Relative Humidity of CFB used for Sensitivity Analysis

Sensitivity Coefficient

The time at which the surface saturation temperature jumps, $t_{jump,}$ was used as a quantitative measure of the effect of adjusting each parameter. A sensitivity coefficient was calculated for each parameter x_i

$$S_i = \frac{x_i}{t_{jump}} \frac{\Delta t_{jump}}{\Delta x_i}$$

The change in the "jump" time for each parameter is shown in Table 41. The calculated sensitivity coefficients are shown in Table 45.

Permeability

The permeability was adjusted $\pm 10\%$ from its base value of $5 \times 10^{-11}\,\mathrm{m}^2$. The effect of this change on the surface temperature, centerline temperature, and mass loss are shown in Figure 305, Figure 306, and Figure 307.

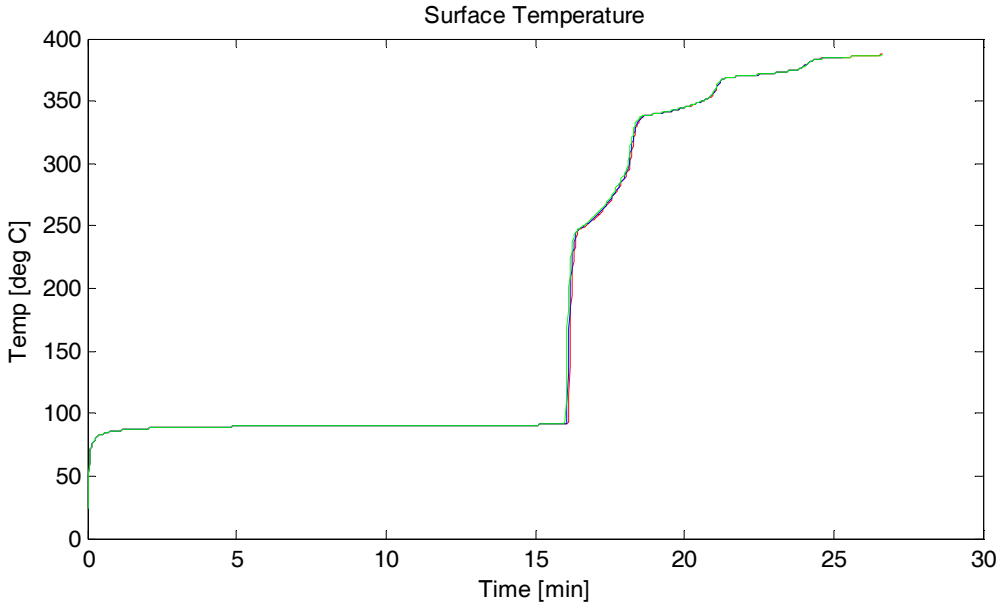

Figure 305 – Effect of Adjusting the Permeability on Radiant Heating of CFB – Surface Temperature

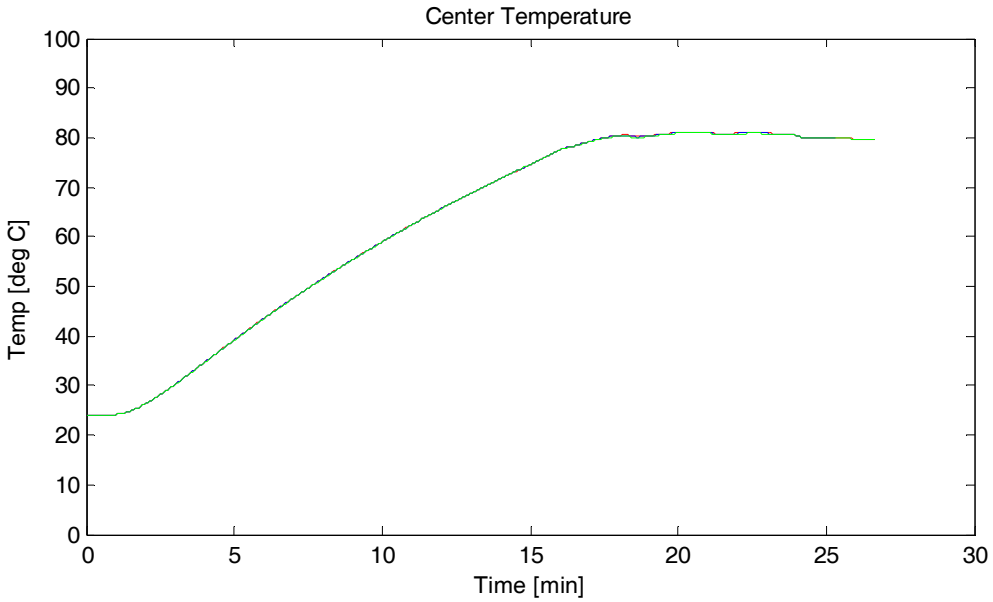

Figure 306 – Effect of Adjusting the Permeability on Radiant Heating of CFB – Center Temperature

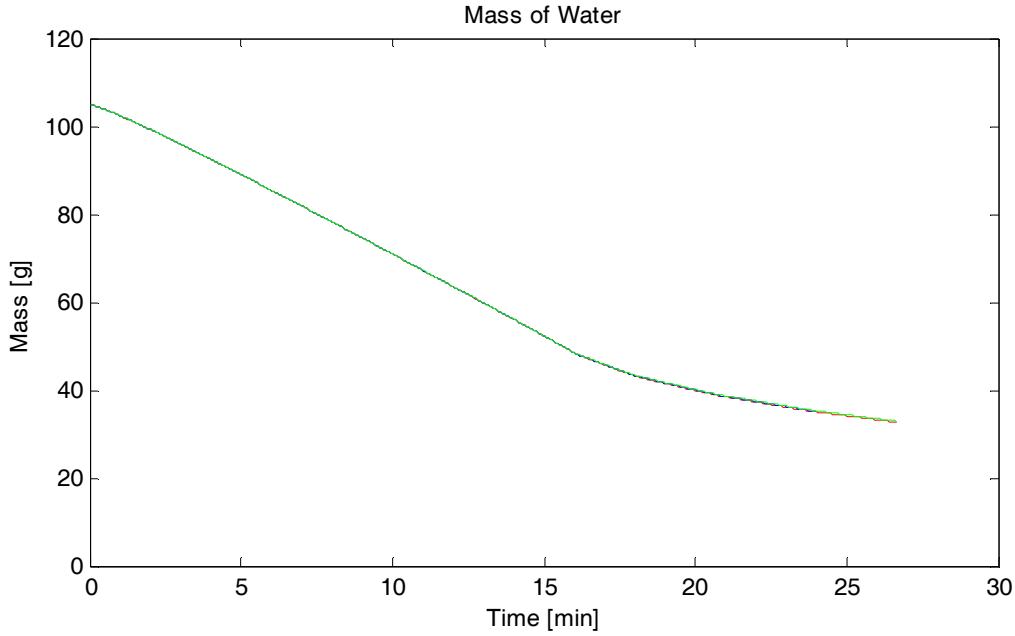

Figure 307 – Effect of Adjusting the Permeability on Radiant Heating of CFB – Mass Loss

Porosity

The porosity was adjusted ±10% from its base value of 0.8. The effect of this change on the surface temperature, centerline temperature, and mass loss are shown in Figure 308, Figure 309, and Figure 310.

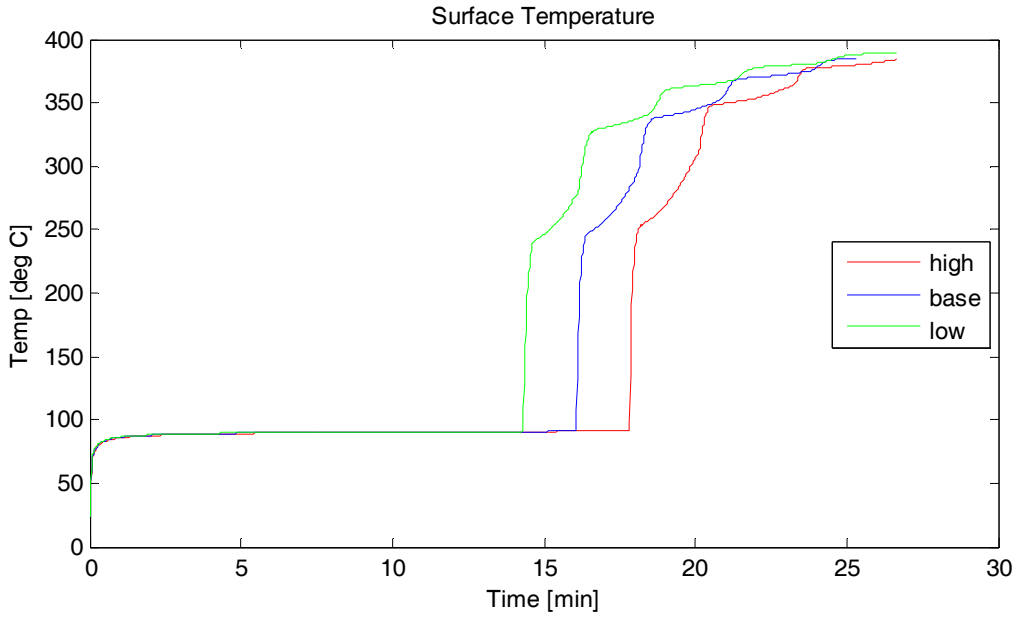

Figure 308 - Effect of Adjusting the Porosity on Radiant Heating of CFB – Surface Temperature

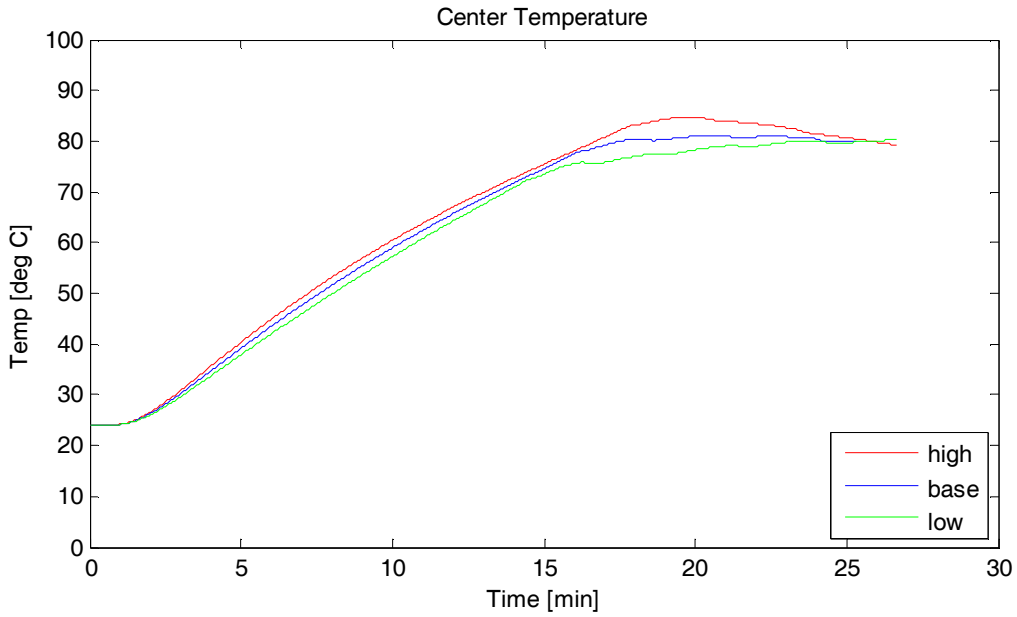

Figure 309 - Effect of Adjusting the Porosity on Radiant Heating of CFB – Center Temperature

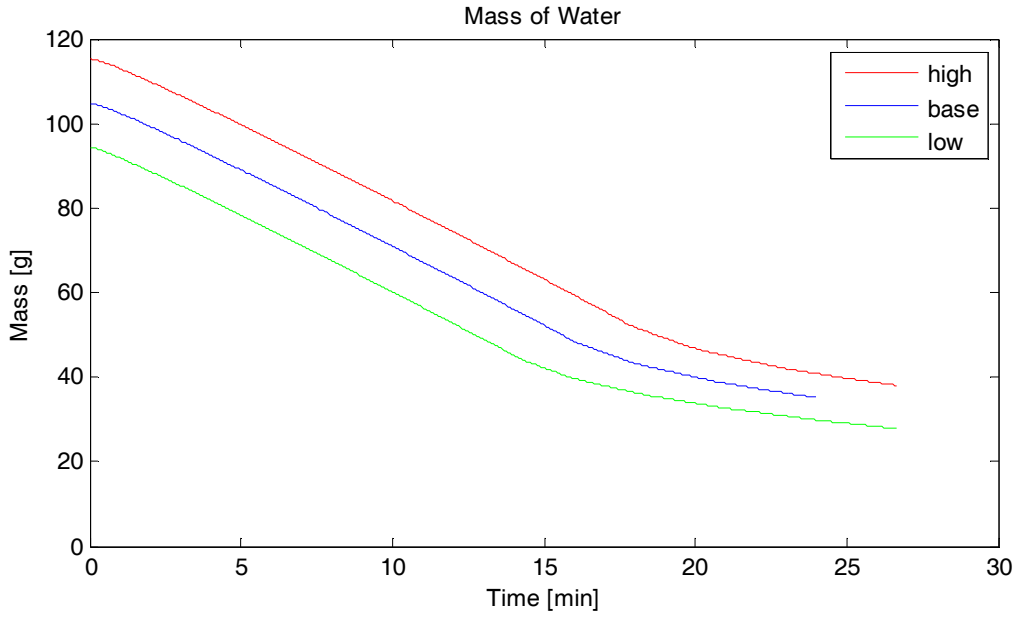

Figure 310 - Effect of Adjusting the Porosity on Radiant Heating of CFB – Mass Loss

It can be seen in Figure 310 that adjusting the porosity while keeping the initial saturation constant at 0.5 has the unintended effect of changing the initial mass of

water in the sample. To test this effect, the porosity was adjusted while keeping the initial mass of water in the sample constant by applying the following constraint

$$S_2 = S_1 \frac{\phi_1}{\phi_2}$$

The effect of adjusting the porosity $\pm 10\%$ subject to this constraint is shown in Figure 311, Figure 312, and Figure 313.

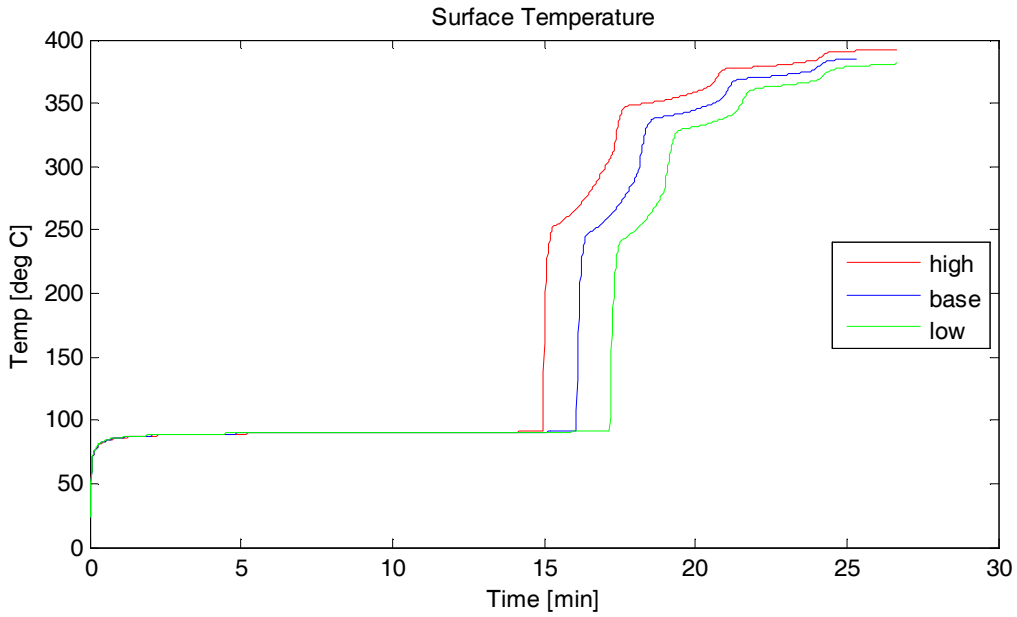

Figure 311 - Effect of Adjusting the Porosity with Initial Mass of Water Held Constant on Radiant Heating of CFB – Surface Temperature

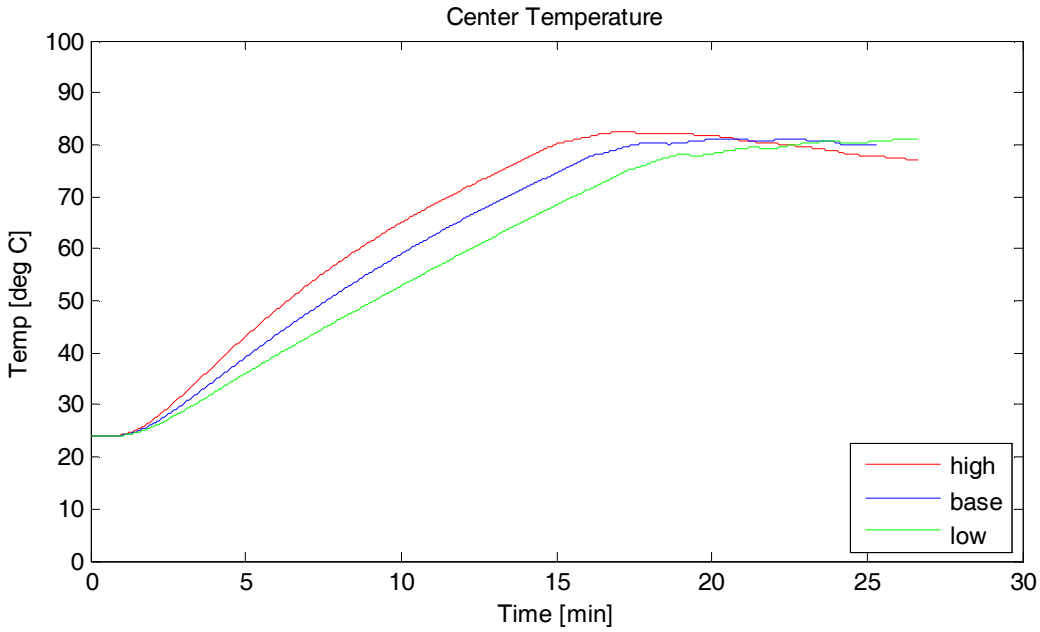

Figure 312 - Effect of Adjusting the Porosity with Initial Mass of Water Held Constant on Radiant Heating of CFB – Center Temperature

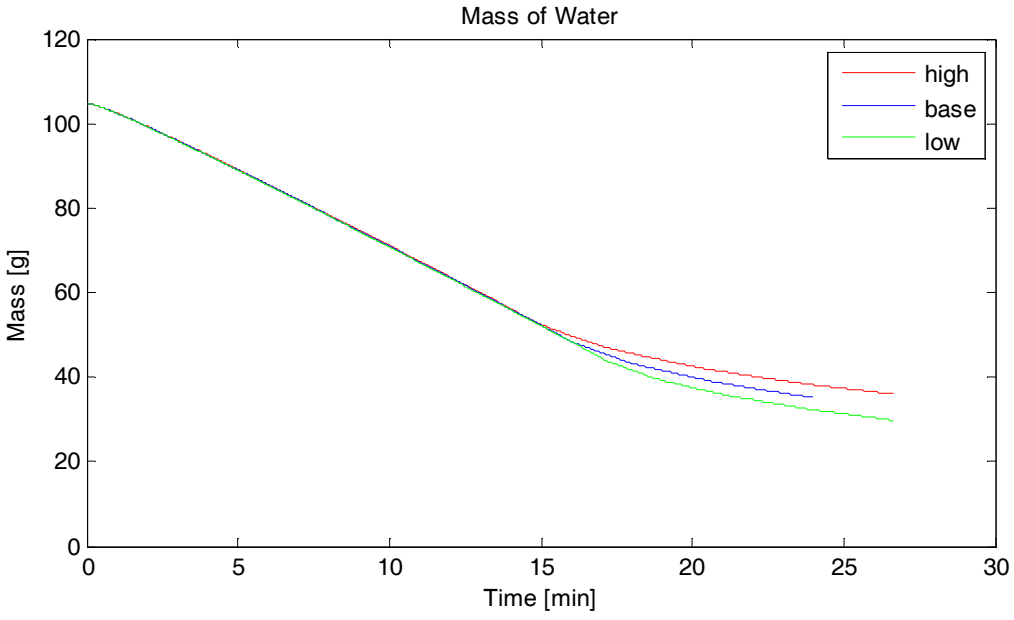

Figure 313 - Effect of Adjusting the Porosity with Initial Mass of Water Held Constant on Radiant Heating of CFB – Mass Loss

Specific Heat

The specific heat of the solid phase was adjusted ±10% from its base value of 1046 J/kgK. The effect of this change on the surface temperature, centerline temperature, and mass loss are shown in Figure 308, Figure 309, and Figure 310.

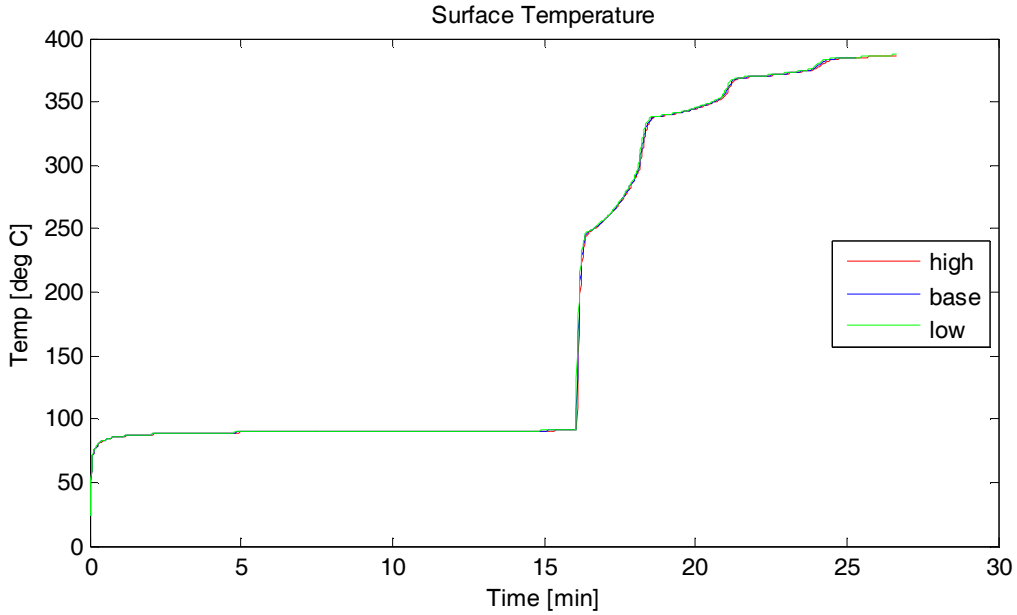

Figure 314 - Effect of Adjusting the Specific Heat on Radiant Heating of CFB – Surface Temperature

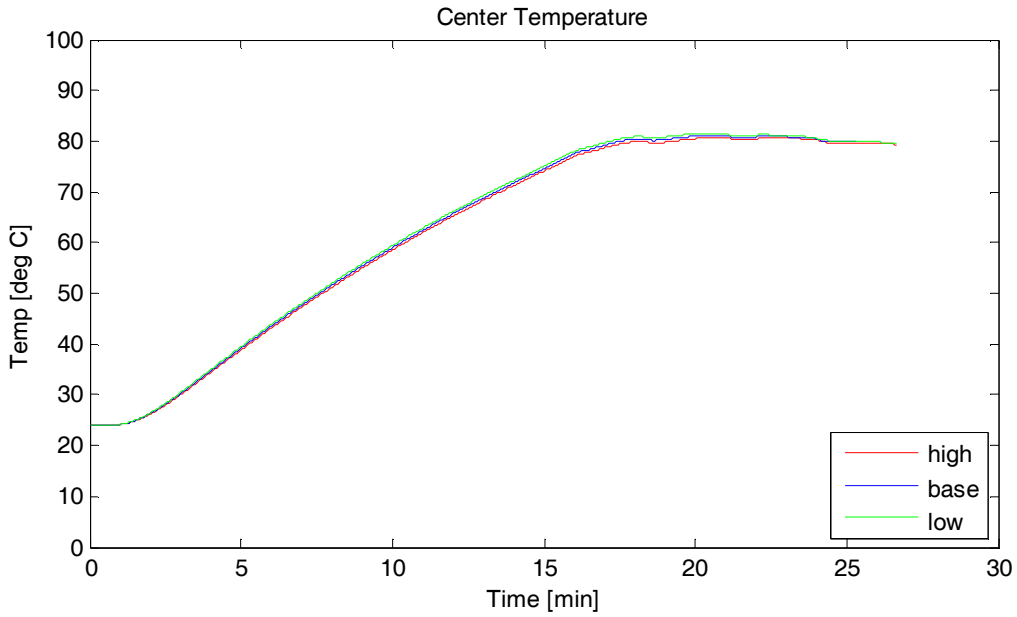

Figure 315 - Effect of Adjusting the Specific Heat on Radiant Heating of CFB – Center Temperature

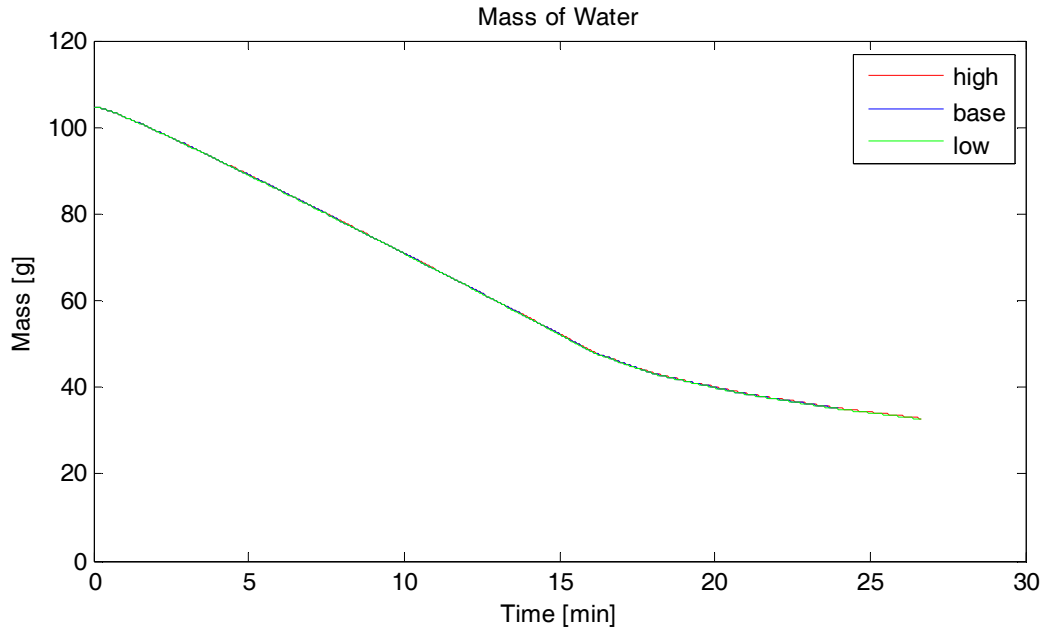

Figure 316 - Effect of Adjusting the Specific Heat on Radiant Heating of CFB – Mass Loss

Thermal Conductivity

The thermal conductivity was adjusted ±10% from its base value of 0.133 W/mK. The effect of this change on the surface temperature, centerline temperature, and mass loss are shown in Figure 317, Figure 318, and Figure 319.

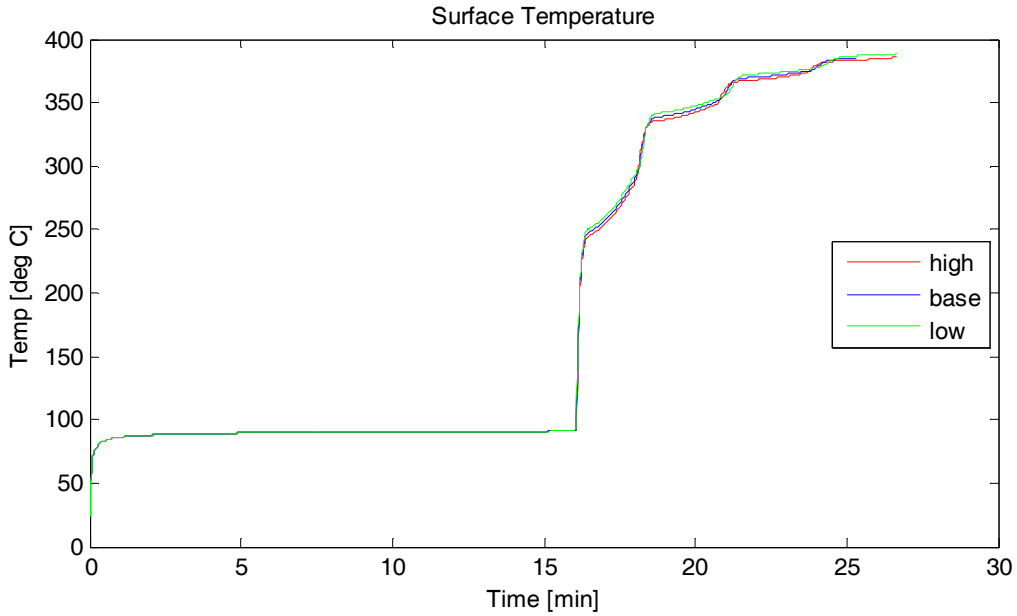

Figure 317 - Effect of Adjusting the Thermal Conductivity on Radiant Heating of CFB – Surface Temperature

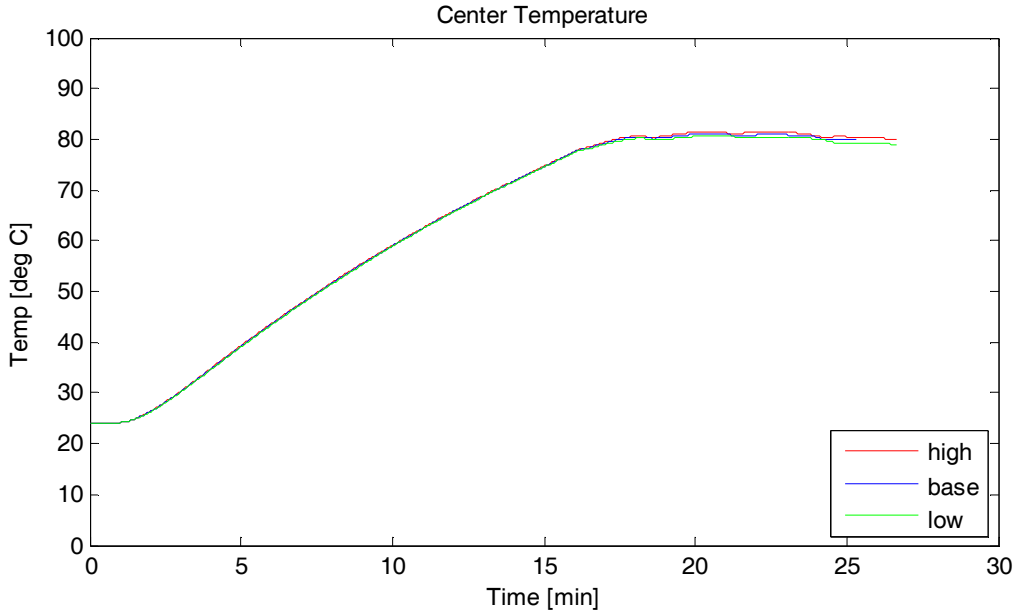

Figure 318 - Effect of Adjusting the Thermal Conductivity on Radiant Heating of CFB – Center Temperature

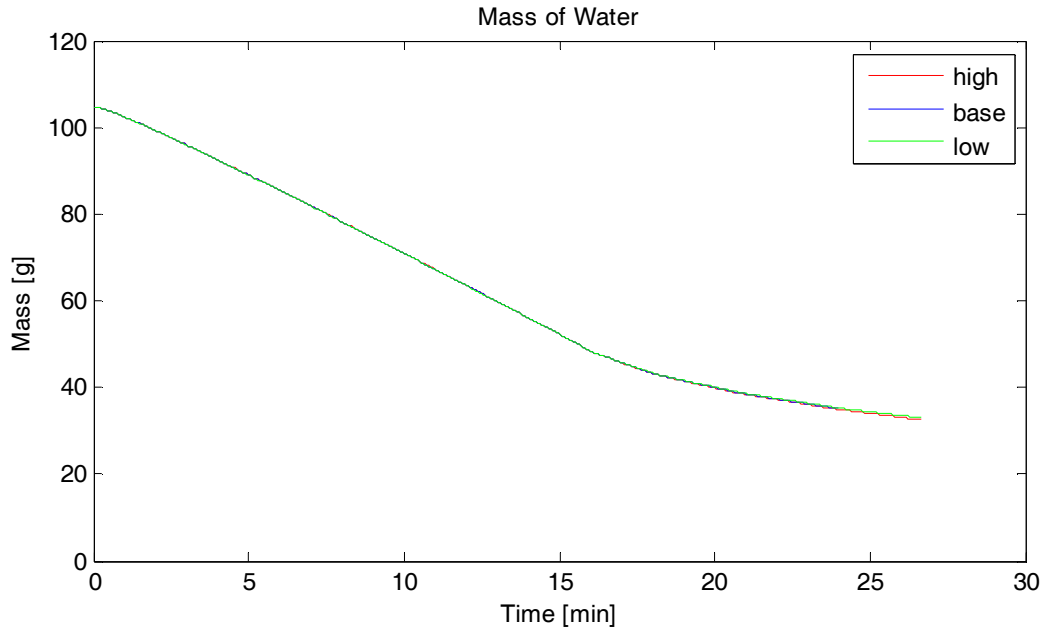

Figure 319 - Effect of Adjusting the Thermal Conductivity on Radiant Heating of CFB – Mass Loss

Density

The density was adjusted ±10% from its base value of 1360 kg/m^3. The effect of this change on the surface temperature, centerline temperature, and mass loss are shown in Figure 320, Figure 321, and Figure 322.

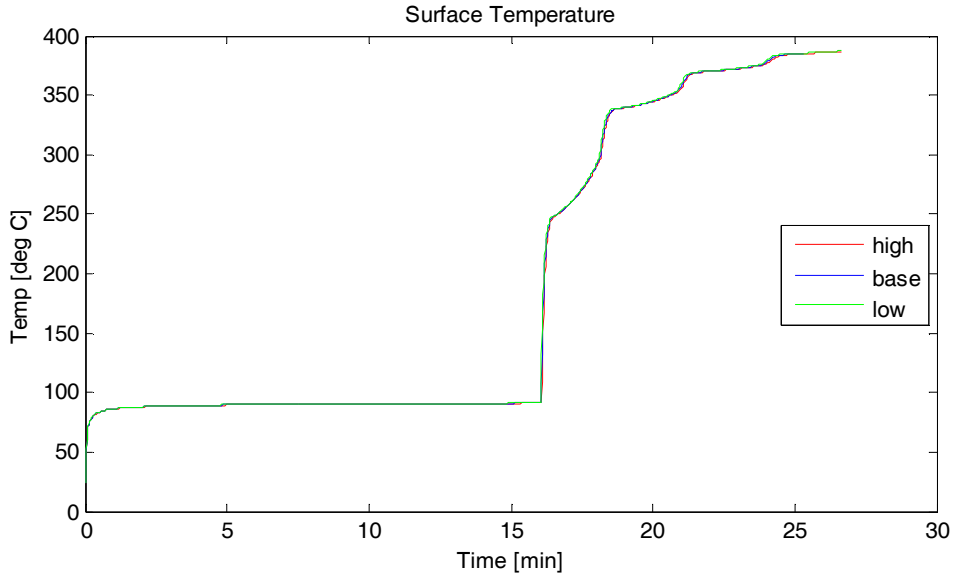

Figure 320 - Effect of Adjusting the Density on Radiant Heating of CFB – Surface Temperature

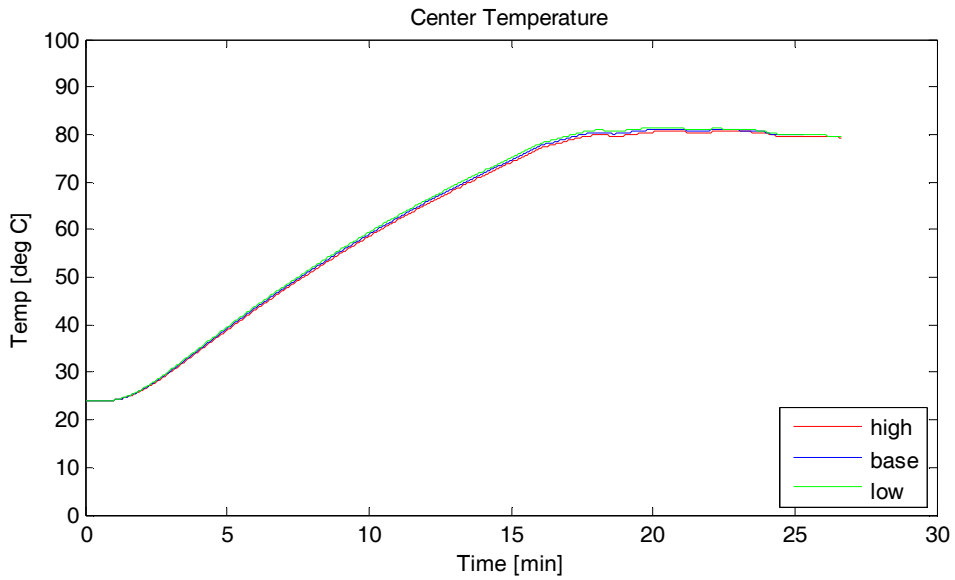

Figure 321 - Effect of Adjusting the Density on Radiant Heating of CFB – Center Temperature

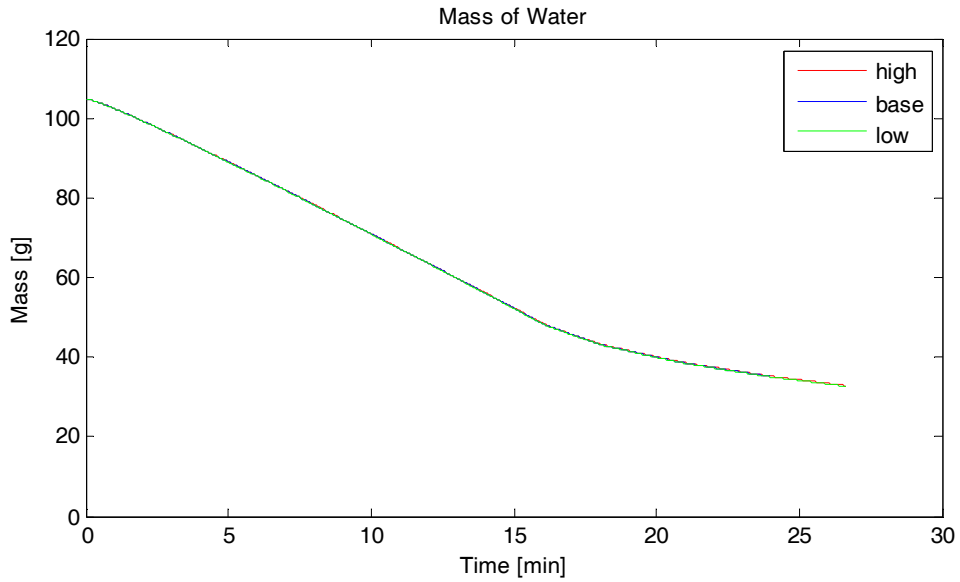

Figure 322 - Effect of Adjusting the Density on Radiant Heating of CFB – Mass Loss

Diffusivity

The diffusivity was adjusted ±10% from its base value of $2.6\times10^{-5}\,m^2/s$. The effect of this change on the surface temperature, centerline temperature, and mass loss are shown in Figure 323, Figure 324, and Figure 325.

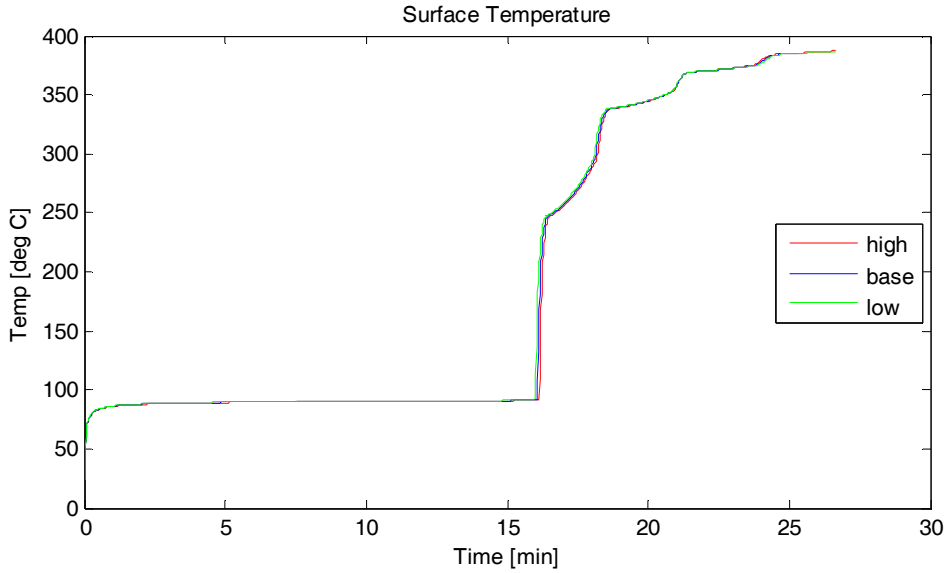

Figure 323 - Effect of Adjusting the Diffusivity on Radiant Heating of CFB – Surface Temperature

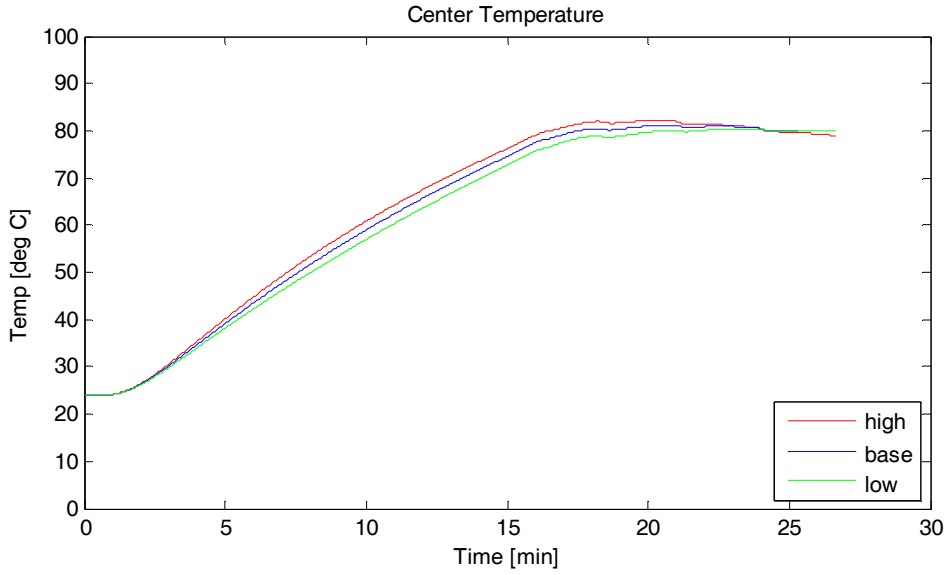

Figure 324 - Effect of Adjusting the Diffusivity on Radiant Heating of CFB – Center Temperature

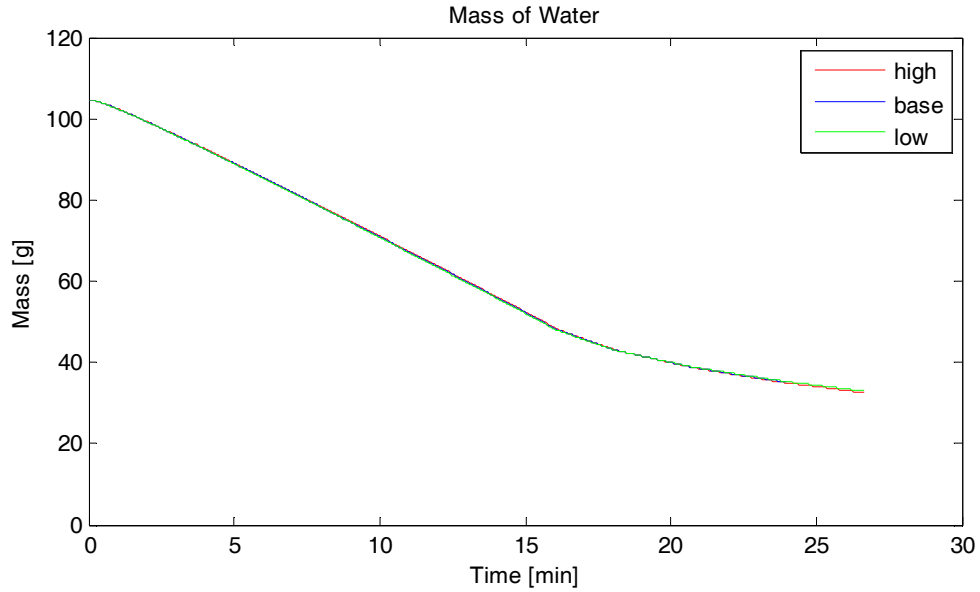

Figure 325 - Effect of Adjusting the Diffusivity on Radiant Heating of CFB – Mass Loss

Heat Transfer Coefficient

The heat transfer coefficient was adjusted ±10% from the value calculated using the correlation described earlier. The effect of this change on the surface temperature, centerline temperature, and mass loss are shown in Figure 326, Figure 327, and Figure 328.

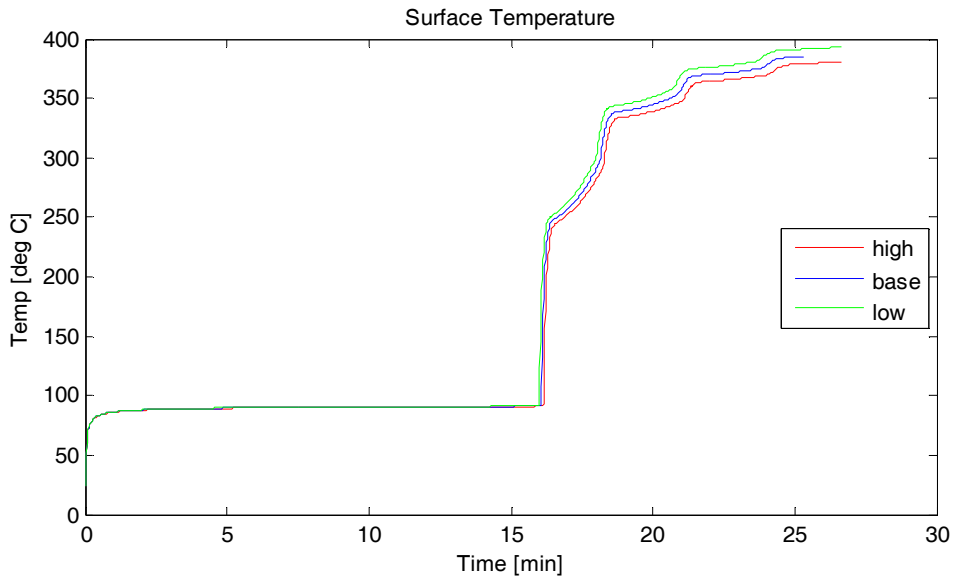

Figure 326 - Effect of Adjusting the Heat Transfer Coefficient on Radiant Heating of CFB – Surface Temperature

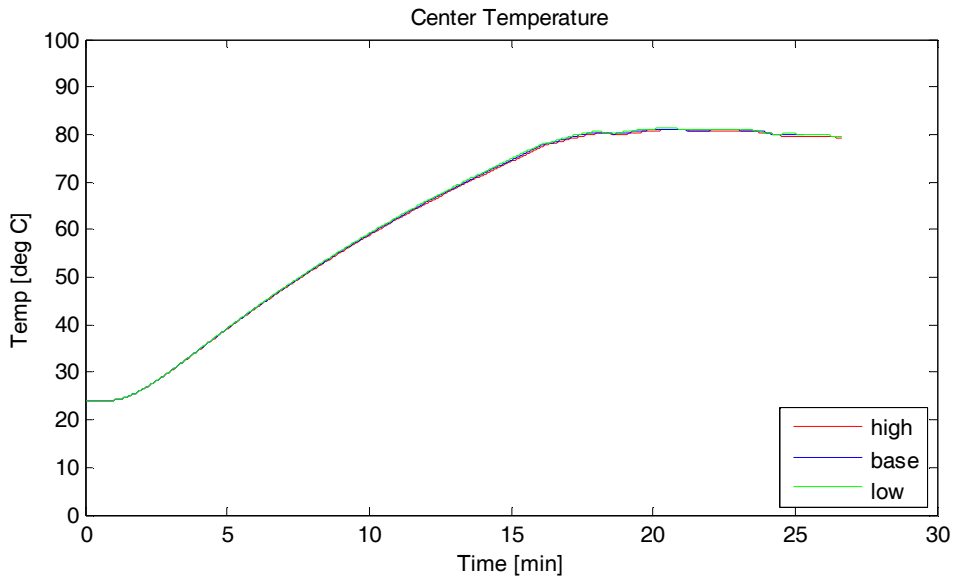

Figure 327 - Effect of Adjusting the Heat Transfer Coefficient on Radiant Heating of CFB – Center Temperature

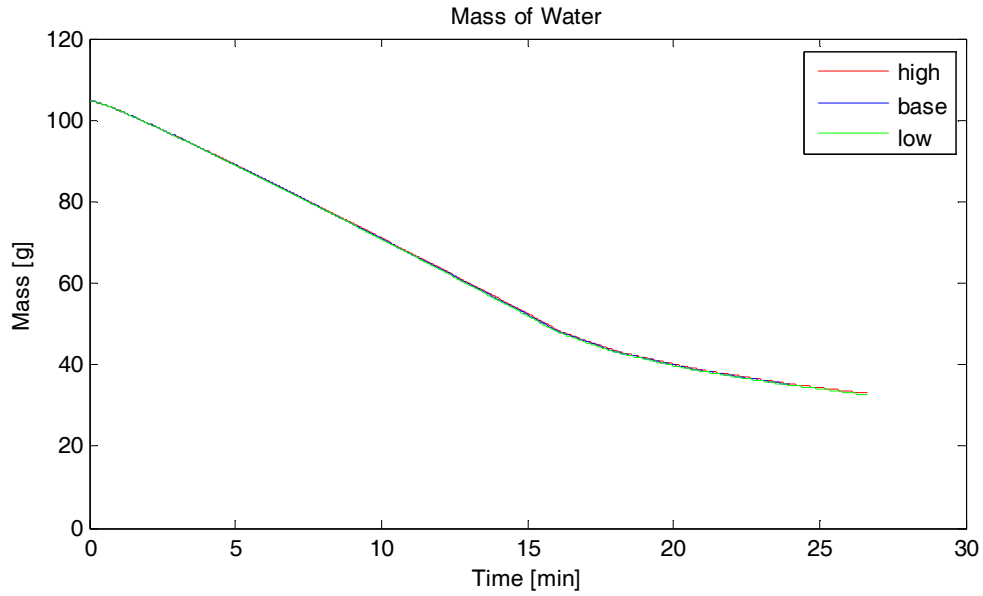

Figure 328 - Effect of Adjusting the Heat Transfer Coefficient on Radiant Heating of CFB – Mass Loss

Mass Transfer Coefficient

The mass transfer coefficient was adjusted ±10% from the value calculated using the correlation described previously. The effect of this change on the surface temperature, centerline temperature, and mass loss are shown in Figure 329, Figure 330, and Figure 331.

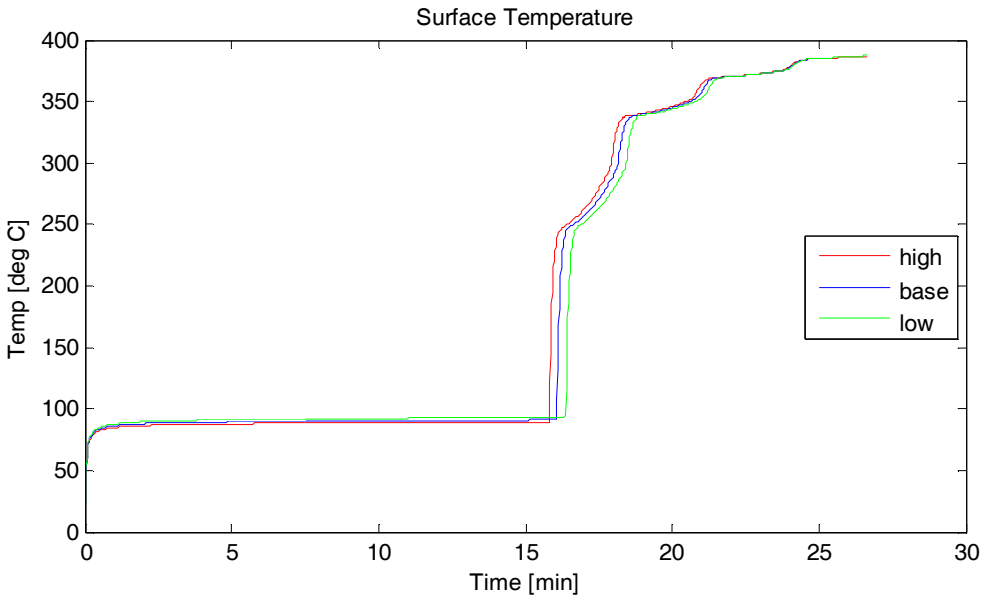

Figure 329 - Effect of Adjusting the Mass Transfer Coefficient on Radiant Heating of CFB – Surface Temperature

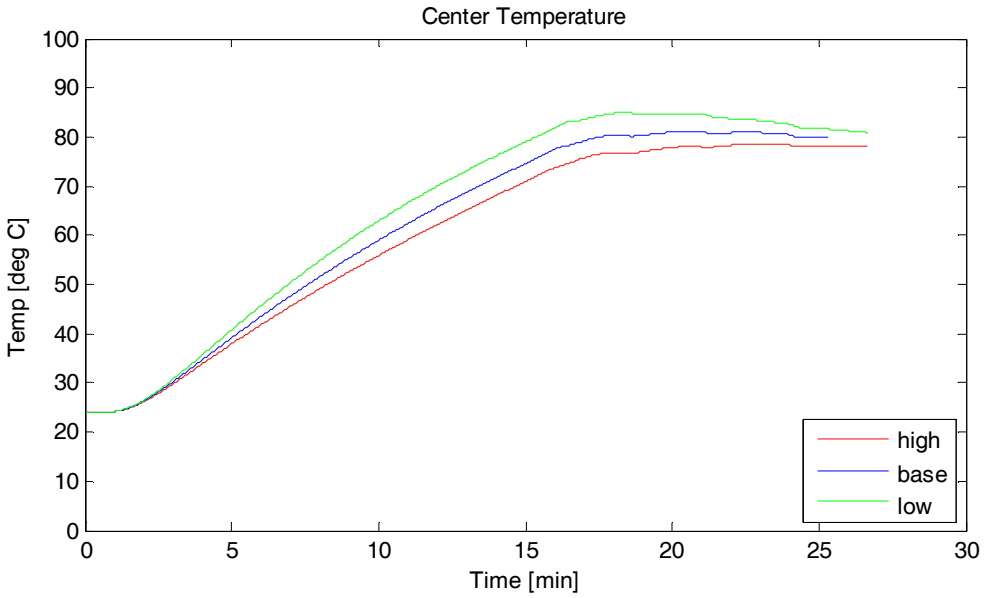

Figure 330 - Effect of Adjusting the Mass Transfer Coefficient on Radiant Heating of CFB – Center Temperature

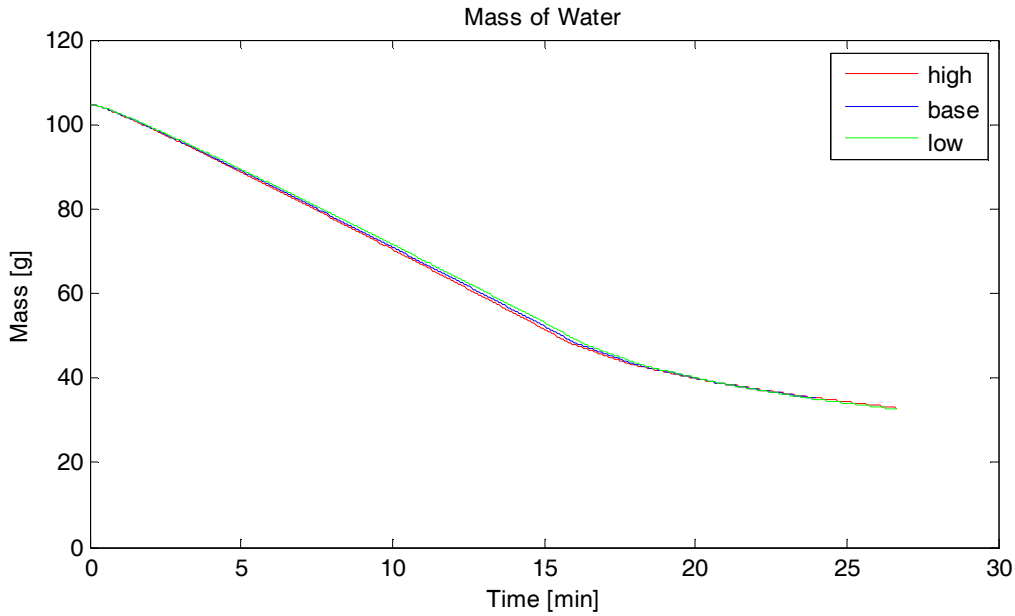

Figure 331 - Effect of Adjusting the Mass Transfer Coefficient on Radiant Heating of CFB – Mass Loss

Relative Humidity

The ambient relative humidity was adjusted ±10% from the base value of 20%. The effect of this change on the surface temperature, centerline temperature, and mass loss are shown in Figure 329, Figure 330, and Figure 331.

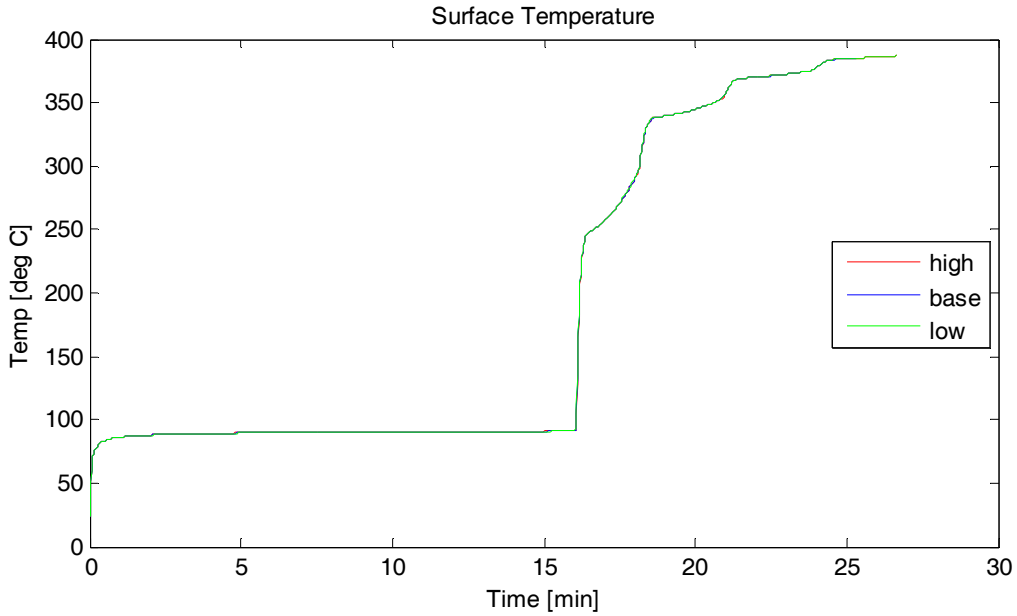

Figure 332 - Effect of Adjusting the Relative Humidity on Radiant Heating of CFB – Surface Temperature

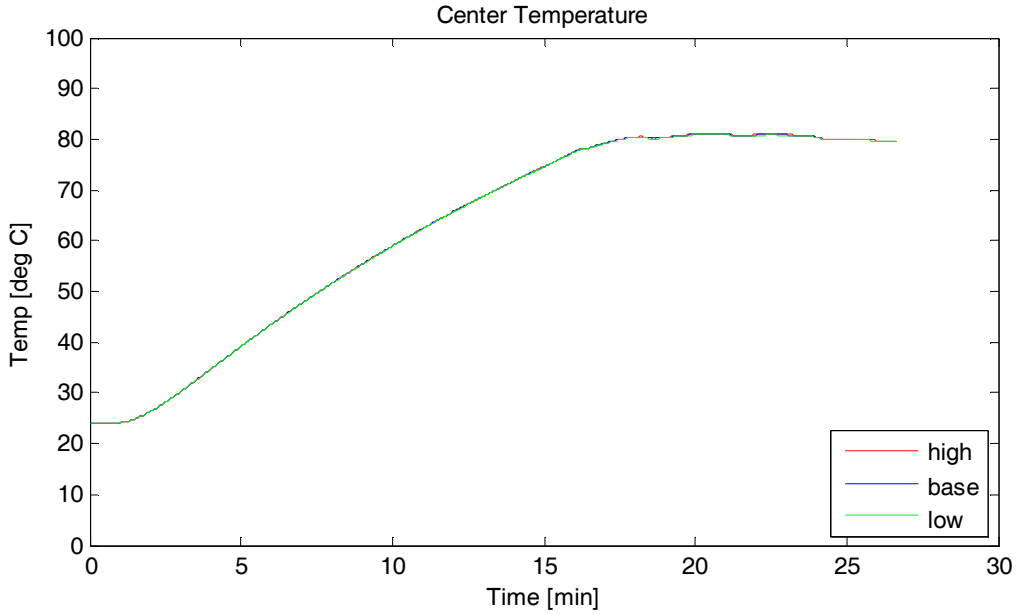

Figure 333 - Effect of Adjusting the Relative Humidity on Radiant Heating of CFB – Surface Temperature

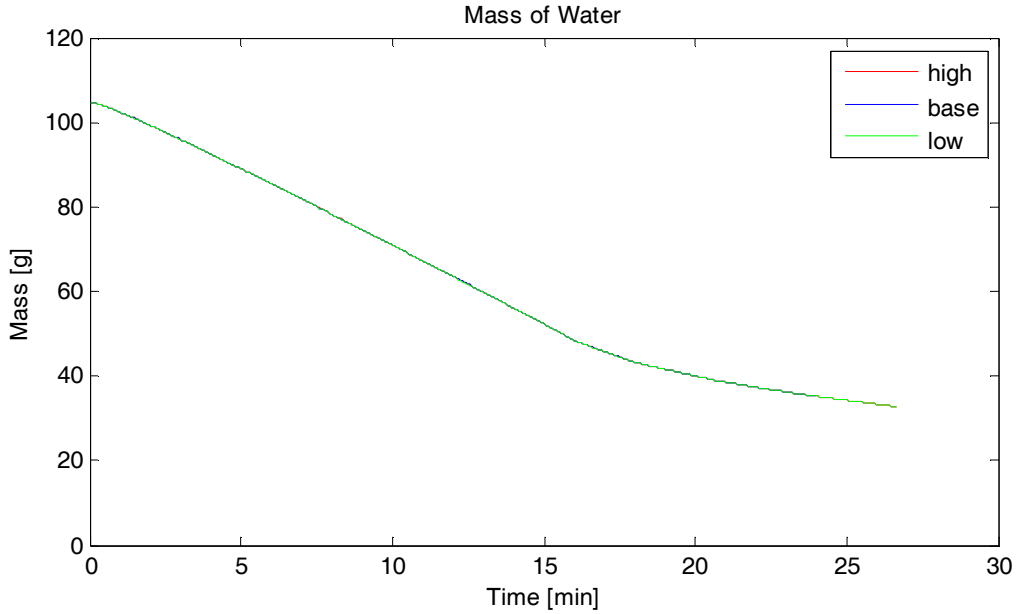

Figure 334 - Effect of Adjusting the Relative Humidity on Radiant Heating of CFB – Surface Temperature

Initial Temperature

The initial temperature was adjusted $\pm 2^0 C$ from the base value of 24°C. The effect of this change on the surface temperature, centerline temperature, and mass loss are shown in Figure 335, Figure 336, and Figure 337.

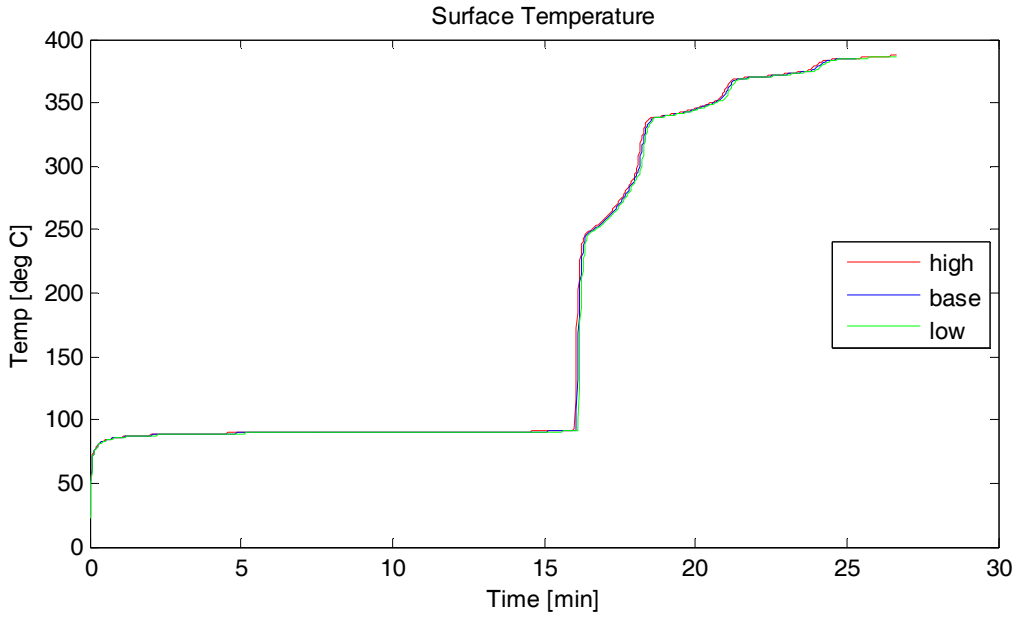

Figure 335 - Effect of Adjusting the Initial Temperature on Radiant Heating of CFB – Surface Temperature

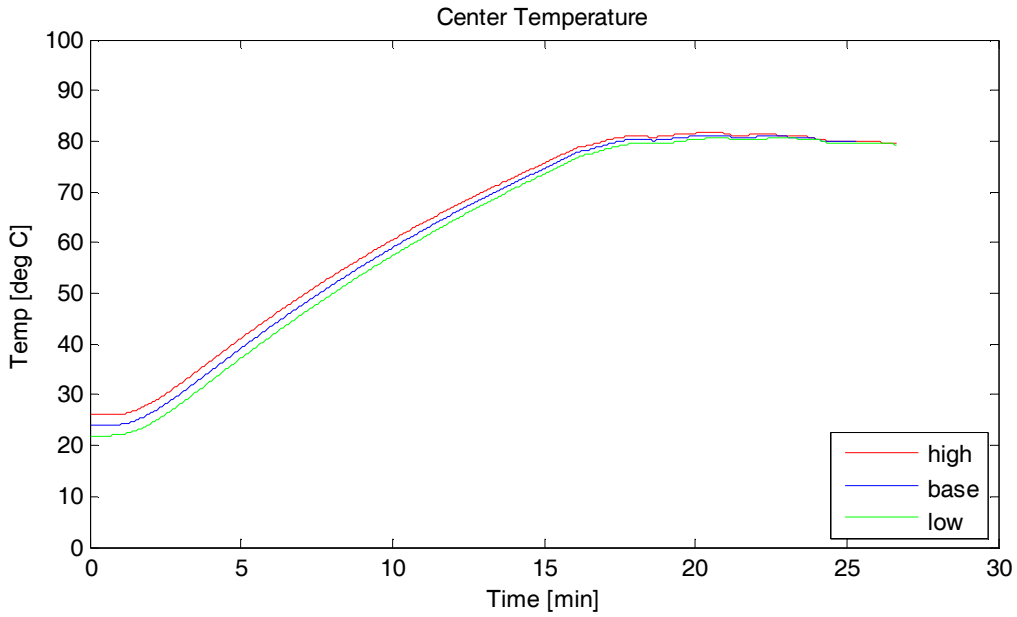

Figure 336 - Effect of Adjusting the Initial Temperature on Radiant Heating of CFB – Center Temperature

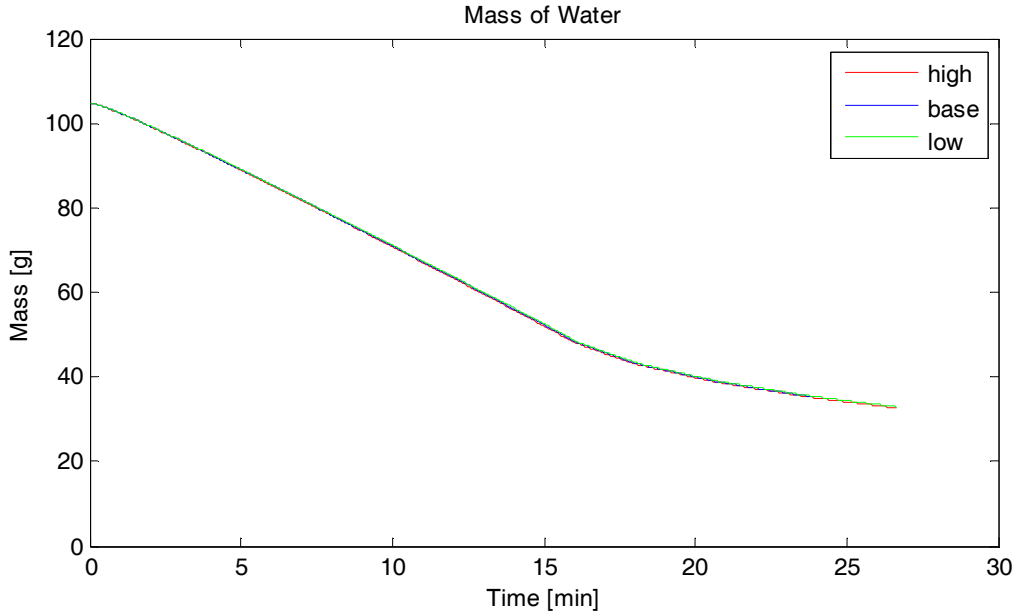

Figure 337 - Effect of Adjusting the Initial Temperature on Radiant Heating of CFB –Mass Loss

Ambient Temperature

The ambient temperature was adjusted $\pm 2^0 C$ from the base value of 24°C. The effect of this change on the surface temperature, centerline temperature, and mass loss are shown in Figure 338, Figure 339, and Figure 340.

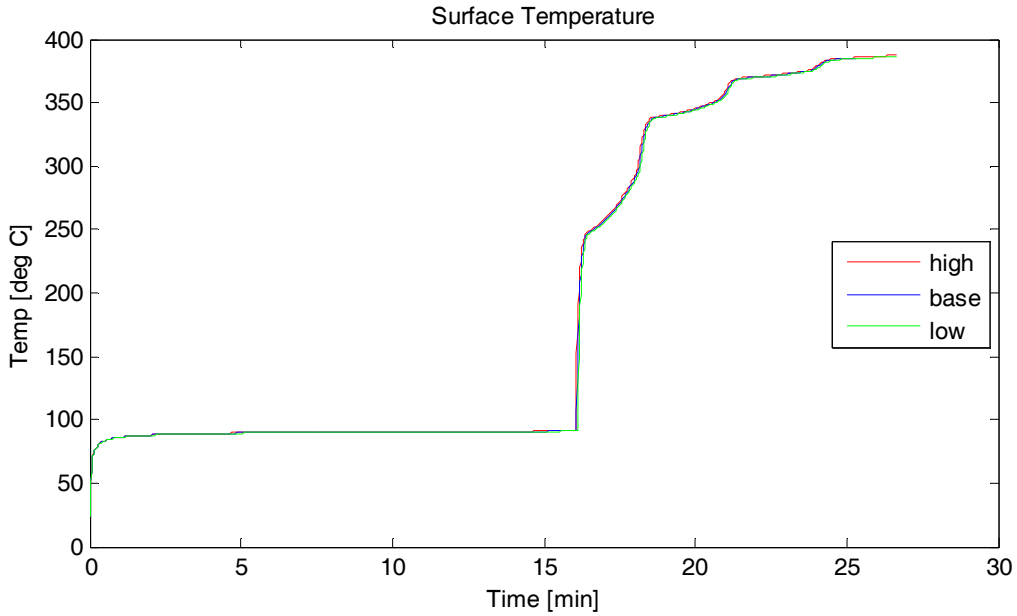

Figure 338 - Effect of Adjusting the Ambient Temperature on Radiant Heating of CFB – Surface Temperature

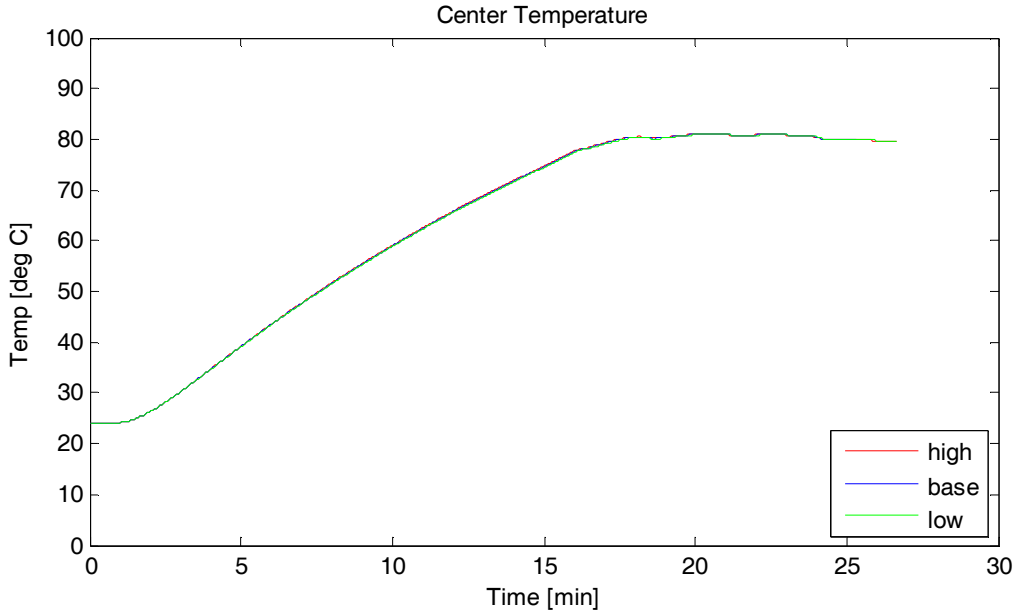

Figure 339 - Effect of Adjusting the Ambient Temperature on Radiant Heating of CFB – Center Temperature

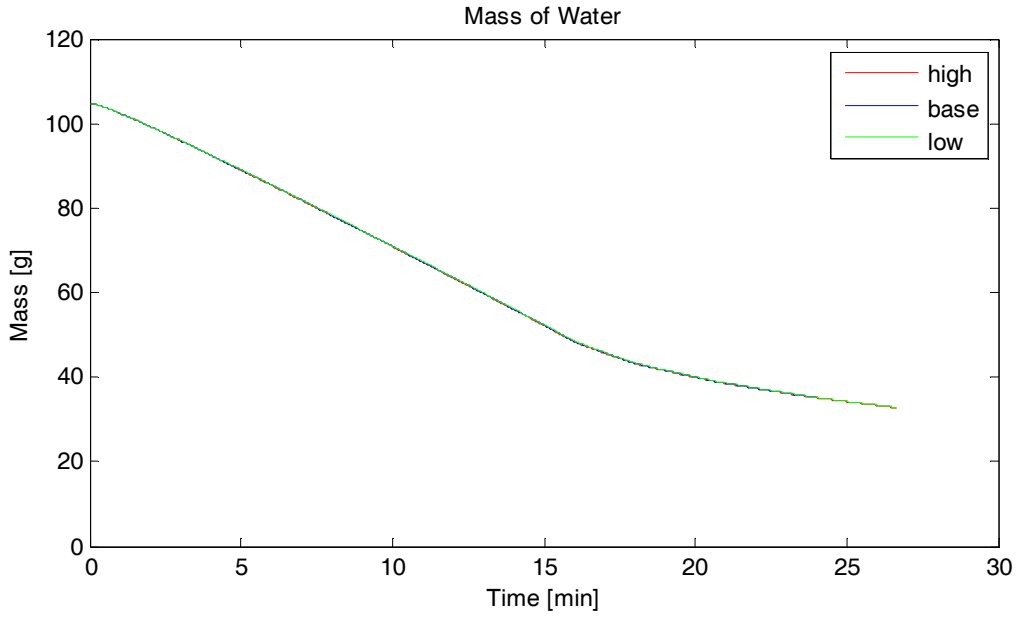

Figure 340 - Effect of Adjusting the Ambient Temperature on Radiant Heating of CFB – Mass Loss

Sample Depth

The sample depth was adjusted ±10% from the base value of 0.0254 m. The effect of this change on the surface temperature, centerline temperature, and mass loss are shown in Figure 341, Figure 342, and Figure 343.

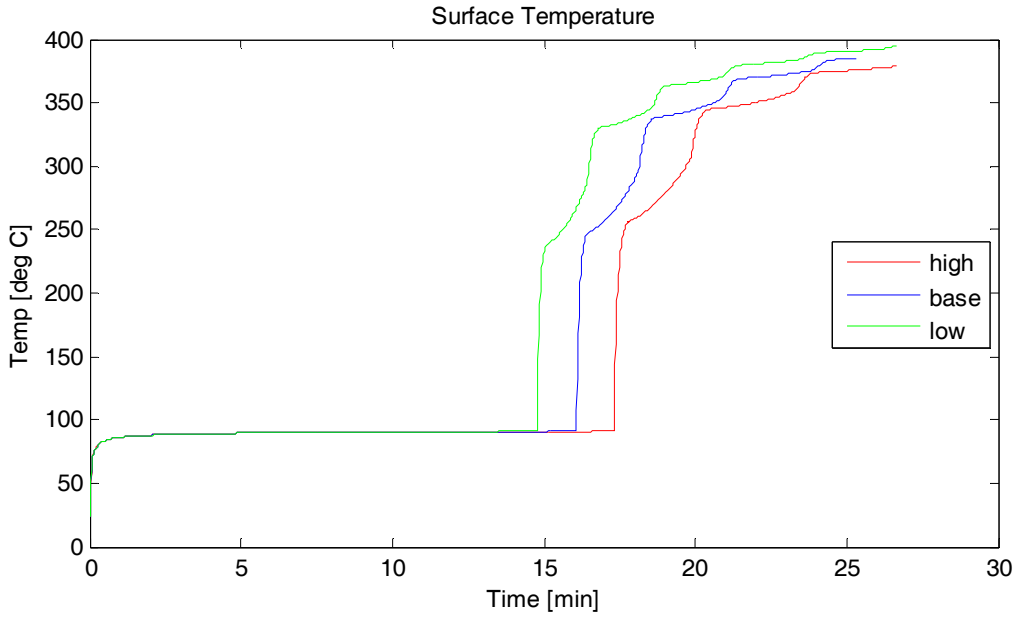

Figure 341 - Effect of Adjusting the Sample Depth on Radiant Heating of CFB-Surface Temperature

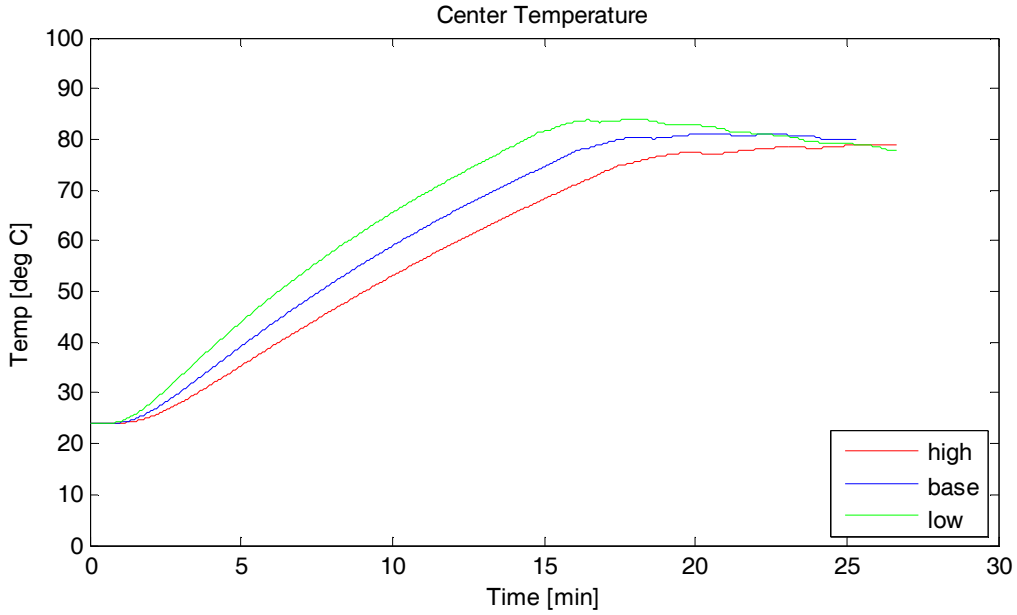

Figure 342 - Effect of Adjusting the Sample Depth on Radiant Heating of CFB-Center Temperature

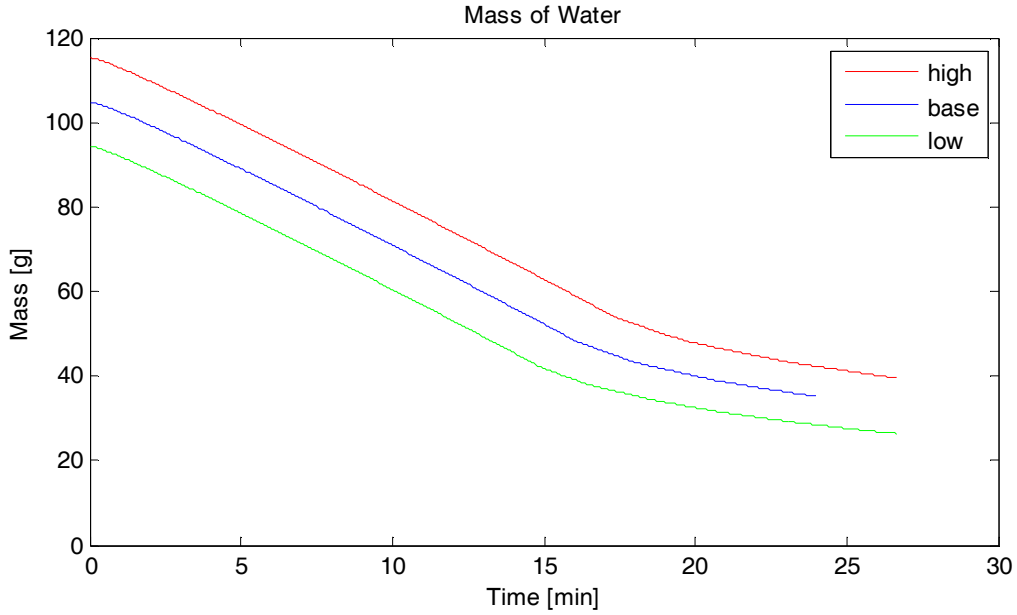

Figure 343 - Effect of Adjusting the Sample Depth on Radiant Heating of CFB-Mass Loss

From Figure 343 it can be seen that adjusting the sample length has the unintended

effect of changing the initial mass of water in the sample. In order to attempt to separate the effects of these two changes to the input parameters, the length of the sample was adjusted ±10% from its base value while keeping the initial mass of water in the sample constant by applying the following constraint

$$S_2 = S_1 \frac{L_1}{L_2}$$

The effect of this change on the surface temperature, centerline temperature, and mass loss are shown in Figure 344, Figure 345, and Figure 346.

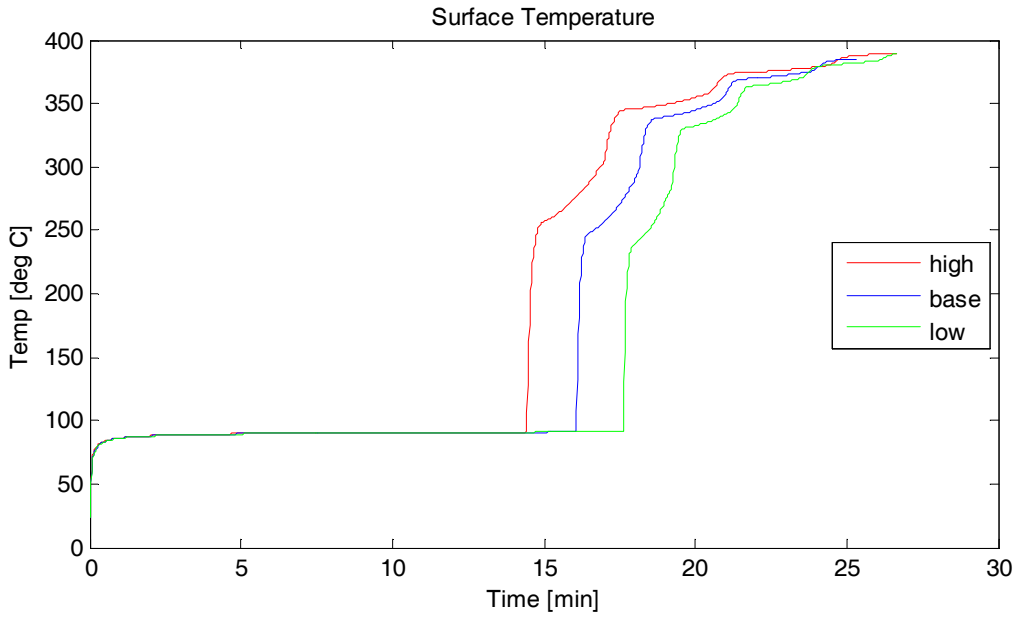

Figure 344 - Effect of Adjusting the Sample Depth with Initial Mass of Water Held Constant on Radiant Heating of CFB- Surface Temperature

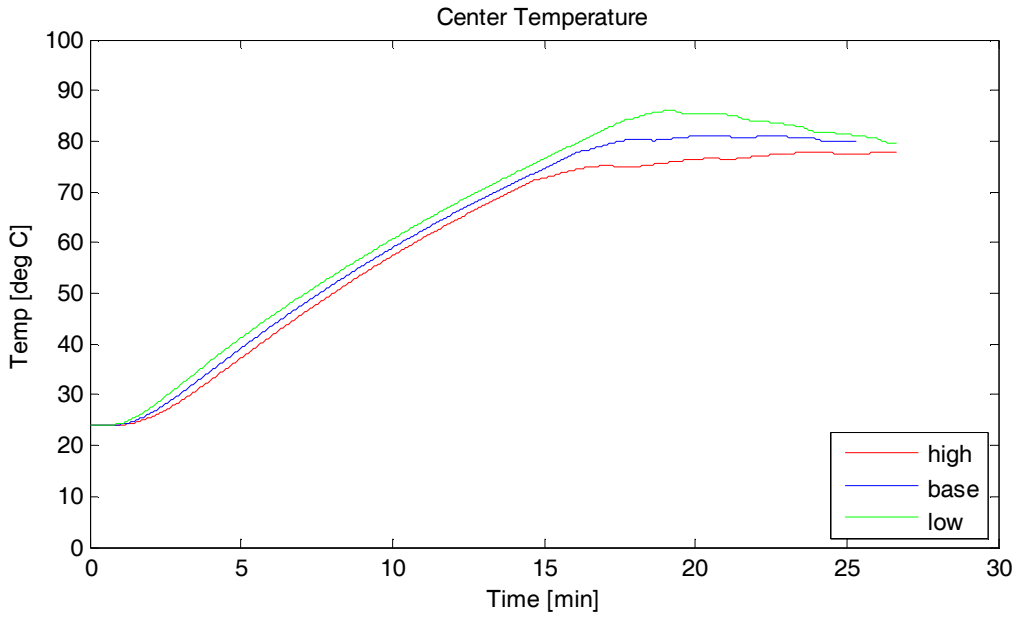

Figure 345 - Effect of Adjusting the Sample Depth with Initial Mass of Water Held Constant on Radiant Heating of CFB- Center Temperature

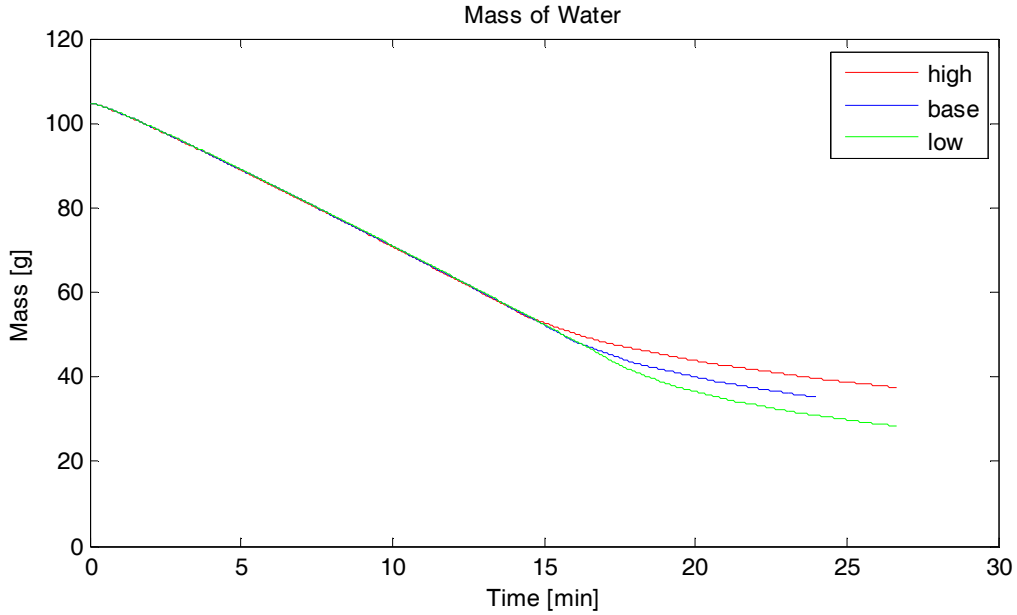

Figure 346 - Effect of Adjusting the Sample Depth with Initial Mass of Water Held Constant on Radiant Heating of CFB- Mass Loss

Initial Water Saturation

The initial saturation was adjusted ±10% from the base value of 0.5. The effect of this change on the surface temperature, centerline temperature, and mass loss are shown in Figure 347, Figure 348, and Figure 349.

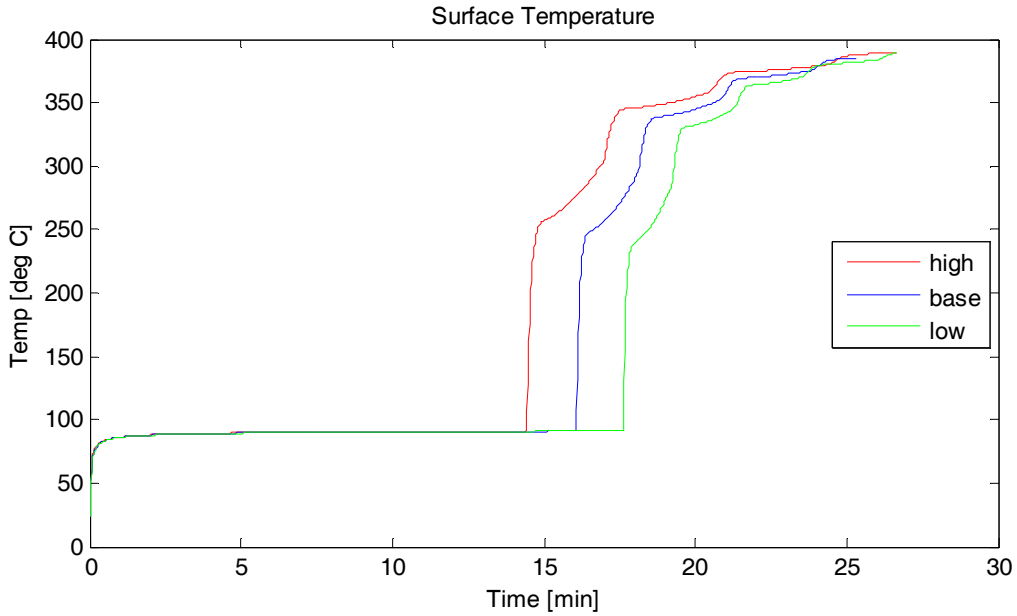

Figure 347 - Effect of Adjusting the Initial Saturation on Radiant Heating of CFB – Surface Temperature

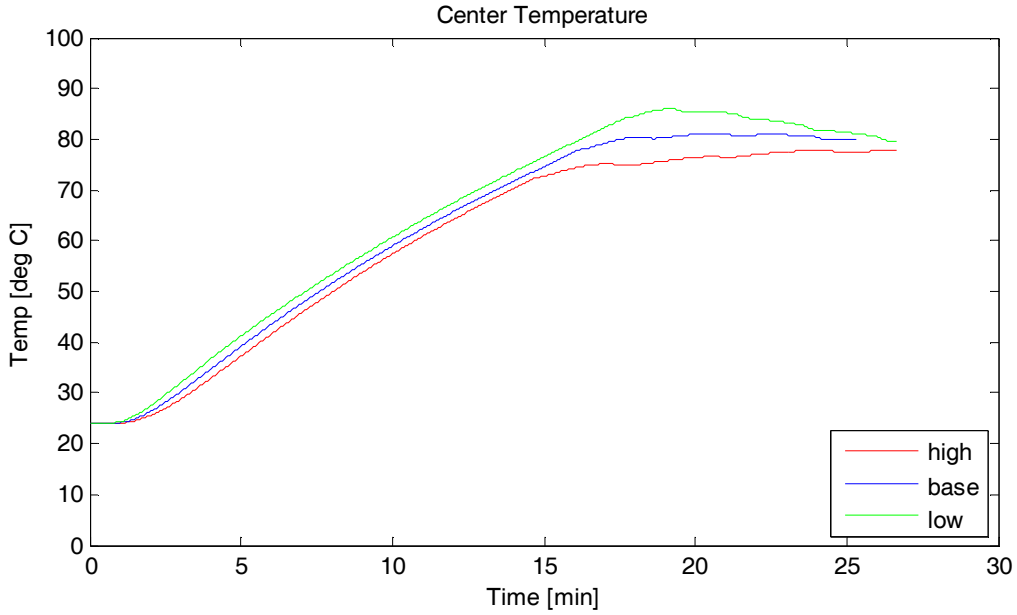

Figure 348 - Effect of Adjusting the Initial Saturation on Radiant Heating of CFB – Center Temperature

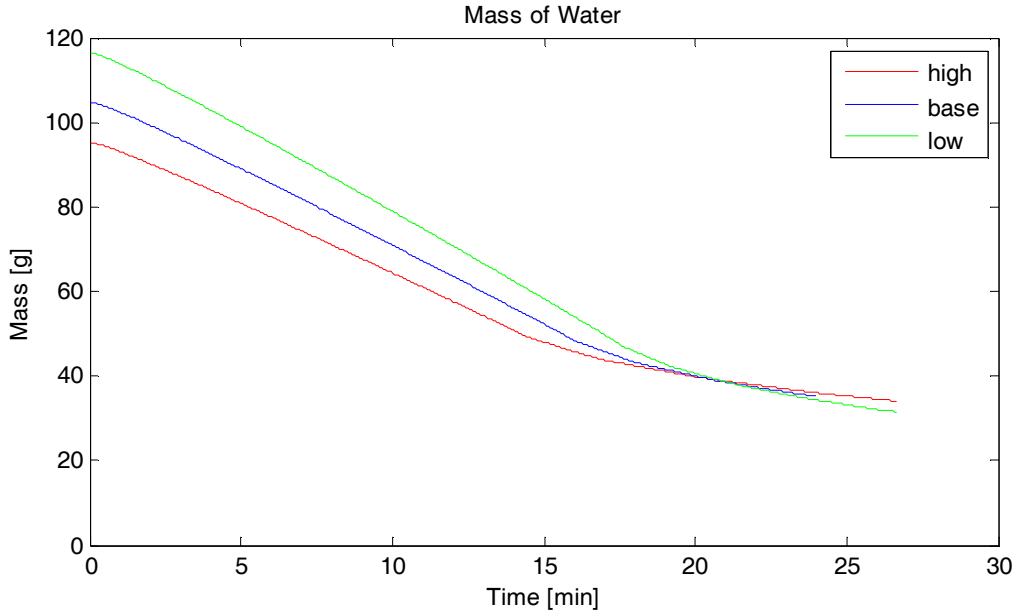

Figure 349 - Effect of Adjusting the Initial Saturation on Radiant Heating of CFB – Mass Loss

Number of Nodes

The initial number of nodes was adjusted from the base value of 25 to a "high" value of 30 and a "low" value of 20. The effect of this change on the surface temperature, centerline temperature, and mass loss are shown in Figure 350, Figure 351, and Figure 352.

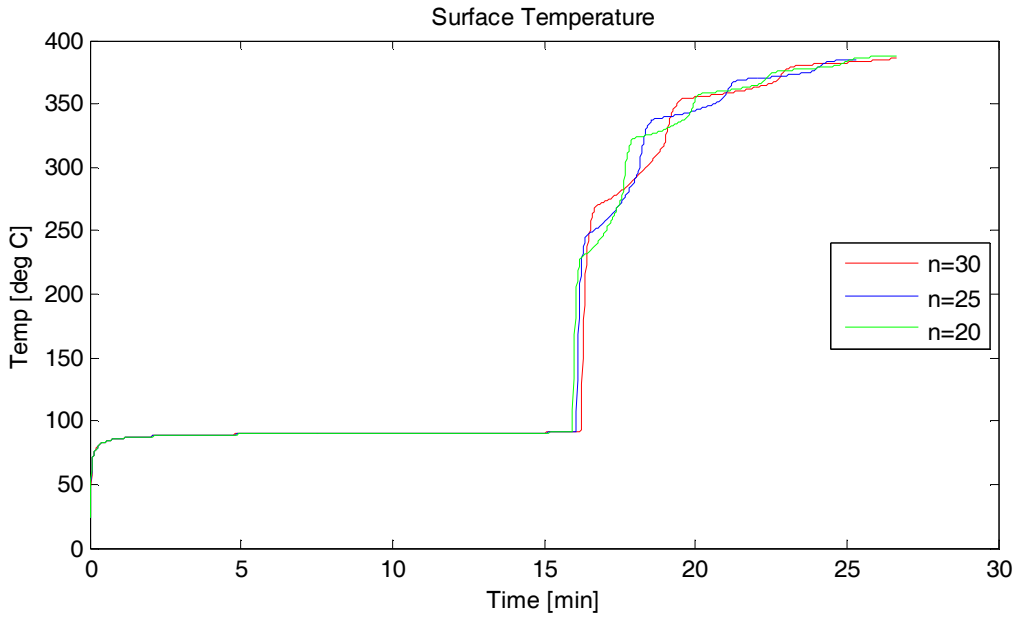

Figure 350 - Effect of Adjusting the Number of Nodes on Radiant Heating of CFB – Surface Temperature

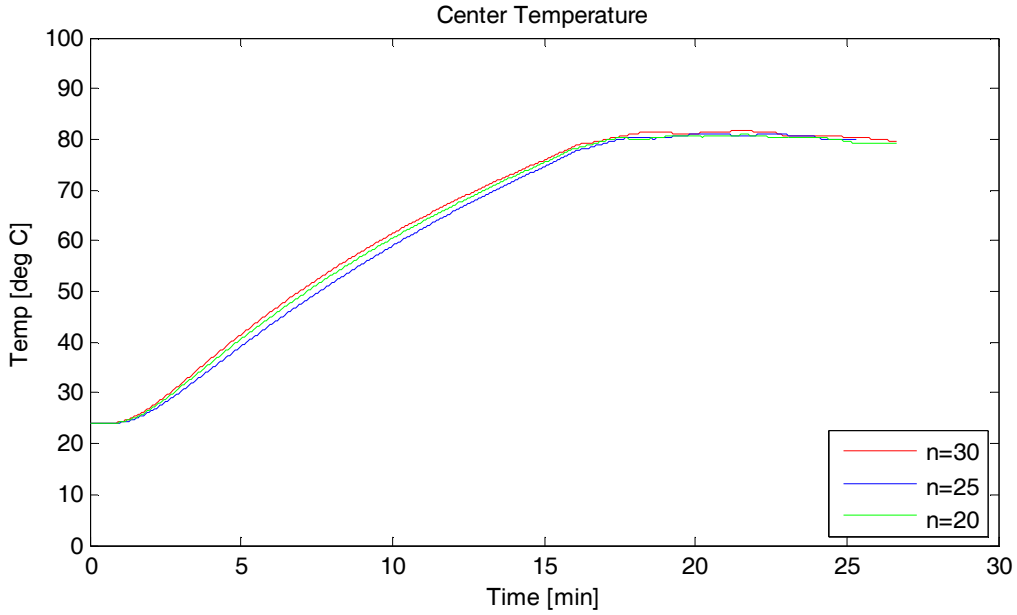

Figure 351 - Effect of Adjusting the Number of Nodes on Radiant Heating of CFB – Center Temperature

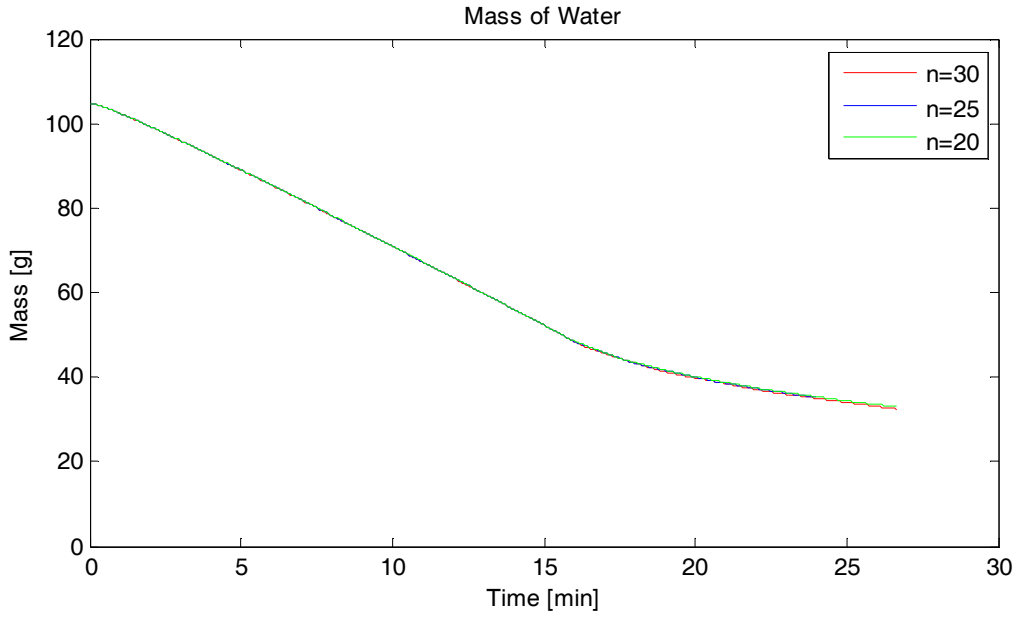

Figure 352 - Effect of Adjusting the Number of Nodes on Radiant Heating of CFB – Mass Loss

Timestep

The time step was adjusted from the base value of 1 second to a "high" value of 1.5 seconds and a "low" value of 0.5 seconds. The numerical solver that switched to a smaller time step when the surface saturation reached the irreducible saturation of 0.15 was still used. The smaller time step was set as the larger time step divided by 1000. This means that for the "high" value of 1.5 second, the small time step was 0.0015 seconds, and for the "low" value of 0.5 seconds, the small time step was 0.0005 seconds. The effect of this change on the surface temperature, centerline temperature, and mass loss are shown in Figure 353, Figure 354, and Figure 355.

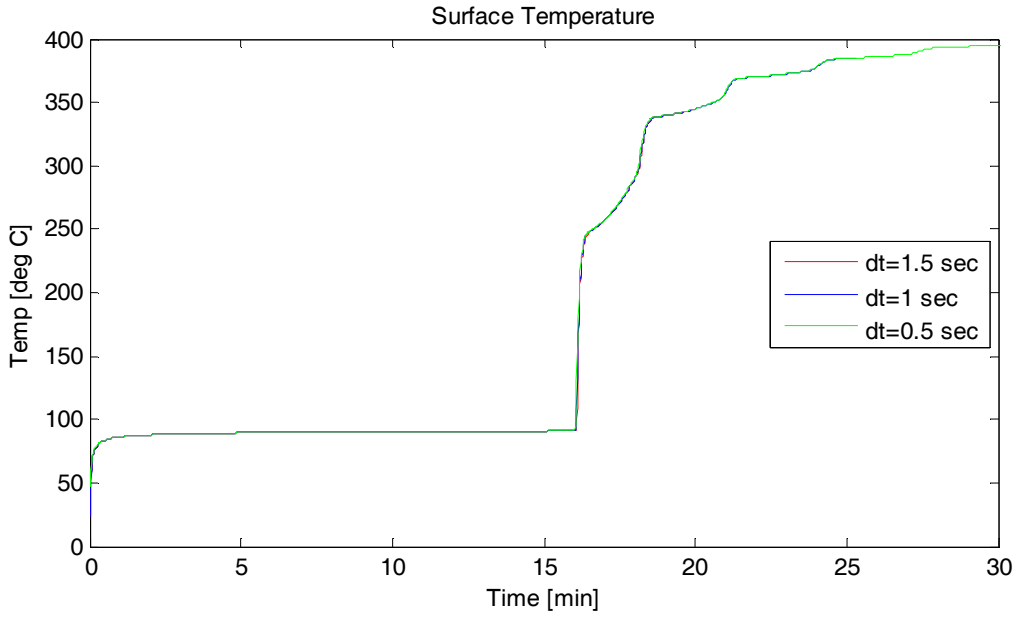

Figure 353 - Effect of Adjusting the Time Step on Radiant Heating of CFB – Surface Temperature

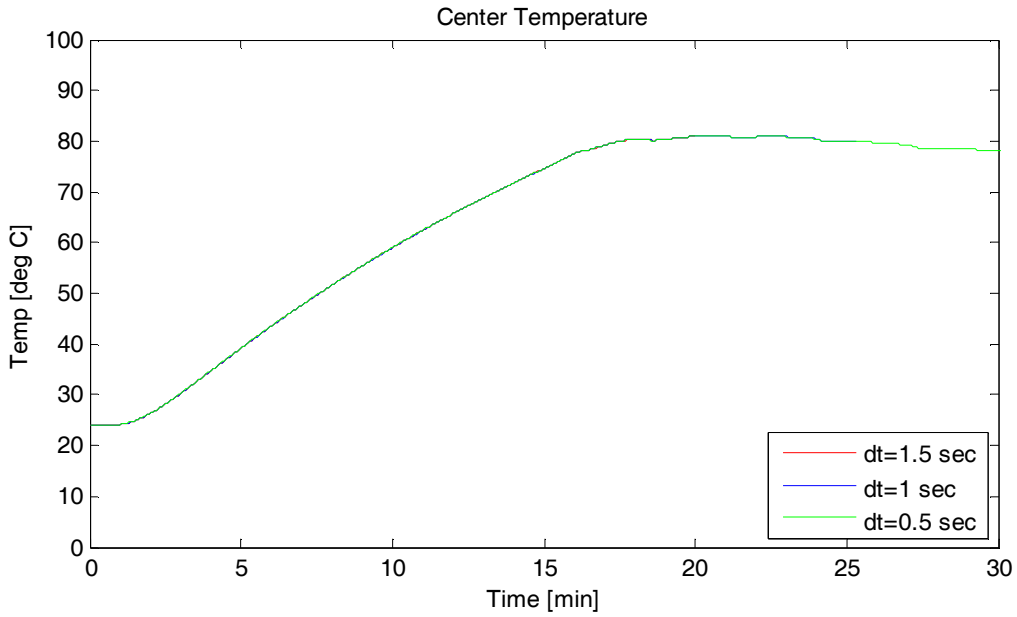

Figure 354 - Effect of Adjusting the Time Step on Radiant Heating of CFB – Center Temperature

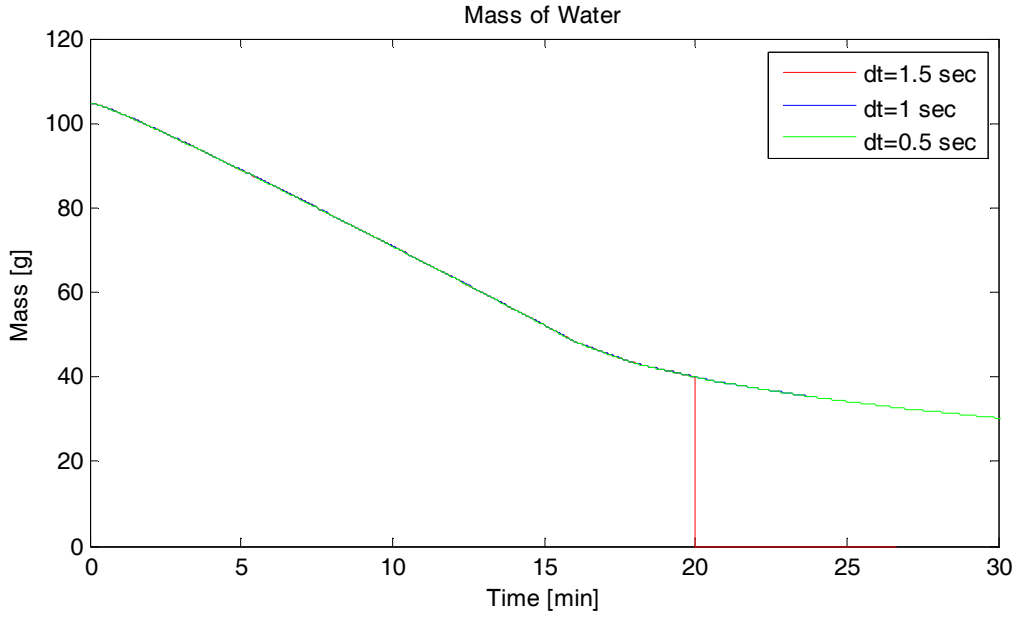

Figure 355 - Effect of Adjusting the Time Step on Radiant Heating of CFB – Mass Loss

Irreducible Saturation

The irreducible saturation was adjusted ±10% from the base value of 0.15. The effect of this change on the surface temperature, centerline temperature, and mass loss are shown in Figure 356, Figure 357, and Figure 358.

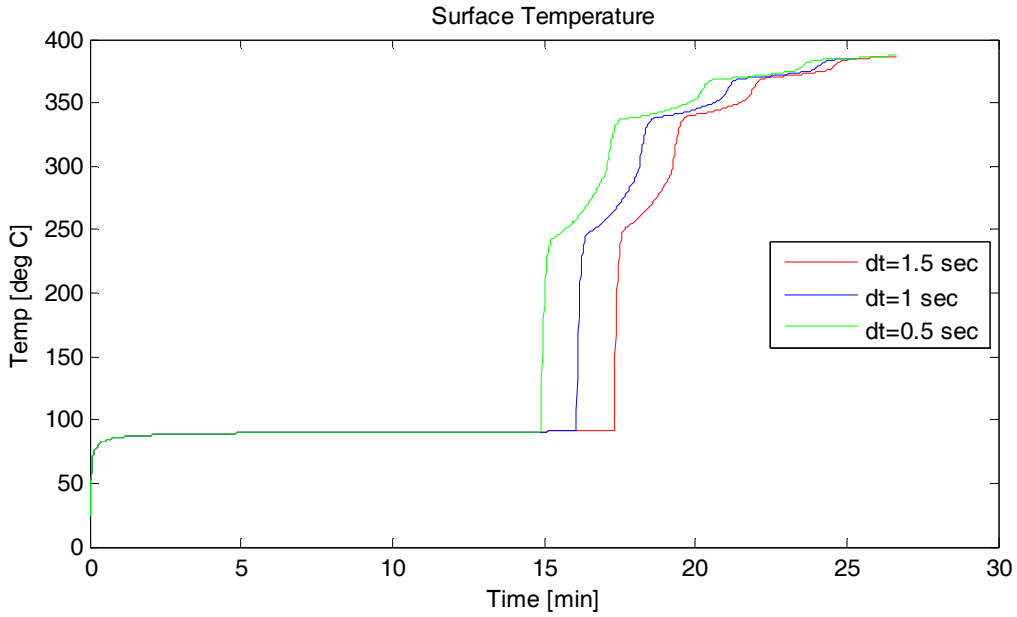

Figure 356 - Effect of Adjusting the Irreducible Saturation on Radiant Heating of CFB – Surface Temperature

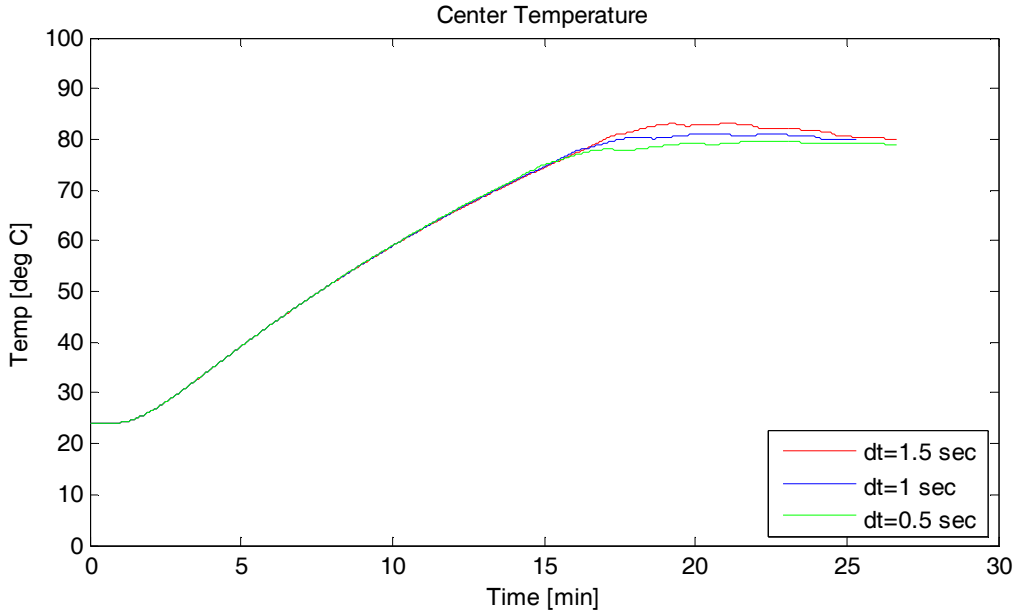

Figure 357 - Effect of Adjusting the Irreducible Saturation on Radiant Heating of CFB – Center Temperature

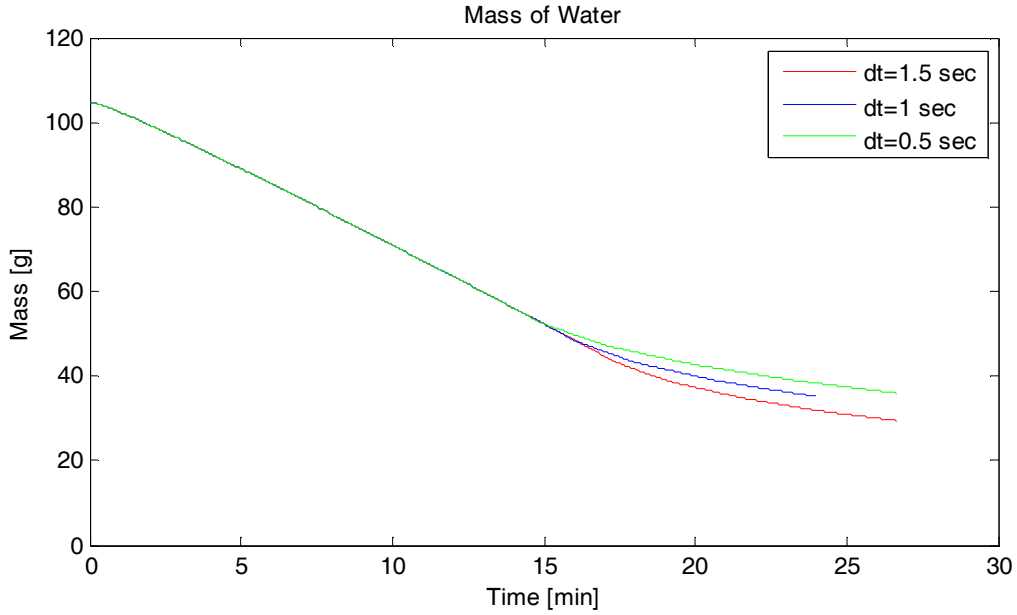

Figure 358 - Effect of Adjusting the Irreducible Saturation on Radiant Heating of CFB – Mass Loss

Radiant Heat Flux

The radiant heat flux was adjusted ±10% from the base value of 20 kW/m^2. The effect of this change on the surface temperature, centerline temperature, and mass loss are shown in Figure 359, Figure 360, and Figure 361.

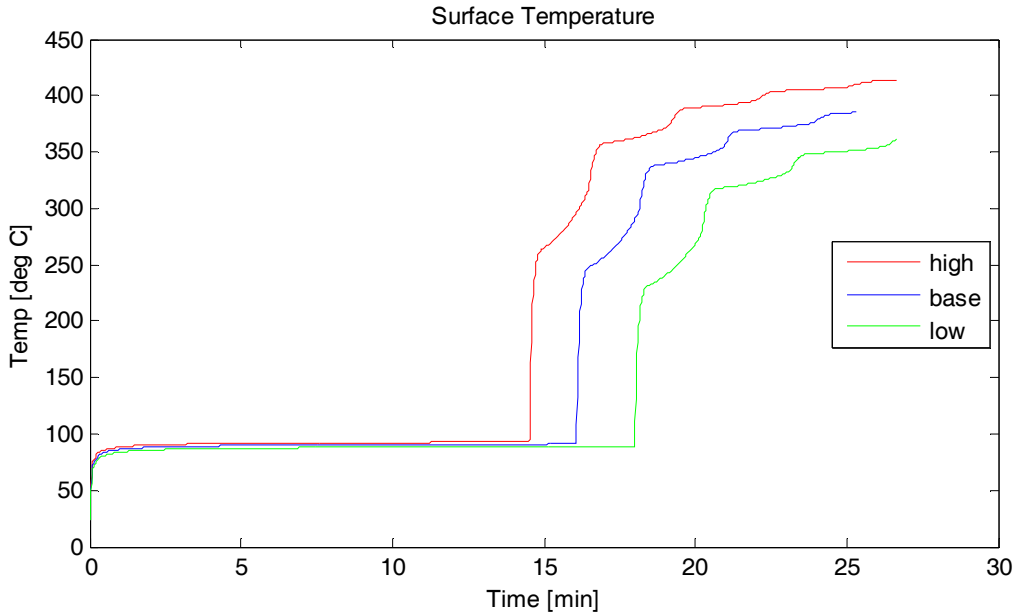

Figure 359 - Effect of Adjusting the Heat Flux on Radiant Heating of CFB – Surface Temperature

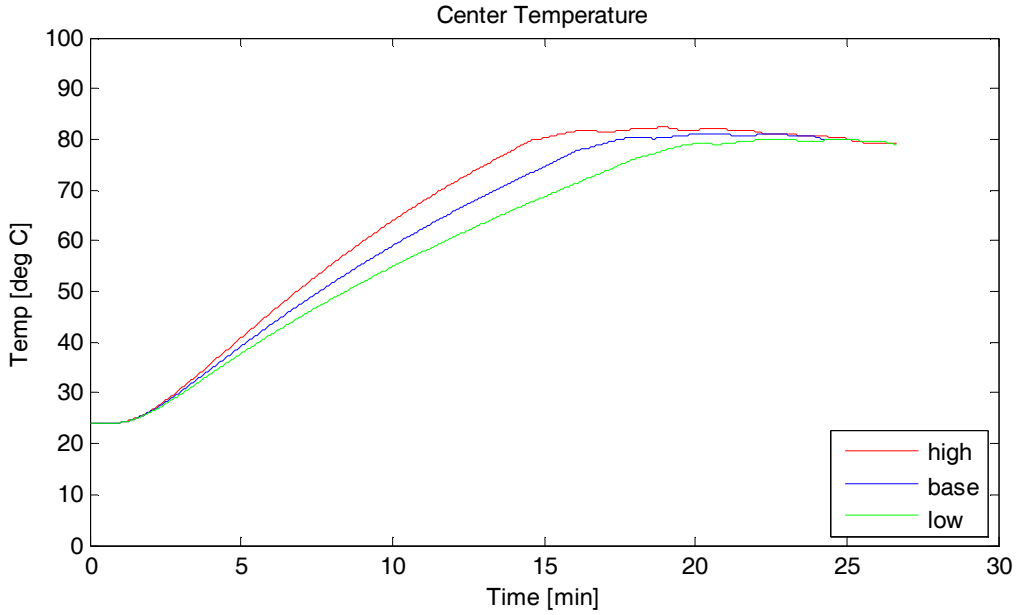

Figure 360 - Effect of Adjusting the Heat Flux on Radiant Heating of CFB – Center Temperature

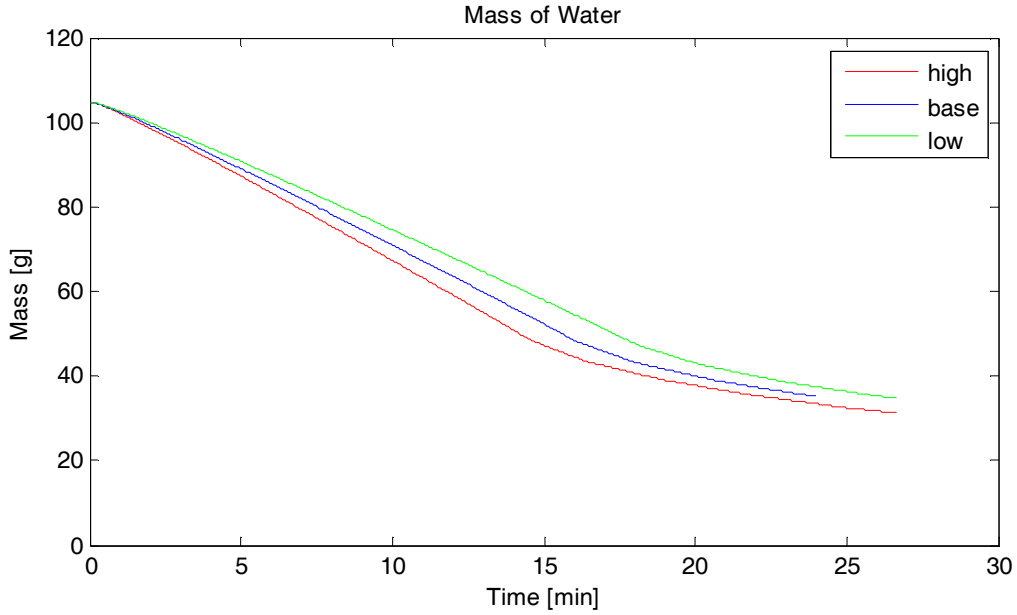

Figure 361 - Effect of Adjusting the Heat Flux on Radiant Heating of CFB – Mass Loss

Surface Emissivity

The surface emissivity was adjusted from the base value of 0.96 to a "high" value of 1.0 and a "low" value of 0.92. The effect of this change on the surface temperature, centerline temperature, and mass loss are shown in Figure 362, Figure 363, and Figure 364.

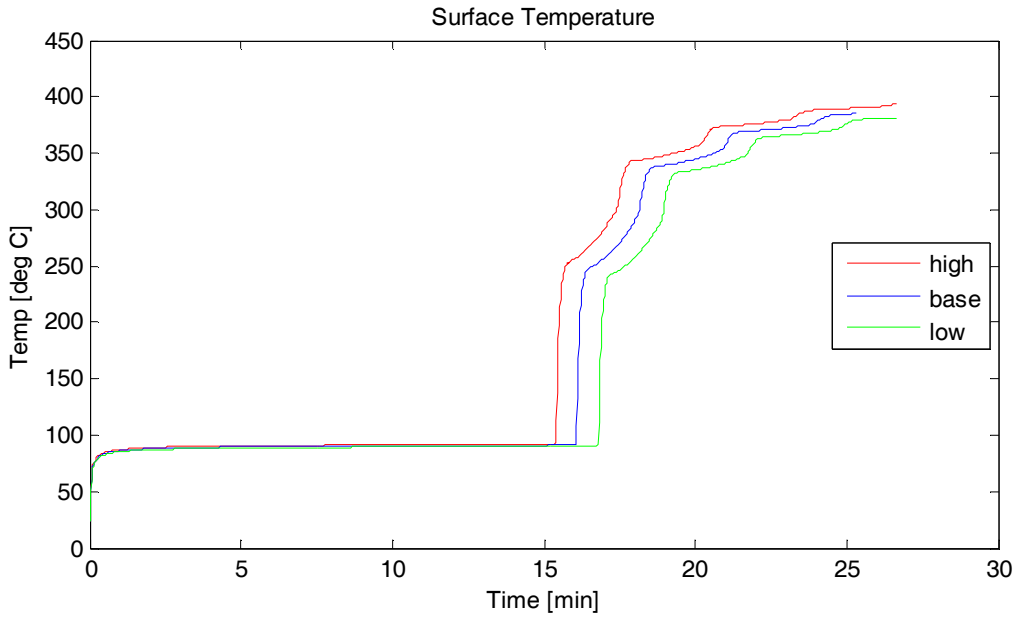

Figure 362 - Effect of Adjusting the Surface Emissivity on Radiant Heating of CFB – Surface Temperature

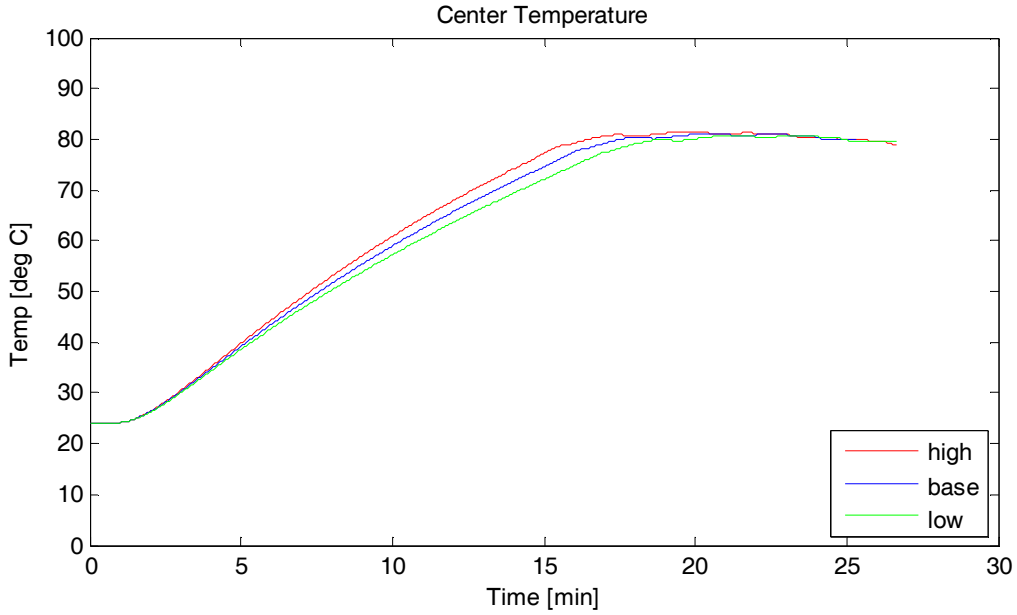

Figure 363 - Effect of Adjusting the Surface Emissivity on Radiant Heating of CFB – Center Temperature

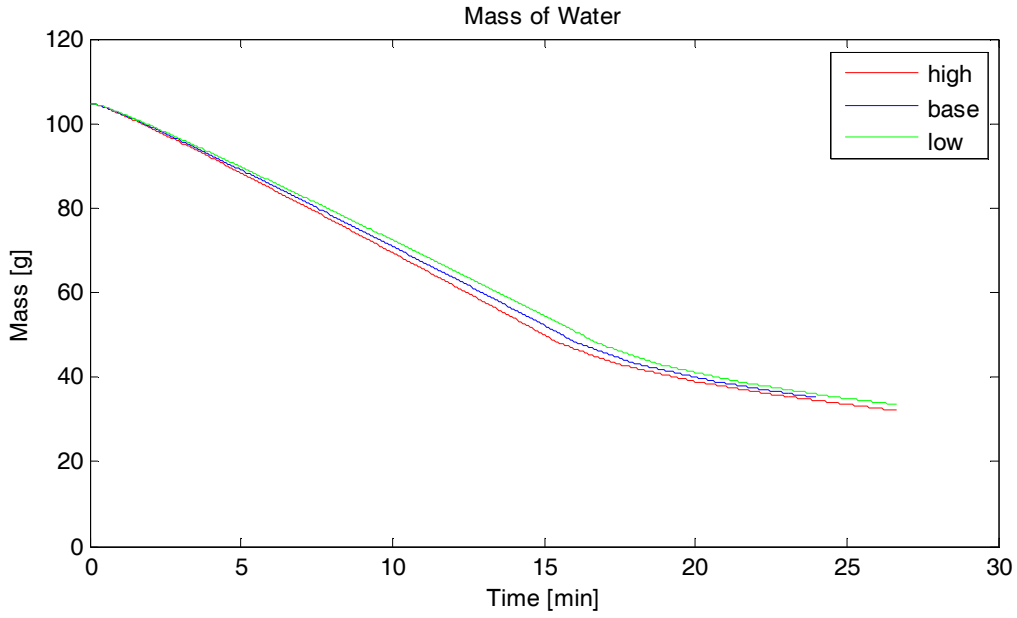

Figure 364 - Effect of Adjusting the Surface Emissivity on Radiant Heating of CFB – Mass Loss

Liquid Relative Permeability

The correlation for the liquid relative permeability was adjusted from the base value to the "high" and "low" correlations shown in Figure 302. The effect of this change on the surface temperature, centerline temperature, and mass loss are shown in Figure 365, Figure 366, and Figure 367.

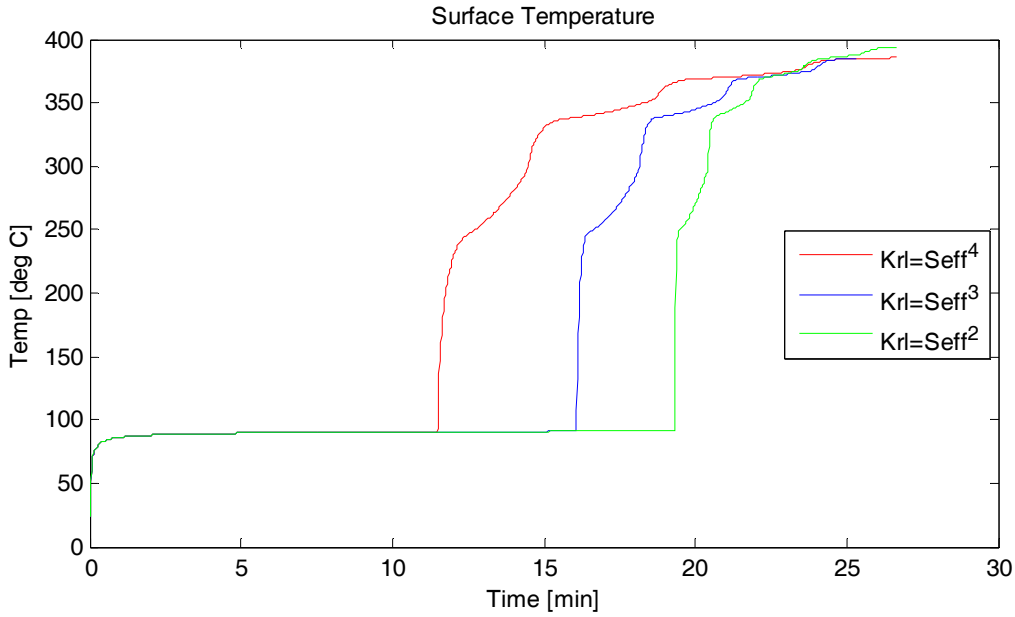

Figure 365 - Effect of Adjusting the Liquid Relative Permeability Correlation on Radiant Heating of CFB – Surface Temperature

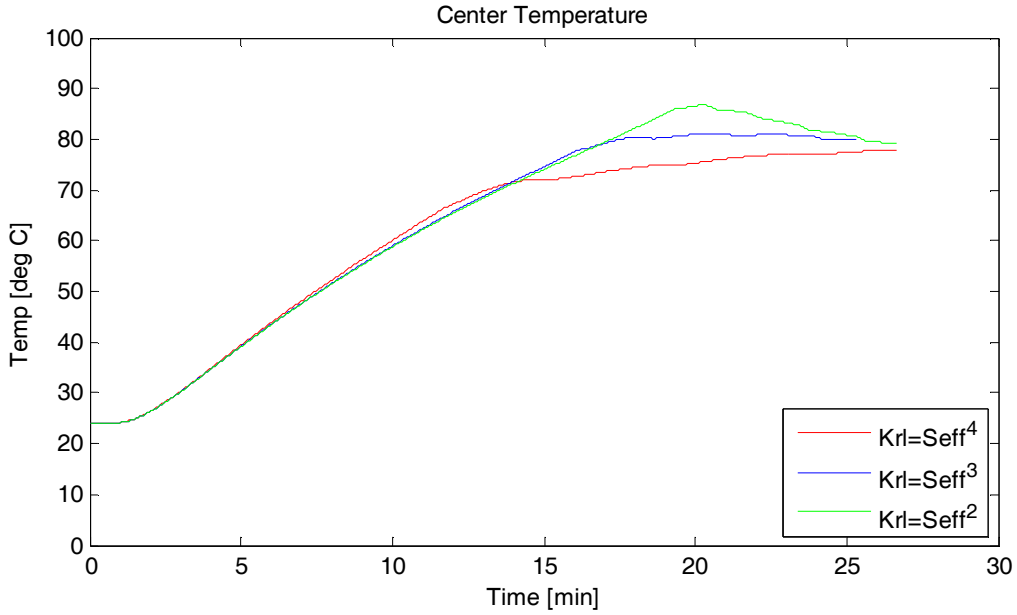

Figure 366 - Effect of Adjusting the Liquid Relative Permeability Correlation on Radiant Heating of CFB – Center Temperature

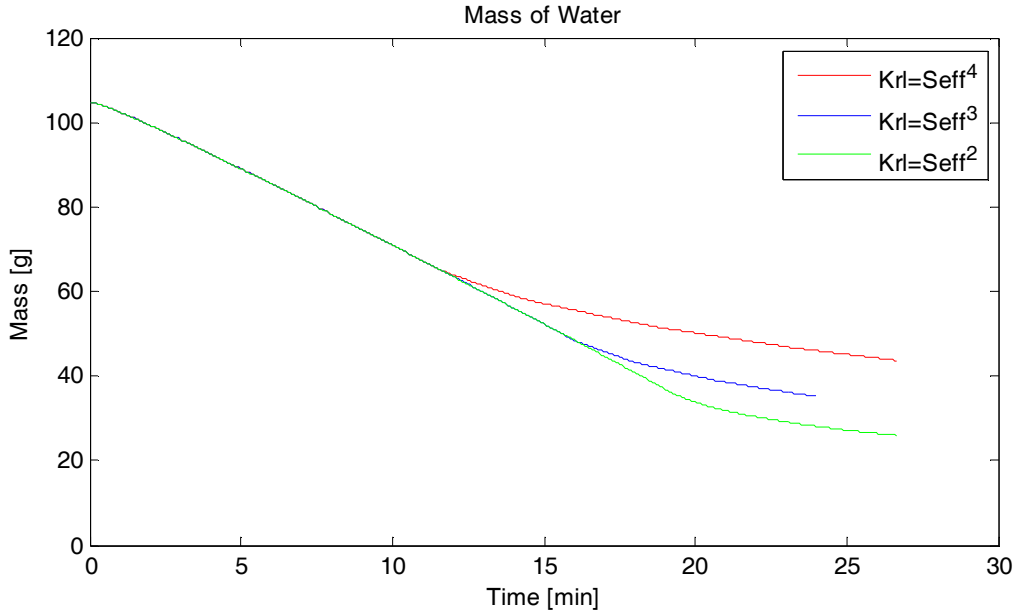

Figure 367 - Effect of Adjusting the Liquid Relative Permeability Correlation on Radiant Heating of CFB – Mass Loss

Gas Relative Permeability

The correlation for the liquid relative permeability was adjusted from the base correlation to the "high" and "low" correlations shown in Figure 302. The effect of this change on the surface temperature, centerline temperature, and mass loss are shown in Figure 368, Figure 369, and Figure 370.

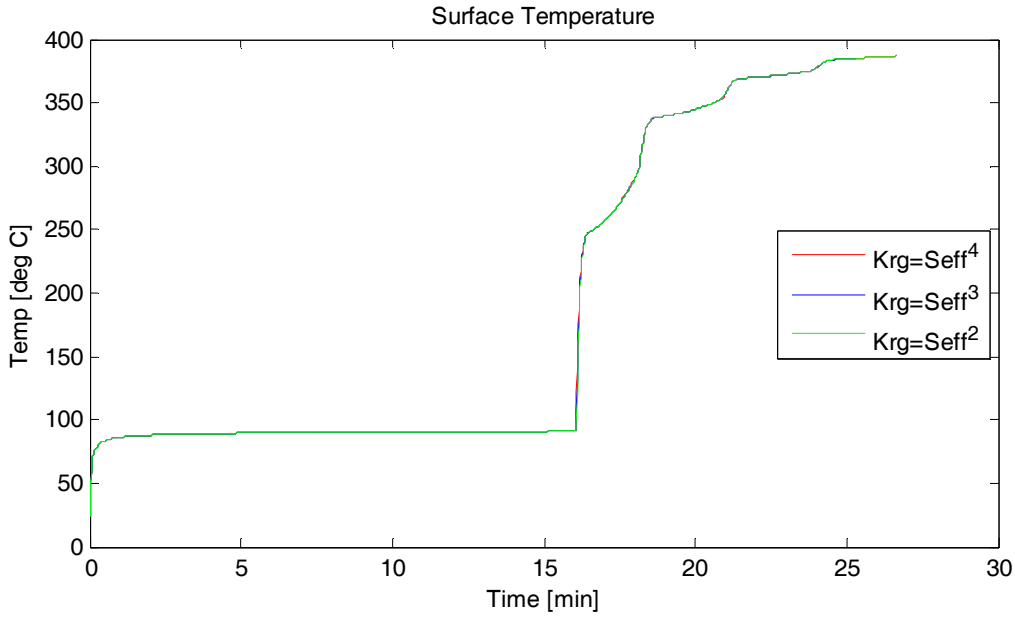

Figure 368 - Effect of Adjusting the Gas Relative Permeability Correlation on Radiant Heating of CFB – Surface Temperature

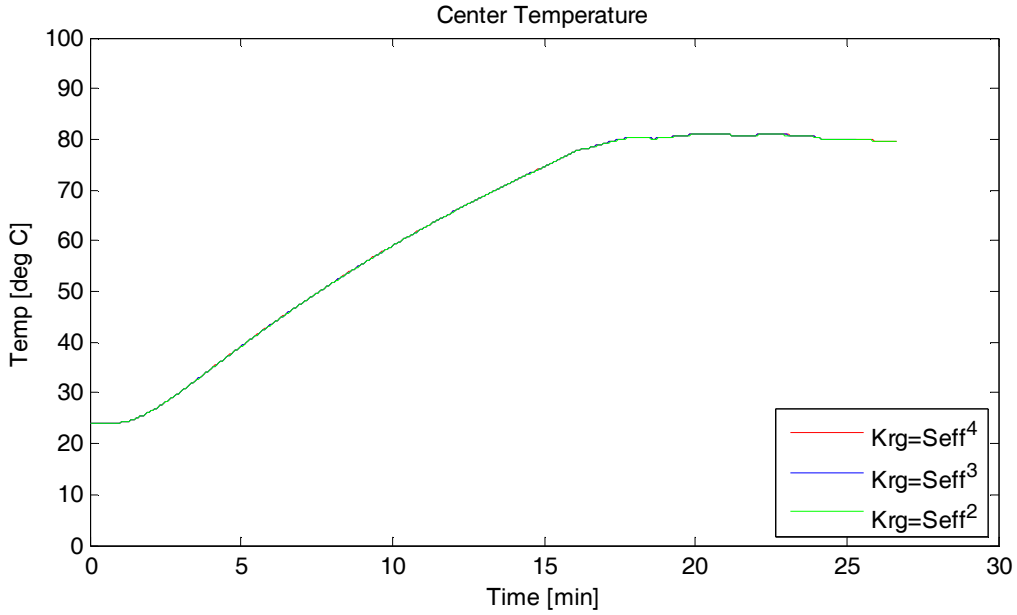

Figure 369 - Effect of Adjusting the Gas Relative Permeability Correlation on Radiant Heating of CFB – Surface Temperature

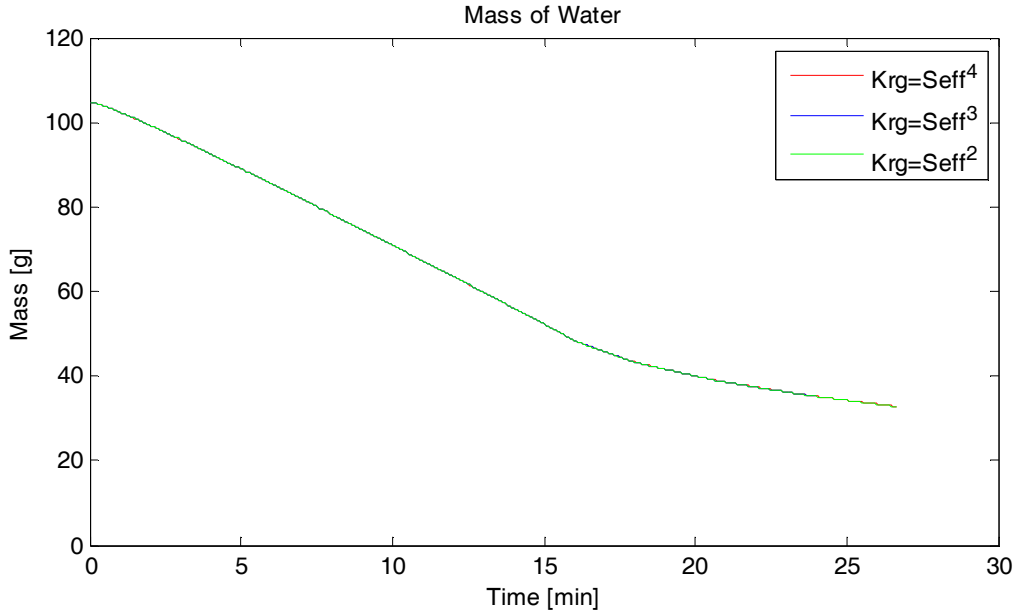

Figure 370 - Effect of Adjusting the Gas Relative Permeability Correlation on Radiant Heating of CFB – Surface Temperature

Capillary Pressure

The correlation for the capillary pressure was adjusted from the base correlation to the "high" and "low" correlations shown in Figure 303. The effect of this change on the surface temperature, centerline temperature, and mass loss are shown in Figure 371, Figure 372, and Figure 373.

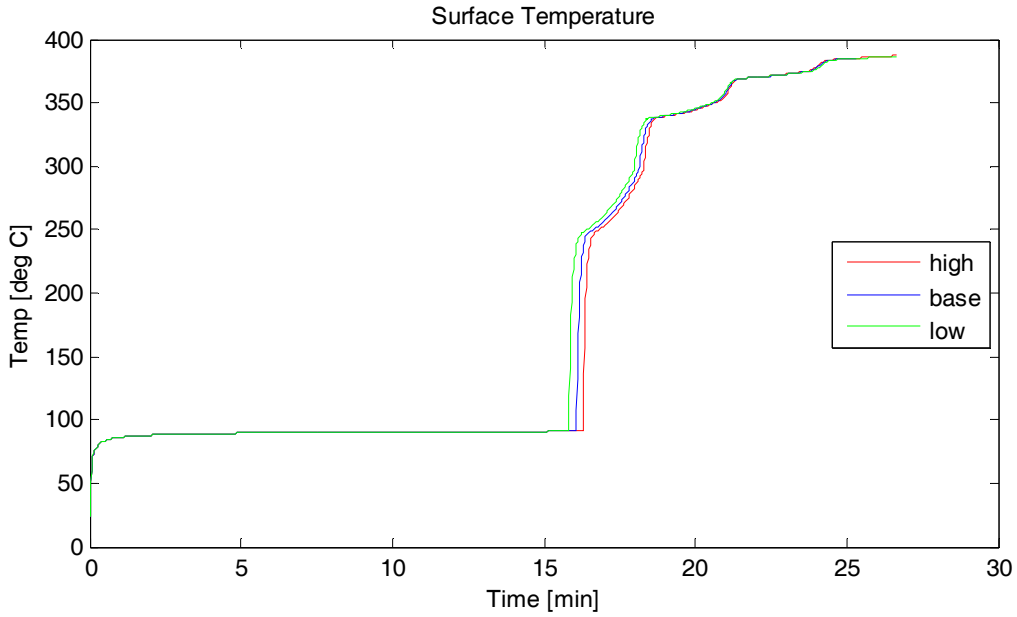

Figure 371 - Effect of Adjusting the Capillary Pressure Correlation on Radiant Heating of CFB - Surface Temperature

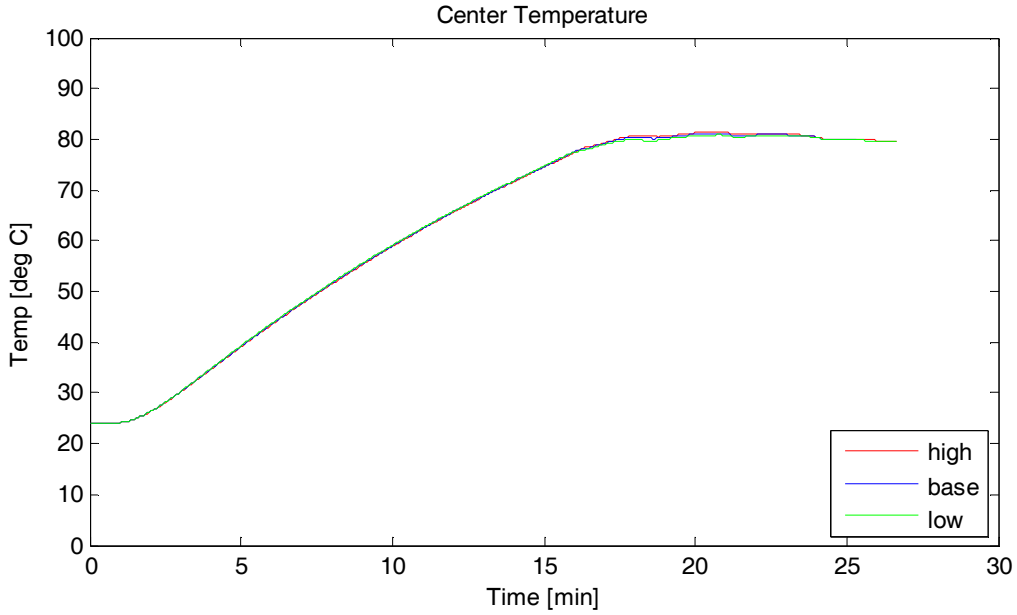

Figure 372 - Effect of Adjusting the Capillary Pressure Correlation on Radiant Heating of CFB - Center Temperature

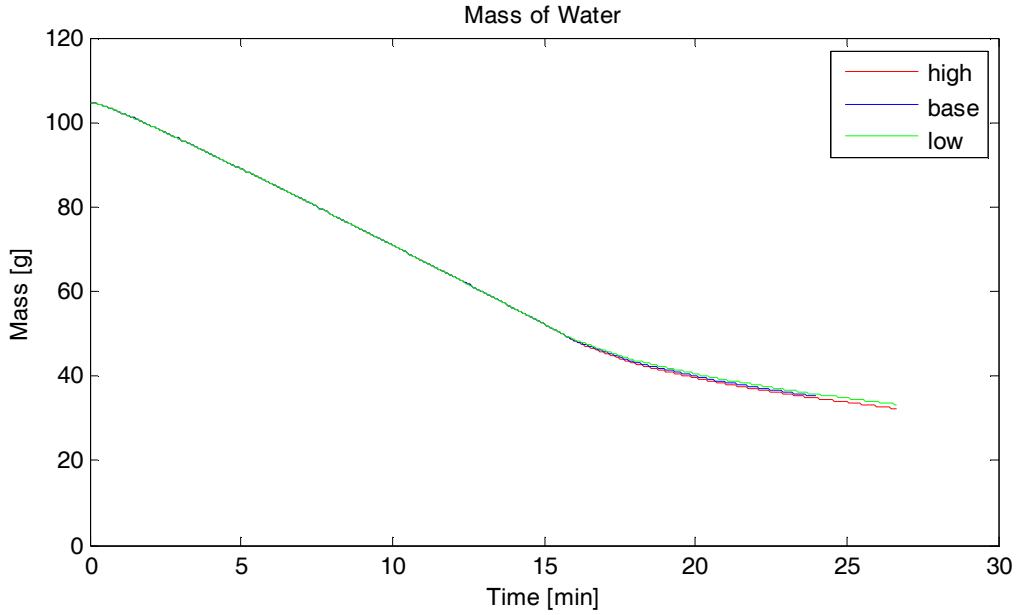

Figure 373 - Effect of Adjusting the Capillary Pressure Correlation on Radiant Heating of CFB - Mass Loss

Relative Humidity

The correlation for the relative humidity was adjusted from the base value to the "high" and "low" correlations shown in Figure 304. The effect of this change on the surface temperature, centerline temperature, and mass loss are shown in Figure 374, Figure 375, and Figure 376.

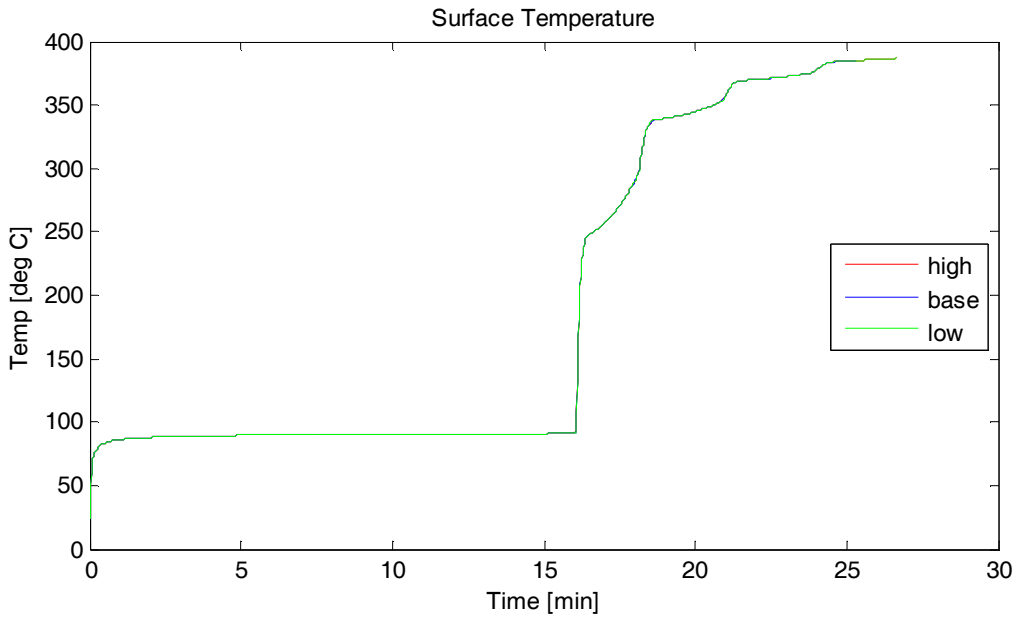

Figure 374 - Effect of Adjusting the Relative Humidity Correlation on Radiant Heating of CFB – Surface Temperature

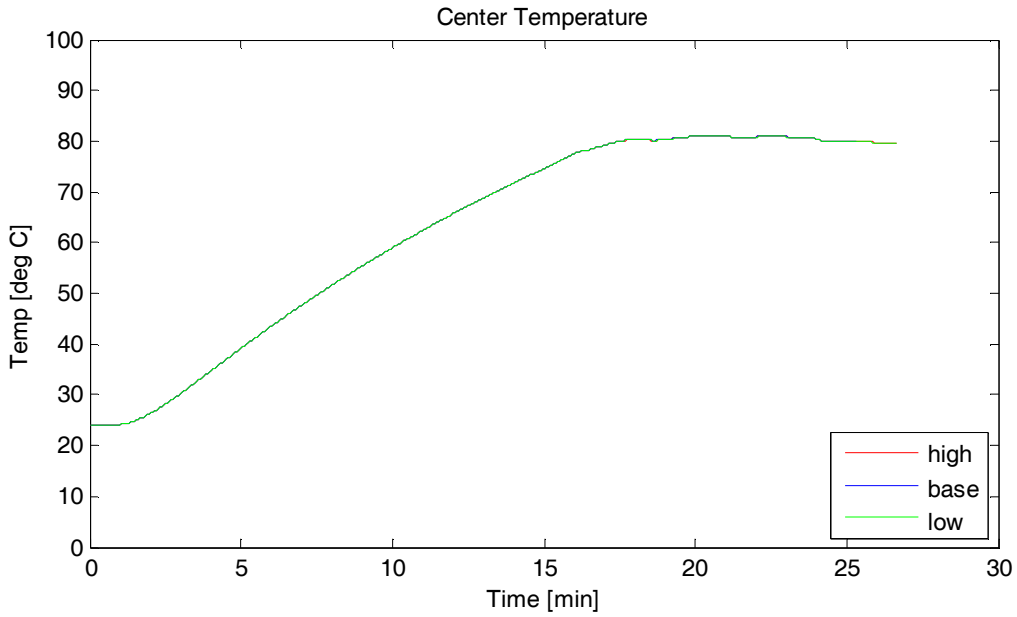

Figure 375 - Effect of Adjusting the Relative Humidity Correlation on Radiant Heating of CFB – Center Temperature

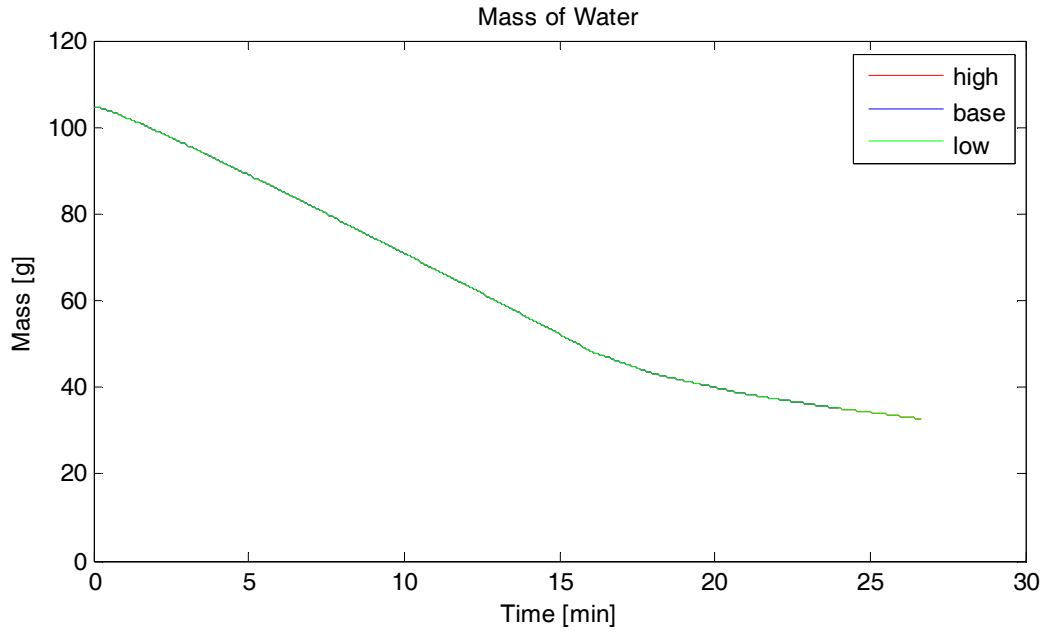

Figure 376 - Effect of Adjusting the Relative Humidity Correlation on Radiant Heating of CFB - Mass Loss

Appendix H. Uncertainty Analysis

The uncertainty of the model output was calculated from the uncertainty of the model input parameters with the highest sensitivity coefficients. For each case, the maximum uncertainty of each input parameter was estimated. The uncertainty distribution of each input parameter is assumed to obey a normal distribution. The maximum uncertainties are assumed to represent three times the standard deviation of the distribution, or a 99.7% confidence interval. This is shown in Figure 377. The center of the distribution (0 standard deviations) represents the base value that has been used for model calculations for the parameter.

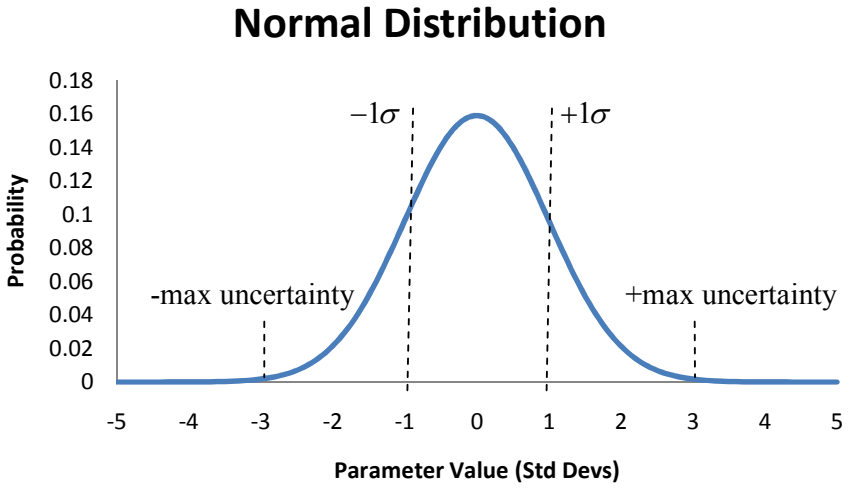

Figure 377- Distribution of Uncertainty of Input Parameters

The upper and lower uncertainty bounds were calculated as follows. The input parameters from the sensitivity analysis with the highest sensitivity coefficients for each validation case were chosen for the uncertainty analysis. The base value of each of these input parameters was adjusted ± one standard deviation in separate simulations, thus representing 68% of all of the possible values of that parameter. All other parameters were held constant for these cases. This was performed for each parameter, and the data from all of the simulations was used to calculate the combined standard uncertainty at each data point in space or time. The combined standard uncertainty for the each model output can be expressed as (ANSI, 1997)

$$u_c^2(y) = \sum_{i=1}^{N} \left(\frac{\partial f}{\partial x_i} \right)^2 u^2(x_i)$$

Where the model output, y, is represented as $y = f(x_1, x_2, .., x_i, ...x_n)$, $u_c(y)$ is the combined standard uncertainty of y, and $u(x_i)$ is the uncertainty of input parameter x_i. Since the current model obtains numerical solutions to the governing equations, the combined standard uncertainty is approximated as

$$u_c^2(y) = \sum_{i=1}^{N} \left(\frac{\Delta y}{\Delta x_i} \right)^2 (\Delta x_i)^2 = \sum_{i=1}^{N} (\Delta y)^2$$

This was used to calculate a reasonable error band for each of the validation cases. This error band represents the sum of the uncertainties associated with adjusting each of the most important input parameters by one standard deviation. The combined standard uncertainty was calculated at discrete points in time and space to provide the error bars for the validation figures.

H.1. CFB Wetting – Type 1 BC

For the two wetting cases with a Type 1 boundary condition (top and bottom wetting), the parameters with a sensitivity coefficient higher than 0.5 were chosen for the uncertainty analysis. These parameters and their uncertainty are shown in Table 50.

Table 50 – Uncertainty of Input Parameters for CFB Wetting

Parameter	Base Value	Max Uncertainty	1 Std Dev
Surface Saturation	0.99	$\pm$ 0.01	$\pm$ 0.0033
Cap Press Coeff 1	0.4	$\pm$ 0.04	$\pm$ 0.0133
Permeability	$5\times10^{-11} m^2$	$\pm\ 2\times10^{-11} m^2$	$\pm 0.66\times10^{-11} m^2$
Porosity	0.8	$\pm$ 0.05	$\pm$ 0.0166
Liq Rel Perm	$K_{rl} = S_{eff}^3$	$\pm$ 1	$\pm$ 0.333
Cap Press Coeff 2	0.364	$\pm$ 0.073	$\pm$ 0.0243

By using 1/3 of the maximum uncertainty of these input parameters the model output for each parameter was calculated. These are shown in Figure 378 and Figure 379. The "+" and "-" symbols in the legend indicate model output for the parameter plus one standard deviation and minus one standard deviation.

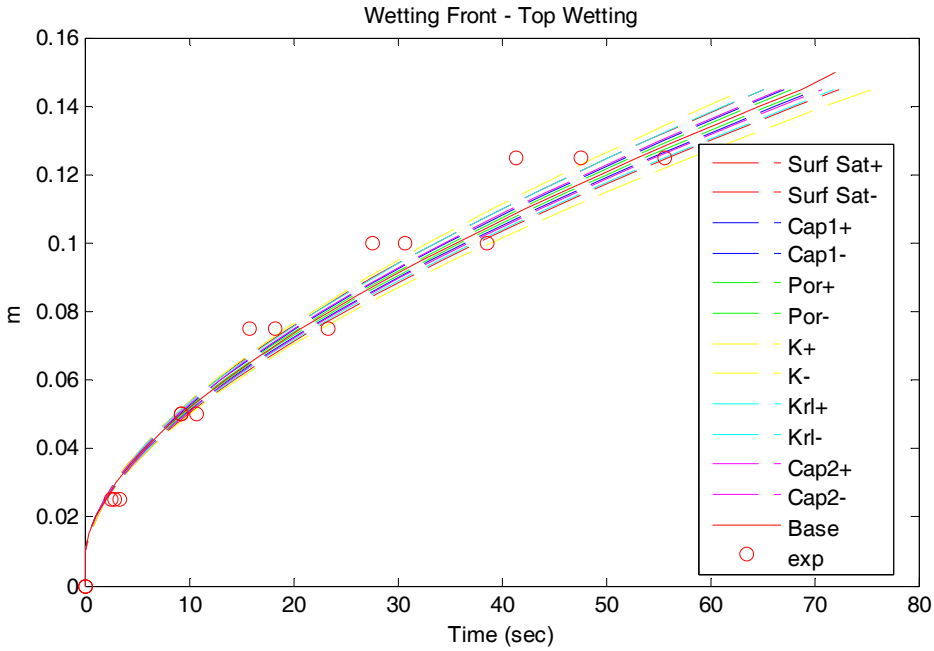

Figure 378 – Effect of Adjusting Parameters on Type 1 BC Wetting of CFB – Top Wetting

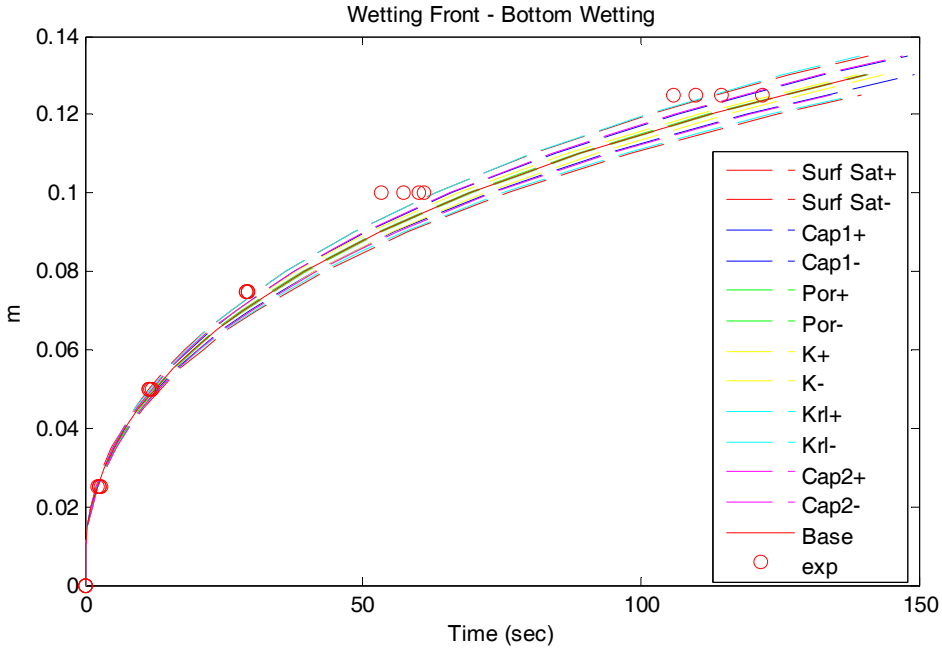

Figure 379 – Effect of Adjusting Parameters on Type 1 BC Wetting of CFB – Bottom Wetting

The combined standard uncertainty of time was calculated at each depth to give horizontal error bars for the output plots. This was determined to be the best means of

presenting the uncertainty. The model is calculating the saturation at nodes of a fixed depth in the material. The wetting front is calculated as the time of arrival of water at these nodes. The model output uncertainty is therefore most easily presented as uncertainty in the time of arrival at each node. The calculated combined standard uncertainty at each node is shown in Figure 380 and Figure 381.

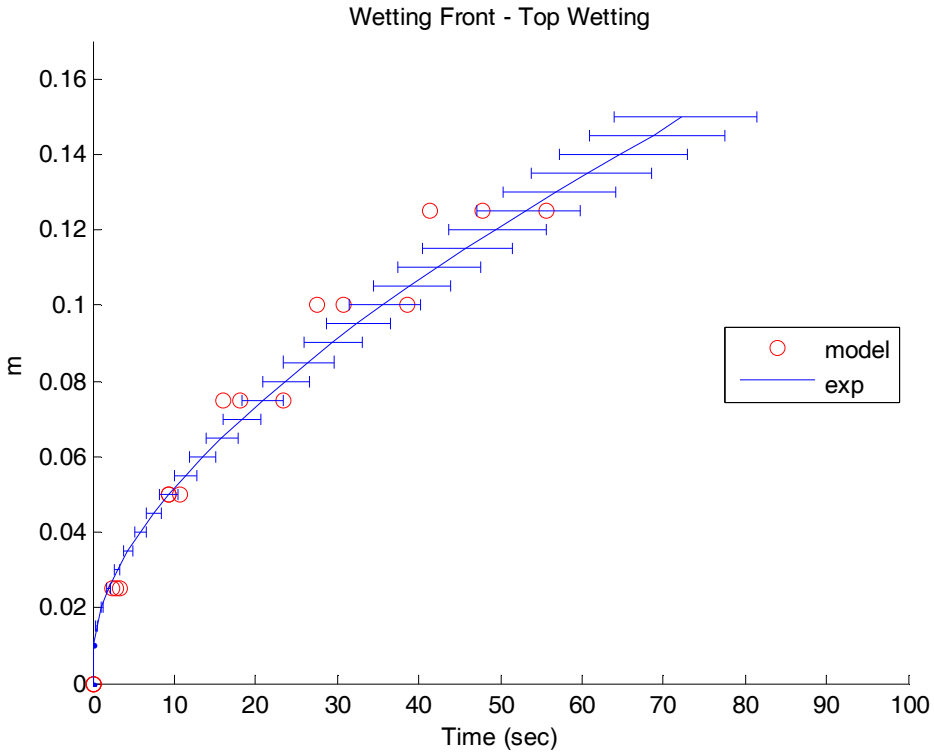

Figure 380 – Combined Standard Uncertainty of Top Wetting of CFB

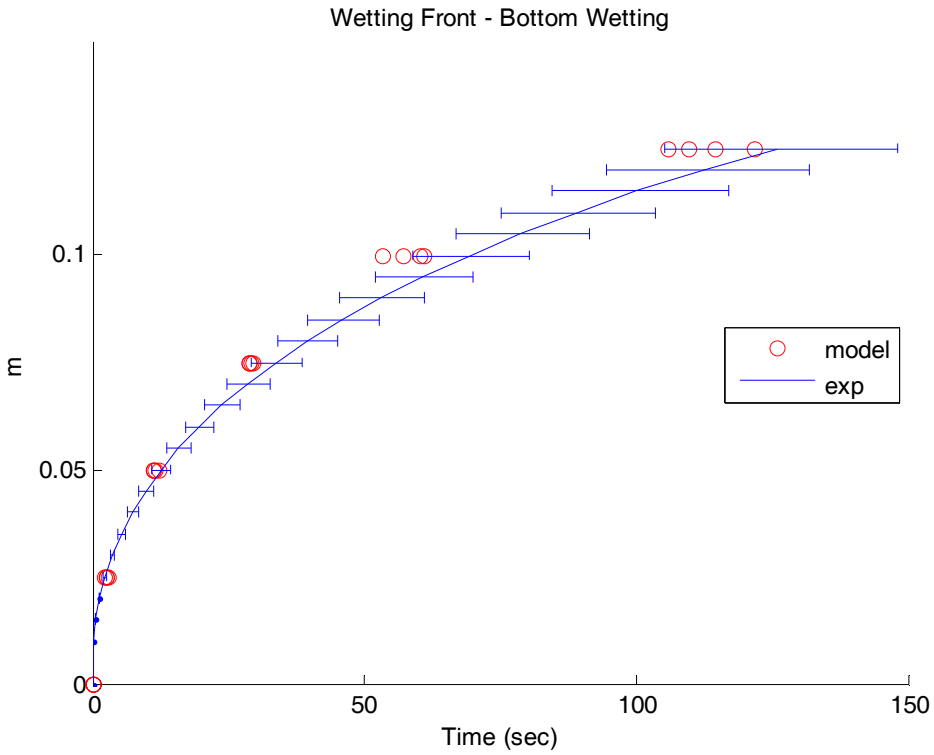

Figure 381 - Combined Standard Uncertainty of Bottom Wetting of CFB

The methods used to estimate the uncertainty of the input parameters will be described in the following sections.

Surface Saturation

The surface saturation base value of 0.99 was estimated by running the model with surface saturation values between 0.98 and 0.999. The results from these simulations cover a wide range that overlaps the experimental data. Since the saturation cannot be greater than 1, and is most likely very close to 1, the uncertainty was assumed to be 0.01.

Cap Press Coeff 1 & 2

The coefficients in the correlation for capillary pressure were adjusted individually to observe the effect of changing each one individually. The uncertainty was estimated by comparing the correlation results to the experimental data. The uncertainty of Coefficient 1 was estimated to be 10%, while the uncertainty of Coefficient 2 was estimated to be 20%.

Permeability

The permeability was estimated from the CFB wetting tests with and without gravity. The permeability in the model was adjusted to obtain the best agreement with the experimental data. The permeability was estimated to be $5\times10^{-11}m^2$ in this manner. From these tests, the uncertainty of the permeability is estimated to be $\pm2\times10^{-11}m^2$.

Porosity

From laboratory tests the ceramic fiberboard was estimated to be 80% porous. The calculations are as follows

$$Width = 6"\pm1/16" = 0.1524m \pm 0.001588m$$
$$Length = 6"\pm1/16" = 0.1524m \pm 0.001588m$$
$$Thickness = 2"\pm1/16" = 0.0508m \pm 0.001588m$$
$$Volume = 0.00118m^3 \pm 6.26\times10^{-5}$$
$$Mass\left(dry\right) = 340g \pm 0.1g$$
$$Mass\left(wet\right) = 1281\pm10g$$
$$Mass\ of\ water\ absorbed = 941\pm10g$$
$$Volume\ of\ water\ absorbed = 0.941kg\frac{1m^3}{1000kg} = 9.41\times10^{-4}m^3 \pm 1\times10^{-6}m^3$$
$$Porosity = \frac{0.000941}{0.0012} = 0.80\pm0.05$$

Liquid Relative Permeability

The liquid relative permeability is assumed be obey the third order correlation that is observed in particulate media.

$$K_{rl} = S_{eff}^3$$

The literature gives correlations for other materials that are power law functions with powers between 2 and 4. This was assumed to be the range of uncertainty in the liquid relative permeability correlation.

H.2. Spray Wetting of CFB

For the spray wetting of CFB validation cases, the model inputs with a sensitivity coefficient greater than 0.5 were chosen to estimate the model uncertainty. These parameters and their uncertainties are shown in Table 51.

Table 51 – Uncertainty of Input Parameters for CFB Spray Wetting

Parameter	Base Value	Max Uncertainty	1 Std Dev
Porosity	0.8	± 0.05	± 0.0167
Water flux	Test 1 - 0.104 kg/m^{2}s Test 2 - 0.128 kg/m^{2}s Test 3 - 0.188 kg/m^{2}s	± 10%	± 3.33%
Liq Rel Perm.	$K_{rl} = S_{eff}^3$	± 1	± 0.333

The model output for each parameter adjusted plus (+) and minus (-) one standard deviation are shown in Figure 382 through Figure 384.

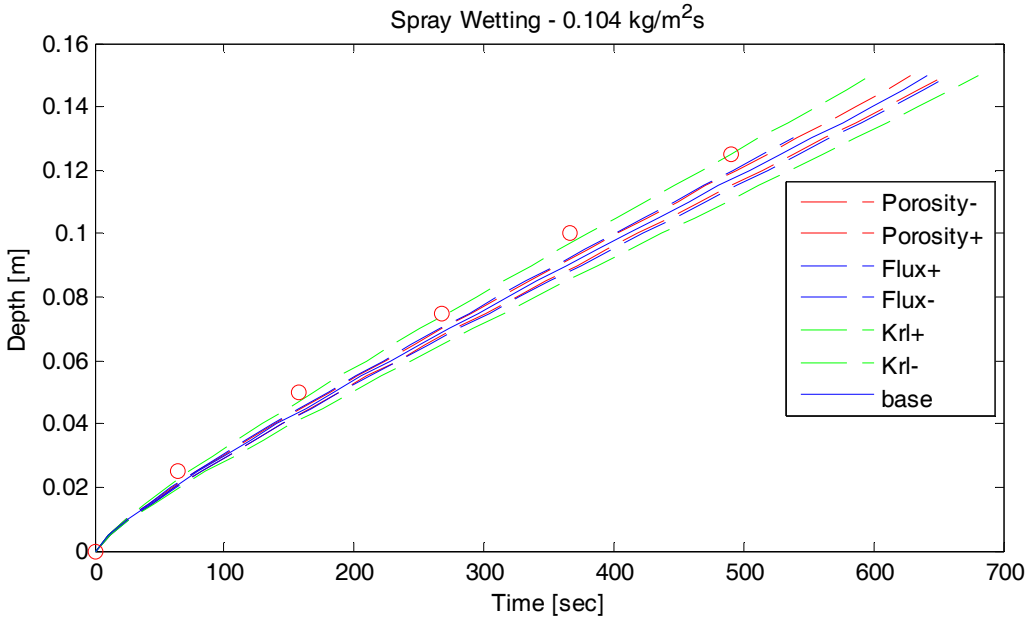

Figure 382 – Effect of Adjusting Parameters on Spray Wetting of CFB– Mass flux = 0.104 kg/m^{2}s

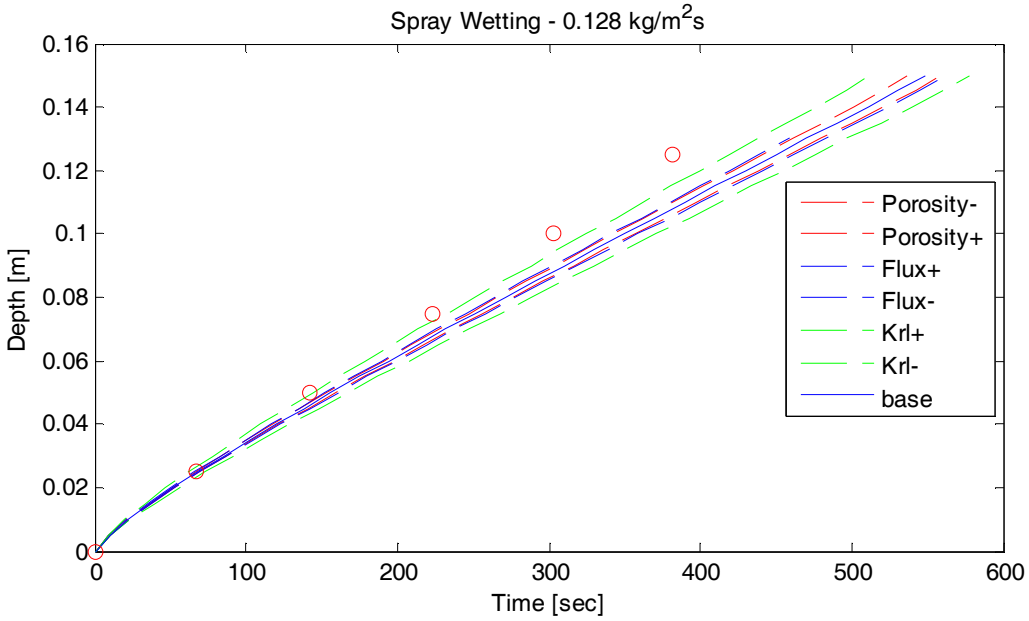

Figure 383 – Effect of Adjusting Parameters on Spray Wetting of CFB – Mass flux = 0.128 kg/m^{2}s

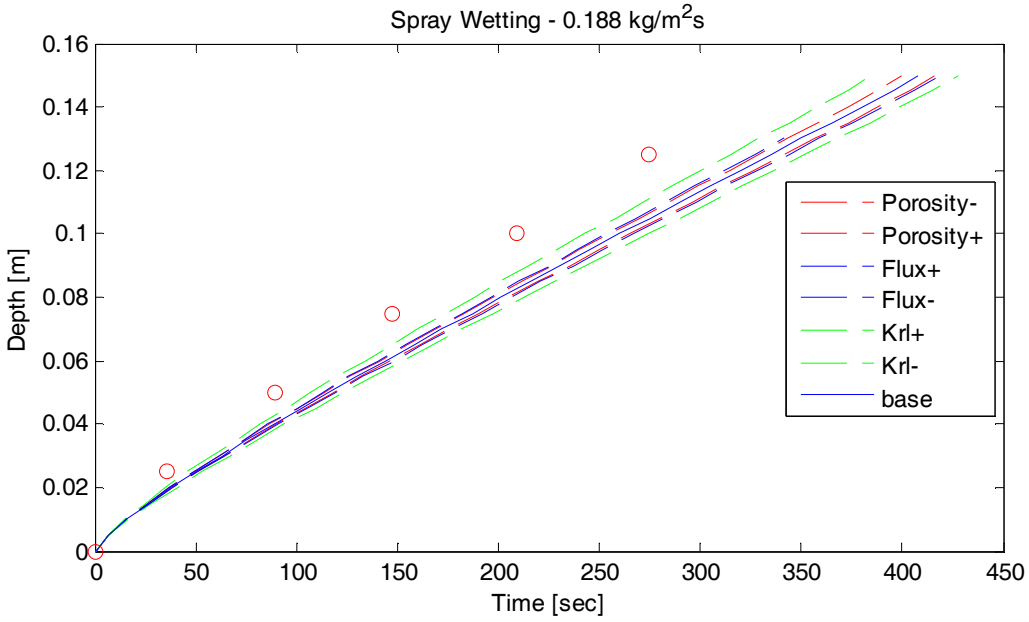

Figure 384 – Effect of Adjusting Parameters on Spray Wetting of CFB – Mass flux = 0.188 kg/m^{2}s

The combined standard uncertainty of time to arrival at each node was calculated for each case. The results are shown in Figure 385, Figure 386, and Figure 387.

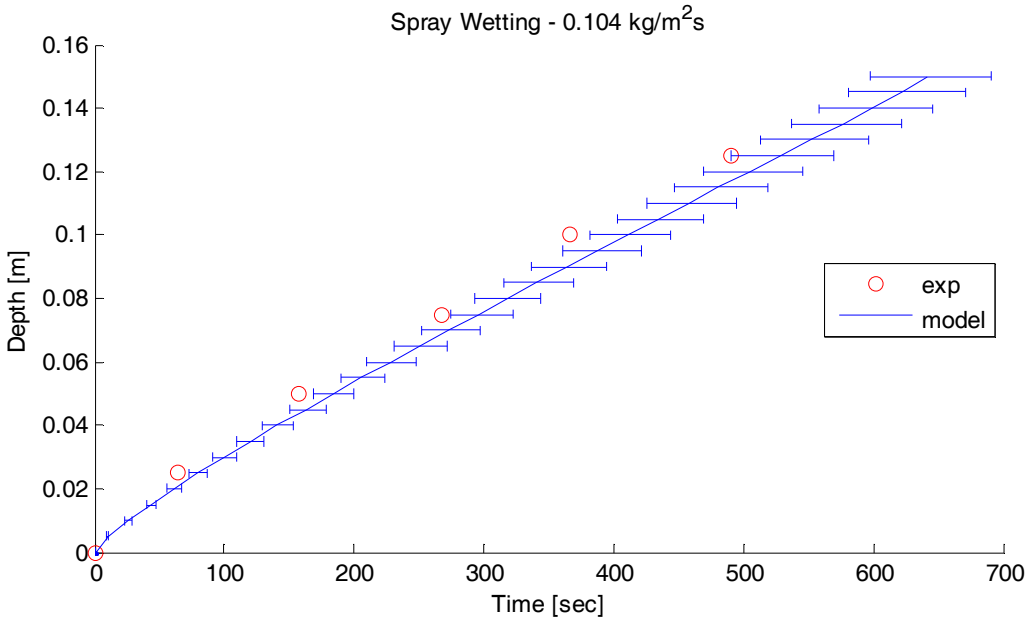

Figure 385 – Combined Standard Uncertainty of Spray Wetting of CFB - – Mass flux = 0.104 kg/m2s

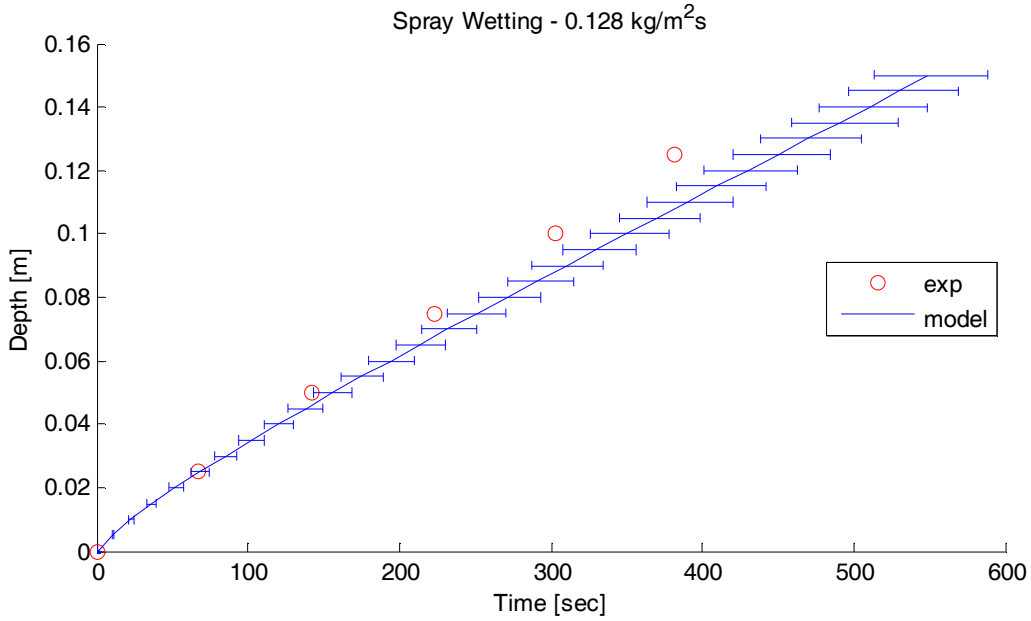

Figure 386 – Combined Standard Uncertainty of Spray Wetting of CFB – Mass flux = 0.128 kg/m^{2}s

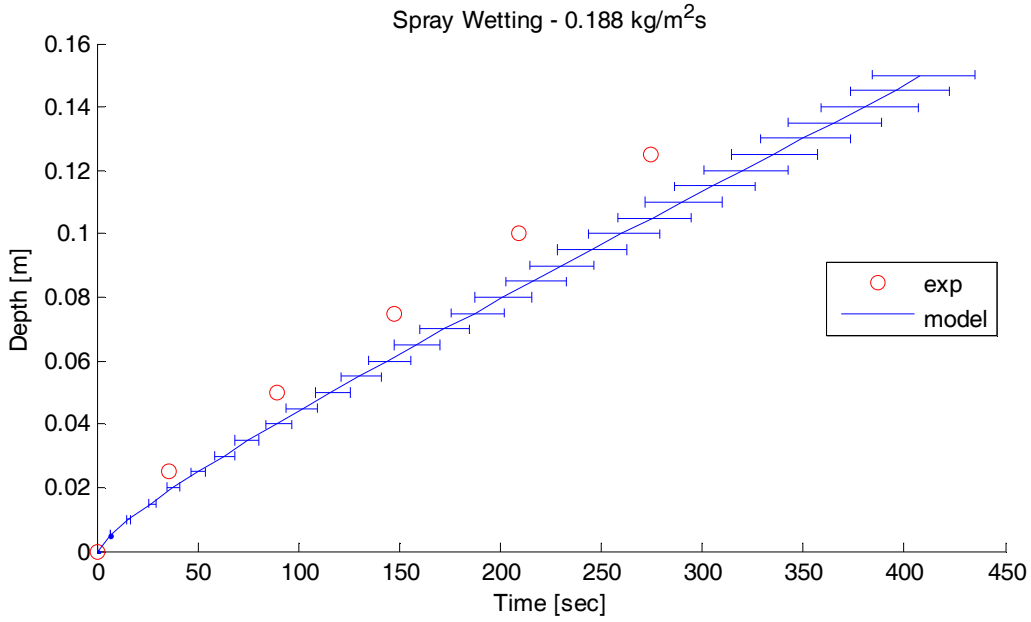

Figure 387 – Combined Standard Uncertainty of Spray Wetting of CFB – Mass flux = 0.188 kg/m^{2}s

Water Flux

The water flux was measured by collecting water from the spray nozzle using a grid of

square tubes. This water was weighed and the mass flux estimated. There was some spatial variation of the mass flux observed over the measurement area. This variation is assumed to be much larger than any uncertainty introduced by water overflow, or uncertainty in the mass measurements. The 4 inch by 4inch square in the center of the spray was observed to have a variation of no more than 20% for any test. Most measurements were within 10% of the spatial average. The maximum uncertainty of the water flux was assumed to be 20%.

H.3. Particulate Media Drying

Parameters with a sensitivity coefficient greater than 0.5 were chosen for the uncertainty analysis of particulate media drying. The parameters and their associated uncertainties are shown in Table 52.

Table 52 – Uncertainties of Parameters for Particulate Media Drying

Parameter	Base Value	Uncertainty	1 Std Dev
Ambient Temp	321K	± 1K	± 0.33K
Initial Saturation	0.915	± 0.015	± 0.005
Heat Trans Coeff	57.7 $W / m^2 K$	± 5.77 $W / m^2 K$	± 1.92 $W / m^2 K$
Relative Humidity	33%	± 2%	± 0.66%
Initial Temp	289.9K	± 1K	± 0.33K

The results of adjusting each parameter by plus (+) and minus (-) one standard deviation on the temperature and mass loss rate are shown in Figure 388 and Figure 389.

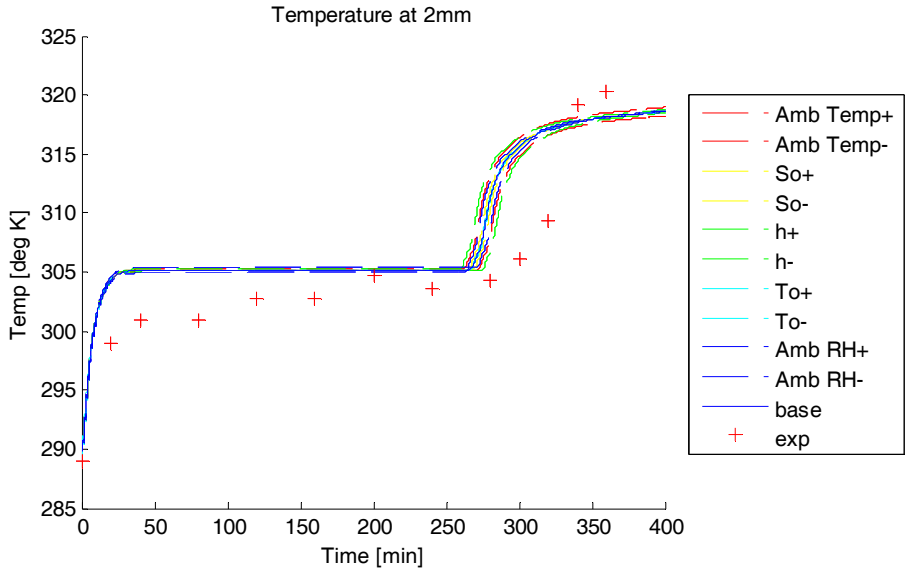

Figure 388 – Effect of Adjusting Parameters on Temperature During Convective Drying of Particulate Media

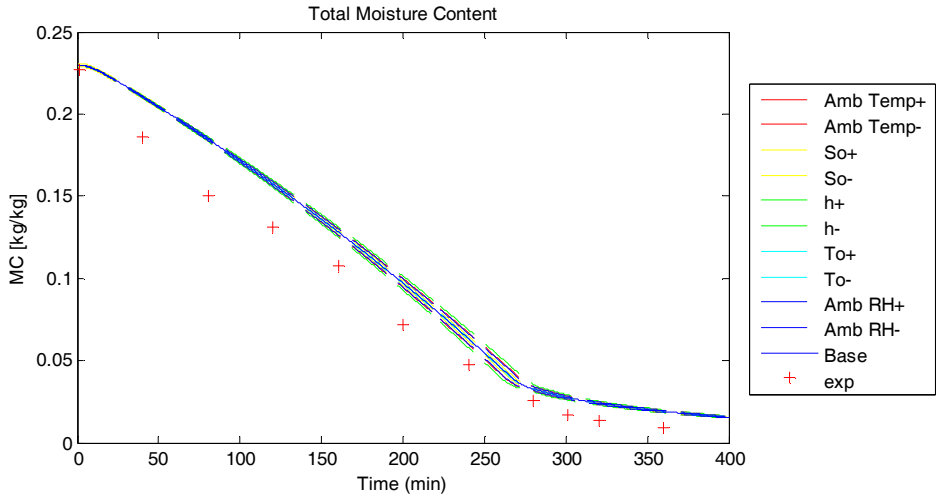

Figure 389 – Effect of Adjusting Parameters on Temperature During Convective Drying of Particulate Media

The combined standard uncertainty for the temperature and mass loss rate is shown in Figure 390 and Figure 391. The uncertainty of time was chosen to be most appropriate to describe the model outputs for this case.

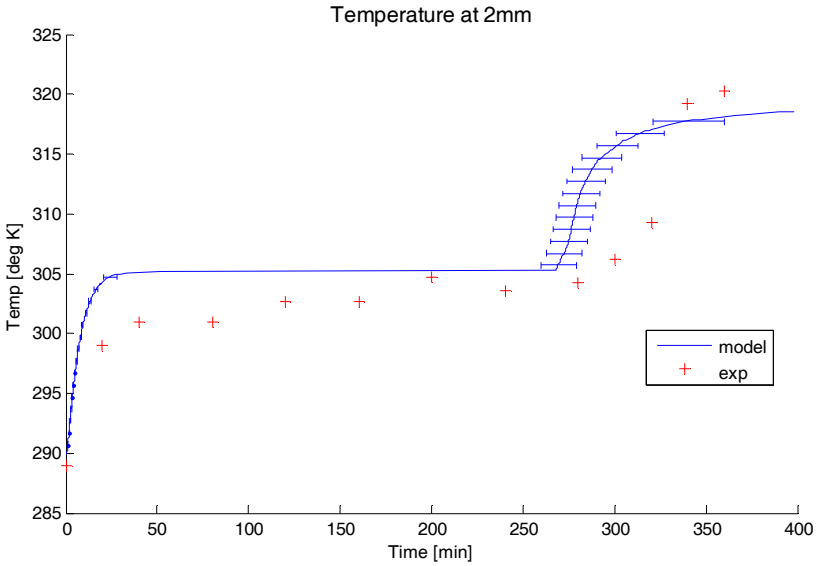

Figure 390 – Combined Standard Uncertainty of Temperature During Convective Drying of Particulate Media

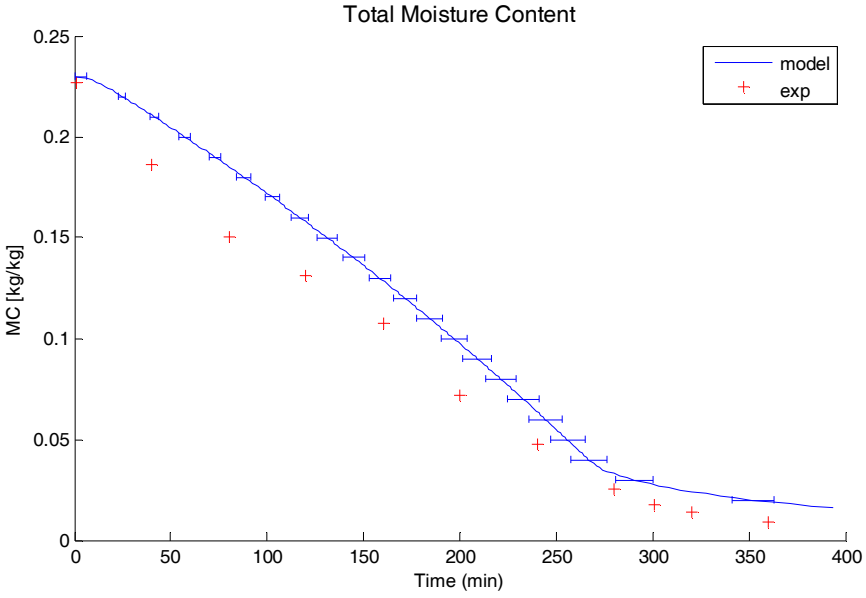

Figure 391– Combined Standard Uncertainty of Mass Loss During Convective Drying of Particulate Media

Ambient Temperature

Lu et al. give the ambient temperature as 321K ±1K. This measurement is most likely made with a thermocouple or thermistor or some other temperature device that has an uncertainty associated with it. The means of obtaining the value of 321 K were not given. From the sensitivity analysis it can be seen that increasing the ambient temperature decreased the jump time.

Initial Saturation

Lu et al. state that the initial saturation in the material is assumed to have a gradient due to gravity, but the surface saturation is 0.9. The model was used to determine the initial saturation that would provide an equilibrium moisture distribution with a surface saturation of 0.9. This was determined to be 0.915. The maximum uncertainty is estimated to be no more than this difference of 0.015. From the sensitivity analysis it can be seen that increasing the initial saturation increased the jump time.

Heat Transfer Coefficient

The heat transfer coefficient was calculated from the mass transfer coefficient, which was determined to have an uncertainty of 8%. The details of this calculation are available in the validation section. From this approach, the mass transfer coefficient was calculated to be $57.7\ W/m^2K$ and assumed to have a maximum uncertainty of 10%, or $\pm 5.77\ W/m^2K$. From the sensitivity analysis it can be seen that increasing the heat transfer coefficient decreased the jump time.

Initial Temperature

The initial temperature is given as 289.9 by Lu et al. and it is believed that this measurement is made using thermocouples in the material. The uncertainty of the ambient temperature is given as ±1K, so this uncertainty will be assumed for the initial temperature as well. From the sensitivity analysis it can be seen that increasing the initial temperature decreased the jump time.

Relative Humidity

Lu et al. give the ambient relative humidity as 33% ±2%. The method of determining this value is not specified. Their value of 2% will be assumed for the maximum uncertainty. From the sensitivity analysis it can be seen that increasing the ambient humidity increased the jump time.

H.4. Brick Drying

Parameters with a sensitivity coefficient greater than 0.1 were chosen for the uncertainty analysis of brick drying. The parameters and their associated uncertainties are shown in Table 53.

Table 53 – Uncertainty of Input Parameters for Brick Drying

Parameter	Base Value	Max. Uncertainty	1 Std Dev
Ambient Temp	80°C	± 2 °C	± 0.66
Initial Temp	25°C	± 2°C	± 0.66
Heat Trans Coeff	f(S)	± 10%	± 3.33
Initial Saturation	0.56	± 0.056	± 0.0187
Length	0.05m	± 0.001	± 0.000333
Liq. Rel. Perm. Coeff	4	± 1	± 0.333

The results of adjusting each parameter in Table 53 by plus (+) and minus (-) one standard deviation on the temperature and mass loss rate are shown in Figure 388 and Figure 389.

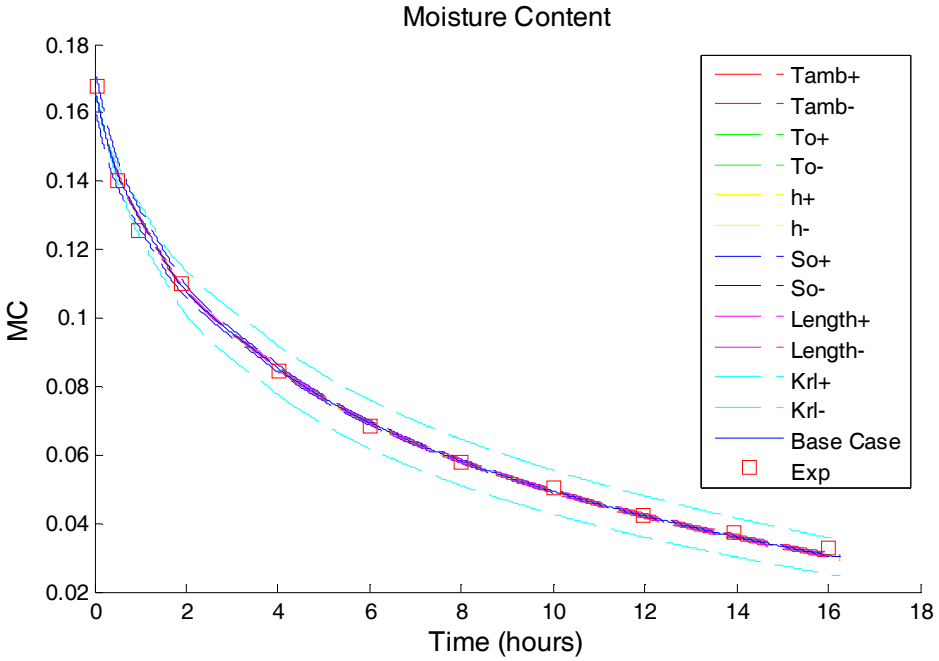

Figure 392 – Effect of Adjusting Input Parameters on Surface Temperature During Brick Drying

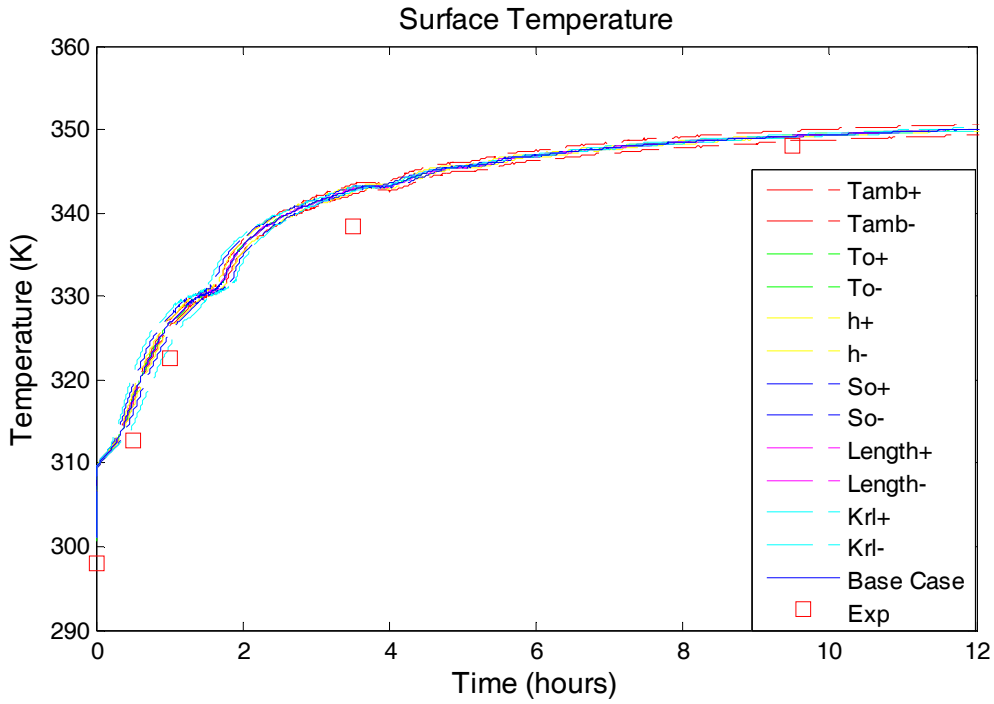

Figure 393 – Effect of Adjusting Input Parameters on Surface Temperature During Convective Drying of Brick

The combined standard uncertainty of the temperature and sample mass were calculated from these results and are shown in Figure 394 and Figure 395.

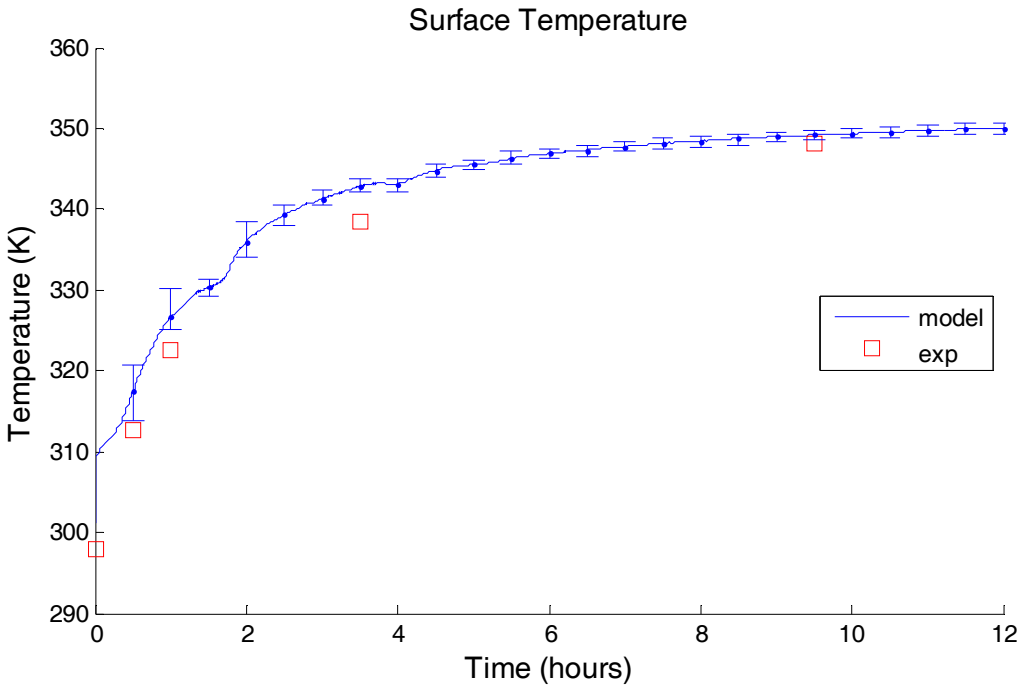

Figure 394 – Combined Standard Uncertainty of Surface Temperature During Convective Drying of Brick

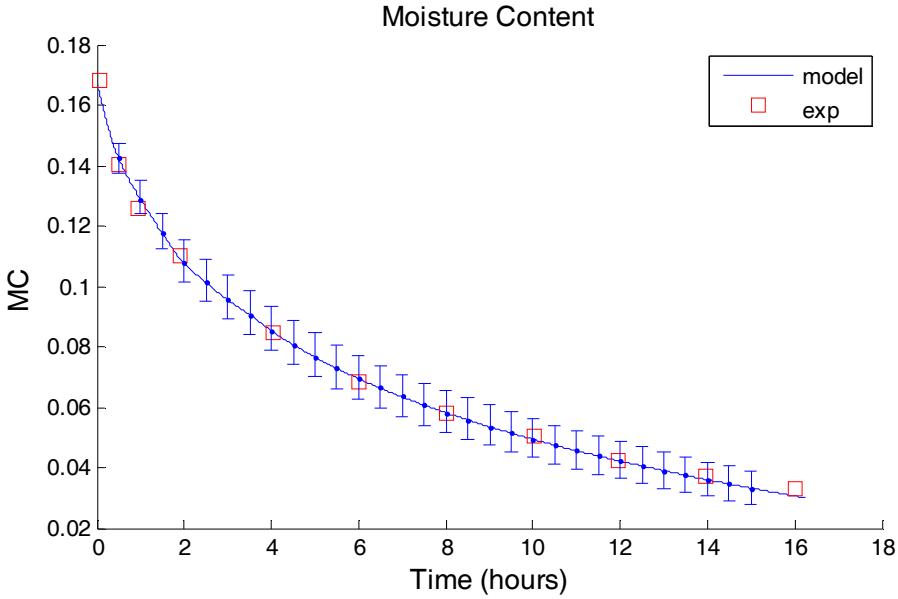

Figure 395 – Combined Standard Uncertainty of Sample Mass During Convective Drying of Brick

The combined standard uncertainty for temperature profiles at several times during the

drying process was calculated and is shown in Figure 396

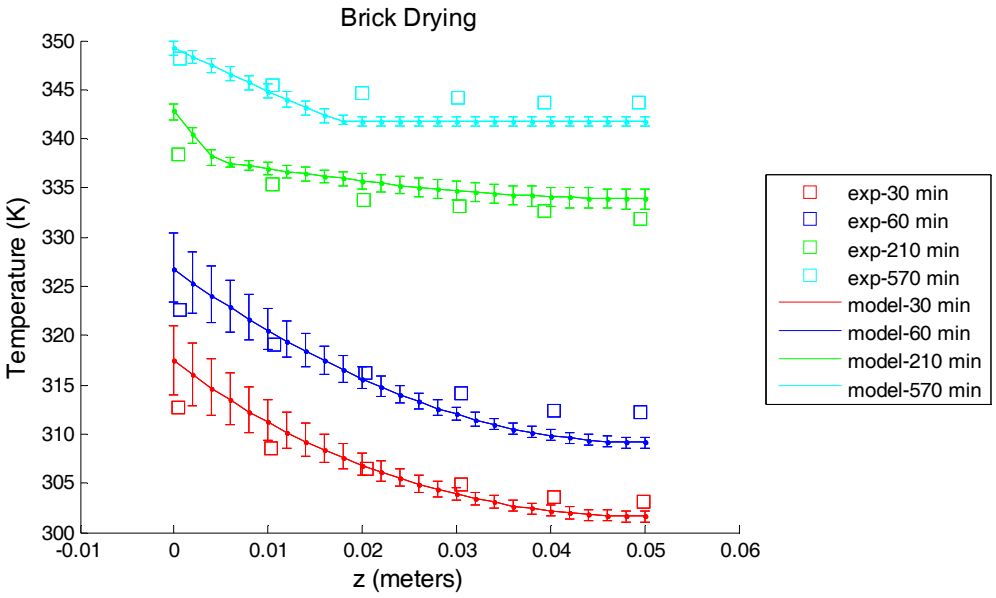

Figure 396 – Combined Standard Uncertainty of Temperature Profiles at 4 Times for Convective Drying of Brick

Ambient and Initial Temperature

Chen and Pei give values of 80°C and 25°C for the ambient and initial temperatures. It is assumed that these values are obtained by thermocouple measurements. The uncertainty of these measurements is assumed to be 2°C.

Heat Transfer Coefficient

Chen and Pei give a correlation for the heat transfer coefficient that is a function of the surface saturation. It is unclear what the saturation of the value calculated from this method is, so an uncertainty of 10% is assumed.

Initial Saturation

The initial saturation of the brick is calculated to be 0.56 from the initial moisture content of 0.168 given by Chen and Pei. This calculation requires a value of porosity, which Chen and Pei give as 0.435. Assume that this porosity has an uncertainty of 0.03, which is the calculated uncertainty of the CFB porosity. This translates into an uncertainty of 6.5% of the calculated uncertainty for the saturation. The depth of the brick slab also has an uncertainty, which is assumed to be 0.001m. If the initial moisture content is calculated using a volume measurement of the brick, then this

uncertainty introduces another 2%. Given these values, assume that the total uncertainty of the initial saturation is no more than 10%.

Length

As mentioned, the length of the sample and the initial saturation are linked. The uncertainty of the depth of the sample is assumed to be 0.001, which is assumed to be a reasonable uncertainty associated with length measurements. Increasing the length decreases the initial saturation value, so the low value of sample length will be used with the high case.

Liquid Relative Permeability Coefficient

The liquid relative permeability is assumed to obey the same fourth order function of saturation as sandstone. Many correlations have been obtained for other materials that obey third order power functions of saturation, so the uncertainty of the liquid relative permeability coefficient is assumed to be ± 1. It can be seen in the sensitivity analysis that increasing the liquid relative permeability coefficient increases the surface temperature.

H.5. Wood Drying

Parameters with a sensitivity coefficient greater than 0.1 were chosen for the uncertainty analysis of brick drying. The parameters and their associated uncertainties are shown in .

Table 54 – Uncertainty of Input Parameters for Wood Drying

Parameter	Base Value	Max Uncertainty	1 Std Dev
Ambient Temp	40°C	$\pm 2^{o} C$	$\pm 0.66^{o} C$
Initial Saturation	0.99	± 0.02	± 0.0066
Heat Trans Coeff	$92.5 W / m^2 K$	$\pm 15 W / m^2 K$	$\pm 5 W / m^2 K$
Initial Temp	10°C	$\pm 2^{o} C$	$\pm 0.66^{o} C$
Length	0.019m	± 0.01	± 0.0033
Density	1500	± 675	± 225

The results of adjusting each parameter in Table 54 by plus (+) and minus (-) one standard deviation on the temperature and sample are shown in Figure 397 and Figure 398.

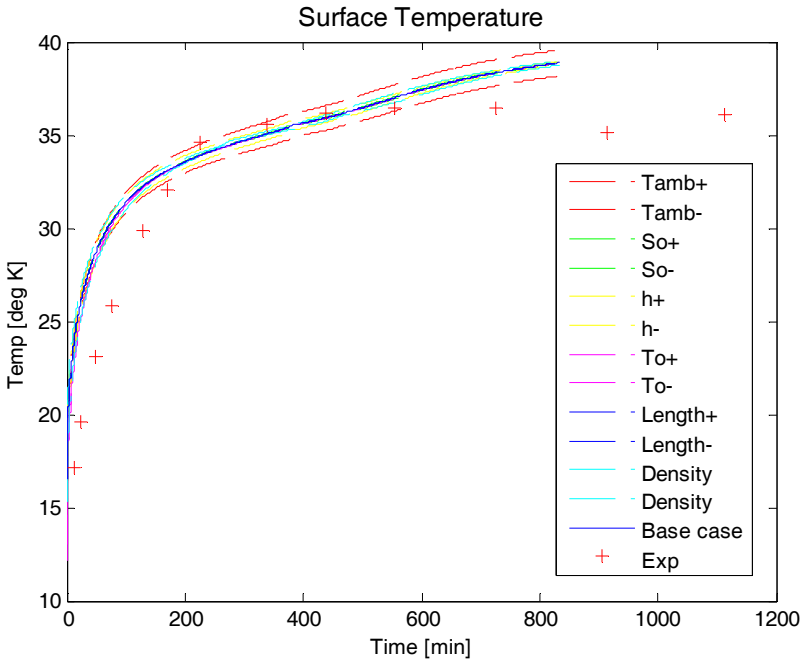

Figure 397 – Effect of Adjusting Input Parameters on Surface Temperature During Convective Drying of Wood

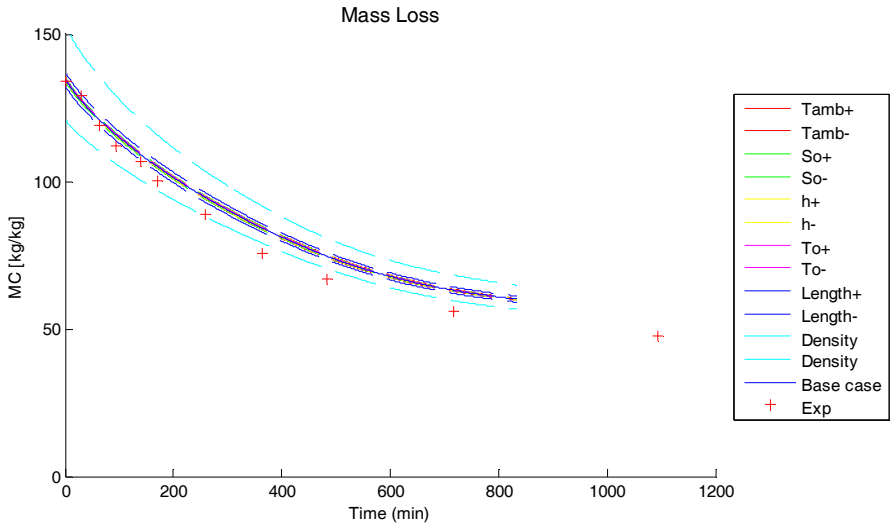

Figure 398 – Effect of Adjusting Input Parameters on Sample Mass During Convective Drying of Wood

The combined standard uncertainty of the temperature and sample mass were calculated from these results and are shown in Figure 394 and Figure 395.

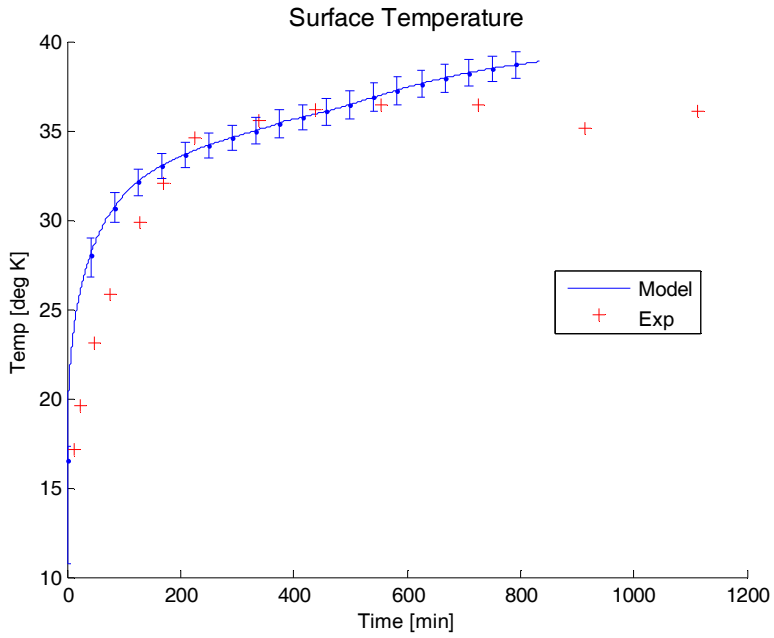

Figure 399 – Combined Standard Uncertainty of Surface Temperature During Convective Drying of Wood

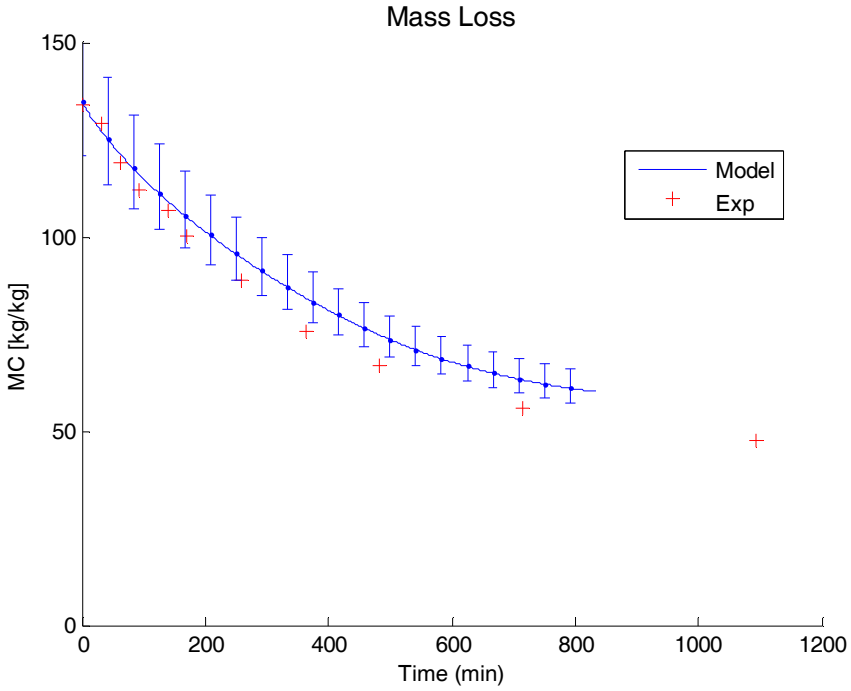

Figure 400 – Combined Standard Uncertainty of Sample Mass During Convective Drying of Wood

Ambient and Initial Temp

The ambient and initial temperature were measured using thermocouples, and therefore assumed to have an uncertainty of $\pm 2^{o}C$.

Heat Transfer Coefficient

The heat transfer coefficient was calculated from the Dittus and Boelter correlation for heat transfer in a duct, using the geometry of the heating apparatus. The details of the experiments are given by Plumb et al. [56]. The exact velocity for the test is not given, just an indication that it was at the upper end of the range of velocities used for a series of tests. If the uncertainty of the velocity is assumed to be $\pm 5m/s$ $(\sim 20\%)$ then the heat transfer coefficient that is calculated will vary by $\pm 15\%$.

Initial Saturation

The wood samples were stored underwater up until right before the test began [55]. The saturation is assumed to be 0.99. Assume that the uncertainty of the initial saturation ranges from 1 (maximum theoretically possible), to 0.97 which is considered a reasonable lower bound for a sample of wet wood stored underwater.

Density

The density of wood was taken as the value of 1500 given by Siau [60]. This represents only the density of the solid wood fibers. The average density of several wood species is given in [57]. The values given have a standard deviation of approximately 15%. The maximum uncertainty was taken to be three times this value.

Length

The wood that was used for the drying test was a standard piece of green 2"×4" lumber that is 17.7" long. When lumber is planed to smooth the surfaces, ¼" is removed from each surface. This produces a board that is 1.5"×3.5" or 0.038m× 0.089m. The model treats this as a one dimensional material with a thickness of 0.019m with a line of symmetry (no-flux conditions) at the back face. The total thickness is assumed to have an uncertainty of 0.002m, which translates unto an uncertainty of 0.001 for the model.

H.6. CFB Heating

Parameters with a sensitivity coefficient greater than 0.5 were chosen for the uncertainty analysis of the CFB heating cases. These parameters and their uncertainties are shown in Table 55.

Table 55 – Uncertainty of Input Parameters for CFB Heating Tests

Parameter	Base Value	Max Uncertainty	+1 Std Dev
Initial Saturation	Test 1 - 0.3 Test 2 - 0.5 Test 3 - 0.7	± 0.043 ± 0.070 ± 0.099	± 0.0143 ± 0.0233 ± 0.033
Radiant Heat Flux	20kW/m^2	± 21kW/m^2	± 0.333 kW/m^2
Surface Emissivity	0.96	± 0.02	± 0.00667
Length	0.0254m	± 0.00151m	± 0.000503
S_{ir}	0.15	± 0.015	± 0.005
Porosity	0.8	± 0.85	± 0.0167
Liq. Rel. Perm. Coeff	3	± 1	± 0.333

The results of adjusting these parameters by plus (+) and minus (-) one standard deviation are shown in Figure 401 through Figure 409.

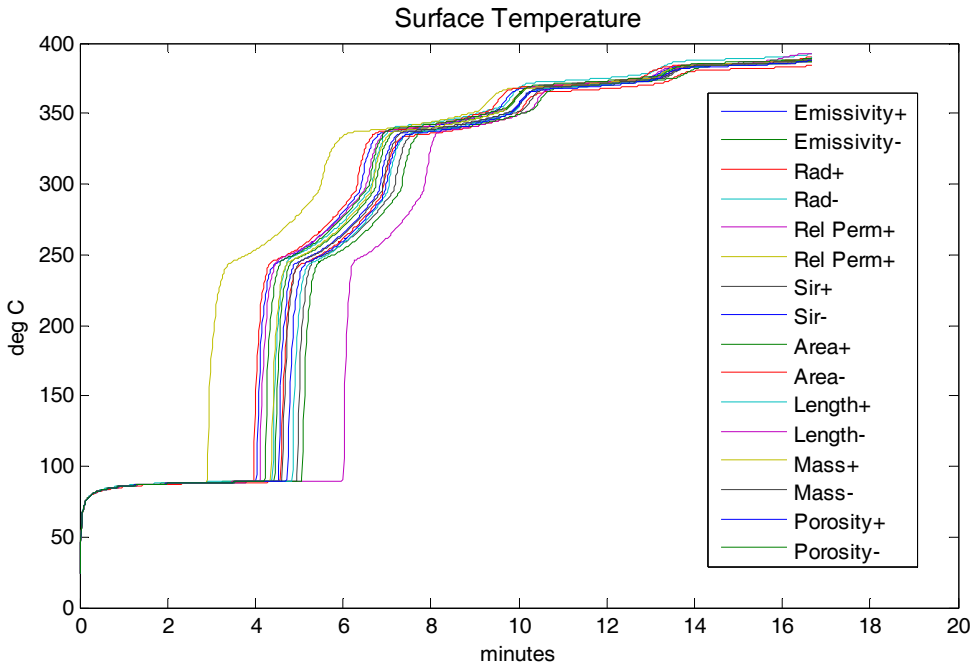

Figure 401 – Results of Adjusting Input Parameters - So=0.3 – Surface Temperature

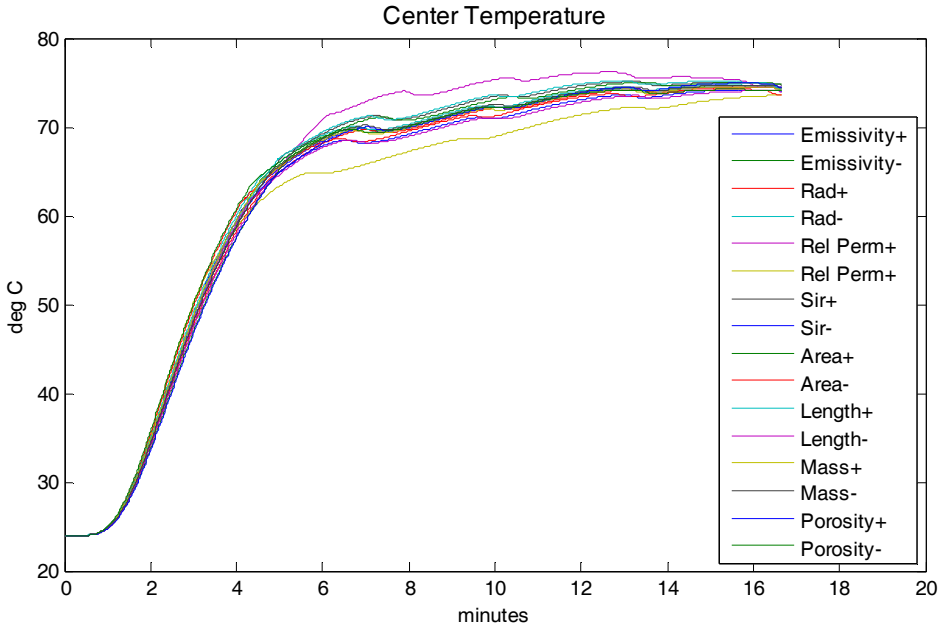

Figure 402 – Results of Adjusting Input Parameters - So=0.3 – Center Temperature

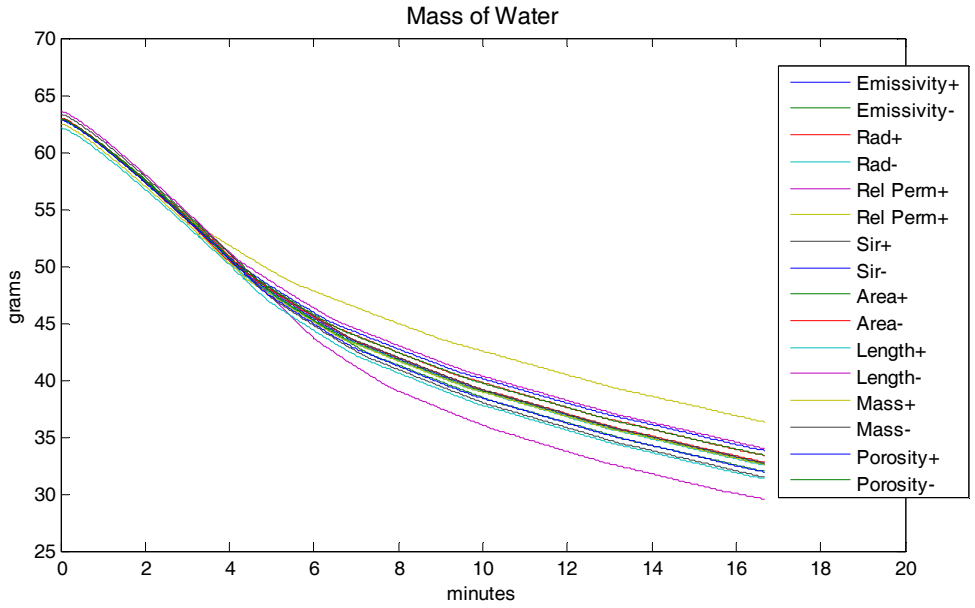

Figure 403 – Results of Adjusting Input Parameters - So=0.3 – Water Mass

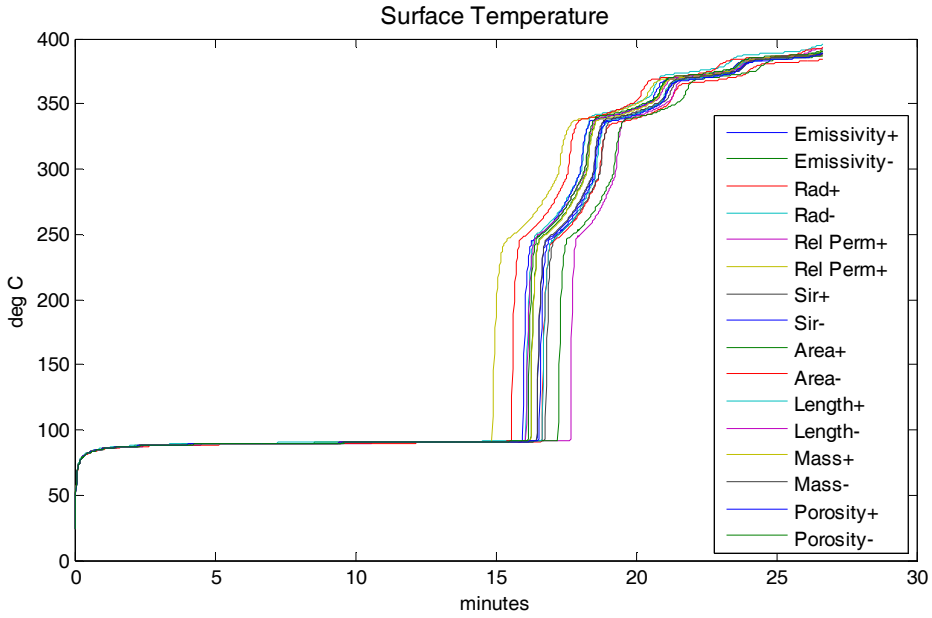

Figure 404 – Results of Adjusting Input Parameters - So=0.5 – Surface Temperature

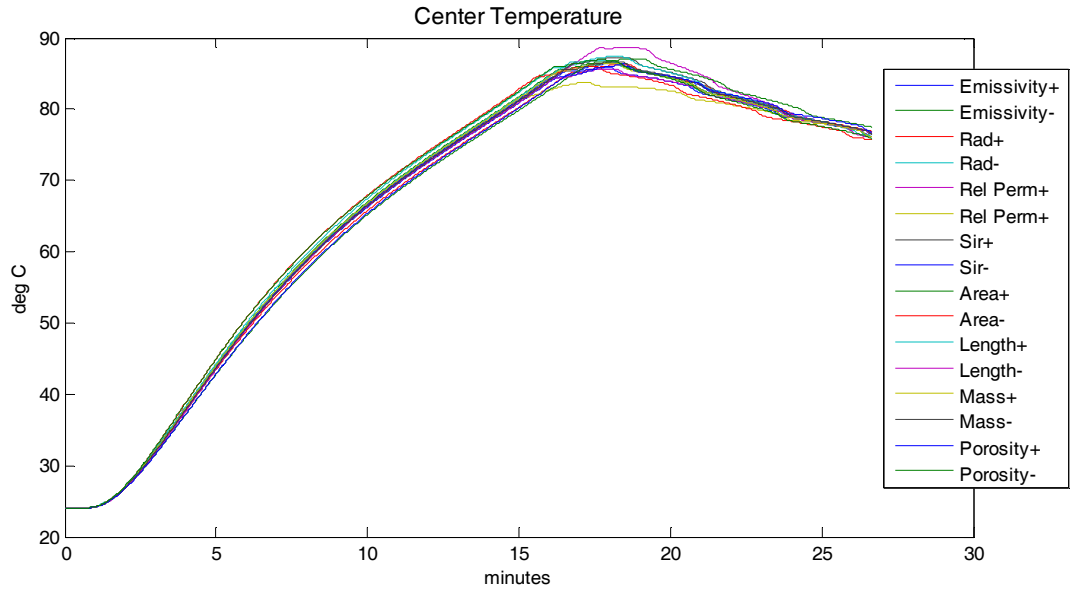

Figure 405 – Results of Adjusting Input Parameters - So=0.5 – Center Temperature

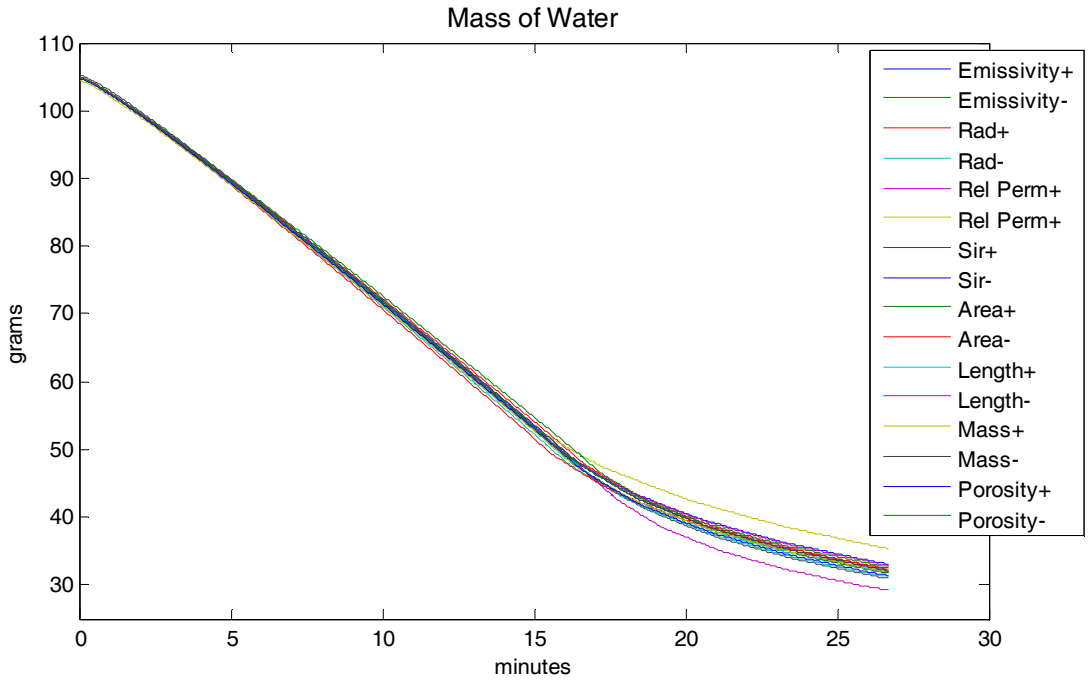

Figure 406 – Results of Adjusting Input Parameters - So=0.5 – Mass Loss

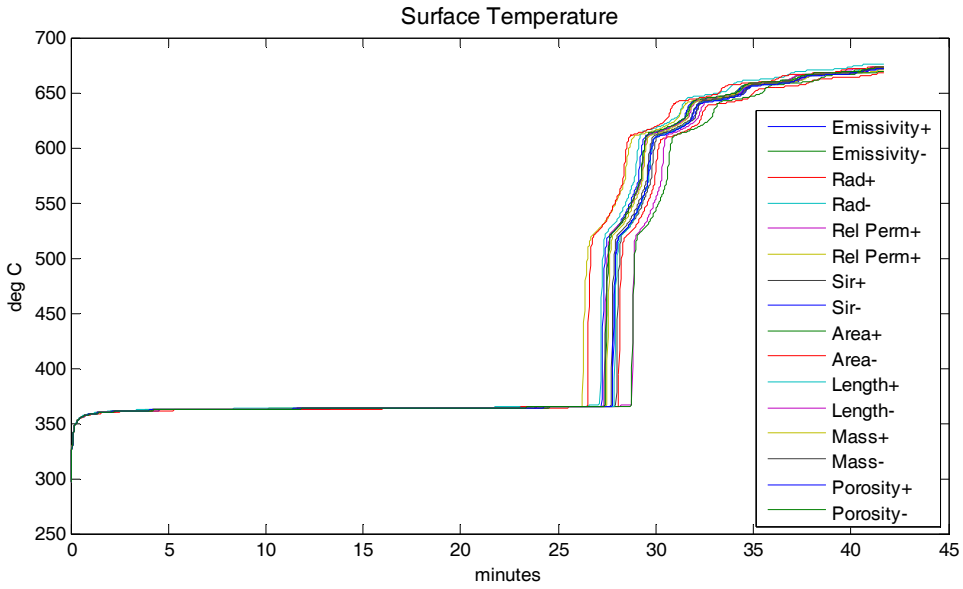

Figure 407 – Results of Adjusting Input Parameters - So=0.7 – Surface Temperature

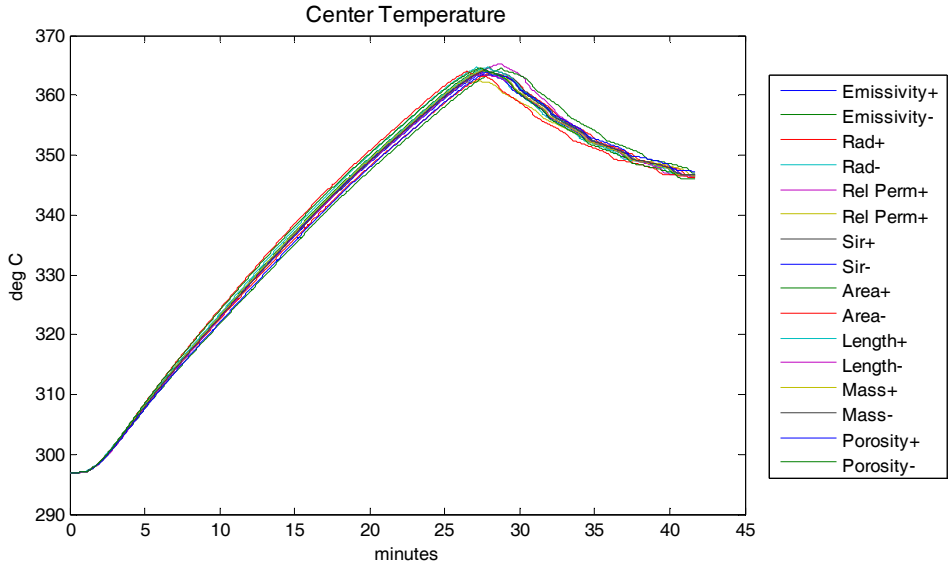

Figure 408 – Results of Adjusting Input Parameters - So=0.7 – Center Temperature

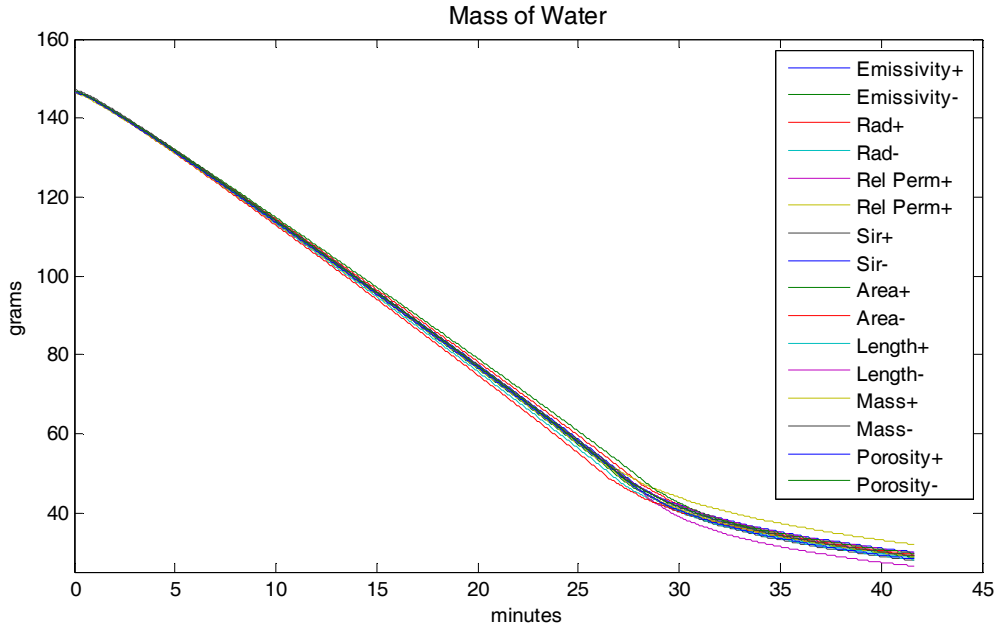

Figure 409 – Results of Adjusting Input Parameters - So=0.7 – Water Mass

These results were used to calculate the combined standard uncertainty. The surface temperature displayed a dramatic vertical jump when the surface dried out, making the calculation of temperature uncertainty problematic. For the temperature, the uncertainty in time was calculated in the horizontal (time) direction for discrete temperature values. This method is better suited to convey the uncertainty in "jump time". For the center temperature and water mass, the vertical uncertainty was calculated. The combined standard uncertainty for the radiant heating of CFB is shown in Figure 410 through Figure 418.

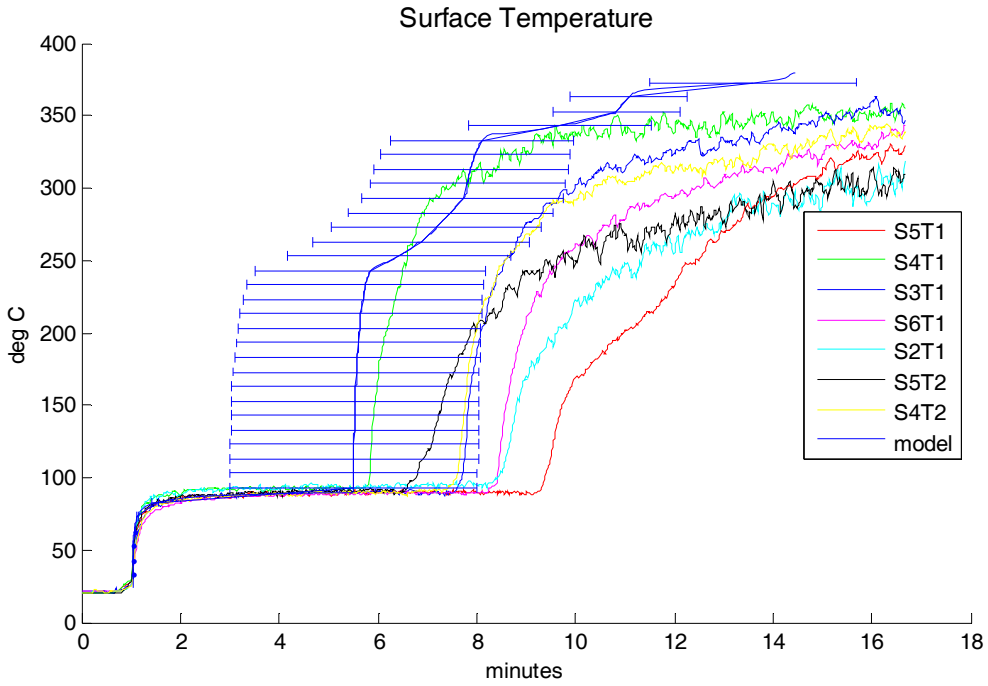

Figure 410 – Combined Standard Uncertainty of Surface Temperature for Radiant Heating of CFB – So = 0.3

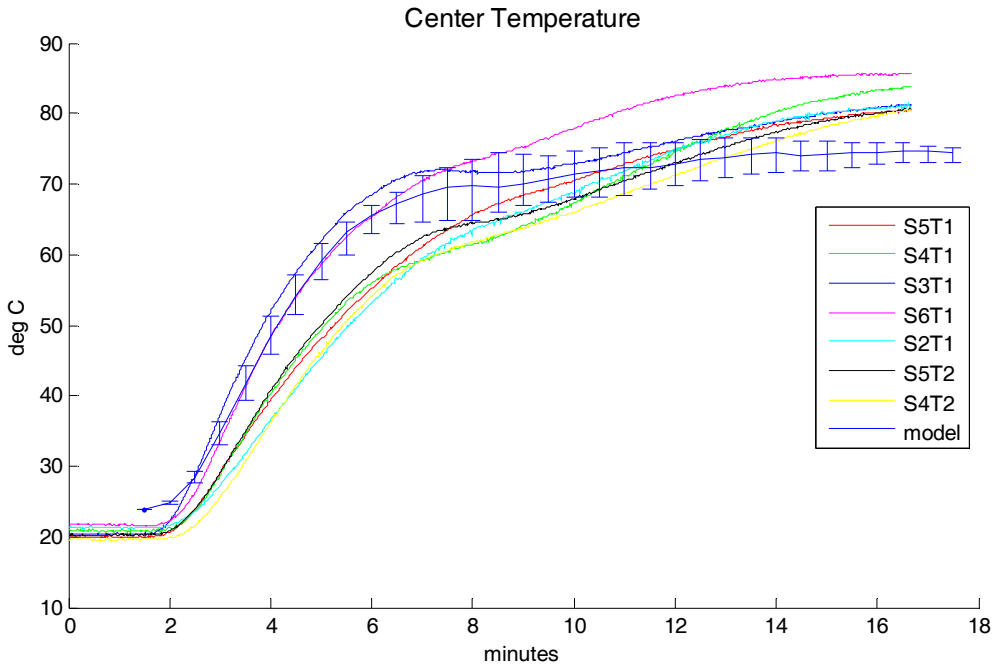

Figure 411 - Combined Standard Uncertainty of Center Temperature for Radiant Heating of CFB – So = 0.3

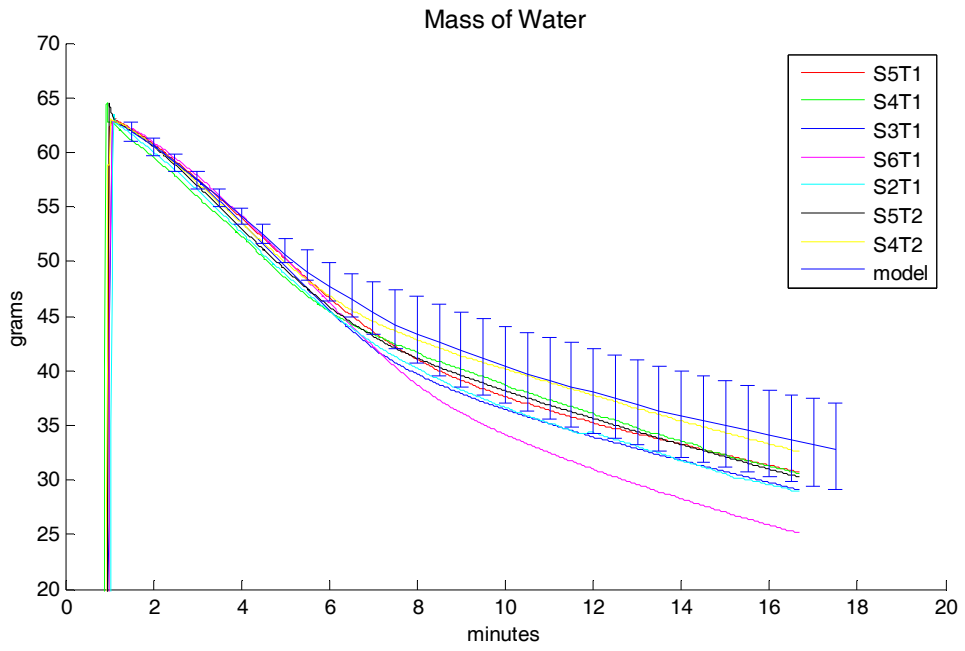

Figure 412 - Combined Standard Uncertainty of Water Mass for Radiant Heating of CFB – So = 0.3

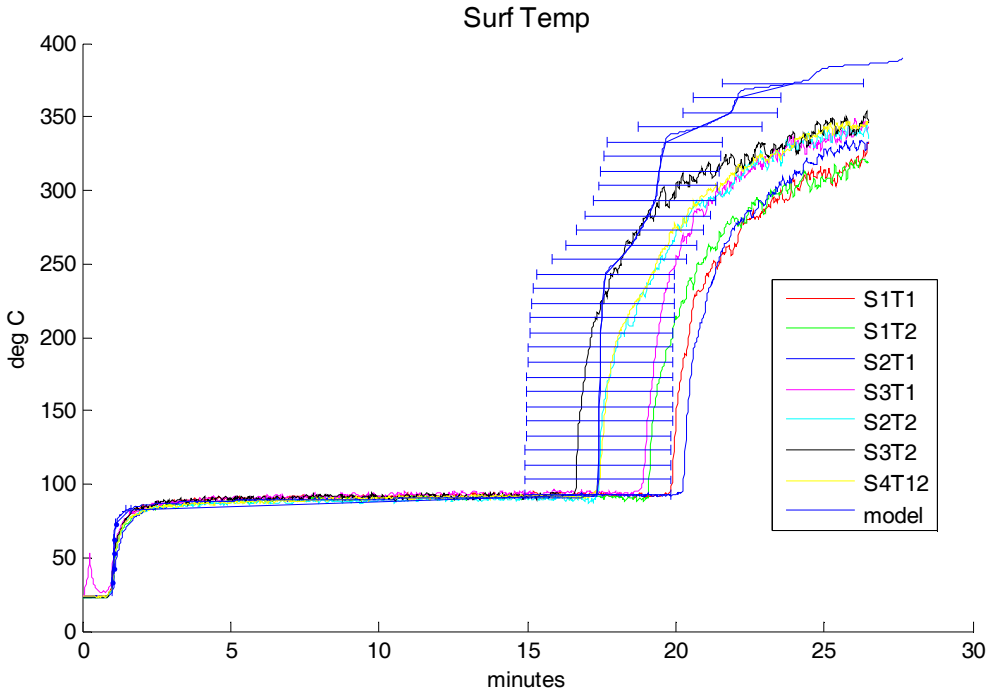

Figure 413 - Combined Standard Uncertainty of Surface Temperature for Radiant Heating of CFB – So = 0.5

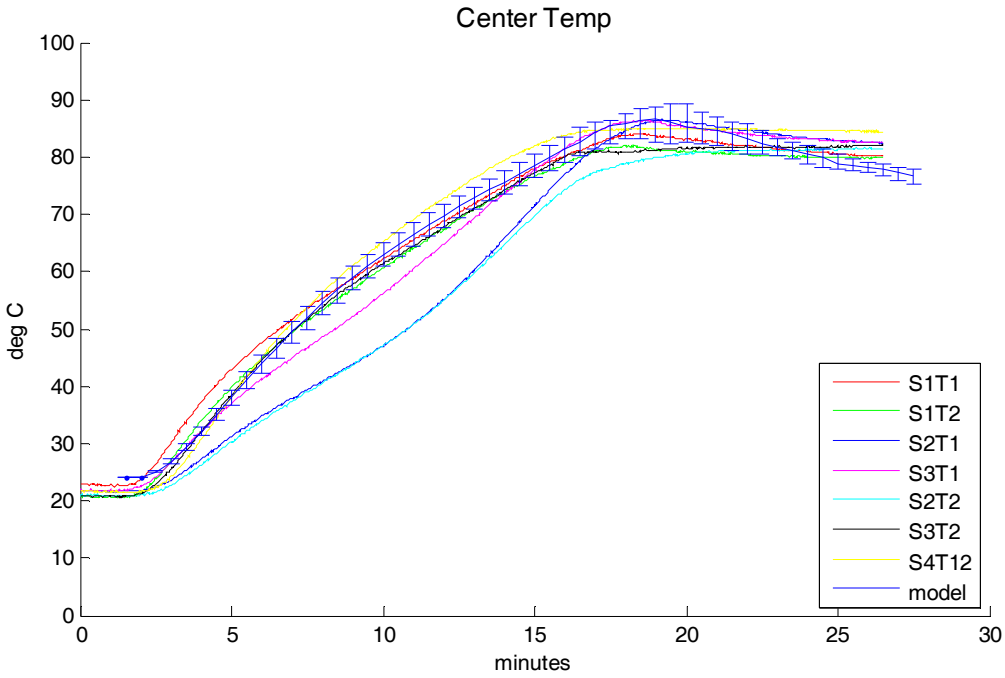

Figure 414 - Combined Standard Uncertainty of Center Temperature for Radiant Heating of CFB – So = 0.5

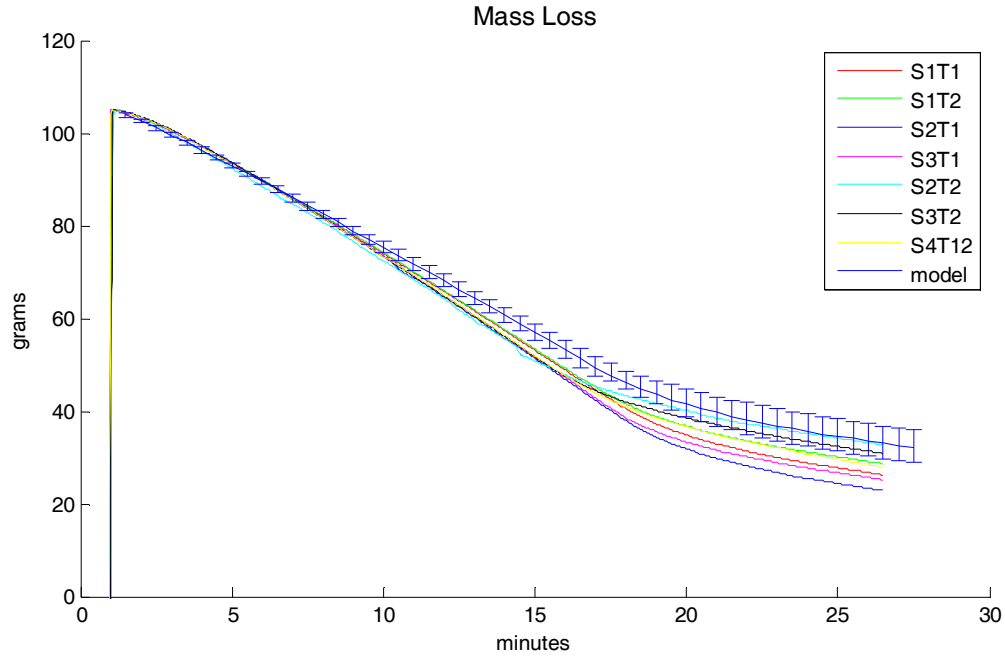

Figure 415 - Combined Standard Uncertainty of Water Mass for Radiant Heating of CFB – So = 0.5

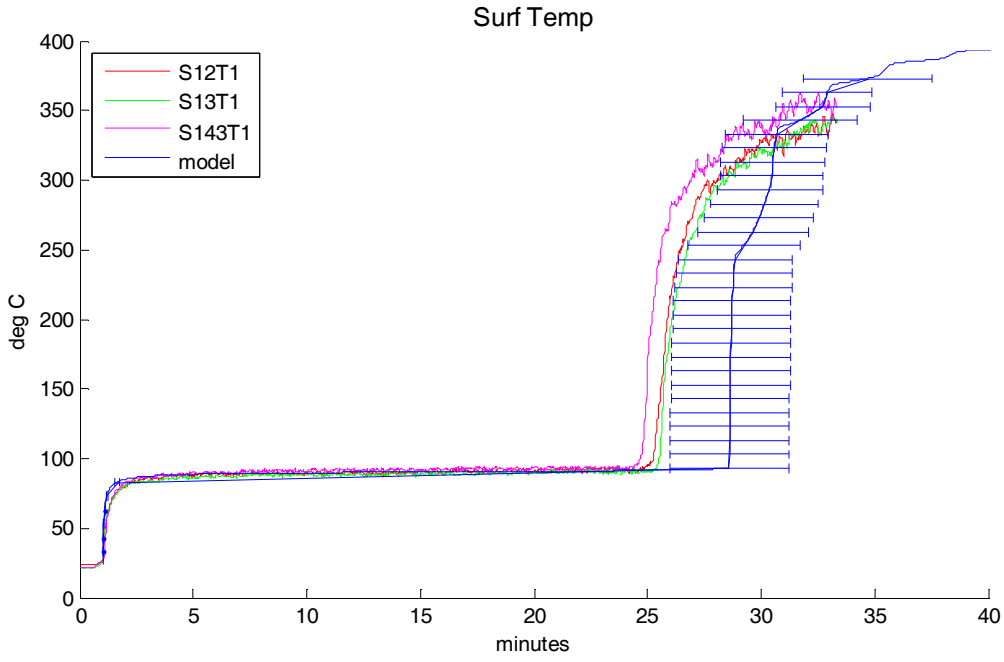

Figure 416 - Combined Standard Uncertainty of Surface Temperature for Radiant Heating of CFB – So = 0.7

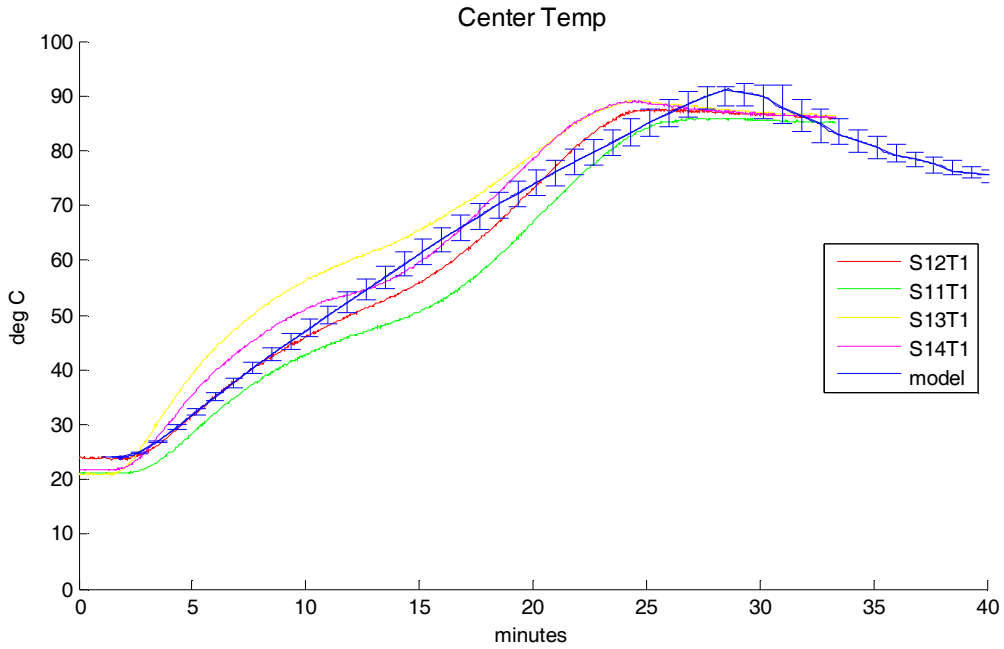

Figure 417 - Combined Standard Uncertainty of Center Temperature for Radiant Heating of CFB – So = 0.7

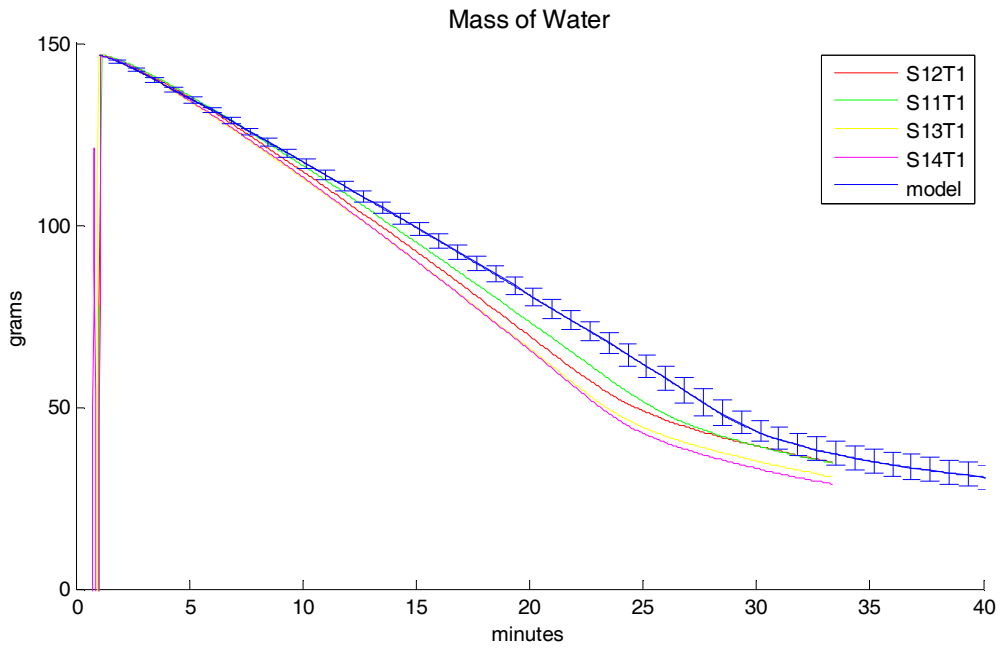

Figure 418 - Combined Standard Uncertainty of Mass for Radiant Heating of CFB – So = 0.7

Methods of Calculating the Uncertainty of Input Parameters

Initial Saturation

The saturation was determined by adding a known mass of water to the samples and assuming identical sized samples. The uncertainty of the water added was 0.5 grams, and the uncertainty of the volume was

Size of CFB Sample

$Length = 4" \pm 1/16" \ \ (0.1016m \pm 0.001588m)$

$Width = 4" \pm 1/16" \ \ (0.1016m \pm 0.001588m)$

$Depth = 1" \pm 1/32" \ \ (0.0254m \pm 0.000794m)$

This combines to give upper and lower uncertainty bounds of the initial saturation. For example the upper bound of initial saturation uncertainty was calculated by assuming that the sample size and porosity was at the lower end of its uncertainty range, and the mass of water added was at the upper end of its uncertainty range.

$$S_o = \frac{V_{water}}{V_{void}} = \frac{105.3 \dfrac{kg}{1000g} \dfrac{m^3}{1000kg}}{(0.75)0.000246m^3} = \frac{0.0001053m^3}{0.0001846m^3} = 0.570$$

By adjusting the mass of water and volume uncertainties in the opposite directions, the lower bound of saturation uncertainty was calculated

$$S_o = \frac{V_{water}}{V_{void}} = \frac{104.3 \dfrac{kg}{1000g} \dfrac{m^3}{1000kg}}{(0.85)0.000279m^3} = \frac{0.0001043m^3}{0.0002372m^3} = 0.440$$

The uncertainty for this case is assumed to be the higher value of 0.07. Using this method, the upper and lower bounds for the other two cases were estimated. From the sensitivity analysis, it can be seen that increasing the initial saturation increases the jump time.

Radiant Heat Flux

The radiant heat flux was controlled by adjusting the temperature of the conical heating element in the cone calorimeter. The value of the heat flux was checked with a calibrated water cooled Schmidt Boelter heat flux gauge. There are uncertainties in the actual radiant heat flux that reaches the sample surface introduced by the uncertainty in the water cooled gauge, the variation in cone temperature over time, and the distance between the cone heater and sample surface. The measured heat flux was observed to oscillate slightly as the electric cone heater relay turned on and off. By moving the heat

flux gauge slightly up and down the variation with distance to the heater could also be observed. This total uncertainty was estimated to be ± 1 kW/m^2. From the sensitivity analysis it can be seen that increasing the incident heat flux decreases the jump time.

Surface Emissivity

The surface emissivity was assumed to be the same as that of asbestos board, which Luikov gives as 0.96. Based on the range of values given by Luikov, the uncertainty of this value was estimated to be 0.02. From the sensitivity analysis it can be seen that increasing the surface emissivity decreases the jump time.

Sample Depth

The CFB samples were all nominally 1" thick, but did exhibit small variation in their thickness. From measuring several samples the uncertainty in their thickness was estimated to be 1/32" or 7.9E-4 m. Since the sample depth uncertainty was used to determine the initial saturation uncertainty, these two parameters are linked. When the initial saturation is adjusted, the sample depth will be adjusted to reflect the calculation of initial saturation. When initial saturation is increased, sample depth is decreased.

Irreducible Saturation

The irreducible saturation is the saturation at which the water in the pores is non-interconnected and water cannot flow. This value was estimated from capillary rise tests using stacks of CFB. From these tests the uncertainty of the irreducible saturation was estimated to be 0.015. From the sensitivity analysis it can be seen that increasing the irreducible saturation decreases the jump time.

Porosity

The porosity of the CFB was determined to be 0.8 by conducting experiments where the maximum amount of water absorbed into a sample was weighed. As discussed previously, the uncertainty of this value is estimated to be 0.05. The uncertainty of the porosity was used for the calculation of the initial saturation, so these parameters are linked. When the initial saturation is increased, the porosity is decreased.

Liquid Relative Permeability

The liquid relative permeability was estimated to be a cubic function of the effective saturation, which is the relation that is observed experimentally in beds of sand, glass spheres, and slabs of sandstone. As discussed previously, the uncertainty of the power

of the correlation was estimated to be ±1. From the sensitivity analysis it can be seen that increasing the power of the correlation decreases the jump time.

Initial and Ambient Temperature

The initial and ambient temperature in the laboratory was estimated to be 24 ±2 deg C. The temperature in the WPI fire science laboratory does not deviate significantly from 24 deg C, but there is some uncertainty associated with any measurement made using a thermocouple, and the samples were sometimes observed to be slightly above or below this value. From the sensitivity analysis it can be seen that increasing the initial and ambient temperatures decreases the jump time.

Mass Transfer Coefficient

The mass transfer coefficient is calculated from a correlation using a Grashof number that accounts for driving forces arising from thermal diffusion effects as well as species diffusion effects. The value that is calculated as a function of the surface temperature does not account for the effect of the ring of insulation that surrounds the sample, or any induced flow patterns arising from the presence of the cone heater above the sample. The effects of phenomena are difficult to estimate, so an uncertainty of 10% is assumed for the mass transfer coefficient. From the sensitivity analysis it can be seen that increasing the mass transfer coefficient decreases the jump time.

Capillary Pressure

The capillary pressure correlation is a function of saturation that was determined from capillary rise tests using stacks of CFB. The correlation is a curve fit to the data points obtained from experiments, and there is some uncertainty associated with the shape and magnitude of the curve. This uncertainty is assumed to be 5% of the value calculated from the correlation. From the sensitivity analysis it can be seen that increasing the capillary pressure increases the jump time.

Complete Bibliography

1. di Marzo, M., and Evans, D., *Dropwise evaporative cooling of high thermal conductivity materials.* Heat and Technology, 1987. **5**(1-2): p. 29-40.
2. di Marzo, M., and Evans, D.,, *Evaporation of a water droplet deposited on a high thermal conductivity surface.* Trans. ASME, J. of Heat Transfer, 1989. **111**: p. 210-213.
3. di Marzo, M., Liao, P., Tartarini, Y., Evans. D., and Baum, H., *Dropwise evaporative cooling of a low thermal conductivity solid*, in *Fire Safety Science – Proceedings of the Third International Symposium*. 1991, International Association of Fire Safety Science. p. 987-996.
4. di Marzo, M., Tartarini, P., Liao, Y., Evans. D., and Baum, H., *Evaporative cooling due to a gently deposited droplet.* International Journal of Heat and Mass Transfer, 1993. **36**(17): p. 4133-4139.
5. Tartarini, P., and di Marzo, M., *The solid-liquid interfacial conditions for dropwise evaporative cooling.* Heat and Technology, 1992. **10**(3-4): p. 57-71.
6. White, G., Tinker, S., di Marzo, M.,. *Modelling of dropwise evaporative cooling on a semi-infinite solid subjected to radiant heat input*. in *Fire Safety Science – Proceedings of the Fourth International Symposium*. 1994.
7. Chandra, S., di Marzo, M., Qiau, Y. M., and Tartarini, P., *Effect of liquid-solid angle on droplet evaporation.* Fire Safety Journal, 1996. **27**(2): p. 141-158.
8. di Marzo, M., *Dropwise evaporative cooling*, in *National Heat Transfer Conference*. 1995: Bologna Italy.
9. Pasandideh-Fard, M., Chandra, S, and Mostaghimi, J., *A three-dimensional model of droplet impact and solidification* International Journal of Heat and Mass Transfer, 2002. **45**(11): p. 2229-2242.
10. Abu-Zaid, M., and Atreya, A., *Transient cooling of hot porous and non-porous ceramic solids.* Transactions of the ASME, 1994. **116**.
11. di Marzo, M., Kidder, C. H., and Tartarini, P., *Infrared thermography of dropwise evaporative cooling of a semiinfinite solid subjected to radiant heat input.* Experimental Heat Transfer, 1992. **5**: p. 101-114.
12. Tartarini, P., Liao, Y., and di Marzo, M., *Transient cooling of a hot surface by droplets evaporation*, in *NIST Interagency Report*. 1993.
13. Tartarini, P., and di Marzo, M. *Evaporative cooling in radiative field*. in *Proceedings of the 10th International Heat Transfer Conference*. 1994.
14. Abu-Zaid, M., *Droplet evaporation on porous and non-porous ceramic solids*

heated from top. Heat and Mass Transfer, 2002. **38**: p. 203-211.

15. Klassen, M., diMarzo M., and Sirkis, J., *Infrared thermography of dropwise evaporative cooling.* Experimental Thermal and Fluid Science, 1992. **5**: p. 136-141.
16. Dawson, H., and di Marzo, M., *An Experimental Study of Multiple Droplet Evaporative Cooling*, in *NIST Interagency Report*. 1993.
17. di Marzo, M., and Tinker, S., *Evaporative cooling due to a sparse spray.* Fire Safety Journal, 1996. **27**(4): p. 289-303.
18. Milke, J.A., Tinker, S. C., and di Marzo, M., *Effect of Dissolved Gases on Spray Evaporative Cooling With Water.* Fire Technology, 1997. **33**(2).
19. Toda, S., *A study of mist cooling – Thermal behaviors of liquid films formed from mist drops on a heated surface at high temperatures and high heat fluxes*, in *Technology Reports*. 1971, Tohoku University.
20. Bonacina, C., Del Giudice, S., and Comini, G., *Dropwise Evaporation.* Journal of Heat Transfer, 1979. **101**: p. 441-446.
21. Bolle, L., and Moreau, J. C. , *Spray cooling of hot surfaces.* Multiphase Science and Technology, 1982.
22. Yu, H.Z., and Jayaweera, Tina, *Water Absorption in Horizontal Corrugated Board Under Water Sprays*, in *FM Global Technical Report*. 2004: Norwood MA.
23. Kaviany, M., *Principles of Heat Transfer in Porous Media*. 2nd ed. 1995, New York: Springer-Verlag.
24. Dullien, F.A.L., *Porous Media - Fluid Transport and Pore Structure*. 1992, San Diego CA: Academic Press.
25. Scheidegger, A., *The Physics of Flow Through Porous Media*. 3rd ed. 1974: University of Toronto Press.
26. Bear, J., *Dynamics of Fluids in Porous Media*. Dover Publications Inc. 1972, New York.
27. Philip, J.R., *The theory of infiltration: 1. The infiltration equation and it's solution.* Soil Science, 1957. **83**: p. 345-357.
28. Philip, J.R., *The theory of infiltration: 2. The profile at infinity.* Soil Science, 1957. **83**: p. 435-448.
29. Philip, J.R., *The theory of infiltration: 3. Moisture profiles and relation to experiment.* Soil Science, 1957. **84**: p. 163-178.
30. Philip, J.R., *The theory of infiltration: 4. Sorptivity and algebraic infiltration equations.* Soil Science, 1957. **84**: p. 257-264.

31. Philip, J.R., *The theory of infiltration: 5. The influence of initial moisture content.* Soil Science, 1957. **84**: p. 329-339.
32. Philip, J.R., *The theory of infiltration: 6. The effect of water depth over soil.* Soil Science, 1958. **85**: p. 345-357.
33. Philip, J.R., *Theory of infiltration.* Advances in Hydroscience, 1969. **5**: p. 215-296.
34. Philip, J.R., and De Vries, D. A., *Moisture movement in porous materials under temperature gradients.* Transactions of the American Geophysical Union, 1958. **38**(2).
35. De Vries, D.A., *Simultaneous transfer of heat and moisture in porous media.* Transactions of the American Geophysical Union, 1958. **39**(5).
36. Whitaker, S., *Heat, mass, and momentum transfer in porous media: A theory of drying*. Advances in Heat Transfer. Vol. 13. 1977: Academic Press.
37. Luikov, A.V., *Systems of differential equations of heat and mass transfer in capillary porous bodies,.* International Journal of Heat and Mass Transfer, 1975. **18**: p. 1-13.
38. Nasrallah, B.S., and Perre, P., *Detailed study of a model of heat and mass transfer during convective drying of porous media.* International Journal of Heat and Mass Transfer, 1988. **31**(5): p. 957-967.
39. Chen, P., and Pei, David C. T., *A Mathematical Model of Drying Processes.* International Journal of Heat and Mass Transfer, 1989. **32**(2): p. 297-310.
40. Ilic, M., and Turner, I. W., *Convective Drying of a Consolidated Slab of Wet Porous Material.* International Journal of Heat and Mass Transfer, 1989. **32**(12): p. 2351-2362.
41. Ni, H., *Multiphase Moisture Transport in Porous Media Under Intensive Microwave Heating*, in *Department of Agricultual and Biological Engineering*. 1997, Cornell University: Cornell NY.
42. Luikov, A.V., *Heat and Mass Transfer in Capillary-Porous Bodies*. 1966, Oxford: Pergammon Press.
43. Bejan, A., *Heat Transfer*. 1993, New York: John Wiley and Sons, Inc.
44. Leverett, M.C., *Capillary behavior in porous solids.* Transactions of the AIME, 1941. **142**: p. 159-172.
45. Spolek, G.A., and Plumb, O. A., *Capillary Pressure in Softwoods.* Wood Science Technology, 1981. **15**: p. 189-199.
46. Baver, L.D., Gardner W. R., and Gardner, W. H. , *Soil Physics*. 4th ed. 1972, New York: John Wiley and Sons, Inc.

47. Moran, M.J., and Shapiro, Howard N., *Fundamentals of Engineering Thermodynamics*. 2000, New York: John Wiley and Sons, Inc. .
48. Haertling, M., *Prediction of Drying Rates*, in *Drying '80*, A.S. Mujumdar, Editor. 1980, Hemisphere. p. 88-98.
49. Ames, W.F., *Numerical Methods for Partial Differential Equations*. 2nd ed. 1977, New York: Academic Press.
50. Saltelli, A., Chan., K., Scott., E. M., *Sensitivity Analysis*. 2000, New York: John Wiley and Sons, Inc. .
51. Institute, A.N.S., *U.S. Guide to the Uncertainty in Measurement*. 1997, Boulder CO: NCSL International.
52. Youngs, E.G., *Moisture profiles during vertical infiltration.* Soil Science, 1957. **84**: p. 283-290.
53. Lu, T., Jiang, P., Shen, S., *Numerical and experimental investigation of convective drying in unsaturated porous media with bound water.* Heat and Mass Transfer, 2005. **41**: p. 1103-1111.
54. Przesmyki, Z., and Strumillo, C., *The mathematical modeling of drying process based on moisture transfer mechanism*, in *Drying '85*, R. Toei, and Mujumdar, A. S., Editor. 1985, Hemisphere: Washington DC. p. 126-134.
55. Plumb, O.A., Brown, C. A., and Olmstead B. A., *Experimental measurements of heat and mass transfer during convective drying of southern pine.* Wood Science Technology, 1984. **18**: p. 187-204.
56. Plumb, O.A., Spolek, G. A., and Olmstead, B. A., *Heat and mass transfer in wood during drying.* International Journal of Heat and Mass Transfer, 1985. **28**(9): p. 1669-1678.
57. DiNenno, P.J., *SFPE Handbook of Fire Protection Engineering*. 3rd ed. 2002, Quincy MA: National Fire Protection Association.
58. Sipe, J., *A Porous Media Model for Sprinkler Wetting*, in *Department of Fire Protection Engineering*. 2010, Worcester Polytechnic Institute: Worcester, MA.
59. Comstock, G.L., *Directional permeability of softwoods.* Wood Fiber, 1970. **1**: p. 283-289.
60. Siau, J.F., *Flow in Wood*. 1971, New York: Syracuse University Press.
61. Spolek, G.A., *A Model of Simultaneous Convective, Diffusive, and Capillary Heat and Mass Transport in Drying Wood*. 1981, Washington State University.
62. Luikov, A.V., *Heat and Mass Transfer in Capillary Porous Bodies*. 1961, London: Pergamon Press.
63. Gebhart, B., Jaluria, Yogesh, Mahajan, Roop. L. and Sammakia, Baghat,

Buoyancy Induced Flows and Transport. 1988: Hemisphere Publishing Corporation.

64. Frank, J.A., *Characteristics and Hazards of Water and Water Additives for Fire Suppression*, in *NFPA Fire Protection Handbook*, A.E. Cote, Editor. 2003, NFPA: Quincy MA.
65. Zalosh, R.G., *Industrial Fire Protection*. 2003, New York: John Wiley and Sons.
66. Chandra, S., and Avedisian, C. T., *Observations of droplet impingement on a ceramic porous surface.* International Journal of Heat and Mass Transfer, 1992. **35**(10): p. 2377-2388.
67. Purtorti, A.D., *Flammable and Combustible Liquid Spill/Burn Patterns*. 2001, Department of Justice: Washington DC.
68. Flynn, D.R., *Response of High Performance Concrete to Fire Conditions: Review of Thermal Property Data and Measurement Techniques*. 1998, NIST Interagency Report.
69. Buchanan, A., *Structural Design for Fire Safety*. 2001, New York: John Wiley and Sons, Inc.
70. Torvi, D., *Heat Transfer in Thin Fibrous Materials Under High Heat Flux Conditions*. 1997, University of Alberta.
71. Gibson, P., *Equations for Multiphase Heat and Mass Transfer in Hygroscopic Porous Media with Applications to Clothing Materials*, in *Navy Report*. 1994: Natick MA.
72. Datta, A.K., and Zhang, J., *Some considerations in modeling of moisture transport in heating of hygroscopic materials.* Drying Technology, 2004. **22**(8): p. 1983-2008.
73. Panton, R., *Incompressible Flow*. 2005, New York: John Wiley and Sons, Inc.
74. Hirschfelder, J.O., Curtiss, C. F., and Bird, R. B., *Molecular Theory of Gases and Liquids*. 1954, New York: John Wiley and Sons, Inc.
75. Williams, F., *Combustion Theory – The Fundamental Theory of Chemically Reacting Flows*. 2nd ed. 1985, Redwood City CA: Addison Wesley.
76. Grew, K.E., and Ibbs, T. L., *Thermal Diffusion in Gases*. 1952: Cambridge University Press.
77. Eckert, E.R.G., *Analysis of Heat and Mass Transfer*. 1972: McGraw Hill.
78. Bird, B.R., Stewart, Warren, E., and Lightfood, Edwin N., *Transport Phenomena*. 2nd ed. 2002, New York: John Wiley and Sons, Inc.
79. Kuo, K., *Principles of Combustion*. 2nd ed. 2005, New York: John Wiley and Sons, Inc.

80. Turns, S., *An Introduction to Combustion*. 2nd ed. 2000, Boston MA: McGraw Hill.
81. Happel, J., and Brenner, H., *Low Reynolds Number Hydrodynamics*. 1986: Martinus Hijhoff Publishers.
82. Rumpf, H., and Gupte, A. R., *Einfusse und Korngrossenverteilung in Wiederstandesetz der Porenstromung.* Chemie Ingenieur Technik, 1971. **43**: p. 367-375.
83. Geankoplis, C.J., *Transport Processes and Unit Operations*. 1978, Boston MA: Allyn and Bacon Inc.
84. Carbonell, R.G., and Whitaker, S., *Fundamentals of Transport in Porous Media*. 1984: Martinus Nijhoff Publishers.
85. Reid, R.C., Prausnitz, J.M., Poling, B.E., *The Properties of gases and Liquids*. 1987, Boston MA: McGraw Hill.
86. Whitaker, S., *Heat and Mass Transfer in Granular Porous Media*, in *Advances in Drying*, A.S. Mujumdar, Editor. 1980, Hemisphere.
87. Slattery, J.C., *Momentum, Energy, and Mass Transfer in Continua*. 1981, Huntington NY: Robert E. Krieger Publishing Company.
88. Whitaker, S., *Fundamental Principles of Heat Transfer*. 1977, Elmsford NY: Pergamon Press.
89. Fox, A.F., and McDonald, Alan T., *Introduction to Fluid Mechanics*. 5th ed. 1998: John Wiley and Sons, Inc.
90. Bristow, J.A., *Paper Structure and Properties*. 1986, New York: Marcel Dekker.
91. Bussmann, M., Chandra, S., and Mostaghimi, J., *Modeling the splash of a droplet impacting on a solid surface.* Physics of fluids, 2000. **12**(12): p. 3121-3132.
92. Huang, C., Bradford, J. M., and Cushman, J. H., *A numerical study of raindrop impact phenomena: The rigid case.* Soil Science Society of America, 1982. **46**(1): p. 14-19.
93. Yarin, A.L., *Impact Dynamics: Splashing, Spreading, Receeding, Bouncing….* Annual Review of Fluid Mechanics, 2006. **38**: p. 159-192.
94. Worthington, A.M., *A Study of Splashes*. 1908, London: Longmans, Green, and Co.
95. Edgarton, H., *Stopping Time: The Photographs of Harold Edgarton*, ed. G. Kayafas. 1987: Harry N. Abrams.
96. Chang, W.-J., and Hills, David J., *Sprinkler droplet effects on infiltration.* Journal of Drainage Engineering, 1993. **119**(1): p. 142-156.

97. Reis, N.C., Griffiths, Richard F., and Santos, Jane M.,, *Numerical simulation of the impact of liquid droplets on porous surfaces.* Journal of Computational Physics, 2004. **198**: p. 747-770.
98. *Approval Standard for Suppression Mode [Early Suppression – Fast Response (ESFR)] Automatic Sprinklers*. Class Series 2008. 2006: FM Approvals LLC.
99. *UL 1767 - UL Standard for Safety for Early-Suppression Fast-Response*. 3rd ed. 2005, Northbrook IL: Underwriters Laboratories Inc.
100. Yuan, S.W., *Foundations of Fluid Mechanics*. 1967, Englewood Cliffs NJ: Prentice Hall.
101. *NFPA 13 - Standard for the Installation of Automatic Sprinkler Systems*. 2002, Quincy MA: NFPA.
102. Siegal, R., and Howell, John R., *Thermal Radiation Heat Transfer*. 2002, New York: Taylor and Francis.
103. Pinkley, L.W., Sethna, P.P. and Williams, D., *Optical constants of water in the infrared: Influence of temperature.* Journal of Optical Society of America 1977. **678**: p. 494-499.
104. Hale, G.M., and Querry, M.R., *Optical constants of water in the 200-nm to 200-µm wavelength region.* Applied Optics, 1973. **12**: p. 555-563.
105. Kondratyev, K.Y., *Radiation in the Atmosphere*. 1969, New York: Academic Press.
106. Ozisik, M.N., *Heat Conduction*. 1993, New York: John Wiley and Sons Inc.
107. Wei, C.K., Davis, H.T., Davis, E.A. and Gordon, J., *Heat and mass transfer in water-laden sandstone: convective heating.* A.I.Ch.E. Journal, 1985. **31**: p. 1338-1348.
108. Lautenberger, C.W., *A Generalized Pyrolysis Model for Combustible Solids*, in *Mechanical Engineering Department*. 2007, University of California at Berkeley: Berkeley CA.
109. Bird, B.R., Stewart, Warren, E., and Lightfood, Edwin N., *Transport Phenomena*. 1960, New York: John Wiley and Sons, Inc.
110. Meyer, R.W., *Influence of pit aspiration on earlywood permeability of douglas fir.* Wood Fiber, 1971. **2**: p. 328-339.